Caractérisation des oscillateurs spintroniques basés sur des couches magnétiques couplées

Elmer Monteblanco Vinces

UNIVERSITÉ DE GRENOBLE

THÈSE

Pour obtenir le grade de

DOCTEUR DE L'UNIVERSITÉ DE GRENOBLE

Spécialité : **Physique de la matière condensée**

Arrêté ministériel :

Présentée par

Elmer Monteblanco

Thèse dirigée par **Ursula Ebels**

préparée au sein **Spintec CEA/CNRS/UJF/G-INP**
et de **l'Ecole doctorale de physique de Grenoble**

Characterization of spintronic nano-oscillators (STNO) based on magnetic coupled multilayer

Thèse soutenue publiquement le **9 Julliet 2014**,
devant le jury composé de :

Monsieur, Alain Schuhl
Directeur Institut Néel, Président
Monsieur, Vincent Cros
Chercheur au Unité Mixte de Physique CNRS/Thales , Rapporteur
Monsieur, Matthieu Bailleul
Chercheur au IPCM Strasbourg, Rapporteur
Monsieur, Grégoire De Loubens
Chercheur au CEA-Saclay DSM/Iramis/SPEC/LNO, Examinateur
Monsieur, Michel Hehn
Chercheur Institut Lamour, Université Lorraine, Examinateur
Madame, Ursula Ebels
Ingénieur au CEA, Directrice de thése, Directeur de thèse
Madame, Daria Gusakova
Chercheur au CEA, Invité

Acknowledgment

This manuscript is also the result of the unconditional support given by especial people in Grenoble and Lima. I would like to gratefully and sincerely dedicate them some words. First of all, I would like to thank Viviana, my wife, for always have trusted in me, for all the support, encouragement and patience given. All the words you gave me in all those moments have given me the confidence and peacefulness to write these today. I love you. I want to thank to my family, my parents (Elmer, Rosa) and my brothers and sister (Jano, Ali, Gabo) for the faith in me, which allowed me to face important challenges and for given me their support in every moment.
My advisor and thesis supervisor, Ursula Ebels, I would like to say thank you for everything you have done for me. I will always remember that things have to be done well, and well means almost perfect. Thank you for the confidence and the opportunity in 2010, I will be a good scientist. Liliana Buda and Daria Gusakova,I feel very grateful with you both, and will never forget for your guidance, understanding and patience.
Felipe Garcia Sanchez (my boss), I do not lie when I say that you are the responsible of this thesis, without you this thesis would not exist, thank you very much your friendship and support at all the time. I am not going to forget the coffee after lunch and football and your most famous expression -No te preocupes, necesitamos de todo un poco-. In particular I would like to thank to the members of the Puya Raimondi for the support to Peruvian students in France. Mr. Robert, Alain, Frederic, Francois, merci beaucoup pour votre gentillesse et votre aide. Je suis heureux pour trouver des gens comme vous, it will be a pleasure to work towards the development of the science and technology in our country.
Williams Savero, we got Grenoble together and we leaved it almost together, thank you very much for been there in all the special moments of this adventure. Argel Estrada, thank you very much for all the support and positives words, I will visit you soon.
SPINTEC friends, my French family, I will always remember you smiling. Emilie and Sylvain, my first friends and office mates for over 3 years, thank for your love and for your great help. It would have been really complicate to be there without you, I will miss you a lot. The nanoscillator group, Juan, Abijhit, Alex (British), Marina (gracias por todas las conversaciones y la ayuda previa), Miguel (que majo eres), Karla (buena vida!!), Christophe (une cigarrette??), Anike and Jerome, thank you to share with me your experience and sorry for the 300 pages of this work. Thank you Maria Marins, and Lavitnia, for your help during the 2010-2011, thank you very much. Kamil, Bertran, Giovanni, Lara, Karol (I wait for you), Alex, Py, Selma,,,Thank you for been a really good guys, you are amazing people. I do not want to forget anybody, thank you very much.

Contents

Abstract

Spin-torque nano-oscillators (STNOs) are promising candidates for integrated radiofrequency (RF) components due to their nanoscale size, the large range of base frequencies that can be covered, as well as the large achievable tuning ranges around the base frequency. The RF signal is obtained due to the spin transfer torque (STT) generating a non-linear magnetization oscillation in a magnetoresistive device. In the past, these excitations were investigated using the picture of a single (or independent) layer. However, many features of the excitation spectra observed experimentally in nanopillar devices cannot be explained considering a single layer. In this thesis we address the important question on the dynamical coupling between the magnetic layers inside a magneto-resistive nanopillar device, to gain a better understanding of the excitation spectra, i.e. the dependence of the frequency and the linewidth on current and applied magnetic field.

A first study is realized for a coupled system, composed by two ferromagnetic layers, coupled by the interlayer RKKY coupling (so called Synthetic Ferrimagnet SyF). Due to the coupling the frequency dependence versus current is different as compared to excitations of a single layer. This is explained by the strong dynamical RKKY coupling. A second study considers a more complex interaction, occurring within standard STNO nanopillar spin valves or tunnel junctions. They are composed by a SyF separated by a metallic or insulating spacer respectively from the single free layer (FL). For this system we take into account besides the RKKY coupling within the SyF, also the dynamical dipolar field coupling and the mutual spin torque (MSTT) between the SyF and the free layer. We find two definite signatures arising from this coupling. The first is a gap in the steady state excitation spectra that is due to the hybridization of the SyF and FL modes in the damped regime. The second is the possibility of the spintorque driven excitation or its harmonics with the damped modes leading to discontinuities in the frequency field dependence when the free layer is dominantly excited. Interestingly this leads to a region of reduced linewidth. Furthermore for SyF layer dominated excitations, the linewidth is lower than in the FL dominated excitations. From these observations we propose a more complex structure, composed by two SyF layers where the single FL is replaced by a SyF.

The results obtained by a combination of experiments, numerical simulations and analytical analysis, demonstrate the important role of the dynamic interactions in nanopillar STNOs and provide routes for designing novel STNO configurations that should lead to improved microwave performances.

Spintronics

Devices based on magnetic materials have driven the development of technology in recent decades, it has occupied a privileged place in science in the past 20 years. To mention are magneto-resistive read heads used in data storage.

In 1991 the company IBM introduced the anisotropic magnetoresistance read heads (AMR) whose operation is based on a change in its resistance (anisotropic) in the presence of a magnetic field. These AMR read heads were much more sensitive than inductive read heads, allowing increased storage capacity of the hard drive. A few years earlier in 1988 and 1989 a new magneto-resistive effect was demonstrated: The giant magnetoresistance (GMR) given years earlier by Albert Fert [Baibich, 1988] and Peter Grümberg [Grünberg et al., 1986] that would lead them to win the Nobel in 2007. This marked a dramatic turning point in the research field and it generated a significant investment towards the integration of magnetic devices in everything related to computer systems and storage. This is one of the few cases in which a scientific breakthrough had a massive impact in technology, in less than a decade, showing its great potential in technological applications. With the discovery of the GMR a new branch of materials science started using magnetism. Based on the effects of electron spin interaction with its environment, called initially spin electronics or spintronics.

Despite the discovery of the GMR, there were certain disadvantages for technological application because for the first magneto-resistive materials used this effect was produced at high fields and the percentage change of resistance was small a room temperature. It was in 1990 that S. Parkin[Parkin et al., 1990] of IBM obtained a significant value of GMR at room temperature, making the spintronic technology a reality. Early, the first devices based on GMR were called spin valves (SV) [Dieny, 1991] in which a significant change of resistance were obtained near to zero magnetic field. IBM introduced it in 1997 as the disk read heads, allowing to read smaller magnetic bits. With the introduction of GMR read heads growth was achieved in the storage density of hard disks of 100 percent

per year (2.4 Gb / sq-inch in 1997 for 70 Gb / sq-inch in 2007).

Other important magneto-resistive devices in current technology are called magnetic tunnel junctions (MTJ). In these devices the magnetic layers are separated by a thin insulating barrier (AlO_3 or MgO) replacing the non-magnetic conductor. The electrons pass from one magnetic material to another by tunneling. Tunnel current is also dependent spin therefore the resistance of these devices (as well as spin valves) depends on the relative orientation of the magnetization of the magnetic layers, showing in general an increase from the parallel state into antiparallel. The change in resistance is known as tunneling magnetoresistance (TMR), and it is much greater than the GMR. It is currently used in the hard disk read heads and in the magnetic random access memories (MRAMs).

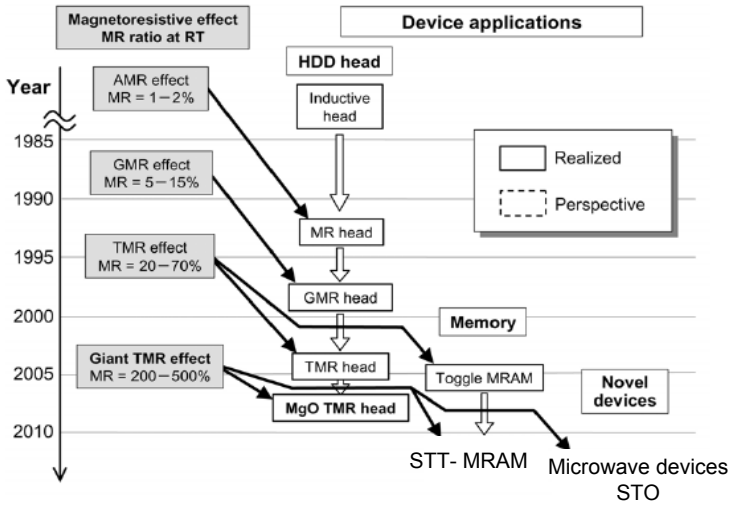

Figure 1 – Schematics of the history and prospects of storage devices, adapted from [Yuasa and Djayaprawira, 2007].

Currently one of the major branches of spintronics is based on the phenomenon of spin transfer torque (STT) predicted by J.C. Slonczewski [Slonczewski, 1996] and L. Berger [Berger, 1996]. The magnetoresistance corresponds to a control of the electronic current passing through of a device such as a SV or MTJ, changing the magnetic state of the structure. Using the STT it is possible to control the magnetization state of the device using a high current density. The STT phenomena, discussed in more detail in chapter 1, is based on the transfer of angular momentum from a spin polarized current to the local magnetization of a magnetic material. The STT has attracted much interest due to technological potential derived from the possibility of reversing the magnetization, generating radio frequency (RF) signals (auto-oscillations) of moving domain walls by applying current.

This thesis is focused on the RF properties induced by STT on a spintronic device, *the spin torque nano-oscillator* (STO). In the last years different STO structures based

on spin valves (SV) [Houssameddine et al., 2010] or magnetic tunnel junctions (MTJ) [Houssameddine et al., 2008], [Houssameddine, 2009], [Cornelissen et al., 2009] were studied in nano-pillars. These devices have shown interesting features such as the current and magnetic field tuning (≈GHz) and narrow linewidth (≈10MHz) at room temperature. However the small power of the STO devices (≈pW for SV and ≈nW for MTJ structures) is a disadvantage of these new devices. The different numerical simulations and experimental studies in STO will be presented as follow:

Part I give us an introduction to this thesis work. Chapter 1 will provide to the reader the concepts to understand the different electronic transport effects, such as the giant and tunnel magnetoresistance and the spin polarized transport. Chapter 2 presents the current context of this thesis work with the most important results to be taking into account during the discussion of our work. In chapter 3, the formalism to the magnetization dynamics and the numerical method used in the simulations will be shown. In the end of this chapter we show the experimental techniques and the characteristics of the STO devices.

Part II presents the numerical results of the thesis. First in chapter 4 we discuss the features of an isolated synthetic ferrimagnet (SyF) structure, taking into account parameters such as the RKKY coupling, the exchange bias field and also the asymmetry. In chapter 5 we will show the case of a standard STO, composed of a SyF and a single ferromagnetic layer. In this case the influence of the dipolar field between the layers in the magnetization dynamics will be studied.

Part III shows the experimental results of the thesis. First in chapter 6 the characterization of the standard STO devices based on spin valves or magnetic tunnel junctions structures is presented. In chapter 7 we show the results of a new structure proposed to improved the linewidth of the STO. This structure is composed by two SyF layers.

Part I

Introduction

Chapter 1

Spintronics - From Ferromagnetism to Spintronics

In this first chapter we will introduce the main concepts of magnetism and spintronics for an overall understanding of the spin torque nano-oscillators (STOs). We will start with the origin of ferromagnetism in materials composed by 3d elements. The concept of spin-polarized transport will be introduced in order to explain the giant magneto-resistance (GMR) and the tunnel magneto-resistance (TMR) effects, the first one discovered in 1988 by A. Fert [Baibich, 1988] and P. Grünberg [G. Binash, 1988] awarded with the Nobel Prize in 2007. Furthermore, the spin-transfer torque effect predicted by Slonczewski [Slonczewski, 1996] and Berger [Berger, 1996], will be introduced. This effect needs to be taken into account in the Landau-Lifshitz-Gilbert equation that describes the dynamics in a ferromagnetic layer. Finally, we will describe the basic features of the interlayer exchange interaction that is important in synthetic ferrimagnet (SyF) systems that are studied within in this thesis.

1.1 Magnetic order and Ferromagnetic materials

Materials can be classified into different groups, materials whose atoms (or ions) have a net magnetic moment equal to zero and materials with a finite net magnetic moment. This last group is divided into sub-groups, depending on the short range and long range magnetic order. Following the schematics of Fig. 1.1 one can see that materials without a net atomic moment belong to the group of diamagnetism. A property of this material

group is that in presence of an external applied field a magnetic moment is induced that opposes the applied field.

Materials with net atomic magnetic moments are called paramagnetic materials when the atomic magnetic moments are all randomly oriented leading to a total volume averaged zero magnetic moment. These materials show a net magnetic moment upon applying an external magnetic field orienting the moments into the direction of the applied field.

Materials with net atomic moments belong to the class of ferromagnetic materials when the atomic moments show a long range order with all moments aligned parallel, exhibiting thus a net spontaneous moment, even in absence of an applied magnetic field. In the case of the sub-group of ferrimagnetic materials, the local magnetic moments are aligned antiparallel (opposing ferromagnetic sub-lattices). When the moments of the different sublattices are unequal then there exists a finite volume averaged net magnetic moment. If the moments of the different sublattices have the same magnitude, the material will be called antiferromagnetic. The spintronics devices studied in this thesis are composed of metallic ferromagnetic and antiferromagnetic materials.

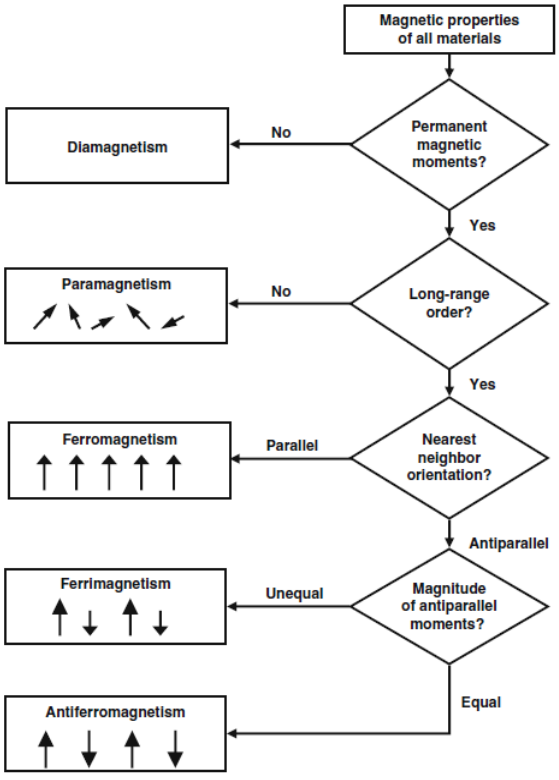

Figure 1.1 – Magnetic order of materials. Diamagnetims, Paramagnetism, Ferromagnetism, Ferrimagnetism and Antiferromagnetism. Adapted from [Stancil, 2009]

1.1.1 Ferromagnetism in matter

The main characteristic of ferromagnetic materials is its spontaneous magnetization in absence of an external applied field. In 1907 the ferromagnetism was explained by P. Weiss using the concept of molecular field (H_m) that would be responsible of the alignment between neighbouring magnetic moments. In 1928, Heisenberg proposed a short-range interaction between these moments to explain the origin of the ferromagnetism. He defined an exchange energy between the neighbour magnetic moments i and j as,

$$E_{ex} = -2J\mathbf{S}_i \cdot \mathbf{S}_j, \tag{1.1}$$

where J is a constant. Depending of the sign of J >0 (<0), the configuration of minimum energy corresponds to the parallel (antiparallel) alignment of the magnetic moments i and j. We have to remark that high temperature disturbs the established alignment, breaking the ferromagnetic order when its value overcomes the Curie temperature (T_C).

Ferromagnetism can be classically understood as a consequence of the Pauli exclusion principle (introduced in 1924) and electrostatic interactions. Electrons that are close to each other have higher electrostatic interaction and need to keep their spin antiparallel (Pauli). Electrons further apart (less electrostatic interaction) can have parallel spins. Hence there is a competition of energies that depends on the material properties (band structure). The minimisation leads to either an antiferromagnetic (AF) or a ferromagnetic (F) long range order of spins. For 3d transition metals it is the latter.

In ferromagnetic 3d transition metals (Fe, Co, and Ni) and its alloys the exchange interaction, responsible for ferromagnetism, leads to a splitting "Δ" (called exchange energy) between the two spin magnetic moment up and down bands. This splitting causes that the spin down electrons (spin magnetic moment[1] parallel to the magnetization) to have lower energy than the spin up electrons (spin magnetic moment antiparallel to the magnetization). The density of states, D(E), of spin up and down bands for a ferromagnetic material is presented schematically in Fig. 1.2.

From the schematic of D(E), it is expected that the *population* of electrons with spin magnetic moment up (denoted by $\uparrow$) to be higher than of the electrons with the magnetic moment down (denoted by $\downarrow$). They are therefore called majority and minority electrons

[1]Magnetic moment associated to the spin of the electron is defined as $\mathbf{m}_\mu = g_e\mu_B\mathbf{S}/\hbar$, where g_e=-2. It is opposite to the spin of electrons.

respectively.

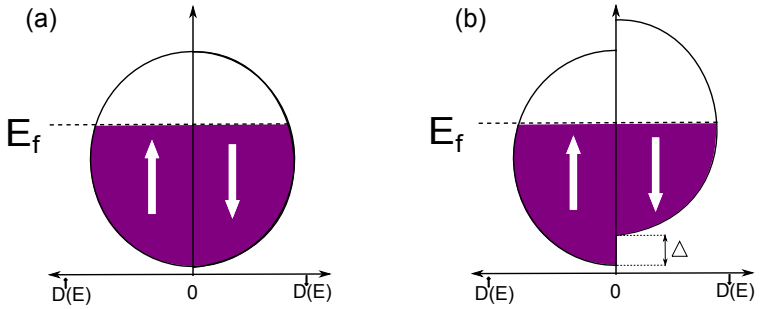

Figure 1.2 – (a)-(b) Schematic of the spin magnetic moment up and down bands as a function of the density of states, D(E), for a non magnetic (a) and a ferromagnetic material (b) respectively. Arrows correspond to the spin magnetic moment.

The number of electrons in each band can be calculated using the Fermi function, *f(E)*, and the density of states, D(E).

$$N_+ = \int_{-\infty}^{+\infty} D(E) f(E_f + \Delta) dE \tag{1.2}$$

$$N_- = \int_{-\infty}^{+\infty} D(E) f(E_f - \Delta) dE \tag{1.3}$$

The net magnetic moment or spontaneous magnetization induced by the splitting of bands in ferromagnetic materials is given by the difference between the number of electrons in the bands, defined as $\mathbf{m}=\mu_0(N_+\text{-}N_-)$[2].

1.2 Spin-polarized transport

In current technologies, the majority of circuits and devices are based on one property of electrons, the *charge*, and ignore another property, the *spin*. This quantum property, in non-magnetic metallic or semi-conducting materials, can be ignored because the number of electrons with spin up and down is the same (50% spin up and 50% spin down). In the case of electrons flowing in a ferromagnetic material this is different.

In order to describe a current flowing in a ferromagnetic material, one can use the two current model considering that both spin up and spin down electrons flow in different channels with different conductivities. This important concept was introduced by Mott

[2]The magnetization is a statistical average of the magnetic moments present in the ferromagnetic layer, defined as $\mathbf{M}=\mathbf{m}/\text{Volume}$, [A/m] or [emu/cm^3]

in 1936 and supported thirty years later by Campell and Fert. The total conductance of a metal is then described by the sum of the conductances of two channels, for majority ($G_\uparrow$) and minority ($G_\downarrow$) electrons,

$$G = G_\uparrow + G_\downarrow. \tag{1.4}$$

The difference in the conductance in both channels means that on average the flow of electrons of one type of spins is not equal to the flow of electrons of the other type of spins, resulting in a spin polarization, i.e. there will be more electrons on average with one type of spin than of the other type. This difference of conductance is explained as follows. The scattering of electrons depends on the number of states available into which to scatter. Due to the band splitting the density of states at the Fermi level are not equal for the spin up and down electrons. Spin up and spin down electrons will thus be scattered differently. In most metals the density of states of the spin down is higher, thus spin down electrons will be scattered more strongly and in consequence their conductance is less. This leads to a spin polarized current when passing a current through a ferromagnetic material, see Fig. 1.4 (a). In contrast, when a current passes through of a non-magnetic metal there will be the same scattering rate for both spins hence the current is unpolarized. This concept of *spin polarized current* is the basis of the development of most spintronics devices, such as magnetic random access memories (MRAMs) or spintronic nano-oscillators (STOs). These spintronics devices are multilayer materials made from magnetic and nonmagnetic thin layers that give rise to the giant and tunnelling magneto-resistance as explained in the next sections.

1.2.1 The Giant Magnetoresistance effect and the Spin Valve device

The giant magnetoresistance effect (GMR) was discovered in 1988 by A. Fert and Baibich [Baibich, 1988] and by P. Grünberg and Binash [G. Binash, 1988]. This effect is a pronounced change in the resistance of a multilayer structure upon sweeping an external magnetic field from positive to negative. A typical magneto-resistance curve of the experimental results of Baibich is shown in Fig. 1.3, in order to explain qualitatively the GMR effect.

This figure shows the change in the resistance as a function of an external magnetic field of a Fe/Cr multilayer at a temperature of 4.2K.

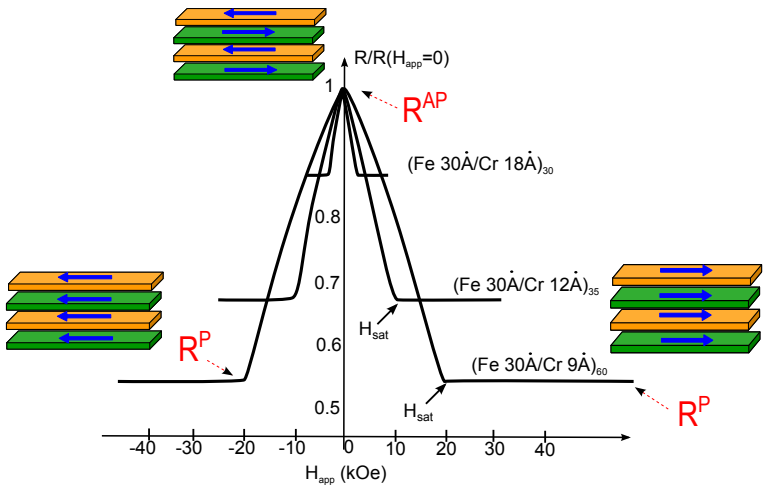

Figure 1.3 – Giant magnetorresistance effect (GMR), measured in multilayer Fe(001)/Cr(001) at 4.2K. The multilayer structure presents high and low resistance, R^{AP} and R^{P} respectively, depending of internal magnetic configuration (due to the external magnetic field value). Adapted from [Baibich, 1988].

For high magnetic fields (positive or negative) the resistance is a minimum, which corresponds to the parallel alignment of the magnetizations in all layers. This low resistance state is labelled as R^{P}. At zero applied field, all layers have an antiparallel magnetization generating a high resistance state which is labelled as R^{AP}. In order to quantify the GMR these two states of resistance must be compared. The GMR is defined by the following equation as,

$$GMR = \frac{R_{AP} - R_P}{R_P} \times 100\%. \tag{1.5}$$

In order to explain the GMR effect, the most basic GMR structure ($FM_1/NM/FM_2$[3]) in CPP configuration, is introduced in Fig. 1.4 (a) and (b). In the first case the magnetizations of both FM layers are oriented in the same direction, defined as the parallel state (P). In the second case both magnetizations remain in the antiparallel state (AP). The change from the parallel to the antiparallel state is generally reached upon varying an external magnetic field.

The explanation of the GMR is based on the spin polarized transport properties mentioned before. In Fig. 1.4 (a)-(b), electrons (↑) and (↓) are flowing into the GMR structure from the left to the right[4]. Each type of electron will use a different channel to pass through the GMR structure. In the parallel (P) configuration, electrons (↑) are majority electrons

[3]This CPP structure is composed by two ferromagnetic layers(FM) and a non-magnetic (NM) metallic layer.

[4]The sign (↑) and (↓) corresponds to the majority and minority electrons.

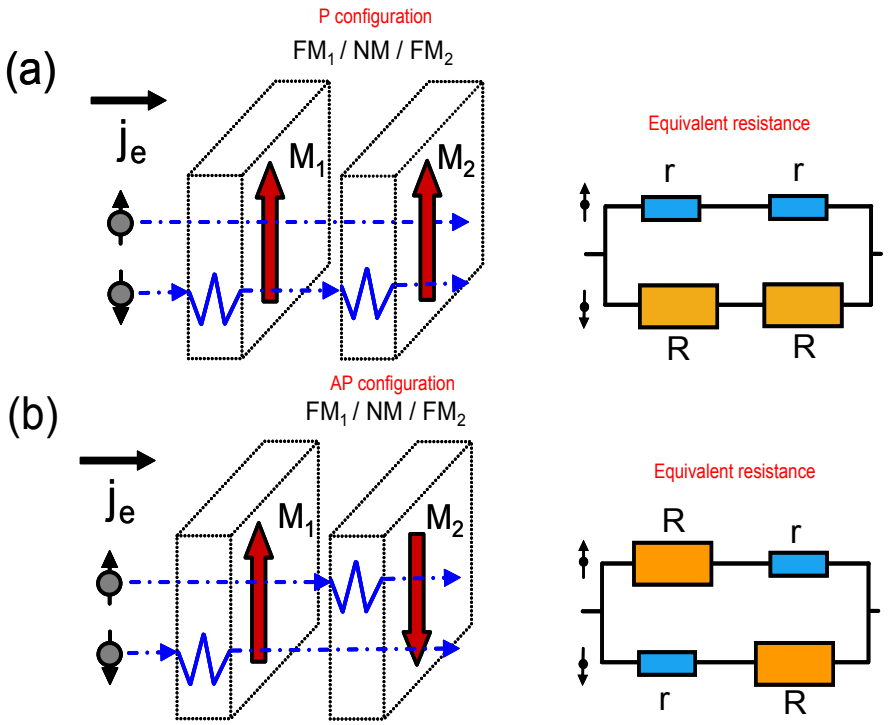

Figure 1.4 – (a)-(b) Schematics of the GMR effect on structure composed by two ferromagnetic (FM) layers separated by a non-magnetic (NM) layer ($FM_1/NM/FM_2$) for the anti-parallel and parallel configuration. Electrons (↑) and (↓) are shown coming from the left. An equivalent circuit is presented next to each case.

in the first and the second layer and thus suffer less scattering. This corresponds to a small resistance r. The other type of electrons, are minority in both layers and thus are more strongly scattered . This corresponds to a high resistance R. The resistance of the structure is represented in the equivalent circuit of the right side where r and R are small and high resistance respectively.

In the case of the antiparallel (AP) configuration, both types of electrons (↑,↓) will be majority in one layer (less scattering) and minority in the other layer (stronger scattering). The resistance of each type of electrons is thus the sum of high and low, yielding the corresponding equivalent circuit shown in Fig 1.4. The equivalent resistances for the P and AP configurations will be R_{AP}=(R+r)/2 and R_P= 2rR/(R+r) where the resistance of the AP state is higher that on P state.

The GMR effect finds its applications in a large variety of field sensor thanks to the revolutionary structure called spin valve (SV), proposed by B. Dieny in 1991 [Dieny, 1991]. The SV opened the possibility to develop the first spintronic device, the hard disk read-head, currently included in all computers. The SV device is composed of two ferromagnetic layers separated by a non-magnetic (NM) metallic material. One of the two FM layers is pinned in one direction by an exchange bias field ($\mathbf{H}_b$), due to the contact with an AF

layer. This FM pinned layer is called *reference layer* and the other one, which can turn into the direction of the applied field, is called the *free layer* (FL), see structures in Fig. 1.5 (a)-(b).

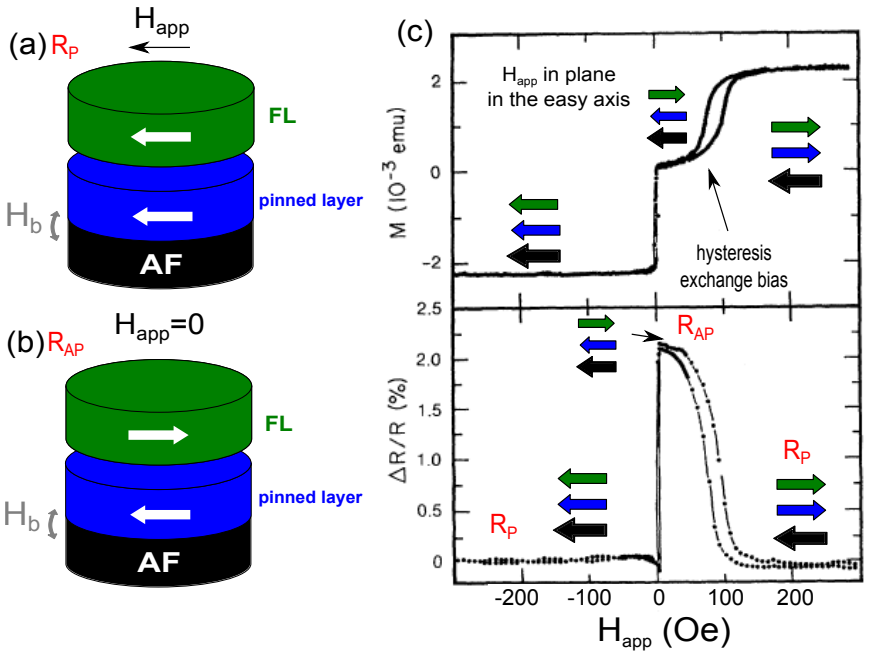

Figure 1.5 – (a)-(b) SV structure, composed by a pinned layer (blue) and a FL (green) which can change its sense following the sense of the applied field. (c) Hysteresis loop and the change on resistance for the spin valve structure, numbers in nanometers, Ag(2)/FeMn(10)/NiFe(15)/Cu(2.6)/NiFe(15)/Si, adapted of [Dieny, 1991]. Arrows represent the magnetization of each layer.

The hysteresis loop and the resistance versus applied field of a typical SV structure [Dieny, 1991] is presented in Fig. 1.5 (c) where it is possible to identify the two resistance states R^P and R^{AP}. In order to improve the SV performance, the structure has evolved into new types of structures. For instance, to reduce the stray field from the pinned layer to the FL and to obtain a more robust pinned layer, the pinned layer has been replaced by a synthetic ferrimagnetic layer (SyF). This is composed by two FM layers, the bottom layer (BL) and the top layer (TL), see Fig. 1.6. The structure and the general features of the SyF layer will be explained in detail in section 1.3.

1.2.2 The Tunnel magneto-resistance effect (TMR) and the Magnetic Tunnel Junction (MTJ)

In the previous section we introduced the GMR effect measured in SV structures, now we will introduce another effect, the spin-dependent electron tunnelling, measured in $FM_1/NM/FM_2$ structures where the non-magnetic material (NM) is an insulator (a tunnel

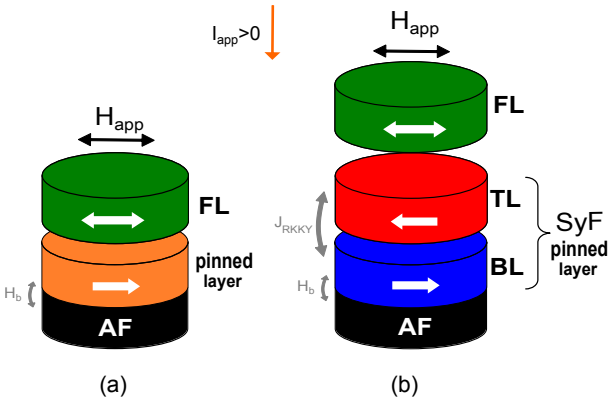

Figure 1.6 – (a) Most basic SV structure. (b) More complex and robust SV structure composed by a FL and a SyF pinned layer. The SyF layer is composed by a two FM layers, the bottom (BL) and the top (TL). Arrows represent the magnetization of each layer.

barrier). In these structures electrons from one electrode (FM_1) will reach (FM_2) by tunnelling through the insulator barrier. These structures are called magnetic tunnel junctions (MTJs).

The concept of tunnel transport or spin dependent tunnelling was introduced by Tedrow and Mersevey in 1971 [P. M. Tedrow, 1971] and four years later Julliere [Julliere, 1975] measured the tunnel magnetoresistance (TMR) in Fe-Ge-Pb and Fe-Ge-Co structures at 4.2K. A change in the resistance of 14% as a function of the external magnetic field was found by Julliere.

Julliere proposed a phenomenological model, where the spin is conserved during the tunnelling process. The electronic current will be proportional to the densities of states $D_1{}^{\uparrow}$ and $D_2{}^{\downarrow}$ at the Fermi energy (E_F) level of the electrodes FM_1 and FM_2, for the majority and minority electrons, see Fig. 1.7. The current through the tunnel barrier, on the P or AP state is given by the following equations,

$$J_P \propto D_1^{\uparrow} D_2^{\uparrow} + D_1^{\downarrow} D_2^{\downarrow}, \tag{1.6}$$

$$J_{AP} \propto D_1^{\uparrow} D_2^{\downarrow} + D_1^{\downarrow} D_2^{\uparrow}. \tag{1.7}$$

The schematics in Fig. 1.7, shows the density of states for a MTJ structure $FM_1/NM/FM_2$ in the parallel (P) and the antiparallel (AP) configuration. In the case of the P state, majority electrons tunnel from a higher $D_1^{\uparrow}$ in FM_1 and remain majority $D_2^{\uparrow}$ in FM_2 while the minority electrons tunnel between two lower density of state ($D_1^{\downarrow} \rightarrow D_2^{\downarrow}$) adding a small contribution of tunnel current. In this configuration, the current is dominated by

the majority electrons. In the AP state we can observe a mix. The majority electrons tunnel from a higher $D_1^{\uparrow}$ into lower $D_2^{\downarrow}$, while the minority electrons tunnel from lower $D_1^{\downarrow}$ to higher $D_2^{\uparrow}$. In this case the current is dominated by a mix of both type of electrons. Since Julliere proposed that the current is proportional to the density the states, equation 1.7, the AP state presents higher resistance than the P state.

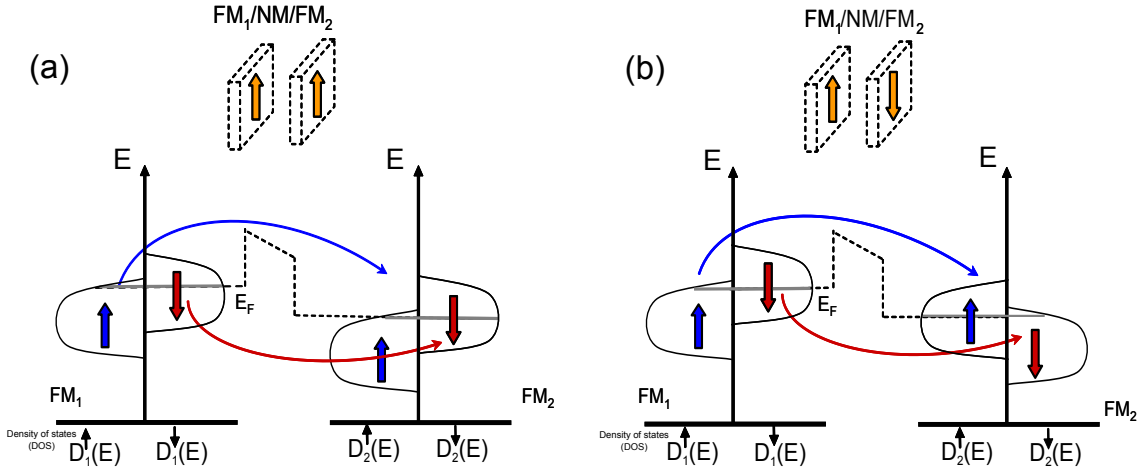

Figure 1.7 – Density of states, D(E), in a MTJ structure FM $_1$/NM/FM$_2$ in the P (a) and in AP configuration (b).

The tunnel magneto-resistance (TMR) can then be expressed as,

$$TMR = \frac{J_P - J_{AP}}{J_P} = \frac{2P_1P_2}{1 - P_1P_2}. \tag{1.8}$$

where $P_i = \frac{D_i^{\uparrow} - D_i^{\downarrow}}{D_i^{\uparrow} + D_i^{\downarrow}}$ is the spin polarization of a ferromagnetic electrode FM_i , i=1,2.

The improvement of deposition techniques since the first experience of Tedrow and Julliere, has allowed the fabrication of MTJ structures showing large TMR at room temperature. In 1995, Moodera [Moodera J. S., 1995] observed at room temperature (295 K) a TMR of 11.8% in MTJs of CoFe/Al_2O_3/Co (or NiFe) .

Yuasa presented in 2007 that the TMR effect in MgO-based MTJs is higher than the TMR using an amorphous Al-O barrier, [Yuasa and Djayaprawira, 2007]. This is due to the coherent tunnelling in the MgO_{001} as a difference with the amorphous Al-O barrier. Tunnelling in a MTJ structure with an amorphous Al-O barrier is illustrated schematically in Fig. 1.8 (a), where the top electrode is Fe(001). In this electrode, many Bloch states coexist with different symmetries of wave functions (Δ_1 for majority electrons, Δ_2 and Δ_5 for the minority electrons), due to the amorphous tunnel barrier, there is no crystallographic symmetry. Due to this non-symmetrical structure, Bloch states can

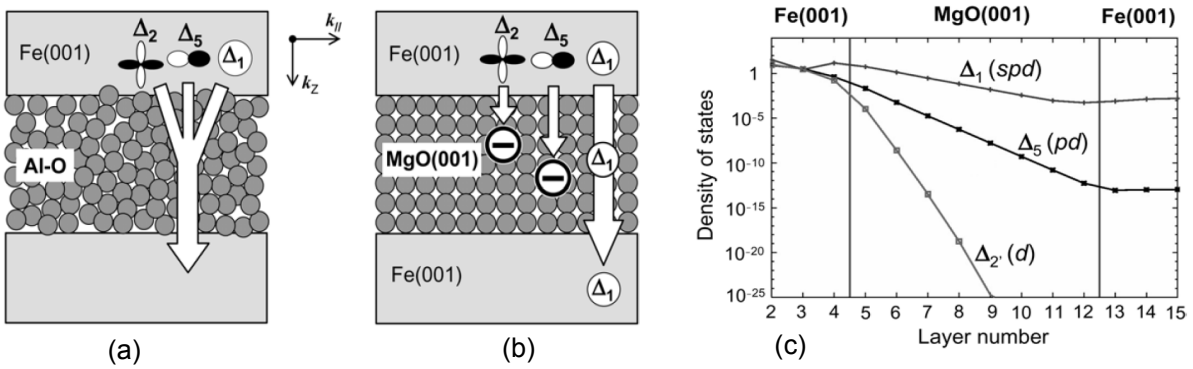

Figure 1.8 – Schematics of the electrons tunneling through (a) amorphous Al-O barrier and (b) crystalline Mg-O (001) barrier. (c) Evolution of the density of states as a function of the numbers of MgO layers. Adapted from Yuasa, [Yuasa and Djayaprawira, 2007]

couple with many different evanescent states in the tunnel barrier of amorphous Al-O and therefore have finite tunnelling probabilities. This tunnelling process is called incoherent tunnelling. In the case of the MgO, coherent tunnelling transport in epitaxial Fe(001)/MgO(001)/Fe(001) MTJ is illustrated schematically in Fig. 1.8 (b). For ideal coherent tunnelling, Fe Δ_1 states are theoretically expected to dominantly tunnel through the MgO(001) barrier. The discovery of a high TMR in MTJ due to MgO produced the reorientation of research towards the improvement in the MgO deposition with a good texture with adjacent ferromagnetic layers.

For instance, epitaxial Fe/MgO/Fe based MTJs are not suitable for commercial devices because they cannot be grown (with the same crystallographic symmetry) in a structure such as in Fig. 1.6 (b) using sputtetring techniques. The antiferromagnetic layer (PtMn or IrMn) induces a fcc crystalline structure in the SyF layer, which produces a mismatching with the MgO (001). The solution of this problem was the MTJ structure CoFeB/MgO/CoFeB deposited by sputtering.

The CoFeB grows amorphous as TL of the SyF (see SyF structure in Fig. 1.6 (b)). The textured MgO (001) barrier can be grown on top of the amorphous CoFeB by sputtering deposition at room temperature. Then, the amorphous CoFeB as FL is grown on top of the MgO. In order to generate a lattice matching i.e crystallize the two CoFeB electrodes in the bcc MgO(001) structure, it is necessary to anneal the devices at 250°C-340°C during at least 1 hour.

The annealing is fundamental to obtain high TMR but it gives rise to several problems such as the degradation of the MgO barrier (pinholes) due to the B or Mn diffusion ([Komagaki et al., 2009], [Takiguchi et al., 2000], [Ikeda et al., 2008], [Kodzuka et al., 2012]) and the reduction of the strength of the RKKY coupling in the SyF layer.

In order to protect the MgO barrier against B diffusion the CoFeB of the TL of the SyF and of the FL can be replaced by CoFeB/CoFe and CoFe/CoFeB bilayers respectively, using a thin CoFe layer (≈ 0.5nm) at the interface to MgO. As shown in [Schreiber et al., 2011] this can increase the TMR from 105% to 192% and reduce the resistance-area product (RA) [5] from 14.5 to $3.4\Omega\mu m^2$ [Schreiber et al., 2011].

1.2.3 Spin Momentum Transfer

In the previous section, we described magnetoresistive effects that can be understood as the control of the current flow through a $FM_1/NM/FM_2$ multilayer structure via the magnetic configuration of FM_1 and FM_2. The inverse of this effect, namely the control of the magnetization state via the spin polarized current is at the base of another important concept of spintronics: *the spin momentum transfer*. This concept has been described theoretically by J. C. Slonczewski [Slonczewski, 1996] and L. Berger [Berger, 1996], predicting that a spin polarized current could drive excitations or the magnetization reversal of a ferromagnetic layer (FM). The first observation of the spin transfer torque (STT) effect was obtained by Tsoi [Tsoi et al., 1998] using a mechanical point contact in a multilayer. In 2000 Katine [**?**] presented the first measurements using a spin valve nanopillar structure, that experimentally confirmed the predictions of Berger and Slonczewski, that it is possible to reverse the magnetization using a spin polarized current with current densities of $(10^{11} - 10^{12} A/m^2)$. This was a major achievement, since these opened new possibilities for technological applications.

Using the schematic of three layers $FM_1/NM/FM_2$ presented in Fig. 1.9 (a) we will explain in a simple and intuitive approach the mechanism of the spin transfer torque. Considering electrons flowing from left to the right. The current is spin polarized in FM_1 thus, spins end up aligned in the direction of $\mathbf{M}_1$. This spin polarization is denoted by $\overline{\mathbf{p}}$, where P is parallel to the magnetization in FM_1, see Fig. 1.9 (a).

When the electrons reach the second ferromagnetic layer FM_2, they interact with the local magnetization $\mathbf{M}_2$ which is misaligned with respect to $\mathbf{p}$. As a result of this, the current will be spin polarized in the direction of $\mathbf{M}_2$ changing the spin angular momentum of the conduction electrons. Since the total angular momentum is conserved, this change in spin angular momentum of the conduction electrons must be transferred to the local magnetization $\mathbf{M}_2$. This transfer of spin angular momentum from the conduction electrons to the local magnetization is equivalent to a torque $\mathbf{T}$ acting on the local magnetization.

[5] In the STO development we look for structure of small RA product ($\sim 1\Omega\mu m^2$) because a reduction of this product will increase the current density trough the structure.

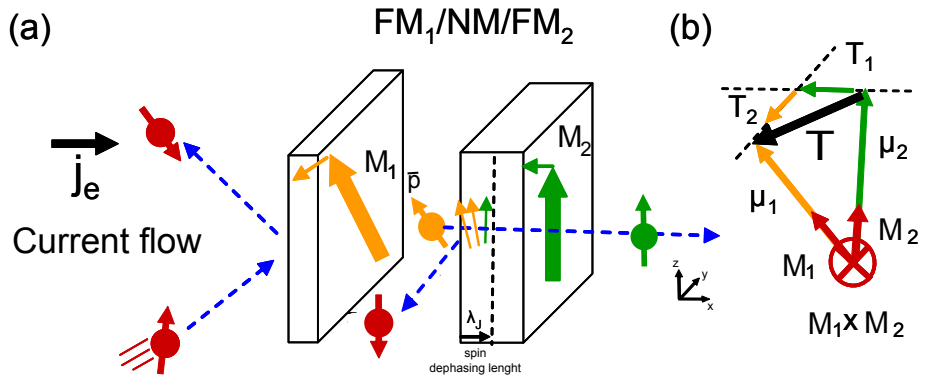

Figure 1.9 – (a) Spin transfer torque in a magnetoresistive structure $FM_1/NM/FM_2$. Electrons flowing from left to right are spin polarized by FM_1 and induce spin momentum transfer in FM_2. In (b), the vectorial schematics of the momentum transmitted by electrons to the local magnetization which are represented by the momentum in μ_1 (ingoing) and μ_2 (outgoing) magnetic moments.

This difference of momentum is described in Fig. 1.9 (b) where we introduced the in-plane schematics of the momentum transfer from μ_1 (electrons conduction moment ingoing) to μ_2 (electrons outgoing). The spin angular momentum μ_1 will change into μ_2. During this interaction the magnitude of the magnetization of FM_2 has to keep constant.

$$\frac{d|\mathbf{m}|^2}{dt} = 2\mathbf{m}.\frac{d\mathbf{m}}{dt} = 0 \tag{1.9}$$

It means that only the perpendicular component of the spin angular momentum is transferred to the local magnetization. The result of eq. 1.9 shows that the temporal change of the magnetization ($\frac{d\mathbf{M}_2}{dt}$) during the interaction is perpendicular to the magnetization $\mathbf{M}_2$. The torque $\mathbf{T}$ is decomposed in two components, $\mathbf{T}_1$ and $\mathbf{T}_2$, acting on $\mathbf{M}_1$ and $\mathbf{M}_2$ respectively[6]. The torque in $\mathbf{M}_2$ can be written as,

$$\mathbf{T}_{\parallel} = a_j \mathbf{m}_i \times (\mathbf{m}_i \times \mathbf{p}). \tag{1.10}$$

where a_j is proportional to the applied dc current such that the torque $\mathbf{T}_{\parallel}$ changes with the current orientation. The symbol $\parallel$ means that the torque is in the plane of $\mathbf{M}_1$ and $\mathbf{M}_2$.

[6]Normally $\mathbf{M}_1$ is insensitive to the torque $\mathbf{T}_1$ due to the pinned or the SyF used as FM_1.

Another extra-torque which appears is known as "field-like term". This field-like torque in $\mathbf{M}_2$ can be written as,

$$\mathbf{T}_\perp = \mathbf{T}_\perp^0 + b_j(\mathbf{m}_i \times \mathbf{p}). \tag{1.11}$$

where $\mathbf{T}_\perp^0$ is the torque at zero voltage and b_j depends of the net current charge. It is possible to write the total torque over $\mathbf{M}_1$ as a sum of two components.

$$\mathbf{T} = \mathbf{T}_\parallel + \mathbf{T}_\perp \tag{1.12}$$

$$\mathbf{T} = a_j\mathbf{m}_i \times (\mathbf{m}_i \times \mathbf{p}) + b_j(\mathbf{m}_i \times \mathbf{p}). \tag{1.13}$$

In this equation, the total torque presents two contributions, a longitudinal $\mathbf{T}_\parallel$ and a perpendicular $\mathbf{T}_\perp$ (to μ_1 and μ_2). In the original prediction, Berger and Slonczewski neglected the perpendicular component of the spin current, getting only the a_j term. The a_j term plays an important role in the devices based with metalic structure, such as SV, while the b_J term in negligible. In the STO devices based on MTJ, the b_J term is not negligible but so far its influence in the excitation spectra is not clear. In this thesis we consider only the $\mathbf{T}_\parallel$

In the next chapter it will be shown that the $\mathbf{T}_\parallel$ term has the form of the Gilbert damping term, following the Landau-Lifshitz-Gilbert-Slonczewski (LLGS) equation which describes the magnetization dynamics taking into account the spin momentum transfer.

1.3 Coupled magnetic System - RKKY phenomena and the Synthetic Ferrimagnet (SyF) layer

In Fig. 1.6 (b) it was shown that using a *Synthetic Ferrimagnet* (SyF) reference (or polarizing) layer has advantages over simple SV structures. The SyF is composed of two layers (top layer (TL) and bottom layer (BL)) separated by a thin non magnetic metallic

spacer layer [7]. In this section we will explain the origin of the magnetic order (AF or F) between the TL and BL of the SyF.

In 1954, Ruderman and Kittel suggested that the magnetic information of the localized magnetic moments could be transmitted (spin polarization) into the surrounding conduction electrons. Kasuya and Yosida ([T.Kasuya, 1956], [Yosida, 1957]) studied the coupling of the localized magnetic moments in rare earth 4f materials with the conduction electrons. They showed that the spin polarization of the surrounding conduction electrons *oscillates* in sign as a function of the distance from the localized magnetic moment and its spin information can be carried over large distances. This coupling is called the Ruderman-Kittel-Kasuya-Yoshida (RKKY) coupling.

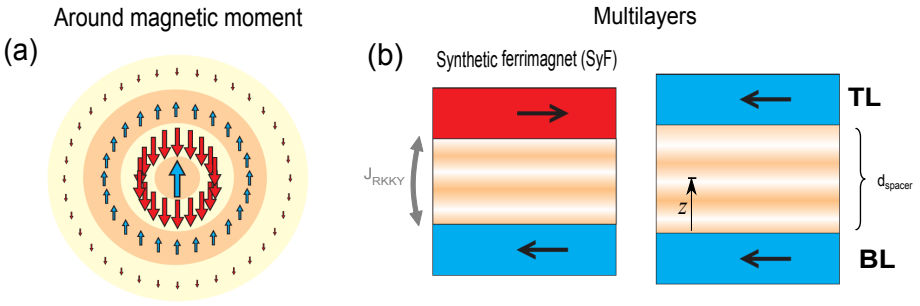

Figure 1.10 – (a) Spin polarization of the conduction electrons around a localized magnetic moment, showing the characteristic RKKY oscillations.(b) In multilayers, the characteristic RKKY oscillations are present between the FM layers. The thickness of the spacer between the TL and BL defined if the RKKY coupling induces an AF or FM coupling between the TL or BL. Adapted from "*Magnetism*"[J. Storn,].

The oscillatory behavior of the RKKY coupling is a result of a general phenomenon due to the wave nature of the conduction electrons in the metallic spacer. Imagine two magnetic moments in an electron sea were the electrons are described as plane wave functions. It is possible to write the exchange RKKY constant J_{RKKY}, which presents an oscillatory behaviour (positive or negative) depending of the distance between the magnetic moments, see Fig. 1.10 (a).

This mechanism can be extended to the case of two ferromagnetic layers separated by a thin nonmagnetic metallic spacer layer (for instance a SyF layer) of the form $FM_1/NM/FM_2$, where the conduction electrons in the spacer will be the media to carry the magnetic information.[8]. In Fig. 1.10 (b), the spin polarization of electrons between two magnetic layers is presented. The relative magnetization alignment (P or AP) in the

[7] Normally the thickness of the metallic spacer is of a few Angstroms. In the case of Ru or Cu it is less than 1nm

[8] This RKKY coupling produces an oscillatory order in the spacer which have been observed by photoemission ([Carbone et al., 1993], [Garrison et al., 1993]

two FM layers depends on the distance between the layers. The J_{RKKY} interaction energy is written as a function of the spacer between the FM layers in the form,

$$J_{RKKY}(z) = J_0 \frac{d_{spacer}^2}{z^2} sin(2\kappa_F z) \tag{1.14}$$

where d_{spacer} is the thickness of the spacer between the FM layers, z is the distance from one FM layer to a point in the spacer, see Fig.1.10, k_F is the Fermi level wave vector.

The theoretical explanations in the frame of band structure calculations were made by Bruno using spacers such as Ag, Cu and Au, for instance [Bruno and Chappert, 1991], [Bruno and Chappert, 1992]. It also includes the influence of the roughness on the period of the oscillations, see Fig. 1.11 (a)-(b). Experimental results from Parkin [Parkin et al., 1990], show the oscillating nature of the interlayer coupling (in terms of the saturation field) for interfaces of Co/Ru, Co/Cr and Fe/Cr, see Fig. 1.11 (c).

Fig. 1.11 (d) shows some experimental results obtained during this thesis work for the optimization of SyF structures. This figure shows the J_{RKKY} coupling strength as a function of the spacer thickness. The value of the RKKY constant was estimated from the saturation magnetization field of the hysteresis loops using the following equation,

$$J_{RKKY} = \mu_0 H_{sat} \frac{M_{S,BL} d_{BL} M_{S,TL} d_{TL}}{(M_{S,BL} d_{BL} + M_{S,TL} d_{TL})} \tag{1.15}$$

The first peak of the Fig. 1.11 (d) corresponds to the highest antiferromagnetic coupling which will be considered as a strong RKKY coupling, $J_{\mathrm{RKKY}} \approx -1$ mJ/m^2. This coupling strength corresponds to ≈0.8nm of Ru thickness. As a weak RKKY coupling we consider values around of $J_{\mathrm{RKKY}} \approx -0.1$ mJ/m^2.

This RKKY coupling is called bilinear because the energy per area is linear in the directions of both magnetization $\mathbf{m}_i$[9].

$$\frac{E_{\mathrm{RKKY}}}{S} = -J_{\mathrm{RKKY}} \mathbf{m}_i . \mathbf{m}_j \tag{1.16}$$

[9]The phenomenologically bi-cuadratic therm was proposed to explain the perpendicular alignment, $\frac{E_{RKKY}}{S}$ =-$J_{2,RKKY}(\mathbf{m}_i.\mathbf{m}_j)^2$

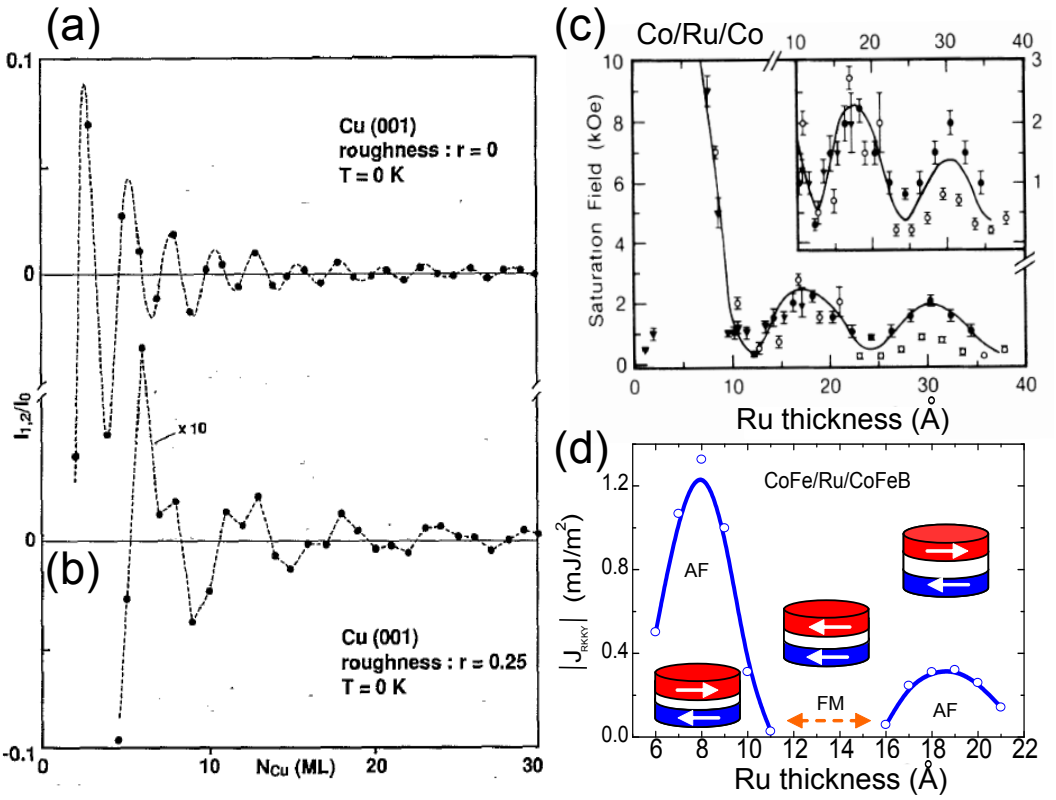

Figure 1.11 – Interlayer RKKY coupling a function of the Cu thickness. Without the interface roughness is presented in (a) or taking into account the roughness in (b), adapted of [Bruno and Chappert, 1991]. Oscillatory behaviour of the saturation magnetization measured by Parkin is shown in (c) for the structure Si(111)/(100Å) Ru/[20Å) Co/t_{Ru} Ru]$_{20}$/(50Å) Ru , deposited at temperatures of •, 40 °C; ∘, 125 °C and × 200 °C. In (d) the oscillatory RKKY coupling of the structure SyF unpinned $Ta(30)/CuN(200)/Ta(50)/CoFe(50)/Ru(x)/CoFeB(20)/Ta(50)$, of different Ru thickness. It is possible to chose the Ru thickness in order to control the strength of the coupling. Thickness in parenthesis are in Å. Sample provided from LETI laboratory.

In the development of the spintronics devices, the texture of the SyF interfaces play an important role, because a roughness of (Å) could change the strength and in consequence the magnetic alignment of the structure or the internal coupling field strength that acts on the magnetic layer.

Chapter 2

Context - Spin Transfer Torque nano-Oscillator (STO)

In chapter 1, some of the fundamental concepts of spintronics were introduced such as the magnetoresistance (GMR, TMR) and the spin momentum transfer. In this chapter, it will be shown how these concepts are used to define a spintronics device called *spin transfer torque nano oscillator* (STO) capable of generating a high frequency voltage signal.

2.1 Spin Transfer Torque Nano-oscillator (STO) nano-pillars

The most basic STO is composed by two ferromagnetic layers, called polarizer and free layer (FL). Generally the magnetization of the FL can be switched between two stable positions by an external magnetic field. In contrast the magnetization of the polarizer is fixed, for instance by exchange biasing using an antiferromagnetic (AF) layer. In Fig. 2.1, a schematics of a STO, emitting an ac signal, is introduced to explain the basic working principle.

A dc current I_{app} is applied through the STO nano-pillar (through a bias tee) spin polarizing the current by the polarizer layer. The spin polarized current will transfer a spin angular momentum to the local magnetization of the FL. This transfer of angular momentum is equivalent to a torque that has to be added to the Landau-Lifshitz-Gilbert (LLG) equation of motion of the magnetization.

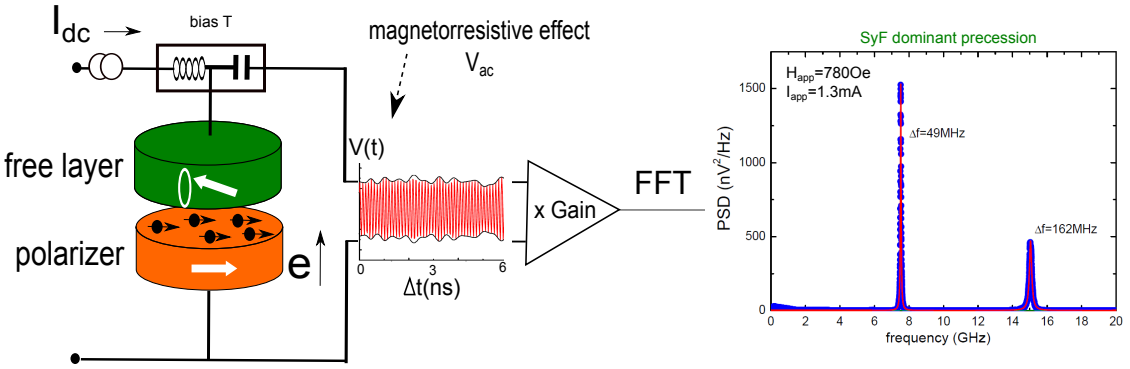

Figure 2.1 – (a) Schema of performance of the STO.

The first term of the LLG equation corresponds to the precession of the magnetization around the effective field in the FM layer, the second term is the damping (energy loss). Due to damping the magnetization will always return back to its equilibrium. Upon adding a spin polarized current of sufficiently large amplitude ($I>I_c$), this damping torque can be compensated by the spin transfer torque (STT), given by the third term in the LLG equation. Here I_c is called the critical current.

$$\frac{\partial \mathbf{M}_i}{\partial t} = \overbrace{-\gamma_0(\mathbf{M}_i \times \mathbf{H}^i_{eff})}^{Precession} + \overbrace{\frac{\alpha}{M_{S,i}}(\mathbf{M}_i \times \frac{\partial \mathbf{M}_i}{\partial t})}^{Damping} + \overbrace{(\frac{\partial \mathbf{M}_i}{\partial t})_{STT}}^{SpinTransferTorque} \tag{2.1}$$

If the critical current (I_c) is reached, the magnetization will start to precess on a stationary trajectory. This precession is called either *steady state oscillations*, *STT mode* or *auto-oscillations*. As it has been introduced in sec. 1.2, the relative position between the magnetization of the FL and the polarizer will define the magneto-resistance of the STO. The precession of the FL magnetization will thus produce via the magneto-resistance, an alternating voltage signal V_{ac} measured across the electrodes of the STO that can be measured on a spectrum analyser after amplification. This conversion from a DC current into an AC output voltage signal defines a nanoscale microwave signal generator whose frequency can be tuned via the applied DC current as well as an applied magnetic field. This frequency tuning via the current is an important feature of the STO signal generator.

The first experiments of microwave signal generation were demonstrated by the Cornell group using a Co/Cu/Py GMR structure [Kiselev et al., 2003]. Since then, many groups have been studying this effect using a variety of different magnetic configurations,for instance [Houssameddine et al., 2007], [Cornelissen et al., 2010], [Hamadeh et al., 2013][1]. The STO structures relevant for this thesis work are shown in Fig. 2.2. In Fig. 2.2 (a) the most basic STO composed by two FM layers, in Fig. 2.2 (b)-(c) the "standard" STO

[1] We will describe furthermore the different STO configurations

(in plane magnetized) composed by a single layer (SL) and a pinned SyF polarizer[2] and in Fig. 2.2 (d) the "perpendicular polarizer" STO which presents three FM layers. A reference (pinned) layer at the top, in the middle of the structure a FL and at the bottom the polarizer (with strong out of plane anisotropy)[Houssameddine et al., 2007].

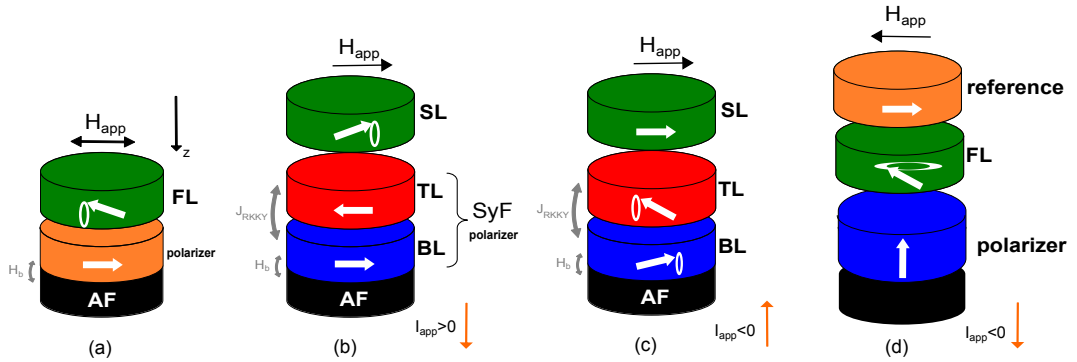

Figure 2.2 – (a) Structures of the basic STO composed by a FL and a polarizer pinned layer. (b)-(c) The standard STO composed by a SyF and a FL in-planed magnetized. It is possible to excited the FL or the SyF changing the sense of the applied current (d) Structure of the perpendicular polarizer STO.

In the most basic concept of STO operation, only excitations in the FL has been considered. However as it is shown in Fig. 2.2 (b)-(c) for the standard STO, upon reversing the current direction it is possible to also excite the pinned layer, using the single layer (SL) as a polarizer. In Fig.2.2 (d) the perpendicular polarizer will spin polarize the electrons perpendicular to the film plane producing excitations out of plane in the FL. In this structure the signal is measured between the magnetization of the FL and the reference layer.

In the following the properties of the excitation spectra will be introduced for the FL excitations using a basic or standard STO configuration.

2.1.1 Excitation state diagrams of a single FM layer

In order to obtain excitations for a STO, a dc current is applied generating different magnetization states in the FL. Depending on the strength of the current and magnetic field it is possible to reach different static or dynamic states. If the dc current is not enough to compensate the damping (i.e. $I<I_c$), only thermally activated damped modes are excited, see Fig.2.3 (a). This damped mode is basically a small amplitude precession mode, with small power and large linewidth. When the dc current is increased, the

[2] In the standard STO the SL is named as the free layer (FL) because it is not pinned by an exchange bias, thus it can turn easily into the direction of the magnetic applied field.

damping starts to be compensated, the linewidth is reduced and the system reaches the auto-oscillation regime when I>I_c. In this point the power starts to increase considerably due to the large precession amplitudes.

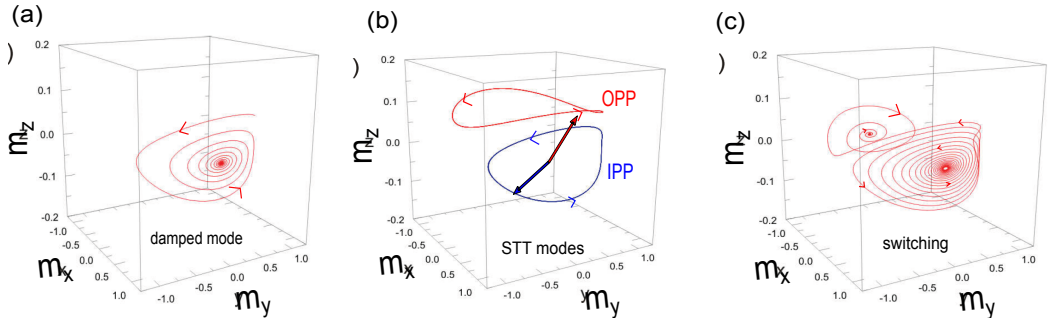

Figure 2.3 – In the state diagram the magnetization could be in the stable state which corresponds to the damped mode (a) or the switching (b). The non stable regime corresponds to the STT mode that could be IPP or OPP precession mode (c).

Here I_c will depend on the applied magnetic field. The magnetization in the STT mode will precess in plane following the tendency of the damped mode or ferromagnetic resonance (FMR) around the minimum energy in plane axis but with large amplitudes (only for the in-plane configuration). This first mode of precession is called the in plane precession or IPP mode. If the current increases more, reaching another critical current, the magnetization can precess out of plane, out of plane precession (OPP) mode, around the axis of maximal energy. The trajectories of the IPP and OPP modes are shown in Fig. 2.3 (b) for high fields. For low fields and large enough current, the STT can switch the magnetization into the opposite direction. The trajectory of magnetization switching is shown in Fig. 2.3 (c) and 2.4(c). After the switching the magnetization will remain in a stable state without excitations.

These regions of static and dynamic states are presented normally in a state diagram as a function of the applied field[3] and current, in order to identify the regions where it is possible to reach STT modes. For instance, the state diagram of a single in-plane magnetized FL is shown in Fig. 2.4 (a) which is deduced from macrospin simulations and defines clearly the boundaries and the states.

In the center of the numerical state diagram ($0<H_{app}<H_u$[4]) a bi-stable region is identified. This region must be avoided because it is not an optimum region for the measurements of STT modes due to the magnetization reversal between two minima of energy, see Fig. 2.4 (c). The magnetization can be reversed from one magnetic state to the other one via the current, P↔ AP (or AP↔ P).

[3]In this type of diagrams the axis of magnetic applied field gives information about the magnetization configuration, i.e parallel (P), antiparallel (AP) (high or low resistance) of the STO.

[4]In a isolated single layer with in-plane magnetization (uniaxial anisotropy, $H_u=2K_u/Ms$)

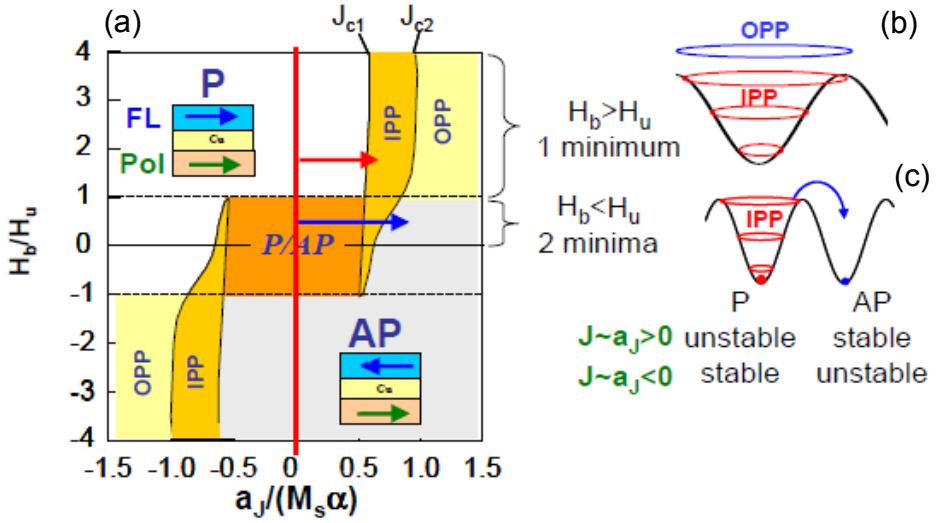

Figure 2.4 – State diagram of the excitations in a in-plane magnetization STO using the term a_J from LLGS equation which is proportional to the I_{app}. We observe the P and AP magnetic state. For a fix value of applied field ($H_{app}>H_u$), sweeping the current we can reach IPP ($I_{app}<J_{c1}$) and the OPP regions ($I_{app}<J_{c2}$) of excitations. For the case of ($H_{app}<H_u$) the system in the bi-stable region (two minimum of energy in right figure) reach a narrow region of IPP excitations.

In Fig. 2.4 (a), for an applied field $H_{app} > H_u$ the IPP ($I_{app}<J_{c1}$) and the OPP mode ($J_{c1}<I_{app}<J_{c2}$) of excitations are clearly defined. Experimental and numerical studies have confirmed the excitation state diagram for a single layer. It is noted that in some numerical simulations the transition between the IPP to OPP regimes show a mixed mode [Bertotti et al., 2005] ,[Zhou et al., 2007] and involves more complex effects of the magnetization dynamics.

In 2003, Kiselev [Kiselev et al., 2003] presented the first experimental state diagram of a multi layer Cu(80)/Co(40)/Cu(10)/Co(3)/Cu(2)/Pt(30) in nanopillars (thickness in nm) at room temperature, see Fig. 2.5 (a)-(b). The shape of the critical lines follow the tendency to the numerical simulations in the macrospin approach of Fig. 2.4 (a).

In the experimental dynamic measurements, the effect of the temperature will play an important role. The temperature generates magnetization fluctuations in the system thus the critical boundaries in the state diagram of STO will suffer changes. This fact makes it difficult to compare the numerical state diagram with the measured experimentally. Schneider studied this influence [Schneider et al., 2007] measuring the state diagrams of a spin valve device at 5K and 300K, see Fig. 2.6 (a)-(b). Comparing the two results it is possible to see how the bi-stable region, denoted by P/AP, is larger for low temperatures. The white dashed line encloses the corresponding bi-stable region. The critical current

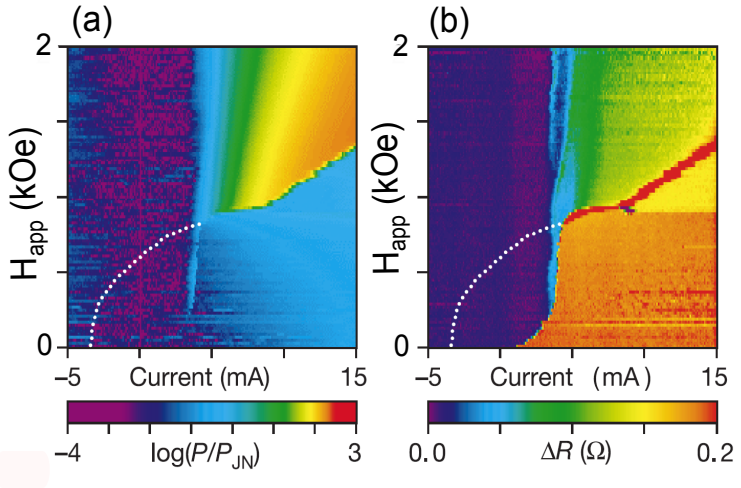

Figure 2.5 – First measurement of a state diagram of excitations. In (a) the colour corresponds to the emitted power in a logarithm scale and in (b) the resistance. Adapted from [Kiselev et al., 2003]

to produce the switching P↔ AP or AP↔ P state is reduced drastically for the case of room temperature.

By taking thermal fluctuations into account in simulations, it is possible to qualitatively reproduce the changes in the state diagram (as a function of the temperature) found experimentally [Xiao et al., 2005].

2.1.2 Frequency dispersion in standard STO nano-pillars

The frequency tuning of the emitted signal of the STO is the most interesting feature. In this section we will show a brief summary of these features for the STT mode of the STOs that has been reported. The frequency tuning as a function of the applied field and dc current was studied in different STO structures (SV, MTJ, Fig. 2.2) and geometries (nanocontact or nanopilars).

2.1.2.1 Frequency dispersion versus applied field

The frequency dispersion as a function of the applied field for a isolated single layer should present a Kittel law tendency i.e increasing frequency with field in a square root like behaviour. Different experiments, using in plane magnetized structures confirm this tendency [Cornelissen et al., 2010], [Houssameddine et al., 2008]. It is important to remark that the damped and the STT mode present this strong dependence (Kittel law)

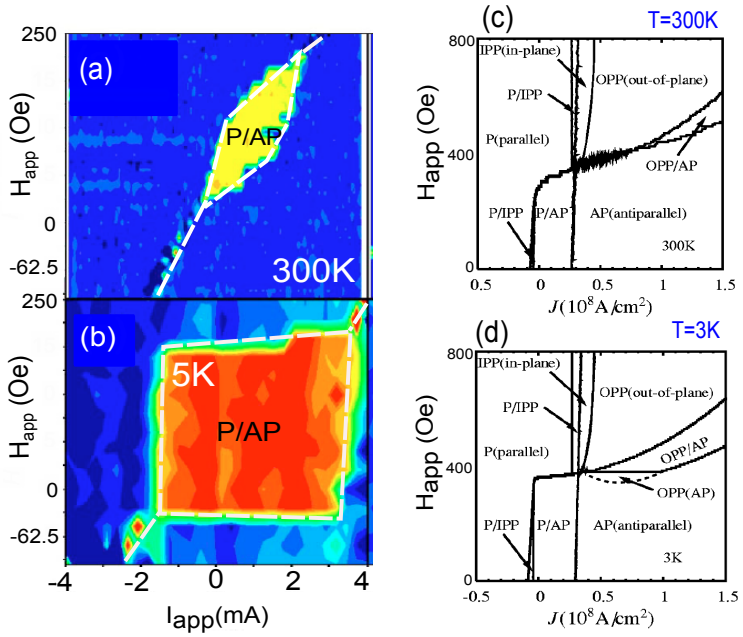

Figure 2.6 – State diagram of the bi-stable region for the case of (a) 300K and (b) 5K. The temperature increases the bi-stable region (enclose by the dash white line). The critical current to generate the switching in the P/AP region is drastically reduced in the case of 300K. (c)-(d) Numerical simulations of the state diagram of a single layer at 3K, and 300 K. Adapted from [Schneider et al., 2007] and [Xiao et al., 2005].

with the applied field. In this sense, it will be the current frequency tuning which will provide the criteria to separate the damped or STT mode. The development of the Kittel law equation (eq. 3.41) will be done in detail in the numerical simulation section 3.1.4.1.

In Fig. 2.7, the frequency dispersion of the STT mode (in the FL) of a standard STO based on MTJ (TMR=100%) structure is shown adapted from [Houssameddine et al., 2008]. The expected Kittel law tendency has been found in the measurements (between 5 and 10GHz) from H_{app}>200Oe (overcoming the bistable region).

An important feature of this result is the characteristic branches A-C presented in the first and second harmonic. i.e the frequency curve is not totally continuous. Superposing the linewidth with the frequency it is noticed that the maximum value of the linewidth correspond exactly to the discontinuity of the frequency dispersion curve. The minimum of the linewidth for this measurement was Δf_{min}=100MHz. The origin of these branches is an open question, however some results of this thesis provide an information of its origin.

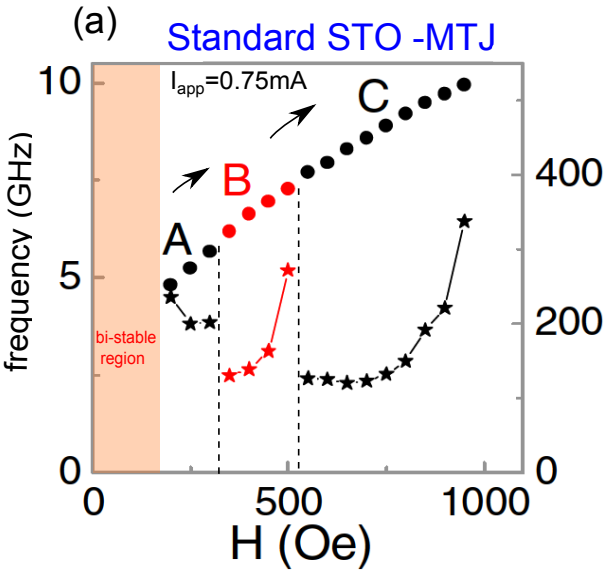

Figure 2.7 – Frequency and linewidth dispersion as a function of the applied field for the FL of a standard STO based on MTJ (TMR=100%). It presents branches in the dispersion curve. The center of each branch corresponds to a minimum of linewidth. This figure was adapted of [Houssameddine et al., 2008]

2.1.2.2 Frequency dispersion versus applied current

An important feature of the FL excitation in the STO is its frequency tuning as a function of the applied current. In Fig. 2.8 the characteristic frequency, linewidth and power of the STO based on MTJ devices are shown. In (a), the frequency dispersion shows the thermal activation regime which is called in this thesis "damped mode", before to reach the critical current I_c. This damped mode is basically a small amplitude precession mode, with small power and large linewidth. When the applied current is close to the critical current, and the system reaches the STT mode, the frequency decreases with the current, giving rise to the name of redshift regime ($df/dI_{app}<0$). It is possible to explain this reduction of the frequency imagining that increasing the dc current, the amplitude of the STT excitations mode increases thus the precession trajectory increases decreasing the frequency. When the system reaches the critical current I_c, the power of the emitted STT signal starts to increase considerably Fig. 2.8 (c), due to the large precession amplitudes and the linewidth presents a minimum (low value), Fig. 2.8 (b).

The geometry of the STO is not limited to a nano-pillar structures, actually there is another structures commonly used for STO devices. It is the nano-contact structure which is shown in Fig. 2.9. Finally, instead of a homogeneously magnetized FL there is also static magnetization of the FL which is a vortex ground state. In the following some features of STO nano-contact and vortex in STO nano-pillars, will be summarized.

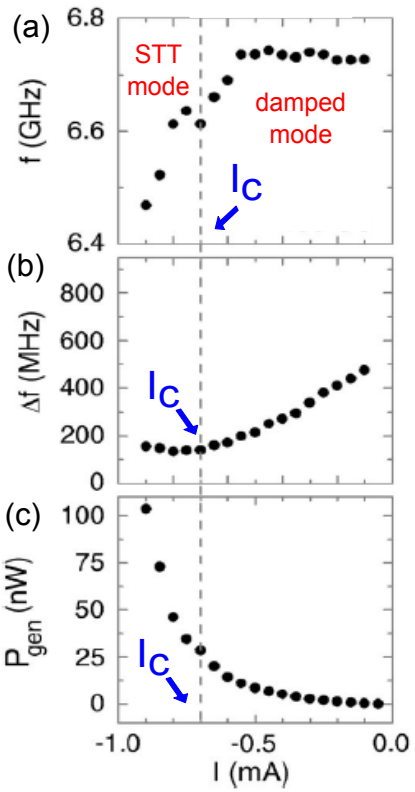

Figure 2.8 – Frequency, linewidth and power as a function of the applied current for a STO devices based on MTJ. The critical current corresponds to the increase of the power and the reduction of the linewidth in both cases. The frequency shows a redshift regime ($df/dI_{app}<0$). Figures were adapted from [Houssameddine et al., 2010]

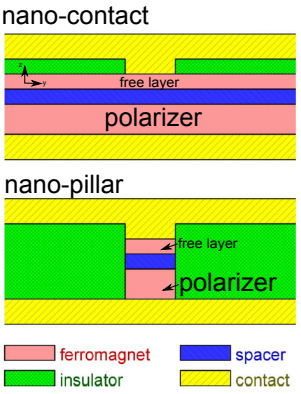

Figure 2.9 – Nano-contact and nano-pillar structure. Adapted from [Slavin and Tiberkevich, 2009]

1. **Nano-contacts**

   In nano-contacts the FL is not bounded in the xy plane, therefore the STT modes in the FL occur in a nano-sized area of the contact (typically of the radius of 10-100 nm). An important feature of nano-contacts is that the dipolar stray field (dipolar field) between the polarizing and free layer are reduced as compared to nanopillars.

2. **Vortex in nano-pilars**

   Many research groups have stimulated the study of STOs because of its interesting features, doing many efforts of research to increase the power of the STOs emission, for example synchronizing many STOs using spin waves [Mancoff et al., 2005], [Kaka et al., 2005], [Demidov et al., 2007] or due to the magneto-static coupling [Gubbiotti et al., 2007] or using an external microwave signal passing through several STOs [Grollier et al., 2006] connected in series. Currently the research is focusing as well on the microwave emission by controlling the precession of vortex induced for STT [Dussaux et al., 2010]. These microwave emissions are characterized by very narrow emission peaks (about 1 MHz) [Ruotolo et al., 2009], [Pribiag et al., 2007a], and a power high emission when the vortex is created in the free layer of a MTJ [Dussaux et al., 2010].

   In a non-uniform magnetization system, the spin polarized current can create excitations of a gyroscopic mode, vortex eigenmodes, [Pribiag et al., 2007b], [Mistral et al., 2008], [Khvalkovskiy et al., 2009], [Deranlot et al., 2010], [Hamadeh et al.,], [Hamadeh et al., 2013]. They present generally low frequencies (200MHZ-2GHz) and narrow linewidths ($<$10MHz).

2.1.2.3 Amplitude and phase noise of a STO

STOs are of interest for integrated microwave devices, however the incorporation of the STO in commercial microwave circuits depends upon two criteria, the output power required value ($\approx$1mW, -10dBm[5]) and the phase noise. In order to meet the first condition, the STO structure based originally on SV (MR=1-10 %,$\approx$pW, -90dBm) has been changed using a structures based on MTJ (MR=50-100 %, $\approx$nW, -60dBm). The STO based on SV structure is easier to fabricate than the MTJ structures and its resistance can be selected to 50 Ω for a good matching with the RF measurement components. In the case of the MTJ structure the insulator character of the MgO barrier gives a resistance between 50-1000 Ω, creating a miss matching in the RF measurement set-up.

[5]The power relation between Watts and dbm is the following, P(dbm)=10log$_{10}$[$\frac{P(W)}{1mW}$]

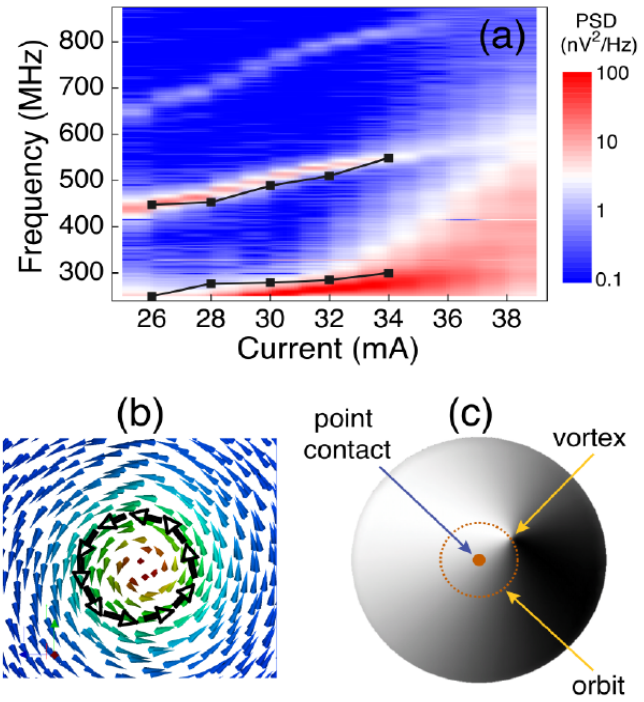

Figure 2.10 – (a) Color map on PSD of a frequency as a function of the applied current for a vortex in a STO. (b) Simulated vortex magnetization profile. (c) Orbit of the vortex (orange) around the contact point. Adapted from [Mistral et al., 2008]

The other condition to meet, in order to know the performance of the STO, is the measurement of the **phase noise**. This parameter is the most useful to find future applications and it can be used to understand the origin of linewidth of the emitted signal, since phase noise and linewidth broadening are two sides of the same coin. It means that the linewidth value of the emitted signal will be a good parameter to provide a first characterization of the performance of the STO. For instance in the case of the standard STO based on SV, the linewidth of the STT mode in the FL was of 200MHz while for the SyF pinned layer the linewidth was 55MHz, [Houssameddine et al., 2010]. In the case of the STO based on MTJ, the linewidth for the STT mode in the FL for devices of high TMR (HTMR) was of 100MHz how ever for the low TMR (LTMR) devices the linewidth is reduced until 10MHz, [Houssameddine et al., 2008]. For vortex excitations, the linewidth could reach the 40KHz, [Hamadeh et al.,]. To understand this, let us consider the voltage signal of equation 2.2. Thermal fluctuations in the magnetic system will induce amplitude and phase fluctuations which take the magnetization out from its trajectory. The real measured voltage V(t) can be described using the following equation,

$$V(t) = [V_0 + \delta a(t)]\cos(\omega_0 t + \varphi(t)), \tag{2.2}$$

where the amplitude fluctuations are denoted by $\delta a(t)$ and the phase fluctuations by $\varphi(t)$. Both represent the temporal fluctuation of the trajectory. The result of the Fourier transform of this voltage is a peak with a finite linewidth. The non-linearity of the system (amplitude and frequency) produces that the phase (which is related with the frequency) will be affected by the amplitude fluctuations. This non-linearity is by the non-linear amplitude and phase coupling parameter ν. A second important non-linear parameter is the non-linear amplitude relaxation f_p, defined in the next section.

During the last years the study of the PSD phase noise (S_φ) of the phase fluctuations φ(t) and amplitude noise ($S_{\delta a}$) of the amplitude fluctuation δa have been measured for the STO based on MTJ structures [Bianchini et al., 2010], [Quinsat et al., 2010] using the Hilbert transform. An example is shown in Fig. 2.11.

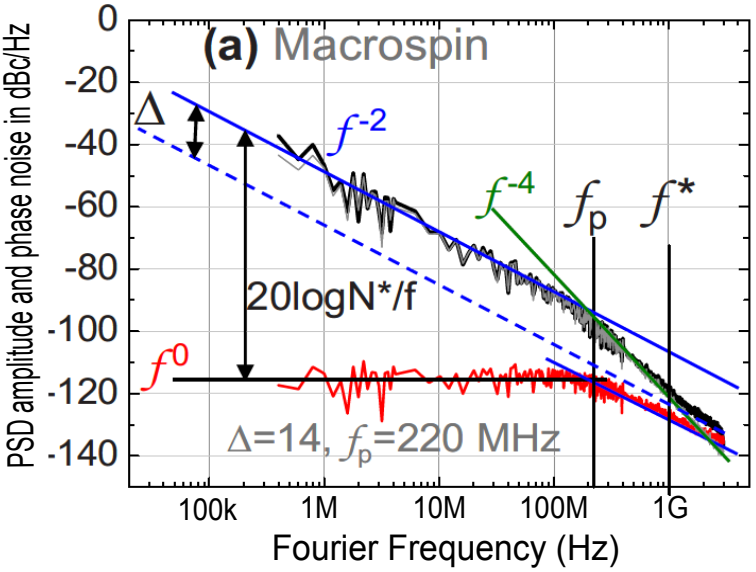

Figure 2.11 – Log-log plot of the PSD of the amplitude and phase noise, using macrospin simulations. Parameters in [Quinsat et al., 2010].

In [Quinsat et al., 2010], M. Quinsat studied the amplitude and phase noise properties as it is shown in fig. 2.11. The inverse power law PSD$\sim 1/f^x$, provide the type of noise that governs the phase fluctuations (x=0 white noise, x=1 *1/f* noise, x=2 random walk noise). When the magnetization is out of its equilibrium trajectory, a restoring force appears to bring it back again. There will be a competition between the spin torque and the attenuation, in order to define the relaxation frequency $f_p=\frac{\Gamma_p}{\pi}$. In Fig.2.11 (a) the log of the PSD amplitude (red) and phase noise (black) are shown. It is noted that the amplitude noise follows a white noise (f^0) up to f_p, then it presents a roll off, following a f^{-2} tendency. It means that the system is damped (into the original position) for $f<f_p$. For $f>f_p$ the system cannot relax to the trajectory and the perturbations are accumulated. For that reason a random walk noise is characteristic in this frequency range. The PSD amplitude noise follows the relation,

$$S_{\delta a}(f) = \frac{2}{\pi} \frac{2\Delta f_0}{[f^2 + (\Gamma_p/\pi)^2)]} \tag{2.3}$$

where Δf_0 corresponds to the statistical properties of the white Gaussian noise source and determines the linewidth of the linear STO. The PSD phase noise (black curves) is always above the PSD amplitude noise, confirming that the more important contribution to increase the linewidth Δf is due to the phase noise. The non-linear amplitude-noise coupling gives to the PSD phase noise an amplitude noise contribution. The PSD phase noise is described by the following equation,

$$S_{\varphi}(f) = \frac{\Delta f_0}{\pi f^2} + \frac{\Delta f_0}{\pi f^2} \frac{\nu^2 f_p^2}{(f_p^2 + f^2)} \tag{2.4}$$

The PSD phase noise presents different regions as a function of the frequency, see Fig. 2.11. For high frequencies $f > f^*$ the tendency is f^{-2} and has a random walk behavior (corresponding to white noise frequency fluctuations ($2\pi f = d\varphi/dt$). For $f_p < f < f^*$, the phase noise falls off as f^{-4}. In this range the random walk is enhanced by the f^{-2} amplitude noise, due to the non-linear amplitude-phase coupling. At low frequencies, for $f < f_p$ the phase noise again becomes like f^{-2}. Here the phase noise is enhanced by the amplitude noise which is proportional to f°in this frequency range.

The difference Δ between the dashed line and the f^{-2} tendency will provide the non-linear parameter $\Delta = 10\log(1+\nu^2)$, which is the amplitude-coupling parameter, see Fig. 2.11.

The derivation of the phase and amplitude noise given here, comes from a universal model which describes the behaviour of the non-linear STO developed by A. Slavin, V. Tiberkevich and J. V Kim, [Kim et al., 2008], [Slavin and Tiberkevich, 2009]. It will provide the theoretical background of the STO excitation properties in autonomous and non-autonomous regime. .

2.1.3 Universal model of the non-linear auto-oscillator

The most important model, to obtain an universal theoretical framework for STOs, is known as the KTS model and is based in the classical quasi-Hamiltonian formalism for spin waves. This model provides a framework to describe the perturbations of the non-linear magnetization dynamics due to noise (amplitude and phase). In this section, we will summarize the important concepts of this model. For a rigorous description we refer

to [Slavin and Tiberkevich, 2009].

In a STO, many spin waves can be excited in the FL but only one of them will reach the steady state oscillation, for which the Gilbert damping term is fully compensated. Using this assumption, this non-linear model is derived from the LLG equation which is written as,

$$\frac{\partial \mathbf{M}}{\partial t} = -\gamma_0(\mathbf{M} \times \mathbf{H}_{eff}) + T_G + T_S \tag{2.5}$$

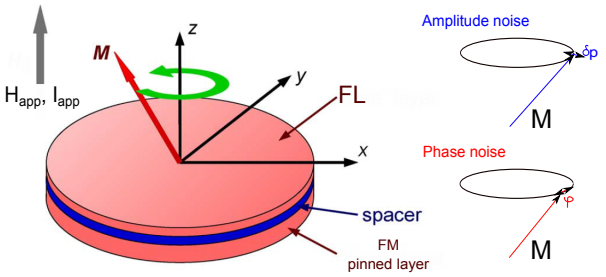

Figure 2.12 – STO structure of the Universal model. The magnetic field and the current is applied perpendicular to the structure. In the right side the amplitude and phase fluctuation. Adapted from [Slavin and Tiberkevich, 2009].

It is possible to rewrite the LLGS equation in another dynamical form, taking into account the damping term and the spin torque term, see eq. 2.6. The magnetization dynamics of the STO can be described by the universal oscillator model represented by the non-linear equation [Slavin and Tiberkevich, 2005], see eq. 2.7.

$$\frac{\partial \mathbf{M}}{\partial t} = \overbrace{-\gamma_0(\mathbf{M} \times \mathbf{H}_{eff})}^{Precession} + \overbrace{\frac{\alpha}{M_S}(\mathbf{M} \times \frac{\partial \mathbf{M}}{\partial t})}^{Damping} + \overbrace{(\frac{\partial \mathbf{M}}{\partial t})_{STT}}^{SpinTransferTorque} \tag{2.6}$$

$$\frac{dc}{dt} = \overbrace{-i\omega(|c|^2)c}^{Precession} - \overbrace{\Gamma_+(|c|^2)c}^{Damping} + \overbrace{\Gamma_-(|c|^2, I)c}^{SpinTransferTorque} \tag{2.7}$$

In eq. 2.7 the first term of the right corresponds to the precession term (conservative), $\Gamma_+(|c|^2)c$ corresponds to the non-conservative or dissipative term (damping term) which leads to the reduction of the spin wave amplitudes with the time. This term depends on the spin wave power defined as $p=|c|^2$ in the limit circle which defines the trajectory. The non-linear positive damping rate $\Gamma_+(p=0)$ represents the half-linewidth of the linear FMR resonance. The term $\Gamma_-(|c|^2)c$ is called the anti-damping which corresponds to the

spin transfer torque effect, Γ_{-}(p)$\approx \sigma$ I(1-p), where σ is called the spin transfer efficiency, σ=$\varepsilon\frac{g\mu_0\mu_B}{2M_0Sd_{FL}e}$ and ε the spin polarization efficiency, e is the electron charge, d_{FL} is the thickness of the FL and S the cross section.

As we know from the LLGS equation, the spin transfer torque creates an effective negative damping for the magnetization precession in the the FL. When the damping is compensated the equation which describes the precession becomes,

$$(\frac{dc}{dt}) = -i\omega(|c|^2)c \tag{2.8}$$

Where the general solution for the eq. 2.8 will be,

$$c(t) = \sqrt{p}e^{[i\omega(p)t+i\phi_0]} \tag{2.9}$$

where ω(p) is the precession frequency and ϕ_0 an initial phase. The non-linear precession frequency depends on the oscillation power $\omega(|c|^2)$ =ω_0+Np, where N is the coefficient of the non linear frequency shift. To find the stationary solution of eq. 2.7, we have to separate the equation into real and imaginary parts, taking into account the fact that the amplitude c is related directly with the power, p =$|c|^2$. The system is described by the two equations,

$$\frac{dp}{dt} + 2[\Gamma_{+}(p) - \Gamma_{-}(p)]p = 0 \tag{2.10}$$

$$\frac{d\phi}{dt} + \omega(p) = 0 \tag{2.11}$$

The first equation corresponds to the dynamics of the oscillation power which is independent of the phase and the second one to the dynamics of the phase.

A solution of eq. 2.10 is p=p_0 constant, where p_0 is found from the equality Γ_{+}(p_0)=Γ_{-}(p_0). This last relation introduces the concept of the loss of energy compensated by the spin transfer term, the total effective damping will be equal to zero[6].

If we consider small perturbations of the auto-oscillation state or limit circle, we are allowed to linearized eq. 2.10 around the mean power p_0, p(t)=p_0+δp(t).

[6]The Γ_{+}(p) increases as a function of the power instead Γ_{-}(p) decreases with it.

In presence of noise, these equations are,

$$\frac{d\delta p}{dt} + 2\Gamma_p \delta p = 2\sqrt{p_0} Re[\tilde{f}_n(t)] \tag{2.12}$$

$$\frac{d\phi}{dt} + \omega_g = \frac{1}{\sqrt{p_0}} Im[\tilde{f}_n(t)] - N\delta p \tag{2.13}$$

where $\tilde{f}_n(t)$=$\tilde{f}_n(t)$e$^{-i\phi t}$, δp$\sim$ e$^{-2\Gamma_p|t|}$ (only in absence of noise) , Γ_p(p$_0$) is the restoration rate, an important parameter of the oscillator. It is possible to obtain Γ_p from the analysis of Fig. 2.11, where f_p=Γ_p/π. From the phase equation, there is no restoring force for that reason the phase is free and accumulates all the fluctuations, corresponding to a random walk behaviour $1/f^2$, see Fig. 2.11.

From the eq. 2.13 it is possible to identify ω_g=ω(p$_0$) which is the generation frequency. The non-linear parameter ν which corresponds to the coupling between the amplitude and phase noise is defined as ν=$\frac{N}{\Gamma_p}p_0$. The PSD of the phase noise presents limits (tendencies) as a function of the frequency, as it has been presented in eq. 2.4.

This summary of the universal model gives a theoretical introduction to the KTS model. Different techniques of telecommunication such as modulation, synchronization and phase looking, used to characterize the STOs, can be explained by the KTS model.

2.1.4 Higher order modes in ferromagnetic layers

STT modes are non-linear modes driven by spin-polarized current and in the linear regime (absent of current), the system is characterized by a multitude of linear spin wave modes. In this section, we will summarize some previous studies. These results are important for the analysis of the spectra, since besides main STT modes other excitations can be seen in the PSD voltage spectra.

Micromagnetic simulation performed by McMichael [McMichael and Stiles, 2005] in 2005, showed the existence of several excitations modes (damped modes) in a ferromagnetic elliptical sample (160×350×5 nm). These damped modes were excited by a field pulses, see Fig. 2.13 on top. As we can observe, damped modes appear in the edges of the sample, with less frequency than the fundamental mode. The fundamental mode is identified as the numbers (1,1). This kind of mode is called a bulk (or volume) mode because it is present almost in all the FM layer. This study revealed the spectra of eigenmodes in a

FM layer [McMichael and Stiles, 2005].

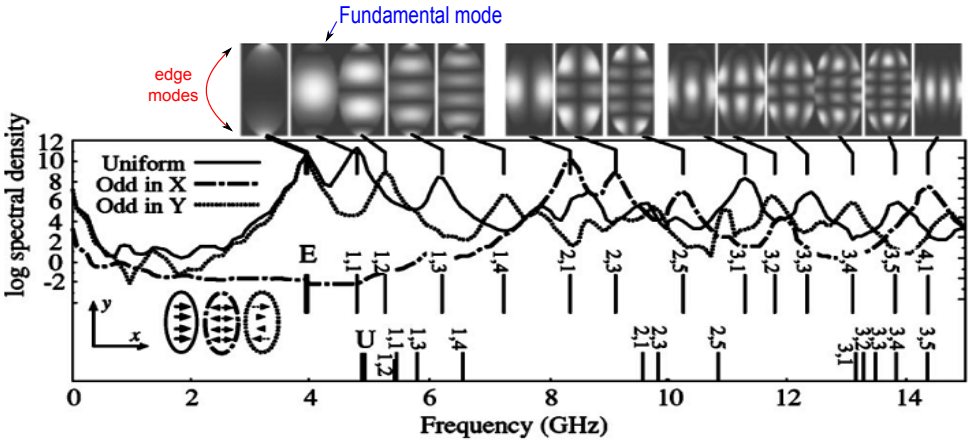

Figure 2.13 – Excitations modes in a elliptical disk obtained using micromagnetic simulation, adapted of [McMichael and Stiles, 2005].

In the same year than McMichel, a study of C. Bayer and G. Gubbiotti appears using Brillouin light scattering and micromagnetic simulations, they proved the existence of different spin modes in arrays of permalloy dots with elliptical and rectangular cross section ([Bayer et al., 2005], [Gubbiotti et al., 2005]). For applied field along the principal axes the solutions can be classified as (i) modes localized near the particle ends, (ii) modes with nodal lines perpendicular to H_{app} (backwardlike modes-BD), (iii) modes with nodal lines parallel to H_{app} (Damon-Eshbach-like modes-DE) and (iv) modes with both parallel and perpendicular nodal lines. For H_{app} along non-symmetry directions only the modes of type (i) are well defined. Others modes are assumed as a hybridization of modes in the above categories.

In Fig. 2.14 (a)-(i), the edge modes symmetric (S), anti-symmetric (AS) and the fundamental mode (F) are shown. On bottom, the angular dependence of the fundamental mode is shown, see Fig. 2.14 (j).

In the numerical simulation of this thesis, we have considered only the fundamental mode, neglecting the higher order modes, since we try to extract the main features of interactions. However it is important to be aware of these higher order modes because in some experiments, higher order modes seem to be present. The existence of these higher order modes (or quantized spin waves modes), in a finite ferromagnetic layer, would provide new features in the emitted spectra. Helmer [Helmer et al., 2010] presented a quantization model of spin waves thermally excited in a standard STO MTJ nano-pillars (RA$\approx$ 16$\Omega\mu$m). The use of a thermal noise source is an excellent technique to study the intrinsic magnetic properties and to understand the nature of the excitations in nano-pillars, see Fig. 2.15 (a). Using this model, it is possible to identify the FL and SyF excitations in the

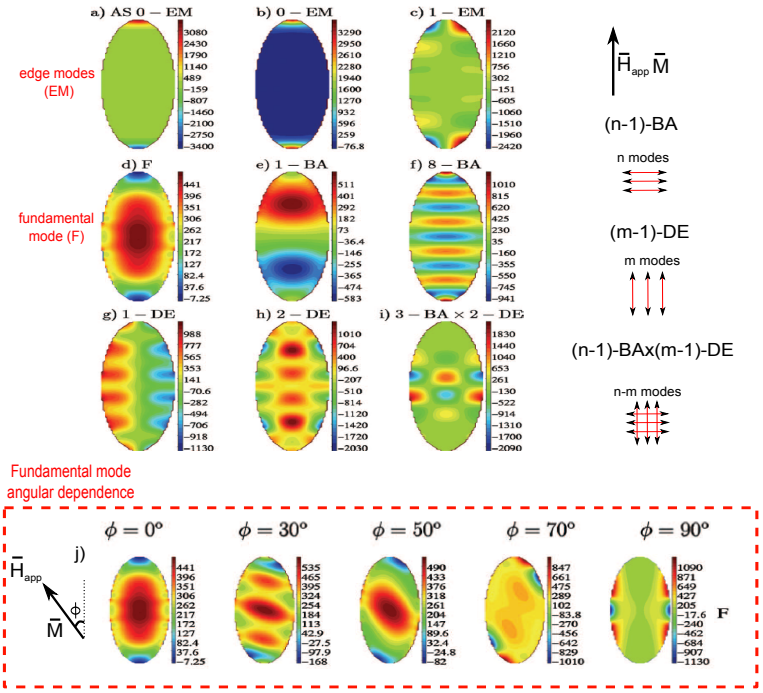

Figure 2.14 – (a) Normal component $m_z(\mathbf{r})$ of the magnetization dynamic of spin modes in ellipses. The edged modes (EM) presented in (a)-(c). The fundamental mode (F) is presented in (d). The BA and DE modes are shown in (e)-(h). Mixed modes are presented in (i).Adapted from [Gubbiotti et al., 2005]. (j) The angular dependence of the fundamental mode. The angle ϕ is measured between the applied field and the major axis of the ellipse.

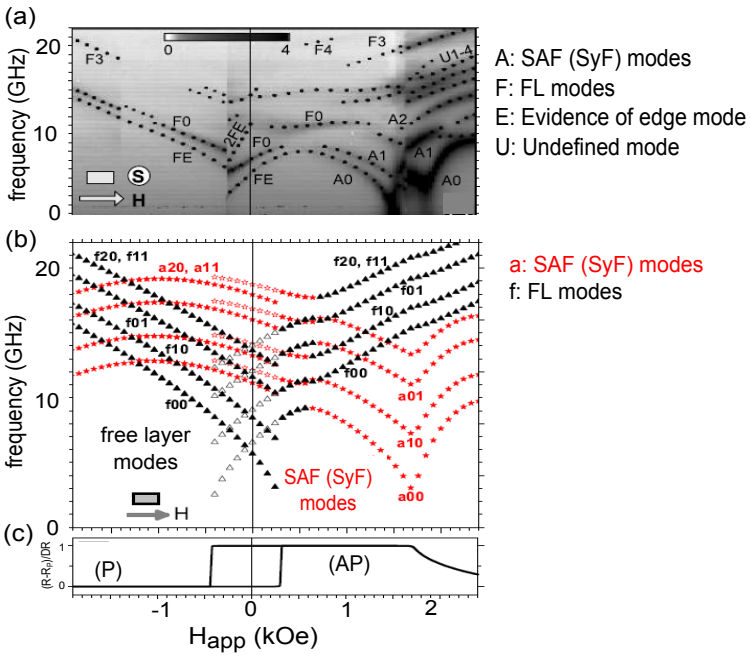

Figure 2.15 – (a) Power spectral density (PSD, log scale) of a nanopillar of $65\times100\text{nm}^2$. F: correspond to the FL modes, A: to SAF (SyF) modes, U: unidentified mode, F0:Fundamental mode of FL (high FL modes are labelled with F1,F2,F3), E: evidence of edge modes, FE: Edge modes. (b) Calculated quantized mode frequencies. (c) The corresponding RH curve of the sample.

sub-critical regime i.e, linear modes, below the critical current (small angle precession), Fig. 2.15 (b). The edge modes (small frequency than the fundamental) were identified because they disappear for high applied field values, the volumetric mode extends throughout the sample destroying edges modes (FE). The characterization of the steady

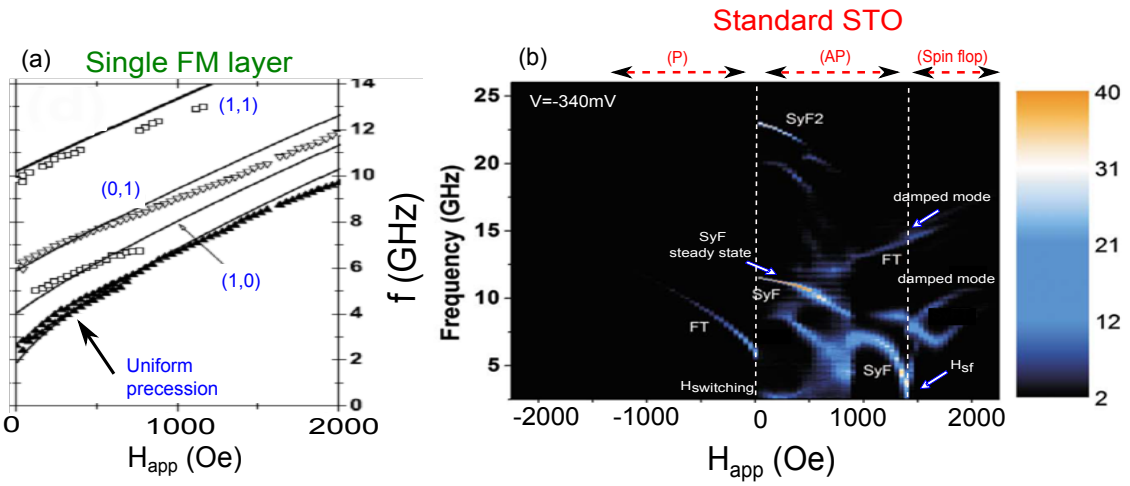

Figure 2.16 – (a) Evidence of damped modes and higher order modes of a FM layer, following the Kittel relation. They are labelled as (x,y), Adapted from Devolder [Devolder et al., 2011]. (b) PSD spectra of the standard STO. It shows the STT and damped modes for ≈340mV. Adapted from Cornelissen [Cornelissen et al., 2010].

state oscillations (STT modes) have to take into account the presence of these higher order modes in the moment of the measurements. The measured spectra of a standard STO will show the STT mode and different higher order modes of the FM layers.

Evidence of different damped modes and higher order modes have been reported by several authors in SV and MTJ structures. For example Devolder [Devolder et al., 2011] studied the thermal stability of an in-plane magnetized structure for MRAMs technologies, see Fig 2.16 (a). It shows the Kittel frequency dependence of the damped and higher order modes, labeled as (x,y). In the case of the standard STO structures, Cornelissen [Cornelissen et al., 2010] showed excitations for the SyF and FL that reveals besides the STT also numerous damped modes, see Fig. 2.16 (b). In this figure for negative applied voltage ≈340mV (negative current) the steady state oscillation in the SyF layer is achieved while the damped modes on the FM layers appears in the spectra. These results are important for his thesis work because (as we will explain further in the chapter 5), the interaction of modes produces new interesting features.

2.2 Outlook of the thesis

Since it was explained in this chapter, the steady state oscillations can be induced in a single free layer (FL), but the experimental results were not well explained considering only an isolated FL or SyF. In this thesis we will show the importance to take into account the dynamical couplings between the layers of the STO structure to understand the frequency dispersion diagrams.

We will start with the study of a basic coupled system SyF, taking into account only the RKKY coupling. We will study the magnetization dynamic, using numerical simulation, as a function of parameters such as the RKKY coupling, the exchange bias field and also the thickness of the layers, see chapter 4 . Then adding a single free layer (FL) to the structure, we will study a more complex system, called the standard STO, see Fig. 2.17, taking into account the RKKY coupling in SyF, the dipolar field between the layers and the mutual spin transfer torque (MSTT) between the SyF and the FL, see chapter 5.

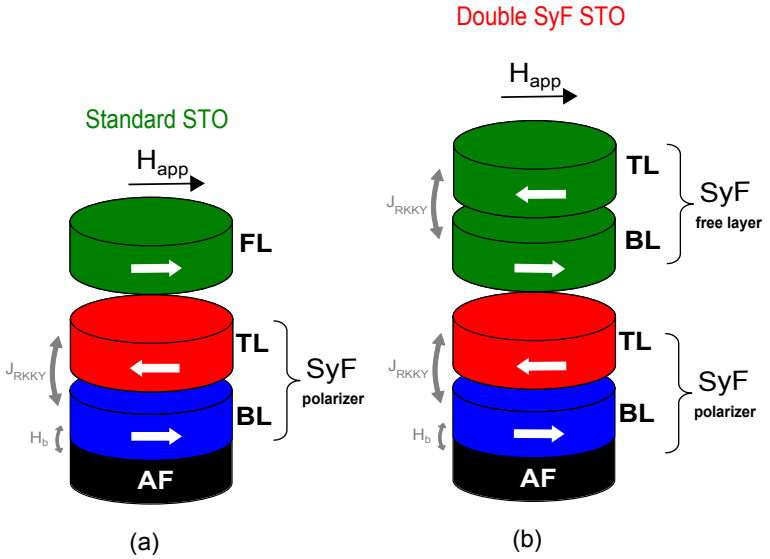

Figure 2.17 – Two types of STO structures are shown. In our reference, positive current values correspond to electrons flowing from polariser to the FL. (a) standard STO structure composed by a FL and a SyF pinned layer. (b) The double SyF (D-SyF) STO composed by a SyF pinned and a SyF FL layer.

In the second part of this thesis we will show the similitude of the numerical simulation with the experimental results. We will explain and identify the several modes on the frequency dispersion diagram, as a function of the field and current. The will found the critical boundaries between the STT and damped modes using the state diagram and the conditions to find the minimum linewidth. The crossing of the STT mode with the hybridized and higher damped modes will study compared with the numerical simulation results, focusing in the linewidth behavior, see chapter 6.

In the end of the thesis, see chapter 7, we show the excitation spectra of the D-SyF STO which is more complex. We used the support of the numerical simulations and the results of the optimization (hysteresis loops) of structures D-SyF in continuous films deposited using sputtering.

Chapter 3

Numerical Simulation and Experimental Techniques

In this chapter we present the numerical and experimental techniques used for the results obtained in chapters 4, 5, 6 and 7. In the first part, the different numerical methods are presented to study the static and dynamic response in single and coupled layers composing the STOs. In the second part, we will present the experimental techniques, including the basic concepts of transmission line theory. In the last part of this chapter, the different STO devices (based on SV and MTJ) that were used for the experimental studies in this thesis will be presented .

3.1 Theoretical Methods for the Numerical Simulations

Numerical simulations are an important aspect for the understanding and the developement of spintronics devices. Simulations help us to understand the static and dynamic magnetization behavior, to predict performances and in the end to suggest new STO structures. The magnetization dynamics of nanoscale systems can be investigated using either macrospin simulations or micromagnetic simulations.

In a macrospin approach, all the spins in a ferromagnetic layer are supposed to point in one direction, as a single macro-spin. The LLG equation is then solved for this single macrospin. By contrast, micromagnetic simulations take into account the spatial variation of the magnetization. The system is subdivided into small cells and the equations

of motion are solved for all the individual spins in all cells, taking into account the different dipolar and exchange interactions between the spins in each cell. This evidently is much more complex and much more time consuming. In the past studies on STOs, macrospin simulations proved sufficient to understand the basic issues of the spin torque driven dynamics of single layers. This is why we adopt this approach here to obtain a first understanding of the basic features for the spin torque driven dynamics of coupled structures.

In the following we present three different numerical approaches that are necessary to obtain **(i)** the static hysteresis loops and with this, the static configuration of the magnetizations in each layer as a function of an applied field, **(ii)** the spin torque driven auto-oscillations and **(iii)** the damped oscillations in the thermally activated regime and the critical boundaries.

3.1.1 Hysteresis loops and energy minimization

Before analysing the dynamic response (damped or auto-oscillation) it is important to know the equilibrium position of the magnetization as a function of field (i.e. its hysteresis loop) and other internal parameters, since this equilibrium determines the restoring torques and with this the frequency of the oscillations. In order to simulate the hysteresis loops the method of total energy minimization is used. Before presenting the method of energy minimization we present the total energy of a single free layer and of a coupled layer structure. The minimisation of this energy will then define the shape of the hysteresis loop.

3.1.1.1 Energetic contributions in a single layer

The total energy of one ferromagnetic layer (as in the case of Fig. 2.2 (b)) is represented by the sum of all the energy contributions, each one of different origin. In order to simplify the equations the reduced magnetization $\mathbf{m}$ is used, which can be expressed in spherical coordinates, $\mathbf{m} = \mathbf{M}/M_S = (\sin\theta\cos\varphi, \sin\theta\sin\varphi, \cos\theta)$. The angles and directions are defined using the coordinated system of Fig. 3.1.

$$E_{\mathrm{T}ot} = E_{\mathrm{Z}eeman} + E_{\mathrm{a}ni} + E_{\mathrm{d}emag} + E_{\mathrm{b}}. \tag{3.1}$$

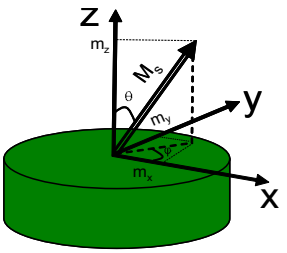

Figure 3.1 – Schema of the coordinated system for the case of a FL.

In the equation, the first term of the right is called **Zeeman energy** term and corresponds to the interaction between the magnetization $\mathbf{M}$ and the external applied field $\mathbf{H}_{app}$. The total (volume averaged) energy to align the magnetic moments into the direction of the applied field is described by,

$$E_{Zeeman} = -\mu_0 \mathbf{M}.\mathbf{H}_{app} \mathrm{V}_{Vol} = -\mu_0 M_S |\mathbf{m}||\mathbf{H}_{app}| \mathrm{V}_{Vol} \cos(\measuredangle \mathbf{M}, \mathbf{H}_{app}), \tag{3.2}$$

The system will reach the minimal value of the Zeeman energy when the magnetization and the applied field are parallel.

In solids, the electron orbitals are not symmetric (spherical) thus, the energy of the electrons depends on the orbital orientation with respect to the surrounding atoms or ions in the crystal. The interaction between the spin and the orbit (spin-orbit coupling, $(\mathbf{L}.\mathbf{S})$) will produce that the energy of the net magnetic moment in the ion depends on its orientation with respect to the axis of the crystal. This dependence is called **magnetocrystalline anisotropy**. In a cubic material the magnetocrystalline anisotropy energy is written by,

$$E_{ani} = K_{\mathrm{u}}^{'}(\alpha_1^2\alpha_2^2 + \alpha_2^2\alpha_3^2)\mathrm{V}_{Vol} + ..., \tag{3.3}$$

where the $K_u^{'}$ corresponds to the cubic anisotropy constant, and α_i corresponds to the angle of projection onto each axis (not to be confused with the damping constant). If the material has only one preferred axis we speak of uniaxial anisotropy whose equation is an expansion in even powers of the angular projection. If the magnetocrystalline anisotropy axis is represented by the unit vector $\hat{\mathbf{n}} = (1, 0, 0)$ its equation has the form,

$$E_{ani} = K_{\mathrm{u}}(1 - (\hat{\mathbf{n}}.\mathbf{m})^2)\mathrm{V}_{Vol} = K_{\mathrm{u}}(1 - m_x^2)\mathrm{V}_{Vol}. \tag{3.4}$$

The shape of the magnetic structure is responsible for another type of anisotropy, finding its origin in the demagnetization energy, which is the third term of eq. 3.1. The demagnetizing energy results from the dipolar charges at the boundaries of the sample, producing a demagnetizing field that opposes the direction of the magnetization. Here we write down the results as a function of demagnetizing field, given by the demagnetization tensor N,

$$E_{demag} = \frac{\mu_0}{2}\mathbf{m}.\mathbf{H}_\mathrm{d}\mathrm{V}_{Vol} = -\frac{\mu_0 M_S^2}{2}\mathbf{m}.\hat{N}.\mathbf{m}\mathrm{V}_{Vol} \tag{3.5}$$

The demagnetizing factors (components of the tensor) depend on the sample shape and for ellipsoids of revolution on the relative axis lengths of the ellipsoid. In the case of thin films, where the ratio between the thickness and the lateral size is much smaller than 1, we can assume that the magnetization lies in the plane of the sample and the corresponding demagnetization factors are $N_x = N_y = 0$ and $N_z = 1$, with

$$E_{demag} = 2\pi\mu_0 M_S^2 \cos^2(\theta)\mathrm{V}_{Vol} \tag{3.6}$$

Rotating the magnetization out of the film plane gives rise to a strong demagnetizing field and energy.

Besides a uniaxial anisotropy, it is possible to create an easy axis with a *unidirectional* anisotropy. This is achieved by an interfacial exchange bias between a ferromagnetic layer and an antiferromagnetic layer. A strong exchange bias field will help to keep the magnetization of the ferromagnetic layer in a given preferential orientation. This leads to the following energy contribution that has the same form as the Zeeman energy contribution and corresponds to the forth energy term of eq. 3.1.

$$E_\mathrm{b} = -\mu_0\mathbf{M}.\mathbf{H}_b\mathrm{V}_{Vol} = -\mu_0 M_S|\mathbf{m}||\mathbf{H}_b|V_{Vol}\cos(\measuredangle\mathbf{M},\mathbf{H}_b). \tag{3.7}$$

In this thesis we investigate the coupling between layers, that can arise from the RKKY interlayer exchange coupling (section 1.3) or from dipolar coupling. We therefore need to consider the total energy of a coupled two layer system consisting of a top layer (TL) and a bottom layer (BL), see Fig. 3.2.

In the following the FM layers will be indicated by the indices i and j.

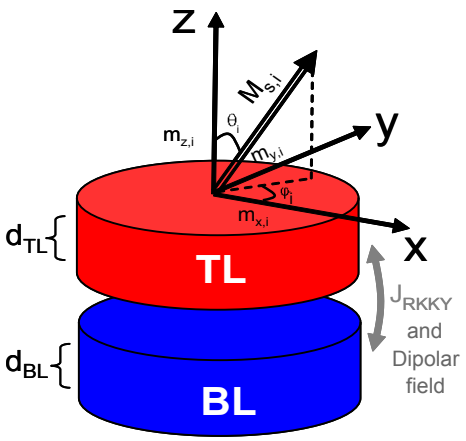

Figure 3.2 – Schema of the SyF layer composed by a TL and BL. The coordinated system on top corresponds to the case for a layer of the SyF.

3.1.1.2 Energetic contributions of a coupled system and hysteresis loop of the SyF

The total energy of the coupled system is the sum of the total energies given by eq. 3.1 of both layers, adding the terms of coupling between the two layers. These terms will be the conservative RKKY and the dipolar coupling which are given by the following equation,

$$E_{\mathrm{Tot}} = E_i + E_j + E_{int}, \tag{3.8}$$

where E_i and E_j are given by eq. 3.1 and E_{int}=E_{RKKY}+E_{dip}.

In absence of dipolar interaction and an applied field, the interlayer RKKY coupling will define the relative orientation between the two magnetizations of the i and j. If the RKKY coupling constant J_{RKKY} is negative (positive) the coupling will be antiferromagnetic (ferromagnetic). Experimentally, it was shown that this coupling oscillates between the AP and P orientation as a function of the spacer thickness, see section 1.3.

The RKKY interlayer coupling energy of eq. 3.8 is written as,

$$E_{\mathrm{RKKY}} = -J_{\mathrm{RKKY}}\mathbf{m}_i.\mathbf{m}_j\mathrm{S} \tag{3.9}$$

where S is the cross section area of the SyF structure, see Fig. 3.2.

In STO nanopillar devices, dipolar interactions have often been neglected, but as it will be shown in this thesis, they can play an important role for the static energies and configurations as well as for the magnetization dynamics.

The derivation of the dipolar interaction energy is presented in the annexe 8.3.1. Solving these equations numerically yields the components of the dipolar interaction, the tensor N_{dip}. The corresponding energy related with the dipolar interaction energy E_{dip} is written in the form,

$$E_{\mathrm{dip}_{i\to j}} = -\mu_0 M_{Si} M_{Sj} \mathbf{m}_i . N_{dip} . \mathbf{m}_j \tag{3.10}$$

where i, j are index of two FM layers.

As an example we show here the total energy of a SyF structure whose j is pinned by an exchange bias field, including RKKY and dipolar interactions between the i and j, see eq. 3.8. The coordinate system defining the easy axis direction is shown in Fig. 3.2.

$$\begin{aligned}
E_{Tot} \;=\; & -\mu_0 M_{S,j}(H_x + H_b)\sin\theta_j\cos\phi_j V_{Vol,j} - \mu_0 M_{S,i} H_x \sin\theta_i \cos\phi_i V_{Vol,i} \\
& -\frac{\mu_0 M_{S,j}^2}{2}(\sin\theta_j^2\cos\phi_j^2 N_{xx,j} + \sin\theta_j^2\sin\phi_j^2 N_{yy,j} + \cos\theta_j^2 N_{zz,j}) V_{Vol,j} \\
& -\frac{\mu_0 M_{S,i}^2}{2}(\sin\theta_i^2\cos\phi_i^2 N_{xx,i} + \sin\theta_i^2\sin\phi_i^2 N_{yy,TL} + \cos\theta_i^2 N_{zz,i}) V_{Vol,i} \\
& +K_{u,j}(\sin\theta_j^2\cos\phi_j^2) V_{Vol,j} + K_{u,i}(\sin\theta_i^2\cos\phi_i^2) V_{Vol,i} \\
& -J_{RKKY}(\sin\theta_j\cos\phi_j\sin\theta_i\cos\phi_i + \sin\theta_j\sin\phi_j\sin\theta_i\sin\phi_i + \cos\theta_j\cos\theta_i) S_{surface} \\
& +\mu_0 M_{S,j} M_{S,i} V_{Vol,i}(N_{xx}^{dipj\to i}\sin\theta_j\cos\phi_j\sin\theta_i\cos\phi_i \\
& +N_{xy}^{dipj\to i}\sin\theta_j\cos\phi_j\sin\theta_i\sin\phi_i + N_{xz}^{dipj\to i}\cos\theta_j\cos\theta_i \\
& +N_{yx}^{dipj\to i}\sin\theta_j\cos\phi_j\sin\theta_i\cos\phi_i + N_{yy}^{dipj\to i}\sin\theta_j\cos\phi_j\sin\theta_i\sin\phi_i \\
& +N_{yz}^{dipj\to i}\cos\theta_j\cos\theta_i + N_{zx}^{dipj\to i}\sin\theta_j\cos\phi_j\sin\theta_i\cos\phi_i \\
& +N_{zy}^{dipj\to i}\sin\theta_j\cos\phi_j\sin\theta_i\sin\phi_i + N_{zz}^{dipj\to i}\cos\theta_j\cos\theta_i) \\
& +\mu_0 M_{S,j} M_{S,i} V_{Vol,j}(N_{xx}^{dipi\to j}\sin\theta_i\cos\phi_i\sin\theta_j\cos\phi_j \\
& +N_{xy}^{dipi\to j}\sin\theta_i\cos\phi_i\sin\theta_i\sin\phi_j + N_{xz}^{dipi\to j}\cos\theta_i\cos\theta_j \\
& +N_{yx}^{dipi\to j}\sin\theta_i\cos\phi_i\sin\theta_j\cos\phi_j + N_{yy}^{dipi\to j}\sin\theta_i\cos\phi_i\sin\theta_j\sin\phi_j \\
& +N_{yz}^{dipi\to j}\cos\theta_i\cos\theta_j + N_{zx}^{dipi\to j}\sin\theta_i\cos\phi_i\sin\theta_j\cos\phi_j \\
& +N_{zy}^{dipi\to j}\sin\theta_i\cos\phi_i\sin\theta_j\sin\phi_j + N_{zz}^{dipi\to j}\cos\theta_i\cos\theta_j).
\end{aligned} \tag{3.11}$$

In case of more than two layers, such as in Fig. 2.17, we have to take into account the different interactions between more than two layers. The equation 8.1 has to be adapted and extended towards the situation under study.

3.1.1.3 Energy minimization and hysteresis loops

In a hysteresis loop the field is swept from a positive to a negative saturation field (and back). In order to find the corresponding equilibrium positions of **M** for each field value one has to minimize the energy of a single layer, eq. 3.8, or a coupled systems eq. 8.1. To find the equilibrium position of the magnetization vectors at a given field value H^{i+1}, the energy minimization takes as initial configuration the equilibrium positions obtained for field H_i, upon sweeping the field. For the magnetization loop M(H) the corresponding magnetization components projected onto the field direction are extracted. For the magneto-resistance curve R(H) one has to use the magnetization component projected onto a reference direction given by the direction of the magnetization of the pinned layer.

The energy minimization of eq. 3.8 or 8.1 makes use of the first derivative and second derivatives of the energy as a function of the characteristic angles, see equation 3.13 where φ_i, φ_j, θ_i, θ_j are the angles for the two layers of eq. 8.1. The energy of a single layer is obtained from eq. 8.1 by setting the energy terms for φ_i and θ_i to zero. The zeros of the first derivatives provide the extrema and the analysis of the second derivatives provides the type of extreme, in our case have to be positive (3.15) to be sure that the angles define the minima of energy.

$$\frac{\partial E_{Tot}}{\partial \theta_{i,j}} = 0 \tag{3.12}$$

$$\frac{\partial E_{Tot}}{\partial \varphi_{i,j}} = 0 \tag{3.13}$$

$$\frac{\partial^2 E_{Tot}}{\partial \theta_{i,j}^2} > 0 \tag{3.14}$$

$$\frac{\partial^2 E_{Tot}}{\partial \varphi_{i,j}^2} > 0 \tag{3.15}$$

We first demonstrate the energy minimization for a single free layer and a single FL pinned by an AF. The corresponding hysteresis loops are shown in Fig. 3.3 for the materials parameters that are introduced in table shown in the inset. Due to the exchange bias H_b=500Oe the hysteresis is shifted into the negative fields.

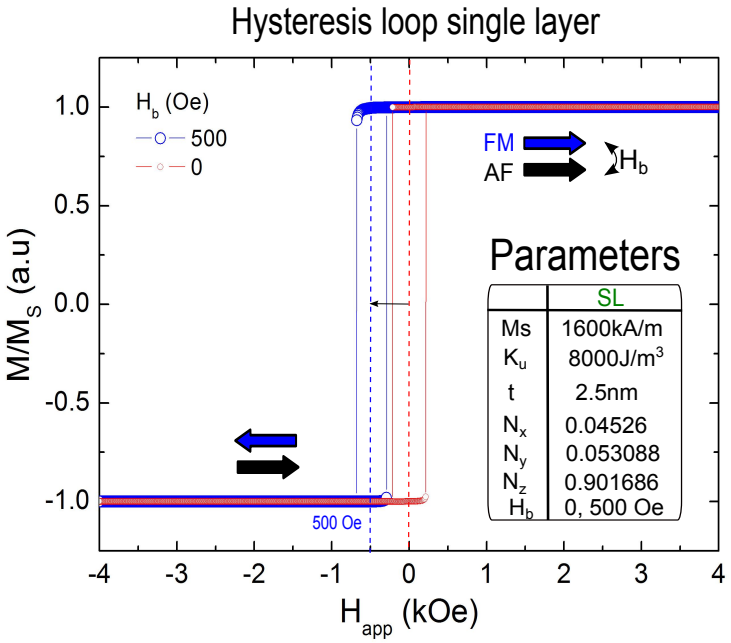

Figure 3.3 – Numerical simulation of the hysteresis loop of a single FM layer which is pinned (blue curve) and unpinned (red curve). Inset: Table of parameters.

For the simulated hysteresis loop of the magnetization configuration of the TL and BL of the SyF structure three regions can be distinguished as a function of field (applied parallel to the easy axis). The first is the plateau region, where both magnetizations remain antiparallel due to the RKKY coupling, close to zero applied field. This is the region where most of the dynamic studies are carried out. The second is the spin flop region, which is defined between the spin flop field H_{sf} and the saturation field H_{sat}. To minimize the energy the TL and BL magnetizations form an angle due to the strong RKKY coupling. This angle decreases gradually with the increase of the applied field, until both magnetizations reach the saturated magnetic state at high fields. The third region is the saturation region (positive, negative), when the applied field is strong enough to keep the two magnetizations (TL and BL) in parallel (P) pointing into the sense of the field. An example of the SyF structure, the angles used to define the magnetization of TL and BL direction and the numerical hysteresis loop of a SyF pinned layer structure is shown in Fig. 3.4.

It will be established in the following of this manuscript, the convention of the name of the SyF structures. As in literature, the SyF layer is called SAF (synthetic antiferromagnet)

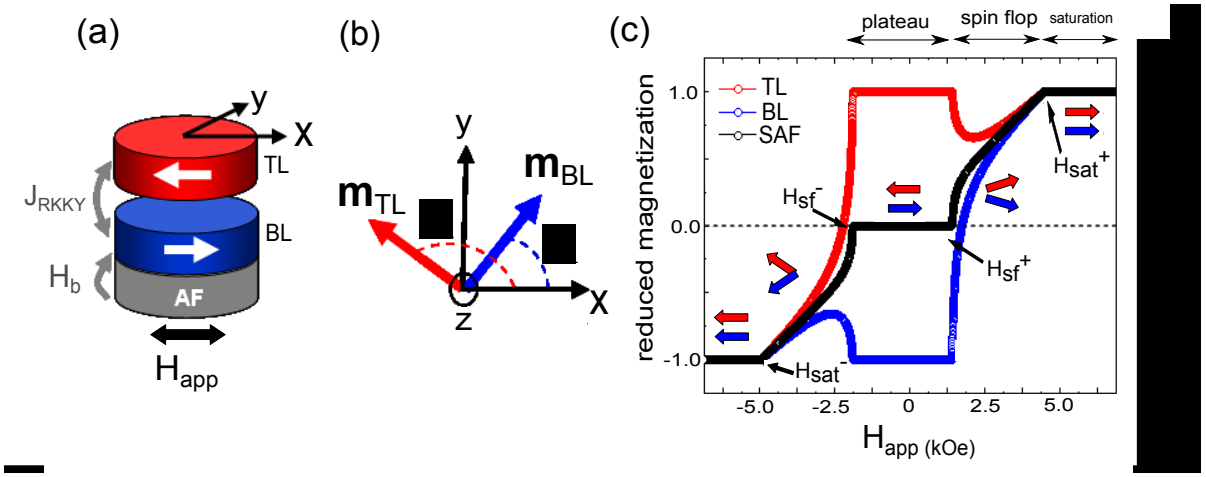

Figure 3.4 – (a) The SyF pinned structure composed by two coupled ferromagnetic layers and in contact with an antiferromagnetic layer. (b) In plane magnetization projections which are defined by angles (φ_{TL} and φ_{BL}) with respect to the easy axis, x. In (c) it is shown the hysteresis loop of a SAF pinned structure (black line, parameters in the text). The behaviour of the TL and BL magnetization is shown in red and blue lines. Arrows correspond to the magnetization direction of each ferromagnetic layer.

when the saturation magnetization M_S and thickness d meet the following condition, $M_{S,TL} \times d_{TL} = M_{S,BL} \times d_{BL}$=0.

The simulation results presented here on the SyF structure, are an introduction to chapter 4, where we will present in more detail numerical simulations on the static and dynamic properties of SyF structures as a function of the RKKY coupling strength and the exchange bias. The parameters used for these simulations are summarized in the table 3.1.

		TL	Ru	BL
Ms		1600kA/m		1600kA/m
K_u	Variable	0, 800, 8000J/m^3		0, 800, 8000J/m^3
t		2.5nm	0.8nm	2.5nm
N_x N_y N_z	Variable	0, 0.045 0, 0.053 0, 0.901		0, 0.045 0, 0.053 0, 0.901
N_{dip}		0		0
H_b	Variable 0 - 500 Oe			
J_{RKKY}	Varible 0.1 - 1 mJ/m^2			

Table 3.1 – Table of parameter for the hysteresis loops in section 4.1. This simulation corresponds to an isolated SyF pinned structure. The parameters used for the numerical hysteresis loop of Fig. 3.4 are indicated by the red squares.

3.1.2 Magnetization Dynamics and Spin Transfer Torque

The main interest of this thesis is the dynamic response in different STO devices under spin momentum transfer. In chapter 2 we already introduced briefly the main features of an STO device and summarized the dynamic properties of a single FM layer known from literature and previous studies of this group. In the following it will be introduced in more detail the macrospin simulations used to study the dynamic properties of coupled magnetic layers of the STO.

3.1.2.1 Landau-Lifshitz-Gilbert (LLG) Equation

The evolution of the magnetization vector $\mathbf{M}$(t) with time is described by the Landau-Lifshitz-Gilbert (LLG) equation taking into account the precession torque and the damping torque, eq. 2.1. In the presence of spin momentum transfer a third term needs to be added and the corresponding equation is called the Landau-Lifshitz-Gilbert-Slonczewski (LLGS) equation, which includes the Slonczewski spin torque term. In order to understand the LLGS equation we will describe the three terms, starting with the precession term and adding then the damping and subsequently the spin torque term.

The precession term is given by eq. 3.16 which describes the magnetization precession around an equilibrium axis without any losses of energy. In order to simplify the equations we used the reduced magnetization m, which can be expressed in spherical coordinates, $\mathbf{m} = \mathbf{M}/M_S = (\sin\theta\cos\varphi, \cos\theta\sin\varphi, \cos\theta)$.

$$\frac{\partial \mathbf{m}}{\partial t} = -\gamma_0(\mathbf{m} \times \mathbf{H}_{eff}) \tag{3.16}$$

Here γ_0 is the gyromagnetic ratio (2.8GHz/T). The effective field, $\mathbf{H}_{eff}$ of eq. 3.16 is given by the derivative of the total *energy density* with respect to the magnetization vector $\mathbf{M}$.

$$\mathbf{H}_{eff} = -\frac{\partial E_{Tot}}{\mu_0 M_S \partial \mathbf{m}}. \tag{3.17}$$

The effective field involves all energy contributions of the ferromagnetic layer (see annexe 8.2) where some terms are a function of the magnetization (demagnetization field and anisotropy field). This dependence gives the non-linear behaviour to this equation and

has important consequences for the magnetization dynamics.

During the precession the module of the magnetization must remain constant. As a consequence the precession of $\mathbf{m}$ occurs on the surface of the unit sphere. This is the reason why the dynamics of the magnetization vector $\mathbf{m}$=(m_x, m_y, m_z) can be described by only two independent variables.

$$\frac{\partial|\mathbf{M}_i|^2}{\partial t} = 2\mathbf{M}_i.\frac{\partial}{\partial t}\mathbf{M}_i = -\gamma_0\mathbf{M}_i.(\mathbf{M}_i \times \mathbf{H}^i_{eff}) = 0. \tag{3.18}$$

The subscript i identifies the effective field acting on one ferromagnetic layer (in the case of a SyF structure it will represent either the TL or BL layer). This equation shows that the precession of the magnetization is along a trajectory of constant energy, since damping is absent in this equation, no energy losses. In a real structure, during the magnetization precession the energy is dissipated into the material due to the coupling between the magnetization and other degrees of freedom (conduction electrons, phonon's).

The damping term in the LLG equation is responsible for the magnetization to come back to the static equilibrium position. It means that the damping term,labelled as ($\mathbf{D}_\alpha$), cannot be tangential to the trajectory but has to be perpendicular to it.

$$\mathbf{D}_\alpha.(\mathbf{M}_i \times \mathbf{H}^i_{eff}) = \mathbf{D}_\alpha.\frac{\partial \mathbf{M}_i}{\partial t}, \tag{3.19}$$

This can be seen from the fact that since $\mathbf{M}_i.\frac{d\mathbf{M}_i}{dt}$=0, $\mathbf{D}_\alpha$ has to be orthogonal to $\mathbf{M}_i$ and $\frac{d\mathbf{M}_i}{dt}$. The direction of $\mathbf{D}_\alpha$ will be defined by the vectorial product $\mathbf{M}_i \times \frac{d\mathbf{M}_i}{dt}$. The damping $\mathbf{D}_\alpha$ is in general not constant and depends on the point of $\mathbf{M}_i$ on the energy surface. The strength of the damping term is a phenomenological constant α which is called the damping parameter. Typical values for alpha are $\alpha = 0.01 - 0.02$ for a ferromagnetic metal. This damping effect is described by the second right term in the Landau-Lifshitz-Gilbert (LLG) equation 3.20.

$$\frac{\partial \mathbf{m}_i}{\partial t} = -\gamma_0(\mathbf{m}_i \times \mathbf{H}^i_{eff}) + \frac{\gamma_0\alpha}{M^2_{S,i}}(\mathbf{m}_i \times \frac{\partial \mathbf{m}_i}{\partial t}). \tag{3.20}$$

3.1.2.2 Gilbert equation enhanced by the Slonczewski term

As it was mentioned in section 1.2.3, J. C. Slonczweski and L. Berger theoretically predicted that in magnetoresistive devices the magnetization can be affected by a spin polarized current. The intrinsic damping of the sample could be counteracted by the spin transfer torque term which gives the necessary energy to the system to continue with the precession. Including this new term to the original LLG equation, it evolves into the LLG equation enhanced by the Slonczewski term, see eq. 1.13. The full LLG enhanced byt the STT term is then,

$$\frac{\partial \mathbf{m}_i}{\partial t} = -\gamma_0(\mathbf{m}_i \times \mathbf{H}^i_{eff}) + \frac{\gamma_0 \alpha}{M^2_{S,i}}(\mathbf{m}_i \times \frac{\partial \mathbf{m}_i}{\partial t}) + \frac{\gamma_0 a_j}{M^2_{S,i}}\mathbf{m}_i \times (\mathbf{m}_i \times \mathbf{p}) + \gamma_0 b_j(\mathbf{m}_i \times \mathbf{p}) \quad (3.21)$$

This equation is called the Landau-Lifshitz-Gilbert-Slonczewski (LLGS). The first term of the transfer the spin is called the Slonczewski which is characterized by the a_j term. This term depends on the applied current. The second term is the *field like* term which influence directly to the effective field. In the case of a STO based on SV the LLGS equation will take into account only the a_j term but also for MTJ's as first approximation we neglect the b_j term, [Petit, 2008]. For numerical evaluation, the LLGS equation will be rewrite in the following form,

$$\begin{aligned} \frac{\partial \mathbf{m}_i}{\partial t} &= -\frac{\gamma_0}{(1+\alpha^2)}(\mathbf{m}_i \times \mathbf{H}^i_{eff}) - \frac{\gamma_0 \alpha}{(1+\alpha^2)}\mathbf{m}_i \times (\mathbf{m}_i \times \mathbf{H}^i_{eff}) \\ &\quad + \frac{\gamma_0 \alpha a_j}{(1+\alpha^2)}(\mathbf{m}_i \times \mathbf{p}) + \frac{\gamma_0 a_j}{(1+\alpha^2)}\mathbf{m}_i \times (\mathbf{m}_i \times \mathbf{p}) \end{aligned} \quad (3.22)$$

where $a_j = j_{app} G(\eta,\theta)$,

$$G(\eta,\theta) = \frac{\hbar[-4 + 0.25\eta^{-3/2}(1+\eta)^3(3+\cos\theta)]^{-1}}{2e\mu_0 M_S d_i} \quad (3.23)$$

The pre-factor $G(\eta,\theta)$ depends on the electron charge e, the layer thickness d_i, the angle θ between the magnetization unit vector $\mathbf{m}_i$, the spin polarization unit vector $\mathbf{p}$, and the spin torque efficiency η. It is the angular dependence of spin accumulation which

important in the case of STO based on SV. In the case of MTJ's the function G is constant.

The above equations show the dynamics of a single magnetic layer $\mathbf{m}_i$. If we want to understand the magnetization dynamics of a coupled system and the role the coupling plays, we have to solve the LLGS equation for all layers simultaneously. These equations are coupled via the effective field, that contains for instance the RKKY or dipolar coupling of one layer to the other (see section 3.1.1.2 above on energy minimization).

Here we like to comment on how the spin torque term is taken into account in the SyF or SAF structure. In most experimental structures the spacer layer between the TL and BL is a thin Ru layer in which the spin polarization is strongly reduced. Consequently in the study of the magnetization dynamics in the SyF, the spin transfer torque between the TL and the BL is neglected and in the numerical simulations presented here for SyF structures, the spin polarized current acts only on the TL and the BL magnetization will precess simultaneously with the TL due to the RKKY coupling.

The dipolar coupling between two layers or the RKKY exchange coupling correspond to a conservative coupling, since they enter into the precession term via H_{eff} and therefore change mainly the precession frequency of the excited modes (more on the spectra of coupled excitations will be presented in chapter 4).

A non-conservative coupling can be taken into account via the spin momentum transfer, which is dissipative. In usual descriptions one distinguishes between one layer (the polarizer) that spin polarizes the current, but whose magnetization remains fixed, while the spin transfer torque acts only on the free layer. However, in reality also the polarizer can evolve in time and feels a spin transfer torque. Thus it is possible to couple the magnetization dynamics of both layers with spin momentum transfer. Here this coupling is called the *mutual spin transfer torque* (MSTT). The STT term in presence of the MSTT is described for layers i and j by the following equations[1],

$$(\frac{\partial \mathbf{m}_i}{\partial t})_{STT} = \gamma_0 j_{app} G(\eta) \mathbf{m}_i \times (\mathbf{m}_i \times \mathbf{m}_j) \tag{3.24}$$

$$(\frac{\partial \mathbf{m}_j}{\partial t})_{STT} = -\gamma_0 j_{app} G(\eta) \mathbf{m}_j \times (\mathbf{m}_j \times \mathbf{m}_i) \tag{3.25}$$

[1] Observe that the sign of the current changes for the opposite layer.

While the above derived LLGS equation describes well the auto-oscillation regime at 0K, the damped oscillations in the below critical regime (I<I_c) are not accessible. They can be investigated, by adding thermal noise to the system via a fluctuating field. Each Cartesian component of the thermal noise field is chosen at random from a normal distribution with a variance so the system relaxes to a Boltzmann distribution at equilibrium. This Brownian fluctuating field $H_{fluc.}$ will be part of the effective field in eq. 3.21. The autocorrelation function that determines the statistics is written by the equation,

$$< H_T^i(t), H_T^j(t') >= \frac{2\alpha k_B T}{\gamma_0 V \mu_0 M_S} \delta_{i,j} \delta(t - t'), \tag{3.26}$$

where the i, j correspond to the Cartesian coordinates and the brackets to the time average [Brown, 1963], [Xiao et al., 2005]. Including thermal noise it will be possible to investigate the linewidth of the auto-oscillation modes [Petit, 2008].

3.1.3 Numerical solution of the LLGS equation

A numerical code developed by L. Buda-Prejbeanu, based on a predictor-corrector H_{eun} described by [Garcia Palacios and Lazaro, 1998], has been used in order to study the magnetization dynamics in different systems. The numerical program solves the Landau-Lifshitz-Gilbert-Slonczewski (LLGS) equation,

$$\begin{aligned} \frac{\partial \mathbf{m}_i}{\partial t} &= -\frac{\gamma_0}{(1+\alpha^2)}(\mathbf{m}_i \times \mathbf{H}_{eff}^i) - \frac{\gamma_0 \alpha}{(1+\alpha^2)} \mathbf{m}_i \times (\mathbf{m}_i \times \mathbf{H}_{eff}^i) \\ &+ \frac{\gamma_0 \alpha a_j}{(1+\alpha^2)}(\mathbf{m}_i \times \mathbf{p}) + \frac{\gamma_0 a_j}{(1+\alpha^2)} \mathbf{m}_i \times (\mathbf{m}_i \times \mathbf{p}) \end{aligned} \tag{3.27}$$

The integration process is based on a predictor-corrector H_{eun} method using a time step of 1 fs. The integration scheme is shown in Fig. 3.5. Taking into account the initial position of the magnetization (m_{x0}, m_{y0}, m_{z0}) it is possible to compute the next position of the magnetization (for each component m_x, m_y and m_z), which are saved each 10000 steps, i.e. each 10 ps.

As a result of the simulations we will obtain the time traces of the magnetization components $m_x(t)$, $m_y(t)$, $m_z(t)$. The total time of integration of the equation has to be large

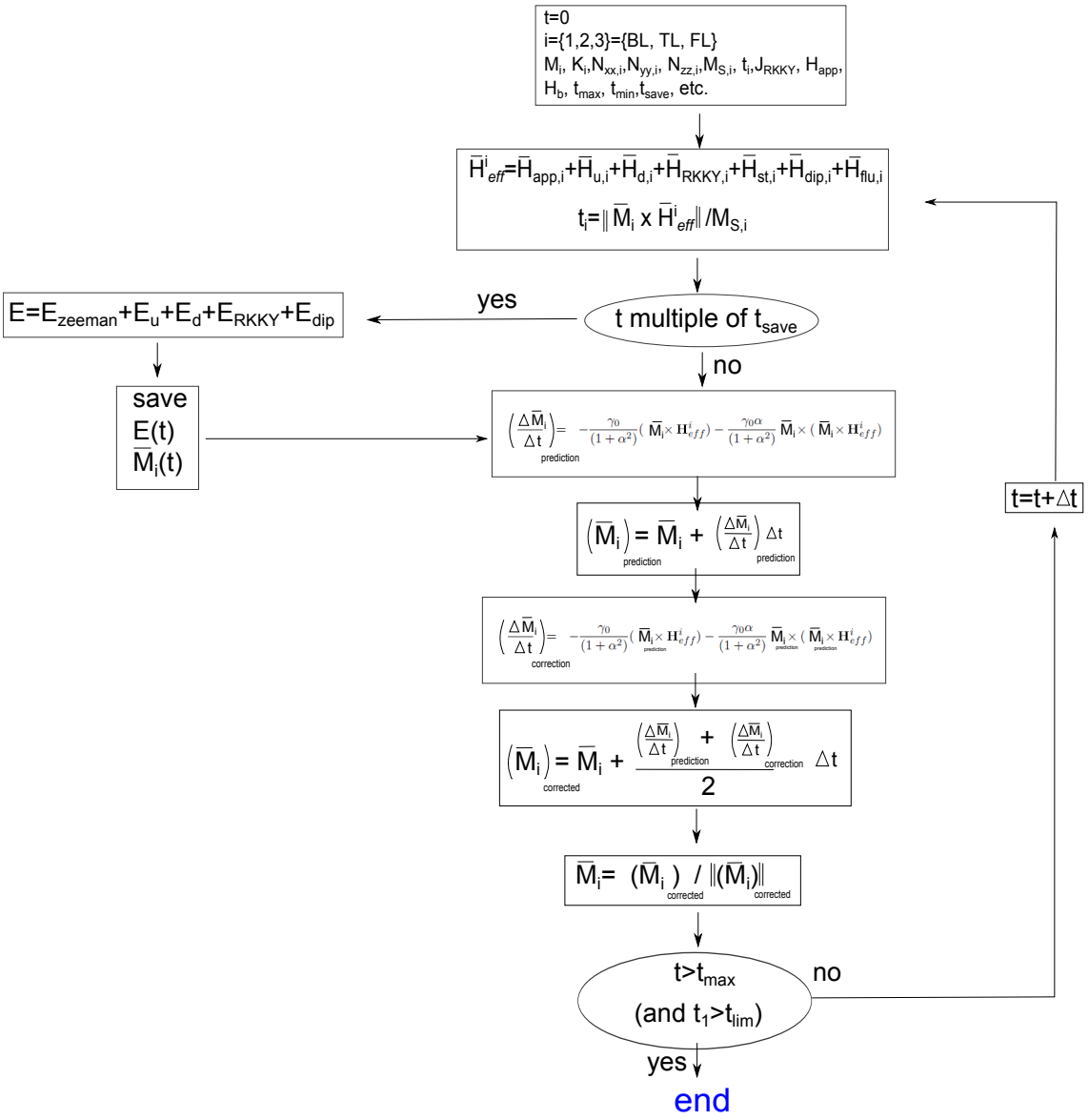

Figure 3.5 – Schematic of the numerical program based on predictor-corrector H_{eun} described by [Garcia Palacios and Lazaro, 1998], used to solve the LLGS equation

(ns) in order to give to the system the time to reach the steady state oscillations and to have sufficient frequency resolution. In the following, the traces and trajectories that will be shown in this section correspond to the numerical simulations of the FL magnetization of a **standard STO**, see table. 3.3.

As an example in Fig. 3.6 (a) and (b) we show the time traces of the $m_y(t)$ component for the FL excitations under STT at 0K. In (a), the current density was $0.1\times10^{12}A/m^2$. This case corresponds to a damped mode, where the current is below the critical current and the magnetization motion is damped, relaxing towards the initial position, see Fig. 2.3 (a). In (b), the current density was $1\times10^{12}A/m^2$ ($\xi=\frac{j_{app}}{j_c}=2.1$) and the $m_y(t)$ component shows the oscillation of the magnetization corresponding to the IPP mode. In Fig. 3.6 (c) we show the $m_z(t)$ component for a value of the current density of $3\times10^{12}A/m^2$ ($\xi=6.3$). This leads to an OPP excitation, compare to Fig. 2.3 (b) and 2.4, that is characterized by an oscillation of m_z whose average value is not zero but has a finite positive or negative value.

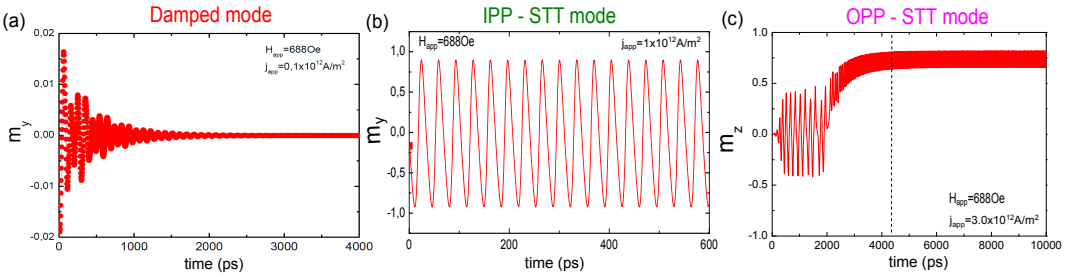

Figure 3.6 – (a)-(b) Examples of the traces of the m_y component for FL excitation of a standard STO in the damped mode and STT mode respectively. (c) The m_z oscillation remains in the positive axis, evidence of the OPP trajectory

Using the time traces of all three magnetization components the different types of excitations are identified plotting the trajectories. As another example we show in Fig. 3.7 the trajectories of the magnetization of the three layers of the standard STO, the BL, TL and FL (blue, red and green respectively), for a uncoupled and coupled system[2]. In the uncoupled cases the applied field was H_{app}=750 Oe. Using a current density of 0.48 and $3.0,\times10^{12}A/m^2$ ($\xi=2.1$ and 6.3)[3] the system reaches the IPP and OPP mode, see Fig. 3.7 (a)-(b). The TL and BL are represented by the red and blue point there are stable without excitations.

In the case of the coupled system, the applied field was H_{app}=688 Oe, see Fig. 3.7 (c)-(d). It is noted that in the coupled excitation, all three layers precess at the same frequency but at different amplitude. In this coupled system, the spin transfer torque counteracts

[2]The uncoupled or coupled correspond the dipolar coupling between the BL, TL and FL in a standard STO.

[3]The super-criticality is defined as $\xi=j_{app}/j_c$.

the damping of the FL. Due to the mutual spin torque between the FL and TL, the TL will precess following the FL movement. To finish, the BL will follow the TL movement due to the RKKY coupling and the three layers will feel the movement of the others due to the dipolar field. If the current density is increased 3.0×10^{12}A/m^2 (ξ=6.3), the FL magnetization will reach the OPP regime, as is introduced in Fig. 3.7 (d).

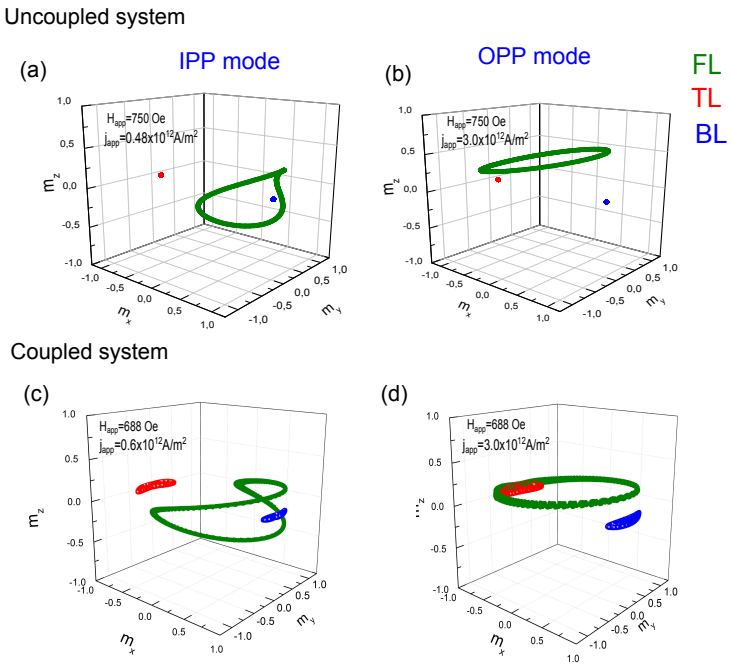

Figure 3.7 – (a)-(b) Examples of the trajectories of the IPP and OPP mode respectively, obtained from the temporal traces. In the OPP regime the component of $m_z(t)$ remains positive, see Fig. 3.6 (c).

Having extracted the components of all three magnetization as a function of the time, the Fourier transform will be used in order to pass from the temporal space to the frequency space. We define the power spectral density (PSD) which is the FFT^2. The PSD can also be calculated from the autocorrelation function R_{xx} of $\mathbf{M}(t)$.

$$R_{xx} = \frac{1}{T}\int M(t)M(t+\tau)d\tau \tag{3.28}$$

$$PSD[M(f)] = \int R_{xx}e^{-2\pi ft}dt \tag{3.29}$$

Analysing the frequency domain spectra, we can extract the number of modes and their corresponding frequency and linewidth. The evolution as a function of the applied current, field or other external or material parameters is an important aspect of the analysis.

In order to generate a state diagram, the spectra are acquired for different field values sweeping (H_{max} to H_{min}). For each field value the current is scanned from some negative to some positive value. The analysis shows for which regions of (current, field) the stationary state of the system is static or dynamic and which steady state mode is excited. An example was shown in Fig. 2.4 and another one is given in Fig. 3.8. In Fig. 3.8 (a) the state diagram is shown and in Fig. 3.8 (b) the dependence of the frequency as a function of field for different values of the current. The interpretation and analysis of these figures is provided in chapter 4.

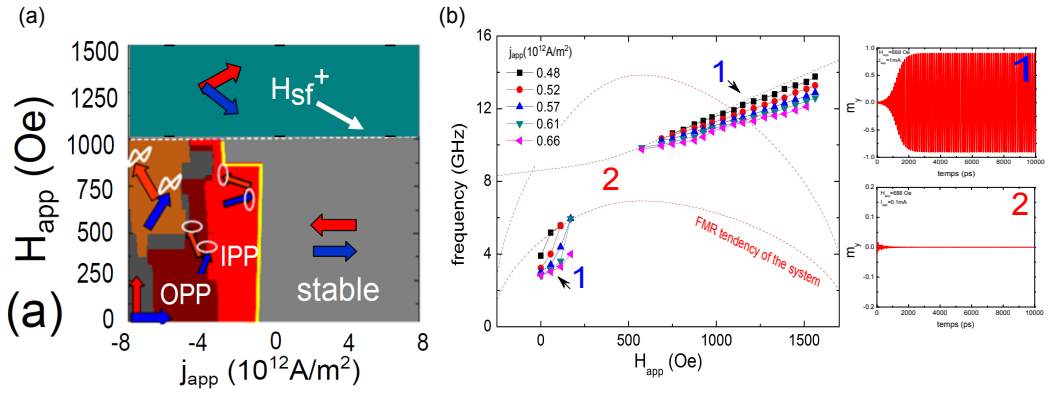

Figure 3.8 – (a) State diagram of a standard STO of a isolated SyF system. It shows the different regions of excitations and the stable states. (b) The frequency dispersion as a function of the magnetic field of a coupled FL-SyF system (standard STO). The number 1 and 2 correspond to the regions where the system reach the critical current (STT mode) and the damped modes respectively. We can observe the temporal traces of these two regimes in the right side.

In Fig. 3.9 we show schematically the different systems that were analyzed numerically during this thesis. The first system studied in chapter 4 is an isolated SyF structure that is spin polarized by an external polarizer whose magnetization is fixed and that is not coupled to the SyF magnetization. This will be done as a function of the RKKY coupling strength, the exchange bias and upon varying the TL and BL thickness and saturation magnetization. This part yields the basic properties of the SyF structure. In the next chapter 5 the SyF is coupled via dipolar interaction and via spin transfer torque to the FL. This represents the analysis of the magnetization dynamics of a standard STO taking the FL-SyF coupling into account. The experimental results are shown in chapter 6. In a final study in chapter 7 the single free layer will be replaced by a SyF free layer.

The parameters used for the numerical simulations of the magnetization dynamics of the isolated SyF structure (chapter 4) are given in table 3.2 and the parameters for the coupled FL-SyF system (standard STO), chapter 5 are shown in table 3.3.

Using the temporal traces of the magnetization it is also possible to compute the magneto-

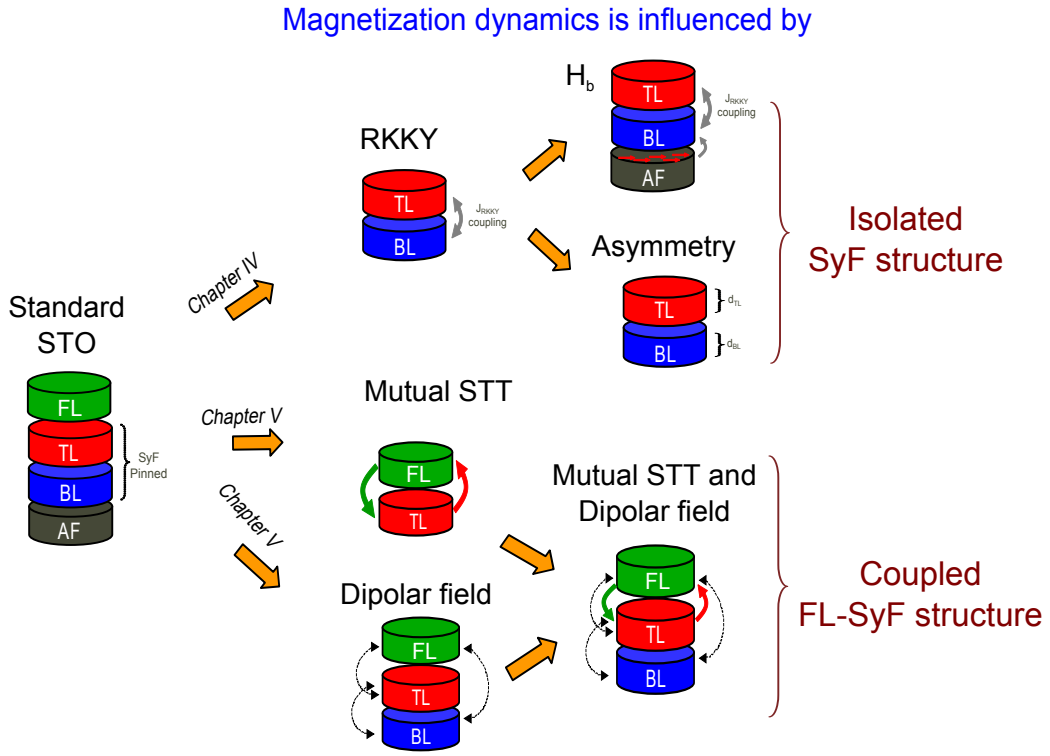

Figure 3.9 – Schematics of the different structures and couplings mechanisms over study in this thesis. First the influence of the RKKY dynamical coupling in a SyF layer as a function of the H_b and its asymmetry will be studied in chapter 4. The interlayer coupling is introduce with the study the dynamic mutual spin transfer torque (between FL and TL) and the dynamic dipolar field between the three ferromagnetic layers. This will be studied in chapter 5.

resistance output voltage of the STO and its corresponding PSD. The output voltage V(t) is,

$$V(t) = I[R_P + \Delta R(\mathbf{m}_{FL}.\mathbf{m}_{TL})/2] \tag{3.30}$$

$$\frac{V(t)}{R_P} = I[1 + MR(\mathbf{m}_{FL}.\mathbf{m}_{TL})/2] \tag{3.31}$$

where R_P is the resistance in parallel, the $\Delta R = R_{AP} - R_P$. This voltage depends of the resistance of the structure. Normalizing the voltage by R_P it is possible to include the MR (GMR or TMR), $MR = \frac{\Delta R}{R_P}$, see equation 3.31.

	SL	Cu	TL	Ru	BL
Ms			1600kA/m		1600kA/m
K_u			8000J/m^3		8000J/m^3
t			2.5nm	0.8nm	2.5 / 3.0nm
N_x N_y N_z			0.045 0.053 0.901		0.045/ 0.051 0.053/ 0.06 0.901/ 0.887
N_{dip}			0		0
H_b	0 - 200 - 500 Oe				
J_{RKKY}	0.1 - 0.5 - 1 mJ/m^2				
α	0.02				
η	0.3				

Table 3.2 – Table of parameters of the stability state diagram (Fig. 3.8 (a)) and the simulations of the isolated system of chapter 4. The top and bottom layer of the SyF are labeled as TL and BL respectively.

3.1.4 Linear excitation modes

As it will be presented in the future chapters, the frequency dispersion of the signal emitted for STO follows the ferromagnetic resonance (FMR) tendency for small values of current of the STT mode. Hence it should be fundamental the study of the FMR modes of the layers which compose the STO, in order to obtain the first idea about the dispersion behaviour. As the standard STO is composed by a FL and a SyF system, the

	FL	Cu	TL	Ru	BL
Ms	1070kA/m		1340kA/m		1600kA/m
K_u	5350J/m^3		6700J/m^3		8000J/m^3
t	3.0nm	3.0nm	3.0nm	0.8nm	2.5nm
N_x N_y N_z	0.051 0.06 0.887		0.051 0.06 0.887		0.045 0.053 0.901
H_b	0		0		500 Oe
J_{RKKY}			-1 mJ/m^2		
α	0.02				
η	0.3				
$\bar{p}$	m_{TL}		m_{FL}		

$$\hat{N}^{dip}_{TL\to FL} = \begin{bmatrix} 2.938884e-25 & 0 & 0 \\ 0 & 3.456266e-25 & 0 \\ 0 & 0 & -6.39515e-25 \end{bmatrix}$$

$$\hat{N}^{dip}_{BL\to TL} = \begin{bmatrix} 3.195453e-25 & 0 & 0 \\ 0 & 3.759008e-25 & 0 \\ 0 & 0 & -6.954461e-25 \end{bmatrix}$$

$$\hat{N}^{dip}_{BL\to FL} = \begin{bmatrix} 1.844209e-25 & 0 & 0 \\ 0 & 2.164428e-25 & 0 \\ 0 & 0 & -4.008636e-25 \end{bmatrix}$$

Table 3.3 – Table of parameters of the frequency versus field dispersion (Fig. 3.8 (b)) and all the simulations of chapter 5.

.

FMR of these two FM layers will be described. In this section the analytical expression of the FMR will be given taking into account the LLG equation without any contribution of applied current (I_{app}). The numerical method used to find the critical current and the linewidth of the FMR mode (for a structure with more than two FM layers) will be introduced in the end of this sub-section.

During the thesis we mean by FMR damped mode in absence of applied current I_{app}=0 while in presence of applied current I_{app}<I_c we speak about a damped mode.

3.1.4.1 Ferromagnetic resonance modes (FMR) in a single layer, sub-critical regime

The analytical expression of the FMR, of a single FM layer, will be obtained taking into account the energy contributions terms in spherical coordinates and using the Smit and Beljers derivation in spherical coordinates, $\mathbf{e}_\rho = (\sin\theta\cos\varphi, \sin\theta\sin\varphi, \cos\theta)$, $\mathbf{e}_\theta = (\cos\theta\cos\varphi, \cos\theta\sin\varphi, -\sin\theta)$ and $\mathbf{e}_\varphi = (-\sin\varphi, \cos\varphi, 0)$.

In order to re-write the LLG equation in terms of the spherical coordinates, the derivative

of $\mathbf{M}$ and the effective field in this coordinate system must be found: $\dot{\mathbf{e}}_\rho = \sin\theta\dot{\varphi}\mathbf{e}_\varphi + \dot{\theta}\mathbf{e}_\theta$, $\dot{\mathbf{e}}_\theta = -\dot{\theta}\mathbf{e}_\rho + \cos\theta\dot{\varphi}\mathbf{e}_\varphi$ and $\dot{\mathbf{e}}_\varphi = -\dot{\varphi}(\sin\theta\mathbf{e}_\rho + \cos\theta\mathbf{e}_\theta)$. The effective field is obtained using the eq. 3.17 for the case of a single layer, which is given by eq. 3.1 and re-writing the effective field in the form of,

$$\mathbf{H}_{eff} = H_\rho\mathbf{e}_\rho + H_\theta\mathbf{e}_\theta + H_\varphi\mathbf{e}_\varphi \tag{3.32}$$

where H_ρ, H_θ and H_φ are the components of the effective field in the basis ($\mathbf{e}_\rho$,$\mathbf{e}_\theta$, $\mathbf{e}_\varphi$). The components of the effective field 3.32 will be found using the gradient operator, $\nabla = \frac{\partial}{\partial\rho}\mathbf{e}_\rho + \frac{1}{\rho}\frac{\partial}{\partial\theta}\mathbf{e}_\theta + \frac{1}{\rho\sin\theta}\frac{\partial}{\partial\varphi}\mathbf{e}_\varphi$, and the equation $\mathbf{H}_{eff} = -\dfrac{\nabla E(\theta,\varphi)}{\mu_0 M_S}$. The precession term of the LLG equation takes the following form in spherical coordinates,

$$\frac{d\mathbf{M}}{dt} = -\gamma_0\mathbf{M}\times\mathbf{H}_{eff} = -\gamma_0(-H_\varphi\mathbf{e}_\theta + H_\theta\mathbf{e}_\varphi). \tag{3.33}$$

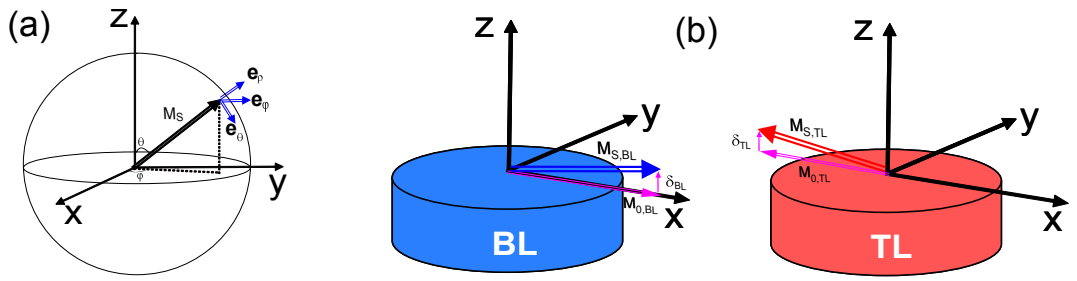

Figure 3.10 – (a) The spherical coordinates used in this section. (b) Schematics of the small deviation of the magnetization for the TL and BL, $M_{Si} = M_{0i} + \delta_i$. This magnetization deviation will correspond to the angular deviation given by eq.3.34 and 3.35.

In equilibrium, magnetization will remain in the state of minimal energy but, when the system is perturbed, the magnetization can be described as a precession around its equilibrium position, defined by (φ_0, θ_0).

$$\theta = \theta_0 + \delta\theta; \qquad \delta\theta << \theta_0 \tag{3.34}$$

$$\varphi = \varphi_0 + \delta\varphi; \qquad \delta\varphi << \varphi_0 \tag{3.35}$$

using a linear development of the energy function one obtains,

$$E_\theta = E_{\theta\theta}\delta\theta + E_{\theta\varphi}\delta\varphi \tag{3.36}$$

$$E_\varphi = E_{\varphi\theta}\delta\theta + E_{\varphi\varphi}\delta\varphi \tag{3.37}$$

where E corresponds to the total energy density of the magnetic system, see eq. 3.1. Introducing these components in the equation 3.33 one obtains,

$$-\frac{M_S}{\gamma}\sin\theta_0\frac{\partial\theta}{\partial t} = E_{\varphi\theta}\delta\theta + E_{\varphi\varphi}\delta\varphi \tag{3.38}$$

$$\frac{M_S}{\gamma}\sin\theta_0\frac{\partial\varphi}{\partial t} = E_{\theta\theta}\delta\theta + E_{\theta\varphi}\delta\varphi. \tag{3.39}$$

The magnetization motion is supposed to be periodic, therefore the solutions of eq. 3.38 and 3.39 will be of the form of $\delta\theta{=}Re(\delta\theta_0 e^{i\omega t})$ with $\dot{\delta\theta} = iw\delta\theta$ for both angles. We will re-write the equation in the matrix form as,

$$0 = \begin{bmatrix} E_{\varphi\theta} + i\omega\frac{M_S\sin\theta_0}{\gamma} & E_{\varphi\varphi} \\ E_{\theta\theta} & E_{\theta\varphi} - i\omega\frac{M_S\sin\theta_0}{\gamma} \end{bmatrix}\begin{bmatrix}\delta\theta \\ \delta\varphi\end{bmatrix} \tag{3.40}$$

The determinant of this matrix has to be equal to zero, in order to find non trivial solutions. The precession frequency ($f = 2\pi\omega$) around the effective field is given by the Smit and Beljers formula in terms of the internal energy derivatives,

$$f = \frac{\gamma_0}{2\pi}\left(\frac{\partial^2 E}{\partial\varphi^2}\frac{\partial^2 E}{\partial\theta^2} - \frac{\partial^2 E}{\partial\theta\partial\varphi}\right)^{1/2} \qquad |\theta_0, \varphi_0. \tag{3.41}$$

In the case of the single FL with an exchange bias, magneto-crystalline and shape anisotropy the frequency will be expressed as,

$$f = \frac{\gamma_0}{2\pi}\sqrt{(H_{app} + H_b + H_u)(H_{app} + H_b + H_u + 4\pi M_s)} \tag{3.42}$$

This equation will describe the uniform mode frequency as a function of the applied field. In Fig. 3.11, the FMR frequency of the FL of the standard STO is plotted with the corresponding hysteresis loop (parameters in table 3.3). During the sweeping from positive to negative magnetic field the frequency goes to zero when the effective field becomes to zero, *mode softening*.

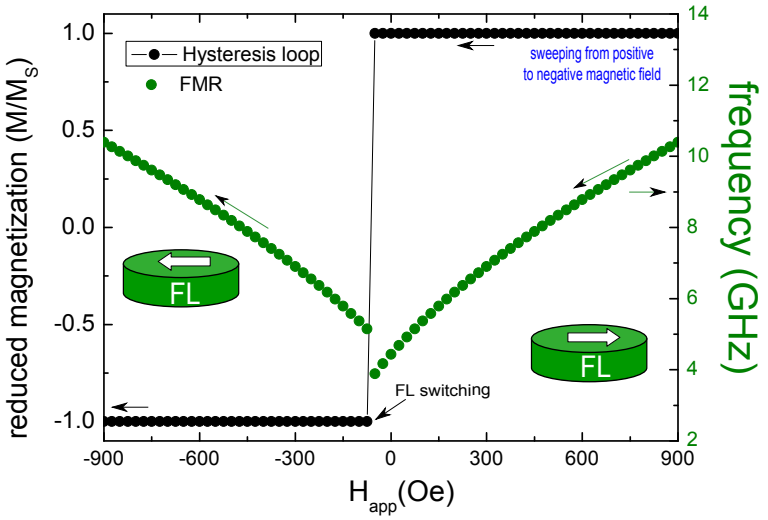

Figure 3.11 – (green)Frequency versus magnetic field, sweeping from positive to negative magnetic field. (black) The corresponding half-hysteresis loop of the FL for the same sweeping. Parameters of the FL on table 3.3 without dipolar field.

3.1.4.2 Ferromagnetic resonance modes (FMR) in a coupled system SyF

Using the same formalism of the previous section, the FMR frequency (I_{app}=0) of a SyF system will be obtained as a function of the total energy, in this case two precession equations should be solved simultaneously.

$$\frac{d\mathbf{m}_{TL}}{dt} = -\gamma_0 \mathbf{m}_{TL} \times \mathbf{H}_{eff}^{TL} \tag{3.43}$$

$$\frac{d\mathbf{m}_{BL}}{dt} = -\gamma_0 \mathbf{m}_{BL} \times \mathbf{H}_{eff}^{BL} \tag{3.44}$$

The linearization of these equations and its characteristic matrix is given in the annexe 8.3, equation 8.21. In contrast to the case of a simple ferromagnetic layer where only one precession mode exists, in the case of a SyF structure two modes co-exist. In Fig. 3.12 (a) we show the numerical simulation of the FMR modes for a single layer, parameter of the single free layer (FL) in Table 3.3. The case of two dynamical uncoupled FM layers (only static coupling between them) is shown in Fig. 3.12 (b) and a coupled SyF structure is shown in Fig. 3.12 (c). The parameter of the FMR modes of Fig. 3.12 (c) are given in Table 3.2.

In Fig. 3.12 (b) the red curve correspond to the TL and the blue curve to the BL pinned by the antiferromagnetic (AF) layer. If a conservative coupling such as the RKKY interaction is introduced, the modes will split at the crossing of their frequencies. This splitting is

proportional to the strength of the RKKY coupling, see Fig. 3.12 (c).

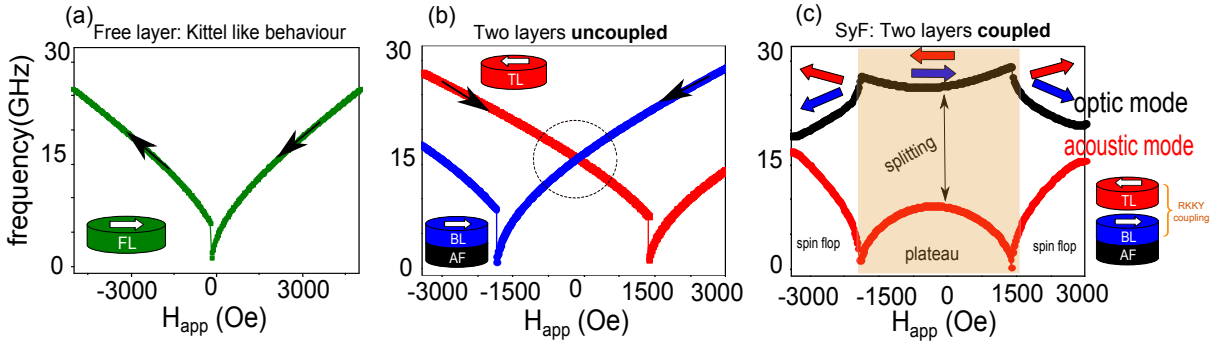

Figure 3.12 – The FMR evolution from a single layer (a), two layers uncouple (b) and in (c) a coupled SyF structure. The introduction of a conservative RKKY coupling to the system of two layer will create a hybridization of the two modes of (b). In a coupled SyF system it is presented two modes with small frequency, the acoustic (red) and optical (black) modes.

In Fig. 3.12 (c) the two excitation modes of the SyF structure are shown. The mode with the small frequency is called the acoustic mode (red) and the mode with high frequency is the optical mode. This definitions comes from the relative phases between the TL and BL magnetizations, Fig. 3.13.

In Fig. 3.13 (a) and (b) we can observe the trajectory of the precession of the acoustic and optical mode. Numbers correspond to the sense of the magnetization trajectory. The acoustic mode corresponds to the two magnetizations precessing in-phase in z and out of phase in the plane xy. The optical mode corresponds to the fact of both magnetizations precess in-phase in the plane xy but out phase in z. Due to the RKKY coupling of the SyF, the optical mode involves high energy due to the relative position of the magnetization in xy, giving rise to high frequencies, see Fig. 3.13 (c).

In section 4.2 the FMR modes of the isolated SyF will be shown, solving the precession term of the LLG equation and the coupled equations numerically. The parameters of those simulation are shown in the table 3.2.

3.1.4.3 Linearisation of the LLGS equation and characteristic matrix of the magnetic system

In the previous section, using standard techniques we found the analytical solution of the linearisation of the LLGS equation of coupled systems such as the standard STO. In the case of this structure, one has to solve three equations simultaneously, corresponding for the FM layers (BL, TL, FL). These equations are coupled by the dipolar field term (inside

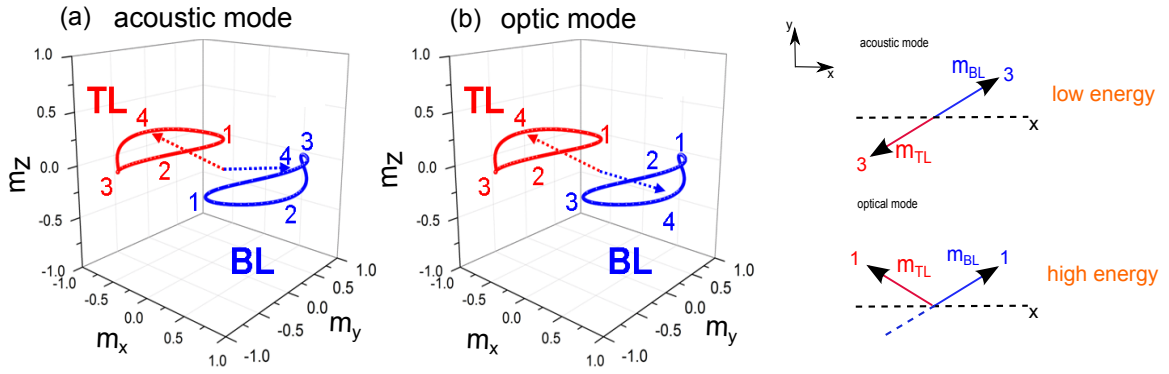

Figure 3.13 – In (a) and (b) is presented the acoustic and optical mode trajectory of the SyF structure. The numbers correspond to the sense of the magnetization in one period. In (c) magnetization position for acoustic and optical modes. The energy due to the RKKY interaction (AP configuration) is smaller in the case of the acoustic mode.

the effective field) and the non conservative mutual spin torque. The method that we will detail in this section will help us to study the excitation modes and the attenuations of the FMR modes (I_{app}=0) and the damped modes ($I_{app} \neq 0$). Studying the attenuation behaviour we will be able to find the critical current I_c where the system becomes unstable (STT modes). In this method the temperature is not taken into account.

The method consists in the linearisation of the torque, $\mathbf{T}=\frac{d\mathbf{M}}{dt}$ around an equilibrium position $\mathbf{M}_0=(M_0,0,0)$[4], taking into account only the a_j term of the spin momentum transfer, see eq. 3.27 (b_j term is neglected).

$$\frac{d\mathbf{M}}{dt} = \frac{d\Delta\mathbf{M}}{dt} = \mathbf{M}_0 + \frac{d\mathbf{T}}{d\mathbf{M}_y}|_{M=M_0}\Delta\mathbf{M}_y + \frac{d\mathbf{T}}{d\mathbf{M}_z}|_{M=M_0}\Delta\mathbf{M}_z \tag{3.45}$$

Each component of the magnetization will present two degrees of freedom, hence the torque $\mathbf{T}=\frac{d\mathbf{M}}{dt}$ can be described by six equations. These equations can be written in the form of a matrix which has to be diagonalised. Supposing a periodic solution of the magnetization of the form $\mathbf{M}=M_o(\pm1,0,0)+(0,n_y,n_z)e^{pt}$, the eigenvalue will be the complex number $p=\lambda+i\omega$. In this kind of solution λ corresponds to the **attenuation** i.e a negative value means that the system will decay into a stable state (damped modes) and a positive value of λ indicates that the system becomes unstable (STT modes). The term ω will correspond to the 2π frequency of the excitation.

[4]Initial magnetization pointing into the x direction.

As an example in Fig. 3.14 (a) and (c), the imaginary part of the eigenvalue which corresponds to the excitation frequency are plotted for the single layer (FL) and for a SyF/AF system. In the case of the SyF the acoustic and optical mode are plotted in the plateau region. In Fig. 3.14 (b) and (d), the corresponding attenuations (λ) of the excitation modes are shown .

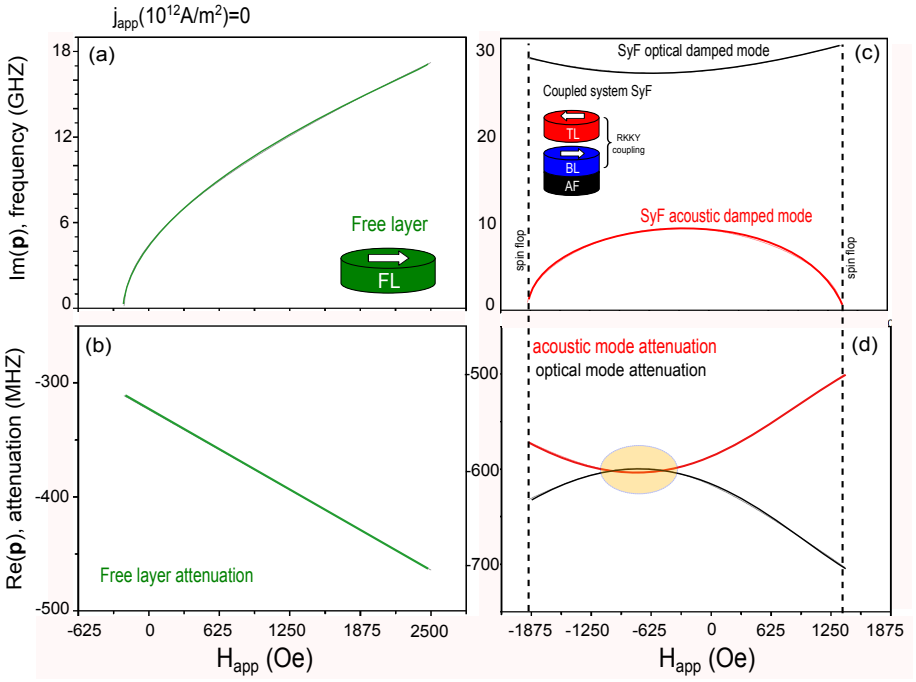

Figure 3.14 – Real (λ) and imaginary (ω) the eigenvalue of the characteristic matrix of a single layer (a)-(b) and a SyF pinned layer (c)-(d). Parameters table 3.3 without dipolar field.

The attenuation of the FL decreases as a function of the applied field. In contrast, the attenuations of the two modes of the SyF show a variable behaviour and a crossing of curves, see orange circle in Fig. 3.14 (d).

The value of the attenuation will give us one criteria to find the critical current of the STT mode because the system in the damped mode will present a negative attenuation (λ). The attenuation will start to increase or decrease as a function of the applied current. When the attenuation of the mode becomes positive, it corresponds already to the STT modes (auto oscillations). The passage from negative to positive defines the critical current, i.e the current where the attenuation is zero: $\lambda(I)=0 \rightarrow I=I_c$.

Using the definition of the Fourier transform (FFT) for the solution $\mathbf{M} \propto e^{pt}$, one obtain a Lorentzian function, as is shown in the following,

$$L(f) = FFT[M(t)] = \int e^{-pt} e^{-2\pi f t} dt = \int e^{-(\lambda + i\omega)t} e^{-2\pi f t} dt \tag{3.46}$$

$$= \frac{1}{\lambda + (\omega + \omega_0)i} \tag{3.47}$$

From the Lorentzian function it is possible to identify the linewidth, which is related with the real part of the eigenvalue of **p**, in the form $\Delta f = \lambda/2$. This is an important result of this method because it provides the possibility to study the linewidth of the FMR and damped modes as a function of the internal and external parameters, solving the characteristic matrix of the system. Coming back to the shadow orange region of Fig. 3.14 (d) the optical mode shows a small linewidth and amplitude than the acoustic mode.

Experimentally, the criteria to find the critical current is to plot the frequency and linewidth as a function of the applied current. Normally for small current, the linewidth presents a first range where it is reduced abruptly and another one where its reduction is less. A straight line can be drawn following the first points (which correspond to the damped regime). The crossing of the extrapolation of the line with the current axis, $\Delta f = 0$, will indicate the critical current, I_c.

In chapter 5, the linearised LLGS will be used in order to obtain the stability diagrams (critical currents), the frequency and the attenuation (and linewidth) of damped modes as a function of the applied field. The parameters used in these simulations are given in the table 3.3.

3.2 Experimental techniques

3.2.1 Basic Concepts of transmission lines

When the wave length of the signal is comparable to the length of the cables and components of the measurement setup[5], the quasi-static approximation that allows one to use Kirchhoff's law is not suitable. We must introduce the electromagnetic waves formalism from Maxwell's equations in order to describe the microwaves propagation along the chain of measurement. The spatial variations of the signal in a transmission line is modeled

[5]For example, 5 GHz corresponds to a wavelength of 6 cm

using the Fig. 3.15. In the circuit, the letter C corresponds to the capacitance and L to the inductance. In the transmission line the signal is propagated in the +z direction. In

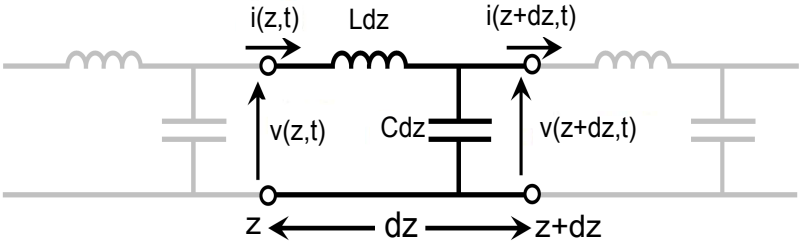

Figure 3.15 – Ideal model of the transmission line.

the telegrapher model, the wave will be propagated in an infinite medium, separated in infinitesimal parts dz, where Kirchhoff laws are validated. The Kirchhoff laws (of voltage and current) applied in the circuit will give us the following equations,

$$v(z,t) = Ldz\frac{\partial i}{\partial t}(z,t) + v(z+dz,t) \tag{3.48}$$

$$i(z,t) = Cdz\frac{\partial v}{\partial t}(z,t) + i(z+dz,t) \tag{3.49}$$

In the case of a lossless system, we will only describe the propagation (v,i) in terms of C and L. In order to find two differential equations to describe the wave inside the transmission line, we will change the form of the previous two equations. We can divide the equation by dz which tends to zero in the limit $dz \longrightarrow 0$. These new equations are called the telegrapher equations. They can be solved simultaneously finding,

$$\frac{\partial^2 v}{\partial z^2} - \frac{1}{LC}\frac{\partial^2 v}{\partial t^2} = 0 \tag{3.50}$$

$$\frac{\partial^2 i}{\partial z^2} - \frac{1}{LC}\frac{\partial^2 i}{\partial t^2} = 0 \tag{3.51}$$

where the solutions of these equations are written as plane wave functions, with the frequency ω, defined as a function of the phase velocity $\omega = \nu_\varphi \kappa$, where ν_φ=1/LC. These solution will be of the form,

$$v(z,t) = (v_0^+ e^{-ikz} + v_0^- e^{ikz})e^{i\omega t} \tag{3.52}$$

$$i(z,t) = (i_0^+ e^{-ikz} + i_0^- e^{ikz})e^{i\omega t} \tag{3.53}$$

where $v_0^{\pm}$ and $i_0^{\pm}$ represent the voltage and current waves amplitudes. The characteristic impedance is defined as $Z_c = \sqrt{L/C}$. In a real case of transmission lines, the resistance R and the conductance G will introduce the losses in the system. The real impedance will be a complex quantity depending on the frequency, $Z_c = \sqrt{\frac{R+i\omega L}{G+i\omega C}}$. In Fig. 3.16, the real circuit of the transmission line is shown. The real impedance of transmission lines

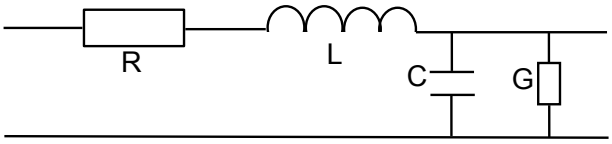

Figure 3.16 – Real model of the transmission line system.

depends on its geometry and electrical properties that could be for example the size of the cables or the dielectric media inside them. Commercial RF elements such as amplifiers, cables, bias-tee present 50Ω of characteristic impedance. The impedance is related with the energy (power) propagation of the wave in the transmission lines. In the case of the resistance, the losses are related with the dissipation of energy.

3.2.1.1 Mismatching of impedance

In the previous section we summarized the transmission lines of a system with a characteristic impedance. The wave will be propagated with the same properties but if two transmission lines with different impedance are connected, we have to introduce interface conditions. In Fig. 3.17 (a) we show the schematic of the two transmission lines (1 and 2) with different impedances, Z_{c1} and Z_{c2}. Considering a plane wave v_1^+ which is traveling

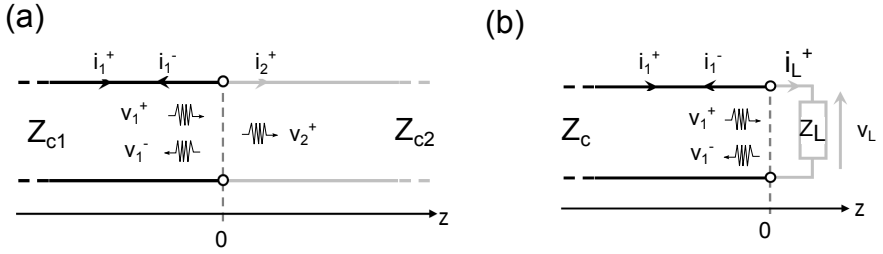

Figure 3.17 – (a) Mismatching between two transmission lines with different impedance in z=0. (b) Transmission line terminated by a load of Z_L.

through the transmission line, from 1 to 2, when this wave reaches the interface, one part of this wave is reflected and the other is transmitted. Hence we define the transmission and reflection coefficients as,

$$\Gamma_{reflex} = \frac{v_1^-}{v_1^+} \tag{3.54}$$

$$\Gamma_{trans} = \frac{v_2^-}{v_2^+} \tag{3.55}$$

The current continuity $i_1^+ = i_1^- + i_2^+$ will help us to write these two coefficients as a function of the two impedances.

$$\Gamma_{reflex} = \frac{Z_{C2} - Z_{C1}}{Z_{C2} + Z_{C1}} \tag{3.56}$$

$$\Gamma_{trans} = \frac{2Z_{C2}}{Z_{C2} + Z_{C1}} \tag{3.57}$$

It is clear now, that a mismatching between the transmission lines will give us a reflection of the incident wave, losses of energy and reduce the transmission power. In our case, we can replace the second impedance for the load impedance Z_L, see Fig.3.17 (b).

$$\Gamma_{reflex} = \frac{Z_C - Z_L}{Z_C + Z_L} \tag{3.58}$$

3.2.1.2 Correction of the STO emitted signal measurement

The correction of the STO emitted signal involves a protocol of measurement which is done automatically by the program of acquisition. The ground signal (amplitude (V) vs frequency (GHz)) is measured before to applied dc current through the STO in order to estimate the bruit which is by default in the measurement. The next step is the measurement of the emitted signal sweeping the dc current or magnetic field. The ground signal is subtracted from the measurements. This results have to be transformed into PSD (nV^2/Hz) which have to be corrected using the transference function G(f).

The ac voltage measurement received by the spectrum analizer have to be corrected using a voltage divider. The Fig. 3.18 represents the voltage divider used to obtain the STO emitted voltage.

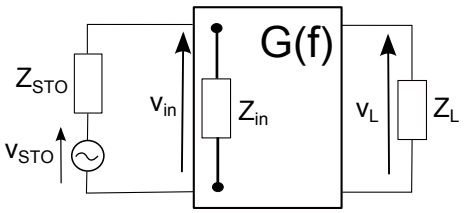

Figure 3.18 – Voltage divider to obtain the correction of the voltage emitted from the STO (V_{STO}) and the measures.

The STO has an impedance defined in the Fig. 3.18 as Z_{STO} which emitted a signal V_{STO} into the setup of measurement. This setup has a gain G(f) and an impedance labeled as Z_{in}. The signal which is measured by the spectrum analizer is represented by V_L on the load of impedance Z_L. Following the voltage divider of Fig. 3.18 we obtain the STO voltage,

$$V_L = G\frac{Z_{STO}}{Z_{in} + Z_{STO}}V_{STO} \tag{3.59}$$

Using this voltage V_{STO}, the dynamical resistance has been calculated as it was explained by Houssameddine [Houssameddine et al., 2007], using the power of the emitted signal. The following equations describe the dynamical resistance as a function of ΔV_L and ΔV_{STO} which correspond to the voltage measured by the spectrum analyser and the voltage of the device respectively. This dynamical resistance will used in the experimental results to identify if the transition from the IPP to OPP mode.

$$\Delta R_{dyn} = 2(2)^{1/2}\Delta R_{rms} = 2(2)^{1/2}\Delta V_L/I_{dc}. \tag{3.60}$$

$$\Delta U_L = (\frac{Z+R}{Z})\Delta V_{STO}. \tag{3.61}$$

3.2.1.3 Microwave transmission and scattering matrix

The previous results highlight the importance of a good matching between the element of our setup. This condition is not always accomplished, generating losses in the STO emitted signal. As it is important to know the real emitted power of the STO, it should be studied the signal when it is transmitted through each RF component (cable,amplifier, bias-tee, etc) of the measurement setup.

The output signal (v_2, i_2) of one element is related with the incident (v_1,i_1) signal by a transmission function, which is represented by a matrix, the transmission matrix (ABCD), Fig. 3.19 (a).

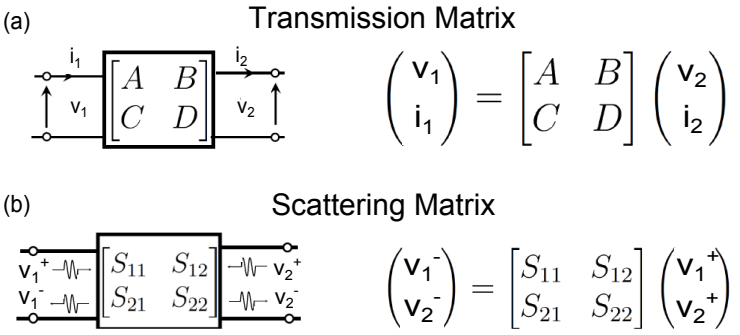

Figure 3.19 – (a) Transmission Matrix (ABCD) with the corresponding input and outputs. (b) Scattering Matrix with the corresponding input and outputs

Using this matrix we can quantify the effect of the element on the signal and find the

transfer function *G(f)* of the experimental setup. This function will be the product of all the individual matrices of each element of the experimental setup. We can obtain the emitted voltage for the STO as a function of the voltage measured, $v_m \approx G(f).v_{STO}$. In order to obtain the T matrix one can measure the scattering matrix S for each component of the chain, using a vector network analyzer (VNA). A completely explanation about the measurement of the scattering matrix component S_{21} is shown by M. Quinsat, [Quinsat, 2012]. In programs used in this thesis to process the data of the measurements the total gain of the setup is included to correct directly the measurement using the individual gain of each element.

The STO devices based on SV has a load impedance between 30-60Ω which is close to the characteristic 50Ω of the chain. Since the STO based on MTJ devices and impedance of 150-1kΩ, the total power is not fully transmitted due to the mismatching of the chain explained above. We should introduce the corresponding correction to have a real value of power emitted by the STO.

3.2.2 Experimental RF measurement

The experimental setup to characterize the STO devices is shown in Fig. 3.20. The STO device will be positioned in the middle of a magnetic field, created by the electromagnet where the sweeping of the magnetic field (from positive to negative and vice-versa) is controlled using a Kepco power supply. The applied dc current is controlled by a current source using an interface with a computer to give us the possibility to obtain automatic measurements. We will explain in the next section that the first measurement in the process to characterized a STO device should be the static measurement of the magneto-resistance (MR) curve.

The applied dc current[6] passes first through a bias-tee component (dc input) and then it is injected into the STO. The dynamic resistance which is generated in the STO, due to the effect described previously, generates an ac voltage measured through the ac output of the bias-tee. This ac signal is amplified before to be measured with the spectrum analyser, in the range of 1 GHz-26 GHz.

The power measured is related directly with the magnetization dynamics through the magneto-resistance effect in the STO. An estimation of the maximun power emitted by

[6]Generally between 1-4mA and 0.1-1mA for STO based on SV and MTJ respectively.

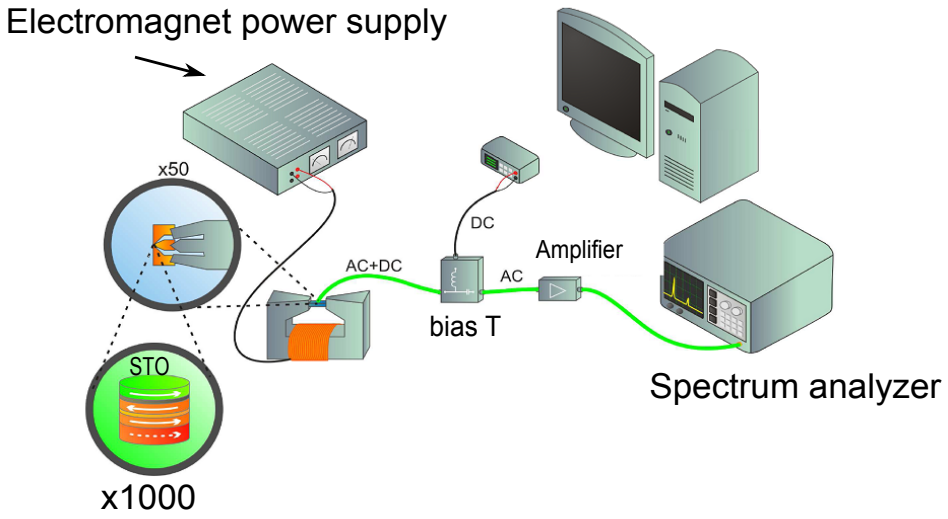

Figure 3.20 – Experimental setup for the static and RF measurements. The sample is exposed to an external controlled magnetic field. A bias-tee allows us to applied dc current to the STO and measure the emitted ac signal separated. This ac signal is amplified (G(f)) and measured with an spectrum analyzer. Adapted from [Houssameddine, 2009]

an STO is given by following equation,

$$P_{out} = I_{dc}^2 R \frac{\beta}{(1+\beta)}(MR)^2 \tag{3.62}$$

where MR corresponds to the GMR ot TMR. For the case of the SV the GMR is around 1% but in the case of the STO based on MTJ the TMR=100%. The factor β=1 correspond to the ideal case of the impedance modeling of the Z_{STO} is equal to 50Ω (β=50Ω/Z_{STO}) an provides non miss-matching of power. The loss of energy in the setup of measurements will be shown later.

During the measurements it was taken into account the reduction of power due to the chain of measurement[7].

[7] In this thesis we will use the Watts (W) as unity of the integral power and the power spectral density (PSD) in V^2/Hz.

3.3 Spin transfer torque (STO) devices

In this section, the STO devices used in this thesis work will be described. The first type of devices have the structure of the **standard STO** nanopillars based on spin valve (SV) and magnetic tunnel junction (MTJ). The second type is the **double SyF STO** (D-SyF) based only on MTJ. In the end of this section, a table with the characteristics of the devices studied in this thesis will be introduced.

3.3.1 Hysteresis loop of a SyF Structure

In order to complement this theoretical framework we present the measured hysteresis loops of two SAF structures. A SAF pinned and a SyF unpinned layer. In Fig. 3.21 (a), the hysteresis loop of the SAF pinned layer shows a total magnetic moment equal to zero in the plateau region. Since the BL of the SAF is pinned in the positive direction, the hysteresis loop is shifted into the negative field values, $H_{sf}^{+} \neq H_{sf}^{-}$. Increasing the negative values of applied field, in the spin-flop region, the BL is turned generating a small hysteresis loop due to the exchange bias field (pointing in the positive direction). In

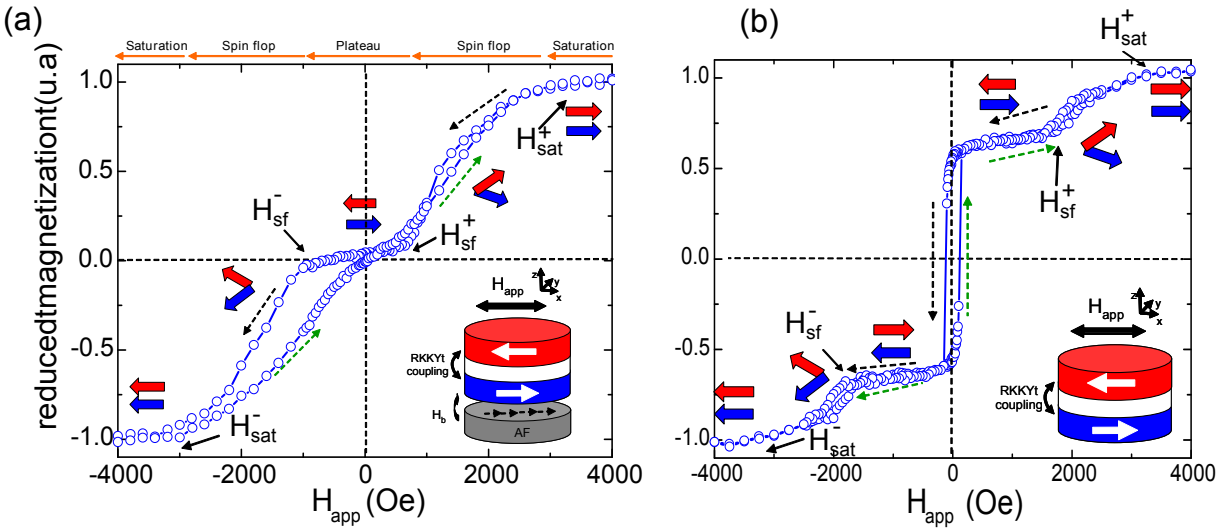

Figure 3.21 – Hysteresis loops of the SAF and SyF. The case of a SAF pinned PtMn(20)/CoFeB(1.5)/CoFe(2.0)/Ru(0.85)/CoFeB(1.5)/CoFe(1.5)/MgO(1.3)/Ru(7) is presented in (a). In (b) we observe the hysteresis loop of the structure Ta(3)/CuN(20)/Ta(5)/CoFe(5)/Ru(0.8)/CoFeB(2)/Ta(5) which is a SyF unpinned. Thickness in parenthesis are in nanometres.

the case of the SyF, see Fig. 3.21 (b), we expect a non zero net magnetic moment in the plateau region because the SyF in the antiparallel state is turned completely (structure

no pinned) when we sweep the applied field from positive to negative (or negative to positive) values. The net magnetic moment of the plateau region will be $M_{plateau} = |M_{S,TL} \times d_{TL} - M_{S,BL} \times d_{BL}|$. As this SyF structure is not pinned, thus the spin flop fields will present the same absolute value, $|H_{sf}^{+}| = |H_{sf}^{-}|$ then the hysteresis loop will be symmetric.

3.3.2 Standard STO nano-oscillator based on spin valve structure

A spin transfer torque nano-oscillator (STO) based on spin valve (SV) structure is the ideal device to start our study. The metallic character of the layers that comprise the STO based in SV will allow us to apply a higher dc current (in comparison with an STO based on MTJ) and hence the observation of many states of excitations, properties and features. The structure of the STO based on SV is the following,

$$\text{PtMn(20)/}\mathbf{\text{CoFe(2.5)}}\text{/Ru(0.8)/}\mathbf{[\text{CoFe(1)/Cu(0.3)}]_2}\text{ /Cu(3)/}\mathbf{\text{FL}},$$

where the FL is layer of $Co_{80}Fe_{20}(1)/Ni_{80}Fe_{20}(2)$, thickness in nanometers. In Fig. 3.23 (c), we present the schematic structure of the standard STO, where each magnetic layer is represented by a different color. The SyF is comprised by the bottom layer (BL) pinned by an exchange bias field (PtMn is an AF layer) and the top layer (TL) which is a laminated layer. The spin valves under study were grown by sputter-deposition using a SINGULUS TIMARIS tool.

All the results discussed in this thesis were found in nanopillars of circular and elliptical cross section. The features and properties of these STO nanopillars could be extended to other devices with different sizes.

In Fig. 3.22 (a) we show the schematics of the mask design of the SV devices. In these devices the easy axis is not in the same direction for all the devices, for that reason it will be necessary to measure the static MR curve in many directions in order to find the real easy axis direction. A correct alignment will provide a good relative position between the layers, especially for the polarizer layer which have to remain in a fixed position.

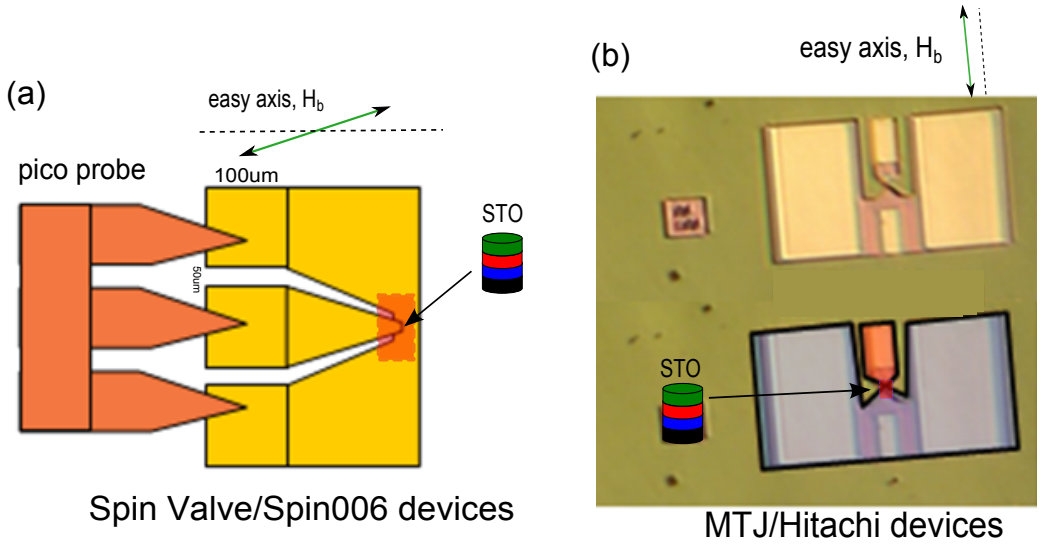

Figure 3.22 – (a) In plane schema of the SV (spin006 P05). (b) MTJ (Hitachi) mask photograph.

3.3.2.1 Static properties of STO based on Spin valve

The static measurement provides us information about the magnetic configuration of the STO that could be for example an AP or P state. It is the typical static curve of magneto-resistance (MR). The MR curves of two STO devices based on SV are presented in Fig. 3.23 (a) and (b) which correspond to a circular and elliptical device respectively. In (b), the color arrows correspond to the sense of the magnetization in each ferromagnetic layer during the sweeping of the field. Each region of the RH curve will be well defined in chapter 4 for the case of the standard STO. In the measurements the external magnetic field was applied in-plane and close to the easy axis direction ($<10°$). The FL magnetization (green arrow) is switched into the direction of the applied field, however the SyF magnetizations (BL and TL) will remain in the anti-parallel state for an important range of magnetic field. As we know, the resistance of the structure depends mainly of the relative position between the FL and the TL magnetizations, due to the GMR effect.

In the MR curves, it is possible to identify the anti-parallel (AP) or parallel (P) magnetic configuration which characterizes the high or low state of resistance. Following the schematic, for positive values of applied field the FL magnetization remains anti-parallel with respect to the TL, see the arrows in Fig. 3.23 (b). Moreover, for high positive values of applied field, the TL starts to turn into the direction of the external field i.e. decrease of the resistance. This critical field value is the spin-plop field $H_{sf}{}^{+}$ and it corresponds to the beginning where the BL and TL start to be aligned in the direction of the applied field, decreasing the resistance of the system. We use the positive and negative spin flop field $H_{sf}^{\pm}$ depending on the sense of the external applied field.

The GMR of the elliptical (GMR 0.6%) and circular (GMR 0.2%) devices are small in comparison with the values obtained in MTJ ($\approx 80\%$) [8].

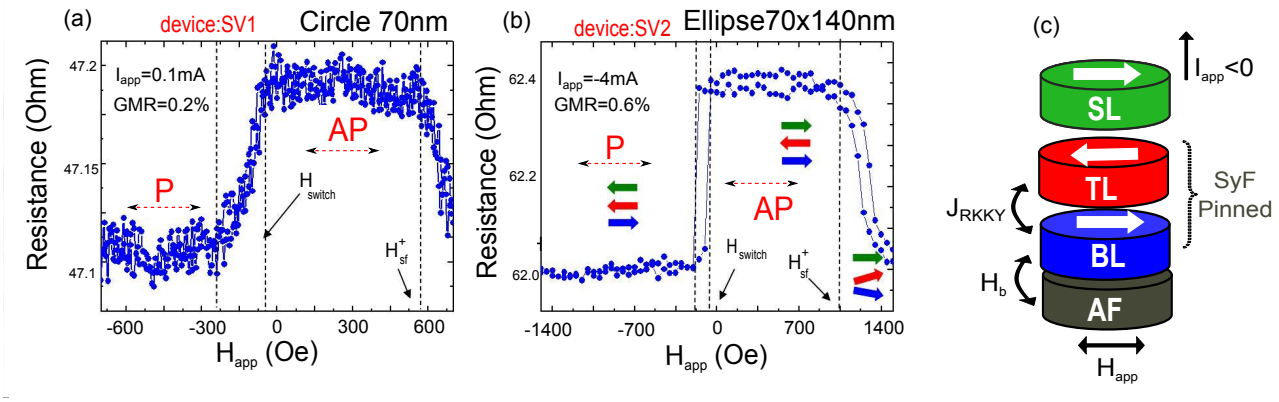

Figure 3.23 – (a)-(b) Typical MR curves for STOs of elliptical (GMR 0.2%, SV1) and circular (GMR 0.6%, SV2) devices. Arrows correspond to the direction of each layer magnetization. The parallel (P) and antiparallel (AP) state of resistance is well defined. We realized that the switching or magnetization reversal of the FL magnetization in the case of the elliptical devices is abrupt. (c) Schematic of the standard STO structure.

In an elliptical device, we notice an abrupt switching of the FL, compared with the MR curve of the circular device, see the devices SV1 and SV2 in the Fig. 3.23 (a) and (b) respectively. Clearly in the case of this circular device, the reversal process is not abrupt[9]. In the RF measurement, normally we started from a high magnetic field it is reduced until zero, in the high resistance state (AP state).

The magnetic configurations of the structure will be crucial in the RF measurements. Therefore, it will be important to find a stable state of resistance, i.e the relative position between the polarizer (TL of SyF) and the free layer (FL) remains constant in the MR curve. In this stable region we will be able to measure the steady state oscillations without the influence of the some reversal of the magnetization.

Therefore a large plateau region is an advantage as is given in the case of the elliptical device (plateau =1050 Oe). It is larger in comparison with the plateau in the case of the circular device (plateau =600 Oe). In order to study the influence of the RKKY coupling and the exchange bias field in the increase of the plateau region we present in section 4.1 the simulated the hysteresis loops of SyF structures.

[8] The study of the STO based in MTJ will be presented in the next section.

[9] Circular devices show an abrupt switching as well but in this case maybe for the angle between the applied field and the easy axis the switching is not abrupt

3.3.3 Standard STO nano-oscillator based on MTJ

In chapter 2 we have presented some features of the STO spin valve devices. In fact, one of the problems that we have to solve, to develop realistic applications, is the increase of the low output power emitted from the STO.

In order to raise the output power, it is better to use a STO based on a MgO MTJ following the results of Yuasa, [Yuasa and Djayaprawira, 2007]. Some studies in STO based on MgO has published by [Cornelissen et al., 2009], [Cornelissen et al., 2010] and [Devolder et al., 2011], due to the high TMR.

The used of the MgO deal with new technical problems, such as the deposition of a good insulating layer of MgO ($\sim$ 1nm)[10], which requires high temperatures ($\sim 340^oC$) to crystallized, [Yuasa and Djayaprawira, 2007]. Normally after the deposition the samples could be annealed (inducing an easy axis and the crystallization).

The annealing temperature could produce Mn diffusion (from the PtMn AF layer), or B (from CoFeB layers) into the other layers, through the MgO barrier, generating pin holes and new interlayer couplings. In addition to this disadvantage, the high current density passing through the structure could degrade the MgO barrier reducing the TMR. The structure of the standard STO based on MTJ as follow,

IrMn(6.1)/**CoFe(1.8)**/Ru(0.4)/**CoFe(2)**/MgO/**CoFe(0.5)**/**CoFeB(3.4)**/Ru/Ta/Ru

As in the case of the SV devices we studied nanopillars with circular or elliptical cross section. The STO structures were realized by Hitachi GST (San José) with small RA (RA=1$\mu\Omega$ m^2). The deposition of the magnetic films were done by D. Mauri and a nanofabrication process by J. Katine.

In the case of the Hitachi devices, see Fig. 3.23 (b), the easy axis which corresponds to the annealing axis is well defined.

[10]The small thickness of the MgO barrier could produces a strong dipolar field between the TL and the FL.

3.3.3.1 Static properties of STO based on MTJ

The hysteresis loops of the standard STO based on MTJ is presented in Fig. 3.24 (a) for a dc current of I_{app}=0.05mA. In this case the TMR is 82%. In comparison with the hysteresis loop of the SV, the insulator character of the MgO barrier increases the resistance of the system. Applying a dc current through the nanopillar a voltage will appear in the interfaces of the MgO barrier, if this voltage is too high the barrier breaks generating pinholes. In our case, a voltage of 300mV is enough to start with the MgO barrier degradation. This voltage is called degradation threshold voltage (V_{th}).

In order to find the V_{th}, it is necessary to sacrifice some devices. Measuring the MR curves and increasing the applied current until the degradation, it is possible to identify the current value and resistance (in the AP state) to calculate the V_{th}. The corresponding current will be I_{th} =V_{th}/R_{AP}.

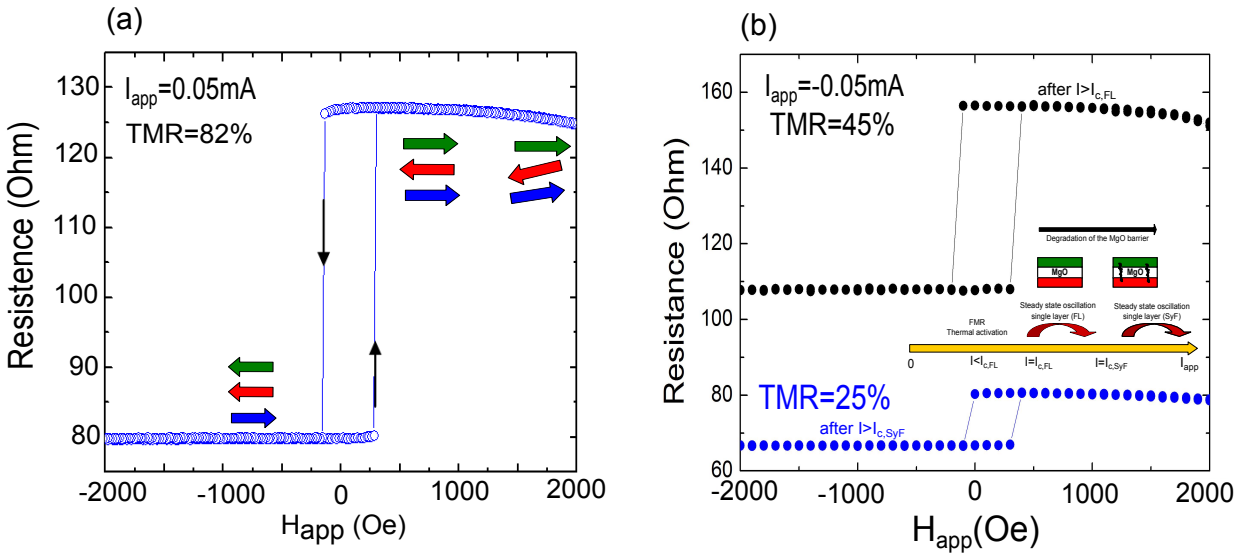

Figure 3.24 – (a) MR curve of a device of a sample ellipse of 65×130nm. (b) Degradation of the MgO barrier after reach the critical current.

The good state of the insulator barrier produces a high value of R_{AP}, however a small I_{th}. This will be a problem in order to reach the critical current of the FL dominant precession ($I_{c,FL}$) and in a second level the critical current of the SyF dominant precession ($I_{c,SyF}$). In Fig. 3.24 (b), we show one example of the evolution of the degradation of the MgO barrier. First the hysteresis loop after the $I_{c,FL}$ was of TMR=42% and after the $I_{c,SyF}$ the TMR is reduced until 25%.

3.3.4 Double SyF STO nano-oscillator based on MTJ

The synthetic ferrimagnet (SyF) has been recently included as a possible FM layer to replace the single FL of a STO. The SyF has the advantage of higher thermal stability, smaller stray magnetic field, faster switching and reduced threshold switching current as compared to single ferromagnetic FL[Zhou et al., 2013]. In this thesis, the static and dynamical features of a Double SyF (DSyF) STO based on MTJ will be studied. The bottom structure of the DSyF STO is similar to the stack of the standard STO of the previous section The DSyF STO has the following structure:

IrMn(6.1)/**CoFe(1.8)**/Ru(0.4)/**CoFe(2)**/MgO/**CoFe(0.5)**/**CoFeB(3.4)**/Ru/**CoFe(3.6)**/CL

where the capping layer (CL) is composed by Ru/Ta/Ru. As in the case of the SV devices we studied nanopillars with circular or elliptical cross section. The STO structures were realized by Hitachi GST (San José) with small RA ($\approx 1\mu\Omega m^2$). The deposition of the magnetic films were done by D. Mauri and a nanofabrication process by J. Katine.

3.3.4.1 Degradation of the MgO barrier

As an example of barrier degradation we show here a study of the degradation of the MgO barrier for the D-SyF STO see Fig. 3.25. The hysteresis loops were measured increasing the applied current until the degradation of the MgO barrier. The curves correspond to the R_{AP} and R_P, red and black curve respectively. The hysteresis loops 1-3 show how the magnetic configuration is destroyed.

Following the protocol described in the previous section 3.3.3.1, the threshold voltage for the DSyF STO is obtained, V_{th}=320mV.

3.3.4.2 Evidence of degradation of the RKKY coupling in the SyF free layer

At the beginning of the development of the D-SyF STO we found different features which supposed that the RKKY coupling in the SyF-FL of the structure will not be the same as in the bottom of the structure. In order to prove our supposition, some magnetic films

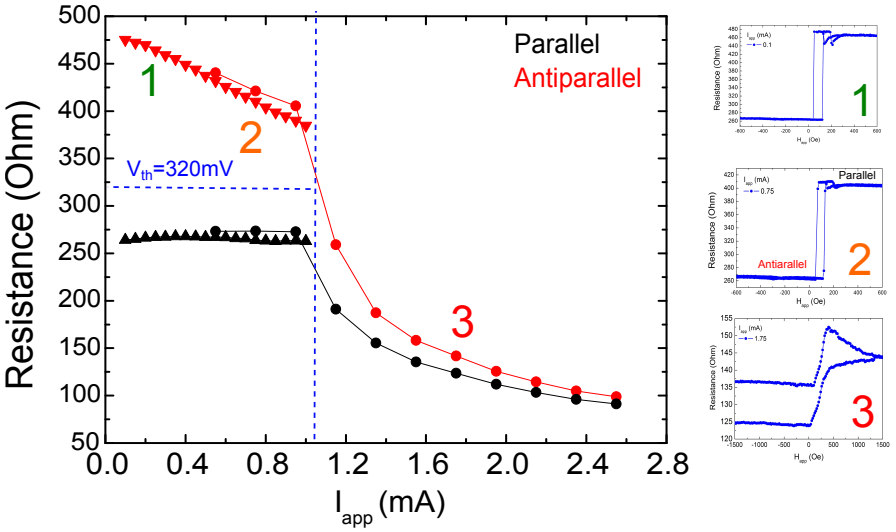

Figure 3.25 – Degeneration of the MgO barrier in a DSyF-STO device. In the right side the hysteresis loops for three different point of the main figure. The abrupt change in the resistance corresponds to the degradation of the barrier. The threshold voltage was found 320mV

were deposited in CEA/LETI by M. C. Cyrille and E. Hassen in LETI laboratory. The structure was the following,

$$\text{Ru(1)/CuN(30)/Ta(5)/PtMn(15)/CoFe(2)/Ru(0.7)/CoFe(3.5)/Cu(3.5)}$$
$$\text{/CoFe(1)/CoFeB(3.5)/Ru(0.9)/CoFeB(3.5)/Ta(5)}$$

The deposition of multilayer transfer and increases the roughness in the interfaces from the bottom into the top of the structure. Therefore the SyF on top of the structure D-SyF STO will show an important complication. As it was shown in section 1.3 the RKKY coupling is quite sensitive to the thickness of the spacer in the SyF (some Angströms). The roughness in the top of the structure will change the RKKY coupling of the SyF-FL.

In Fig. 3.26 (a) we can observe the hysteresis loop of a DSyF STO based on SV. Arrows correspond to the magnetizations of the FM layers. In Fig. 3.26 (a) the zoom of the plateau of the SyF-FL is shown. We validated that the RKKY coupling of SyF-FL has decreased in comparison with the RKKY coupling of the SyF pinned layer. For different D-SyF STO structures, this behaviour was confirmed.

Using the equation 1.15 it is possible to estimate the RKKY coupling of both SyF. We found that the SyF on bottom presents a $J_{RKKY}^{SyF-pinned}$=-0.65mJ/m^2 and J_{RKKY}^{SyF-FL}=0.005mJ/m^2. The RKKY coupling could be increased if the thickness of the layers are reduced but it won't be significant .

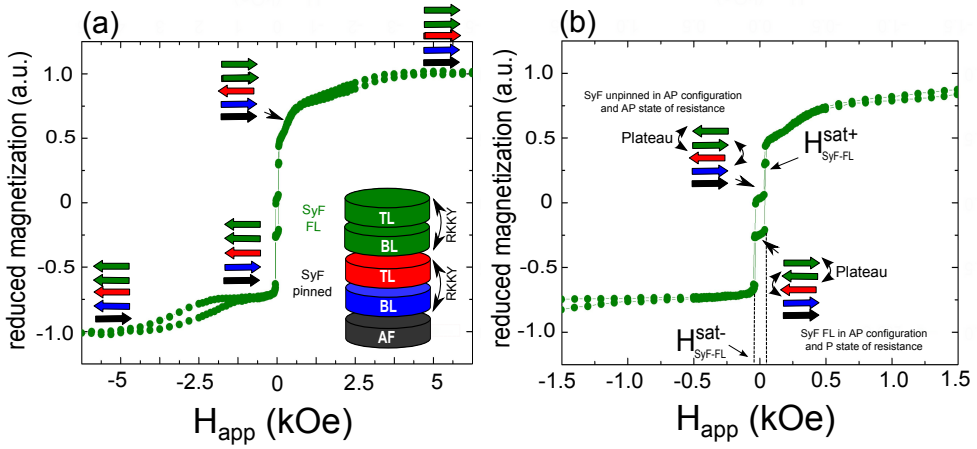

Figure 3.26 – (a) Optimized of the plateau in the DSyF-FL of the structure of a D-SyF spin valve. Arrows correspond to the magnetization of the structure. (b) The plateau of the SyF on top showed an important reduction of its size in comparison with the with the SyF polarizer.

In conclusion, due to the roughness of the structure we can not expect that the RKKY coupling of the SyF-FL shows the same strength as the SyF pinned on the bottom of the structure. Moreover, the magnetization dynamics will be affected directly for this weak value of the RKKY coupling.

3.3.5 List of devices

The characteristic of the STO devices studied in this thesis are summarized in the table 3.27.

Devices	Diameters	GMR/TMR (%)	R_{AP} (Ohm)	R.A (Ohm.µm^2)
SV1	C70nm	0.6	47.2	—
SV2	E70x140nm	0.2	62.4	—
SV3	E100x130nm	0.3	23.16	—
SV4	E100x130nm	0.45	25.17	—
SV5	E70x140nm	0.52	38.65	—
MTJ1	E90x190nm	54	110	1.4
MTJ2	E80x160nm	60	160	1.6
MTJ3	E65x130nm	48	225	1.5
MTJ4	E55x100nm	16	335	1.4
D-SyF1	E55x100nm	60	800	2.1
D-SyF2	E65x130nm	70	360	1.39
D-SyF3	E65x130nm	60-30-20	340-172-162	1.39
D-SyF4	E65x130nm	75-38	380-215	1.3
D-SyF5	C85	80	450	0.6

Figure 3.27 – Table of devices studied in this thesis.

3.3.6 Estimation of the static dipolar field in devices

The static dipolar field between the FM layers of the STO devices was is estimated along the x axis, in order to obtain a first picture of the coupling strength due to this stray field. The components of the dipolar tensor were calculated using the method described in the annex A, section 8.3.1.

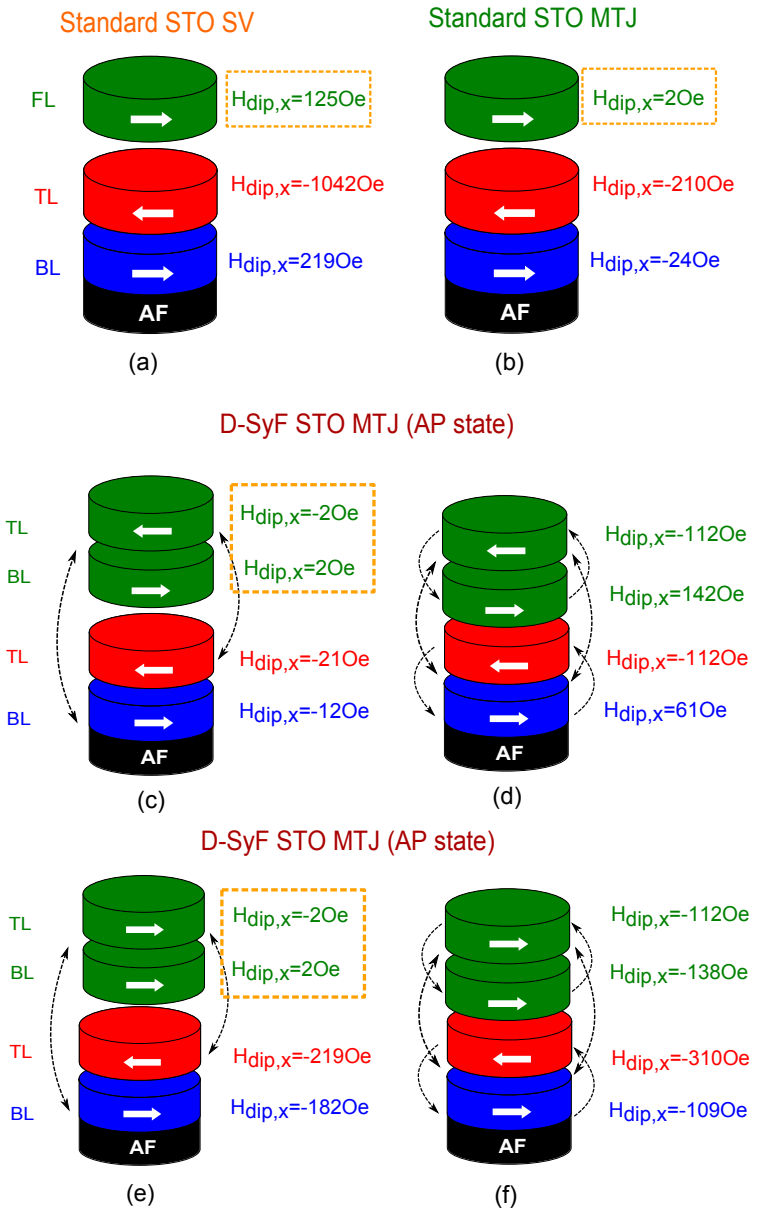

Figure 3.28 – The estimate static dipolar field in the x direction was found for each FM layer of the different structures over study described in this section. The standard STO based on SV (a) and MTJ (b), and the D-SyF in (c)-(d) for both magnetic configurations of the SyF on top.

In the case of the standard STO based on SV, see Fig. 3.28 (a), the static dipolar field

was estimated in 125Oe[11], for an elliptical device E65x70nm2. The same parameters has been used in numerical simulations of chapter 5, see Table 3.3. In the case of the Standard STO based on MTJ, the optimization of the devices produces a small dipolar field, only 2Oe, see Fig. 3.28 (b). The parameters used are shown in Table 3.4 which are the same used for the D-SyF STO.

The dipolar field between the SyF and the single FL of the standard STO based on MTJ is reduced even if the distance between the SyF and the single FL is 1nm. Changing the thickness of the FM layers and the magnetization we can optimize the stack.

	SyF-FL				SyF pinned		
	TL	Ru	BL	MgO	TL	Ru	BL
Ms	1470kA/m		1112.5kA/m		1060kA/m		1470kA/m
K_u	7957.75J/m^3		7957.75J/m^3		7957.75J/m^3		7957.75J/m^3
t	3.6nm	0.8nm	3.9nm	1.0nm	2.0nm	0.8nm	1.8nm
N_x N_y N_z	0.042085 0.078372 0.879543		0.044620 0.083119 0.872260		0.027061 0.050280 0.922658		0.024952 0.046343 0.928705
H_b			0		0		1000 Oe
J_{RKKY}	-0.1 mJ/m^2				-1.5 mJ/m^2		
α	0.02						
h	0.3						
$\bar{p}$			m_{TL}		m_{BL}		

Dipolar tensor

$N^{dip}_{x,BL\to TL}$ = 1.706766x10^-25
$N^{dip}_{y,BL\to TL}$ = 3.195475x10^-25
$N^{dip}_{z,BL\to TL}$ = -4.902441x10^-25

$N^{dip}_{x,BL\to BL}$ = 2.172154x10^-25
$N^{dip}_{y,BL\to BL}$ = 4.071497x10^-25
$N^{dip}_{z,BL\to BL}$ = -6.243651x10^-25

$N^{dip}_{x,TL\to BL}$ = 3.079646x10^-25
$N^{dip}_{y,TL\to BL}$ = 5.773958x10^-25
$N^{dip}_{z,TL\to BL}$ = -8.853604x10^-25

$N^{dip}_{x,BL\to TL}$ = 1.435170x10^-25
$N^{dip}_{x,TL\to TL}$ = 1.860979x10^-25
$N^{dip}_{x,BL\to TL}$ = 5.075982x10^-25

$N^{dip}_{y,BL\to TL}$ = 2.666935x10^-25
$N^{dip}_{y,TL\to TL}$ = 3.476933x10^-25
$N^{dip}_{y,BL\to TL}$ = 9.517479x10^-25

$N^{dip}_{z,BL\to TL}$ = -4.102105x10^-25
$N^{dip}_{z,TL\to TL}$ = -5.337912x10^-25
$N^{dip}_{z,BL\to TL}$ = -1.459346x10^-24

Table 3.4 – Parameters of numerical simulation of the D-SyF structure. These are the same parameters used for as the standard STO based on MTJ only for the first three layers.

For the structures D-SyF STO we estimate the static dipolar field for two magnetic configurations of the SyF on top or free layer (SyF-FL). In Fig. 3.28 (c)-(d) in the AP configuration (plateau region) and in 3.28 (e)-(f) when the SyF-FL is already in the saturation region. For (c) and (e) we have taken into account only the dipolar field from the FM layers of the opposite SyF. An in the case of (d) and (f) the whole interactions. We observe that the structure of the D-SyF was optimized to reduce the dipolar field of the TL of the SyF-FL in -2Oe.

In conclusion, we should expect in the case of the standard STO based on SV an important

[11] See annexe sec:Calculation of the Effective field in SyF

influence of the dynamical dipolar field[12]. In the case of the standard MTJ Hitachi based on MTJ the influence have to be reduced dramatically due to the optimization of the devices. The case of the D-SyF could be an intermediate case.

[12]During the precession of the magnetization, the dynamic dipolar field (three components) under each FM layer of the structure will change its amplitude periodically.

Part II

Numerical Results of Spin Transfer Torque Nano-Oscillators

Standard STOs are composed of a SyF pinned layer and a single FL, depending on the current direction it is possible to excite (in the picture of uncoupled FL-SyF) the FL or the SyF layer, see Fig. 2.2. Main features of FL excitations are well known from literature (experiment and simulations), however SyF excitations have been less studied. The study of the magnetization dynamics in the SyF and FL layers is a fundamental step to understand the features and behaviours of the emitted signal of a standard STO. In this magneto-resistive device the static and dynamic resistance depends mainly on the relative position between the TL and FL magnetizations. This fact leads us to find numerical solutions (trajectory and position) of the magnetization in the SyF and FL, firstly without taking into account the couplings between them. Therefore in the first chapter of this part of this thesis work, the spin torque driven excitations of isolated SyF will be studied using the macrospin approach, see Fig. 3.29.

In chapter 5, it will then be addressed the FL-SyF coupled system (standard STO), taking MSTT and dipolar coupling into account. These different mechanisms of dynamical coupling between the layers will change the features of the excitation. In this coupled system depending on current direction there will be dominant FL or dominant SyF excitations, but they will suffer changes due to dipolar coupling. Aim of the chapter is to reveal the difference of isolated FL and isolated SyF excitations as compared to FL and SyF excitations in a coupled structure.

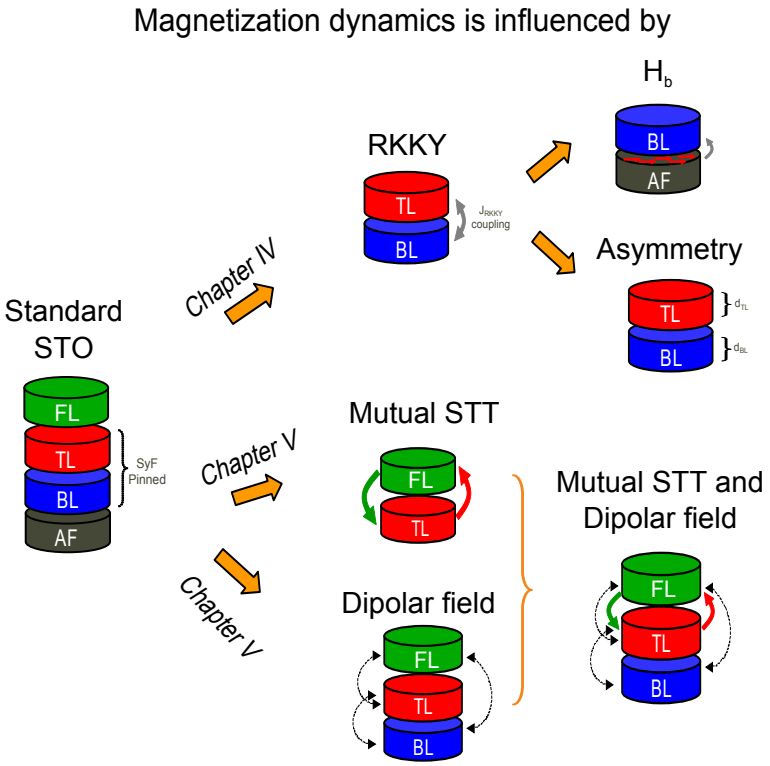

Figure 3.29 – Schematics of the different structures and couplings mechanisms over study in this section. First the influence of the RKKY dynamical coupling in a SyF layer as a function of the H_b and its asymmetry. The interlayer coupling is introduce with the study the dynamic mutual spin transfer torque between the FL and the TL, and in the end it was added the dynamic dipolar field between the three ferromagnetic layers.

Chapter 4

Study of an Isolated SyF System

In this chapter we address the spin torque driven excitations for an isolated SyF structure, that consists of two ferromagnetic layers (TL and BL) that are coupled via RKKY interaction and where one of the layers (BL) can be coupled to an AF. The dynamic response is analysed as a function of the RKKY and AF coupling strength, as well as a function of TL and BL thickness and saturation magnetization. Before addressing the dynamic response one has to consider the static properties of these different SyF configurations. Therefore the corresponding static hysteresis loops will be analysed in the first section of this chapter, and the dynamics is presented in the second section. The dynamic properties of the sub-critical (damped modes) and auto-oscillations regime will be presented.

4.1 Static simulations of the SyF structures based of STO

In this section, the influence of different intrinsic parameters, such as the magneto-crystalline anisotropy, the shape anisotropy, the RKKY coupling strength and the exchange bias field on the hysteresis loop is analysed for an isolated SyF structure.

We start the discussion with a compensated SyF structure that we call synthetic antiferromagnet (SAF) [1]. A pinned SAF structure which is usually part of standard STO devices is shown in Fig. 4.1 and will be taken as a reference for the studies on the dif-

[1] A SyF structure compensated means that the product $M_{S,TL} \times d_{TL} = M_{S,BL} \times d_{BL}$. This compensation reduces the static stray field from the SyF on the FL, see Fig. 2.2. This structure is called synthetic antiferromagnet (SAF)

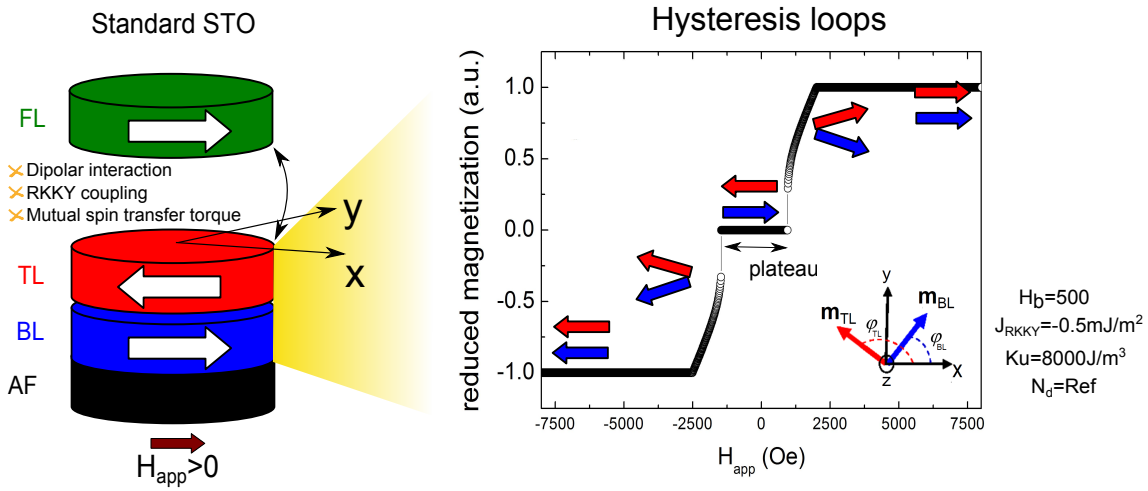

Figure 4.1 – The standard STO structure and the hysteresis loop of the SAF pinned layer. Inset: The coordinate system with the angles which define the position of the TL and BL magnetization. Arrows correspond to the magnetization of each layer.

ferent SyF configurations. The corresponding parameters used for the simulations such as the saturation magnetization of the layers ($M_{S,TL}, M_{S,BL}$), the thickness's (d_{TL}, d_{BL}), the magnetocrystalline anisotropy ($K_{u,TL}, K_{u,BL}$) and the demagnetizing factors (N_x, N_y, N_z) are indicated by the red squares in table 3.1. The RKKY interaction is relatively strong (-0.5mJ/m^2). The exchange bias field for the pinning of the BL by an AFM is $H_b = 500Oe$ [2].

After introducing the hysteresis loop of the reference pinned SAF and defining the parameters that characterize the hysteresis loop, we will analyse the changes of these parameters as a function of the anisotropy, exchange bias and RKKY interaction strength. In order to simulate the hysteresis loops the method of energy minimization is used which was introduced in sec. 3.1.1.3.

The main features of a SAF hysteresis loop have already been presented in sec 3.1.1.3, Fig. 3.4. We remind here, that there are three regions, the plateau region for fields $H_{sf}^{-}<H_{app}<H_{sf}^{+}$ (with H_{sf} the spin flop field), the spin flop region for $H_{sf}^{\pm}<H_{app}<H_{sat}^{\pm}$ and the saturation regions $H_{app}>H_{sat}^{\pm}$. The corresponding relative positions between the magnetizations of the TL and BL are represented by the colour arrows in Fig. 4.1. In the spin-flop region the external field counteracts the effective field of the RKKY coupling, thus breaking the antiparallel alignment of the plateau and reorienting the magnetization into the field direction. The magnetization direction of one of the layers turns first into the direction of the applied field and due to the strong coupling both magnetizations will form an angle, to minimize both Zeeman and exchange energy. This angle disappears

[2] These factor have been approximated for an ellipse of 60x70nm

gradually with the increase of the applied field, more specifically reaching the saturation region. It is reached when the two magnetizations are parallel (P) to the applied field.

In the following it will be shown how the spin-flop field $H_{sf}^{\pm}$ and the saturation field $H_{sat}^{\pm}$ are changed upon changing the different material and coupling parameters.

4.1.1 Magnetocrystalline anisotropy and exchange bias field

In order to show the influence of the magneto-crystalline anisotropy constant (K_u) on the hysteresis loop, any other contribution to define an easy axis is eliminated. Therefore the demagnetizing factors (N_x, N_y, N_z) and exchange bias field (H_b) are fixed to zero as compared to the compensated SAF reference structure (Table 3.1).

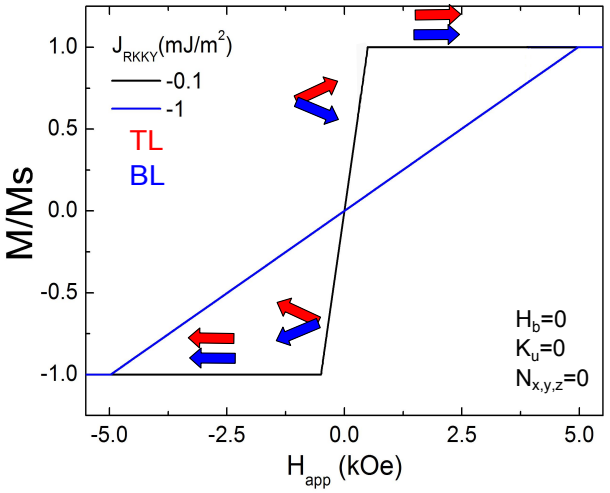

Figure 4.2 – Hysteresis loop of a completely symmetric structure (SAF) for $K_u = 0$. The reversal of the magnetizations is a continuous rotation of the BL and TL.

The completely symmetric SAF structure shows for $K_u = 0$ a hysteresis loop that is characterized by a linear variation of the magnetization between $H_{sat}^{\pm}$ without a plateau, see Fig. 4.2. The reversal takes place via a continuous rotation of the magnetizations of the TL and BL, where they are antiparallel only in zero field. This behaviour is the same for weak and strong RKKY coupling, where the only difference is the value of the saturation field that is indicative of the RKKY coupling strength, see in the annexe the expression of the values $H_{sat}^{\pm}$ in eq. 8.5.

In Fig. 4.3 (a) and (b), the influence of the K_u is shown for two values of the RKKY coupling (a) J_{RKKY}= -0.1mJ/m^2 and (b) J_{RKKY}= -1mJ/m^2 (weak and strong RKKY

coupling).

Introducing an uniaxial magnetocrystalline anisotropy K_u [3], to both the TL and BL layers of the SAF, the plateau region appears, where the size of the plateau (i.e. $\Delta H = H_{sf}^{+} - H_{sf}^{-}$) depends on the value of the anisotropy energy K_u and on the RKKY coupling strength. This appearance of the plateau means that a totally symmetric system has an energy minimum where the magnetizations stays anti-parallel over a certain field range. In addition to the plateau, a bi-stable region appears around the spin-flop field in the case of weak RKKY coupling Fig. 4.3 (a), for K_u=8000J/m^3($H_u \approx$100 Oe). Arrows correspond to the sweeping direction of the magnetic field. The appearance of the hysteresis shows that for these parameters the system can get stuck in a local energy minimum which is not a global energy minimum.

The effective magnetic field arising from the RKKY coupling depends on the strength of the coupling and on the thickness of the layers. For instance the effective field of the BL $H_{eff,BL}$ due to the weak RKKY coupling (J_{RKKY} =-0.1mJ/m^2) to the TL is H_{BL}=225 Oe for equal M_S. The magnetic field associated with the RKKY coupling is obtained using,

$$H_{RKKY} = -\frac{J_{RKKY}}{\mu_0 M_{S,i} d_i}. \tag{4.1}$$

For a strong coupling (J_{RKKY} =-1mJ/m^2) it will be ten times higher. These values of field give us an idea on the importance of the RKKY coupling and will help us to define a robust SAF structure. The saturation field depends only slightly on the anisotropy for strong RKKY coupling but is shifted in the case of weak RKKY coupling.

The spin flop fields and saturation fields can be determined from the energy minimisation given in section 8.1. This has been done by [Gusakova et al., 2009] and the equations are 8.4 and 8.5.

4.1.2 Exchange bias and Demagnetized factors

In the next step, we will analyse the influence of a positive exchange bias field (H_b), to fix the BL magnetization in one direction, see Fig. 4.3 (c)-(f), for the two cases of RKKY coupling. The exchange bias field pins the BL magnetization into the positive direction giving to the structure a unidirectional anisotropy. The result of the exchange

[3] The magnetic field associated with magnetcristalline uniaxial anisotropy is $H_u = 2K_u/\mu_0 M_S$.

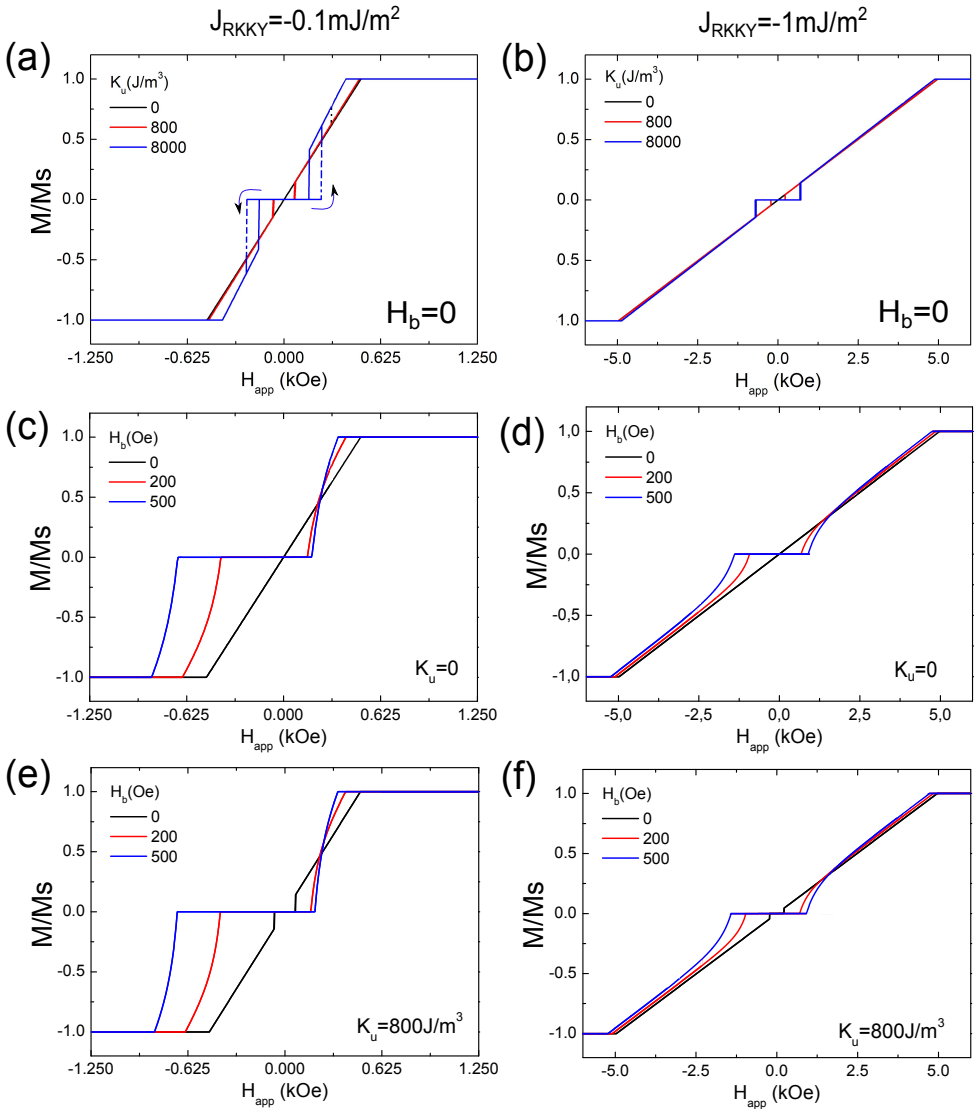

Figure 4.3 – (a)-(b) Hysteresis loops of the reference SAF structure using a constant of J_{RKKY}=-0.1mJ/m^2 (weak) and -1 mJ/m^2 (strong), without demagnetizing field $N_x = N_y = N_z = 0$ or H_b=0. It is observed a small plateau close to zero applied field and a bistable region for K_u=800, 8000J/m^3. This plateau increases for the strong RKKY coupling, see (b). In (c) it is shown the influence of the exchange bias field, H_b, creating a larger plateau for $H_b \neq 0$Oe. For an strong RKKY coupling the plateau increases 10 times. In (e) is introduced a K_u=800J/m^3(e) the plateau appears for the black curve, corresponding to H_b=0Oe. In (d)-(f) the presence of a hysteresis appears for H_b=200 and 500 Oe, which correspond to the BL reversibility.

bias is that in the case of zero anisotropy (Fig. (c),(d), that it also induces a plateau, but with different positive and negative spin flop fields. The width of the plateau increases with increasing exchange bias. Including the anisotropy, the plateau is reinforced, i.e it becomes larger. As in the previous case, the anisotropy field also changes the saturation field in the case of weak RKKY but does affect it only weakly in the case of strong RKKY.

The size of the spin-flop region is reference of the strength of the exchange bias field because it corresponds to the magnetic field value to break the magnetization pinning. The RKKY coupling will define the saturation magnetization value due to the competition of the RKKY coupling to keep the magnetization in the AP state and the external magnetic field which wants to break this state to saturate the SAF.

Keeping the exchange bias H_b and anisotropy field H_u constant and changing RKKY coupling (Fig.(c) and(d)) we will see that the plateau is much affected by RKKY. The difficulty is that the plateau is defined almost by equal amounts by H_{RKKY}, H_b, and H_u. In the case of weak RKKY, the exchange bias can dominate the plateau but not in the case of strong RKKY, see the hysteresis loops in Fig.4.7.

In section 2.1.1 is has been shown that if the self oscillations (STT modes) occur in a bi-stable area, the magnetization could change its position into another energy minimum. In order to avoid the hysteresis loop with bi-stability regions the SAF should present larger RKKY coupling, to neglect the influence of K_u, see Fig. 4.3 (b). However introducing a strong H_b, the region between the plateau and the spin flop show a small hysteresis loop. It corresponds to the reversal behaviour of the BL magnetization which is pinned in the positive direction.

4.1.3 Demagnetization energy

The shape anisotropy for elliptical sized samples (as used in the experiment) is one form of a uniaxial anisotropy and will have the same effect as the magnetocrystalline anisotropy. Including thus the shape anisotropy, in addition to a uniaxial anisotropy and an exchange bias field, will increase symmetrically the plateau region, as shown in Fig.4.4.

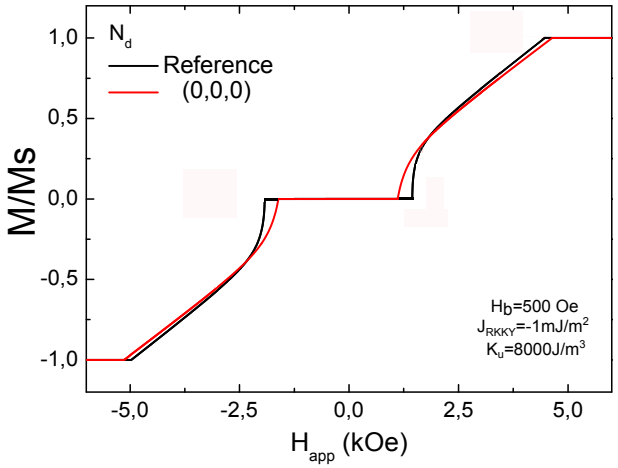

Figure 4.4 – Hysteresis loops of the reference SAF structure with and without demagnetized factors. For $Nx \neq Ny \neq Nz \neq 0$ the plateau increases in both senses.

4.1.4 Magneto-resistance curves

In order to obtain the RH curve from the SAF M(H), we use in the simulation a FL magnetization whose is switched in zero applied field. The RH curve corresponds of the relative position between the FL and the TL, which are shown with color arrows, see Fig. 4.5. The high resistance will be the AP state and the low resistance for the P state. The AP state will correspond to the positive applied field and the P state for negative applied field. The study of the STT modes will be focused in the AP state i.e. from the FL switching value to the positive spin flop value H_{sf}^{+}.

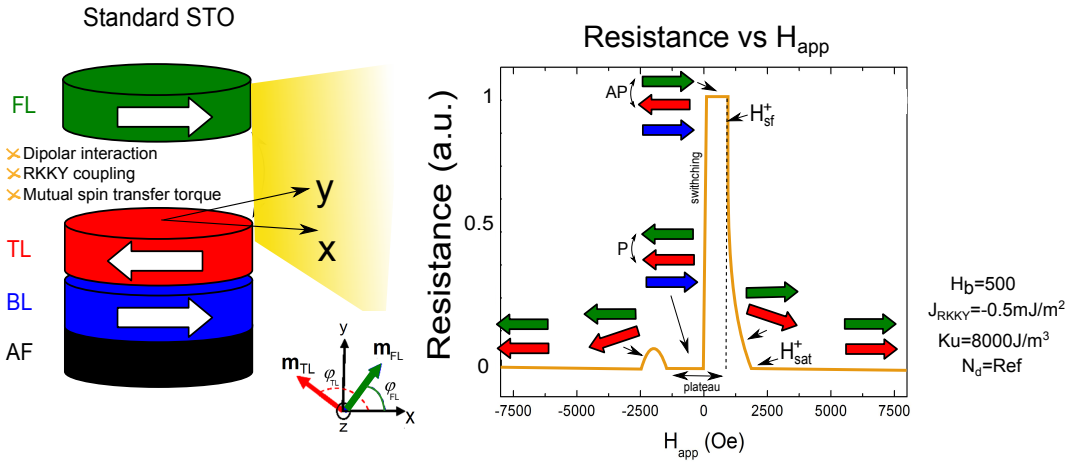

Figure 4.5 – Resistance versus applied field (RH) curve of the standard STO which is proportional to the relative position between the FL and the TL. Arrows correspond to the magnetizations. The parameters of the SAF correspond to the reference of Table 3.1 but with J_{RKKY}=-0.5mJ/m^2. The FL has been chosen to switch in zero applied field for convenience. The corresponding M(H) of this R(H) is shown in Fig. 4.1.

In this section, the different hysteresis loops and the RH curves were shown as a function of

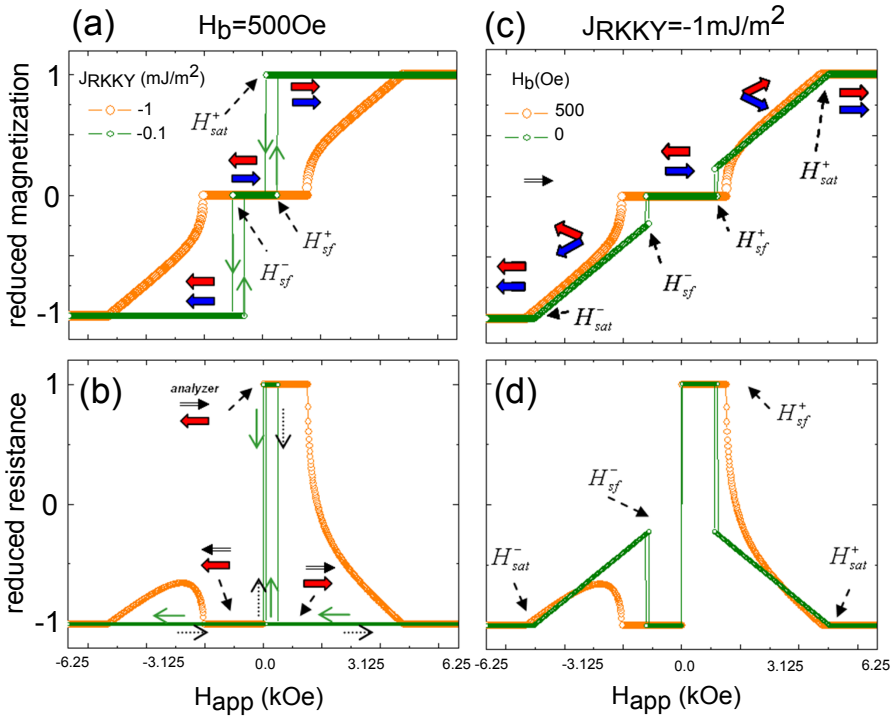

Figure 4.6 – (a) and (b) correspond to the hysteresis and RH loops of the SAF reference using two values of RKKY coupling (J_{RKKY} =-0.1 and -1 mJ/m^2). In (c) and (d) is shown the hysteresis and RH loops of the SAF reference but the pinned (H_b=500 Oe) and unpinned (H_b=0) structures.

the exchange bias field and the RKKY coupling. In Fig. 4.6 the orange curves (hysteresis and RH curve) correspond to the reference SAF structure, parameters in Table 3.1.

4.1.5 Summary

In Fig. 4.7 we show the positive/negative spin-flop fields and the positive saturation field, as a function of either H_b or J_{RKKY}. It will be introduced the size of the plateau (H_{sf}^{+}-H_{sf}^{-}), because it gives us the anti-parallel configuration of the SAF. We will compare results from numerical simulations with analytical equations, 8.4 and 8.5. The solid points correspond to the simulation values and the dashed line corresponds to the analytical solution of equations. The agreement between the analytical predictions and numerical simulations for different values of the RKKY coupling is very good.

The bi-stability on the hysteresis loop of the SAF with weak RKKY lead us to define, for the static analytical solutions of Fig. 4.7, the characteristic fields as follows. The saturation field $H_{sat}^{\pm}$ is calculated supposing that the magnetic state of the SAF passes from the saturation to the spin-flop or to plateau region. Unfortunately it is not possible

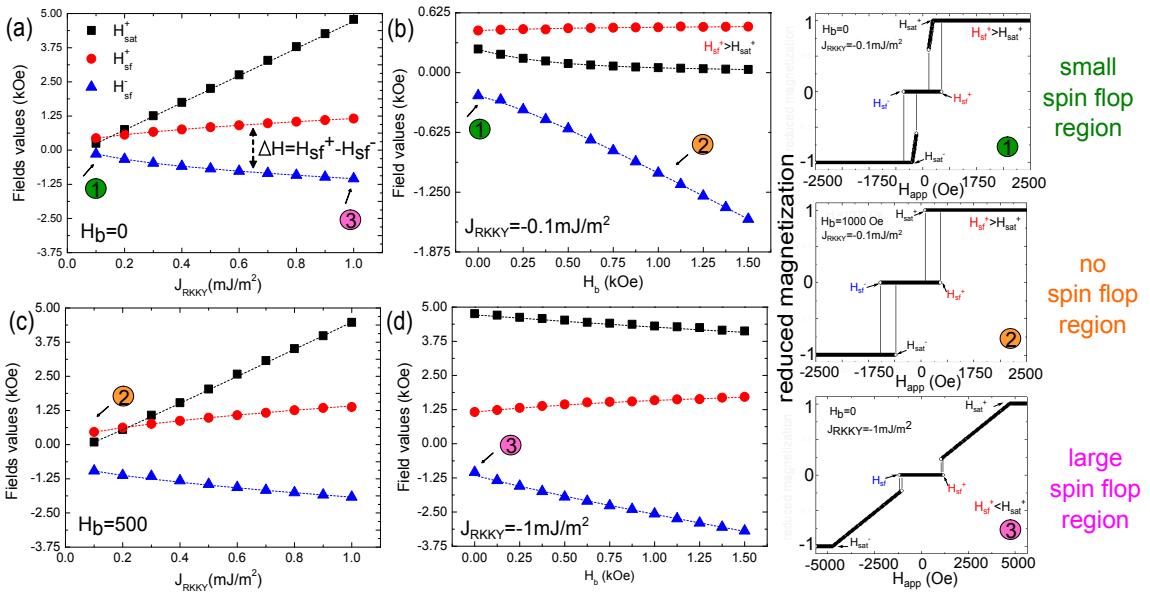

Figure 4.7 – The saturation magnetization, the spin flop field values and the size of the plateau region are presented as a function of the RKKY coupling for a SAF unpinned and pinned respectively in (a) and (c). In (b) and (d) they are presented as a function of the exchange bias field, for a weak and a strong values of RKKY coupling. Solid points correspond to the simulation loops and the dash lines corresponds to the analytical equations 8.4 and 8.5. The others parameters are the same as in the SAF reference, see Table. 3.1

to calculate the $H_{sat}^{\pm}$ coming from the spin flop to the saturation. The spin flop field $H_{sf}^{\pm}$ is determined supposing that the magnetic configuration passes from the plateau to the spin flop or directly to the saturation region.

In Fig. 4.7 (a), it is shown that by increasing the RKKY coupling the internal field becomes strong and it is necessary to apply a stronger field to counteract its influence and to break the anti-parallel magnetic configuration. The positive spin-flop field increases with the RKKY coupling and in particular for the case of the unpinned SyF layer it is symmetric. The arrow corresponds to the plateau size value. There is strong dependence of the RKKY coupling on the H_{sat}^{+}. Therefore the magnetization curves present a negligible hysteresis and the magnetization process is reversible. For the case of weak values of the RKKY coupling J_{RKKY}=-0.1mJ/m^2, see the hysteresis loops of points 1 and 2 in the right side of Fig. 4.7, the system presents hysteresis.

In Fig. 4.7 (b) it is shown the case of a weak RKKY. The strong dependence of the exchange bias field in the H_{sf}^{-} value is shown. It corresponds to a reversal process of the pinned BL. In the case of this exchange biased SAF layer the asymmetry between the two spin-flop field values is a common feature.

In Fig. 4.7 (c), the SAF pinned structure (H_b=500 Oe) is studied. In comparison with the case of the SAF unpinned, the plateau is not symmetric and, moreover, the positive spin flop field and the plateau are increased for all the values of RKKY coupling. The exchange bias field pinning the BL produces high stability in the system. There is a competition between the applied field which wants to break the anti-parallel magnetization configuration and the RKKY field enhanced by the exchange bias field. In this case it is necessary to apply more external field to break the AP configuration.

In Fig. 4.7 (d) the plateau region increases showing the strong dependence and the positive saturation field decreases. In agreement with the Fig. 4.7 (b) for a strong exchange bias field, if the RKKY coupling is weak the H^+_{sat} will be smaller than in the case of a strong RKKY coupling.

From these results we can conclude that in order to optimize the STO it is important to develop a SyF layer with high exchange bias field and RKKY coupling because it will provide a large plateau which corresponds to a large region of anti-parallel magnetic configuration of the SyF. However, these parameters can affect the critical currents and frequency of steady state oscillations and therefore simulations of the dynamics are necessary at this step to assess this question. The structures with weak RKKY coupling could be of interest for MRAMs technologies due to the abrupt switching.

A summary of different hysteresis loops of SyF structures are shown in Fig. 4.8. In (a) and (b) we compare the hysteresis loops of the SyF pinned and unpinned. Due to the large asymmetry d_{TL}=5nm, d_{BL}=2nm and the strong RKKY coupling, in the plateau region the BL is pointing into negative field, overcoming the exchange bias and generating hysteresis. In (b), H_b=0 the SyF switches completely close to zero field. Changing the thickness of the layers d_{TL}=2.5nm, d_{BL}=5nm, we observe in (c) the negative total net moment in the plateau region. Reducing the RKKY the saturation field decreases and the spin flop region disappears, see (d). Decreasing the exchange bias the a small spin flop region appears in (e) and decreasing more the SyF is switched, in (f). For zero exchange bias the hysteresis loop of (g) is equal to (b) but with the opposite magnetization direction in the plateau region. Changing the thickness of the BL, d_{BL}=3 and 3.5nm the total magnetic moment in the plateau region varies, see (i)-(j).

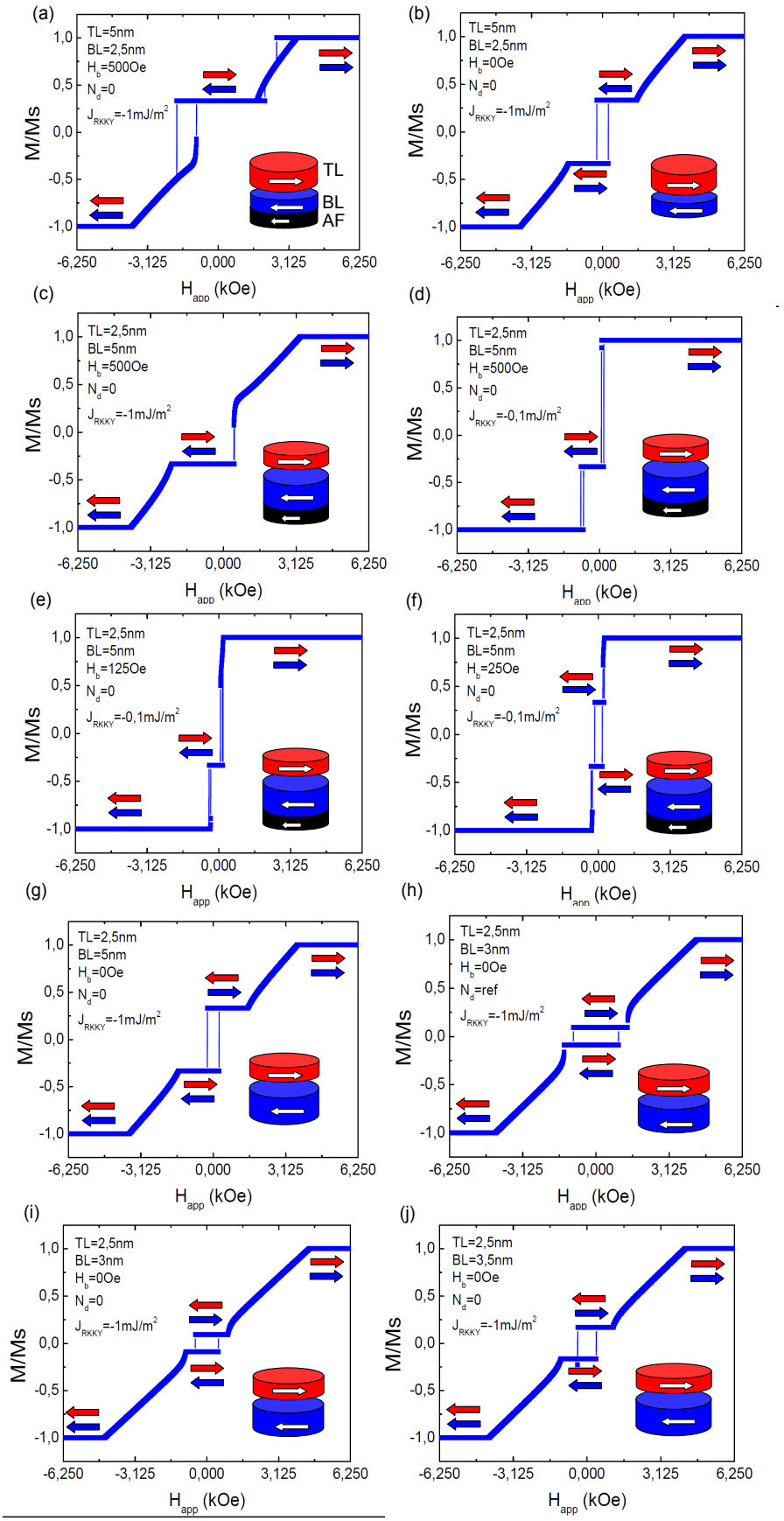

Figure 4.8 – Summary of hysteresis loops of SyF structures based on SAF reference

4.2 Magnetization Dynamics and Spin Transfer Torque

In this section we analyze numerically the dynamic response of an isolated SyF structure and we present a systematic study of the influence of the RKKY coupling, exchange bias and the symmetry of the SyF on the excitation spectra. It should be pointed out, that this corresponds to a standard STO, where the FL is fixed (in the positive direction of the applied field) and acts as an external polarizer, that spin polarizes the current. Spin momentum transfer is then considered only to occur for the TL, since the spacer between the TL and BL is supposed to reduce the spin polarization. The BL is excited only due to the RKKY interaction[4]. The parameters of the SyF reference structure used for the numerical simulations are given in table 3.1. In order to understand the STT driven auto-oscillations of the SyF, we first present the excitation spectra of the FMR modes (j_{app}=0)[5].

4.2.1 Sub-Critical regime, damped modes of spin tranfer nano-oscillators

The ferromagnetic resonance (FMR) or damped modes at small values of current density ($j_{app}<j_c$) will provide a first understanding of the STT modes under large current ($I_{app}>I_c$). The damped modes are magnetization excitations around the local effective field at small amplitudes of precession. In experiments, these damped modes can be observed in the sub-critical regime below the critical current and occur due to thermal excitation. Therefore these modes are called often thermal ferromagnetic resonance (TFMR).

The procedure of how to calculate the frequency and attenuation of damped oscillations has been described in chapter 3, using the linearization of the LLG or LLGS equation. The main feature of the damped excitations of the SyF system is that the frequency versus field dispersions of the dynamically uncoupled system splits at the crossing of the frequencies, generating two new normal modes: the acoustic and the optic mode. This procedure has been used to calculate the frequency-field dispersions for the SyF structures shown in Fig. 4.9 where the corresponding hysteresis loops and the RH curves are giving in Fig. 4.6.

In Fig. 4.9 we compare the FMR curves of a pinned SAF for two values of the exchange

[4]In this case the FL is fixed in the positive direction of the applied field as in the case of the results in Fig. 4.6.

[5]In this section of numerical results we use de current density j_{app} (A/m^2) instead the current in mA.

bias field $\mathbf{H}_b$=500 and 0 Oe and for two values of the RKKY coupling, J_{RKKY} =-0.1mJ/m^2 and -1mJ/m^2. The red and blue arrows correspond to the TL and BL magnetizations.

The conditions for Fig. 4.9 (a) should be compared to the green hysteresis loop of Fig. 4.6 (a) that shows that for this weak value of RKKY coupling, the spin flop region is absent and that the magnetization switches abruptly from the saturation region to the plateau region. These abrupt changes translate into abrupt jumps in the frequency field dispersion that is shown for sweeping the applied field from negative to positive values (pink circles) and from positive to negative (black circles). Both the acoustic and optic modes are shown, whose frequency shows concave and convex curvatures respectively in the plateau region and increases with field in the saturation region.

In chapter 3 only the numerical methods were introduced, showing that in the case of a SAF the splitting leads to an acoustic and optic type of mode. In Fig. 4.10 we show the phases of the m_y and m_z magnetization components of these damped modes, for the SAF structure of Fig. 4.9 (a) and (c). The applied field was fixed at H_{app}=300 and 500 Oe (plateau and saturation region) and without current density at j_{app}=0. For these simulations the temperature was T=0K.

In the plateau region, the acoustic mode shows the m_y components out of phase while the m_z remain in phase, reducing the RKKY energy. In contrast the case of the optical mode presents the m_y components in phase while the m_z components are out of phase. Therefore the mode with small energy is the acoustic mode. The case of the saturation region (H_{app}=500Oe) is different since the magnetic configuration of the SAF changes, both magnetization (TL, BL) point into the sense of the magnetic field. The acoustic mode shows the m_y components out of phase and the m_z in phase. In the case of the optical mode the m_y components are in phase moving together but the m_z components are out of phase. This optical mode will be the low energy mode in the saturation region.

An example of the FMR dispersion of the acoustic mode for strong RKKY coupling is shown in Fig. 4.9 (b) for two values of H_b=0, 500 Oe. As indicated in chapter 3, the splitting between the acoustic and optic modes increases for increasing RKKY. This is why the optic modes are pushed to much higher frequencies in Fig. 4.9 (b) as compared to Fig. 4.9 (a). A second difference between weak and strong couplings is that in (b) the spin flop region is well pronounced, so that there are specific features in the dispersion to be seen between the plateau and saturation region, that are absent in the weak coupling case. The frequency dispersion in a SyF depends on the magnetic configuration. The positions of the TL and BL magnetizations in the spin flop region are canted that makes the frequency dispersion more complicated in this region.

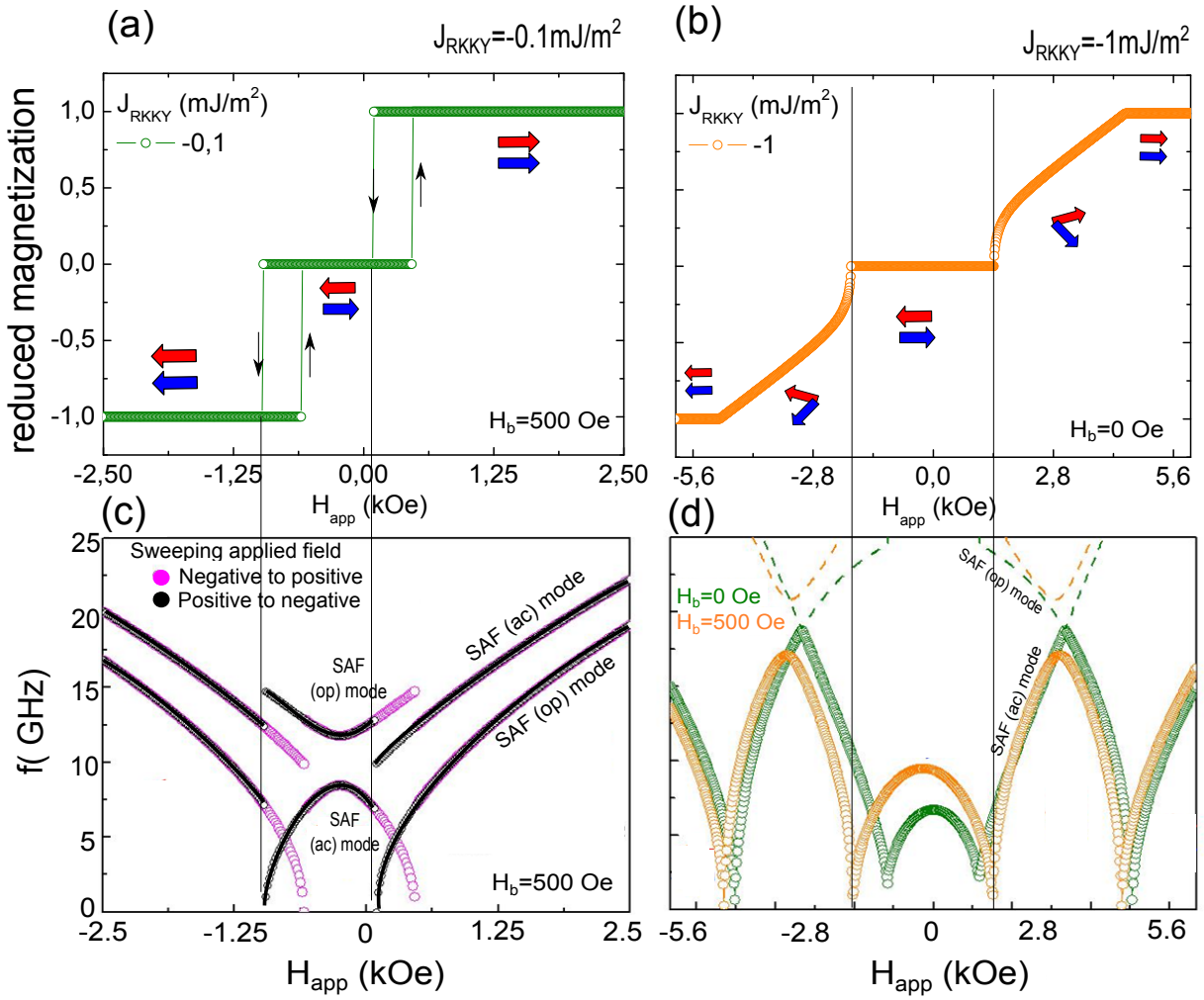

Figure 4.9 – (a),(b) The hysteresis loop of the SAF reference (parameters table 3.1) for J_{RKKY}=-0.1 and -1mJ/m^2 respectively (same hysteresis of Fig. 4.6). In (b) it is presented the hysteresis loops of a pinned and unpinned SyF structure (H_b=0 and 500Oe). In (c) the FMR modes are presented for the reference SAF pinned with a RKKY coupling of J_{RKKY}=-0.1mJ/m^2. The shape of the FMR curve changes with the sweeping sense of the applied field. This is represented by the black and pink circles. (d) FMR modes of the reference SAF pinned and unpinned structure. The colour arrows correspond to the magnetization direction (of the TL and BL).

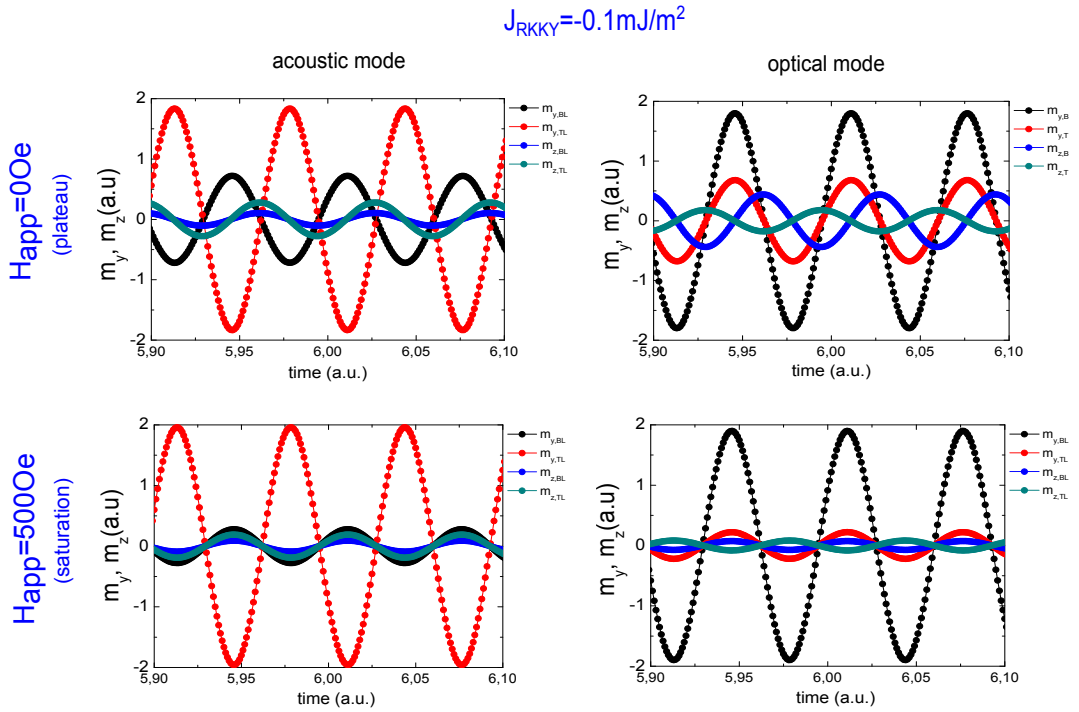

Figure 4.10 – Acoustic and optic damped modes j_{app}=0 from the linearisation of the LLGS equation for an isolated SAF corresponding to the Fig. 4.9 (c) (parameters table 3.1). The applied field was fix in 0 and 500Oe (plateau and saturation region). The temporal evolution of the components m_y and m_z are shown.

The hysteresis loops corresponding to the FMR loops are shown in Fig. 4.6 (c)-(d). The asymmetry of the plateau in the case of H_b=500 Oe is reflected in the FMR loop that is also shifted to negative fields. The phases between the components m_y and m_z for the curve of Fig. 4.9 (d) is shown in the Fig. 4.11.

In the sub-critical regime (damped modes) the SAF will present two well defined modes, but when the system approaches the critical current, only one mode will evolve into the STT.

For applications we are interested to stabilize excitations at low or zero applied field. This is why the study of the FMR and the steady state oscillations will focused on the plateau region only and this mainly for positive values of the applied field, see Fig. 4.9 (c),(d).

The magnetic configuration will determine the FMR tendency. In return the measurement of the FMR dispersion can be used to better understand the magnetic configuration of the structure. This statement will be used in the experimental result to understand the frequency dispersion of the D-SyF STO, composed by two SyF layers.

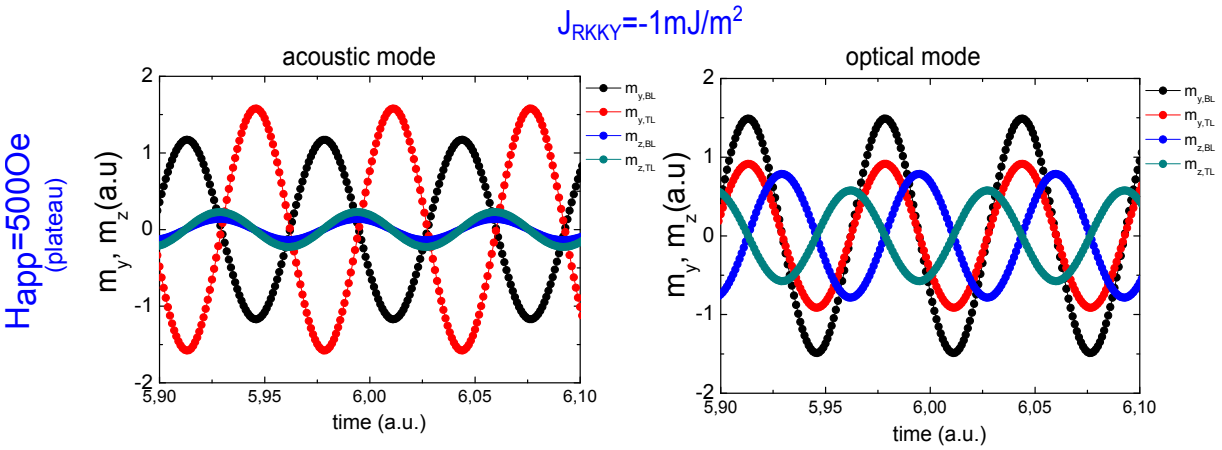

Figure 4.11 – Acoustic and optic damped modes j_{app}=0 from the linearisation of the LLGS equation for an isolated SAF (parameters table 3.1. The STT mode of the SAF will be the evolution of one of these modes. The phases between the component m_y and m_z are shown.

4.2.2 Influence of the exchange bias field in steady state oscillations of the SyF

In this section we will address the steady state excitations of different SyF structures as a function of the exchange bias and RKKY coupling strengths. As it has been discussed in the section above (analysis of damping on current), the acoustic mode will be driven into steady state for negative applied current. The concept of linearization (chapter 3), only provides information on the stability of the modes, but cannot be used for the analysis of the dynamics above the critical regime, because the relative amplitudes decrease. Therefore the LLGS equation (eq. 3.21) is solved numerically using the method of section 3.1.3, taking the same isolated pinned SAF structure as a reference, see table 3.1. For these simulations a FL switching in zero applied field is included, as in a real STO device, however it is emphasized, that the FL plays here only the role of the polarizer and its magnetization remains fixed. We start the discussion for constant RKKY and varying the exchange bias field.

4.2.2.1 State diagrams

As it has been explained in chapter 3, in order to obtain a better understanding on the external parameters to reach the steady state oscillations one should establish a state diagrams that shows for which conditions of the applied field and applied current density the system is in a stationary steady state or in a static state, see Fig. 3.5. We start our discussion with the state diagram of the reference pinned SAF for which the RKKY

coupling is J_{RKKY} =-1mJ/m^2 and the exchange bias field is H_b= 500 Oe, and then discuss the changes for different weaker values of the exchange bias field, H_b=0, 200 Oe (Table 3.1). The corresponding diagrams and trajectories of the different dynamic states are presented in Fig. 4.12 (a)-(c). Only the AP state between the TL and the FL layer is examined, for which a negative current j_{app} destabilizes the SAF. The hysteresis loops and RH corresponding to H_b=500 and H_b=0 Oe are those of Fig. 4.12 (d) and the FMR modes of Fig. 4.9 (d).

The state diagrams show the different regions of static and dynamic states, for positive fields of the plateau region starting from zero field to 0<H_{app}< H^+_{sf}. The arrows correspond to the magnetization direction of the TL (red arrow) and BL (blue arrow). Since the system is an isolated SAF, the position of the FL magnetization will be always in the same direction as the applied field.

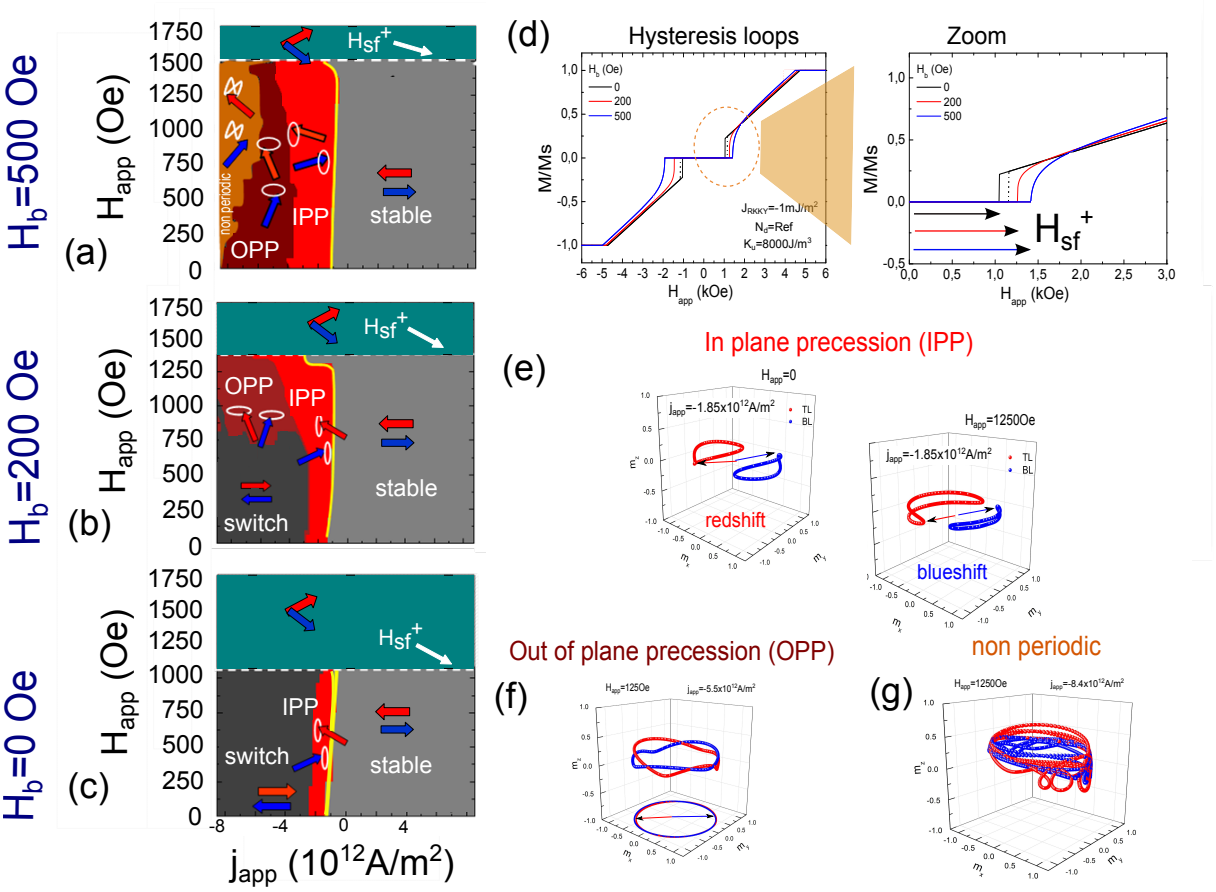

Figure 4.12 – (a)-(c) Evolution of the magnetization dynamics in the state diagrams applied field vs. apply current density for different values of exchange bias field (H_b=500, 200, 0 Oe). All the cases correspond to SAF structure with a J_{RKKY}=-1mJ/m^2 (parameters in table 3.1). It is shown the different regions of magnetization dynamics, the in-plane precession (IPP), out plane precession (OPP), and also the stable regions. (d) The corresponding hysteresis loops of the three SAF structures with a zoom in the region of study. (e)-(g) Different excitations regimes, IPP, OPP and non periodic regimes.

For the state diagram of the reference SAF Fig. 4.12 (a) the magnetizations of the SAF remain in a stable state for positive currents (electrons flowing from the TL into the FL in the standard STO), i.e. there are no excitations of the SAF for these values of applied current and both magnetizations remain their initial antiparallel magnetic configuration. For negative values of applied current density it is possible to obtain steady state oscillations, (electrons flow from FL as polarizer into the SAF layer). If the negative current density reaches a critical value, the in plane precession (IPP) is the first mode to be observed, (the critical current density is represented by the yellow line) represented by the red region in Fig. 4.12 (a). Increasing the current density, the IPP oscillations develop into the out of plane precession (OPP) mode where the magnetization oscillates around the axis of maximal energy (wine region of the diagram). The trajectories of the IPP and the OPP modes are shown in Fig. 4.12 (e)-(f). It should be noted here that the IPP mode develops from the acoustic FMR mode discussed in the previous section. For the OPP mode the out of plane components of both the TL and BL are pointing together into either the positive or negative direction while the in plane components are out of phase, see the components phases on Fig. 4.13.

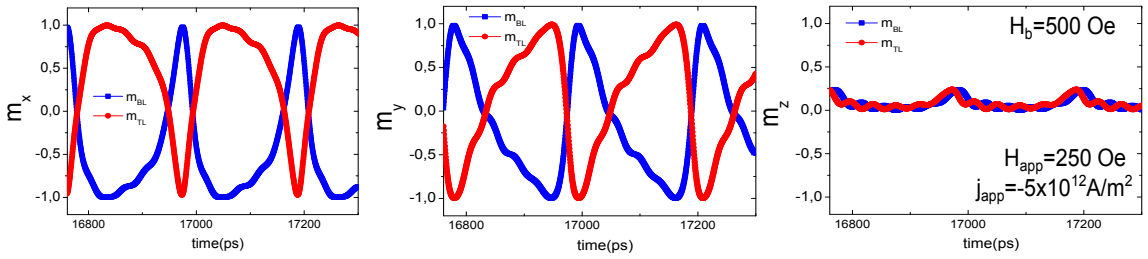

Figure 4.13 – Phases of the OPP mode for H_{app}=250 Oe and j_{app}=-5×10^{12}A/m^2.

If the current density is further increased, the system reaches a non-periodic excitation mode (orange region in the diagram). A non periodic trajectory is shown in Fig. 4.12 (g). We can observe that it continues in a OPP trajectory but with small IPP sub-trajectories. All three types of dynamic excitations exist up to the maximum field of H^+_{sf} ≈1500 Oe, which is the static spin flop shown in Fig. 4.12 (d). This diagram shows that it is possible to stabilize steady state oscillations for the SyF in the plateau region, and in particular in zero applied field.

In Fig. 4.12 (b) the corresponding state diagram is shown for a similar SyF structure as in Fig. 4.12 (a) but for a lower exchange bias field of H_b=200 Oe. In consequence the spin-flop field is a bit lower (1312.5 Oe) than for H_b=500 Oe (1500 Oe). There are three distinct difference as compared to the reference SyF structure: (i) in low applied fields the region of IPP excitations is reduced and (ii) the transition to the OPP mode is replaced by a switching of the SAF (dark grey region in the diagram Fig. 4.12 (b)), where both the TL and BL switch their orientation; (iii) in higher applied fields up to H^+_{sf} the OPP

region is increased and the region of the non-periodic excitations has disappeared.

In Fig. 4.12 (c) the state diagram for an unpinned SAF structure is shown, with a spin flop field of H_{sf}^{+}=1000 Oe. The IPP region is further reduced with a lower current for the transition to the region of the SAF switching in the whole field range. The OPP region is absent.

In all three cases the critical current j_c separating the static and the dynamic states (yellow line) does not depend strongly on the exchange bias field, since the RKKY interaction is much stronger and most likely dominates the critical current.

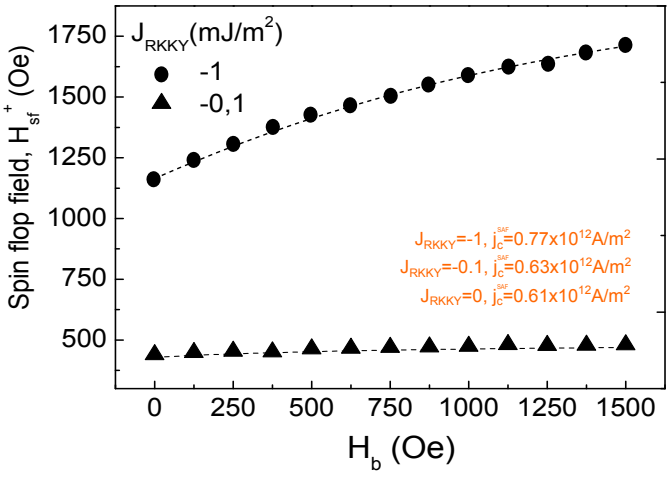

Figure 4.14 – Spin flop field dependence for two SAF structures (parameters table 3.1) for J_{RKKY}=-0.1 and -1mJ/m^2 using numerical simulations. The dashed line (red and black) correspond to the eq. 8.4 of [Gusakova et al., 2009]. The critical current of the SAF (j_c^{SAF}) was found for the SAF in the plateau region (H_{app}=0) using the eq. 4.2 adapted from [Gusakova et al., 2009].

In Fig. 4.14 it is shown the dependence of the spin flop field H_{sf}^{+} as a function of the H_b for the reference SAF structure (parameters table 3.1) for J_{RKKY}=-0.1 and -1mJ/m^2. The dashed line (red and black) corresponds to the analytical value using the eq. 8.4. We obtain the critical current of the SAF structure (J_{RKKY}=0, -0.1 and -1mJ/m^2) using the eq. 4.2 of [Gusakova et al., 2009], see inset on Fig. 4.14.

$$j_{plateau}^{SAF} = -\frac{\alpha}{G}(H_{app} + H_{RKKY} + H_{an} + H_d) \tag{4.2}$$

The occurrence of the switching region can be qualitatively explained as follows. The TL feels directly the spin torque and can be reversed when the current density is high enough. However, only for zero exchange bias, the BL is completely free to follow the

movement of the TL due to the RKKY coupling and can switch as well. This is why in the case of H_b=0 the switching region is very large. For non-zero exchange bias, the BL feels a competition between the exchange bias from the AF and the RKKY coupling from the TL that is driven by spin transfer torque. When the exchange bias is too strong the reversal of the SAF (i.e. both the TL and BL) is suppressed and as a compromise the system transits into the OPP mode. The intermediate case of Fig. 4.12 (b) where there exists a switching region in low field and an OPP region at higher fields can be explained by the fact that the external field is in the direction of the BL magnetization, see Fig. 4.1. For low field this does not contribute too much to keep the BL in the field direction and the BL can switch when the TL wants to switch due to STT. However in higher fields, the BL is more and more stabilized by the external field and does not want to switch and as a compromise the OPP mode is established.

The non periodic region is present only for high values of RKKY coupling and high values of applied current density. The strong AP coupling of the structure will induce this non-coherent behaviour between an OPP and IPP trajectories. The system wants to remain in the AP state (to minimize the energy) but in the OPP both magnetization shows the same m_z direction (high energy), see Fig. 4.13. This competition could be the origin of the non-coherent precession.

4.2.2.2 Frequency dependence on Field and Current for the IPP mode for varying the exchange bias

We will now address the dependence of the frequency as a function of the applied field (easy axis direction) and current density focusing first on the IPP modes. The frequency as a function of the applied field is shown for the reference pinned SAF for the different exchange bias fields in Fig. 4.15 (a)-(c). For values of the current density close to the critical current the frequency is close to the frequency of the acoustic ferromagnetic resonance (FMR) mode (damped modes) up to the spin-flop field. It is known from the IPP mode of an isolated single layer (e.g. the FL) that the frequency vs field follows the FMR dependence but that upon increasing the current the frequencies decrease and that the f vs H_{app} dispersions are more or less parallel down shifted in frequency (frequency red shift for the full field range), see Fig. 4.16.

In the case of the unpinned SAF structure H_b=0 Fig. 4.15 (c) such a frequency redshift is observed for all fields up to the spin flop field. In the case of non-zero exchange bias, Fig. 4.15 (d) and (e), this is quite different. Only in low fields the frequency is red-shifted upon increasing current, while in higher fields the frequency is shifted upwards (blue-shifted)

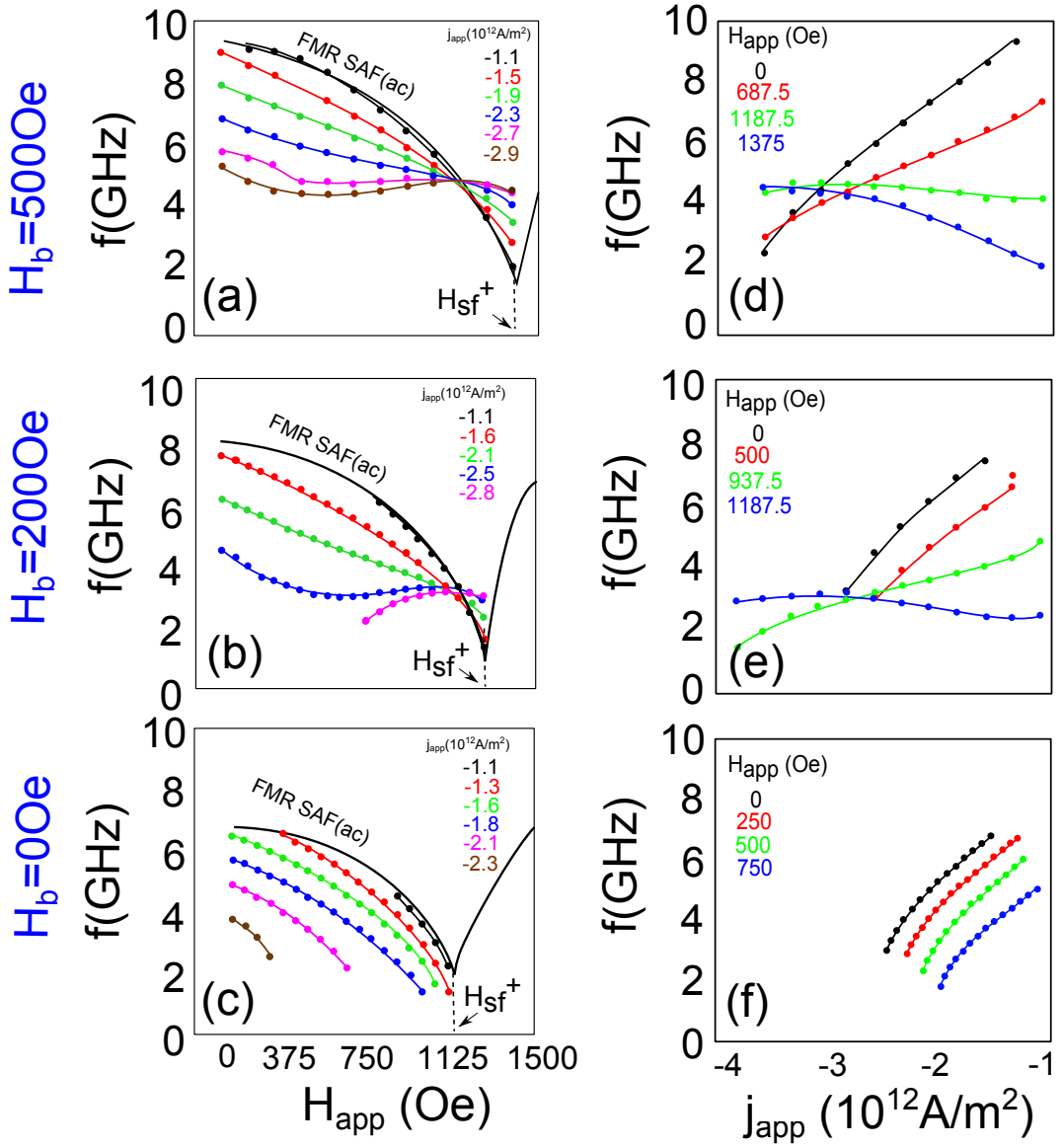

Figure 4.15 – The oscillation frequency is studied as a function of the applied field (a)-(c) and as a function of the current density in (d)-(f). It is shown that the tuning (df/dj_{app}) changes for high values of applied fields in the case of a SAF pinned structure (d) and (e) in contrast with the case of a SAF unpinned layer (f).

above the value of the FMR frequency. As a consequence there is a field value H_{cross}^{STT} at which all the frequency-field curves cross. For H_b=500 Oe and 200 Oe, this crossing field is H_{cross}^{STT} ≈1125 Oe (at 5GHz and f=3 GHz). An increase of the exchange bias field will reduce the amplitude of the BL precession (TL precession also due to the RKKY) therefore we note that the frequency of the acoustic IPP mode increase as a function of the exchange bias field.

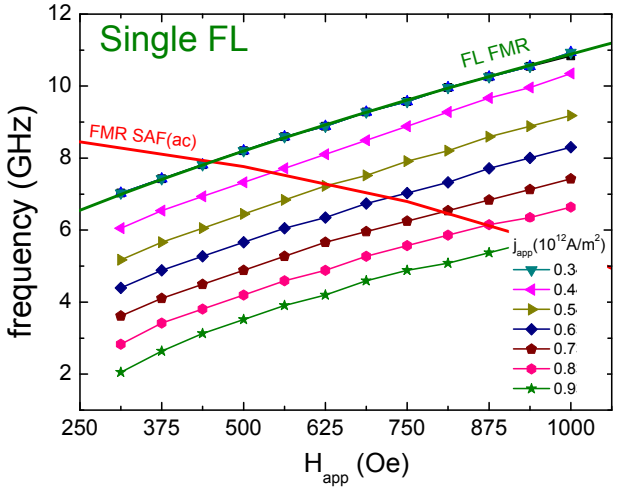

Figure 4.16 – Single FL frequency dispersion as a function of the applied field. Parameters in table 3.3 without taking into account the dipolar field and the MSTT. The STT mode are parallel to the FMR more j_{app}=0.

This change from frequency redshift to frequency blueshift is an important feature of the SAF excitations since it will be possible to tune the frequency from $df/dj_{app}<0$ to $df/dj_{app}>0$ upon changing the in-plane applied field and to study other dynamic properties (such as the linewidth or synchronisation) as a function of the frequency shift. An explanation of this change from redshift to blueshift will be presented in section 4.2.5.

The change from redshift to blueshift regime in the SAF structures is evidenced more clearly when plotting the frequency vs current for different applied field values Fig. 4.12 (d-f). The SAF structures with H_b=500 and 200 Oe show frequency redshift for $H_{app}<H_{cross}^{STT}$ and frequency blueshift for $H_{app}>H_{cross}^{STT}$ while the unpinned SAF shows only redshift, Fig. 4.12 (f).

In conclusion, the magnetization dynamics in a SAF is strongly affected by the exchange bias field. Thus in order to develop an STO using a SAF excitation layer, it will be important to take into account that the region of excitation of the steady state IPP mode depends on the value of the exchange bias field without an important change of the critical current. On the other side, the low switching current density (TL opposite to the magnetic field) in the case of the unpinned SAF layer makes it a good candidate for MRAM technologies, in comparison to the single FL.

4.2.3 Influence of the RKKY coupling in the steady state oscillations of the SAF

In the previous section the influence of the exchange bias field for the case of a SAF structure with a strong RKKY coupling, J_{RKKY}=-1mJ/m^2 was studied. In this section we will analyse the dependence of the STT modes on the RKKY coupling strength with medium J_{RKKY}=-0.5mJ/m^2 and weak J_{RKKY}=-0.1mJ/m^2 coupling for constant exchange bias of H_b=0, 200 and 500 Oe. Corresponding hysteresis loop are shown in Fig. 4.17.

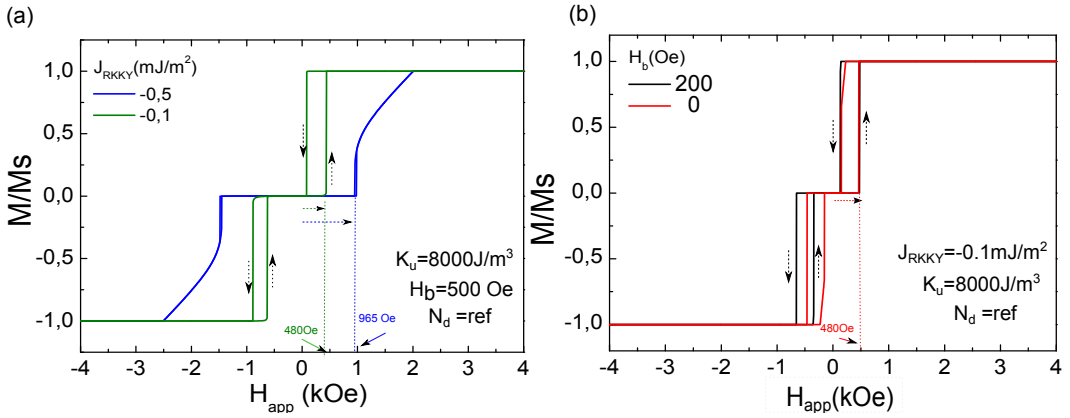

Figure 4.17 – Hysteresis loops of a SAF pinned (parameters in table 3.1) for medium J_{RKKY}=-0.5mJ/m^2 and weak J_{RKKY}=-0.1mJ/m^2 coupling. The horizontal arrows denote de region where we will focus the study of the magnetization dynamics ($0<H_{sf}^{+}$).

The saturation field obtained from the hysteresis loop of Fig. 4.17, in the case of J_{RKKY}=-0.1mJ/m^2 is close to 480Oe for the three cases of H_b=0 ,200 ,500Oe. We notice that a small spin flop region appears only in the case of H_b=0.

4.2.3.1 State diagrams

The dynamic state diagram, applied field vs applied current density, for J_{RKKY}=-0.5mJ/m^2 is shown in Fig. 4.12 (a). As compared to the case of J_{RKKY}=-1mJ/m^2, in Fig. 4.18 (a), the spin-flop field is reduced to H_{sf}^{+} ≈1000 Oe, in agreement with the static simulations in Fig. 4.17. The dynamic states also reveal some differences. First upon increasing the current above the critical current an IPP mode is excited that transits into an OPP mode at higher current and for fields below 500 Oe. This OPP mode is similar to the one in Fig. 4.12, where both the TL and BL have the same out of plane magnetization component. Upon further increasing the current (H_{app}<500 Oe) the system reaches a new stable state ($switch_2$, dark grey region), where the TL is out of plane while the BL remains in-plane given by the exchange bias field direction. For higher values of applied field H_{app}>500 Oe,

the region of OPP precession is reduced and the OPP precession becomes non-coherent and non-periodic. It corresponds to the orange region in the diagram (non periodic) of Fig. 4.18 (a).

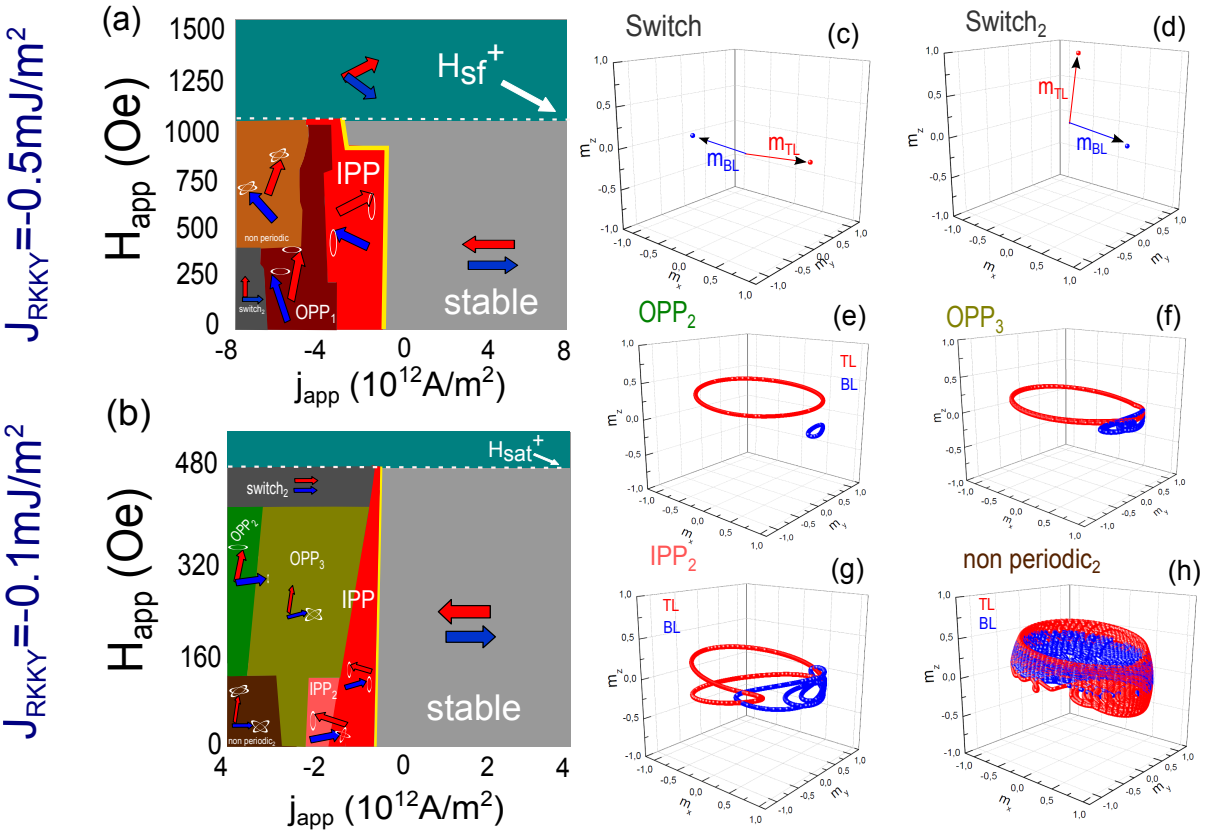

Figure 4.18 – Evolution of the magnetization dynamics in the state diagrams applied field vs. applied current density for different values RKKY coupling, J_{RKKY}=-0.5 and -0.1 mJ/m^2 (a), (b) respectively. These should be compare with the case of J_{RKKY}=-1 in Fig. 4.12 (a). Figures (c)-(h) show the trajectories for the different regions in the state diagrams.

The state diagram for weak RKKY coupling J_{RKKY}=-0.1mJ/m^2, is shown in Fig. 4.18 (b). As a consequence of this weak coupling, the structure is easily saturated by the applied field (H_{sat}^+=480Oe) and the spin-flop region disappears. This fact is in agreement with the results of static loops, see Fig. 4.17 (a). The IPP mode region becomes small (notice that the current scale is not the same). If the current density is increased, the spin transfer torque induces an OPP mode, however it is different than the OPP mode described before. In this case only the TL magnetization precesses on an OPP trajectory while the BL precesses on a non coherent IPP trajectory (OPP_3, dark yellow region) since the RKKY coupling is not strong enough to take the BL magnetization out of the plane as in the case of J_{RKKY}=-0.5mJ/m^2, Fig. 4.18 (a). For small values of applied field, $H_{app}<$ 160 Oe the system remains in IPP mode but the BL shows an exotic behaviour around the x axis (IPP_2, pink region), see Fig. 4.18 (g). Increasing further the applied current, for $H_{app}<$125Oe, the oscillations of the TL precesses in a non coherent trajectory (brown

region on the diagram, non periodic$_2$) and for H_{app}>125Oe the BL precess with a small amplitude in IPP mode while the TL continues in a OPP mode (OPP$_2$, green region in the diagram).

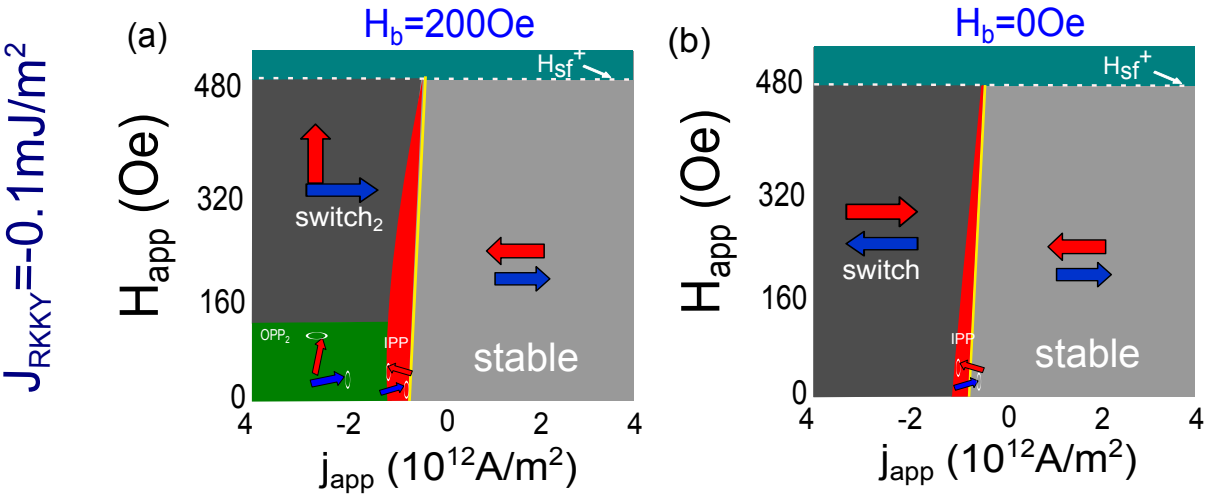

Figure 4.19 – Evolution of the magnetization dynamics in the state diagrams applied field vs. applied current density for different values RKKY coupling, J_{RKKY}=-0.1 mJ/m^2 for H_b=200 Oe and 0 Oe (a), (b).

The state diagram for weak RKKY coupling J_{RKKY}=-0.1mJ/m^2, for H_b 0, and 200Oe are shown in Fig. 4.19. These structures are also easily saturated by the applied field (H^+_{sat} ≈480Oe) as in the previous case, see Fig.4.17. The spin-flop region is absent. For the case of a SAF with H_b=200Oe, the IPP mode region becomes smaller. If the current density is increased (for small values of applied field, H_{app}< 125 Oe), the spin transfer torque induces an OPP$_2$ mode. For H_{app}> 125 Oe the system shows a stable region (switch$_2$) where the TL is switched pointing perpendicular to the plane. The case of a SAF unpinned with weak RKKY coupling shows an even smaller region of IPP oscillations, see Fig. 4.19 (b). Increasing the current in all the range of applied field the SAF is switched completely, see the trajectories in Fig. 4.18 (c).

The reduced region of IPP oscillations is of little advantage for microwave applications. However, the occurrence of the OPP mode in zero applied field can be potentially of interest, since OPP modes will give rise to a larger output signal as compared to IPP modes, since they make use of the full MR change from the P to AP alignment when using an in-plane reference layer to produce the MR signal. We will study the frequency tuning of the OPP precession in this chapter.

4.2.3.2 Frequency dependence on Field and Current for the IPP mode

The frequency dependence as a function of field and current is shown respectively in Fig. 4.20 for J_{RKKY}=-0.5 and -0.1mJ/m^2. It shows the same dependence as compared to the reference SAF with J_{RKKY}=-1mJ/m^2 with a transition from frequency redshift to frequency blueshift vs current, see Fig. 4.15 (a) upon increasing the applied field. In Fig. 4.20 (a), the field value corresponding to the crossing of frequencies (≈5GHz) is reduced in comparison with the case of strong RKKY coupling, see Fig. 4.15 (a), (approximately in ≈350Oe).

In the case of J_{RKKY}=-0.1mJ/m^2, Fig. 4.20 (c) the applied field dependence shows that there is no more crossing between redshift and blueshift and there is only redshift vs current as shown also in Fig. 4.20 (d). In comparison with the case of an strong RKKY coupling the system reaches the OPP mode easily, i.e the TL feels more free to go out of plane and precess on OPP mode.

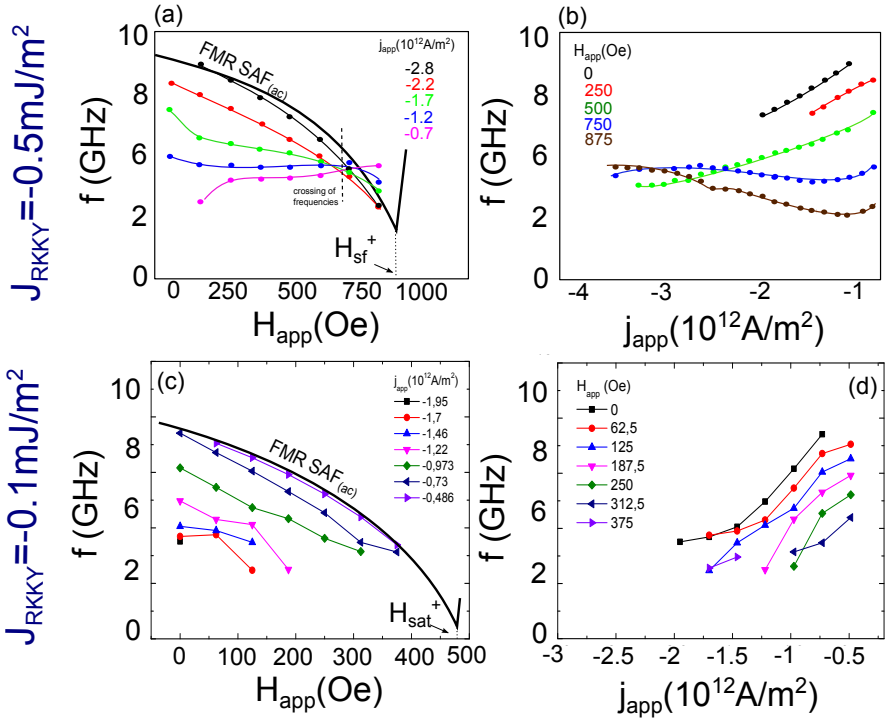

Figure 4.20 – The oscillation frequency is studied as a function of the applied field (a)-(b) and as a function of the current density in (c)-(d). It is introduced that the tuning (df/dj$_{app}$) changes for high values of applied fields in the case of a SAF pinned structure (d) and (e) in contrast with the case of a SAF unpinned layer (f).

To summarize, the RKKY coupling as well as the exchange bias field play an important role for the dynamic excitations of a pinned SAF structure. A weak RKKY coupling results in a small region of the IPP mode and the BL magnetization is unable to follow the motion of the TL magnetization in the OPP mode. If the exchange bias is strong

enough the BL magnetization will remain in the direction of the exchange bias field. The RKKY coupling also influences the frequency tuning, where a blueshift regime only appears for SAF structures with a strong RKKY and non zero exchange bias.

4.2.3.3 The out of plane precession, OPP

The possibility to obtain a OPP precession of the SAF could be of interest for applications. In Fig. 4.21 (a) we present the frequency dispersion as a function of the applied current density for the reference SAF pinned by H_b=500Oe. We chose four values of applied field in the redshift (H_{app}=0, 750Oe) and blueshift (H_{app}=1200, 1375Oe). The IPP mode transits into the OPP generating an abrupt jump.

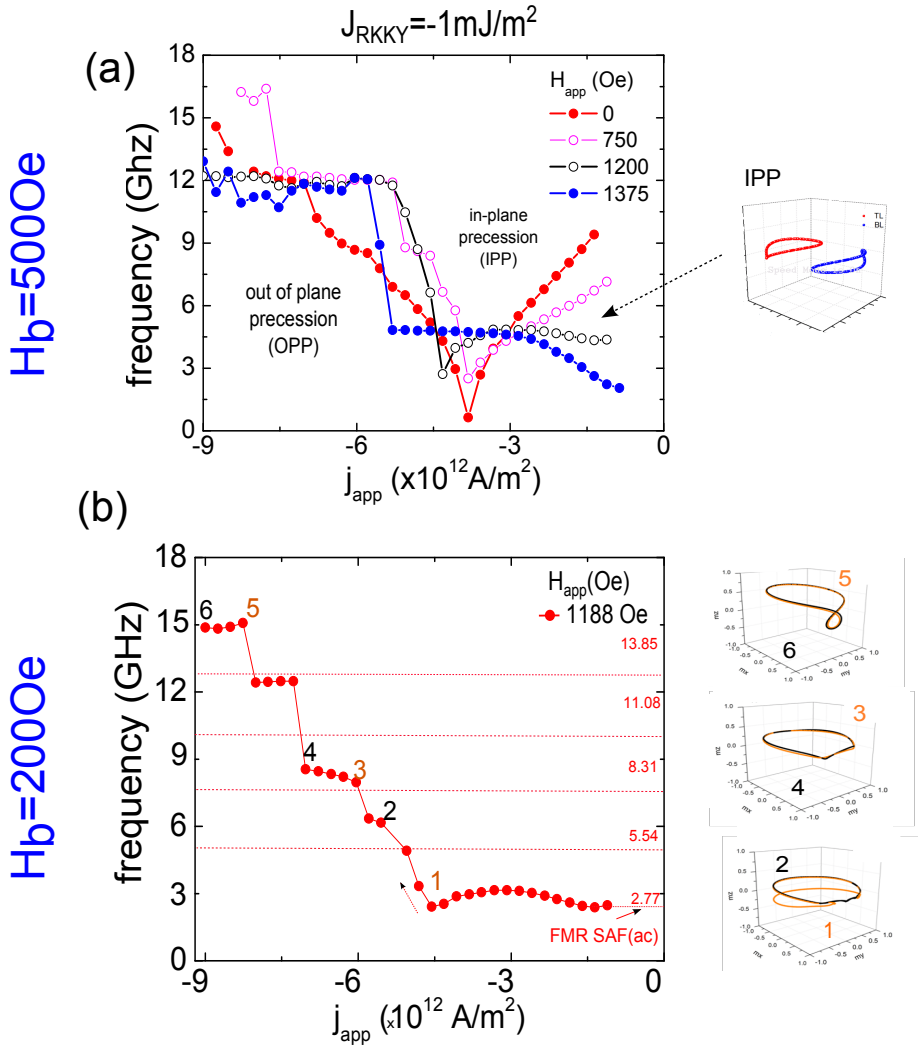

Figure 4.21 – (a) Frequency tuning as a function of the current for the SAF of reference (H_b=500Oe) of Fig. 4.12 (a), for four values of H_{app}=0, 750, 1200, 1375Oe. In (b)-we show the case of a SAF with H_b=200Oe, for H_{app}= 1188Oe. We observe jumps and a flattening in the OPP regime j_{app}<-5×10^{12}A/m^2.

In Fig. 4.21(b), the case of a SAF pinned by H_b=200Oe is shown, for H_{app}=1188Oe. We can observe the IPP and OPP region. In the OPP regime the frequency present jumps and flat regions (constant frequency). In comparison with the case of H_b=500 these jumps are not obvious and the flattening region is larger.

4.2.4 Influence of the asymmetry in the steady state oscillations of the SyF

In the previous section, the frequency tuning (df/dj_{app}) displayed a change from redshift to blueshift upon increasing the applied fields. This change occurs in SAF structures with strong RKKY coupling and when one of the layers is pinned by an AF. The SAF itself is symmetric (i.e. same parameters for the TL and BL, see table 3.1). However, the exchange bias as well as the external field induce an asymmetry in terms of the torques that act on the two layers. We therefore investigated whether a different type of asymmetry will produce the same effect on the frequency current tuning. Instead of exchange biasing one of the layers, we break the symmetry by using a non-compensated SyF with different thicknesses so that the product is $M_{S,TL} \times d_{TL} \neq M_{S,BL} \times d_{BL}$.

In the following we will be compare the results of the unpinned SAF (H_b =0 Oe, see Fig.4.12 (c), and Fig.4.16(c)-(f), with d_{BL}=d_{TL}=2.5 nm against a SyF of unequal thicknesses of the BL, d_{TL}=2.5 nm and d_{BL}=3.0 nm, see Fig.4.22, but otherwise the same parameters as the unpinned SAF. The symmetry of the system will be broken due to (i) the change of the strength of the effective field arising from the *RKKY coupling*, since it depends on the thickness of each layer 1.15 and (ii) the different *shape anisotropy* fields since they depend also on the thickness[6].

Upon comparing Fig. 4.12 (c) with Fig. 4.22 (a) we first note that the spin-flop field is enhanced in the uncompensated SyF. Secondly at higher fields the IPP region is larger, where upon increasing current an OPP mode appears. In lower fields, the IPP mode changes into a switched state upon increasing current, that is similar to the switched state of the unpinned SAF, with a reversal of both the TL and BL.

For the IPP mode we can see from Fig. 4.22 (b) that the asymmetry of the uncompensated SyF induces a cross over from frequency redshift to blueshift (vs current) upon increasing the field. There is a crossing point H_{cross}^{STT}(≈3.5GHz) as in the case of the pinned SAF, see Fig 4.15 (a)-(b). The field value for the crossing point does not change a lot with the

[6]Changing the K_u we can induce also a asymmetry but it is not to strong as in two mentioned cases.

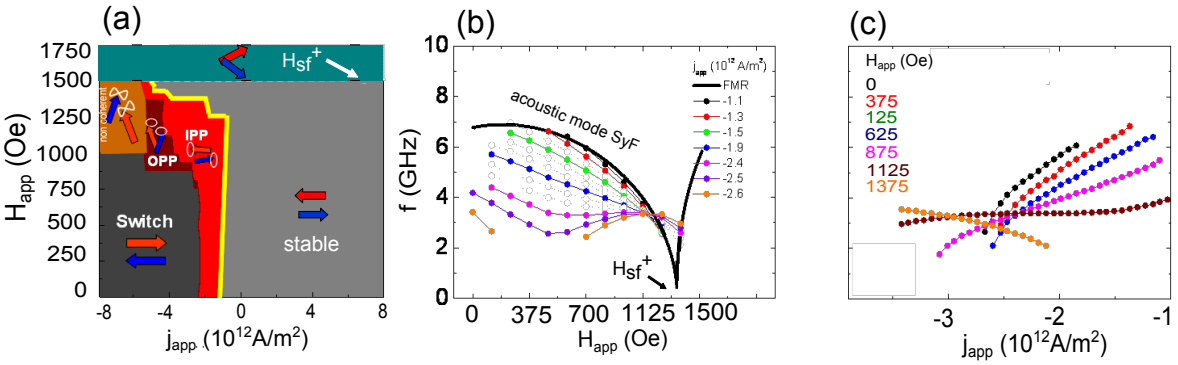

Figure 4.22 – In (a), the state diagram of a non compensated SyF unpinned layer is presented (H_b= 0 Oe) for an asymmetric structure with a RKKY coupling of J_{RKKY}=-1mJ/m^2. The Frequency of oscillations as a function of the applied field is presented in (b) and the frequency as a function of the current density in (c). The thickness of the BL remains in d_{BL}=3.0nm but the thickness of TL is now d_{TL} =2.5nm. We can observe the change in the tunability in comparison with the case of the compensated SyF unpinned layer in Fig. 4.12 (i).

asymmetry if the RKKY coupling remains invariant, see Fig. 4.15(a), Fig. 4.15(b) and Fig. 4.22(b), (H^{STT}_{cross} ≈1125 Oe). The transition from redshift to blueshift is clearly seen in Fig. 4.22(c) in the plot of the frequency vs current density.

These results are important, because one can now envisage designing an STO where the single FL of the standard STO is replaced by an unpinned SyF to obtain almost the same dynamical features of a pinned SAF, see Fig. 4.23.

The simulation results of the unpinned SAF and the unpinned SyF will be a first step to understand the excitation spectra in such a double SyF (D-SyF) STO that will be studied experimentally in chapter 7.

4.2.5 Evolution from the redshift and blueshift regime in SyF

An important feature of the STOs and more specifically when the SyF layer is excited, is the change in the frequency tuning df/dj$_{app}$ (as a function of the applied current), from redshift to blueshift with the increase of the external applied field, see Fig. 4.15 (d)-(e). In order to take advantage of this feature we should understand its origin. The understanding of this effect will help to design and create new devices, with specific characteristics. In this section we will describe the precession of the IPP regimes of the SyF and an explanation of the origin of the blueshift will be proposed.

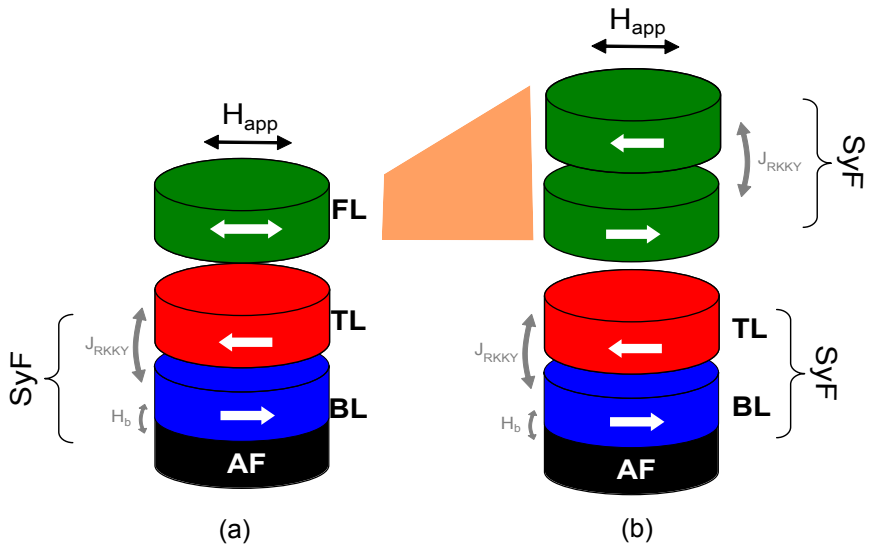

Figure 4.23 – In the standard STO the FL could be replaced by a SyF unpinned which remains the same properties already measured in a SyF pinned layer.

As we know, the IPP mode of the STT excitations is given around the axis of minimal energy, defined by the effective field of the magnetic structure. In each position of the magnetization precession (trajectory), the energy contributions present different values[7].

The static energy surface of the SyF structure as a function of the angles φ_{TL} and φ_{BL} (see inset of Fig. 4.1) will give us information about the state of minimal energy for one value of applied field[8]. In the energy projection (φ_{TL} versus φ_{BL} in Fig. 4.24 (a)-(c)), it is possible to distinguish the minimal values of energy as blue valleys and the highest state of energy as red valleys. In these simulations the component out-of plane of the magnetization is neglected for these small values of current density.

In Fig. 4.24 (a), we show the energy surface of the SAF unpinned structure (H_b=0 Oe), secondly in Fig. 4.24 (b) the case of the reference SAF pinned structure (H_b=500 Oe) and in Fig. 4.24 (c) the last case will correspond to a SyF unpinned structure (H_b=0 Oe and $d_{TL} \neq d_{BL}$). The black dash line which to the values of the static energy in the anti-parallel magnetization configuration with $\varphi_{TL} - \varphi_{BL} = \pi$.

In each case of Fig. 4.24 the magnetic field was H_{app}=0.8H_{sf}^{+}, always close to the spin-flop field value, in order to analyse the blueshift regime. In the case of the unpinned SAF, Fig. 4.24 (a), it is observed that the shape of the valley of minimal energy remains along the dash black line with a small deflection due to the TL magnetization sense (opposite to the applied field).

[7] The total energy during the precession is written as a sum of different contributions, see eq. 3.1. In the SyF the TL (BL) is pointing into the negative (positive) x axis.

[8] The angles define the magnetization position

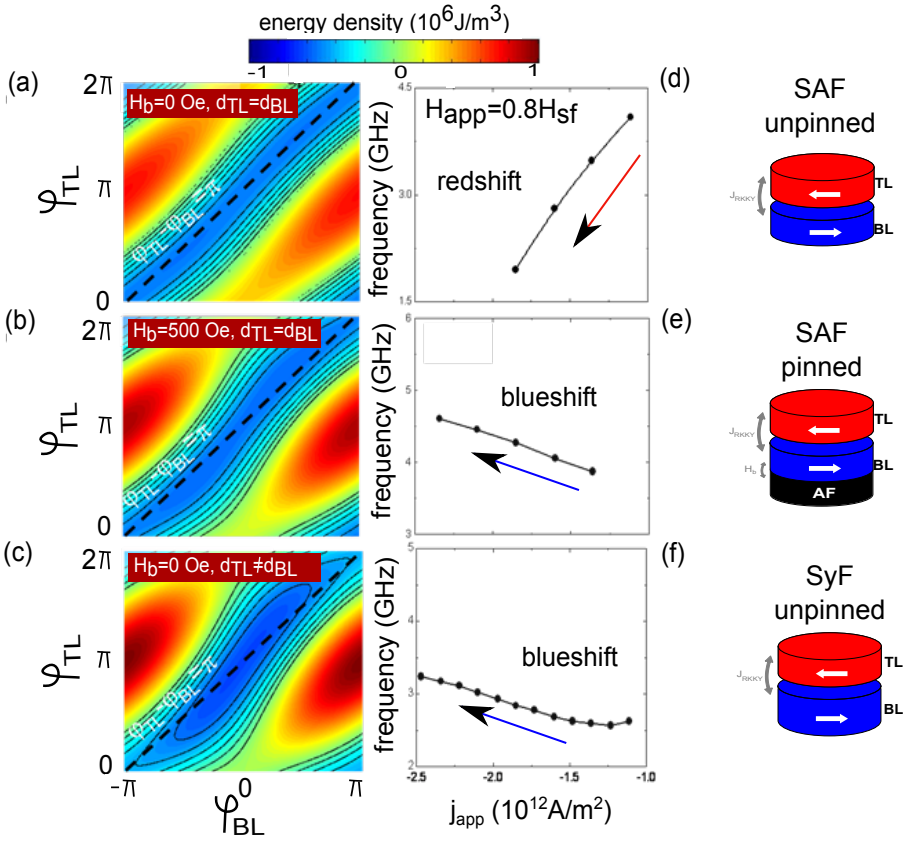

Figure 4.24 – Static energy surfaces neglecting the out of plane component of the magnetization for a RKKY coupling of J_{RKKY} =-1 mJ/m^2 and an applied density current of j_{app}=-1.85× 10^{12} A/m^2 for a SAF unpinned (H_b =0, d_{TL} =d_{BL}) in (a), for a SAF pinned (H_b=500 Oe, d_{TL}=d_{BL}) in (b) and a SyF unpinned (H_b=0, $d_{TL} \neq d_{BL}$) in (c). The dash line in each figure corresponds to the anti-parallel magnetization position, $\varphi_{TL} - \varphi_{BL}$=$\pi$. The applied field value was H_{app}=0.8H_{sf}^{+}, in order to be in a blueshift regime. In (d), frequency versus applied current in the redshift regime is presented, in the asymmetric structures the energy surface is distorted and the blueshift regime appears.

Comparing the static energy of the symmetric structure with the next two asymmetric cases Fig. 4.24 (b) and (c), a change is observed in the shape of the valley of minimal energy. The dash line gives us information about the deflection from the anti-parallel state of magnetizations of TL and BL. In the asymmetric systems the minimum energy is not given by the anti-parallel state but by a configuration that is deflected from AP state.

Now let's focus in the case of the SAF reference which is pinned by an antiferromagnetic layer. The static energy surface for all the possible angles φ_{TL} andφ_{BL} is given in Fig. 4.25 for two field values corresponding to the redshift regime (H_{app}=0 Oe) and to the blueshift regime (H_{app}=1375 Oe). The dashed black lines correspond to a strict antiparallel alignment of the TL and BL magnetizations, $\varphi_{TL} - \varphi_{BL} = \pi$. For low applied fields (redshift regime), the static energy surface presents a valley of minimum energy which extends along $\varphi_{TL} - \varphi_{BL} = \pi$ line with the absolute energy minimum (static equilibrium) at φ_{BL}=0,$\varphi_{TL} = \pi$. The situation changes for higher applied fields (blueshift regime). The valley deviates significantly from the $\varphi_{TL} - \varphi_{BL} = \pi$ line, while the absolute energy minimum remains at φ_{BL}=0, $\varphi_{TL} = \pi$. This asymmetry is mainly due to the fact that the applied field in the case of the BL acts in the same direction as the RKKY field while for the TL it opposes the RKKY field.

This rotation of the energy valley (with the increasing of field) away from the $\varphi_{TL} - \varphi_{BL} = \pi$ line has an important consequence for the spin torque driven dynamics of the IPP SyF mode occurs around the energy minimum. In order to see this on the static energy surfaces, we superpose (in white) the total in-plane energy of the SyF motion along the trajectories of the BL and TL, with the corresponding angles φ_{TL} and φ_{BL}. This dynamical in plane energy is represented by the white closed line on the energy surface, Fig. 4.25 (a). This white line follows the energy valley in both cases (for smaller and higher fields). From this we can see that for low applied fields (redshift regime) the TL and BL magnetizations stay almost antiparallel on all points along the IPP trajectory. In contrast to that, for higher applied fields (blueshift regime) the antiparallel alignment is not maintained. This is shown in more details by the XY-projection of the trajectories in Fig. 4.25 (b). Indeed in the case of low fields the TL and BL trajectories have approximately same amplitudes, while with increasing field the amplitude of TL magnetization is larger than that of BL. The latter case, at the turning points (noted as 1 and 3 in Fig. 4.25 (b)) the TL and BL magnetizations have a maximum deviation from the antiparallel configuration. The TL magnetization experiences the maximum of RKKY field coming from the BL. This field is indicated by the double arrow in Fig. 4.25 (b). As a result, both layers will feel an additional dynamical torque due to the RKKY interaction. This torque is proportional to the vector product$(\mathbf{m}_{BL(TL)} \times \mathbf{m}_{TL(BL)})$ which is largest when the deviation of the

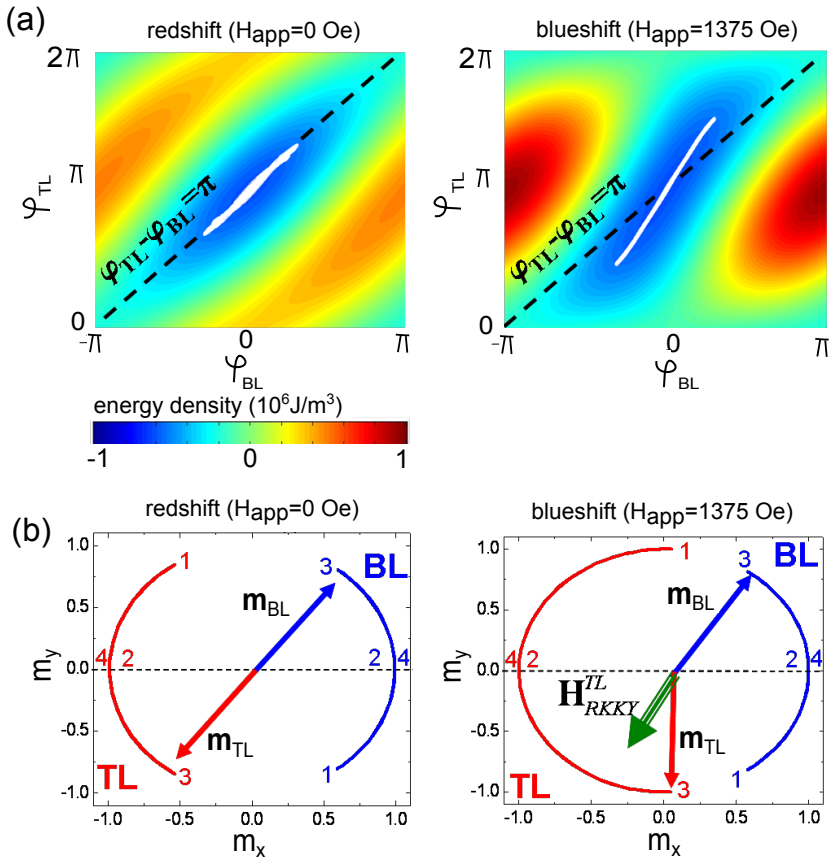

Figure 4.25 – (a) Static energy surfaces (color map) as a function of possible in-plane angles φ_{TL} and φ_{BL} for two field values. The color scale is the same for both energy surfaces. Dashed black lines correspond to the potential situation when the magnetizations of TL and BL are strictly antiparallel with $\varphi_{TL} - \varphi_{BL} = \pi$. Closed white lines correspond to the in-plane angles φ_{TL} and φ_{BL} extracted from simulated trajectories. (b) XY-projections of the magnetization trajectories for TL and BL

expression $\varphi_{TL} - \varphi_{BL}$ from π is largest.

The above reasoning for increasing field at constant current applies also when increasing the current at constant field. For this we remind that the amplitude of the IPP mode increases with increasing current. In Fig. 4.26 (a), we show the evolution of the BL and TL in-plane angle amplitudes φ_{BL} and $\varphi_{TL} - \pi$ as a function of applied current. An important difference between redshift and blueshift regimes can be observed. While in the redshift regime the in plane amplitudes of the TL and BL magnetizations stay very similar, in the blueshift regime the difference between the two in-plane amplitudes is much more important resulting in a increase of the dynamic torque due to the RKKY interaction.

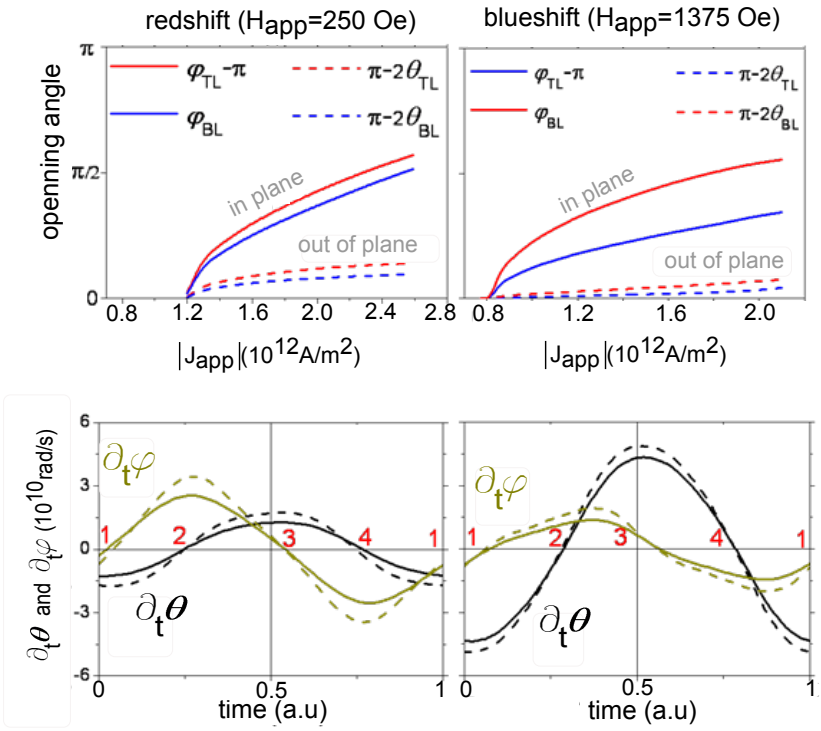

Figure 4.26 – (a) Solid lines: BL and TL in-plane angles amplitudes $(\varphi_{BL}, \varphi_{TL} - \pi)$. Dashed lines: BL and TL out-of-plane angles amplitudes $(\pi - 2\theta_{BL}, \pi - 2\theta_{TL})$. (b) Rate of change of the in-plane and the out-of-plane angles as a function of normalized time for one oscillation period. Solid lines correspond to the current density $|j_{app}| = 1.36 \times 10^{12} A/m^2$ and dashed lines correspond to $|j_{app}| = 1.6 \times 10^{12} A/m^2$

To illustrate how this additional dynamic torque affects the frequencies and the transition from the redshift to the blueshift regime we analyse the local velocities along the trajectory. For this we show in Fig. 4.26 (b) the evolution of the rate of change of the in-plane $(d\varphi_{TL}/dt)$ and out-of-plane angles $(d\theta_{TL}/dt)$ vs. time for one period of oscillation. In the redshift regime the variation of both components has the same order of magnitude. The evolution of the frequency as a function of current is not much affected by the RKKY interaction and the slope df/dj_{app} stays negative $(df/dj_{app} < 0)$ as in the case

of a single free layer. In contrast to that in the blueshift regime it is the amplitude of the out-of-plane velocity $d\theta_{TL}/dt$ which dominates over the in-plane velocity $d\varphi_{TL}/dt$. At the turning point 3 of the trajectory the amplitude of the out-of-plane component has its maximum with a main contribution coming from the RKKY interaction giving the most important contribution to the overall velocity. Thus the evolution of frequency as a function of current is strongly affected by the dynamical RKKY interaction. In the case of blueshift the dominance of the out-of-plane component of velocity becomes important enough to inverse the usual tendency and changes the slope df/dj_{app} from negative to positive ($df/dj_{app} > 0$). We compared two extreme cases of low and high fields. The evolution from the redshift to the blueshift regime is gradual for intermediate values of applied fields. This means that the contribution of the additional torque due to the dynamic RKKY interaction field to the resulting velocity becomes more and more important with rising field.

In conclusion, the strength of the conservative RKKY coupling generates many features in the magnetization dynamics of the SyF structure. It transforms the damped modes of two FM isolated layers into a coupled system with two excitations modes, the acoustic and optic. In asymmetric SyF structures the steady state oscillations present different amplitudes of the BL and TL magnetization during the precession, for high values of applied field. As a consequence, if the conservative RKKY coupling is strong enough, a dynamic torque due to RKKY coupling produces the change in the tuning of the frequency, as a function of the current, changing from redshift $df/dj_{app} < 0$ to blueshift $df/dj_{app} > 0$.

Chapter 5

Study of a Standard STO

In this chapter we address the spin torque driven excitations for a standard STO structure, that consists of a SyF pinned layer and a single ferromagnetic layer. The dynamic response is analysed taking into account the dipolar field interaction between the three ferromagnetic layers and the mutual spin torque (MSTT) between the FL and the TL of the SyF. The dynamical studies in this chapter will be structured as follows:

1. **The mutual spin torque (MSTT)**. It is a non conservative coupling between the FL and the TL of the SyF, which permits us to study the magnetization dynamics using the most simple coupling. This has been addressed by D.Gusakova [Gusakova et al., 2009], [Gusakova et al., 2011] and we will summarize the results for comparison. In this study we suppose that the spin transfer torque occurs simultaneously in the FL (TL polarizes the electrons) and in the TL of the SyF (FL polarizes the electrons), creating precession in all the layers. This coupling presents some specific features, but it will be seen later on, that the dipolar coupling is more important.

2. **The dipolar field interaction and MSTT**. We will take into account the dipolar field (conservative coupling) between all the ferromagnetic layers and the MSTT between the FL and the TL, as in the previous case. This is the most realistic model for nanopillar structures used in experiments, where dipolar fields are present.

For the dynamical studies we defined the same structure as used by Gusakova [Gusakova et al., 2009], in order to compare the results with previous studies, parameters in Table 3.3. Before addressing the dynamic response we will study the influence of the dipolar field interaction on the static hysteresis loop.

5.1 Hysteresis loop influenced by the dipolar field

This section will provide an idea about the magnitude of the influence of the dipolar field in the static hysteresis loops of the SyF pinned layer and the single FL which composes the standard STO. We used the parameters of table 3.3, with and without dipolar field. In Fig. 5.1 (b)-(d) the arrows show the sense of the dipolar field between the layers.

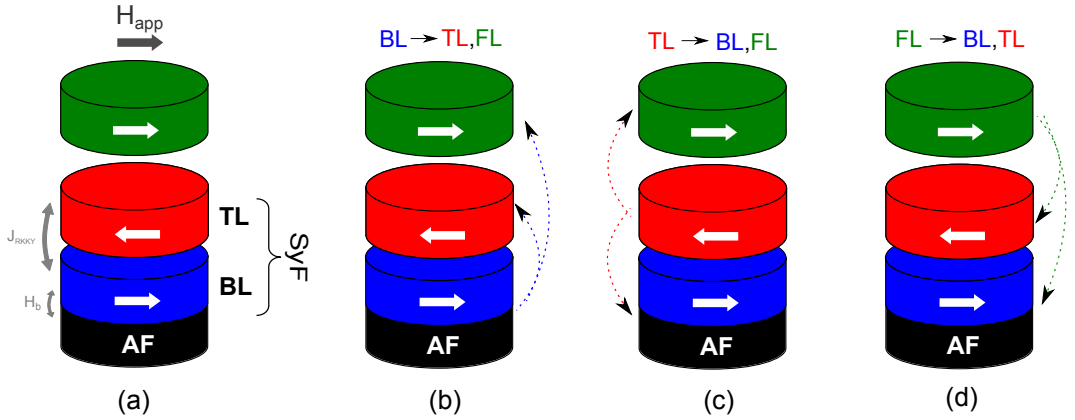

Figure 5.1 – (a) Standard STO and (b)-(d) the dipolar field interaction between the layers. Parameters in table 3.3.

Fig. 5.1 (b) shows for the case of $H_{app}>0$, that the dipolar field from the BL stabilizes the direction of the TL but destabilizes the FL. Similarly, the dipolar field from the TL, Fig. 5.1 (c) stabilizes the FL and the BL, while the dipolar field from the FL, Fig. 5.1 (d) stabilizes the TL but destabilizes the BL. Using equation 3.10 we quantified the static dipolar field (in the X direction) over the layers. We found that the $H_{dip,BL}$=219Oe, $H_{dip,TL}$=-1043Oe and $H_{dip,FL}$=125Oe.

The Fig. 5.2 shows the hysteresis loop of the BL, TL, total SyF and FL magnetizations for an isolated system and a coupled system (static dipolar field in the x direction). The spin flop value H_{sf}^{+} of the SyF increases by ≈360Oe, from 1410Oe to 1770Oe. The switching of the FL is shifted into negative fields ($H_{switching}$= -274Oe and -35Oe), the total dipolar field from the TL ($H_{dip,TL\longrightarrow FL}$=497.28Oe) and BL ($H_{dip,BL\longrightarrow FL}$=-372Oe) will stabilize the magnetization of the FL into positive values of magnetic field.

The parameter of the dipolar field component, in the x direction, from the TL (2.938×10^{-25}) is larger than the corresponding one for the BL (1.84×10^{-25}), because they are related to the geometry of the system and with the distance between the centres of the layers. The absolute value of the dipolar magnetic field from the BL to the FL is reduced as compared to the dipolar field from the TL to the FL.

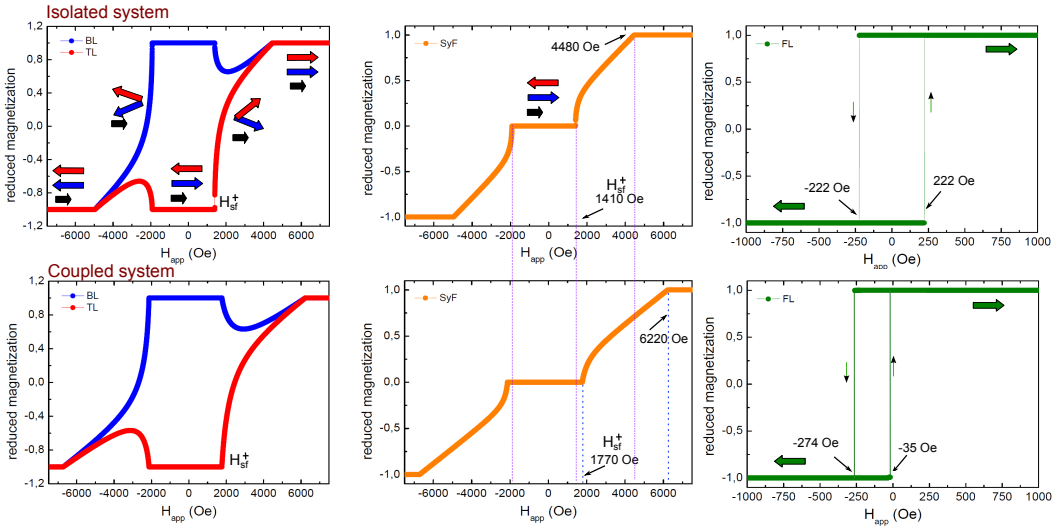

Figure 5.2 – Hysteresis loop of the TL, BL (SyF) and FL for the isolated and coupled system. The static dipolar field (x axis) over the layers calculated are $H_{dip,BL}$=219Oe, $H_{dip,TL}$=-1.043Oe and $H_{dip,FL}$=125Oe. Parameters in table 3.3.

In Fig. 5.3 we overlap the hysteresis loops of the FL and SyF for the isolated and coupled system. The yellow region indicates the range of field ($H_{FL}^{switching}$<H_{app}<H_{sf}^{+}) where the system remains in the AP state (high resistance). Arrows in the inset represent the layers magnetizations. Due to the dipolar field the AP state increases by 414Oe, from 1630Oe to 2044Oe. In this region we will study the magentization dynamics.

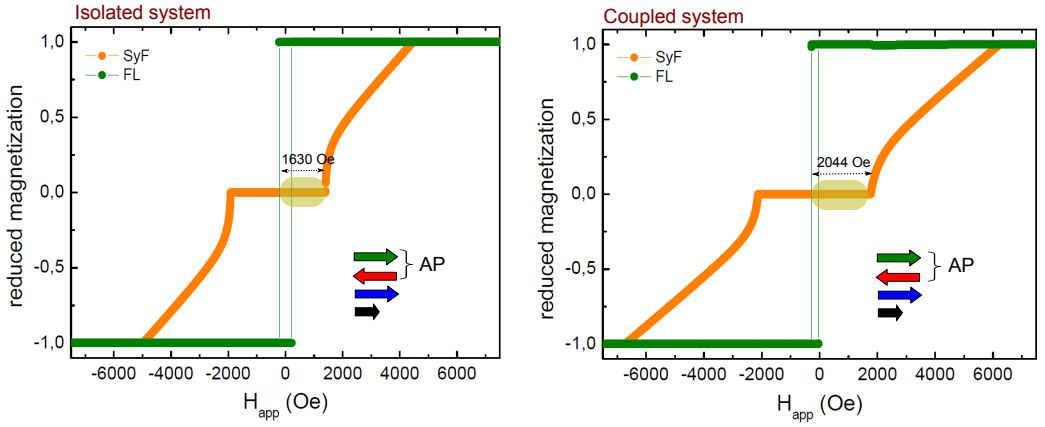

Figure 5.3 – The AP magnetic configuration between the TL and the FL is shown for the isolated and coupled system. The influence of the dipolar field produces an increase of the AP state (yellow region), from 1630Oe to 2044Oe. Parameters in table 3.3.

5.2 Magnetization dynamics in standard STO

In the numerical methods of chapter 3 we have shown how to solve a coupled system by the example of two layers, which are part of the SAF. In this chapter we will solve three

equations, corresponding to FM layers of the standard STO (FL, TL, and BL) considering the following interactions. In the case of the SyF the BL is coupled via exchange bias to an antiferromagnetic layer (in the positive x direction). The RKKY coupling is responsible for the interaction between the TL and the BL of the SyF. The FL and TL are coupled via a mutual spin torque effect (MSTT). This means that the MSTT destabilizes the initial AP state, for positive and negative current. The destabilizing effect of the spin transfer torque effect occurs on the FL (TL) for positive (negative) values of current density. The BL will follow the movement of the TL due to the RKKY coupling. The dipolar coupling is taken into account between the three FM layers. Due to these interaction all the three layers BL, TL and FL will precess simultaneously.

In this chapter and in the following of this thesis, when the systen is in the AP state and the current (or current density) is positive, we will define the STT driven excitation (j_{app}>j_c) as **FL dominant precession**. In this case, the FL shows a larger amplitude in comparison with the TL or BL (SyF layer) precession. For negative values of current, the STT driven excitation will be called **SyF dominant precession**, see Fig. 5.4.

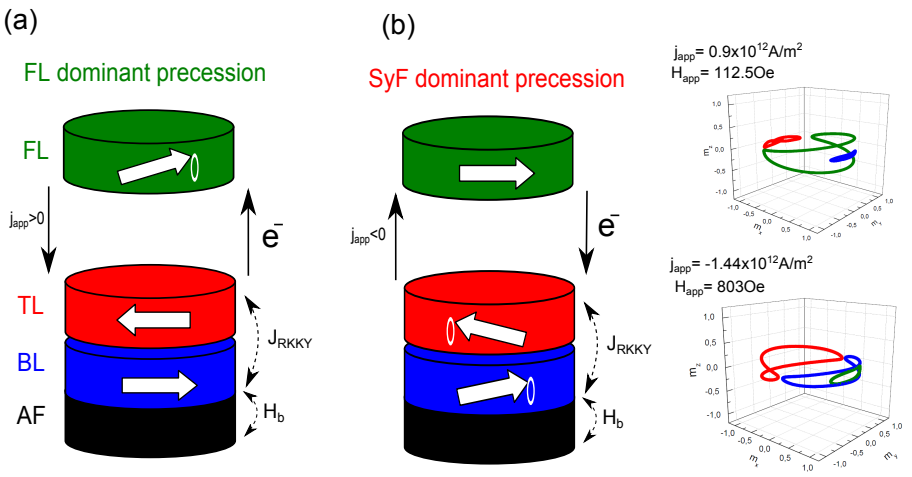

Figure 5.4 – (a) State current-field diagram of a standard STO without take into account the dipolar field interaction between the layer. An example of standard STO used to simulate the state diagram is introduced in (b). Figure has adapted from [Gusakova et al., 2009]. In (c) the standard STO adding the dipolar field interaction. Parameters in table 3.3.

We will start this section by summarizing the results from D.Gusakova et al on MSTT coupled standard STO.

5.2.1 Mutual spin torque in magnetization dynamic of the standard STO

As a first study of the coupling in a standard STO our group has considered the MSTT between the TL and the FL, [Gusakova et al., 2009], [Gusakova et al., 2011]. The MSTT is introduced in the LLG equation using the STT term, which takes the form of the equation 5.1 to 5.3. The current polarization will be the unity vector pointing into the direction of the FL (TL) magnetization for each layer, as it is shown in the equations,

$$(\frac{\partial \mathbf{m}_{FL}}{\partial t})_{STT,FL} = \gamma_0 j_{app} G_{FL}(\eta) \mathbf{m}_{FL} \times (\mathbf{m}_{FL} \times \mathbf{m}_{TL}) \quad (5.1)$$

$$(\frac{\partial \mathbf{m}_{TL}}{\partial t})_{STT,TL} = -\gamma_0 j_{app} G_{TL}(\eta) \mathbf{m}_{TL} \times (\mathbf{m}_{TL} \times \mathbf{m}_{FL}) \quad (5.2)$$

$$(\frac{\partial \mathbf{m}_{BL}}{\partial t})_{STT,BL} = 0 \quad (5.3)$$

The state diagram of the MSTT coupled standard STO (H_{app} versus I_{app}) is shown in Fig. 5.5, adapted from [Gusakova et al., 2009]. In comparison with the state diagrams shown in chapter 4 where the polarizer is fixed, here the coupling between the FL and the SyF generate the magnetization precession in all the layers but with different amplitudes for both senses of applied current, see Fig. 5.4.

The sweeping of magnetic field from the saturation will allow us to observe the excitations also in the spin flop and saturation regions (arrows correspond to the magnetization directions of each layer). The red lines denote the critical currents for the SyF[1] excitations and the green line for the FL excitations.

As in the previous chapter, our study is focused on the positive region of the plateau, $0<H_{app}<H_{sf}{}^{+}$, where the FL and the TL magnetization remain anti-parallel (AP). This region is indicated by the shadow yellow rectangle in Fig. 5.5.

[1]Gusakova called the structure SAF, since it is close to be compensated, ($M_S d_{TL}$=4020 μA and $M_S d_{BL}$=4000 μA)

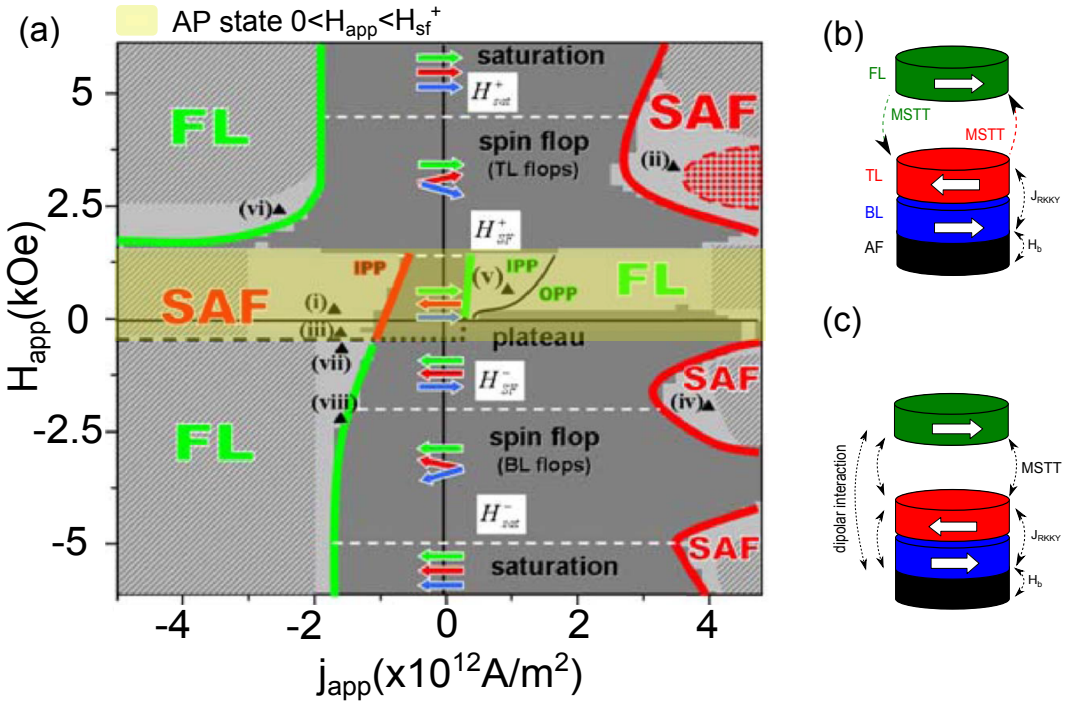

Figure 5.5 – (a) State current-field diagram of a standard STO without take into account the dipolar field interaction between the layer. An example of standard STO used to simulate the state diagram is introduced in (b). Figure has adapted from [Gusakova et al., 2009]. In (c) the standard STO adding the dipolar field interaction. Parameters in table 3.3.

5.2.1.1 Frequency tuning influenced by the mutual spin torque

The simulations of Gusakova et al. have shown coupled excitations where in positive current the FL is dominantly excited and in negative field the SyF is dominantly excited. In the following we will address the frequency versus current and frequency versus field dependence of the FL and the SyF for the coupled system in comparison to the uncoupled system. This reveals some basic features of the interaction.

First of all, the frequency tuning versus field of a single FL (without any interaction with other layers) will be compared with the results of Gusakova [Gusakova et al., 2011] taking into account the MSTT between the single FL and the TL of the SyF in a standard STO structure. The influence of this non conservative coupling is shown in Fig.5.6.

In an isolated system, the frequency versus magnetic field (f vs.H_{app}) of the single FL and the acoustic mode of the SyF are shown as green and red lines, respectively in Fig. 5.6 (a). Its frequency versus H_{app} dependence will follow the Kittel like law with the frequency increasing with the field. Upon applying a positive current the FL is driven into auto-oscillations.

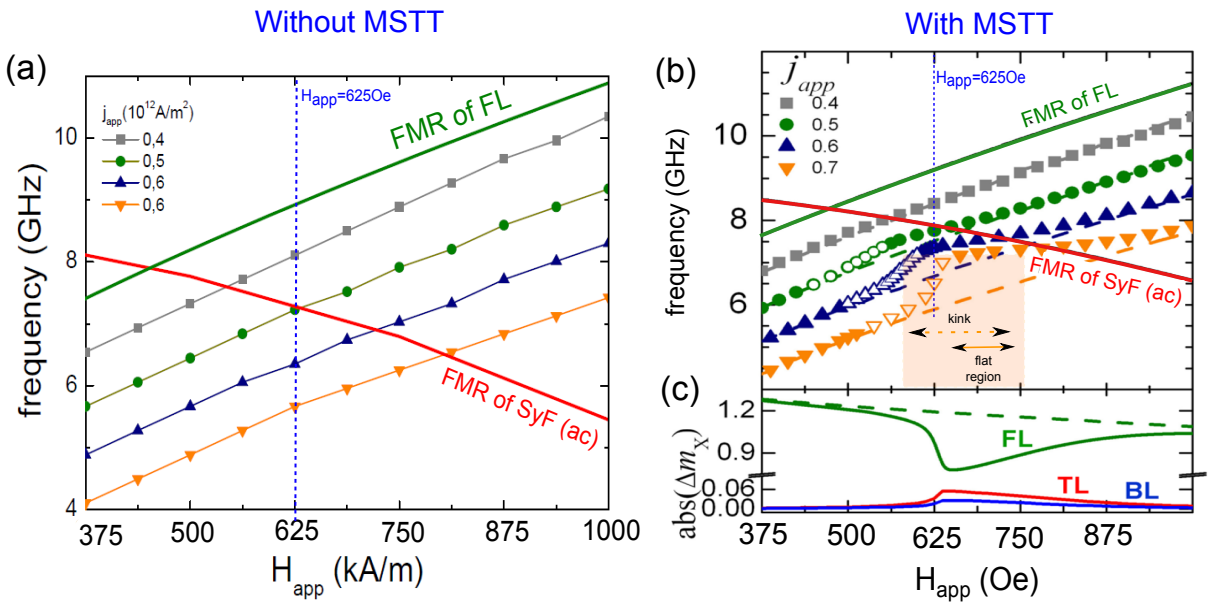

Figure 5.6 – In-plane precession frequencies of the FL dominant as a function of the applied field, for several values of dc current (10^{12}A/m^2). In (a) the frequency dependence calculated for a structure without MSTT. In (b) taking into account the MSTT. We notice the deflection of the tendency close to the crossing of the modes. This interaction has two regions, the kink and the flattening. The different amplitudes (BL, TL, FL) in the region of interaction are shown in (c). Parameters of the standard STO structure is shown in table 3.3. (b) and (c) adapted from [Gusakova et al., 2011]

For current larger than $j_c \approx 0.3\times10^{12}$A/m^2, the frequency dispersion (f vs H) of the STT modes are more or less parallel down shifted (redshift).

In the case of MSTT interaction between the FL and the TL of the standard STO, which is shown in Fig. 5.6 (b), the frequency field dispersion will be altered, for current and field values where the SyF FMR frequencies cross the STT FL frequencies (ranged 560 to 750 Oe). Close to the crossing, the STT mode of the FL dominant precession ($\approx 0.5\times10^{12}$A/m^2) starts to be pulled towards the FMR SyF$_{(ac)}$ mode (red line), following its tendency and generating a kink and a flattening in the f vs H dependence. This deviation increases with the current, $\approx 0.7\times10^{12}$A/m^2, showing a larger field range where f vs H is flat. During this interaction, the amplitudes of the magnetization precession changes for the three layers. Close to the region where f vs H is flat, the amplitude of the FL is not increased with the dc applied current. It is found instead, that its amplitude is reduced as the TL and BL of SyF amplitudes increase, see the Δm_x components of the precession in Fig. 5.6 (c). This is interpreted as the energy being transmitted to the FL by the spin polarized current is transferred partially to the TL of the SyF. In consequence the amplitude of the steady state oscillation in the FL is reduced.

This effect is explained qualitatively as a resonance phenomenon, where the STT from

the FL (that oscillates at the FL frequency) drives the FMR mode of the SyF. When the FL and SyF frequencies are the same, the SyF is driven into resonance.

It is instructive, to also consider the frequency current dependence. For this the magnetic field is set at H_{app}=625Oe, see the blue dashed line in Fig. 5.6 (b). The frequency tuning (f vs j_{app}) is shown in Fig. 5.7 (a) (for a T=400K) where the black curve corresponds to the isolated FL (without MSTT) and the red one to the coupled system, taking into account the MSTT. In the case of the isolated FL (black curve), the frequency shows the normal frequency redshift with current. In the case of the coupled system (red curve), increasing the current density, the system shows a region of current values where the f vs I dependence is flat (deviated from the isolated FL tendency). Increasing more the current density the system comes back to the isolated f vs I dependence. The overall deviation between the coupled and uncoupled frequency dispersion versus current is called kink[2].

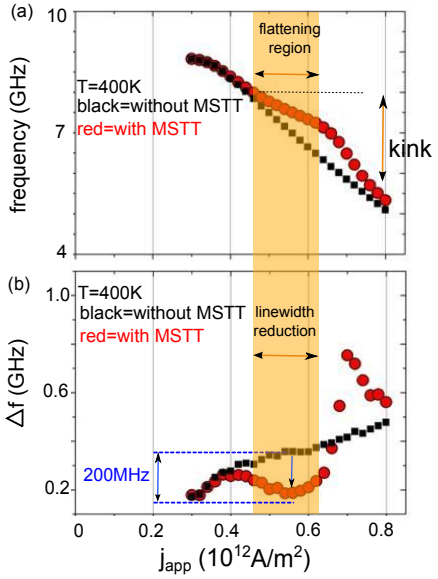

Figure 5.7 – Frequency and linewidth of the FL excitation for a standard STO with coupled FM layers by MSTT (red curves) an isolated FM layers (black curves). (a) Frequency dispersion as a function of the current density. We observe the kink which correspond to the interaction of the FMR of SyF with the FL excitation.(b) Linewidth as a function of the current density where it is shown the reduction of the linewidth in the kink region of (a). For this simulations the applied field was fixed on H_{app}=625Oe and the temperature at T=400K. Figure from D. Gusakova.

The numerical simulations of Fig. 5.7 have been done at 400K in order to include thermal fluctuations and measure the linewidth of the signal which is shown in Fig. 5.7 (b). Here, the linewidth is compared for the case with and without MSTT coupling. In the case of the isolated FL the linewidth increases with the current density but in the case of MSTT coupling, we observe a reduction of linewidth (orange shadow region). This reduction of

[2]For small values of current (or field) the kink shows a continuous behaviour, however increasing these parameters the kink shows two branches, separated by a jump.

the linewidth of 200MHz appears just in the corresponding flattening region of Fig. 5.7 (a), in the same current range where the kink starts.

The reduction of the linewidth is interpreted as a reduction of the non linear amplitude-phase coupling ν of the system. From theory, the amplitude phase coupling enhances the linewidth following the equation 5.4. ν is proportional to $(\mathrm{df/dI}_{app})/\Gamma_p$. Hence a reduction in $\mathrm{df/dI}_{app}$ will give rise to a reduction of the linewidth.

$$\Delta f = \Delta f_0(1+\nu^2) \propto (1+(\frac{df/dI_{app}}{\Gamma_p})^2) \tag{5.4}$$

We expect to find the minimal linewidth in the region where the frequency varies slowly with respect to the current density, df/dI_{app}, small orange region of Fig. 5.7. We can conclude that at least in the case of a coupled system via MSTT, there will be deviations from the uncoupled tendency of the STT modes close to the crossing of STT mode with FMR. These deviations will generate a flattening of the frequency dispersion (df/dI_{app}) generating a reduction of the linewidth, see eq. 5.4.

5.2.2 Influence of the mutual spin torque and the dipolar field in the magnetization dynamic of the standard STO

Frequency current tuning of a isolated system, standard STO

In the previous section we discussed the results taking into account the MSTT coupling only. Here we will also include the dipolar interaction. Before to start this discussion we remind the FL and SyF frequency and linewidth vs current dependence of the uncoupled system (T=400K).

For positive current, larger than the critical current, the FL STT mode is stabilized. It shows first the IPP redshift and then for larger currents evolves into the OPP blueshift mode. The linewidth decreases in the linear regime (damped mode) and for currents just above the critical currents in the STT mode. In Fig. 5.8 the linewidth reaches a minimum value of 155MHz (H_{app}=1250Oe and j_{app}=0.45 $\times$ 10^{12} A/m^2) and then increases in the IPP regime until reaches the OPP mode.

For negative current density the SyF is excited. As we discussed in chapter 4 we can see

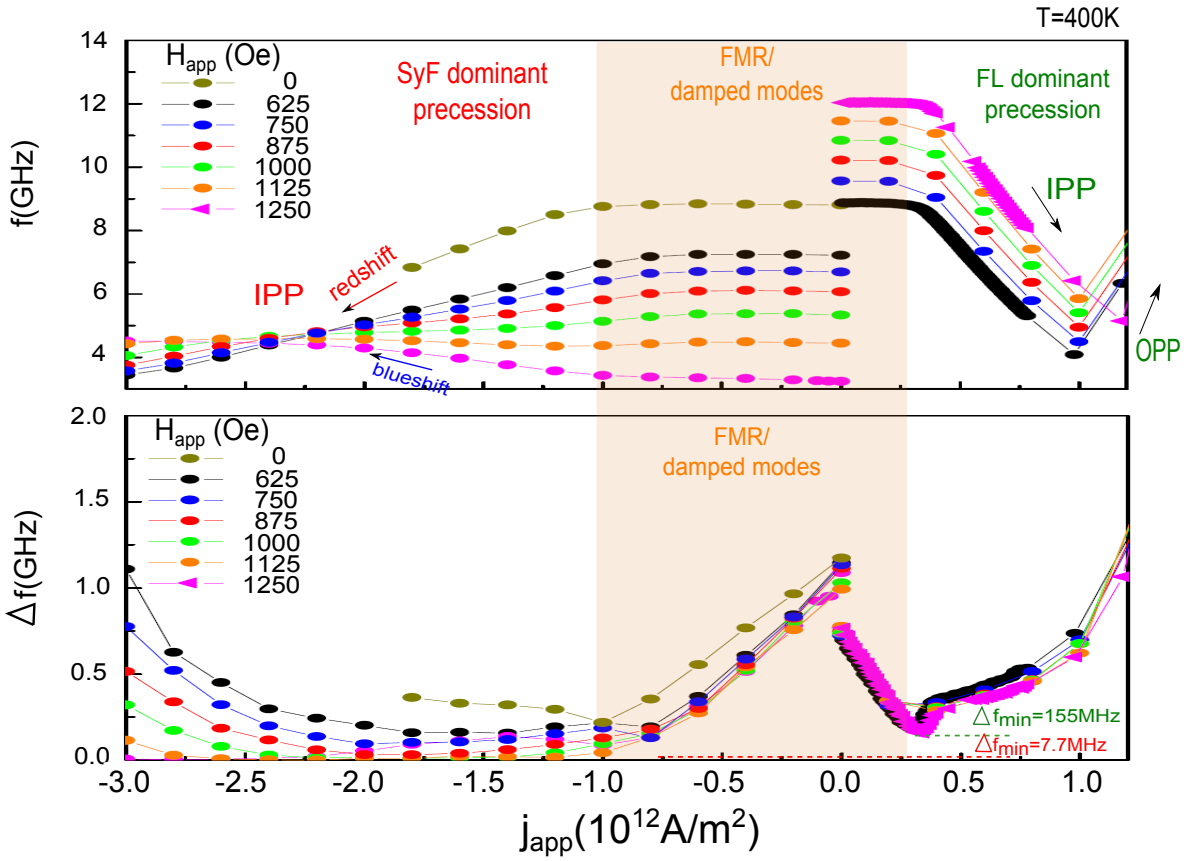

Figure 5.8 – Frequency tuning and linewitdh as a function of the current density, for H_{app}=0 to 1250 Oe. The frequency of the SyF dominant precession shows the redshift and blueshift regime and the FL dominant precession the evolution from IPP to OPP regime. The smaller linewidth of the SyF is Δf_{min}^{SyF}=7.7MHz and for the FL of Δf_{min}^{FL}=155MHz.

the transition from redshift into the blueshift regime. The linewidth shows small values of 7.7MHz for the blueshift region (H_{app}=1250 Oe and j_{app}=-2.6 $\times$ 10^{12} A/m^2), less than the FL STT mode.

Frequency tunning of a coupled system, standard STO

We now start with the presentation of the dynamics taking into account the dipolar interaction and the MSTT. We should mention that experimentally the dipolar field is always present in this type of nano-pillar structures but not in nano-contacts[3].

The strength of the dipolar field is determined by three parameters (i) the spacer between the FM layers, (ii) the M_S of the FM and (iii) the thickness of the FM. In the case of the interaction between the three ferromagnetic layers, the dipolar tensors and the parameters of the simulations are given in table 3.3.

Before addressing the STT excitations, we first consider in the next section the subcritical regime of the coupled FMR modes of the three layer system as well as the stability upon applying a spin torque via current, i.e we will find the regions where the system is stable (initial or reversed static state) or unstable (steady state oscillation or non periodic dynamics), using the method described in section 3.1.4.3 and complemented by the numerical simulations which are described in section 3.1.3.

5.2.2.1 Sub-critical regime in the standard STO

In the sub-critical regime, the frequency dispersion of an isolated FL shows the tendency of the Kittel-law FMR mode, described by eq. 3.41. Furthermore the frequency of an isolated coupled SyF structure shows two excitation modes, acoustic and optical modes, see Fig. 4.9 (d). In Fig. 5.9 (a) are shown the three modes corresponding to an isolated SyF system (BL and TL) and FL in the range of $H_{FL,switching}$<H_{app}<H^{+}_{sf}. The isolated FMR modes (j_{app}=0) of the SyF and the FL will intersect close to H^{cross} $\approx$460Oe. In Fig. 5.9 (b) we included the static dipolar field which shifts the FL switching into negative values and the spin flop value of the FMR acoustic mode of the SyF into positive values, see Fig. 5.2. These shifted occurs because the dipolar field stabilized the AP configuration between the FL and the TL magnetization.

The dipolar coupling between the SyF layer and the FL will give rise to new hybridized

[3]The STO structures investigates in this thesis are nano-pillars of about 100nm of diameter.

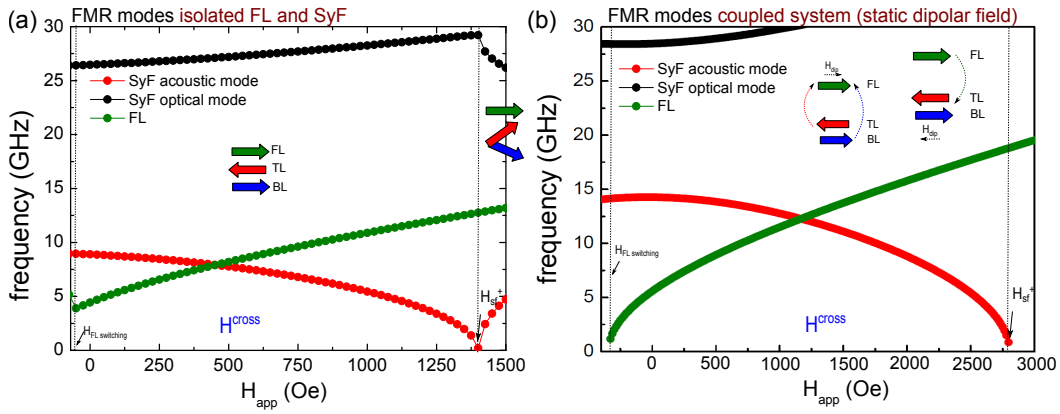

Figure 5.9 – (a) FMR modes for the isolated SyF and FL layer of the standard STO. The acoustic and optical mode of the SyF are shown in red and black. the FMR of the FL in green. The crossing field is labelled as H^{cross}. (b) The FMR of the standard STO over the influence of the static dipolar field between the layers.

modes, similar to the acoustic and optic mode splitting of the SyF. These new hybridized modes are shown in Fig. 5.10 (a) as a function of the magnetic field in a region which corresponds to the range $H_{FL,switching}<H_{app}<H^{+}_{sf}$.

In Fig. 5.10 (a) the hybridized modes (solid circles) are shown together with modes of Fig. 5.9 (a), the isolated layers (dash lines). We observe the acoustic and optical mode will show a splitting, creating a frequency range without excitations.

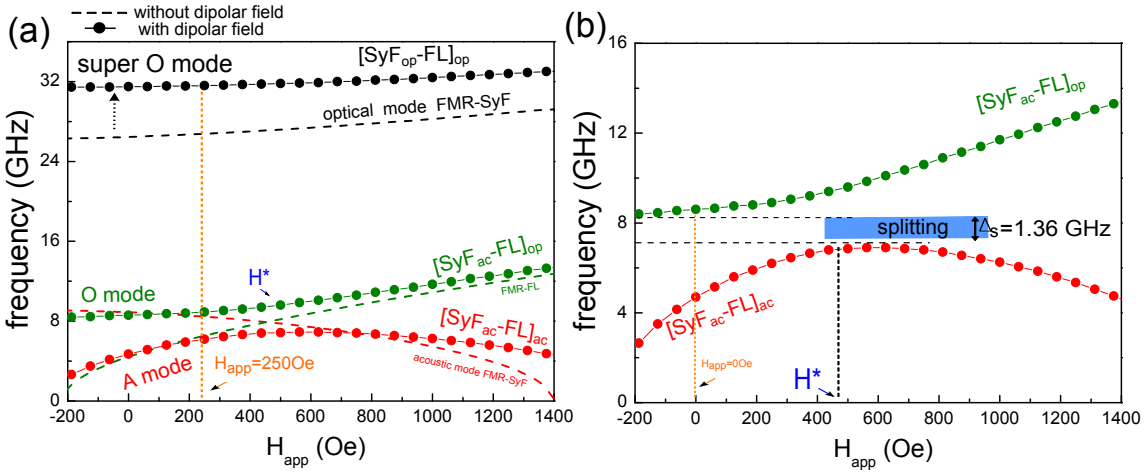

Figure 5.10 – Hybridization of modes for the standard STO. (a) Dash lines correspond to the FMR modes of the SyF and FL. Solid circles correspond to the hybridized modes. (b) Splitting (Δ_S) between the acoustic and optical mode of the standard STO.

In Fig. 5.10 (b) we show a zoom of the magnetic field region corresponding to the crossing of modes. One can observe clearly the splitting between the two lower modes.

The frequency dispersion of the FMR (damped) modes will be labelled as is indicated in Fig. 5.10. The A=$[SyF_{ac}\text{-}FL]_{ac}$ and O=$[SyF_{ac}\text{-}FL]_{op}$ mode derive mainly from a hybridis-

ation between the FL mode and the acoustic mode of the SyF, and the SO=$[SyF_{op}\text{-}FL]_{op}$ mode from the optic SyF mode that is pushed towards higher frequencies. To better understand the labelling of A and O we have a look at the phases of the m_y and m_z component, keeping in mind that a 180° (0°) phase shift of the m_y component is characteristic for an acoustic (optic) mode.

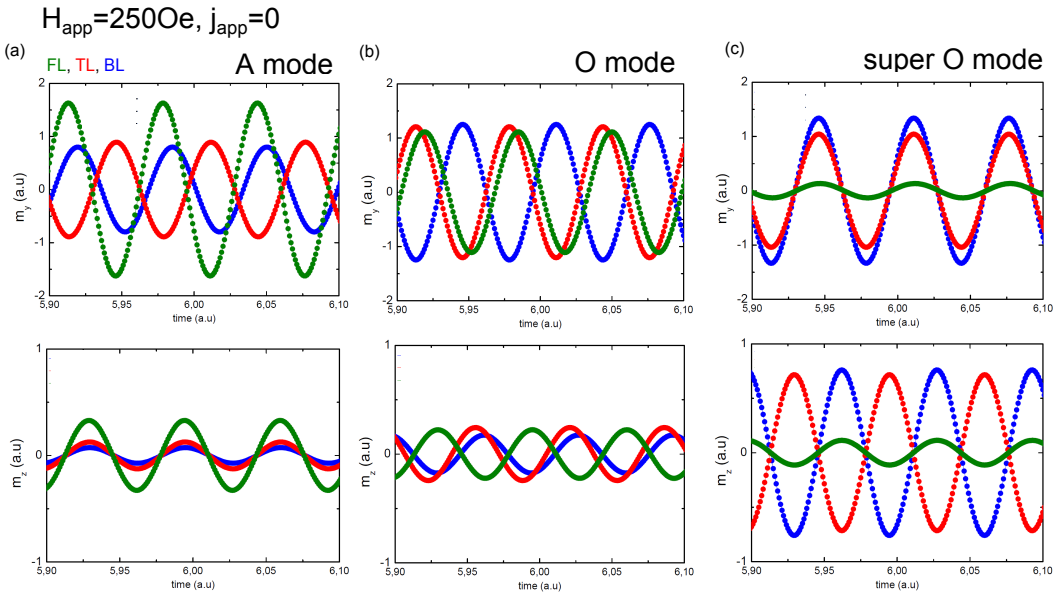

Figure 5.11 – Temporal traces of the m_y and m_z component of the FMR (damped) modes (j_{app}=0). (a) Acoustic (A) (b) optical (O), and (c) super optical (SO) relative phases for H_{app}=250Oe. In A and O modes the m_y components of the SyF are out of phase (strong RKKY coupling) while in the SO both are in phase. The m_y of the FL is in phase with the TL for the O and SO but out of phase for the A mode. The m_z of the TL and FL are in phase in A and out of phase in O and SO. In A the FL changes its phase in A and O. The energy of the super O mode is higher because the system have to overcome the RKKY coupling.

In Fig. 5.11, we show the temporal traces of the m_y and m_z components, calculated from the eigenvectors (0, n_y, n_z) of the characteristic matrix of the system, for zero current density j_{app}=0. The A and O mode of Fig. 5.11 shows the m_y component of the TL and BL in the anti-parallel state (strong RKKY coupling). The m_y phase of the FL with respect to the TL is out of phase for the A mode and in phase for the O mode. The SO mode shows the m_y component of the three layers in phase. The m_z component of the TL and FL are in phase for the A mode and out of phase for the O and SO mode.

In the following we will focus the study in the two modes with lower frequency of Fig. 5.10 (b), however at the end of this chapter we will show that the third mode also plays a role in the behavior and tendency of the fundamental STT mode.

5.2.2.2 Attenuation of the excitations modes

Upon applying a current, we have seen for single layers (section 3.1.4) that the FMR (damped) modes ($\propto e^{pt}$, $p=\lambda-\omega i<0$) can become unstable and transit into a STT. This transition is defined by the *attenuation* (λ), that goes from negative (damped) to positive (unstable). The zero value of the attenuation then defines the critical current. This method (section 3.1.4.3) is used here for the coupled system (standard STO) in order to find the frequency and the attenuation of the damped excitations around the equilibrium axis. In Fig. 5.12 we show the numerical results of the attenuations λ for the damped A and O mode as a function of the current density. The red shadow region is a numerical solution that will not be taken into account.

The attenuation increases or decreases with current depending on the field value. For instance (Fig. 5.12) for the A mode at low fields, the attenuation decreases with increasing negative current and then goes to zero. This zero crossing defines the critical current $j_c(H)$ as a function of the applied field. For larger field values, the dependence is reversed, and the attenuation increases from zero with current. For the O mode the behaviour is similar, but the tendency is reversed for low and high fields. Using this type of plots of the attenuation vs current, it is possible to determine the critical boundaries of the state diagram, see section 5.2.2.3.

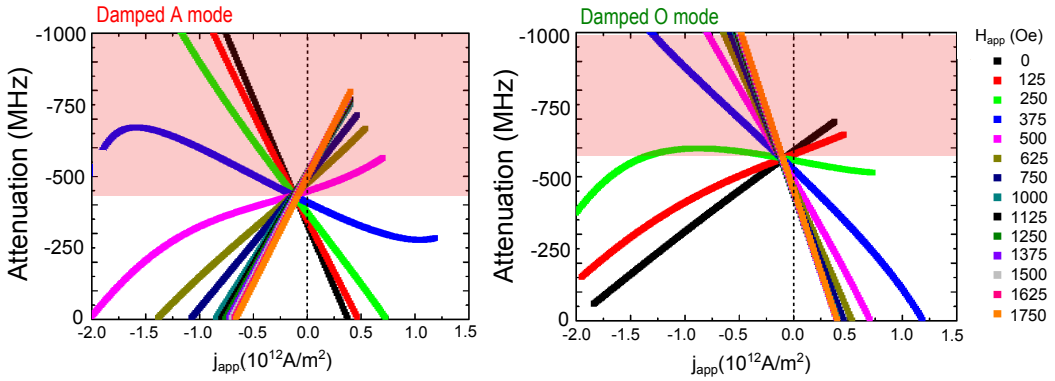

Figure 5.12 – Attenuation in the linear regime for A and O mode of the standard STO. The attenuation decreases as a function of the current density (positive and negative) only for some conditions of magnetic field. In order to a better understanding we should avoid the red shadow region in the plot, see explanation on the text. Parameters in table 3.3.

Since we have been investigating the hybridisation of the modes for the frequency field dependence, we now analyse the frequency and the attenuation as a function of field upon increasing the applied current (and with this the STT) from zero. In Fig. 5.13 (a) and (b) the evolution of the frequency ($\omega=2\pi f$) (top row) and the attenuation (λ) (bottom row), are shown as a function of the magnetic field for different values of current. They

represent the real and imaginary part of the eigenvalues of the characteristic matrix for the standard STO system[4].

In (a) and (b) the dashed lines correspond to the isolated FL and SyF damped modes for j_{app}=0. In all the field range the attenuation λ remains negative, i.e the system will be stable thus the frequency of the excitations corresponds to the damped modes $[SyF_{ac}\text{-}FL]_{ac}$ and $[SyF_{ac}\text{-}FL]_{op}$ (A and O modes).

At low fields the A mode is determined by the FL and the O mode by the SyF, while at high fields this is reverse. The attenuation for high and low magnetic fields follows the tendency of the isolated system but close to H^* (splitting), the attenuation changes for both layers, even at zero current i.e the spin transfer torque is not responsible for this effect. When only one layer has large amplitude, it determines also the damping, when both layers have equal amplitude, then both layers damping will contribute, hence in one case the damping increases and in the other it decreases.

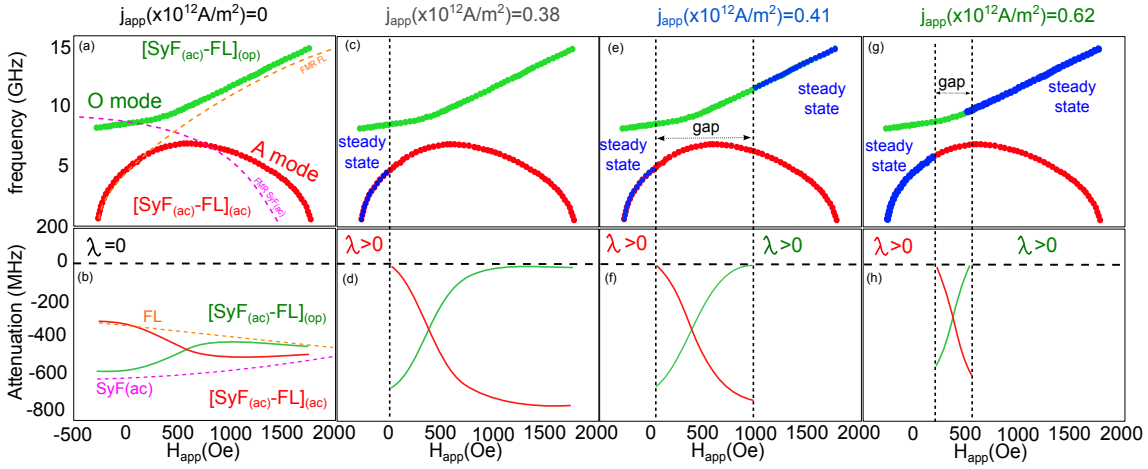

Figure 5.13 – Figures show the real and imaginary part λ and ω=2πf of the eigenvalue of the characteristic matrix for the standard STO system. They correspond to the attenuation λ and the frequency (f) respectively. We present the evolution of the curves as a function of the current density (positive) in the sub-critical and critical regime.

Introducing the spin transfer torque ($j_{app} \neq 0$) the attenuation will change the sign of λ. For positive current we will see that the damped mode will be driven into steady state for which the attenuation has a lower absolute value. First the frequency and the attenuations are shown for different values i.e FL dominant precession for $j_{app} > j_c$ in Fig. 5.13 (c)-(h). For j_{app}=0.38$\times$ 10^{12} A/m^2 the attenuation of the A mode goes to zero at low applied field values ($-281 < H_{app} < 0$). This means that in this field range the A mode transits to an STT mode. In the other field range the A mode as well as the O mode

[4]During the linearization of the system we supposed a solution of M in the form $\sim M_0 e^{pt}$ where the eigenvalue p= λ+2πfi.

remain a damped mode.

Upon increasing the current to j_{app}=0.41 and 0.62× 10^{12} A/m^2 the attenuation of the O mode at higher fields goes to zero. This means that in the corresponding field range the O mode transits into a STT mode, while the A mode at higher field remains damped, as well as the O mode at lower field values. This means that upon increasing field there is first a low frequency STT A mode and the O mode is damped. Then there is a field range where are only two damped modes exist. This is followed by a field range where the STT mode is at higher frequency (O mode) and the damped mode is the low frequency mode (A mode). The field region where there is no STT mode, we call here **'gap'**.

The STT modes will remain with the same relative phases as the damped modes. This is shown in Fig. 5.14 for H_{app}=0, 688Oe and for j_{app}=0.52, ±1.1 and -3.3×10^{12}A/m^2. The phases of the m_y component of the STT A and O modes are close to be since there is a small phase-shift, as we showed in the case of Fig. (b),(c) and Fig. (a),(d), respectively.

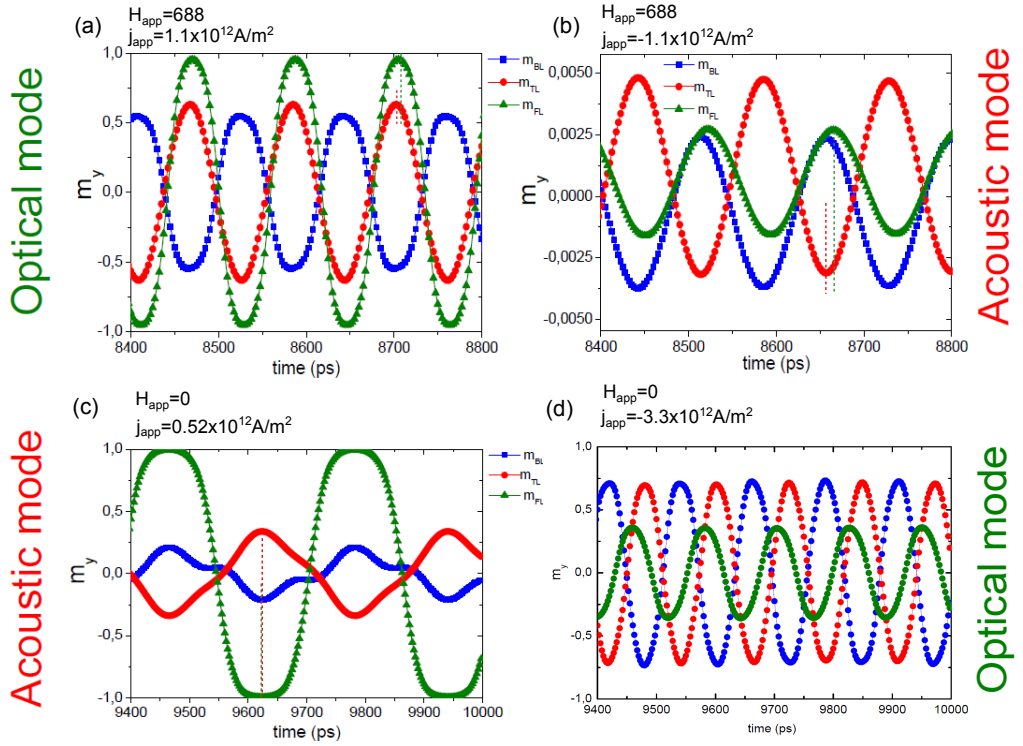

Figure 5.14 – Temporal traces of the m_y component of the STT and damped modes for positive and negative current density. (a) and (b) after the gap, H_{app}=688Oe (high magnetic field) and (c) and (d) before the gap, H_{app}=0Oe

Now we come to negative current values. The case of small current density j_{app}=-0.07 × 10^{12} A/m^2 is shown in Fig. 5.15 (a)-(b). In comparison with j_{app}=0 A/m^2 of Fig. 5.13 (a), the attenuation of the damped modes are reversed. Increasing the current density to j_{app}=-1.3 × 10^{12} A/m^2 we obtain the steady state oscillations only in the A mode and

for high magnetic field values, see Fig. 5.15 (c)-(d). Increasing more the current density, j_{app}=-1.75 $\times$ 10^{12} A/m^2 we can observe the STT A and O modes low fields, separated by a gap, as in the case of the positive current, see Fig.5.15 (e)-(f). The O mode of the SyF dominant precession (small values of magnetic field) needs high current density to be excited (large j_c) therefore in the experiments this mode will be the more difficult to observe.

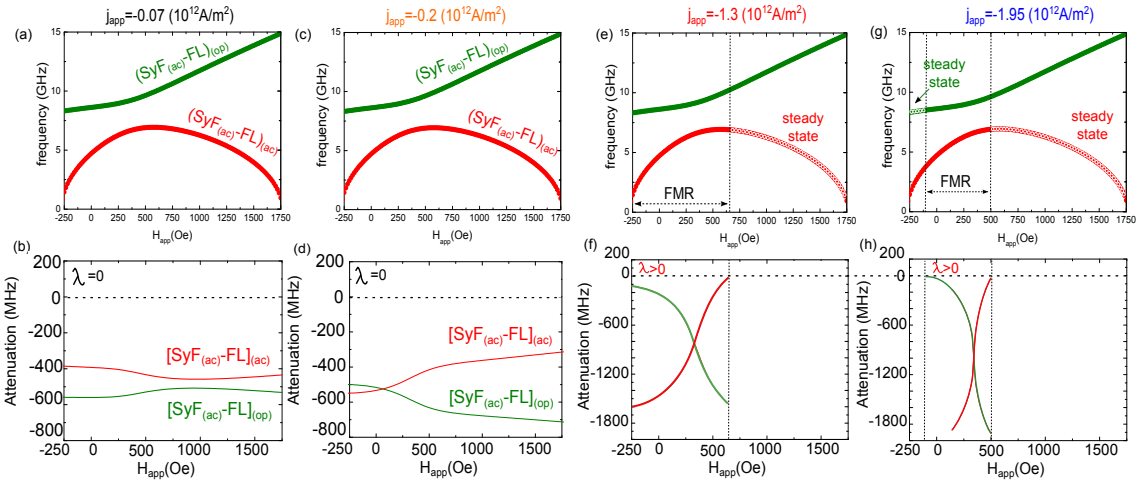

Figure 5.15 – Figures show the real and imaginary part λ and ω=2πf of the eigenvalue of the characteristic matrix for the standard STO system. We present the evolution of the curves as a function of the current density (negative) in the sub-critical and critical regime.

An important feature is the splitting Δ_S which is created between the A and O hybridized modes, see Fig. 5.10 (b). Similar to the splitting between the damped acoustic and optical mode of the SyF (RKKY coupling), this splitting will be given by the strength of the dipolar field coupling. In Fig. 5.16 (a) the frequencies of the A, O mode and the splitting Δ_S are shown as a function of the current density.

We observe a decrease of the frequencies of the A and O mode in the sub-critical and above critical regime which is observed also in the behaviour of the splitting. This decrease is not symmetric. At zero current density the splitting is around Δ_S $\approx$1.36GHz (j_{app}=0). The Δ_S as a function of the current density show a small change in the linear regime, 32MHz for positive and 72MHz for the negative current density. For positive current density above j_c, the splitting suffers an increase of 500MHz. Then the splitting decreases as a function of the current density until 0.96GHz. In the STT mode for negative current, the splitting decreases 200MHz. In Fig. 5.16 (b) we show the size of the gap as a function of the current density. We notice that the gap is not symmetric. For the positive current density the gap is closed first than for negative current density.

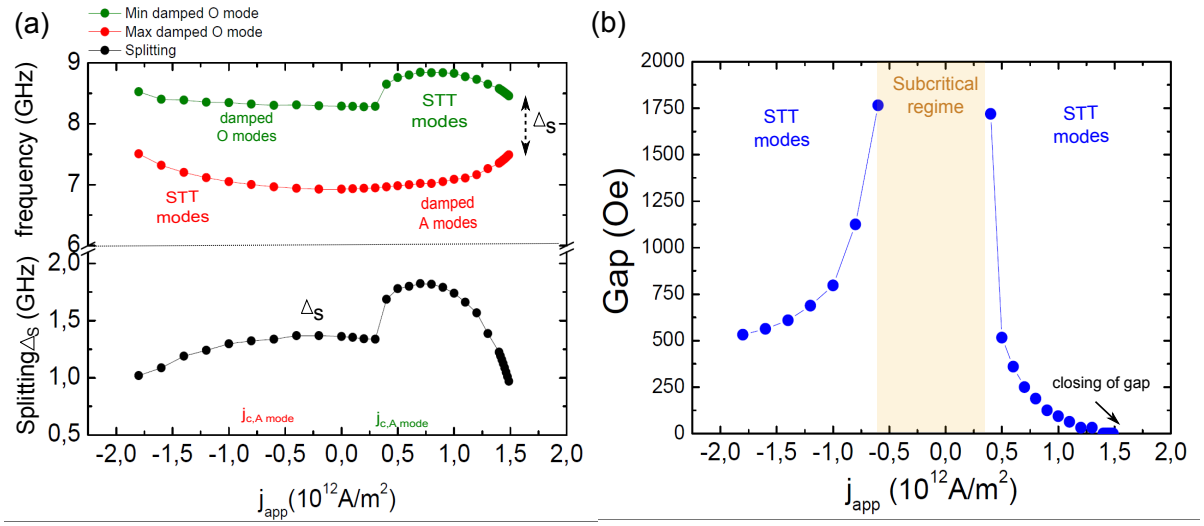

Figure 5.16 – (a) The maximum value of the acoustic mode (red curve), the minimum value of the optic mode (green curve) and the splitting (black curve) in the sub-critical and in the auto oscillations regime. The critical current density for the FL dominant precession is j_c=0.4×10^{12}A/m^2 and for the SyF dominant precession j_c=-0.6×10^{12}A/m^2.

5.2.2.3 Stability of the standard STO

The linearisation in section 3.1.4.3 provides a general solution for the magnetizations in the damped regime in the form of $\sim M_0 e^{pt}$ where the eigenvalue is p= λ+2πfi. Using the analysis of the attenuations λ and the stability conditions as a function of the magnetic field and current one can construct the characteristic state diagram with critical boundaries (H_{app} vs j_{app}), for each condition (j_{app}, H_{app}). As it has been described in the section 5.2.2.2 the value of the attenuation λ=0 will define the critical boundary, i.e transition from stable to unstable states.

We start showing the state diagram for the case of a standard STO without dipolar field interaction, only MSTT, see Fig. 5.17 which is a zoom of Fig. 5.5. The unstable state corresponds to the region in red color, stable to the grey color and the spin flop region is the grey color and the black color corresponds to the region where the FL is switched. The yellow lines correspond to the critical lines. In the case of the FL excitations, positive current density, the critical line increases linearly (but weakly) with field. In the case of the SyF excitation, negative current density the critical current decreases with the applied magnetic field.

In the following, we will study the influence of the dipolar field on the state diagrams. We used the dipolar tensor which has been multiplied by scalar factors = 0.1, 0.25, 0.5, 0.75 in order to simulate different strengths in the dipolar field. The influence of the dipolar field on the state diagram is presented in Fig. 5.18.

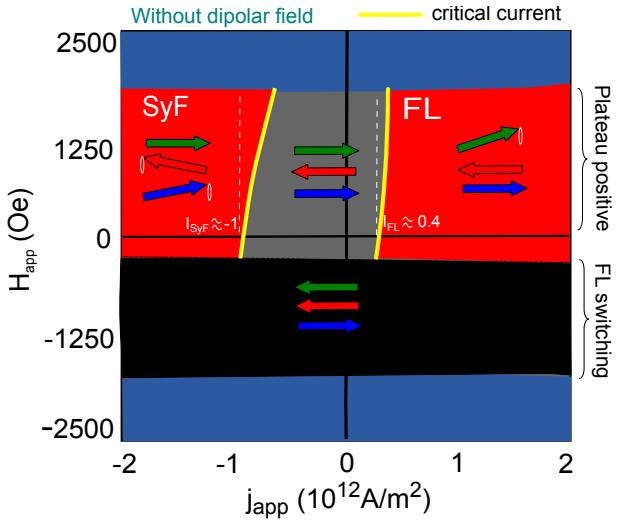

Figure 5.17 – Critical lines in the state diagram of the standard STO without take into account the dipolar field. In the state diagram the color arrows represent the magnetization direction of each FM layer in the STO (blue correspond to the BL, red to the TL and green to the FL). Parameters in table 3.3.

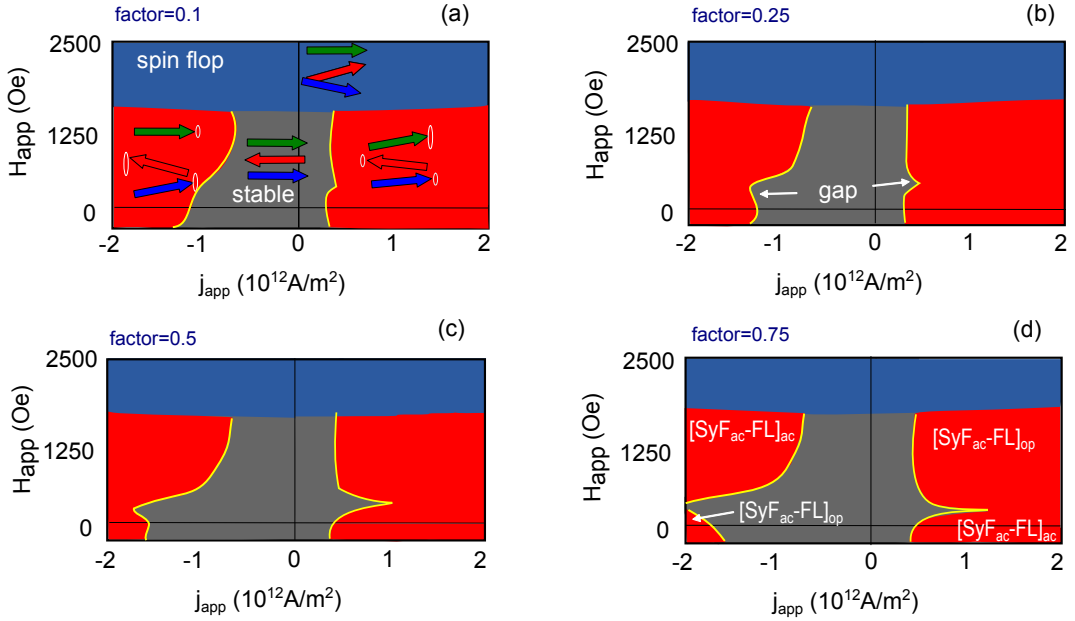

Figure 5.18 – State diagrams of the standard STO for different values of the factor of proportionality which multiply the dipolar field tensor. (a)The arrows represent the magnetization of each ferromagnetic layer. The red region corresponds to on stable region (steady state oscillations or chaos). The grey region correspond to the stable state and the spin-flop region is the green-metal color. The increase of the dipolar field created a gap (b). The labels of each region are presented in (d).

First we will explain the state diagram of the Fig. 5.18 (a) which corresponds to a dipolar field multiplied by a factor 0.1. If we compare with the Fig. 5.17 which corresponds to the state diagram of the isolated system (without dipolar field), we observe that a small gap is created, i.e for certain values of applied field and applied current the steady state oscillations does not exist. As we presented in Fig. 5.13, under the influence of the dipolar interaction a gap occurs as a function of field, where the STT modes vanish and only damped modes exist. This gap closes upon increasing current density. Upon increasing the dipolar interaction from 0.1 to 1 one can see that the current required to close the field gap increases, or in other words the field gap increases with increasing dipolar coupling between the layers.

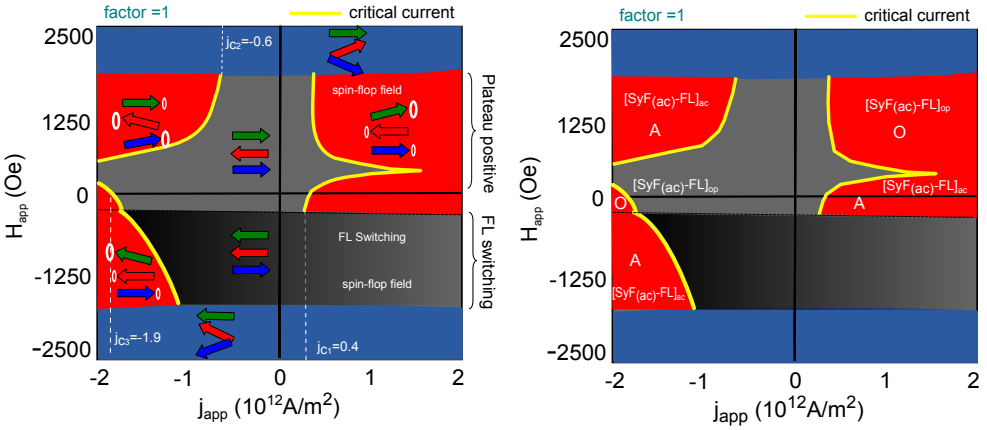

Figure 5.19 – State diagram of the standard STO for a factor=1. Yellow lines correspond to the critical current density. Three values of critical current density are defined j_{c1}=0.4 for the FL dominant precession, j_{c2}=-0.6 and j_{c3}=-1.9 for the SyF dominant precession.

We show the critical current density using the yellow lines in the state diagram of Fig. 5.19. Since the FL is less rigid than the SyF layer (the FL it is not pinned and it is not a coupled system) its critical current, j_{c1}=0.4×10^{12}A/m^2 , will be smaller than the SyF current density, j_{c2}=-0.6×10^{12}A/m^2 and j_{c3}=-1.9×10^{12}A/m^2 at H_{app}=0. The gap for the SyF is larger than for the case of the FL and higher current is needed to close it.

In conclusion, the dipolar field is an important parameter which changes the behaviour of the STT modes creating a gap and three hybridized modes of excitations. These results were also corroborated by Sung and Kudo, [Lee et al., 2012] and [Kudo et al., 2012] at the same time as we did our studies presented here.

5.2.2.4 Frequency tuning of the FL dominant precession ($j_{app}>0$)

As it has been explained before, when the current density overcomes the critical current value the excitations transit from the sub-critical into the above critical regime. The damping is counteracted and the system reaches the state of auto-oscillations (STT modes).

In this section, we will discuss first the frequency dispersion as a function of the applied field of the STT mode. In this study we neglect the thermal fluctuations i.e T=0K. Fig. 5.20 shows the frequency dispersion in the FL dominant regime (positive current density).

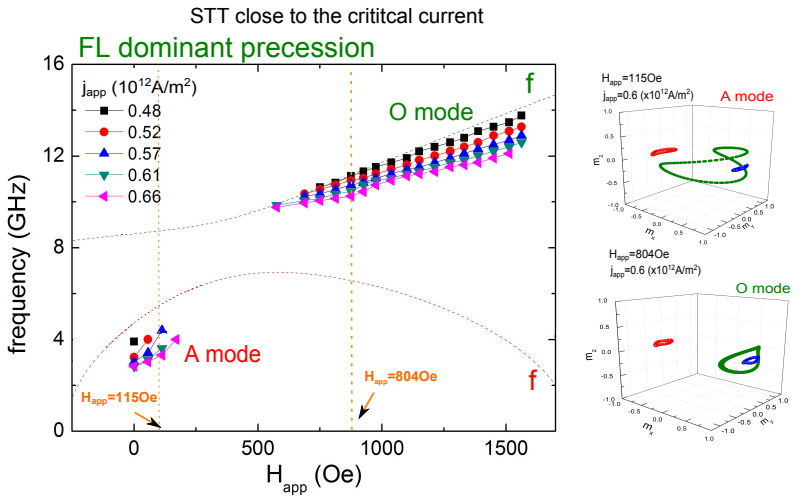

Figure 5.20 – (a)-(b) Frequency of the STT modes versus magnetic field for positive current density. The FL and SyF dominant precession are represented by solid points and the FMR hybridized modes in dash lines. In the right side of both figures the IPP trajectories for the A and O mode are shown.

Low current density on FL dominant precession ($j_{app}>0$)

We will start to study the auto-oscillations for small values of current density i.e close to the critical value (j_{app} ≈0.48 × 10^{12} A/m^2 and j_{app} ≈-1.03 × 10^{12} A/m^2). In Fig.5.20 (a) the STT A and O mode is shown for the FL dominant precession which follow the FMR tendency (dashed lines). As in the case of a single isolated FM layer the frequency decreases as a function of the current density i.e both modes (A and O) are redshifted from the FMR frequency dependence.

For the range of low current values shown the STT A and O mode are separated by the gap which decreases as a function of the current density as seen from the state diagram of Fig.5.19. The frequency at the critical current seems to be constant around ≈10 GHz, for different field values. The trajectories of the IPP A and O modes are shown in the right

side for two values of applied field and j_{app}=0.6 × 10^{12} A/m^2. As it was predicted, the FL dominant precession corresponds to an amplitude larger for the FL trajectory. The amplitude of the FL in the O mode is smaller than in A mode due to the strong applied field in the X direction which stabilize the magnetization in that sense.

Intermediate current density on FL dominant precession (j_{app}>0)

The frequency dispersion of the FL dominant precession for higher current density (from j_{app}= 0.7 to 0.9 × 10^{12} A/m^2) is shown in Fig. 5.21 (a), where the STT A and O mode remain in the IPP regime. In the case of the A mode the system continues with the same tendency and the gap decreases. In contrast, for the STT O mode we notice an important change from the FMR tendency. The frequency as a function of the magnetic field shows a strong deviation: the frequency vs field is first relatively flat (df/dH_{app}≈0) and then there occurs a more or less abrupt increase, in the form of a continuous kink (lower current) or a discrete jump (higher current). In section 5.2.2.5 the kink and jump will be investigated in more detail. Before we come to this, we show some more features of the STT modes.

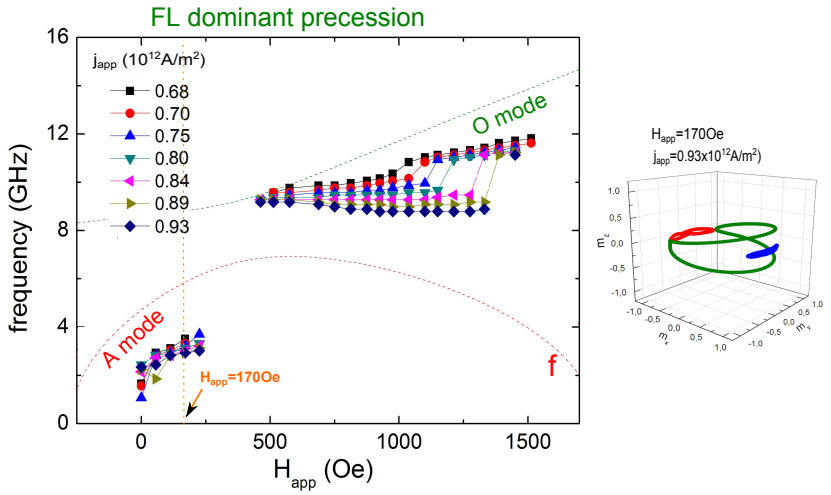

Figure 5.21 – Frequency versus magnetic field for several values of positive current density. The FL dominant precession are represented by solid points and the FMR hybridized modes in dash lines. (a) The frequency dispersion modes A and O are separated for the characteristic gap. In (b), increasing the current density the gap size decreases. Close to the crossing between the O STT mode and the A damped mode, the frequency dispersion shows a kink which becomes in a splitting.

High current density on FL dominant precession (j_{app}>0)

Increasing more the current density, j_{app}>1.1-1.9 × 10^{12} A/m^2, see Fig. 5.22, it is observed that the gap between the A and O mode is already closed. Around the figure we show

the trajectories for different field values and for a fixed current density (j_{app}=1.9 × 10^{12} A/m^2), see colour circles in the Fig. 5.22.

Following the frequency dispersion for j_{app}>1.9 × 10^{12} A/m^2, we notice first that for small field values H_{app}=397Oe, the A mode reaches the OPP regime (H_{app}=56.4Oe), see trajectory on the left side of the figure. In H_{app}=170Oe and 284Oe the system is in a transition regime from IPP to OPP mode, giving rise to a noisy frequency dispersion. Depending on the radius of the OPP precession, the size of the m_z component will change and also the dipolar field over the TL and the BL [5]. Secondly for H_{app}=170Oe and 284Oe the system shows a noisy IPP regime.

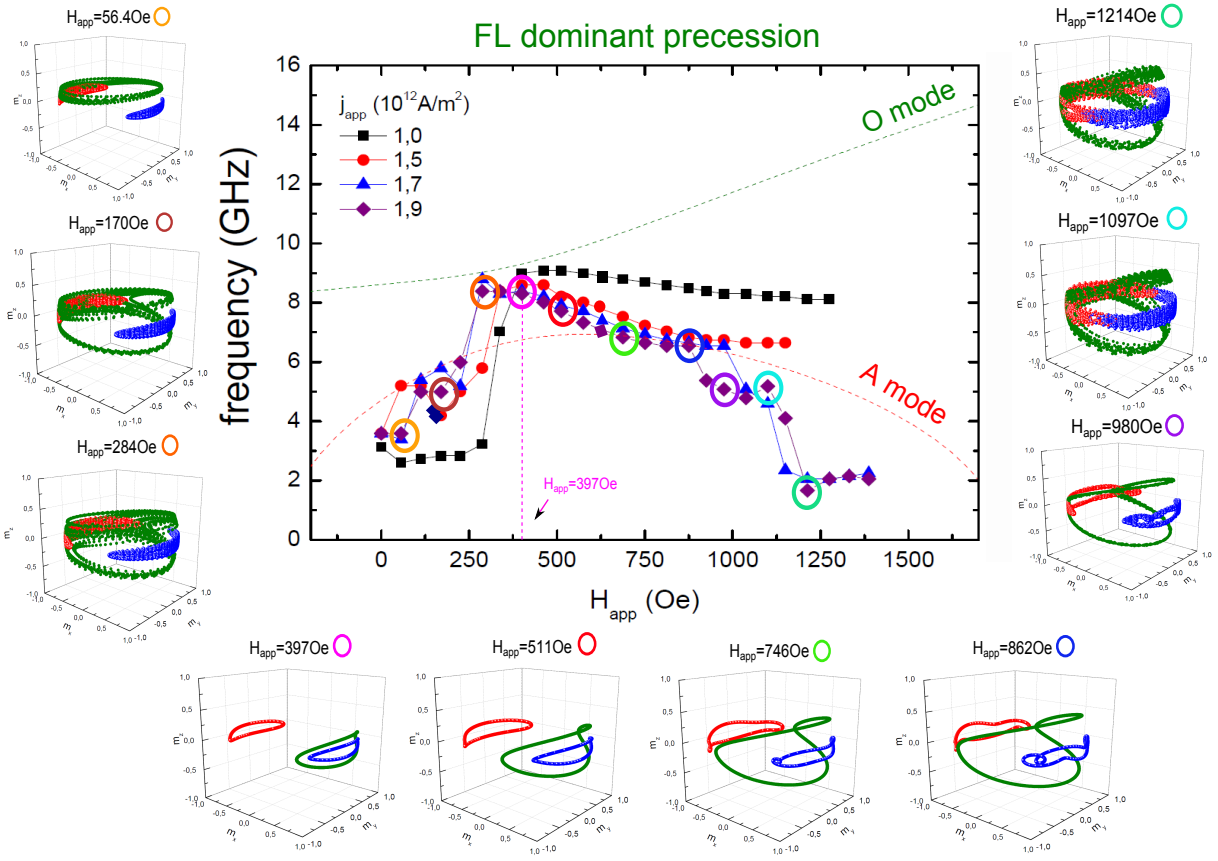

Figure 5.22 – Frequency versus magnetic field for several values of positive current density. The FL dominant precession are represented by solid points and the FMR hybridized modes in dash lines. The frequency dispersion modes A and O are not more separated for the characteristic gap. The A mode is already in a OPP regime showing a noisy tendency.

Increasing the field 387Oe<H_{app}<862Oe, the system shows a stable IPP mode. We observe the increase of the FL, TL and BL amplitudes as a function of the field and the distortion of the TL and BL precession trajectories. In this range of current and field, the frequency decreases, an opposite behaviour with the increase of frequency shown at small current values, see Fig. 5.20. For high field values, but less than the spin flop field, the IPP

[5] The OPP precession for high m_z component will be shown in the inset of Fig. 5.39 (b).

regime shows a jump and it becomes more noisy.

Looking for the origin of this kind of behaviours (noisy A mode region or deviation of the FMR O mode tendency) in the standard STO, we simulated the same system taking into account only the dipolar field between the layers (MSTT was neglected). The frequency dispersion as a function of the applied field is shown in Fig. 5.23. There are many similarities with the frequency dispersion of the total coupled system (MSTT + dipolar field) shown in Fig. 5.21, namely the A and O mode of the FL dominant precession are shifted from the FMR tendency, the gap is closed for high values of current density and a kink or jump of the STT O mode appears close to H_{app}≈1250Oe. As a difference with the case of dipolar and MSTT coupling, now close to the spin flop value we observe STT O mode excitations that present different dependence than in the previous case, see Fig. 5.22.

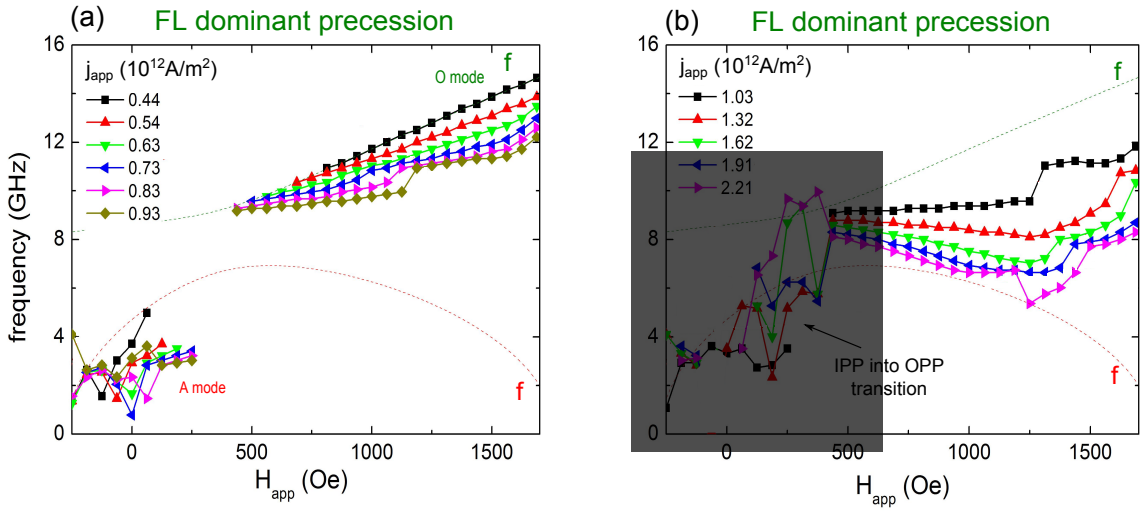

Figure 5.23 – Frequency versus magnetic field for several values of positive current density. The FL dominant precession O mode are in solid circles and the FMR hybridized modes in dash lines. (a) Current density values are close to the critical value. The interaction between the super O mode (3f) with the damped super optical mode (f) is shown in a form of a kink. (b) Increasing the current density the kink becomes in a splitting of modes.

In the following, a brief study of the STT A mode frequency tuning as a function of the current density will be presented. After this study we will continue with a study of the origin of the kink and jump shown in the frequency dispersion versus applied field H_{app}≈1250Oe, in Fig. 5.21 and Fig. 5.23.

A mode as a function of the current density (j_{app}>0)

The state diagram of Fig. 5.24 shows the orange region under study, which correspond to the STT A mode of the FL dominant precession (j_{app}>0) at small magnetic fields.

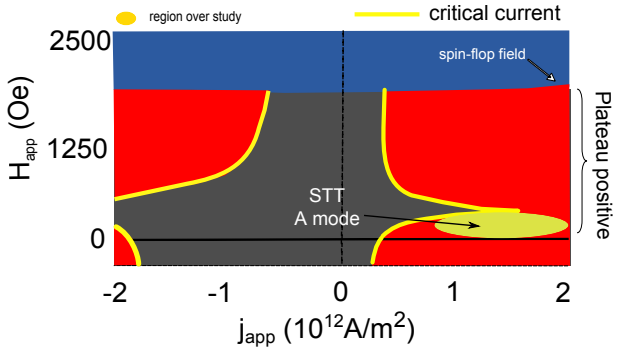

Figure 5.24 – The orange region in the state diagram (H_{app} vs. j_{app}) indicates the region over study.

The frequency tuning of the A mode (see Fig. 5.22) as a function of the current density is presented in Fig. 5.25. We chose three values of small magnetic field (0, 112.5, 225 Oe) to study the STT A mode before the gap. In the Fig. 5.25, we can observe that the frequency remains constant (FMR (damped) mode) until it reaches the critical current. For increasing j_{app}, the damped (sub-critical) regime transits to the steady state oscillations (IPP regime), then the frequency decreases (redshift). Increasing the current density, this IPP mode evolves into the OPP mode.

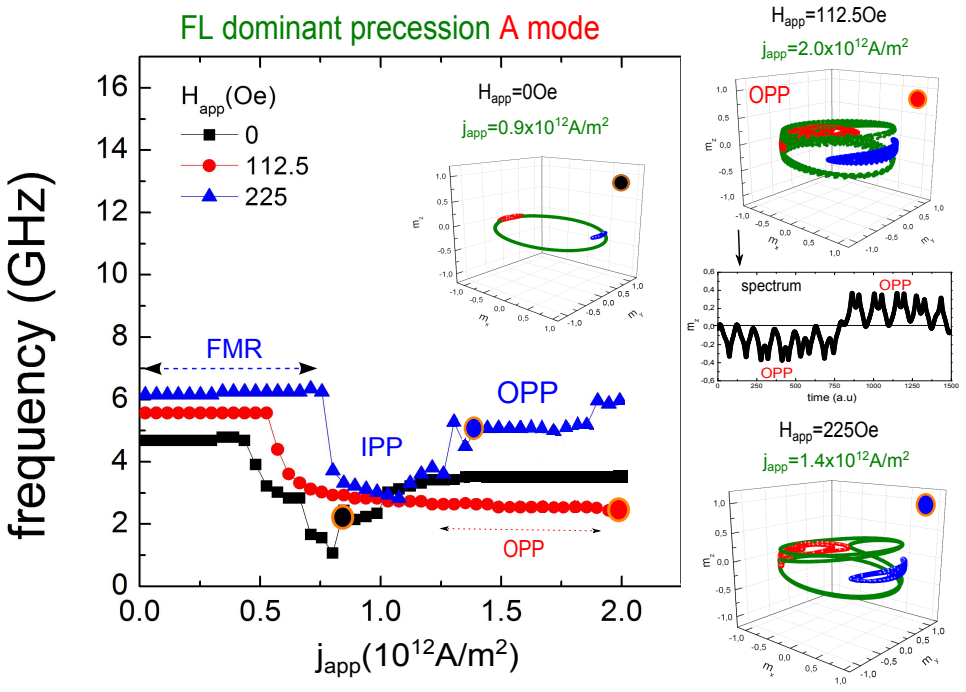

Figure 5.25 – Frequency tuning corresponding to the A mode as a function of the current density for H_{app}=0, 122.5, 225 Oe. (a) The A mode present a small region of IPP precession which evolves into the OPP oscillations.

In the right side of Fig. 5.25, we show the trajectories for H_{app}=112.5 Oe and j_{app}=1.53

and 2.0 $\times$ 10^{12} A/m^2. Overcoming the IPP regime the system enters to a OPP. The temporal trace of the m_z component shows that the system remain in the OPP regime[6] but changing the sign of the m_z component (positive and negative).

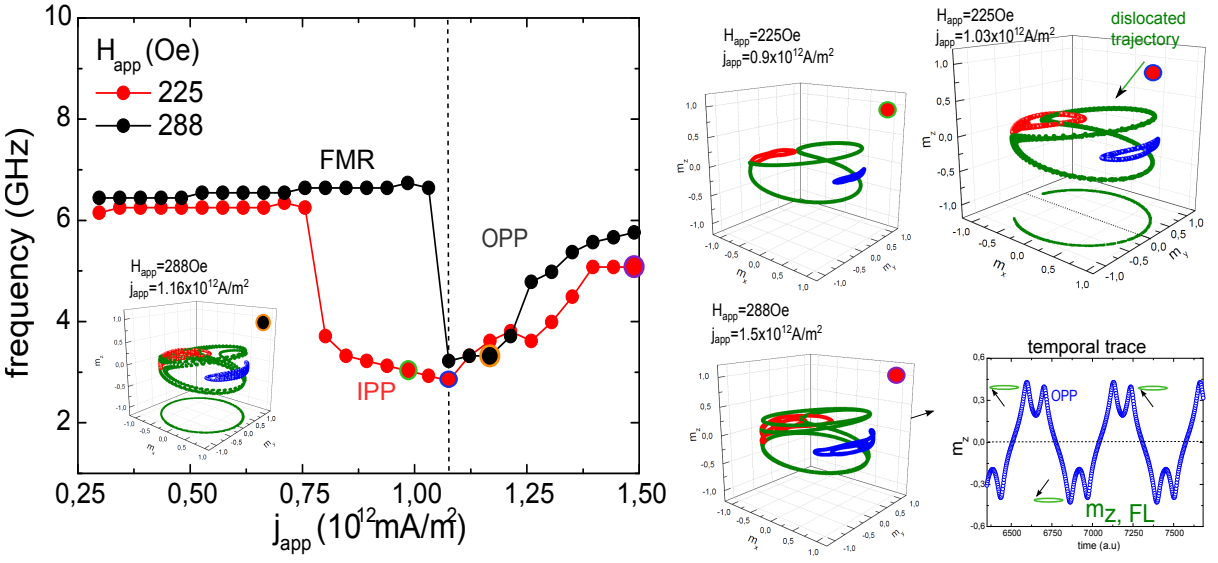

Figure 5.26 – Frequency tuning corresponding to H_{app}=225 and 288Oe (A mode) as a function of the current density. The IPP mode of the H_{app}=225Oe shows a small region (0.25x10^{12}A/m^2) which evolves into a OPP oscillations. For H_{app}=280Oe the system goes almost directly from the FMR (damped) mode to the OPP regime.

The frequency dispersion for two field values close to the gap (H_{app}=225Oe and 288Oe) is given in Fig. 5.26. In the case of H_{app}=225Oe the IPP regime (redshift) is small and evolves into the OPP which shows blueshift regime (frequency increases with the current density values). We found that the FL dominant precession show a non symmetric trajectory for 1.03 $\times$ 10^{12} A/m^2, see right top figure.

In the case of H_{app}=288Oe, the system reaches directly an OPP type regime above the critical current, see inset in the figure for 1.16 $\times$ 10^{12} A/m^2. In the right side of the Fig. 5.26 we can observe the different trajectories of the frequency dispersion and the temporal trace of this of the OPP mode (H_{app}=288Oe and 1.5 $\times$ 10^{12} A/m^2). The behaviour of the f vs I for H_{app}=288Oe is similar to the observed by [Houssameddine et al., 2008] and it could be a a possible interpretation. In that case, a standard MTJ STO with low TMR (LTMR) was characterized finding that it is possible to apply high current density values. In our simulations the jump from the damped mode to STT OPP mode shows the highest critical current.

In conclusion, the tuning (df/dj$_{app}$) in the IPP region for small values of magnetic field shows the redshift regime for a small range of current density. The condition of the

[6] If the component m_z remains with the same sign $\pm$ the system will be in OPP regime. i.e IPP reme is suppressed

maximum range was found for H_{app}=112.5 Oe, see Fig. 5.25. Moreover it will be possible to measure excitations in the OPP regime if the critical current is high enough.

5.2.2.5 Interaction of the STT modes with damped modes

Now, we will address the specific feature observed for the STT O mode. The state diagram of Fig. 5.27 (a) shows the purple region under study, which corresponds to the STT O mode of the FL dominant precession (j_{app}>0) for fields larger than the gap (high magnetic fields), see Fig. 5.27 (b). In this region we observe an important feature (kink and jump) which will be studied in the next section.

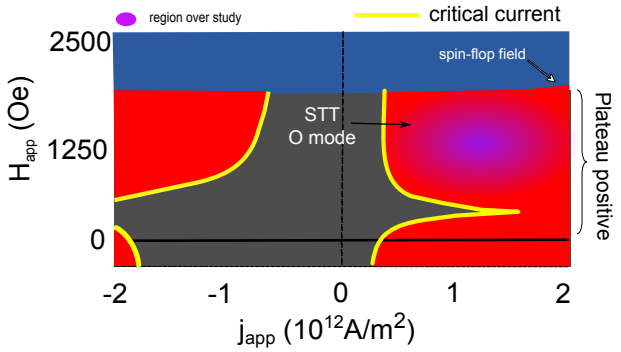

Figure 5.27 – State diagram (H_{app} vs. j_{app}) shows the STT O mode region (purple) over study.

In the previous section 5.2.2.3 we have discussed how damped modes can couple in the linear regime and how they are driven into STT upon applying a current (spin torque). To summarize these results, the dipolar coupling between the FL mode and the SyF modes leads to three hybridised modes that we call A, O , SO modes. The two lower frequency A and O mode can be driven into STT depending on the sign of the current and the field, while no condition has been found in the simulations for which the high frequency SO is driven into steady state. These results are not much altered when including or not the MSTT coupling between the FL and the SyF, see Fig. 5.23. A different situation has been presented in section 5.2.1 where only the non conservative MSTT has been considered between the FL and the SyF. The numerical studies reveal that the fundamental STT FL excitation can interact with the fundamental damped SyF mode when their respective frequencies cross. This leads to characteristic deviations in the frequency field and frequency current dependence, as well as a reduction of the linewidth in given range of field and current where the coupling is most efficient. In section 5.2.2.3 we also presented the results on the frequencies vs field for the STT O mode of the dipolar + MSTT coupled STO that revealed similar deviations in the frequency dependence as for

MSTT coupling only. We therefore extend in this section the studies on the coupling of the STT mode with damped modes to include the dipolar interaction. We will see here that the SO mode can play an important role.

In order to have a first idea on the possible coupling between the STT mode and the damped modes we show in Fig. 5.28 the three hybridized modes (A, O and SO modes) and some of their harmonics. From this figure we can predict possible crossings and interactions: For positive current the O mode is in STT at higher fields. The damped O mode frequency crosses with the frequency of the second and third harmonics of the damped A mode. Furthermore the third harmonic of the damped O mode (at higher fields) can cross with the SO. These crossing could be potentially the origin of the jumps or kinks observed.

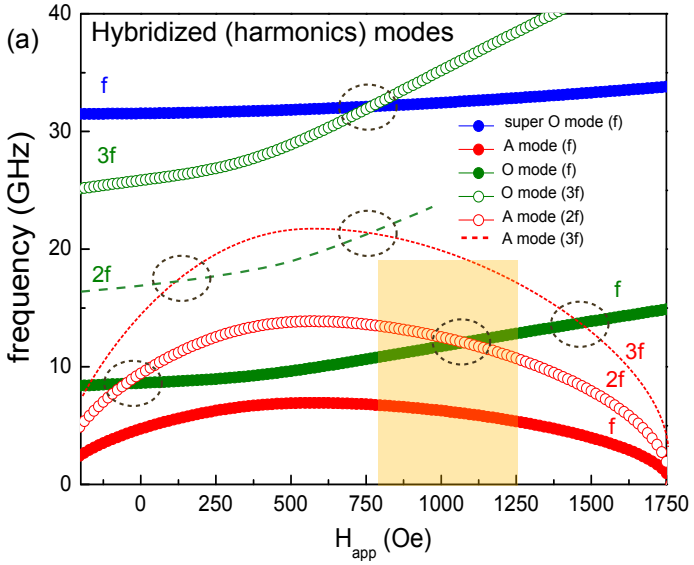

Figure 5.28 – (a) Frequency versus magnetic field for the three hybridized FMR modes (A, O and SO modes). We include the harmonics of the A mode (2f) (3f) and the O mode (2f) and (3f). The dashed circles correspond the possible interaction of modes. The shadow region corresponds to the jump of Fig. 5.29.

Similarly for negative current the A mode is driven into STT at higher fields and its second and third harmonics frequency can cross the damped O mode. We do not consider the lower field A and O STT mode, since at higher currents that are required for interactions the A mode transits into OPP and the O mode is difficult to be excited.

From the following discussion, it will be shown that this 'naive' picture of the crossing of damped modes can provide a guide, but that the frequency shift of the STT modes as a function of current as well as of the damped modes needs to be taken into account. Before coming to this we analyze more closely the evolution of the frequency as a function of field upon increasing the current.

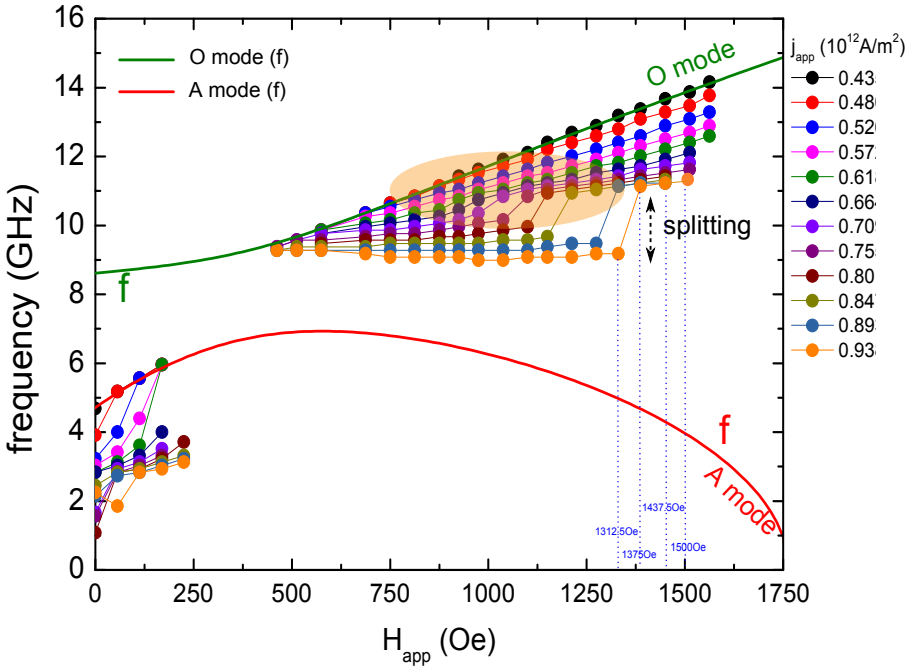

Figure 5.29 – (a) Frequency dispersion versus magnetic field for several values of positive current density (FL dominant precession). The frequency dispersion is shown in solid circles while the FMR hybridized modes and the harmonics are shown in dashed lines. (b) Frequency versus magnetic field for the three hybridized FMR modes (A, O and SO modes). The orange region correspond to the crossing of modes close to the STT jump.

The frequency dispersion of the STT O mode and the FMR modes are shown in Fig. 5.29 as a function of the magnetic field, for the FL dominant precession at T=0K. Comparing Fig. 5.29 with Fig. 5.28 we notice that in the range of the splitting there are two possibilities of crossing of modes: The fundamental STT O mode with the 2f damped A mode or the 3f STT O mode with the SO damped mode.

Introducing temperature to the system, we will have the possibility to analyse the STT modes and the damped modes simultaneously in the FFT ($m_{y,FL}$) frequency spectrum[7]. In Fig. 5.30 we show the spectrum (H_{app}=1312.5Oe and $j_{app}=0.93\times10^{12}A/m^2$) of the FL dominant precession (O-mode) (≈9.5GHz). We observe the damped A mode (≈2.1GHz) and SO mode (≈33GHz). We identify also the harmonic of the damped A and O mode. In the following, we will look for the evidence of the interaction in the STT frequency dispersion due to the crossing of the damped modes.

A first interpretation of the jump was the interaction of the STT O mode with the 2f FMR A mode, see Fig. 5.31 (a). We investigate the current dependence of the A mode when the STT O mode has reached ($j_{app}>0$), see Fig. 5.31 (b). The green region indicates the current range where the STT O mode is reached.

[7]The previous numerical results were calculated at 0K.

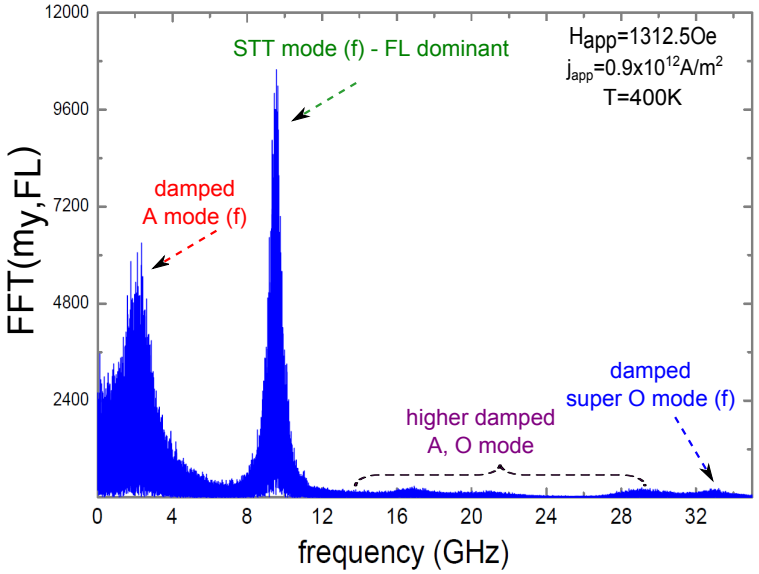

Figure 5.30 – Frequency spectrum simulated for a H_{app}=1312.5Oe and j_{app}=0.9×10^{12}A/m^2. The higher peak corresponds to the STT O mode of the FL dominant precession. The damped A and SO modes and higher harmonics are shown.

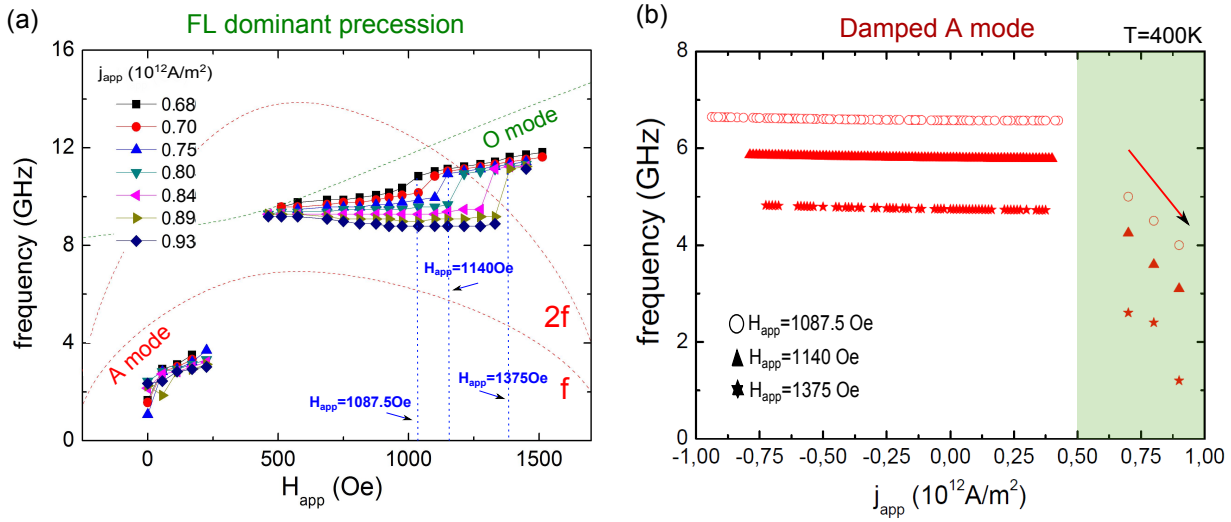

Figure 5.31 – (a) Frequency dispersion as a function of the applied field (FL dominant precession). The red dashed line correspond to the fundamental and second harmonic of the FMR A mode. (b) Frequency tuning of the damped A mode is shown as a function of the current density, for three values of applied field, H_{app}=1087.5, 1140 and 1375 Oe. This damped mode is red-shifted strongly as a function of the current density (≈1.2GHz).

In the damped A and O mode region (j_{app}<0.5×10^{12}A/m^2) the frequency does not change considerably but when the STT O mode is reached, the frequency of the A mode decreases. It is red-shifted strongly as a function of the current density (≈1.2GHz). This current dependence is strong. The decrease moves the crossing of STT O mode and damped A mode to frequencies that are much lower than the kink or jumps observed. The crossing of the 2f damped A mode can therefore be excluded as the origin of the kink or jump.

We now analyse the case of the crossing between the SO damped mode with the STT O mode. In the Fig. 5.32 we show the A and SO damped modes as a function of the current density. We notice that the SO mode shows a negligible shift in comparison with the damped A mode. This difference in frequency of SO mode and A mode can be qualitatively explained by the fact that when the STT O mode has a large amplitude. This also means that the FL has a large amplitude. In this non-linear regime the A, O and SO modes are most likely no more the proper base to describe the dynamics. The modes will mix, and a given excitation should be described as a superposition of the A, O and SO mode. Since the A and O mode are closer in frequency (than the SO mode and the A or O mode), their relative contributions to the lower frequency damped mode will be more important and in consequence the frequency shift of the initial A mode is stronger than for the SO mode.

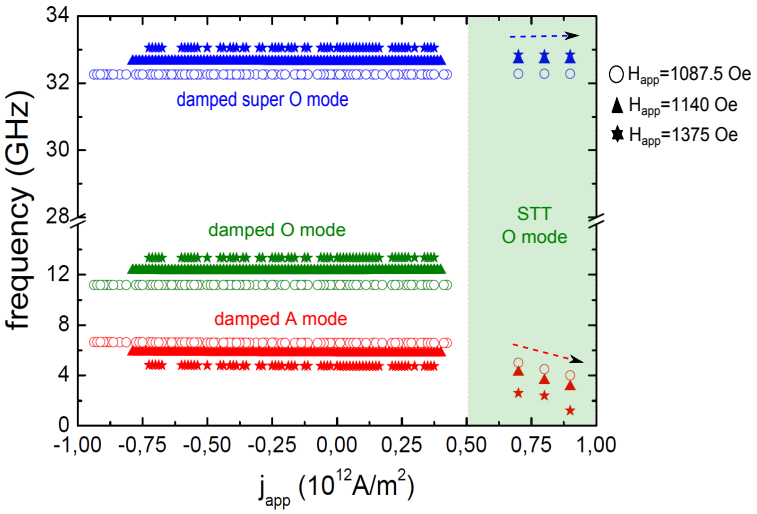

Figure 5.32 – (a) Frequency tuning of the A, O and super mode are shown as a function of the current density, for three values of applied field, H_{app}=1087.5, 1140 and 1375 Oe. (b) The damped super O mode shows a negligible shift but the damped A mode is red-shifted strongly as a function of the current density (≈1.2GHz).

In the following we will show a careful analysis of the STT O mode that have been done around the jump or kink. From the simulations at T=0K we observe a hysteresic behaviour around the kink (jump), see Fig. 5.33 (a). In Fig. 5.33 (b) and (c) we show the frequency spectrum in the bi-stable region finding that only one peak appears, the

fundamental of the STT O mode on each branch. In absence of the thermal noise the damped modes are not visible (T=0K).

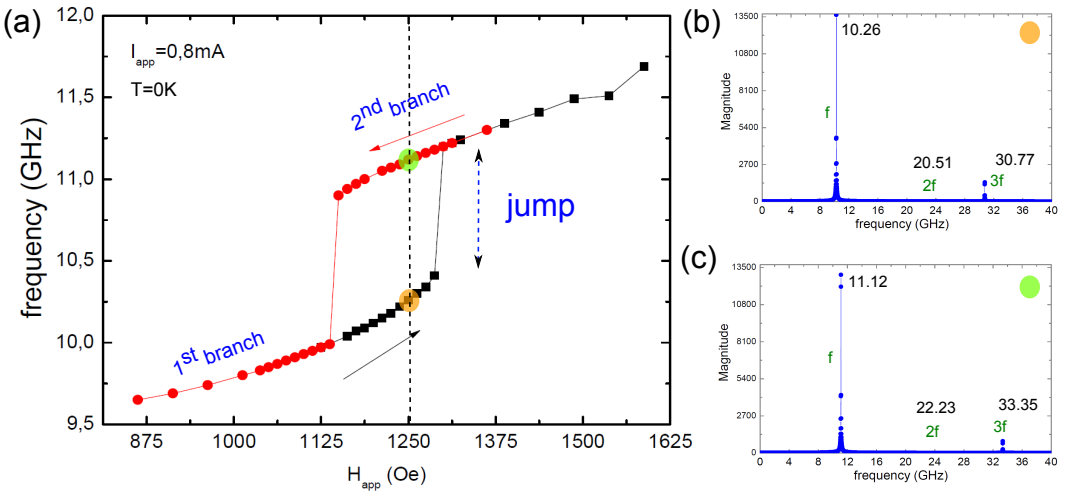

Figure 5.33 – (a) Frequency versus field dispersion around the kink for j_{app}=0.8×10^{12}A/m^2 at T=0K. Arrows show the sense of the field sweeping (red and black). (b)-(c) Frequency spectrum for H_{app}=1250Oe for both senses. The damped modes are not visible.

The evolution of the frequency dispersion of the STT O mode, as a function of the field for 0.7, 0.8 and 0.9 ×10^{12}A/m^2 are shown in Fig. 5.34 (a) at T=400K. The sweeping of magnetic field was from 250Oe to 1750Oe and is represented as solid symbols. The super O mode is indicated by the f/3 dashed blue line and the O mode (green line). As we showed in Fig. 5.32 the SO mode does not reveal a strong change of frequency with current density.

In all the cases, increasing the magnetic field the frequency increases in the first branch of the STT O mode. However, close to the crossing of modes (jump) the excitation spectrum shows two peaks, see Fig. 5.34 (b)-(c). The second peak is represented by the solid triangles close to the damped SO mode (f/3) in Fig. 5.34 (a). This coexistence is indicated by the shadow regions.

The fitting of the peaks for H_{app}=1200Oe is shown in Fig. 5.34 (b)-(c) where we show the fundamental STT O mode (f) (b) and its third harmonic (3f) (c). In (c), we notice the appearance of another peak between the (3f) STT O mode and the SO mode.

In order to analyse the evolution of the frequency spectrum as a function of the magnetic field, before and after the kink/jump, we will fix the current density in j_{app}=0.9×10^{12}A/m^2, see Fig. 5.35. We observe the frequency spectrum of the FL dominant excitation for H_{app}= 1312.5 (a)-(b), 1375Oe (c)-(d), 1437.5 (e)-(f) and 1500 Oe (g)-(h). The first two fields are placed just before the jump (frequency vs H_{app}).

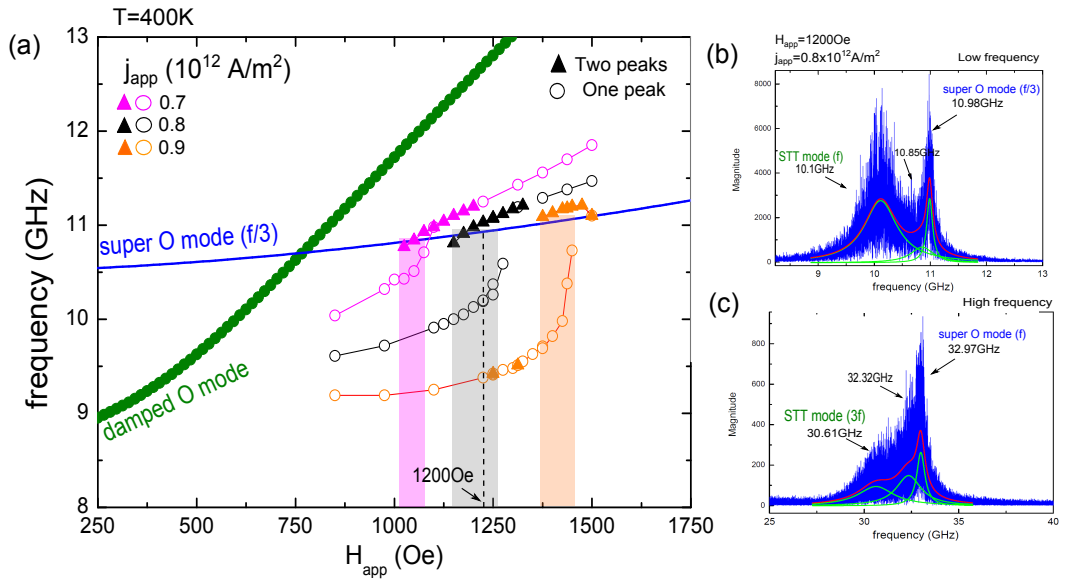

Figure 5.34 – (a) Frequency as a function of the magnetic field. The A mode, O mode and the super O mode are introduced as red, green and blue curves. In (a) the frequency dispersion for j_{app}= 0.7, 0.8 and 0.9 $\times 10^{12}$A/m^2 in the region of the crossing of the 3f STT mode with the FMR super O mode is shown (represented by the f/3 FMR super O mode). (b)-(c) Frequency spectrum for H_{app}=1200Oe and j_{app}= 0.9 $\times 10^{12}$A/m^2 for both senses. The damped modes are not visible.

In Fig. 5.35 (a) and (c) we can observe that the fundamental STT mode (9GHz and 9.71GHz) and in (b) and (d) the corresponding 3f harmonics, 29GHz and 29.9GHz. The damped super O mode is shown in (b) and (d) at 32.8 GHz and 33.28 GHz respectively. In (a) and (c) the f/3 of the damped super O mode at 11GHz and 11.09GHz. We notice the appearance of a second peak close to the STT O mode, see Fig. 5.35 (c), when the damped super O mode crosses the 3f harmonic of the STT mode. As it is not possible to excite two STT modes, the appearance of the second peaks corresponds to the disappearance of the first one, probably by a hopping between them.

For high magnetic fields, the STT O mode is at 11.17GHz, just the same frequency (f/3) of the damped super O mode, see in Fig. 5.35 (e). We notice that the crossing of modes has already occurred, the damped super O mode is in the left side of the Fig. 5.35 (f) and (h) at 32.8 GHz and 32.41 GHz. The linewitdh of the STT excitation is reduced from Δf=720MHz in the case of Fig. 5.35 (a) to , Δf=98MHz in Fig. 5.35 (e) exactly when the (3f) STT O mode interacts with the damped super O mode. This smaller linewidth corresponds to a smaller df/dj$_{app}$ as we will discuss in section 5.2.1.1 below.

The interaction between the modes is summarized in Fig. 5.36. We plot the frequency of the (3f) STT O mode and the damped super O mode as a function of the magnetic field for j_{app}= 0.8, 0.85 and 0.9 $\times 10^{12}$A/m^2. We indicate the crossing of modes with the shadow

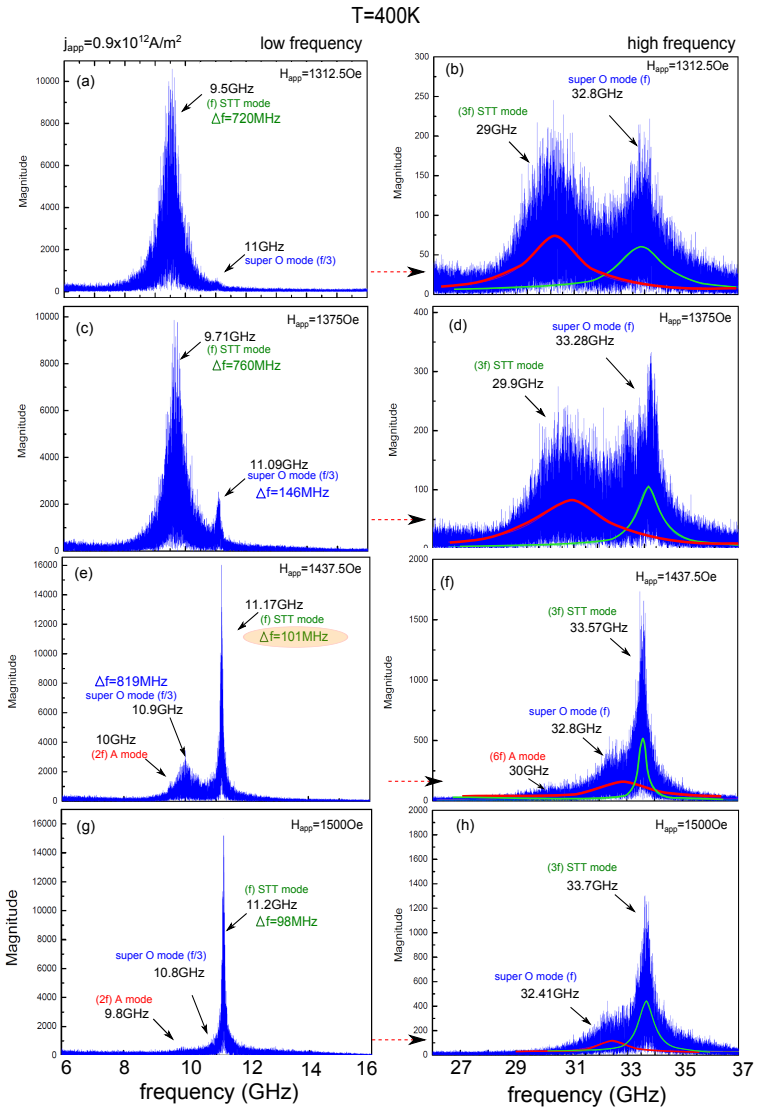

Figure 5.35 – Spectrum of the standard STO for H_{app}=1312.5Oe (a)-(b), 1375Oe (c)-(d) (before the jump) and 1437.5Oe (e)-(f), 1500Oe (g)-(h) (after the jump) for $j_{app}=0.9\times10^{12}A/m^2$. In (a),(c),(e) and (g) the peaks of the fundamental STT O mode and the super damped O mode (f/3). For high frequencies (b),(d),(f) and (h) the third harmonic of the STT O mode has jumped into high frequencies in comparison with the damped O mode.

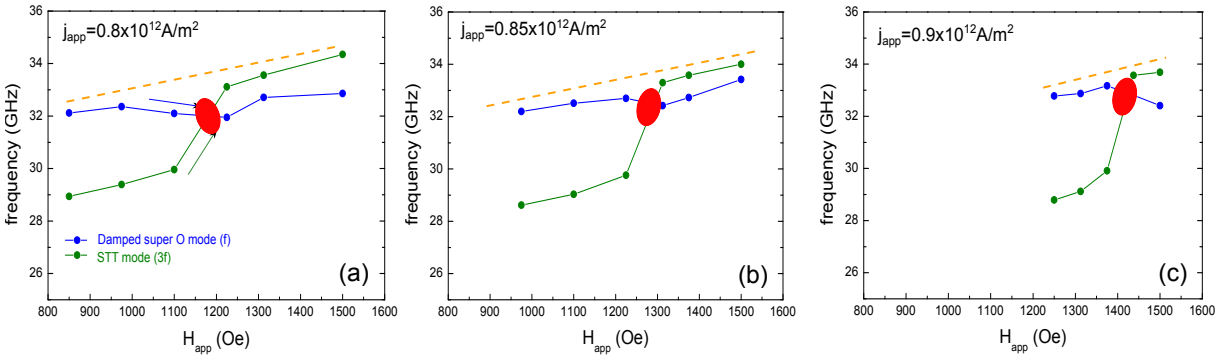

Figure 5.36 – Frequency as a function of the magnetic field, for spectrum of the standard STO for j_{app}=0.8, 0.85, 0.9×10^{12}A/m^2. The green (blue) curve corresponds to the frequency of the (3f) STT mode (damped super O mode). After the crossing the STT mode (3f) follows the tendency of the damped super O mode (flattening region of Fig. 5.29).

red region. On the crossing of modes the fitting is complicated due to the proximity of both peaks. We realize that far away from the crossing the (3f) STT O mode follows the tendency of the damped mode, see yellow dashed line. In conclusion, after the jump the STT O mode take the characteristic of the damped super O mode.

The linewidth as a function of the magnetic field in the jump region is shown in Fig. 5.37 for the higher intensity mode only. An important decrease in the linewidth appears after the jump.

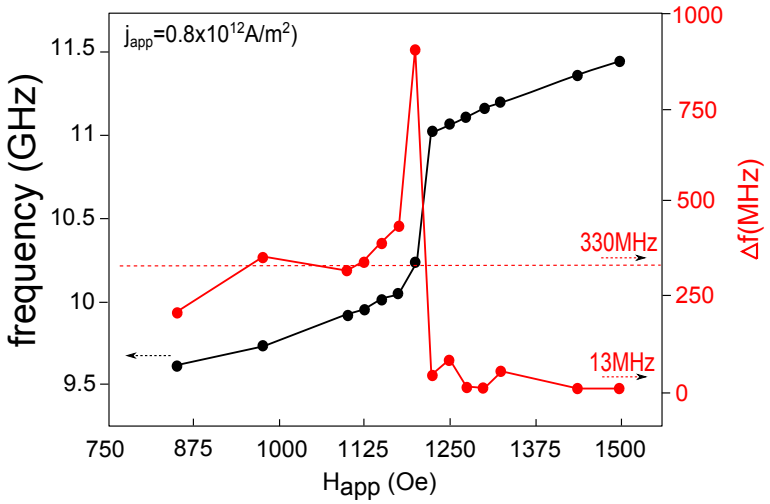

Figure 5.37 – Frequency and linewidth dispersion of the standard STO as a function of the magnetic field for j_{app}=0.8×10^{12}A/m^2.

The fact that the kink and jump is attributed to the interaction between the (3f) STT O mode with the damped super O mode does not mean that the A mode does not suffer any change in the corresponding frequency field and current range. In Fig. 5.38 (b) we show the frequency dispersion for the damped A mode. First we notice that for a dynamical precession the softening of the A mode decreases by around 250Oe to H_{app} ≈1500Oe

(softening means $\omega \longrightarrow 0$). Moreover we observe that in the region of the interaction (STT mode with damped super O mode) the damped A mode shows deflections, see shadow pink, grey and orange regions. *The deflections follow the kinks and jumps of the STT-O mode*. We interpret this as follows: In the non-linear regime the excited modes are a linear combination of the three modes hybridized A, O and SO modes of the linear regime. For this fact, any change in some of this linear modes will affect, in different magnitude, the hybridized modes of the system.

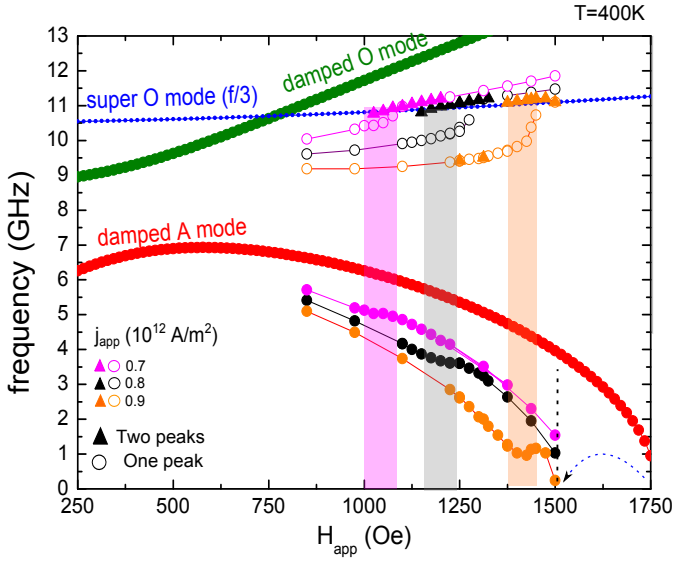

Figure 5.38 – Frequency dispersion of the STT O mode and the damped A mode as a function of the magnetic field for 0.7, 0.8 and 0.9 $\times 10^{12}$A/m^2 in the region of the crossing of the (3f) STT mode with the damped super O mode is shown (represented by the f/3 FMR super O mode) the damped A mode shows a deviation in the regions of the interaction.

Frequency and linewidth versus current density ($j_{app}>0$)

In the following we analyse the current dependence of the frequencies of the STT O mode ($H_{app}>400$Oe) at T=0K in order to obtain an understanding of their tendencies. Fig. 5.39 (a) and (b) show the STT O mode frequency versus current density. In the figure (a), the frequency dispersion (for magnetic fields close to the gap) show a redshift regime and a discontinuity (jump) for high values of current density. This jump (high current density) correspond to the crossing of the STT O mode with the damped SO mode. If the magnetic field increases as it is shown in Fig. 5.39 (b), we can observe the same tendency. We will focus the analyse in the kink of (11GHz) which evolves into a jump (1000Oe$<H_{app}<$1500Oe). At high current density the system will evolves into OPP precession that is not considered here.

We will add temperature to the system T=400K, in order to study also the linewidth behaviour around the interaction between the modes and in order to quantify the FL or

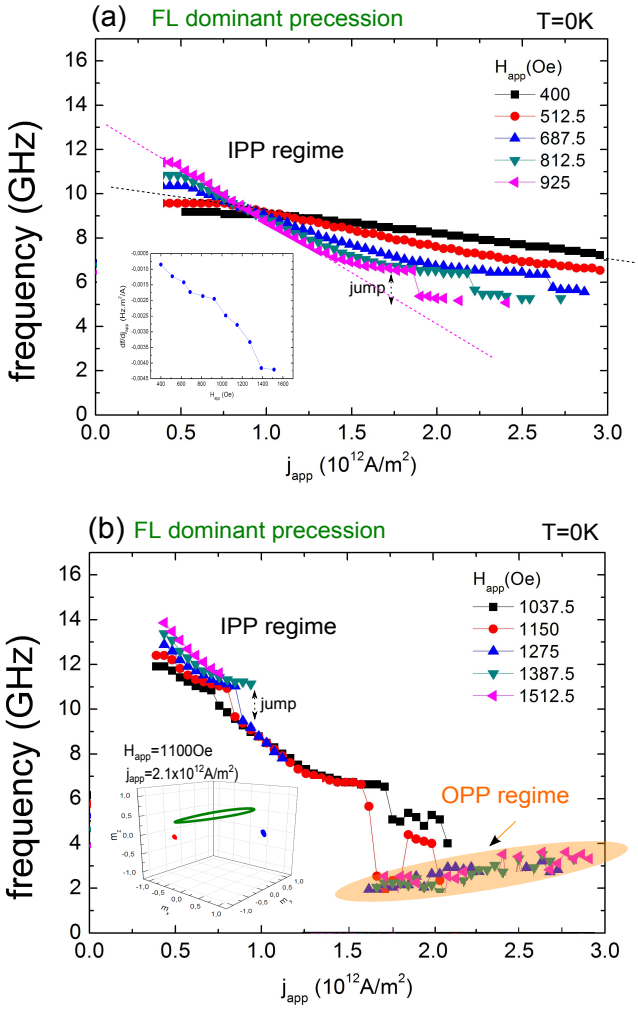

Figure 5.39 – Frequency tuning as a function of the current corresponding to the STT O mode. (a) Frequency dispersion (small magnetic fields) shows a jump for high current values (interaction with damped A mode) while in (b) the frequency dispersion (high magnetic fields) shows the jump in the interaction with the super O mode (f/3 dashed blue line).

SyF dominant precession linewidths. The interaction of the (3f) STT mode of the FL dominant precession with the damped super O mode of the system is shown in Fig. 5.40 (f vs j_{app}) for two magnetic field values (H_{app}=625 and 1250Oe). In both figures the green curve corresponds to the FL dominant precession (positive current density) and the red curve to the SyF dominant precession (negative current density). The shadow regions (in red and green) indicate damped modes of both cases ($j_{app} \neq < j_c$). The blue dashed lines in Fig. 5.40 (a)-(b) indicates the hybridized damped super O mode (≈32.8GHz) at (f/3) ≈11GHz.

In Fig. 5.40 (a), for $j_{app}>0$ there is no crossing between the green curve (STT O mode) and the blue dashed line (damped super O mode f/3), thus one cannot distinguish any interaction (kink or jump). In contrast, Fig. 5.40 (b), the projection of the f/3 damped super O mode into the STT mode of the FL dominant precession creates a jump, as in the case of T=0K.

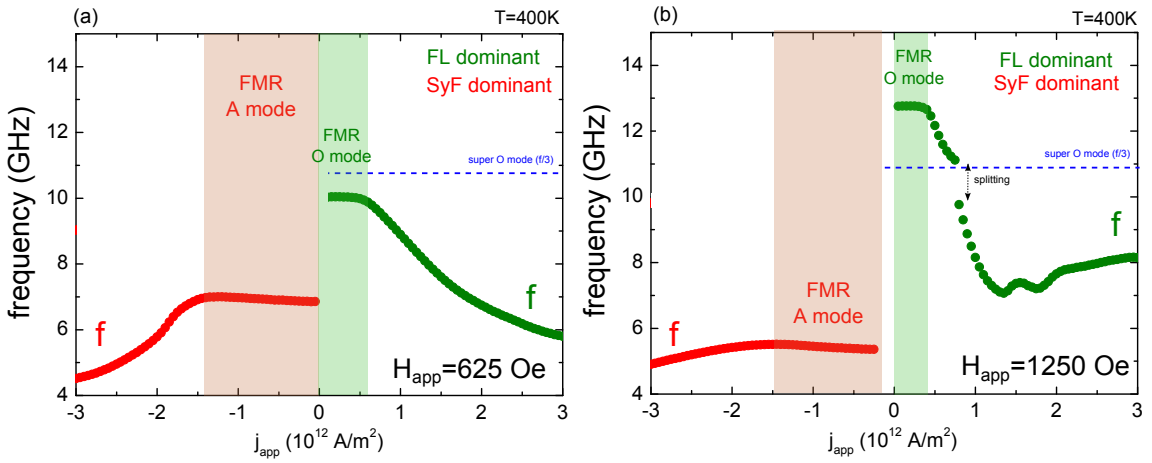

Figure 5.40 – Frequency dispersion as a function of the current density at T=400K. For positive (negative) current density we observe the FL (SyF) dominant precession (green and red curves). the dashed blue line corresponds to the damped super O mode hybridized mode. In (a) the super damped O mode do not interact with the (3f) of the FL dominant precession. In (b) the interaction shows the splitting.

Analysing the linewidth for these two fields values, see Fig. 5.41, a linear tendency is found for the damped modes regions (for both senses of current density) as it has been predicted in section 5.2.2.2, Fig. 5.12. In Fig. 5.41 (a), H_{app}=625Oe, the linewidth shows deviations for both sense of current density, that we cannot identify as the crossing of modes. Looking at the blue dashed line, there is no crossing of the f/3 damped SO mode with the damped O mode. In the case of H_{app}=1250Oe, see Fig. 5.41 (b), the crossing of modes gives rise to the splitting (jump) for the FL dominant precession for $j_{app} \approx 0.7\times10^{12}$A/m^2. The blue shadow region shows a flat region of f vs j_{app} (low df/dj_{app}) before the jump and a decrease of the linewidth. We can relate this behaviour with the decrease of the linewidth explained in section 5.2.1.1, see Fig. 5.7, where we shown the

deviation of the frequency versus field curve in the region close to the crossing of the modes. This was related with the decrease of the non-linear parameter ν and a reduction of the linewidth. The linewidth behaviour can provide information about crossing of modes.

In Fig. 5.42 (a) (H_{app}=0Oe) the blue dashed line crosses the (3f) FL dominant precession, $j_{app} \approx 0.5\times10^{12}$A/m^2. In Fig. 5.42 (b) super O mode (f/3) crosses the (3f) FL dominant precession. In both figures, the linewidth of the FL dominant precession shows a turning point close to the crossing of the modes, indicated by the blue shadow region. It has found that the linewidth in the STT regime is smaller for the SyF than for the FL dominant precession in the case of H_{app}=0Oe (linewidth of $\Delta f \approx 88$MHz) but not at all in the case of H_{app}=125Oe.

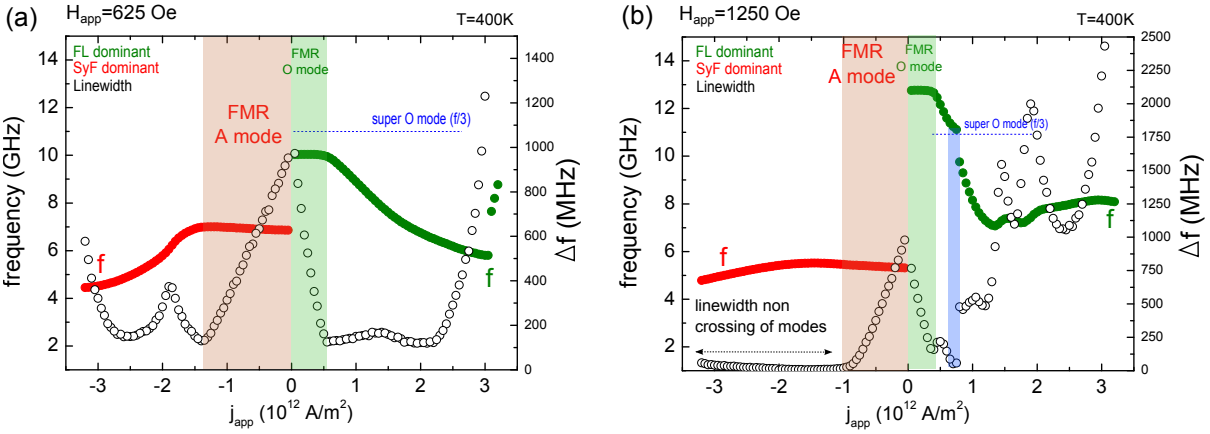

Figure 5.41 – Frequency dispersion and linewidth as a function of the current density, for magnetic field of H_{app}=625 ans 1225 Oe in (a) and (b). For positive current density (green curve) the dominant FL excitation is presented and for negative current density, (red curve) the dominant SyF excitation. The circles in grey correspond to the linewidth in both sense of current. In both cases the damped super O mode (f/3), is presented.

Summarizing, the crossing of the damped SO mode with the STT mode will generate a kink or jump in the frequency and a reduction of the linwidth. An interesting feature shows the SyF dominant precession for H_{app}=1250 Oe, see 5.41 (a). In the entire range of negative current the linewidth does not show any deflection or discontinuity. This fact corresponds to the absence of crossing modes, the STT mode for the SyF dominant precession is not affected by the damped super O mode. The linewidth show the smaller value $\Delta f \approx$ 10MHz.

Now we will analyse the jump in the STT O mode, in the regions where the interaction between the modes shows an influence on the linewidth. In order to study the frequency dispersion and linewidth as a function of the current density ($j_{app}>0$) the magnetic field was fixed in H_{app}=850, 975, 1100 and 1225Oe, close to the jump of the FL dominant

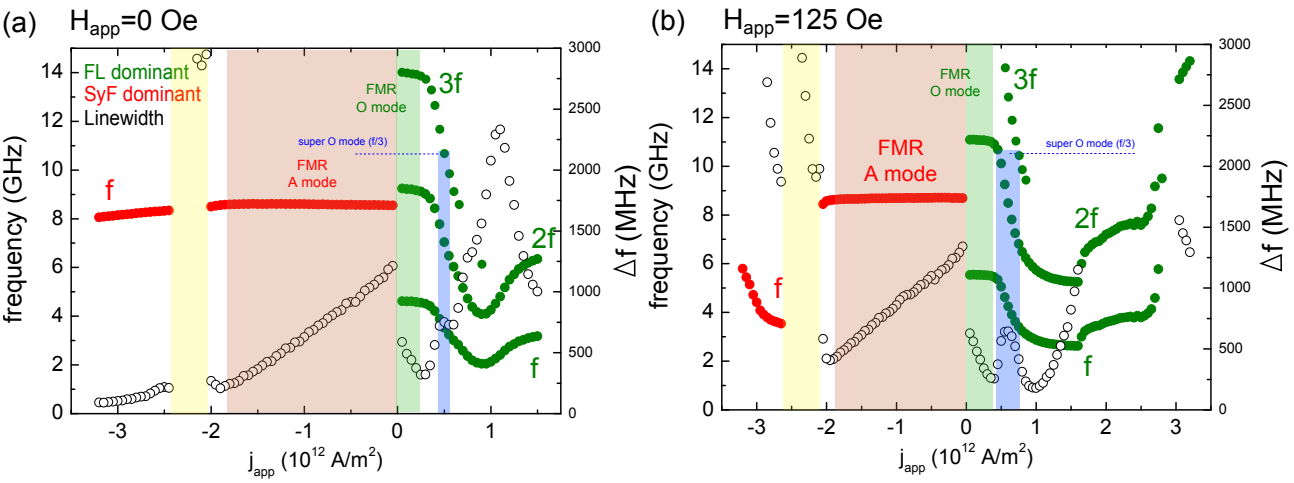

Figure 5.42 – Frequency and linewidth dispersion as a function of the current density for H_{app}=0 and 125 Oe (a) and (b) respectively. The circles in grey correspond to the linewidth for both sense of current. The super damped O mode crosses the (9f) STT mode of the FL dominant precession in both cases.

precession described in Fig. 5.41 (b). In Fig. 5.43, the black curve corresponds to the frequency of the STT O mode. It is possible to observe the evolution (as a function of the magnetic field) of the kink, starting with a flat part (b) and evolving towards a jump (d) for high values of current density.

Looking into the linewidth at H_{app}=850 Oe we can observe how it increases as a function of the current density without an important deviation. Increasing the magnetic field to H_{app}=975Oe, we notice that the kink appears in the frequency dispersion while the linewidth shows a deviation, see blue shadow region. In the kink region the linewidth decreases and after this increases (yellow shadow region). We notice also that the reduction is in agreement with the flat region of the frequency, where the df/dj_{app} is smaller, reducing the non linear parameter ν, as it has been explained in section 5.2.1.1 in equation 5.4, [Gusakova et al., 2011].

The emitted spectra before and after the jump is shown in Fig. 5.44 for H_{app}=1225Oe. The FFT of the temporal traces of the m_y component (green, pink and orange circles, j_{app}=0.75, 0.8 and 0.85 $\times 10^{12}$A/m^2), are shown. In the case of the pink circle we observe two peaks (3f of the damped super O mode ≈10.2GHz and the STT O mode ≈11.02GHz). The linewidth of the STT O mode decreases from 90MHz into 30MHz just before the jump, in the bi-stable and flattening region.

In conclusion, the macrospin simulations shows that the crossing of the STT O mode (FL dominant precession) with the damped SO mode will generate a distortion in the frequency dispersion diagrams (versus field and current). The linewidth will be also

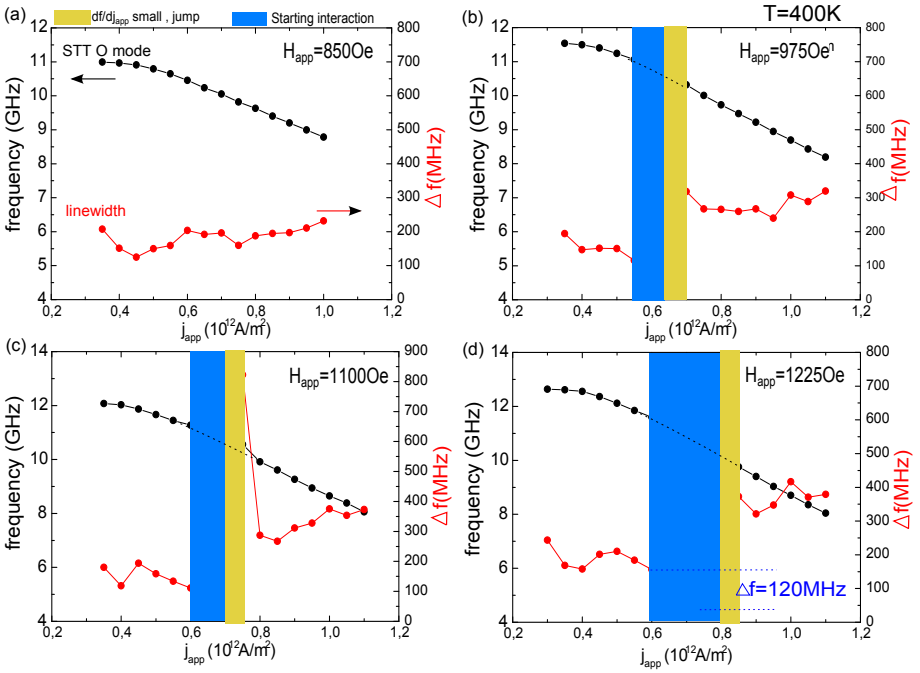

Figure 5.43 – Frequency and linewidth dispersion as a function of the current density, for H_{app}=850, 975, 1100 and 1225Oe. The blue region correspond to the beginning of the interaction (3f) harmonic of the STT mode with the damped super O mode, small df/dj_{app}. The evolution from a kink towards a jump is shown.

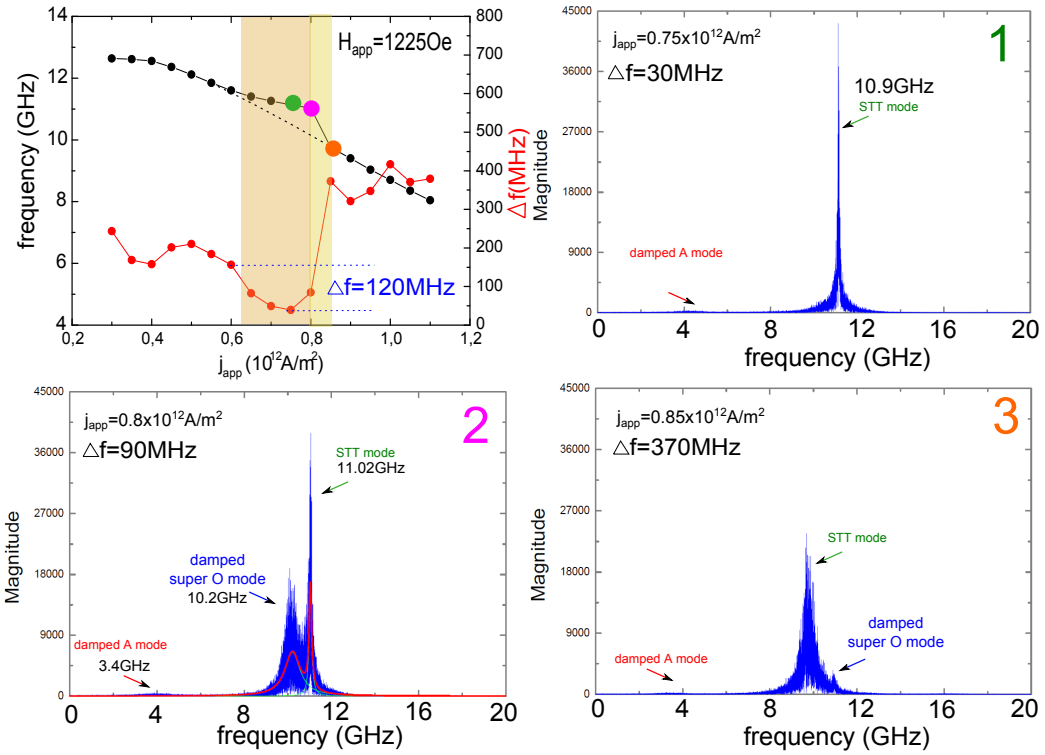

Figure 5.44 – Frequency dispersion (f vs.j_{app}) for H_{app}=1225Oe. Amplitude of the peaks for j_{app}=0.75, 0.8 and 0.85 $\times 10^{12}$A/m^2 around the splitting. Before the jump (2) in the flat region the linewidth shows its minimum value Δf=30MHz.

strongly affected. This crossing of modes for some conditions will reduce the linewidth in a small window of current density and field, improving the quality of the emitted signal. However the overall minimum linewidth obtained for the STO was found for the SyF dominant precession, in the blushift regime.

The minimum linewidth for the FL dominant precession was of $\Delta f_{min}{}^{FL}$= 38MHz for H_{app}=375Oe and j_{app}= 2×10^{12}A/m^2, and for the SyF dominant precession was $\Delta f_{min}{}^{SyF}$= 6.4MHz for H_{app}=1250Oe and j_{app}=-1.6×10^{12}A/m^2, in the blueshift regime. As we explained in section 4.2.5, for high values of magnetic field, the dynamic RKKY torque increases, given rise to a more stable precession leading into a reduction of the line width. Comparing the FL and the region of the smaller linewidth corresponds to the blueshift regime of the SyF dominant precession.

5.2.2.6 Frequency tuning of the SyF dominant precession (j_{app}<0)

Changing the sense of the current density we can study the features of the SyF dominant precession. This coupled layer has shown interesting transition from redshift (df/dj_{app}<0) to blueshift (df/dj_{app}>0). Moreover in this last regime the system shows the overall smaller linewidth.

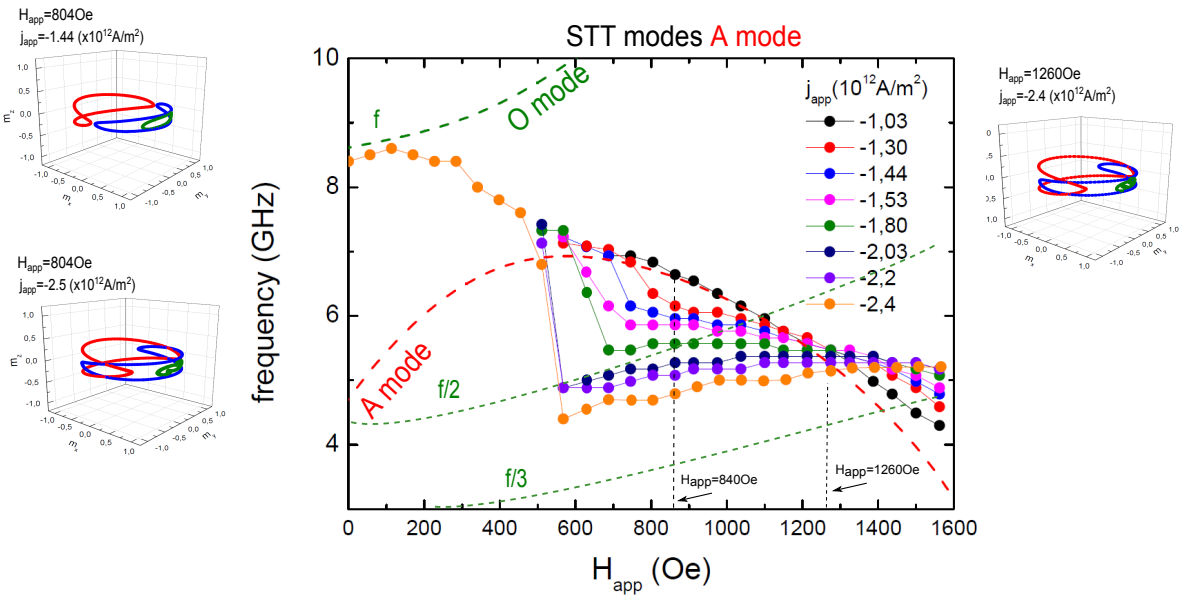

Figure 5.45 – Frequency versus magnetic field for several values of negative current density. The SyF dominant precession are represented by solid points, the FMR hybridized A mode by red dashed lines and the fundamental, f/2 and f/3 FMR O mode in green dashed lines.

In Fig. 5.45 is shown the STT A mode of the SyF dominant precession as a function of the magnetic field, for several values of current density from j_{app}=-1.03 to -2.4 $\times$ 10^{12} A/m^2

(solid circles). The red dashed line corresponds to the acoustic FMR A mode of system which gives the first tendency for the STT modes. The green dashed lines correspond to the fundamental, f/2 and f/3 FMR O mode.

As in the case of the FL dominant precession the STT modes are shifted from the FMR tendency increasing the current. Close to H_{app}=1260 Oe, the STT modes present a crossing point, as in the case of the isolated SyF, see Fig. 4.15. This crossing point separates the redshift regime (left side) and the blueshift regime (right side).

The behaviour of the frequency dispersion is similar to the case introduced in sec. 4.2.2 for the case of an isolated SyF. Under these conditions of current and field the SyF will remain in the IPP regime, see trajectories in Fig. 5.45. Another observation is, that the STT A mode seems to suffer a kink around f=≈6GHz, starting at -1.3× 10^{12} A/m^2 and a jump for -2.4× 10^{12} A/m^2 In order to conclude that this is really an effect of the crossing of modes we need more simulations with temperature.

5.2.2.7 Magneto-resistance frequency dispersion

In chapter 4 and in the previous sections we showed the numerical simulation taking into account the FFT of the temporal traces of the m_y component, which corresponds to the precession around the fixed y axis. Now in this section we will obtain the frequency diagrams (MR-diagrams) taking into account the FFT of the temporal traces of the product $\mathbf{m}_{TL}.\mathbf{m}_{FL}$ (MR effect), see equation 3.30. The MR-diagrams are a more realistic picture because the voltage measured depends of the angle between both magnetizations. In this section we will look for similarities and differences between these both cases and they will be compared later with the experimental results of the standard STO in chapter 6.

FL dominant precession T=400K

The frequency as a function of the magnetic field for the FL dominant precession, 0.4 and 0.6 × 10^{12} A/m^2 are shown in Fig. 5.46 at T=400K. The frequency dispersion for the $m_{y,FL}$ are shown in Fig. 5.46 (a)-(b) and for the m_{TL} component in Fig. 5.46 (c)-(d). In order to find the origin of these the differences, we show in Fig. 5.46 (e)-(f) the frequency dispersion of the $\mathbf{m}_{TL}.\mathbf{m}_{FL}$.

For these figures the magnitude of the FFT of the temporal traces has been normalized for each H_{app} value, i.e we will show the FMR damped modes and the STT modes. This

will be useful because in the measured frequency diagrams of the STO based on MTJ the damped modes will be present. The yellow colour corresponds to high amplitude of the FFT, and dark colours to small magnitudes. The thickness of the excitations corresponds to the linewidth. The red and green lines included in Fig. 5.46 (e)-(f) will indicate the field range of the damped modes in the frequency diagram and to identify only the STT A and O modes.

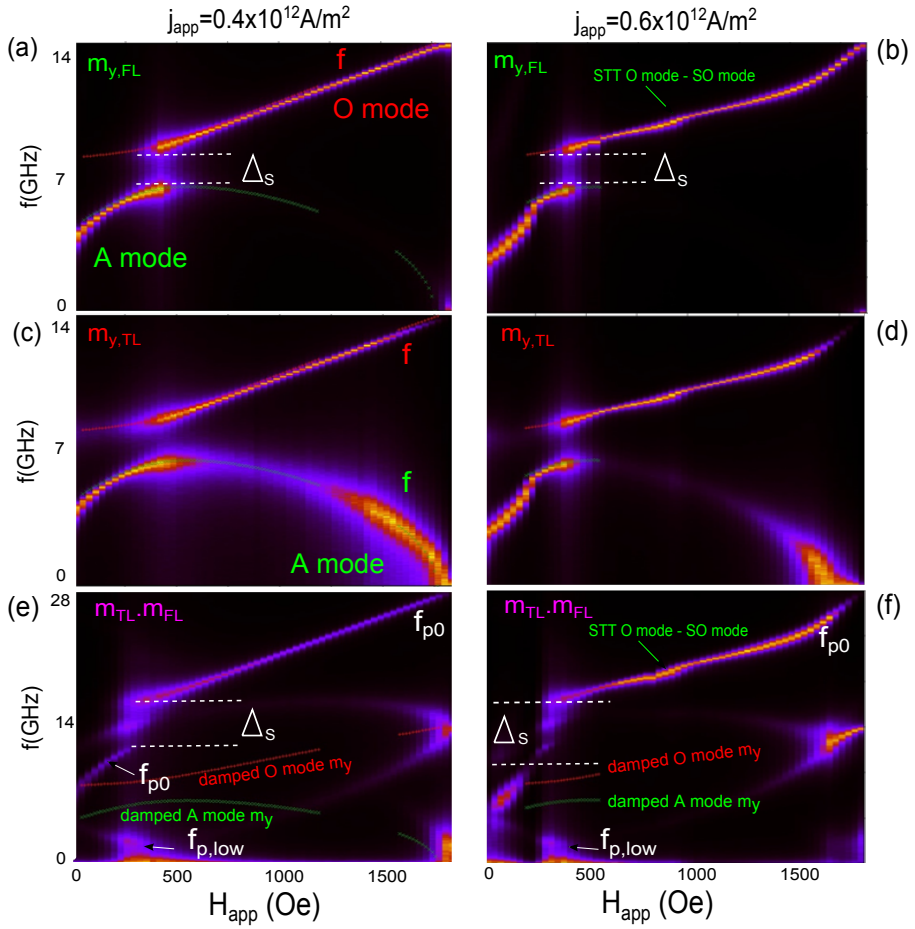

Figure 5.46 – Frequency dispersion as a function of the applied field is shown for j_{app}=0.4 and 0.6×10^{12}A/m^2 (FL dominant precession). The diagrams correspond to the excitations (T=400K) for the FL (a)-(b), TL (c)-(d) and the inner product of the components $\mathbf{m}_{TL}.\mathbf{m}_{FL}$ (e)-(f). The yellow colour corresponds to high magnitude of the excitation spectrum. The region of damped A and O mode are indicate by the red and green lines, in all the other field range the STT modes are present. In all the cases the linewidth of the signal corresponds to the thickness of the mode. The interaction between the STT O mode- damped SO mode is show for high current density 0.6×10^{12}A/m^2. Due to the presence of the damped modes, the splitting seems to be closed.

In Fig. 5.46 (a)-(d) the STT modes show the splitting between them and the same tendency of the FMR damped mode. In the case of the MR diagrams 5.46 (e)-(f) the frequency is the double than in (a)-(d). We observe that in Fig. 5.46 (e)-(f) the damped modes appear clearly due to the normalization of the FFT amplitude. For that reason the splitting seems to be closed. We observe that in the region of the gap a positive low

frequency ≈2GHz damped mode appears and in the splitting ≈14GHz as well. In the following we will shown the similarities and difference of the MR diagrams ($\mathbf{m}_{TL}.\mathbf{m}_{FL}$) in comparison with the previous results of this chapter.

Similarities:

1. **Presence of the gap and splitting**. In Fig. 5.46, the frequency dispersion diagrams and MR-diagrams for 0.4-0.6× 10^{12} A/m^2 show the STT A and O mode, separated by the characteristic gap (damped modes) and the splitting. The size of the gap is reduced with the increase of the current density, see red and green lines in Fig. 5.46 (e)-(f).

2. **Interaction between modes**. In Fig. 5.46 (b), (d) and (f), the evidence of the interaction between the STT O mode with the damped SO mode is shown close to H_{app} ≈1100Oe.

3. **STT A mode**. For high current density, 0.6× 10^{12} A/m^2 in Fig. 5.46 (c), the STT A mode shows a noisy frequency dispersion, which corresponds two the non-periodic OPP modes.

Differences:

1. **Double of frequency**. In the MR-diagrams, Fig. 5.46 (e)-(f) show the double of frequency in comparison with the diagrams corresponding to the $m_{y,FL}$ and $m_{y,TL}$ component (a)-(d).

2. **Low frequency modes**. Around H_{app}=400Oe (region of the gap) the MR diagrams shows a low frequency mode (1-2GHz), see Fig. 5.46 (e)-(f)

SyF dominant precession T=400K

Similarly for the case of the SyF dominant precession, see Fig. 5.46, j_{app}=-1.0 ×10^{12}A/m^2 we obtain the MR diagram with the different excitation modes that will be compared in chapter 6. We observe that in (c) the splitting seems to be closed and a low frequency modes appears in the range of field of the splitting. In the case of T=0K we simulated the MR diagram for showing a sort of modulation. An open question will be if it is possible to observe the same modulation for T=400K, i.e. for higher current density values.

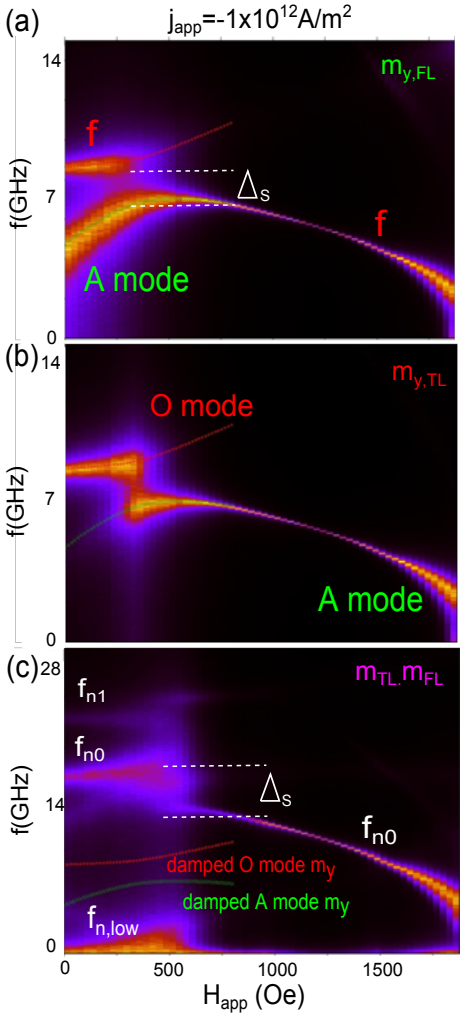

Figure 5.47 – Frequency dispersion as a function of the applied field is shown for j_{app}=-1.0 $\times 10^{12}$A/m^2 (SyF dominant precession). The diagram correspond to the excitations (T=400K) for the FL (a), TL (b) and the inner product of the components $\mathbf{m}_{TL}.\mathbf{m}_{FL}$ (c). The yellow colour corresponds to high magnitude of the excitation spectrum. The region of damped A and O mode are indicate by the red and green lines, in all the other field range the STT modes are present. In all the cases the linewidth of the signal corresponds to the thickness of the mode. Due to the presence of the damped modes, the splitting seems to be closed.

Extra modes in the MR diagram

The most important feature of the MR diagrams is the appearance of new modes which change the original spectra of the obtained by the FFT of the temporal traces of the m_y component.

In Fig. 5.48 (a) (positive current density) we identify the extra modes with a dashed yellow circles. In the splitting, which separates the STT A and O mode we noticed one new mode, labelled $f_{p,ex}$. The presence of this mode will generate the visual effect of the absence of the splitting. We have to remark that the appearance of this mode is accompanied for the low frequency mode $f_{p,low}$, in the same range of field. Using this fact we will identify later the region of the splitting.

For high fields two new modes, labelled f_{ex1} and f_{ex2} converge in the (f/2) STT O mode which appears also only in the MR diagrams for positive current density.

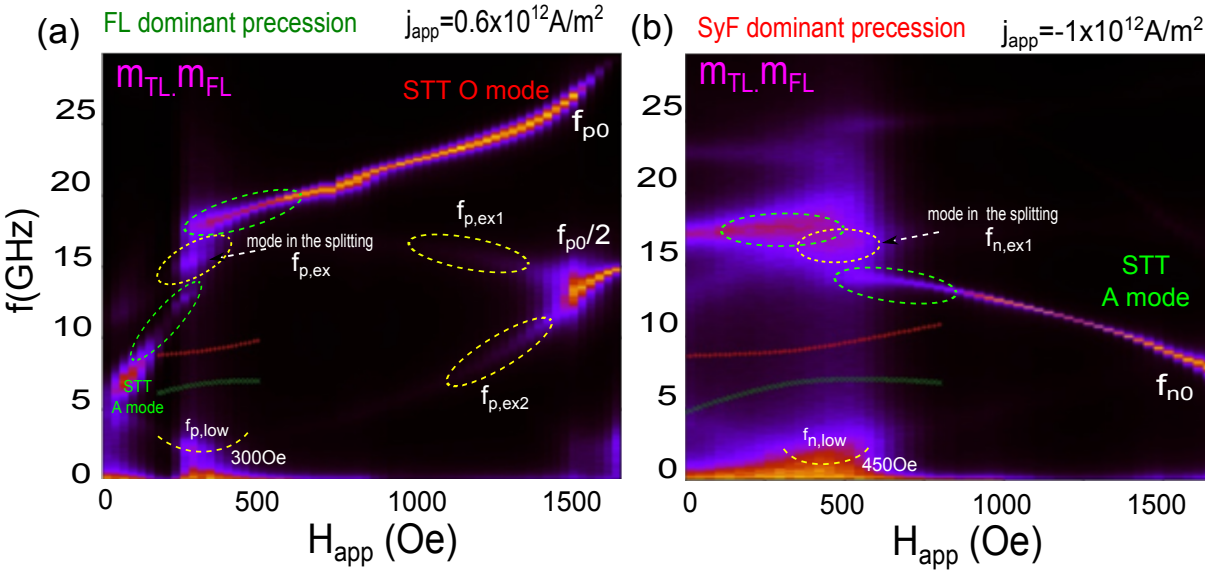

Figure 5.48 – The MR diagram of the frequency dispersion as a function of the applied field is shown for j_{app}=0.6 (a) and -1×10^{12}A/m^2 (b), FL and SyF dominant precession. The yellow circles indicate new modes in the diagram and the green circles the modes close to the splitting. A low frequency mode appears in the region of the gap.

In Fig. 5.48 (b) (negative current density) we identify again a new mode in the splitting, labeled f_{ex4}. The presence of this mode will generate also the visual effect of the absence of the splitting but as in the case of positive current we should be able in the experiments to separate the three modes. We have to remark that the appearance of this mode is accompanied for the low frequency mode $f_{n,low}$, in the same range of field. We notice that the $f_{n,low}$ appears for higher values (H_{app} ≈450Oe) than the $f_{p,low}$ (H_{app} ≈300Oe).

We can provide an hypothesis of the origin of the modes in the MR diagrams. The $\mathbf{m}_{FL}$ components could be described as a mix of sinusoidal functions, in the for of (Acos(ωt)+Bsin(ωt+Δm$_x$), Ccos(ωt)+Dsin(ωt+Δm$_y$), Ecos(ωt)+Fsin(ωt+Δm$_z$)) where Δm represents the phase noise in the system. The product $\mathbf{m}_{TL}.\mathbf{m}_{FL}$ will be represented as:

$$\approx A'Cos(2\omega t) + B'Sin(2\omega t + \Delta m) + C'Sin(2\omega t + \Delta m) + D'Cos(\omega t + \Delta m) + E' + ..(5.5)$$

We observe that the fundamental mode is represented as a modulated terms with ω, 2ω and low frequencies modes close to zero. The MR diagrams shows the double of frequency than the frequency dispersion of the m$_y$ component.

The Fig. 5.48 (a) and (b) will be the used in the chapter 6 two identify excitations modes of the frequency diagram of the standard STO.

Part III

Experimental Results of Spin Transfer Torque Nano-Oscillators

This part of the thesis corresponds to the experimental results of the measurement and characterization of the STO emitted signal. These results are presented in two chapters, which correspond to the standard STO results in chapter 6 and to the structure D-SyF STO in chapter 7. The outline of this chapter is summarized in the following,

1. **Presence of the gap**. In the first part of this chapter the evidence of the presence of the **dipolar coupling** will be shown which will play an important role in the magnetization dynamics. This will be evidenced by two features. Firstly, the appearance of a gap in the state diagrams (H_{app} vs I_{app}) for both senses of applied current, in agreement with our numerical predictions, see Fig. 5.18. Secondly, we will identify the different *hybridized excitation modes* in the linear or damped regime using the frequency dispersion as a function of the external magnetic field. These damped modes will give us the tendency of the auto-oscillation (above critical regime) for small values of current (small precession amplitude), where the excitation could be FL or SyF dominant precession[8]. Moreover for the SyF dominant precession, the change of the frequency tuning df/dI_{app} from redshift (negative) to blueshift (positive) regime will be shown, which is due to the strong **dynamical RKKY coupling**.

2. **Interaction between excited modes**. In the second part we present the interaction of the STT modes and the damped modes for the FL and SyF dominant precession.

[8]The dominant precession corresponds to the larger amplitude of oscillation corresponding to the FL ($I_{app}>0$) or the SyF layer ($I_{app}<0$) in the region over study (AP state).

Chapter 6

Spin transfer torque nano-oscillators

Experimental results of the standard STOs will be presented in this chapter. These results will be compared with the numerical predictions of chapter 5. In the past, this kind of structures have been analysed but without taking into account the different interlayer coupling (between the FL and SyF layers). At the end of this chapter we will be able to introduce a universal description of the state diagram of the STO. In this thesis work, it has been characterized the standard STO nanopillars based on SV and MTJs[1] introduced in the section 3.3.2 of chapter 3.

6.1 Demonstration of the gap in the state diagrams of excitations

The relevance of the dynamical dipolar field on the magnetization dynamics has been already introduced using numerical simulations, see chapter 5. The appearance of a gap in the dynamic state diagrams (H_{app} vs I_{app}) is a signature of the presence of the dipolar coupling in the system.

In the experiments (as in the numerical simulations), we focus our study in the region where the relative magnetic configuration between the TL and the FL remains in the AP (high resistance state). We use the same reference of measurement as in the simulation results, i.e for positive (negative) values of dc current the electrons flow from the TL (FL) of the SyF into the FL (TL of the SyF). It means that for positive dc current the FL will

[1] These samples were introduced in sec.3.3

be excited dominantly into the steady state oscillations (I_{app}>I_c).

The first measurement will be the static MR curve, in order to identify the P and the AP state, the values of the GMR or TMR (depending on the samples) and the values of the spin flop and saturation field.

The RF measurements begin with the dynamic state diagrams (H_{app} vs I_{app}) of the standard STO devices, in order to find the magnitude of applied field and current that the system needs to reach the auto-oscillations.

6.1.1 STO based on SV devices

Fig. 6.1 (a) corresponds to the MR curve a STO device **SV1**[2]. The arrows correspond to the TL (red) and FL (green) magnetizations. The study of the excitation modes will be limited to the orange shadow region of the MR curve (Fig. 6.1 (a)), which corresponds to the positive region of the SyF plateau where the TL and FL remain AP.

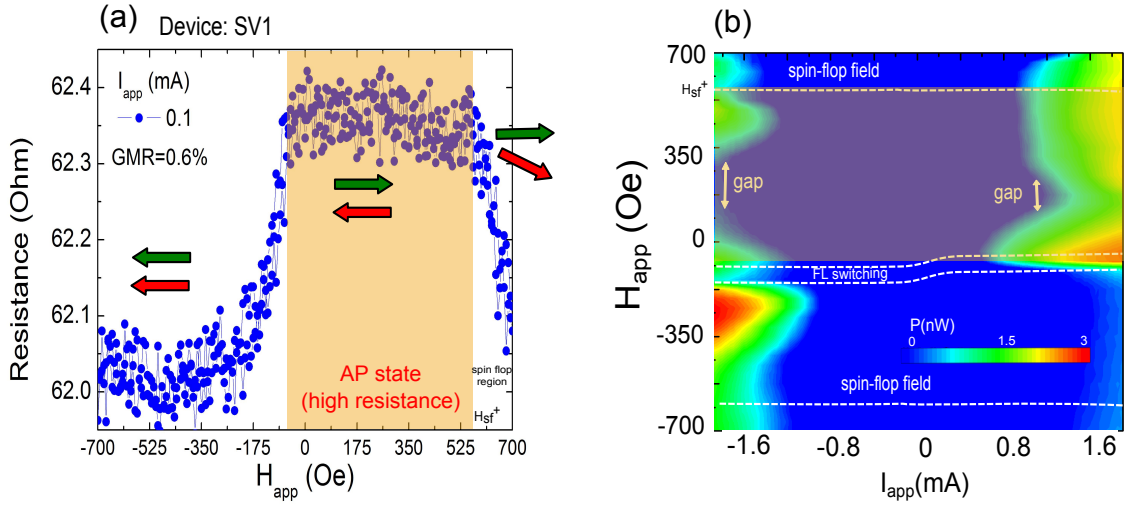

Figure 6.1 – (a) MR curve of SV1 device of GMR=0.6%. The RF measurement is focused in the AP state (orange region). Arrows correspond to the magnetization, FL (green) and TL (red). (b) State diagram of auto-oscillations as a function of magnetic field and applied current. The blue region corresponds to the stable state or damped mode, the red one to the highest integrated power. The shadow region in the diagram corresponds to the AP configuration of the hysteresis loop. The dash lines indicates the FL switching and the spin flop value.

The state diagram of the STO device **SV1** is shown in Fig. 6.1 (b), where the blue region

[2]The devices are describes in sec.3.3, SV1 is a SV circular device of 70nm of diameter

represents the damped regime (stable region) and the red region corresponds to the power in Watts of the emitted signal. We should remark that the integrated power is the total power emitted (in the total frequency range) for the STO (for a fixed value of dc current and applied field). In some cases the integrated power could include several modes with non negligible amplitude. For STO based on SV devices the amplitude of the emitted signal of the damped excitation or linear regime is negligible, and in all the measurements the appearance of a peak corresponds to auto oscillations. In the case of STO based on MTJ the emitted power of the damped excitation modes is not negligible and it could change the details of boundaries of the dynamic state diagram.

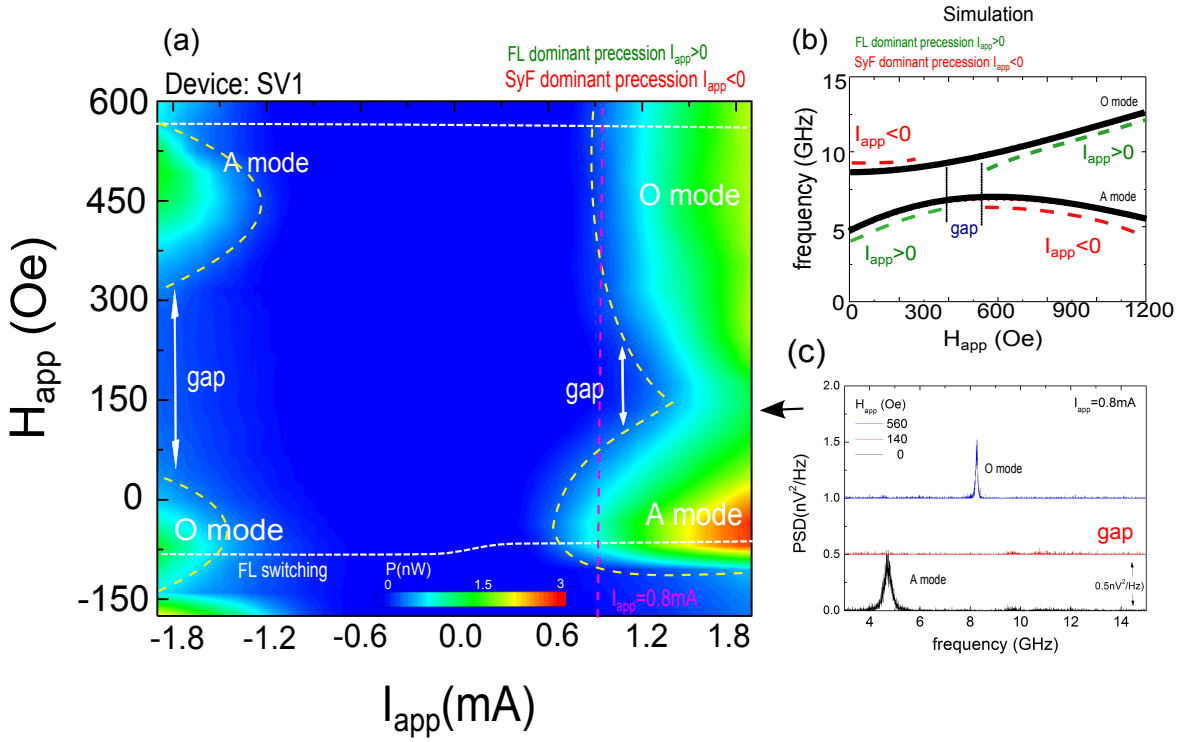

Figure 6.2 – (a) Zoom of the state diagram (Fig.6.1 (b)) in the AP region. The FL and SyF dominant precession in the A and O mode (I_{app}>0 and I_{app}<0 respectively) are observed separated by the characteristic gap (evidence of conservative dipolar coupling). Yellow dash line corresponds to the critical currents. (b) Numerical simulation of the hybridized damped A and O modes (black lines). The green and red dash lines represent the FL and SyF dominant precession respectively. (c) PSD of the peaks for three values of magnetic field and a fix current I_{app}=0.8mA, see pink dash line on state diagram (a)

In Fig. 6.2 (a), the zoom of the AP region of the state diagram (Fig.6.1 (b)) shows two gaps between the excitation regions for positive and negative current, which is a signature of the dynamic dipolar coupling. As it has been predicted by numerical simulations the gaps separate the excitation regions and satisfy the relation gap_{SyF}>gap_{FL}. Clearly the critical current (dash yellow line in Fig. 6.2) for the FL dominant precession is lower in comparison with the critical current of the SyF dominant precession.

As it has been shown in the numerical simulations, the A and O modes correspond to the acoustic and optical hybridized damped modes respectively. For example in Fig. 6.2 (b), the numerical simulation of the O mode of the SyF dominant precession will correspond to the red dash line close to zero field or the O mode of the FL dominant precession to the green dash line for high fields. This was explained and defined in section 5.2.2.1.

The pink dash line for I_{app}=0.8mA in Fig. 6.2 (a) indicates the position on the state diagram for which the PSD spectra are shown in Fig. 6.2 (c). In the gap region there is no STT excitation. The static MR curve of the device **SV2**[3] is shown in Fig. 6.3. It

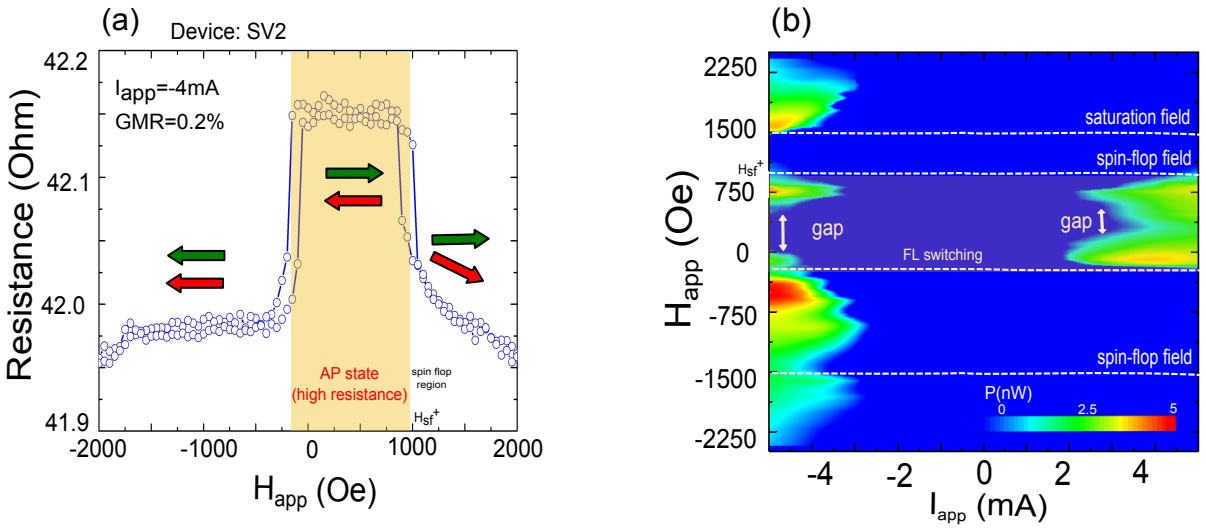

Figure 6.3 – (a) MR curve for the device SV2. The RF measurement will be focused in the AP state (orange region). (b) State diagram of auto-oscillations as a function of magnetic field and applied current. The orange shadow corresponds to the AP state of the hysteresis loop. Dash lines correspond to the FL switching, spin flop and saturation field values.

presents a larger plateau, in comparison to the **SV1**, see Fig. 6.3 (a)[4]. The state diagram of Fig. 6.3 (b) shows many regions of excitation but the study will focus in the orange region of the MR curve of Fig. 6.3(a). The zoom of the region of interest (AP state) is shown in Fig. 6.4. In total more than 20 SV devices were measured, with circular and elliptical cross section, finding for all of them the characteristic gaps in their state diagrams.

[3]This is an elliptical device of 70x140nm based on SV.

[4]In order to reach high magnetic fields the low temperature experimental setup has been used. It was described in chapter 3.

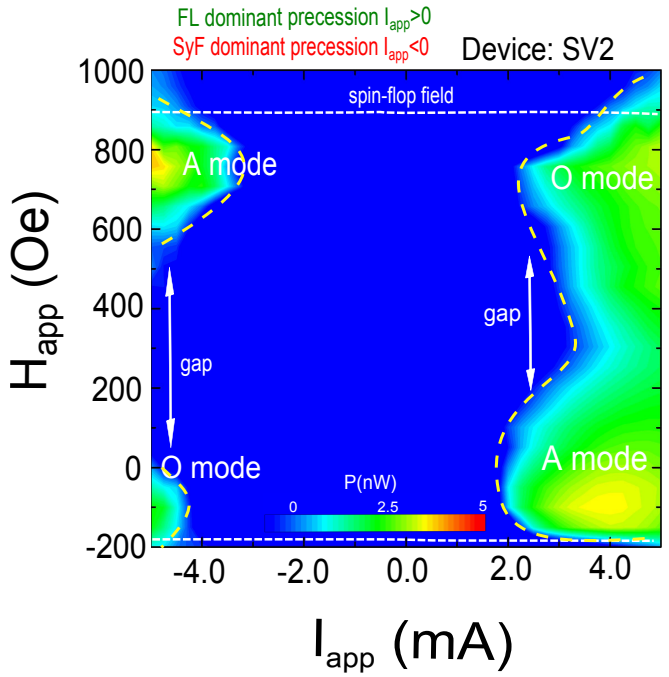

Figure 6.4 – (a) Zoom of the state diagram in the AP region for device SV2. The different modes are separated by the characteristic gap.

6.1.2 STO based on MTJ devices

This kind of state diagram is not specific of the SV, it is also found for STOs based on MTJs. For many devices the insulator character of the MTJ devices (high resistance) does not make it possible to reach the critical current for the SyF dominant precession without degradation of the MgO barrier[5]. For that reason in some cases only the damped excitations are measured. How to determinate the threshold voltage (degradation voltage) to avoid the destruction of the MgO barrier was shown in section 3.3.3.1.

The MR curves of the standard STOs based on MTJ are presented in Fig. 6.5 (a) and (c) which correspond to the device **MTJ1** [6] and for the device **MTJ2**[7] respectively. As in the case of the SV study, the orange shadow region in the MR curves indicates the AP region.

The state diagrams of a standard STO are shown in Fig. 6.5 (b) and (d). In the case of these MTJ STOs we should be sure that the excitation measured is already in the steady state oscillation. In order to separate the auto-oscillations from the damped excitations,

[5]If the MTJ has large resistance a small dc current value will be enough to reach the threshold voltage (V_{th}) and degrade the sample.
[6]MTJ1: elliptical 90×190nm device of TMR 54%
[7]MTJ2: elliptical 80×160nm device of TMR 60%

the critical current has to be found using the linewidth criteria. The linewidth as a function of the dc current (applied magnetic field fixed) will present a characteristic tendency. An extrapolation of the tangential line until $\Delta f=0$ will provide the critical current. The frequency dispersion as a function of the applied dc current will be introduced in section 6.3.4 to show the protocol that has been used to identify these modes.

In the case of the state diagram of Fig. 6.5 (b), the excitation regions correspond to the damped excitations of the A and O modes, due to the small applied dc current for this device. The dash line corresponds to the region where the damped modes appear. If we increase the current as in the case of Fig. 6.5 (d), the excitation regions will be composed by a mixture of the STT modes or auto-oscillations (high power) and damped excitations (low power).

The diagram of Fig. 6.5 (d) is almost in agreement with the numerical simulated diagram and shows the characteristic gap which separates the excitations regions (in the AP state) for both sense of current. In the P state we did not measure any excitation with high power.

The conclusion of the measurement of several devices based on MTJ structures is that the diagram of the STT modes are in agreement with the numerical simulated diagram. In the case Fig. 6.5 (d), it is not possible to reach the O mode of the SyF dominant precession ($I_{app}<0$) due to its intrinsic high critical current. In contrast for SV devices this O mode is reached for $I_{app}<$-4mA, an impossible value of applied dc current for the STO based on MTJ studied here.

In order to start with the study of each excitation region on the state diagram it is necessary to identify the modes, using the frequency dispersion diagram.

6.2 Identification of the excitation modes in STO based on spin valve

In the following, the frequency dispersion diagrams (f vs H_{app}) will be introduced in order to identify the spin transfer torque auto-oscillations. These steady state excitations will be called in the following STT modes ($I_{app}>I_c$) to separate them from the damped modes ($I_{app}<I_c$).

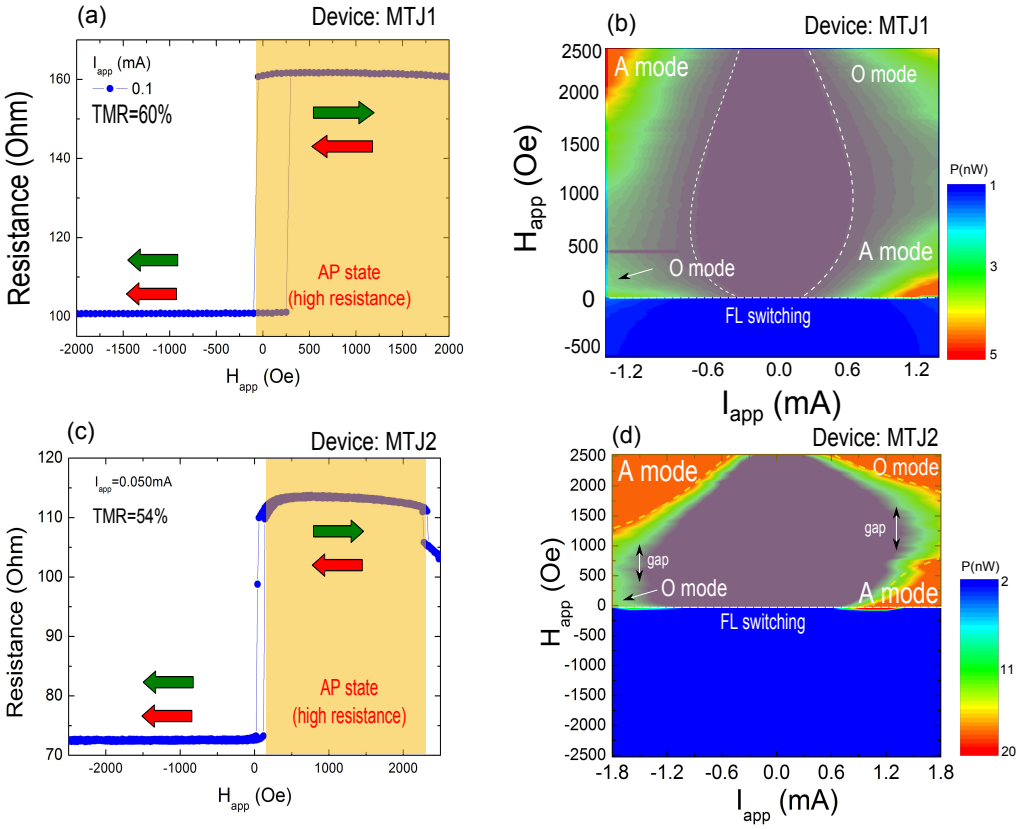

Figure 6.5 – In (a) and (c) MR curves for the MTJ1 and MTJ2 devices. In (b) and (d) the corresponding state diagrams are introduced. In (b) the state diagram of the damped mode is presented. It is not possible to reach the auto-oscillations. In (d) the system reaches the auto-oscillations and it is possible to identify the characteristic modes.

In order to identify the acoustic $[SyF_{ac}\text{-}FL]_{ac}$ and optical $[SyF_{ac}\text{-}FL]_{op}$ modes, they are labelled as A and O modes. In the next section we introduce the frequency versus magnetic field diagrams, for a fixed value of dc current (positive or negative).

6.2.1 Steady state oscillations of FL dominant precession $I_{app}>0$ in AP state

The frequency dispersion (f vs H_{app} and I_{app}=2mA) for the **SV2** is shown with its corresponding MR curve in Fig. 6.6 indicating the AP state.

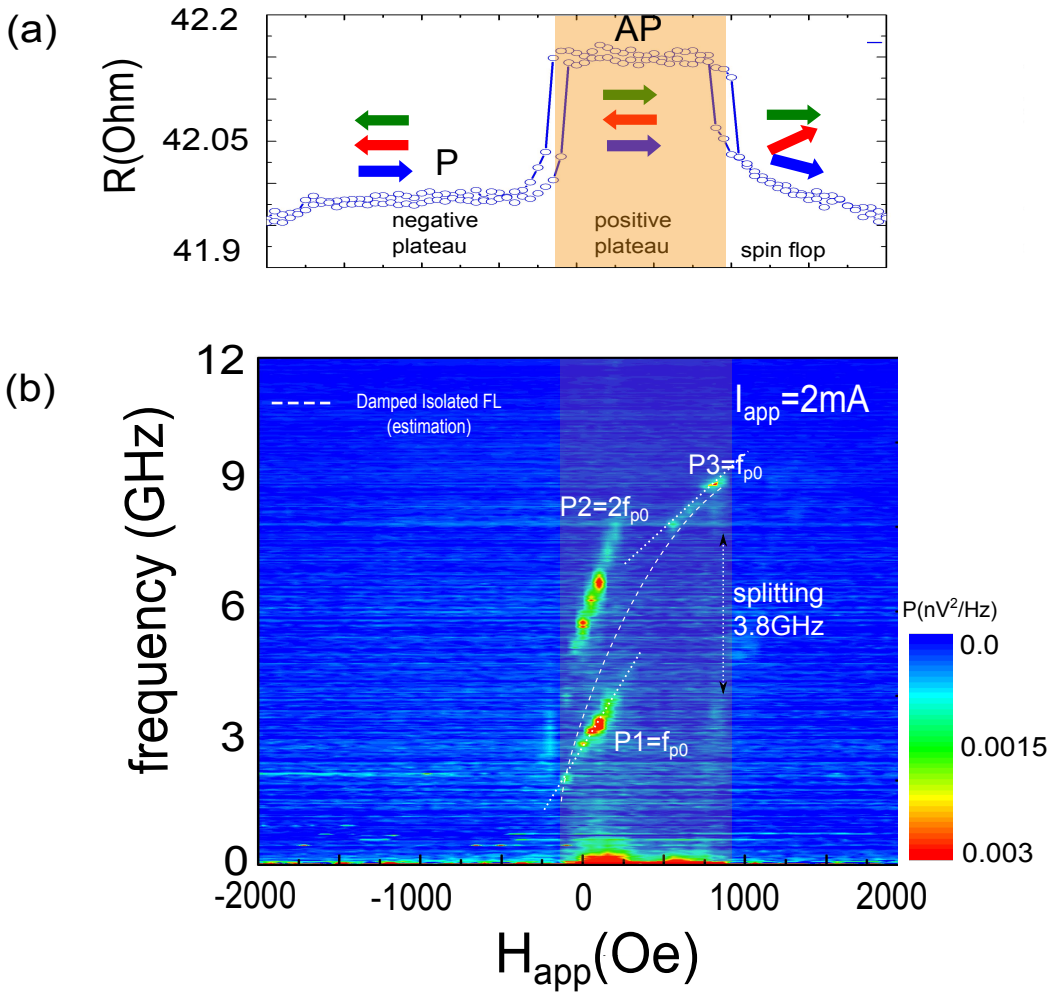

Figure 6.6 – (a) MR curve of the SV2 device. Arrows correspond to the magnetization direction of the FM layers. The study of the excitations will be focus in the orange region (AP state, high resistance). (b) Frequency dispersion diagram as a function of the applied field (I_{app}=2mA). We identify three modes (P1=f_{p0}, P2=$2f_{p0}$, P3=f_{p0}) as the $\mathbf{m}_{TL}.\mathbf{m}_{FL}$ frequency dispersion in numerical simulations of Fig.5.46. This line is drawn as a reference of the tendency of the damped mode of a isolated single layer (as a visual reference).

Due to the negligible power of the damped excitation modes in SV structures they will not be visible in the diagram. The frequency dispersion for a dc current of I_{app}=2mA (FL dominant precession) is shown below the MR curve for the same range of field, see Fig. 6.6 (b)[8]. It is possible to observe three modes, P1=f_{p0}, P2=$2f_{p0}$, P3=f_{p0} in the positive plateau region (high resistance). These modes have already been identified in the frequency dispersion diagram, see Fig.5.46 in numerical simulations section. The white dash line corresponds to the tendency of the FL damped excitation of an isolated single layer. It is introduced in order to help with the identification of the STT modes.

In order to show that the P1 and P3 correspond to the FL dominant precession, in Fig. 6.7 (b) we remind schematically the tendency of the hybridized A and O damped modes (black solid lines) and the FL dominant precession (green dash lines). In Fig. 6.7 (a) the peaks (power spectral density (PSD) of the A and O modes of the FL dominant precession are shown for a range of applied field from 0 (AP state) to 1000 Oe (spin flop region). The red peaks correspond to the A mode for low frequency and small fields, the blue ones correspond to the O mode of high frequency and large fields. In the spin flop region the TL magnetization is switched into the positive direction of the applied field and the excitation modes will change (small black peaks). In some cases the switching of the TL is not abrupt, generating a gradual increase of the angle between the TL and the FL. This fact will increase the spin torque, as it will be presented in the next section, Fig. 6.23 (b). In the following, the dashed lines are not at fit of the FMR modes, but they are drawn as a guide to the eye to help us to identify the mode character[9].

The yellow dashed lines included in the frequency diagram of Fig. 6.7 (c) correspond to the estimation of the hybridized damped A and O modes. The vertical white dashed lines identify the gap between the two STT modes and the horizontal dashed line shows the splitting between the modes. It is noted that P2 is the harmonic of P1 and the characteristic gap separates P1 from P3. From this we identify the STT P1 mode as the A mode and P3 as the O mode of the FL dominant precession. Both deviate from the isolated FL tendency (Kittel law). Measurements for fields outside the AP sate, did not reveal any excitation at positive current.

[8] This is an elliptical device of 70x140nm based on SV.

[9] It is not possible to fit the hybridized modes but we can calculated and approximate dashed lines using some parameters

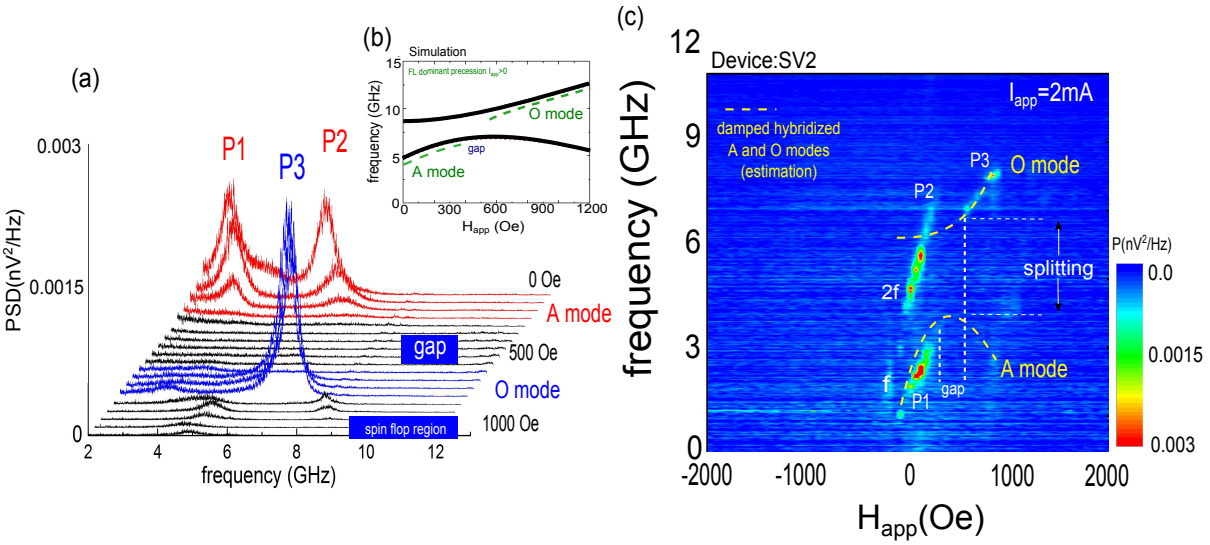

Figure 6.7 – (a) PSD peaks of the FL dominant precession which are separated by a gap between the A and O modes. The STT P1 mode is the harmonic of P2. (b) Numerical simulation of the hybridized A and O modes (black solid lines) and the FL dominant precession (green dash line). (c) Frequency dispersion diagram as a function of the applied field for 2mA of current. The dash yellow lines are included as a reference of the tendency of the hybridized damped A and O modes.

6.2.2 Steady state oscillations of SyF dominant precession $I_{app}<0$ in AP state

We now continue with the identification of the excitation modes but applying negative values of dc current. As it has been shown in the state diagrams, the critical current to reach the SyF dominant precession is larger than in the case of a single layer, therefore a dc current of -5mA has been applied in order to generate SyF dominant precession (following the current values obtained from the state diagram, see Fig. 6.4 (b)).

The MR curve of Fig. 6.8 (a) will help the identification of the modes in the corresponding different regions (P , AP state or spin flop) of the frequency dispersion diagram of Fig. 6.8 (b).

In the region of interest (AP state) three excitation modes are identified, N1=f_{n0}, N2=f_{n0}, N3=$2f_{n0}$, see Fig. 6.8 (b). In the frequency dispersion diagram of Fig. 6.8 (b), are included the acoustic mode of the isolated SyF structure, which is represented by the white dashed line. The excitation modes in the other regions (such as the P state or the spin flop region) will be described later.

In order to help with the identification of the modes, the dashed lines (corresponding to

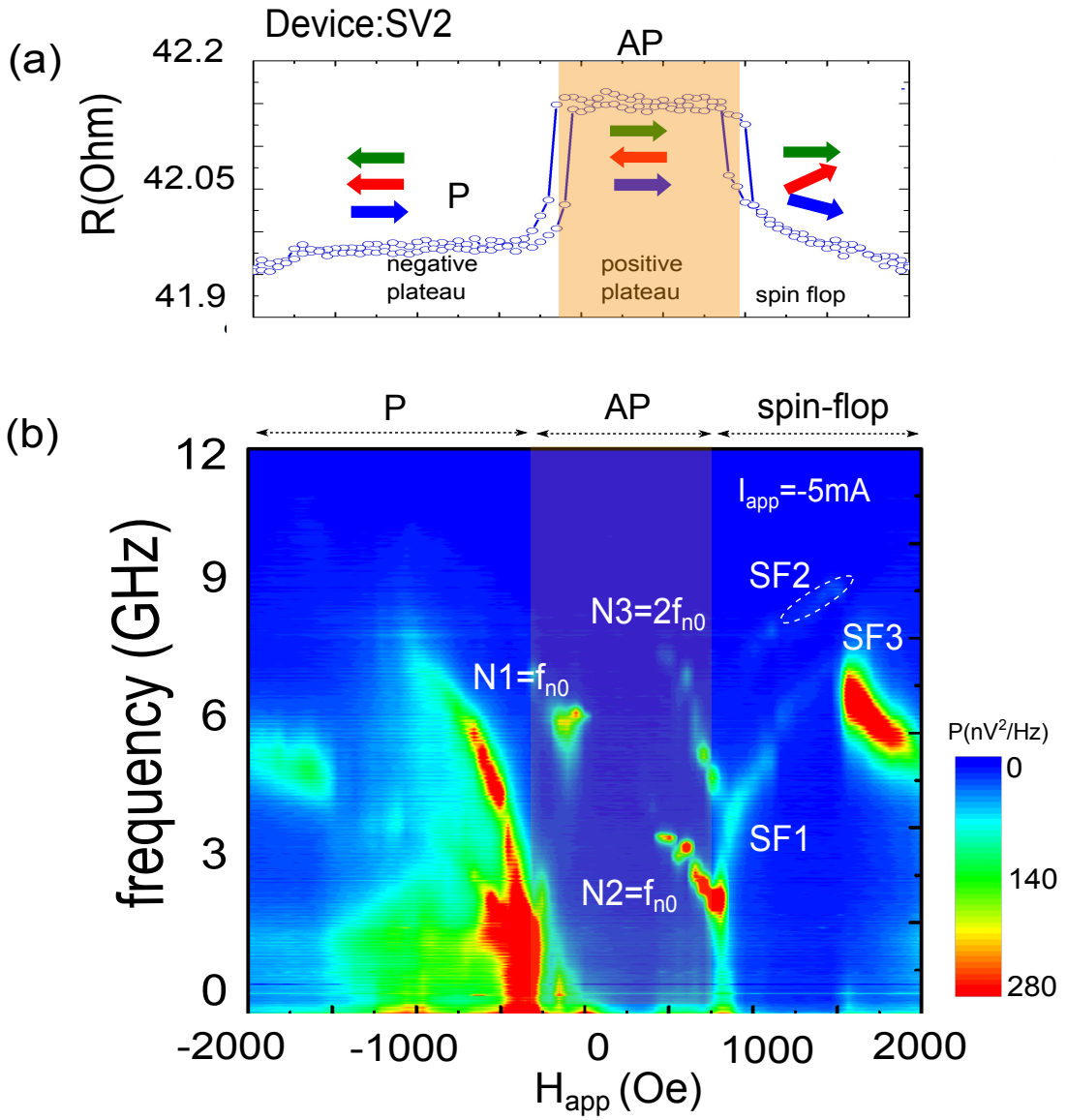

Figure 6.8 – (a) MR curve of the SV2 device. (b) Frequency dispersion diagram as a function of the applied field for I_{app}=-5mA. Firstly, in the interest region we identify three modes N1=f_{n0}, N2=2f_{n0}, N3=f_{n0}, as the $\mathbf{m}_{TL}.\mathbf{m}_{FL}$ frequency dispersion in numerical simulations of Fig.**??** (a) and 5.46. In the spin flop region we identify the modes SF1,SF2 and SF3.

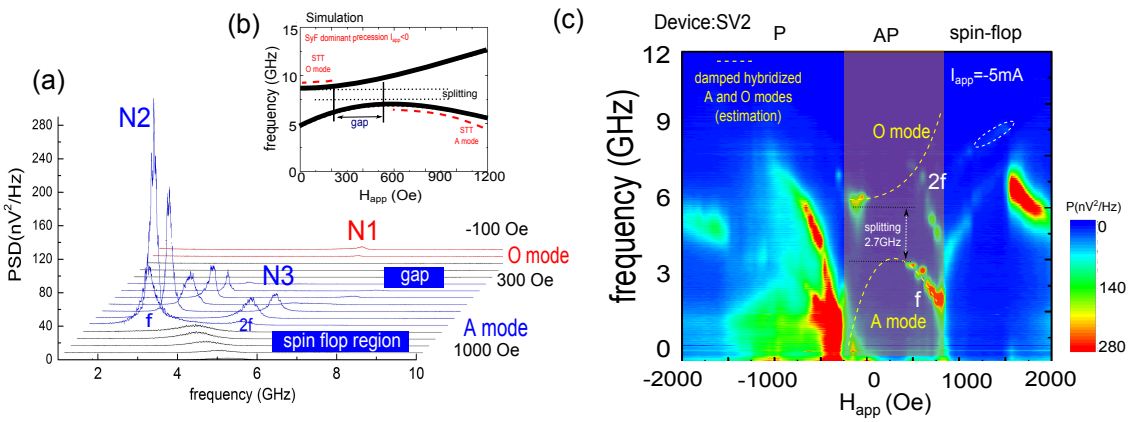

Figure 6.9 – (a) PSD peaks for several values of applied field. (b) Simulated frequency dispersion diagram. The damped hybridized damped A and O modes and the SyF dominant precession modes (red dash lines). (c) Frequency dispersion diagram as a function of the applied field. Yellow dash lines indicate (as a reference) the hybridized damped A and O modes.

the hybridized modes for some parameters) are shown in Fig. 6.9 (b) (in the AP state). The tendency of the hybridized damped A and O modes are represented by the solid black lines and the SyF dominant precession corresponds to the red dashed lines (I_{app}<0). It is possible to identify the N1 and the N2 STT modes as the O and A mode respectively of the SyF dominant precession. The PSD peaks of these STT modes are shown in Fig. 6.9 (a) (for -100 Oe<H_{app}<-1000 Oe, AP state) where it was found that the N3 is the second harmonic of N2. The maximum PSD found for the SyF dominant precession was PSD_{max}=280nV^2/Hz around 500Oe which is really more important in comparison with the corresponding PSD for the FL dominant precession PSD_{max}=0.03nV^2/Hz. In the frequency dispersion diagram of Fig. 6.9 (c) we noted a splitting of 2.7GHz between the STT A and O mode. The dashed yellow lines indicates as a reference the A and O modes (using some parameters).

6.2.3 Steady state oscillations I_{app}<0

Parallel (P) region (H_{app}<$H_{switching}$)

As it was shown in the state diagrams, for negative values of current it is possible to find modes in the P state (for the FL dominant precession), due to the reflected electrons from the TL of the SyF.

In the P state (H_{app}<-250Oe for **SV2**), the stable state of the SyF is favoured for negative

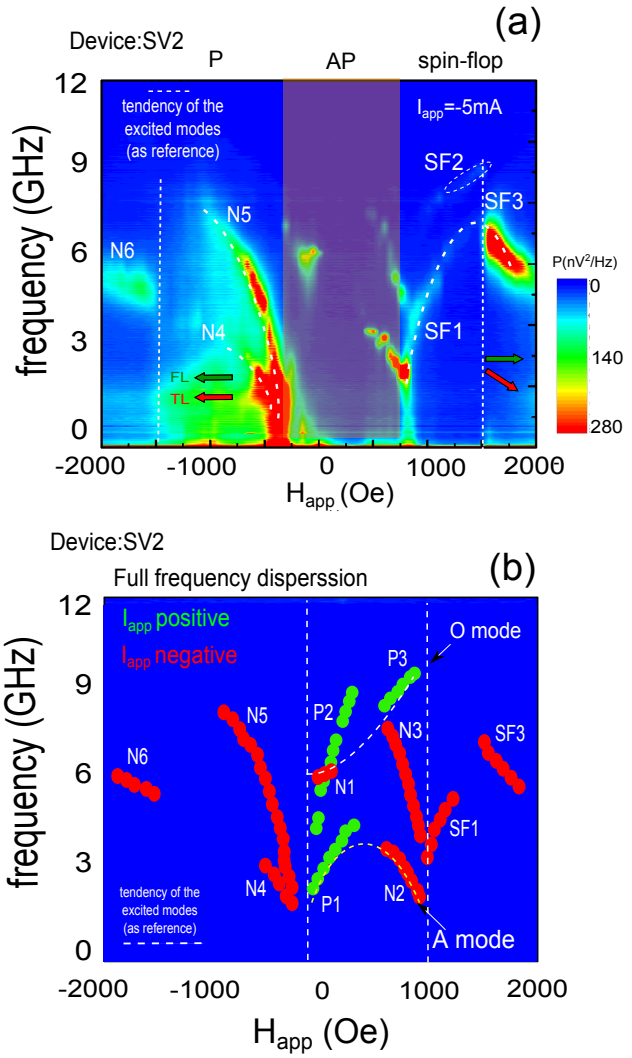

Figure 6.10 – (a) Frequency dispersion as a function of the applied field shows excitations modes N4 and N5 in the P (H_{app}<-250) and the modes SF1-SF3 in the spin flop regime (H_{app}>700Oe, and H_{app}<-1000Oe). (b) Superposition of FL and SyF dominant precession in order to observe the whole frequency dispersion diagram. The yellow dash lines correspond to the hybridized A and O damped modes as a visual reference.

current, however excitations in the FL can be induced, which will follow the tendency of the Kittel law, see Fig. 6.10 (a). It is possible to identify two modes, N4 and its harmonic N5. As it is shown in the state diagram of Fig. 6.3 (b) , (H_{app}<-250 and I_{app}<0) the critical current for the FL dominant precession in the P state is smaller than the corresponding one of the SyF dominant precession, (H_{app}<-250 and I_{app}>0). The STT N4 mode follows the Kittel law dispersion curve, without an appearance of a gap.

Spin flop region in the AP state, $\mathbf{H_{app}}$>$\mathbf{H_{sf}}$

In the positive spin flop region, the excitation modes N6 and N7 are identified. The N6 mode corresponds to the first part of the gradual switching of the TL in the spin flop region, see Fig. 6.10 (a). When the TL is switched into positive values of applied field the N6 mode disappears. The mode N7 appears when the FL and TL magnetization start to become parallel. In the negative spin flop region the N8 mode is identified.

6.2.4 Summary

In Fig. 6.10 (b) the superposition of all the modes in the frequency dispersion diagram is shown. The FL and SyF dominant precession are represented by the green and red circles, I_{app}=2mA and -5mA respectively. Each STT mode is labelled (P1-P3 and N1-N8). The tendency of the damped A and O mode is introduced as a yellow dash line. In the AP state (region between the two vertical white dashed lines) it is observed that the STT modes of the FL and SyF dominant precession (which are P1, P3 for I_{app}>0 and N1, N2 for I_{app}<0), follow the A and O damped mode tendency. The P1 and N2 are the acoustic mode and N1 and P3 the optical mode.

6.2.5 Angular dependence of frequency dispersion

The RF characterization of the STO devices is not trivial. There is one parameter to take into account which could change notoriously our results. It is the angle with respect to the easy axis (of the sample) in which the magnetic field is applied. The frequency dispersion diagram (f vs H_{app}) will change drastically if the direction of the magnetic applied is changed. In order to identify the excitation modes we will present results for the diagrams for three different directions of applied field. It is represented by the angle between the easy axis and the applied field 0, 30 and 50 degrees. The applied current was I_{app}=±4mA.

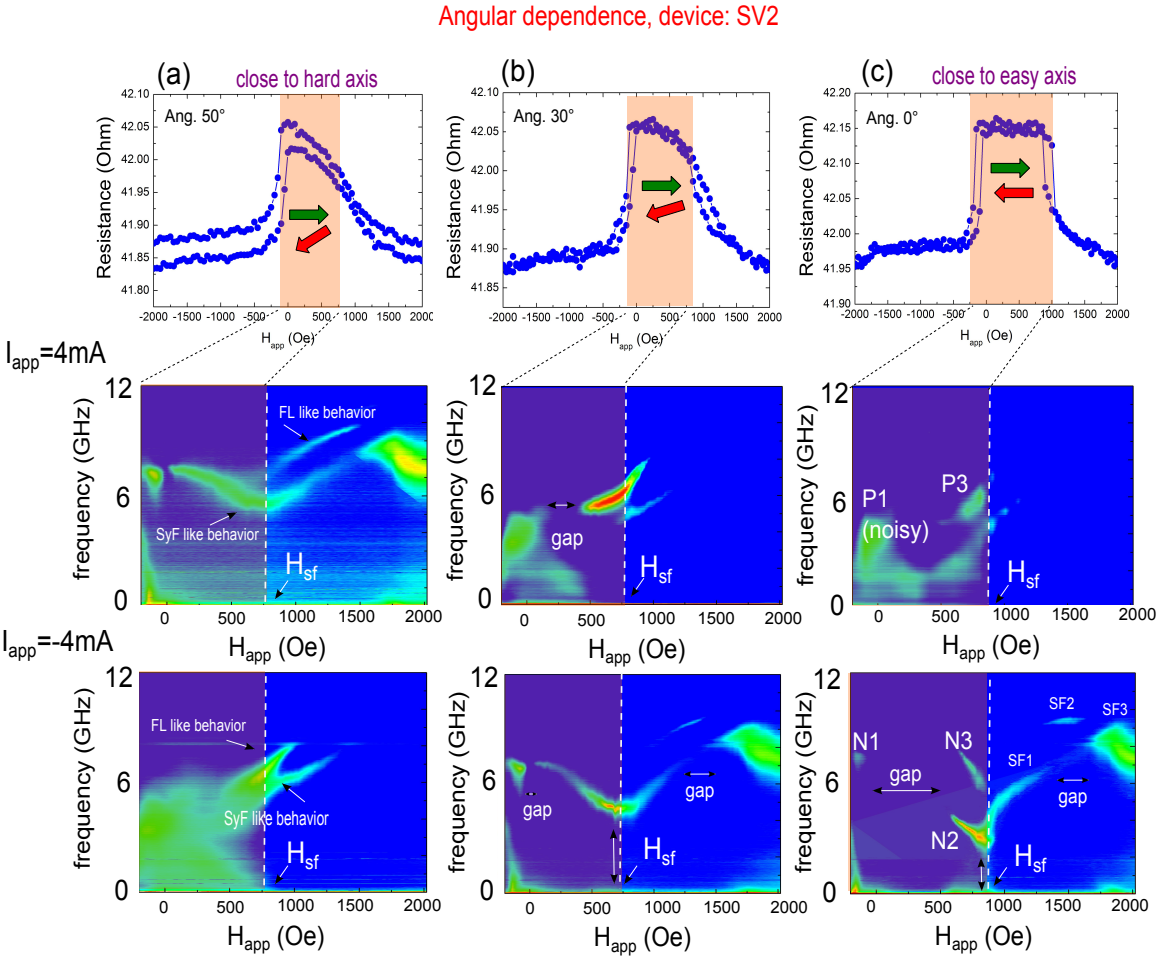

Figure 6.11 – The MR and the frequency dispersion as a function of the magnetic field is presented for 3 different angles. The direction angle of the magnetic field is measured with respect to the easy axis. In column (a) for 50 °, in (b) for 30 ° and in (c) in the easy axis, 0 °. The applied current was I_{app}=±4mA.

In the column (c) of Fig. 6.11 we show the result for ≈0° with the MR curve on top showing the AP state on orange shadow region. Below the MR curve we show the frequency dispersion diagram for positive and negative dc applied current (I_{app}=±4mA). We identify the excitation modes P1, P3, N1, N2, N3. The P1 mode is well define in Fig. 6.7 (c) for I_{app}=2mA, but already in the transition regime (IPP⟶OPP) as it is shown, in more detail, the Fig. 6.23 (b)-(c) for high values of positive dc current.

We will now discuss the situation for an angle of 30° (with respect to the easy axis), see column (b) of Fig. 6.11. Due to the non co-linearity between the applied field direction and the axis of annealing, the FL magnetization will be pointing into the direction of the applied field. The MR curve shows a reduction of the plateau. In the frequency dispersion diagram (I_{app}>0) we realize that the P3 excitation mode increases its power. In the case of I_{app}<0 the frequency dispersion shows that the gap between N1 and N3 decreases. Moreover the minimal linewitdh value of the N3 STT mode increases (Δf≈85MHz⟶300MHz).

In the case of 50°, see Fig. 6.11 (a), the MR curve is distorted from the MR of 0°. The frequency dispersion diagram changes completely its original behaviour. For I_{app}>0 the excitation modes seem like a mix between the FL and SyF dominant precession.

In Fig.6.12 (a)-(b) the frequency and linewidth of the **SV2** device is presented. It is noticed that N1 and N2 are separated by the gap until a field angle of 30° with respect to the easy axis. From this value the gap shows a small jump (blue curves, H_{app}=0). The linewidth is minimum (≈85MHz) when the applied field is aligned close to the easy axis in the N2 excitation mode.

In conclusion, it will be important to measure close to the easy axis, because the linewidth at 0° appears to be lowest, and in addition we will be sure that the TL of the SyF pinned layer is not reorient.

6.3 Identification of the excitation modes in STO based on magnetic tunnel junction

In contrast to the SV spectrum, the STO based on MTJ shows together the damped modes and the STT modes. The damped modes are present always in the measurements due to the high TMR of the MTJ devices. In this section we will start with the identification of the damped modes of the MTJ i.e in the sub-critical regime, I_{app}<I_c and then with the

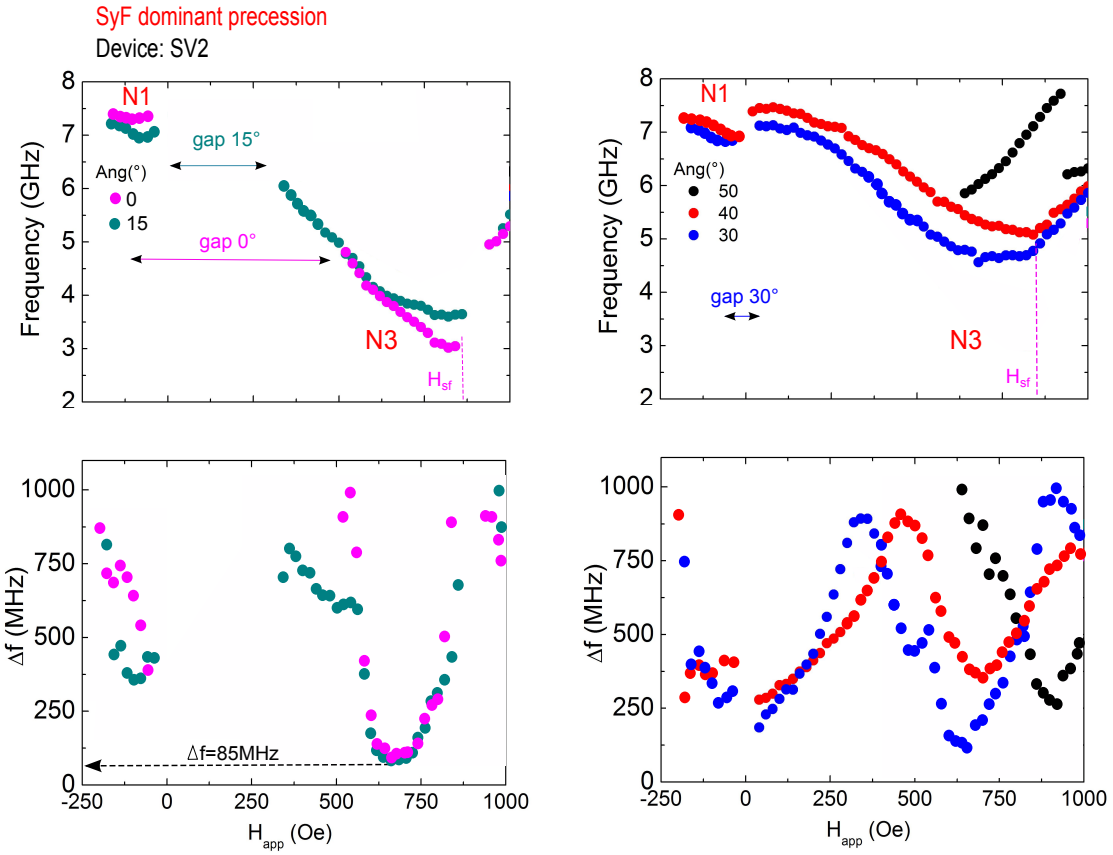

Figure 6.12 – (a) Frequency dispersion as a function of the magnetic field direction ($H_{app}\measuredangle$ easy axis = 0, 15, 30, 40 and 50 degrees). (b) The corresponding linewidth as a function of the magnetic field direction.

STT modes $|I_{app}|>|I_c|$. We will compare it were possible the features of the SV with the MTJ STOs.

6.3.1 Damped modes, the sub-critical regime ($I_{app}<I_c$)

We show in Fig. 6.13 (a) the MR curve of the device **MTJ4**[10]. In order to obtain a well defined hybridized modes, the angle of applied field was ϕ=30° because for this angle the hybridized A and O mode are well defined[11]. The arrows represent the relative position of magnetization (AP or P) between the TL and FL, see Fig. 6.13 (a).1. The frequency spectrum as a function of the magnetic field is shown in Fig. 6.13 (b)-(c) for ±1mA. In these diagrams the dashed lines correspond to the A and O damped modes which are included in the spectrum as a visual guide. We identify the two branches of the A mode (for small and high magnetic field), labelled as M1 and M2. In both cases of I_{app} we observe the characteristic gap in the A mode (between 1000Oe-1700Oe).

For higher frequencies (14-20GHz) in Fig. 6.13 (b) and (c) we identify the damped O mode. This O mode shows for both senses of current two branches, labelled as M3 and M4, for high magnetic field (≈2500Oe). They are separated by a gap. We will label the two small branches of the O mode for small magnetic field shown in Fig. 6.13 (b) further. The splitting between the A and O damped mode is higher in the case of positive current, 3.2GHz versus 2.9GHz for negative current.

It was shown in the numerical simulations in section 3.1.4.3 that the critical current of the modes are found when the extrapolation of the linewidth Δf (dashed lines in Fig. 6.14) reaches zero, $I_{app}=I_c$. In Fig. 6.14 we show Δf as a function of the current density for different values of applied field for both damped A modes (M1 and M2) and damped O modes (M3 and M4). The critical currents for all the modes are higher than I_c>1mA.

The spectra of MTJ devices do not show only the damped modes corresponding to the hybridized modes, but also higher order modes. These modes are indicated in the frequency dispersion diagram in Fig. 6.15 (a)-(b). The higher order modes are superposed using dashed white lines. We labelled the higher order modes as M_{xy}, where x corresponds to the main mode M_x and y corresponds to a mode that comes next upon increasing the frequency, but having (approximately) the same slope as M_x.

We indicated the higher order damped modes with parallel to M1 and M2. They are

[10] Elliptical device E55x100nm with a TMR=16%

[11] Beyond we will show the angular dependence of the frequency dispersion diagrams.

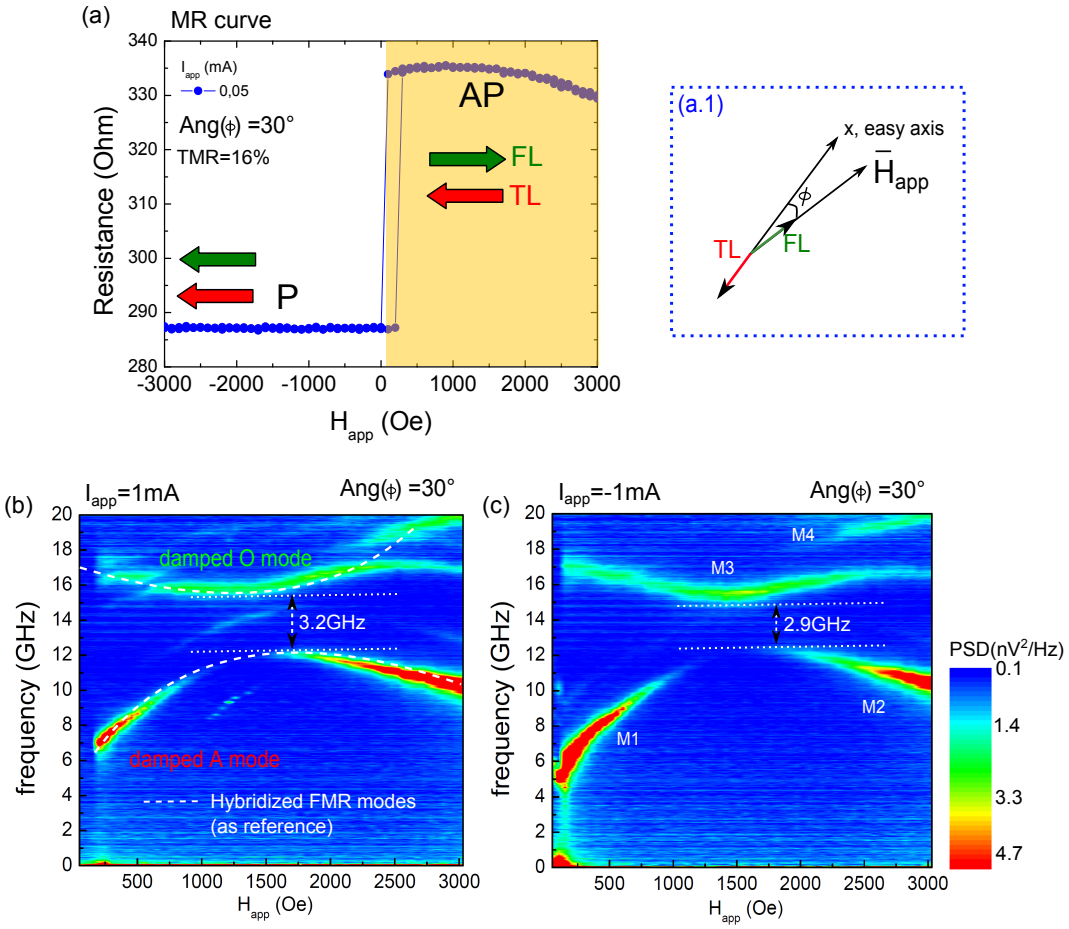

Figure 6.13 – In (a) the MR curve of the MTJ4 for ϕ=30°. Arrow correspond to the magnetization (a).1. In (b)-(c) PSD of the frequency versus applied field. The damped optic (O) and acoustic (A) modes of the standard STO are shown for ±1mA. The dashed lines indicate the damped modes in the frequency diagram. The splitting Δ_S is shown for both cases.

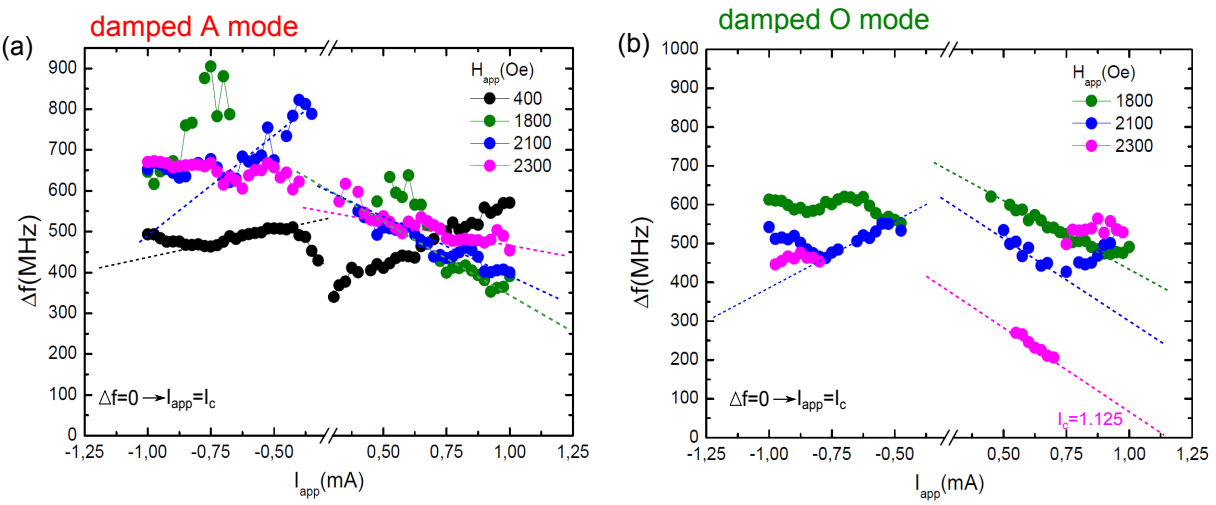

Figure 6.14 – Linewidth as a function of the applied current (positive and negative) for different values of applied field for MTJ4. For the damped A and O modes (a)-(b) respectively. The dashed lines do not cross the I_{app} axis as a prove of the sub-critical regime or damped modes.

labelled as M_{11}, M_{12} and M_{13}, M_{22}, M_{22} and M_{23}. These damped modes were also discussed by Helmer, [Helmer et al., 2010]. The macrospin simulations of chapter 3 do not predict these higher modes because in this approach the magnetization is simulated as a unidirectional vector. The higher order modes are quantized spin waves, which need a micromagnetic approach.

In Fig. 6.15 (a), the frequency dispersion of the M3 damped O mode close to zero field shows two splitting, which could be due to the crossing of the higher order mode M_{12} and M_{13}. These crossing of modes are not seen in the case shown in Fig. 6.15 (b) for negative current.

A further point to indicate is that in this device for positive current above 0.9mA, we observe two narrow modes (87MHz) in the gap region. They are separated by ≈2.2GHz from the damped A mode.

6.3.2 Angular dependence of frequency diagram of MTJ

The dispersion diagrams (frequency versus applied field) of the STO based on MTJ, **MTJ3**[12] show a change if the angle of magnetic field application varies (with respect of the easy axis). In Fig. 6.16 we show the evolution of the frequency dispersion diagram from an angle 10° until 40°. In all the scenarios, the applied dc current was ±1mA. The

[12]MTJ3 device (ellipse of 65×130nm and TMR=48%

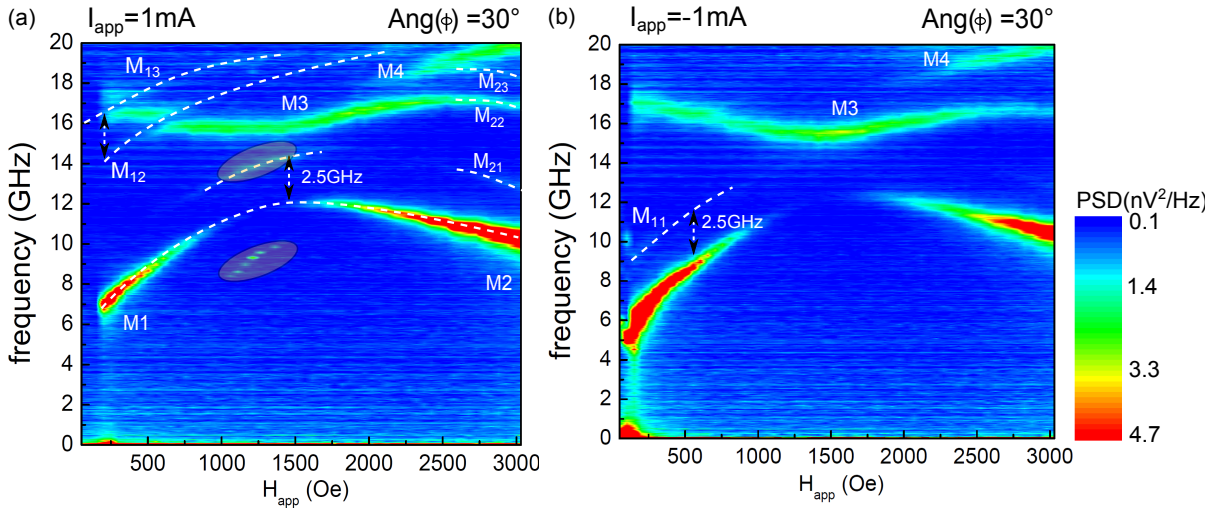

Figure 6.15 – (a)-(b) PSD of the frequency for the optic (O) and acoustic (A) modes of the standard STO, for ±1mA. The dashed lines indicate the higher order modes in the frequency diagram. For this device in (a) the region of the gap shows two modes, orange shadow regions. Device MTJ4.

diagram shown in the previous section was for 30° and it seems the case shown in Fig. 6.16 (h) and (i), with a reduction of the splitting (from 3GHz for MTJ4 to 2GHz for MTJ3).

As we were expecting, in the MR loops, 6.16 (d), (g) and (j), the AP state show a deflection in comparison with the case of 10° 6.16 (a), due to the turning of the FL magnetization. For high fields the magnetizations of the SyF pinned layer reach the spin flop region gradually.

Also, it shows in this figure that changing the magnetic field angle, the frequency dispersion diagram changes, from a STT mode in (b) into the damped A and O modes, see 6.16 (c)-(l). The relative position between the TL and the FL of the structure could influence the strength of the spin torque term, see equation 3.23 and the system remains in the damped regime. The splitting (Δ_S) between the damped A and O mode now is clear (≈3GHz) around 1000Oe. In comparison with the case of the SV devices splitting measured is smaller (3.8GHz for positive current and 2.7GHz for negative in SV).

In Fig. 6.17 (b), we show the frequency field dispersion for I_{app}=-1mA and for a magnetic field angle of 30° . In Fig. 6.17 (a) the peaks of the emitted signal are shown. The excitation modes M1 and M2 are separated by the characteristic gap, while the M3 presents a continuous evolution until H_{app}=1600Oe. The black dashed lines in (a) and white in (b) show the visual tendency of the corresponding damped A and O modes.

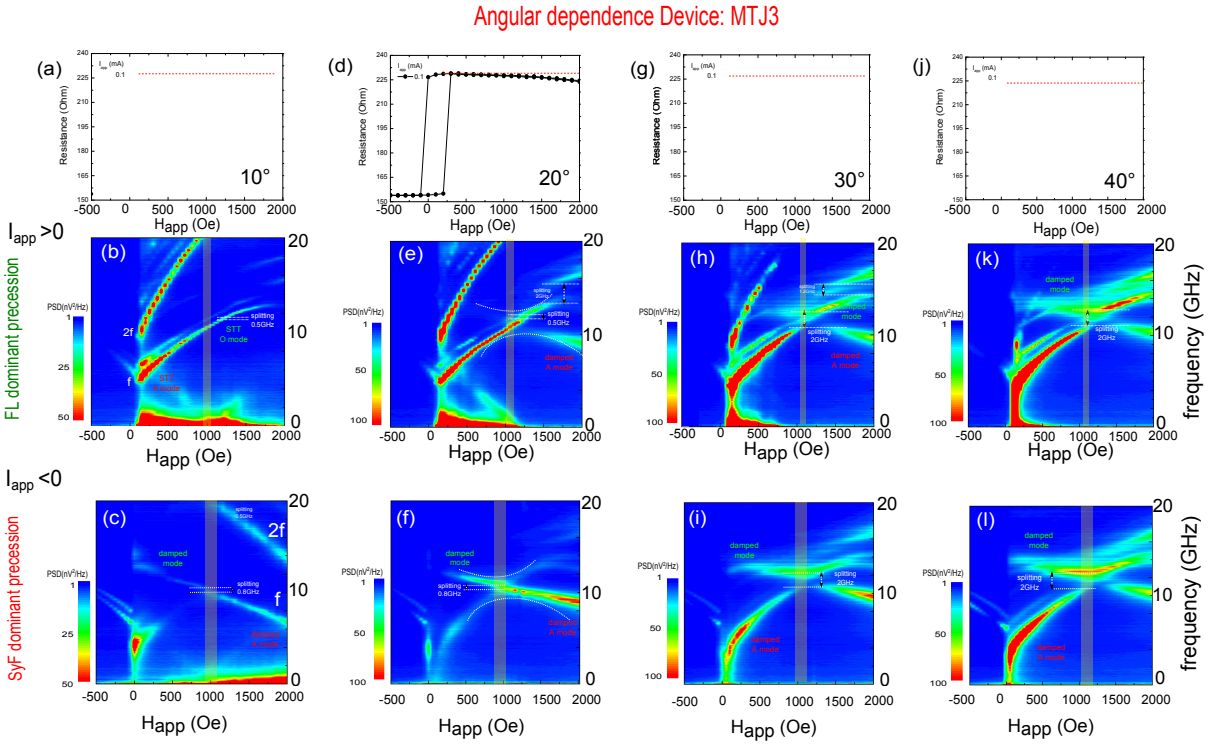

Figure 6.16 – Angular dependence of the state diagram frequency versus applied field. The damped hybridized A and O modes appears clearly when the angle of application of the magnetic field is deviated from the easy axis. The applied current was I_{app}=±1mA and the the MTJ3.

In Fig. 6.17 (b) we can notice that the PSD is higher for STT A mode. Close to the gap the A and O excitations have to show a comparable Δf value, but due to the relative phases between the TL and the FL the damped O mode will show more intensity. In the case of the A mode both magnetizations are out-of phase in the axis y, and for the O mode they are in phase. Following the assumption that the relative position between the FL and TL will define the power of the emitted signal in some regions the O mode will be high power than the A mode.

In Fig. 6.17 (b) the gap (950 Oe<H_{app}<1250 Oe) of the A mode disappears but the O mode remains excited. Moreover, its amplitude is increased. In order to explain this feature it should be necessary to come back to the study of the stability in the numerical simulation and observe the attenuation of the damped modes, see Fig. 5.15.

In Fig. 5.15, the attenuation presents an alternating behaviour for the A and O mode. For small magnetic fields, the A mode will be less attenuated but in the gap the A and O mode present a comparable attenuation and for high fields will be the O mode less attenuated.

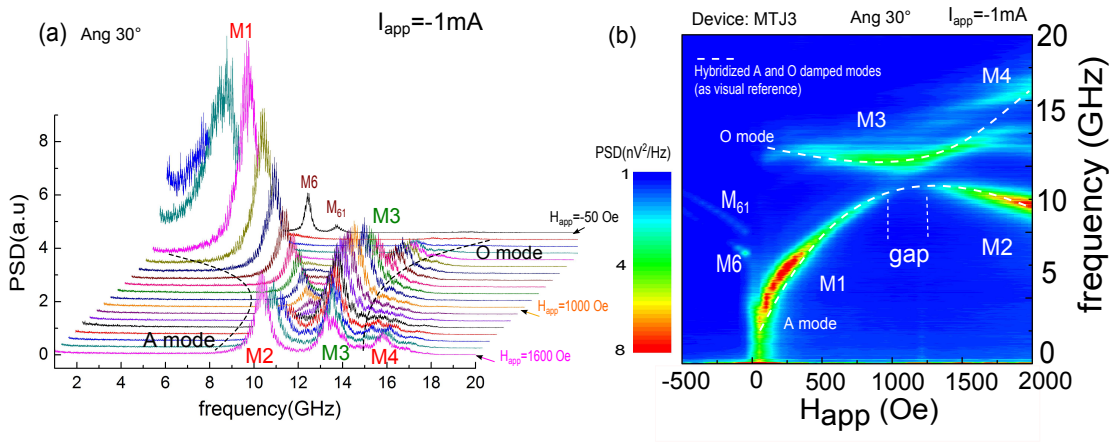

Figure 6.17 – (a) PSD for different peaks of the emitted signal as a function of the applied field (MTJ1 device). The modes are identified as M1-M4 and M6-M_{61}. The dashed lines correspond to the tendency of the damped A and O modes (visual reference). In (b), the frequency dispersion as a function of the applied field is shown. The applied dc current was I_{app}=-1mA.

The summary of the labels for the SV and MTJs damped modes are shown in Fig. 6.18 to help to identification.

In the following we show the STT modes of the SyF and FL dominant precession for an angle close to 0°, in order to obtain the smaller linewidth.

6.3.3 STT modes of the SyF dominant precession (I_{app}<0)

Upon increasing the current the system will transit from the damped hybridized modes[13] towards the STT mode. However, the measured frequency dispersion diagram will show a mix between damped A, O, higher order modes and the STT mode[14].

In order to know whether one excited mode is already in the steady state oscillations, we look at the linewidth as a function of the applied current. The extrapolation of the tangential of low current to zero (i.e Δf=0) yields an estimation of the critical current I_c[15].

In Fig. 6.19 (a) is shown the MR curve (orange region indicate the AP state) for a **MTJ3**[16]. The frequency dispersion diagram for negative current I_{app}=-1mA is shown in

[13]The PSD of the damped modes are not negligible.
[14]FL or SyF dominant precession for positive or negative current respectively.
[15] For instance we can see Fig. 6.52 for the device **MTJ2**.
[16]Elliptical device E65x130nm and TMR=48%

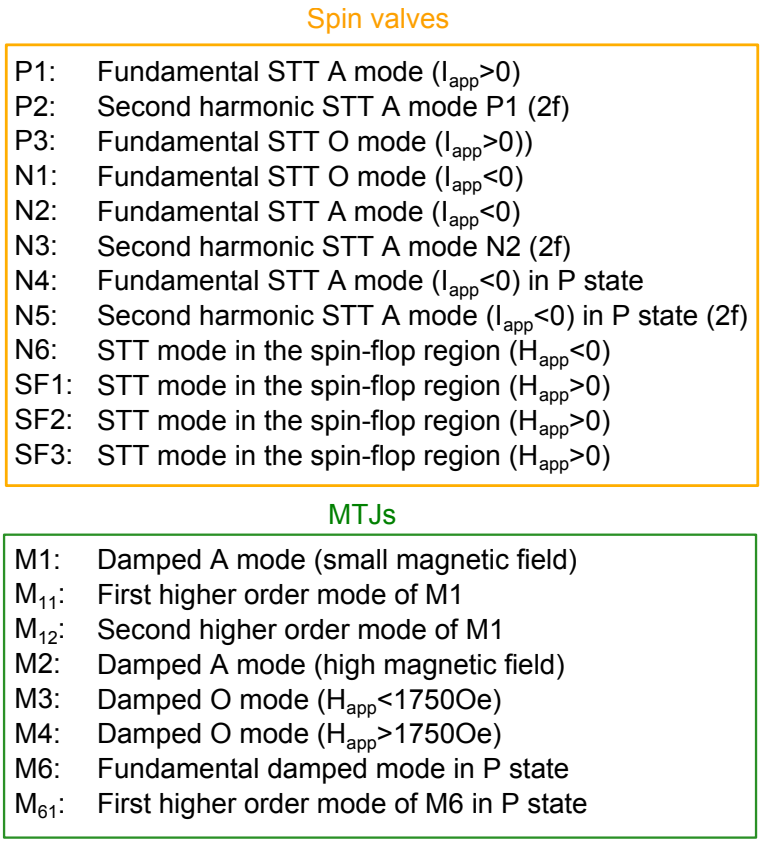

Figure 6.18 – Labels of modes used for the SV and MTJs.

Fig. 6.19 (b), where the SyF layer is mainly excited. It is identified in the AP state, the damped O mode for small values of magnetic field, and the STT A mode for high values of magnetic field (close to the spin flop value). Also the damped A mode M1 and the harmonic (2f) STT A mode. In the P state region we observe the M6 and M_{61} damped and higher order modes respectively.

The critical current to excite predominately the SyF layer is higher than the corresponding one to the FL, so for I_{app}=-1mA only the STT A mode is reached. Between the damped O mode and the STT A mo we observe a small splitting of 0.8GHz which is almost closed by a small damped mode. The low frequency peak appears also for this sense of current as it was predicted with the MR diagrams in section 3.3.6. We notice that the (2f) damped O mode will disturb the normal tendency of the damped O mode.

Comparing with the SV case, it is possible to identify that the STT A mode corresponds to the N2, the STT O mode to N1 and N4 to M6.

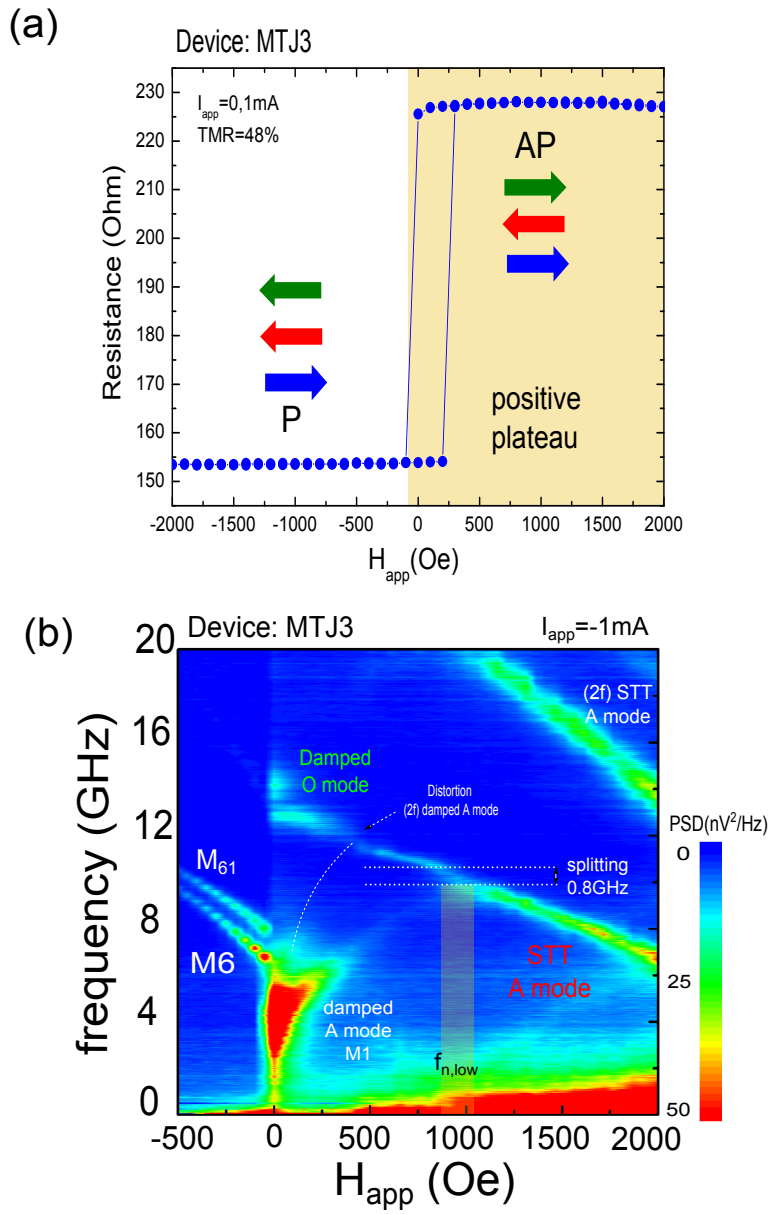

Figure 6.19 – (a) MR curve of the MTJ3. Arrows correspond to the magnetization of the layers. (b) Frequency dispersion as a function of the applied field for I_{app}=-1mA. The STT A mode and the damped modes are identified. A splitting of 0.8GHz between the damped O mode and the STT A mode appears around 1000Oe. A distortion around 400 Oe is shown in the damped O mode. Device MTJ3

6.3.4 STT modes of the FL dominant precession (I_{app}>0)

In this section the corresponding frequency versus field dispersion diagram of the **MTJ3** device is shown in Fig. 6.20 for a positive dc current. In this case also the direction of the applied field less than 10°, close to the easy axis (to obtain the minimum linewidth). Using the PSD of the magneto resistance shown in Fig. 5.48 (a) we will identify additional features in the frequency versus field diagram that should be studied in this section.

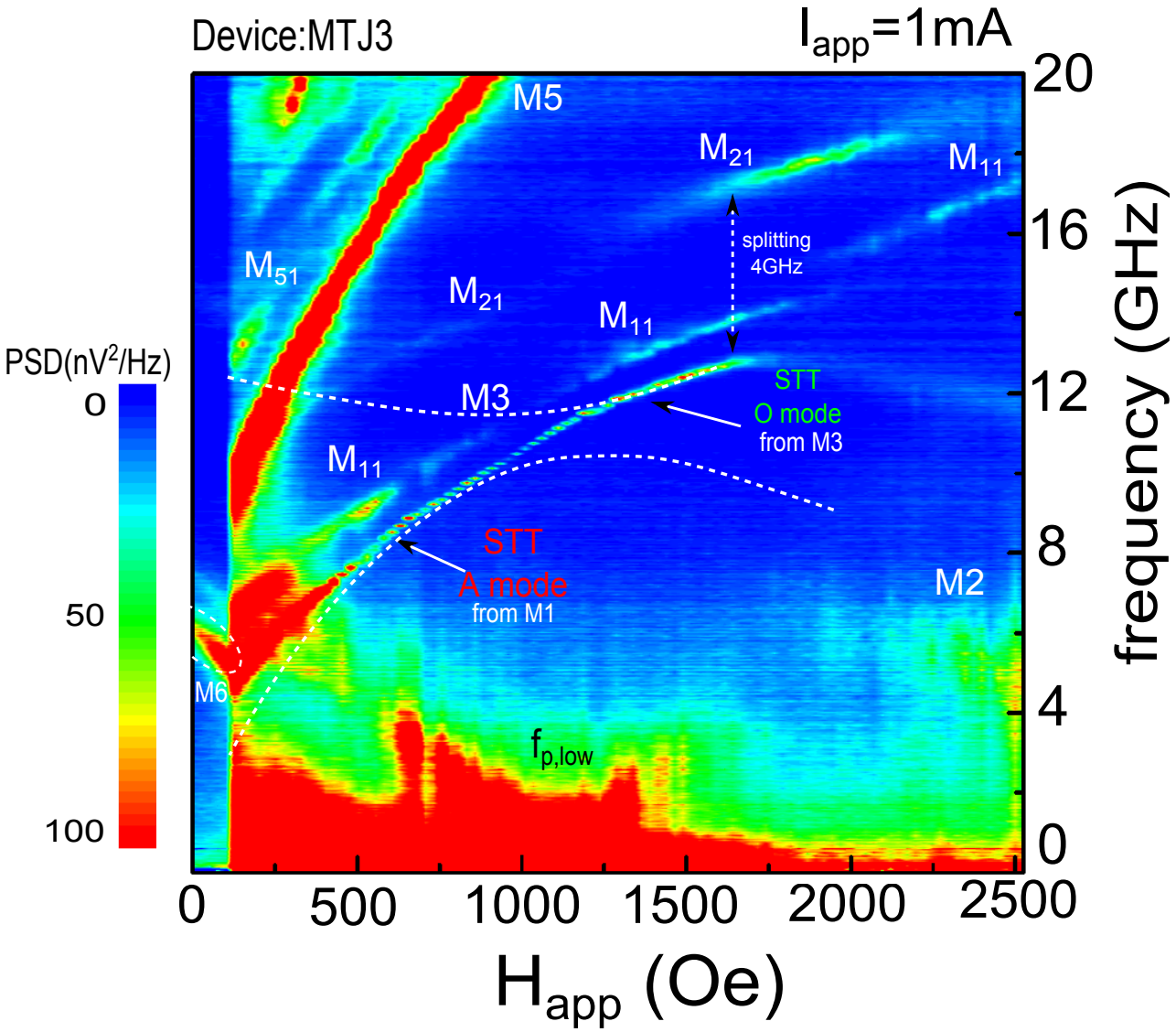

Figure 6.20 – The frequency dispersion as a function of the applied field. The state diagram shows the damped and the STT A and O modes. An additional peak of low frequency, H_{app}=≈1000Oe appears. The damped modes as M5=2M1, M2 and M6 and the higher order mode as M_{11}. The applied dc current was I_{app}=+1mA. Dashed lines represent the M1 and M3 damped modes of Fig. 6.16

.

In Fig. 6.20 we identify the STT A mode (small fields) as the evolution from the M1

mode, and the STT O mode (≈12GHz) which is the evolution from the M3 mode. The expected splitting (Δ_S) between the STT A and O mode disappears for these conditions (angle less than 10°). We include the dashed lines which identify the M1 and M3 damped modes from Fig. 6.16, (angle 30°). We observe also in Fig. 6.20 a noisy low frequency signal $f_{p,low}$ for H_{app} around the range of field of the splitting, ≈1000Oe.

From the PSD of the magneto resistance shown in Fig. 5.48 (a) we know that in the splitting region a peak with small amplitude appears closing the splitting and a low frequency peak appears. This should be the reason why we cannot observe the splitting.

An interest feature is that the STT O mode stopped around ≈1750Oe and another mode (17GHz) identified as M_{21} increases its PSD.

Measuring different devices we notice the presence in almost all the cases of the higher mode M_{11}, separated by ≈1GHz from the main M1 mode. The hybridized damped A mode (high fields) is labelled as M2 and the second harmonic of M1, labelled as M5.

In Fig. 6.21 we show the PSD of the peaks of frequency dispersion of Fig. 6.20 (b). The colour correspond to the different region of the diagram. The blue region show the smaller linewidth (19MHz) and the black curves the smaller STT modes with small PSD peaks. After the frequency dispersion changes its slope, see green region. In the brown region we observe a splitting or change of the mode from 12GHz STT O mode into 16GHz. This could be a change from the STT O mode to the M_{21} mode or the jump of the interaction of the STT O mode with the damped SO mode.

In Fig. 6.22 (a) we show a zoom of the frequency and linewidth dispersion as a function of the magnetic field. The minimum linewidth found in this device was of ≈19MHz in the STT A mode in 850Oe.

In comparison with the standard STO based on SV (e.g **SV1** device, see Fig. 6.6), we identify that the STT A mode corresponds to P1, the harmonic of the STT A mode (M5) to P2 and the STT O mode to P3.

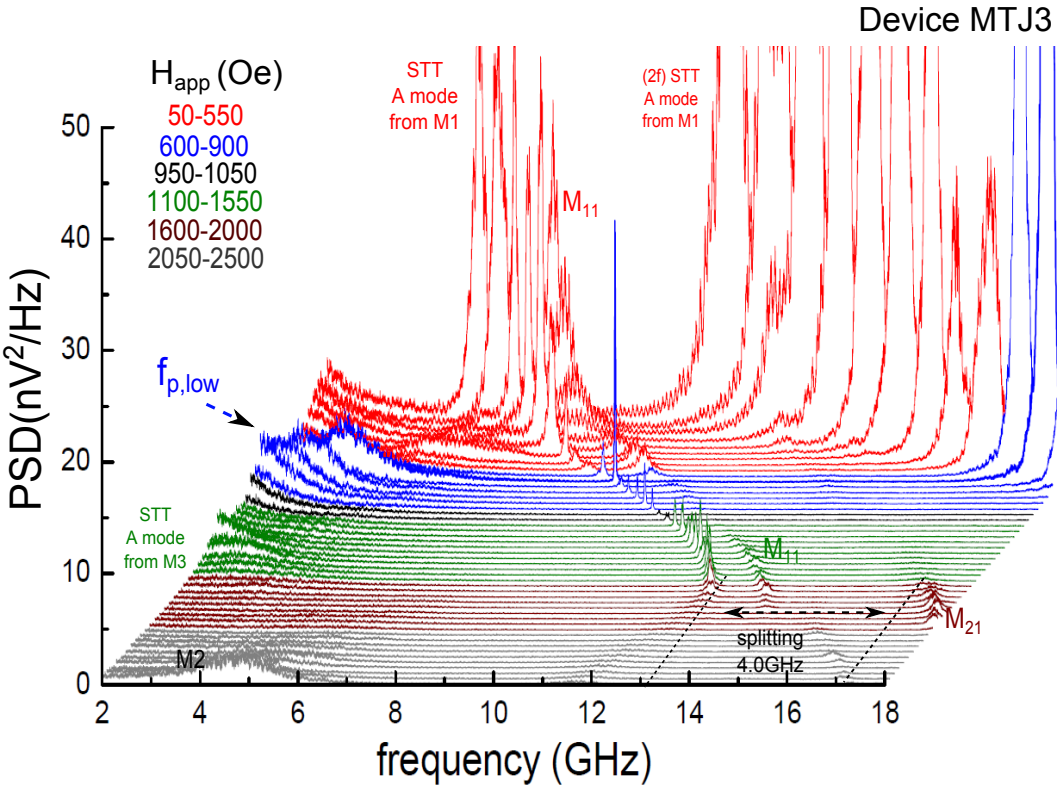

Figure 6.21 – PSD spectra, frequency versus applied field for I_{app}=1mA, FL dominant precession. The red colour represents the STT A mode for small fields (50Oe-550Oe). The higher order mode M_{11} is shown close the STT A mode. The blue region corresponds to the small linewidth in the STT A mode and where the low frequency field appears $f_{p,low}$, (600Oe-950Oe). The smaller STT mode appears (950-1050), black region. The STT O mode (1100Oe-1550Oe) shows the splitting in the brown region (1600Oe-2000Oe). For the grey region the M2 mode appears (2050Oe-2500Oe).

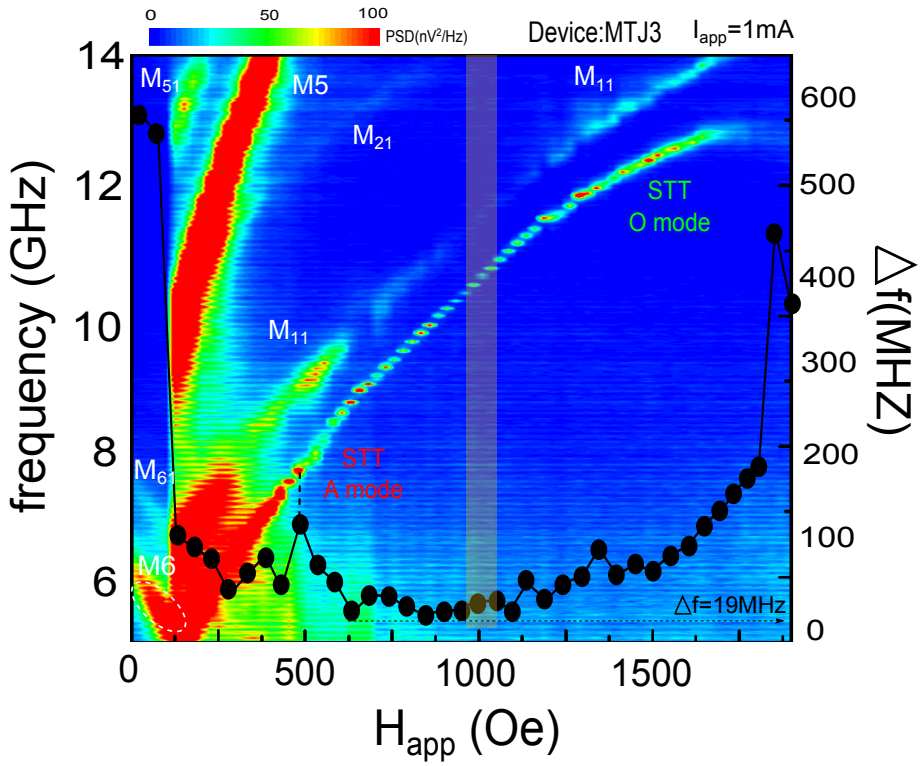

Figure 6.22 – A zoom of the frequency dispersion of Fig. 6.20 (b). The dashed lines are included as a visual reference of the splitting between the STT A and O mode. The linewidth is included, showing a minimum value of 19MHz around 850Oe.

6.4 STT modes frequency tuning as a function of magnetic field and current

One important feature of the STO is the capability to change the frequency (some GHz) of the emitted signal as a function of the applied magnetic field. Moreover, in the standard STO the auto-oscillation can be achieved in a FL or in a SyF pinned layer, changing the sense of the applied current. It produces a new mechanism of frequency tuning, current tuning. In this section we analyse some further characteristics of the frequency tuning in the standard STO first for the case of the structure based on a **SV** and then for based on a **MTJ** structure.

6.4.1 Frequency tuning in the STO based on SV structure

6.4.1.1 Frequency versus magnetic field

FL dominant precession, $I_{app}>0$

This study will begin with the FL dominant precession modes in the AP state, $I_{app}>0$. The STT A and O modes (P1 and P3) present the A and O damped modes tendency and they are separated by the characteristic gap. In Fig. 6.23 (a)-(b), the frequency dispersion of the STT modes as a function of the applied field is shown for I_{app}=1.1mA and 1.85mA respectively. The white dashed lines are used as a guide of the hybridized damped modes (A and O). The vertical white dashed lines at (≈-125Oe) correspond to the switching of the FL (negative applied fields) and the spin flop value (≈600Oe). These measurements correspond to the **SV1** device. If we compare the two dispersion diagrams, Fig. 6.23

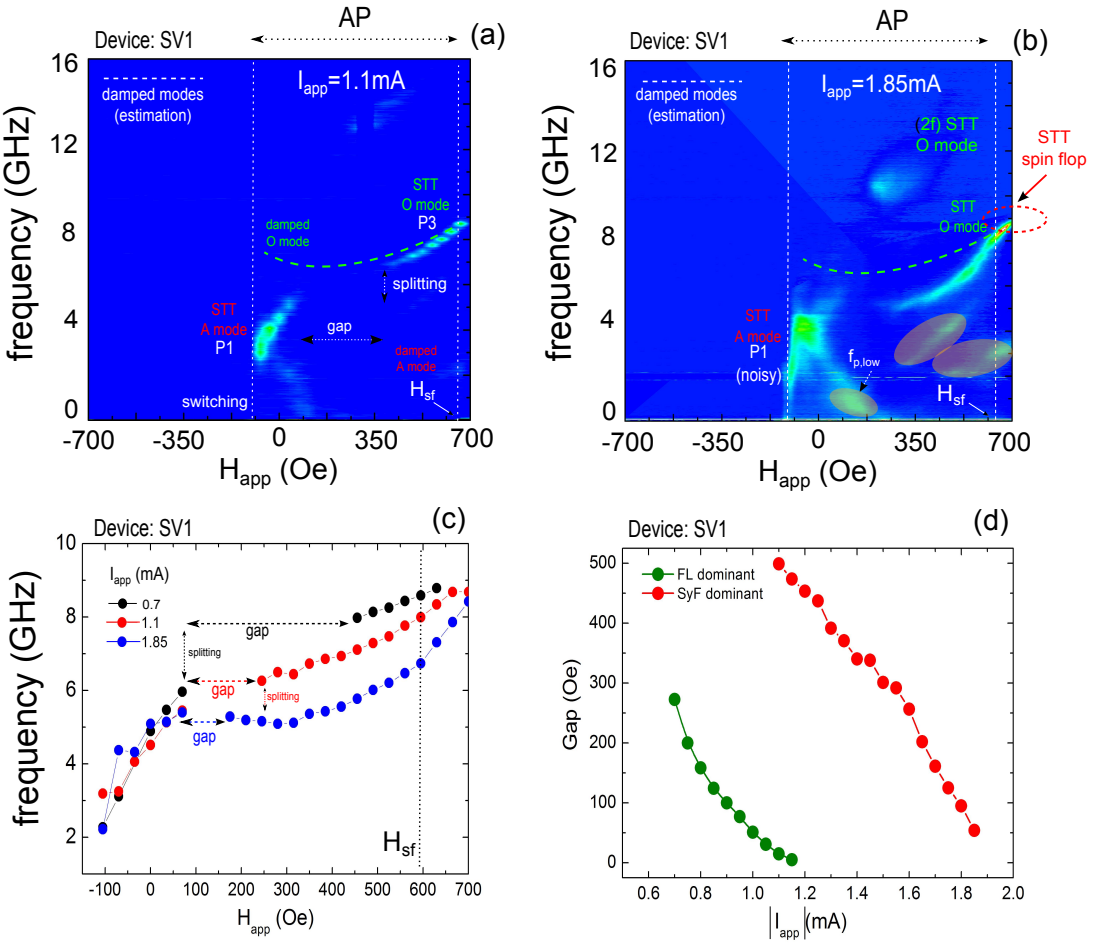

Figure 6.23 – Frequency dispersion versus applied field for the SV1 device. In (a)-(b) we observe the auto-oscillation dispersion for positive applied current (I_{app}=1.1 mA and 1.85 mA), FL dominant precession. The dash yellow lines represent the damped tendency of the A and O hybridized modes (I_{app}=0). In (c) we can observe the frequency versus applied field dispersion for I_{app}=0.7, 1.1 and 1.85mA. (d) The closing of the gap_{FL} and gap_{SyF} is introduced as a function of the current.

(a)-(b) it must be observed that P1, STT A mode (low field values), follows its Kittel like tendency, i.e increase of frequency with magnetic field. We notice that for higher currents, I_{app}=1.85mA, the P3 (STT O) mode is deviated from the hybridized damped O mode indicated by the green dashed line.

The STT O mode is also measured in the spin flop field region (H_{app}>6000e), see red circle in Fig. 6.23 (b). An intense peak appears (Δf=198MHz). It is possible because after the spin flop field the TL of the SyF starts to be deviated from its antiparallel position. This change in its direction will change the relative angle between the TL and the FL (pointing in the positive direction). The spin transfer torque under the TL will change showing a signal with higher amplitude.

As it has been shown in the state diagrams, in the frequency versus applied field dispersion the characteristic gap (distance between the STT A mode (P1) and STT O (P3) modes) is closed as a function of the applied current. In Fig. 6.23 (c), the gap is reduced if the applied current increases from 0.7 mA to 1.85 mA.

The closing of the gap for the FL and SyF dominant precession is shown in Fig. 6.23 (d) as a function of the absolute value of applied current. The gap is closed for the FL dominant precession (in green) which shows a smooth decrease.

Another feature is the appearance of low frequency modes (orange shadow region in Fig. 6.23 (b)) for high values of applied dc current. at least one has been predicted in the PSD of the magneto resistance shown in Fig. 5.48 (a).

SyF dominant precession, I_{app}<0

The SyF dominant precession modes are reached applying negative values of dc current. As it was shown in the state diagrams (Fig. 6.4) the critical current in this case is higher than in the FL dominant precession. An important feature of the SV devices is the capability to endure high dc current values without the destruction of the STO structure therefore it is possible to study the SyF dominant precession without the limitation of the dc current value. In Fig. 6.24 (a)-(b), we show the frequency dispersion of the SyF dominant precession as a function of the applied magnetic field values (for the same **SV1** device). The dashed lines correspond to the damped hybridized A and O modes. In order to reach the N1 mode of the SyF dominant precession (small values of applied field) it is necessary to apply high dc current values. The critical current for the N1 and N2 mode for this device were $I_{c,N1}$ ≈-1.4mA and -1.0mA respectively, deduced from the frequency versus field diagram with the appearance of the mode. For that reason in Fig. 6.24 (a) which corresponds to I_{app}=-1.1mA the N1 mode is not totally perceptible. However for I_{app}=-1.85mA in Fig. 6.24 (b), this mode is clearly identified. Both modes are separated by the characteristic gap, signature of the presence of the dipolar field. The gap decreases as a function of the dc current (see Fig. 6.23 (d)). the PSD of the magneto resistance shown in Fig. 5.48 (a)

In Fig. 6.24 (c) it is presented the evolution of the peaks measured as a function of the applied field for a dc current of -1.1mA. The amplitude are presented in arbitrary units and with an offset. The N1 mode appears at -105 Oe with a frequency close to 6 GHz, and it increases its frequency until the gap. After the gap in 350 Oe the N2 mode appears, in the A mode, decreasing until the spin-flop field value.

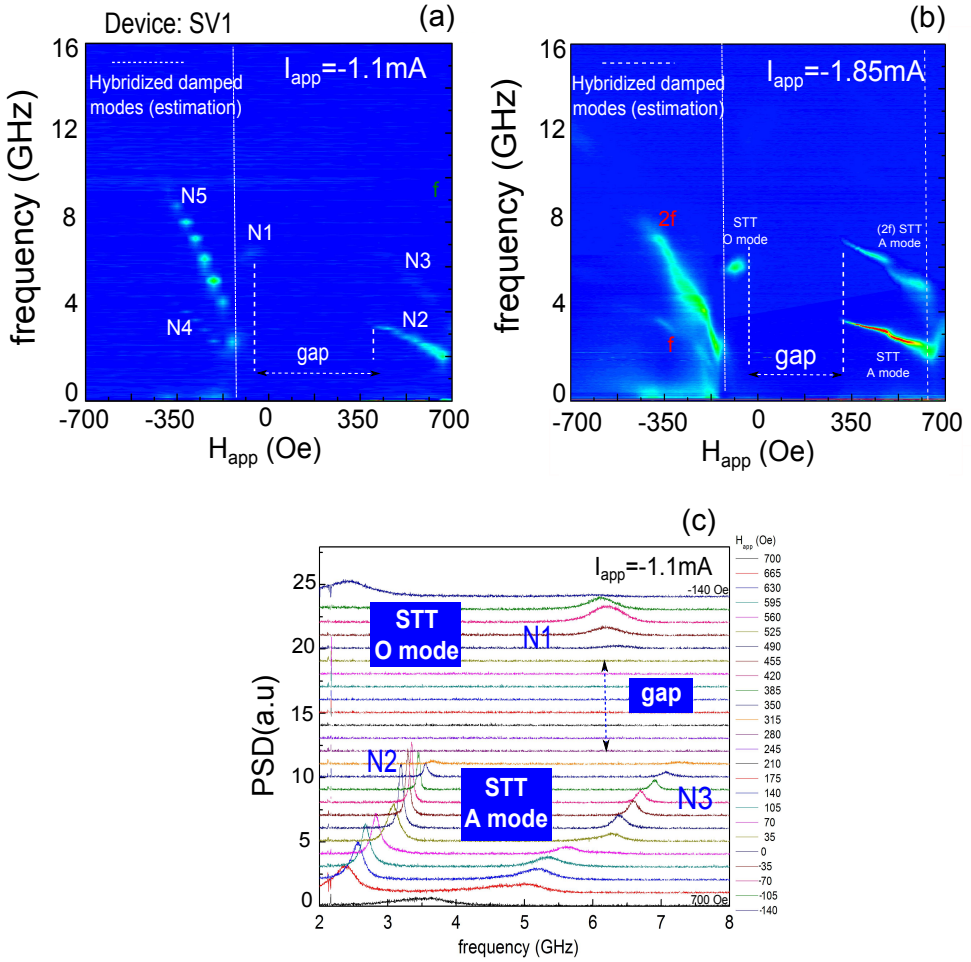

Figure 6.24 – (a)-(b) Frequency dispersion as a function of the applied field for the SyF dominant precession, I_{app}=-1.1mA and -1.85mA respectively. In (c) we observe the spectral emission measured for the case (a) where we can observe the N1, N2, N3 modes. The N1 and N2 mode are separated by the characteristic gap.

In the case of the **SV2** device, it is observed the same N1-N5 modes, see Fig.6.25. Something special is the appearance of the mode N9 close to the N1 mode. The size and the high dc current applied to this kind of devices could be the explanation of this additional mode. This could be a higher order mode. Something that is important to remark is that both modes N1 and N9 show a narrow linewidth, $\Delta f_{min,N1}$=32.4MHz (H_{app}=52.5Oe), $\Delta f_{min,N9}$=53.4MHz (H_{app}=35Oe) . As it is not possible to obtain (at least we can not prove it) two modes of steady state oscillation in the same layer, we propose a hopping between these two modes in steady state oscillations, see Fig. 6.25 (b). Another feature

of this **SV2** device is the soft kink or deviation in the tendency of the excitation modes in the P state which does not present an obvious gap in the measured field range.

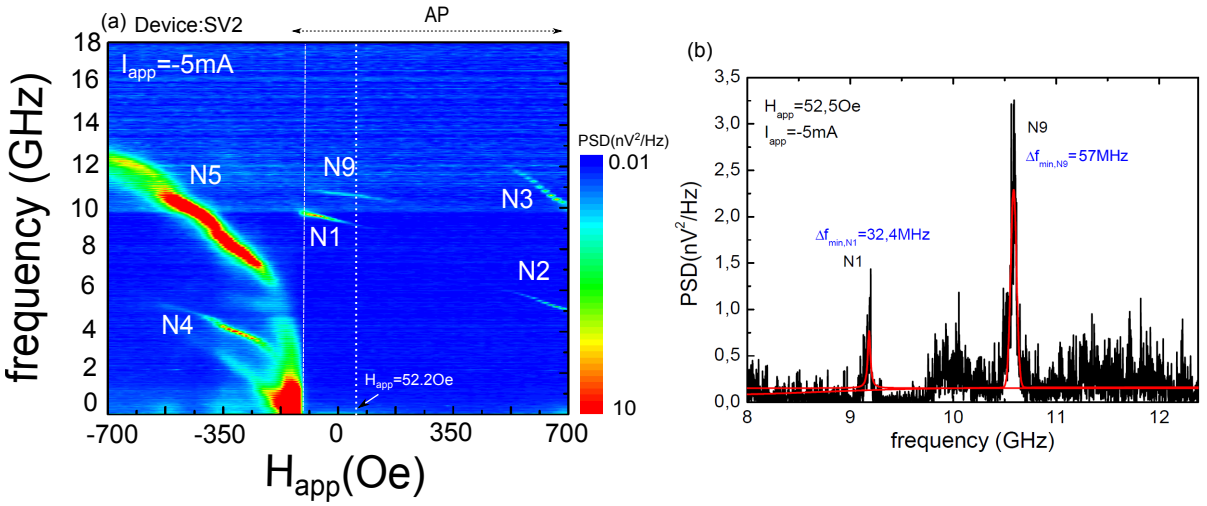

Figure 6.25 – (a) Frequency dispersion for the SV2 device shows the same excitations modes distributions but with a mode which is attributed to the high dc applied current. (b) The PSD peaks of N4 and N9 are show.

The motivation to study the excitations in the SyF pinned layer was investigate the linewidth in comparison with the linewidth of the FL. In Fig. 6.26 (a) we show for **SV2** a comparison of linewidth versus applied field, where $H_{app}>0$ for SyF and $H_{app}<0$ for FL excitations. As can we seen the minimum linewidth for the SyF is 12MHz (N2 high fields) in the AP state and for the FL is 34MHz (N4 in the P state). It is interesting to note that the linewidth of the FL in the P state is lower than in the AP state (≈700MHz), see Fig. 6.26 (b). At 0 field, a peak appears for a small range of field (≈158MHz).

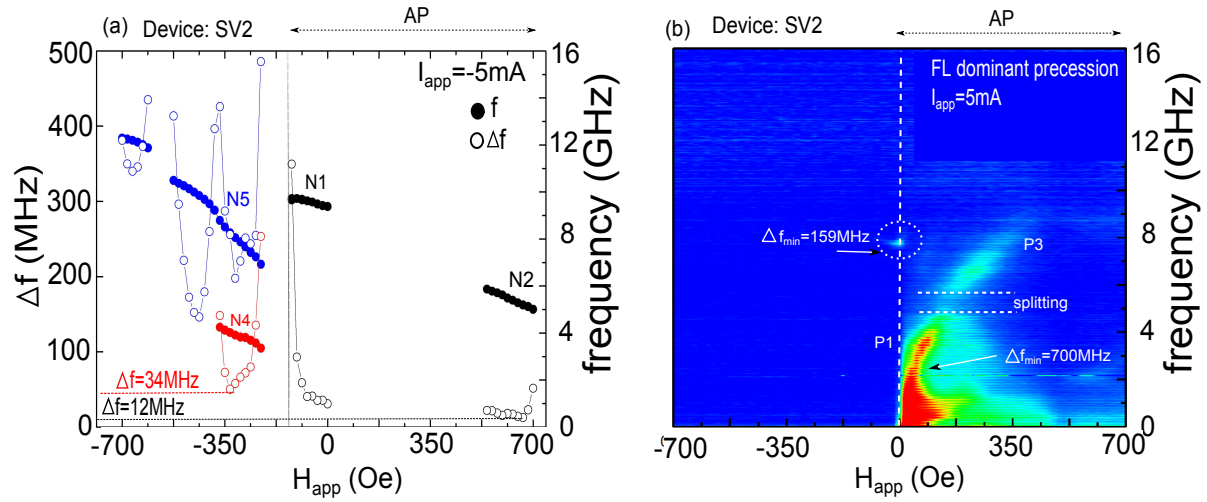

Figure 6.26 – The frequency and linewidth versus applied field. The minimum linewidth Δf=12MHz was found for high fields in N2. In the P state the minimum linewidth was Δf=34MHz in N4. N5 presents jumps when the frequency changes of branch.

6.4.1.2 Transition from redshift ($df/dI_{app}<0$) to blueshift ($df/dI_{app}>0$) regime

In the numerical simulation, we have shown a region of high fields and negative current where the frequency tuning as a function of the current changes from $df/dI_{app}<0$ to $df/dI_{app}>0$. It is identified in the numerical state diagram of Fig. 6.27 as the yellow shadow region.

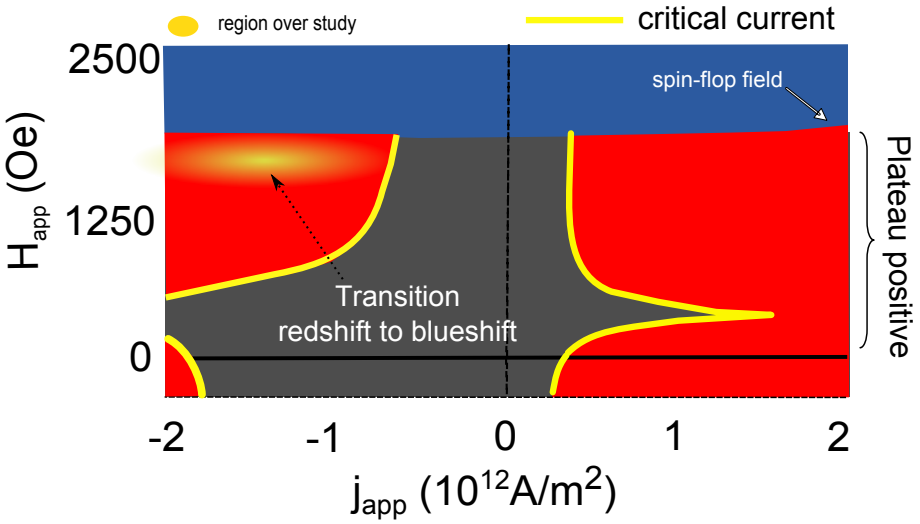

Figure 6.27 – The region of the transition from redshift to blueshift regime is identify in the simulated state diagram.

Frequency versus applied field

In Fig. 6.28 (a) the frequency versus applied field of the device **SV1** is shown. As in the results of the numerical simulations, Fig. 4.12 (d), we observe a transition from redshift (low fields) to blueshift (high fields) and a crossing of the frequency versus applied field at a characteristic field H^*_{cross}. This is an experimental verification of the numerical predictions. An important feature to remark here is that the linewidth is minimum (≈40MHZ) in the blueshift regime, see Fig. 6.28 (b). In Fig. 4.12 (d) we observe that the frequency decreases ≈4GHz but in Fig. 6.28 (a) ≈0.2GHz in the redshift regime H_{app}=325Oe. This small change produces that in the frequency versus current diagram the curves does not intersect each other.

In Fig. 6.29 we show the frequency dispersion as a function of the magnetic field for the device **SV4**. We observe the field value H^*_{cross}. In the inset of this figure is shown the magneto resistance curve with the orange shadow region which indicates the region of this transition.

Frequency versus current

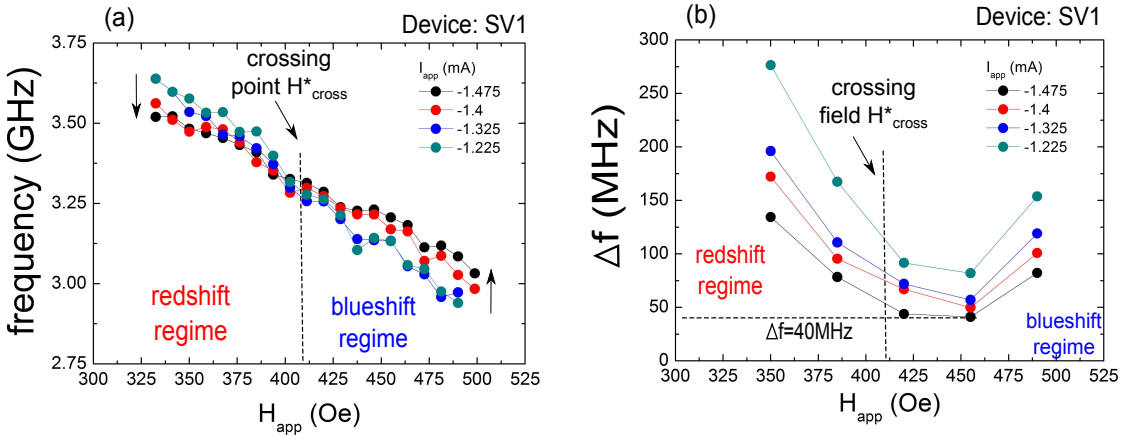

Figure 6.28 – (a) Frequency as a function of the applied field (SV1 device) for the SyF dominant precession which presents a predicted crossing point (vertical dashed line). (b) The minimum linewidth is found in the blueshift regime.

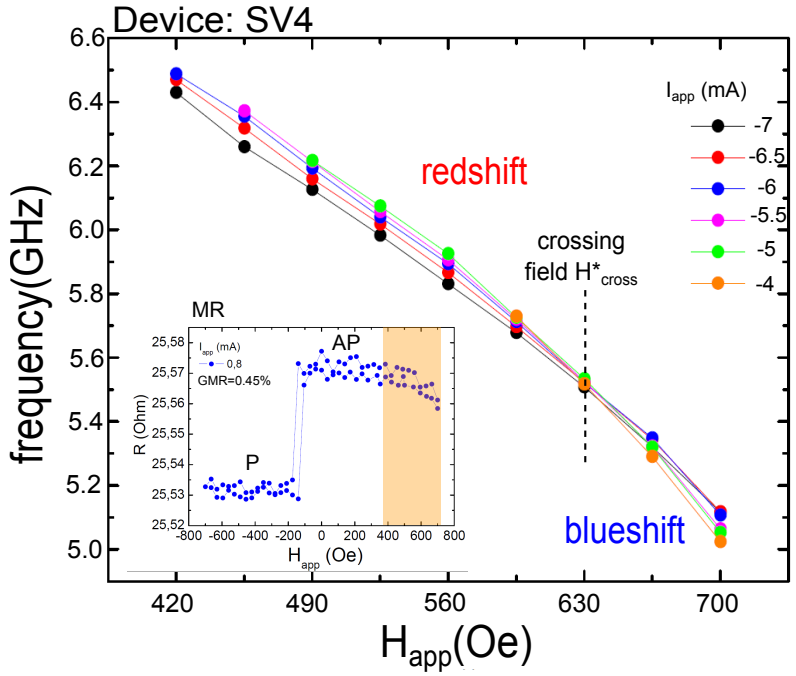

Figure 6.29 – Frequency as a function of the applied field (SV4 device) for the STT mode N2 which presents a predicted crossing point (vertical dashed line). Inset: curve magneto resistance. The region under study is shown in orange.

Now we will show the frequency and linewidth as a function of the current density in the transition. As it was shown and explained in section 4.2.5 of numerical simulations, the SyF dominant precession present a change in its tuning df/d$|I_{app}|$, from negative to positive with the increase of the external magnetic field. The evolution from redshift to blueshift regimes is presented for the device SV1 in Fig. 6.30. The dynamic RKKY coupling in the SyF pinned layer will be the origin of a dynamical torque which increases the frequency of the precession. The asymmetry of the SyF pinned layer will lead to different amplitudes of precession for high fields, increasing the dynamical torque will present its maximum value.

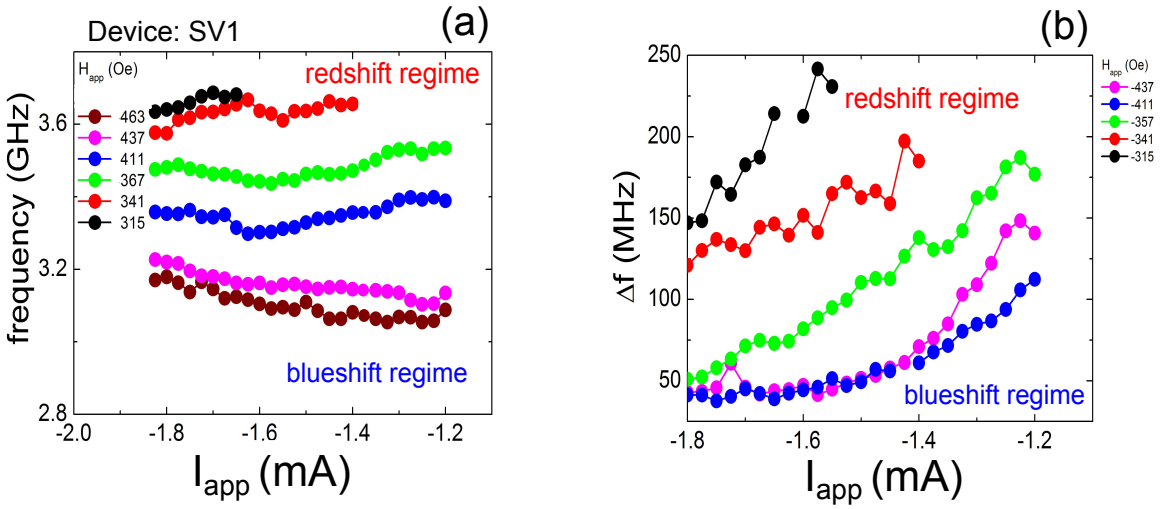

Figure 6.30 – (a) Evolution from the redshift to the blueshift regime for a standard STO SV1 device. In (b) we can observe the minimum linewidth for the case of the blueshift. This reduction of the linewidth could be associated to the dynamical torque which gives stability to the magnetization precession.

In Fig. 6.30 (a), a gradual change from redshift to blueshift regime is observed for device **SV1**. The linewidth presents a minimum in the blueshift regime, see Fig. 6.30 (b), where the dynamical RKKY torque is maximal. For the device SV1, the minimum linewidth for the redshift regime is 55MHz, and in the case of the blueshift regime 30MHz.

Another example of the redshift to blueshift transition is shown for the device **SV4** in Fig. 6.31, confirming the results of the device **SV1**. Here the lowest linewidth is of 12MHz.

6.4.1.3 STT A and O mode, SyF and FL dominant precession.

The SV devices are a good type of structure to study the features of the frequency tuning, due to the high values of dc current that it can endure. In this section we will shown the frequency al linewidth tuning of the STT A (P1 and N2) and O (P3) mode for the FL

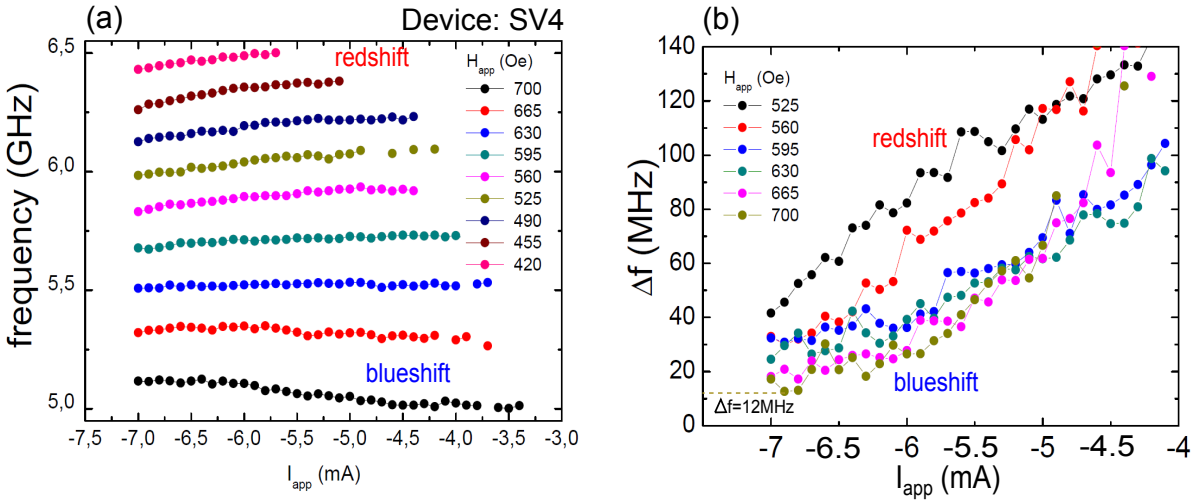

Figure 6.31 – (a) Evolution from the redshift to the blueshift regime for a standard STO SV4 device in the frequency versus current diagram. In (c) we observe the minimum linewidth for the case of the blueshift.

dominant precession.

STT A mode $I_{app}>0$

We start with the frequency tuning as a function of the current of the STT A mode corresponding to small magnetic fields and high current, see orange shadow region in Fig. 6.32. In the numerical simulations we found that the STT A mode evolves from IPP to a OPP regime upon increasing the dc current.

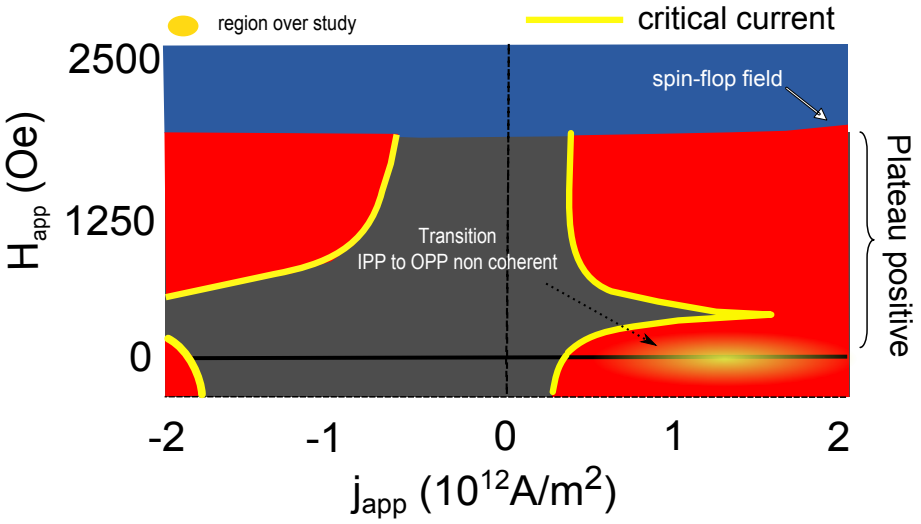

Figure 6.32 – The region of the transition from IPP to the non coherent OPP is identified in the simulated state diagram.

The frequency and linewidth versus current of the STT A mode is shown for **SV1** in Fig. 6.33 (a). We observe that for small positive current values, the behaviour is the

usual one of a free layer: redshift in the frequency dependence with current. A higher current the linewidth of the STT excitation becomes larger, showing a noisy region in the figure, I_{app}>1.1mA. We have superposed (solid circles) the tendency of the peaks in the noisy region (high current values). The orange pink follow the redshif regime of the main mode, however a second peak appears showing a blueshift regime (pink circles). The numerical simulations for a coupled system predicts a narrow region of IPP excitations, which evolves into a hopping between a non periodic OPP precession and another mode, see Fig. 6.33 (b).

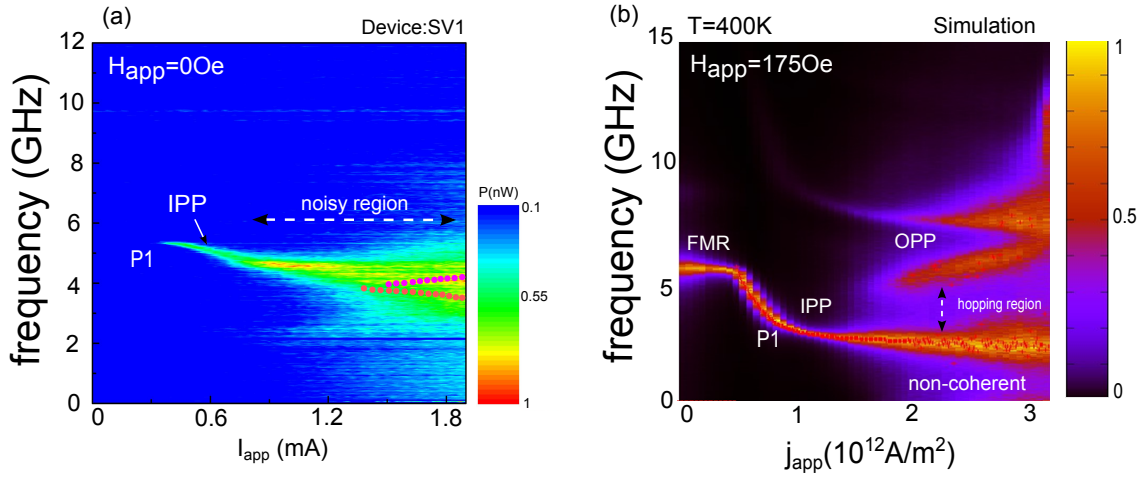

Figure 6.33 – (a) Frequency tuning as a function of the applied current for H_{app}=0 Oe (FL dominant precession, I_{app}>0). We can observe the evolution of a narrow IPP mode into a noisy region. (b) Numerical simulation of the frequency dispersion of (a) at 400K. Parameters in table 3.3.

In Fig. 6.34 (a)-(b), the frequency and linewidth for H_{app}=0 and 35Oe are shown. First, the linewidth reaches a minimum in the IPP regime ≈150 and 100MHz at 0.55mA in (a) and 0.42 in (b) respectively. We observe a dramatic change in the tendency, into blueshift for H_{app}=35Oe while for H_{app}=0 remains in a redshift regime (another mode). Comparing with the Fig. 6.33 (b) seems that the system chooses between the modes.

Increasing the dc current the linewidth increases fast and there is a clear change in the slope of the frequency dispersion, giving even rise to a new behavior, including a blueshift regime. We can compare this case with the numerical simulations in Fig. 5.25 and 5.26.

These features, as well as the conditions for which it takes place (low field and high current) fit with what is expected for an out of plane precession mode (OPP mode), for which the amplitude decreases (i.e. the frequency increases and the integrated power decreases) with the current. Our assumption is in agreement with our simulations (see Fig. 6.35 (a)) and with reference [Kudo et al., 2012] which by macrospin simulations predicts that the acoustic IPP mode is only stable in a very narrow current range. Moreover, the system

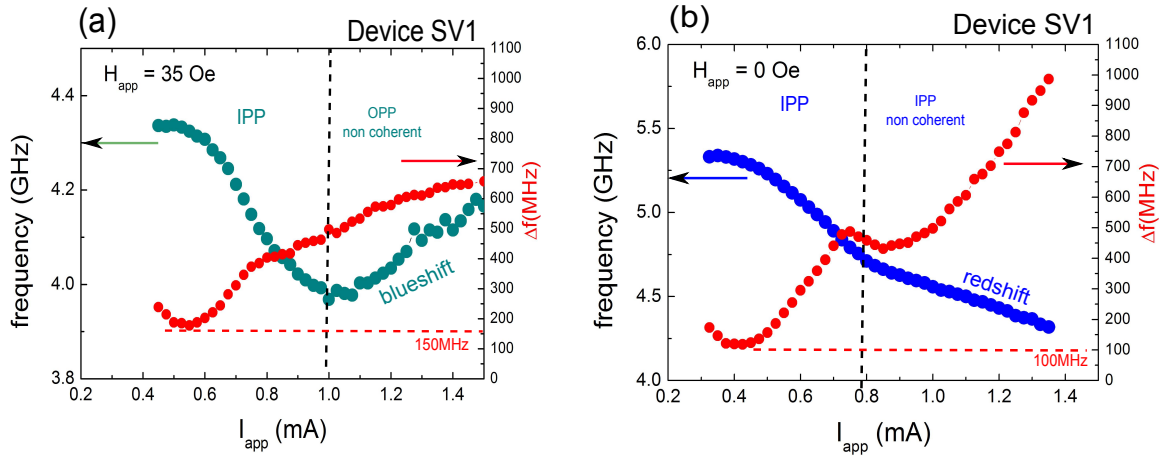

Figure 6.34 – Frequency and linewidth as a function of the applied dc current for the STT A mode. (a) For H_{app}=35Oe and (b) H_{app}=0.

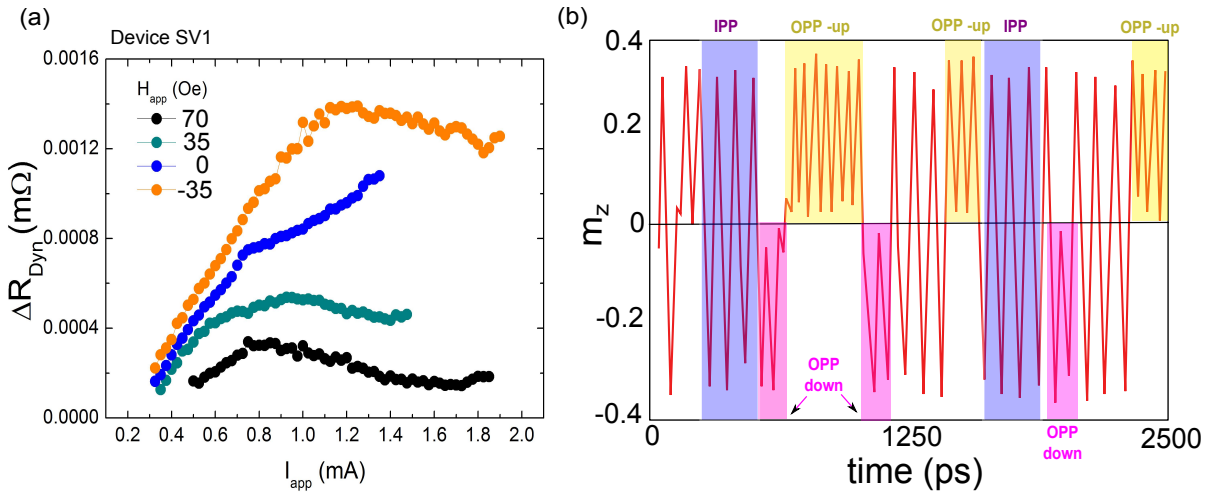

Figure 6.35 – (a) Dynamical resistance of the device during the precession. (b) Temporal trace of the OPP regime and non coherent regime.

reaches an unstable OPP mode which is characterized by a broadening of the linewidth mode with random hopping of the FL between the out-of-plane precession trajectories, see Fig. 6.33 (b). In order to test further our assumption of the system going into an OPP mode, we have studied the dynamical resistance of the system of this region as a function of the current for different fields, Fig. 6.35 (b). The dynamical resistance has been calculated as explained on reference [Houssameddine et al., 2007], using the equations 3.60 and 3.61, where ΔU and ΔU_{gen} correspond to the voltage measured by the spectrum analyser and the voltage of the device respectively.

As can be seen in Fig. 6.35 (b), the dynamical resistance increases for low currents of the IPP mode until it reaches a maximum and decreases with the current when the system reaches the new mode. This fact supports our assumption of an OPP mode because the precession amplitude (and therefore the angle between the FL trajectory projection and the reference layer) decreases with current in an OPP mode and therefore the resistance as well.

To further appoint this, we show results of device **SV3**, see Fig. 6.36. We can observe the evolution from the IPP into the noisy region.

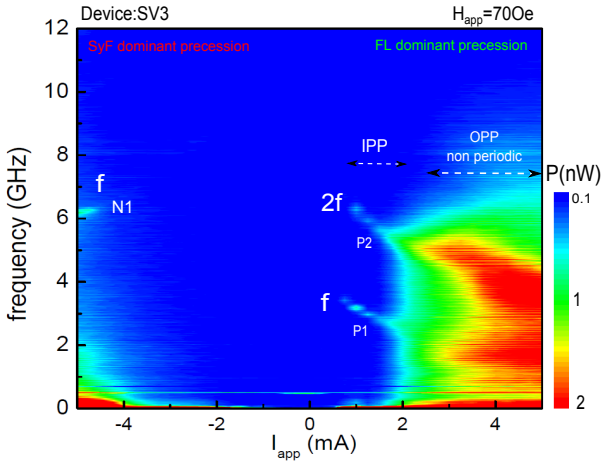

Figure 6.36 – (a) Frequency tuning as a function of the applied current for H_{app}=70 Oe (FL dominant precession, I_{app}>0 for SV3 device). We can observe the evolution of a narrow IPP mode into the noisy region.

STT O mode

The STT O mode for the FL dominant precession is indicated in Fig. 6.37 for high values of field.

The frequency versus current of the excitations of the STT O mode of the FL domi-

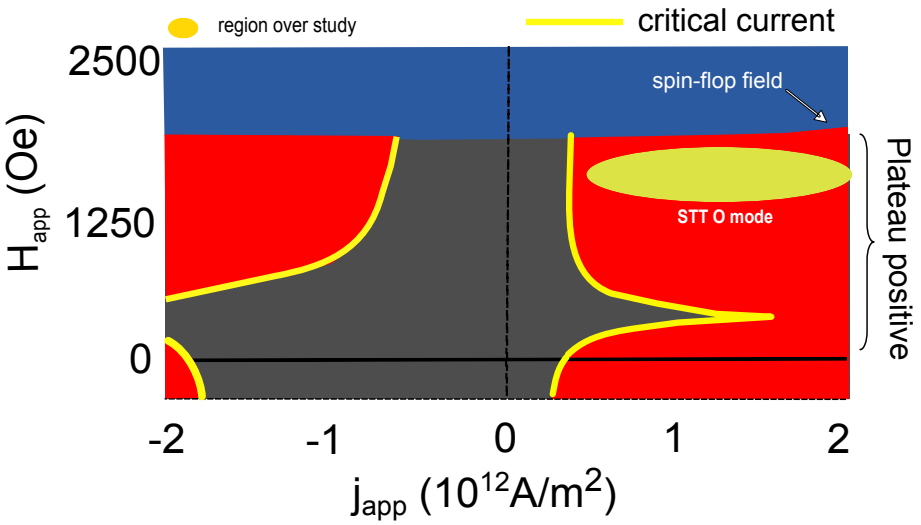

Figure 6.37 – Region of the STT O mode for FL dominant precession.

nant precession are shown in Fig. 6.38 (a). These excitations show a redshift regime $df/d|I_{app}|<0$ as in the case of an isolated FL. This regime is presented for the excitation in the AP state ($H_{app}<H_{sf}$) and in the spin flop region ($H_{app}>H_{sf}$) close to the H_{sf}^{+} value (compare with Fig. 6.23).

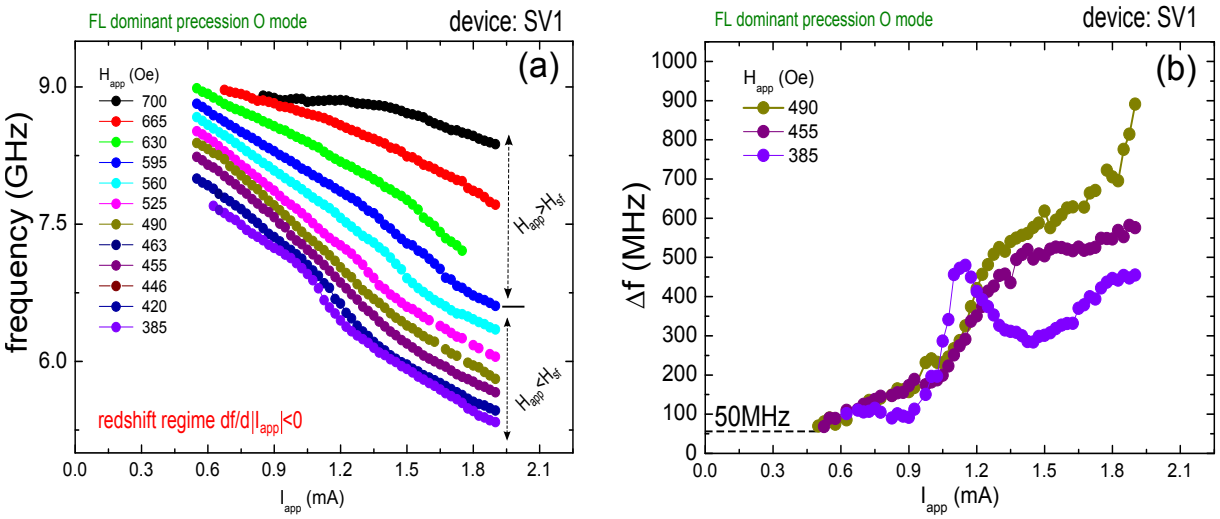

Figure 6.38 – (a) Frequency versus applied dc current for several values of applied field (In the AP state and in the spin-flop region). These STT modes correspond to the FL dominant precession on the O mode. They have been found in the redshift regime (as an isolated single FL). The linewidth for H_{app}=385, 455 and 490Oe is shown in (b).

The highest frequency tuning df/dI_{app} in this case is 1.8GHz/mA. These values correspond to the magenta curve of Fig. 6.38 (a) for H_{app}=525 Oe. Below 385Oe the exitation appears over I_{app}=1.1mA because correspond to the closing of the gap region.

The excitation in the spin flop region has an increased the amplitude, 3nW (Fig. 6.23 (b)) but the tuning decreases, as it is noticed in Fig. 6.38 (a) for H_{app}=700 Oe. For this magnetic field value the $\partial f/\partial I_{app}$ will be only of 0.53 GHz/mA.

The linewidth as a function of the current for the corresponding STT O mode of the FL dominant precession increases as a function of the current for all fields, see the Fig. 6.38 (b). It has been chosen three values of magnetic field, corresponding to the 385, 455 and 485Oe of Fig. 6.38 (a). In all these cases the minimum linewidth is found close to the critical current.

In this O mode of the FL dominant precession it is possible to observe some kind of kinks or deflections for $H_{app}<H_{sf}$. The origin of these perturbations will be discussed in the next section.

6.4.2 Interaction between the STT mode and the damped modes for a STO based on SV

An important motivation of this thesis is to find answers for some open questions presented in the measurements of the frequency dispersion diagrams of previous works and publications, [Houssameddine et al., 2008], [Houssameddine et al., 2010], [Cornelissen et al., 2010], for instance the appearance of difference branches in the frequency dispersion diagram..

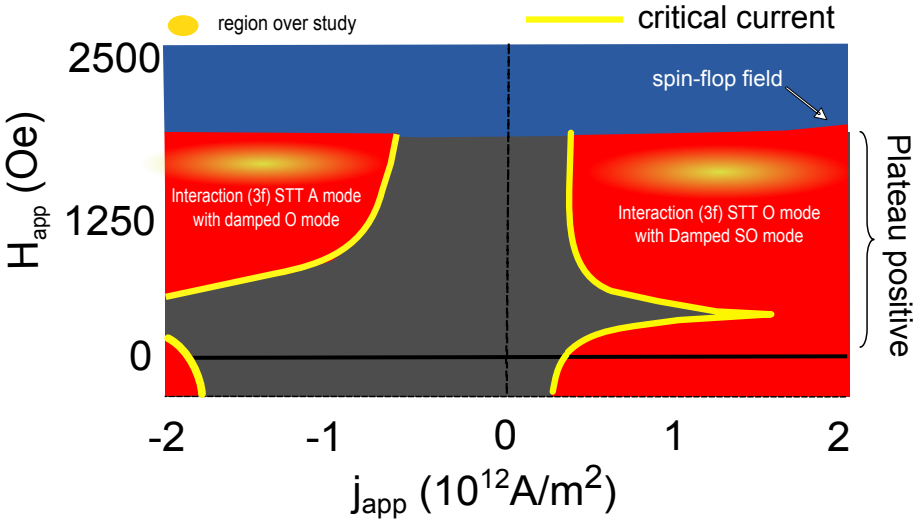

Figure 6.39 – Region of the interaction of the STT A and O mode for the SyF and FL dominant precession with the damped modes.

The frequency dispersion of the STT A and O modes FL or SyF dominant precession

present jumps or kinks (deviations) from the usual tendency. We will study the STT modes taking into account the interaction with the damped modes in the spectrum. We will study SV and MTJs devices. The region of interactions are shown in Fig. 6.39.

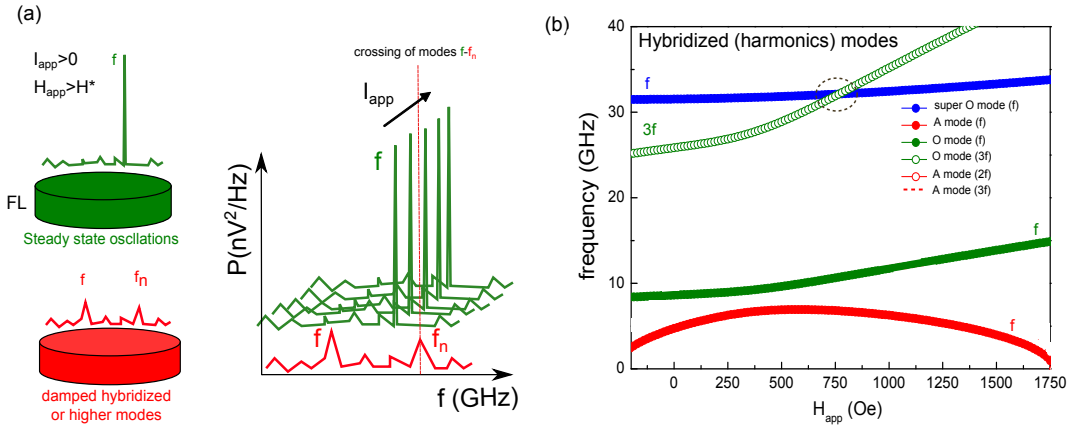

Figure 6.40 – Schematic of the interaction between the modes in the RF measurements. In (a) for positive applied current the FL dominant precession is excited but other damped (or higher order) mode could be present. The schematic of the crossing between the steady state oscillation in the system with a damped mode f_n. The hybridized damped modes are shown in (b). The black dashed circle shows the crossing of the (3f) damped O mode with the damped SO mode.

As it has been shown in the previous sections, the hybridized damped modes and the confined higher modes of the FM layers will appear in the measured spectrum. In Fig. 6.40 (a) we show one example of interaction between the STT mode and the damped f_n mode from simulation. The STT mode and the hybridized damped mode show a current tuning $df/dI_{app}{}^2$ (GHz/mA). We can sweep the dc current to tune the emission signal measured in the spectrum analyser, see Fig. 6.40 (b). Therefore, when the STT mode frequency is close to the frequency of the damped mode both modes interact. The frequency versus magnetic field shows the regions (black dashed circle) of crossing between the modes, see Fig. 6.40 (b).

We observe via simulations a kink or a jump (Fig. 5.31) which is interpreted by the STT O mode interacting with the damped SO mode. Numerically (in the macrospin approach) the effects of the interaction between STT mode with other damped (or higher order) modes are excluded. However in the experimental measurements (especially in STO based on MTJ), the others damped and higher modes will appear creating a distortion in the STT peak.

In this section we will show some evidence of the numerical prediction for the interaction between the damped mode with the STT modes.

6.4.2.1 Evidence of interaction between the STT O mode (FL dominant precession) with a damped SO mode in SV structure

Frequency versus magnetic field

In the numerical simulations of chapter 5 we have shown that the frequency dispersion versus field of the standard STO will show a gap, which separates the STT A mode from the STT O mode for both senses of current. Furthermore an interaction between the STT O mode for the FL dominant precession with the damped super optic (SO) mode, for high fields. These numerical predictions were found in experiments, see Fig. 6.41 for the device **SV5**. The dashed line indicate the tendency without interactions in the region of the kink.

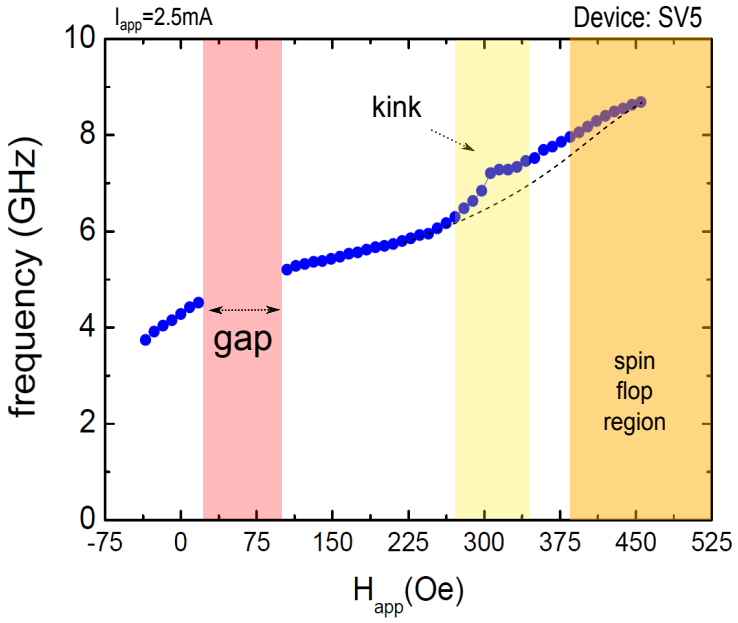

Figure 6.41 – Frequency versus magnetic field dispersion, I_{app}=2.5mA. Device SV5.

The linewidth is affected for this interaction as we show in Fig. 6.42 (a). The linewidth of the STT O mode shows a reduction of 267MHz in the flattening frequency region, see yellow shadow region. This is an experimental verification that confirms the reduction of the non linear parameter ν in the interaction between the STT O mode and the damped SO mode. Gusakova given the origin of this effect to the MSTT between the FL and TL layers but taking into account only the interaction of the fundamental modes. In the numerical simulation we found a maximum decrease of 317MHz for $j_{app}=0.8\times10^{12}$A/m^2, see Fig. 6.42 (b).

This feature is observed also in the device **SV1** as a function of the field in Fig. 6.43. We observe that the frequency shows an kink for 315Oe$<H_{app}<$450Oe close to the gap. The blue dashed line indicates the tendency without the kink. In this case the decrease of the

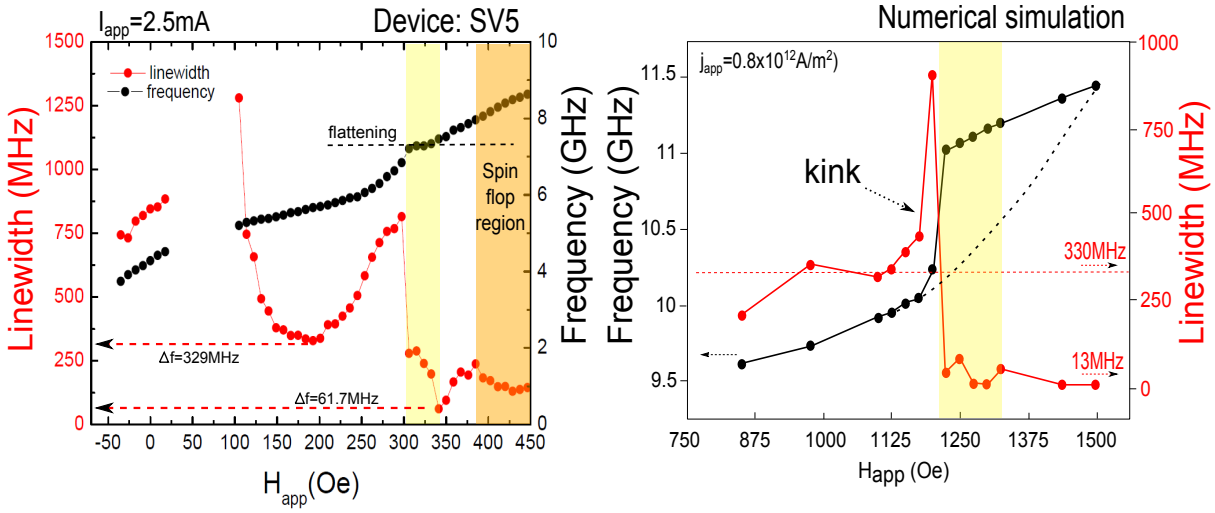

Figure 6.42 – (a) Frequency and linewidth versus magnetic field dispersion, I_{app}=2.5mA. (b) Numerical simulation of the frequency and linewidth for the interaction between the STT O mode and the dampes SO mode, see Fig. 5.21. Device SV5.

linewidth is not quite large as in the previous case of device **SV5**. The inset shows the frequency versus field diagram for all the range of field.

Frequency versus current

We start discussing **SV1** for the frequency versus current dependence. The STT O mode (P3) shows a kink which we interpret as an evidence of the interaction with a damped SO mode. This FL dominant precession is characterized by an important tuning (as a function of the external magnetic field and current), see Fig. 6.38 (a).

In Fig. 6.44 (a) we show the frequency versus applied field diagram for I_{app}=1.1mA in order to first identify the modes; P1 close to zero and P3 where we will observe the interaction. The vertical dashed line corresponds to a cut in H_{app}=385Oe. In Fig. 6.44 (b) we show the frequency and the linewidth as a function of the current for the fixed H_{app}=385Oe. The dashed lines are shown in order to visualise the linewidth for the case of an isolated system, without taking into account the dynamic couplings (MSTT or dipolar field), and following the numerical result of Fig. 5.7. The red shadow region indicates the flattening of the frequency. In this region we found a reduction of the linewidth of 62.4MHz from the supposed isolated case, as in numerical simulations, see Fig. 5.7. Following the theory, equation 5.4, the linewidth is reduced if the df/dI_{app} decreases i.e the system loses the non linearity. In the orange region, the linewidth presents an abrupt increase, which corresponds to a large $|df/dI_{app}|$.

As it has been introduced in numerical simulations, the interaction between the STT O

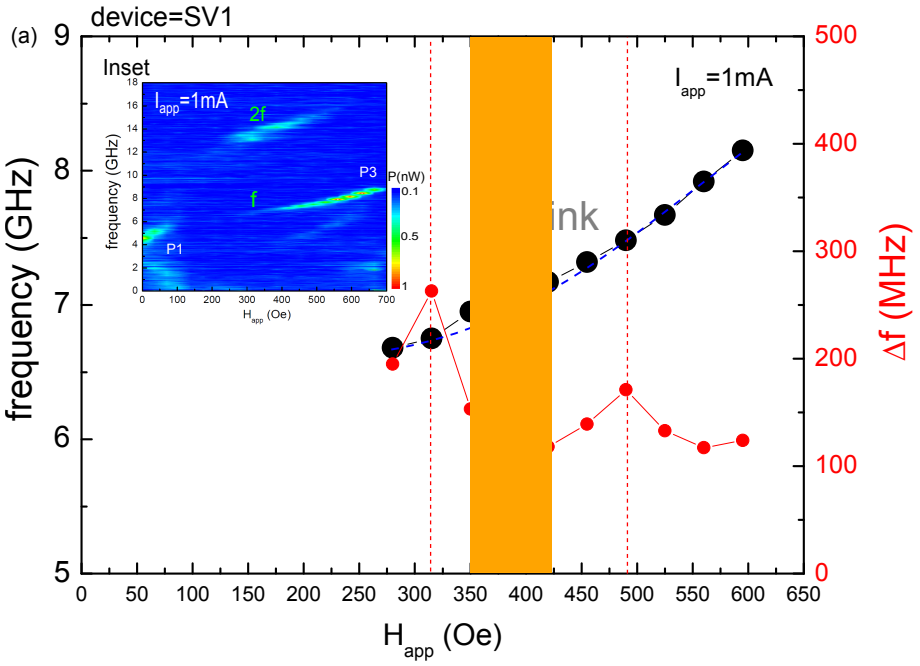

Figure 6.43 – (a) Frequency and linewidth versus magnetic field dispersion, I_{app}=1mA. The minimum linewidth corresponds to the flattening of frequency. Inset: Frequency dispersion as a function of the field. Device SV1.

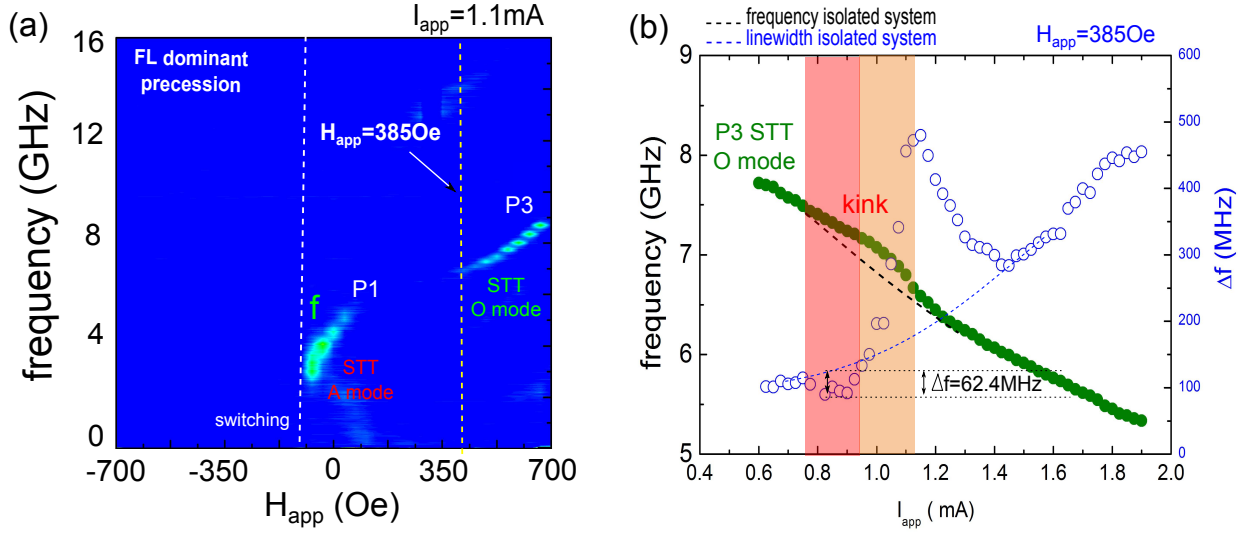

Figure 6.44 – (a) Frequency versus magnetic field diagram. The P1 and P3 STT modes are shown for I_{app}=-1.1mA. (b) Frequency tuning as a function of the applied dc current of the P3 STT O mode for H_{app}=385Oe. The dashed lines are plotted to give us one idea of the curves in a isolated system, following predictions shown in Fig. 5.7.

mode and the damped SO mode produce a kink or a jump and the corresponding decrease of linewidth. In order to be sure that the kink corresponds to this interaction we show the spectra for the device **SV1** applying H_{app}=385Oe and I_{app}=1.425mA, see Fig. 6.45 (a). It shows the STT O mode and the damped A mode peaks. The frequency versus applied current of the damped A mode shows a tuning of ≈1GHz/mA, see Fig. 6.45 (b). In order b sure that the kink is not an interaction between the STT O mode and the damped A mode we plotted the corresponding harmonics, see Fig. 6.45 (c). We confirm that the modes does not cross.

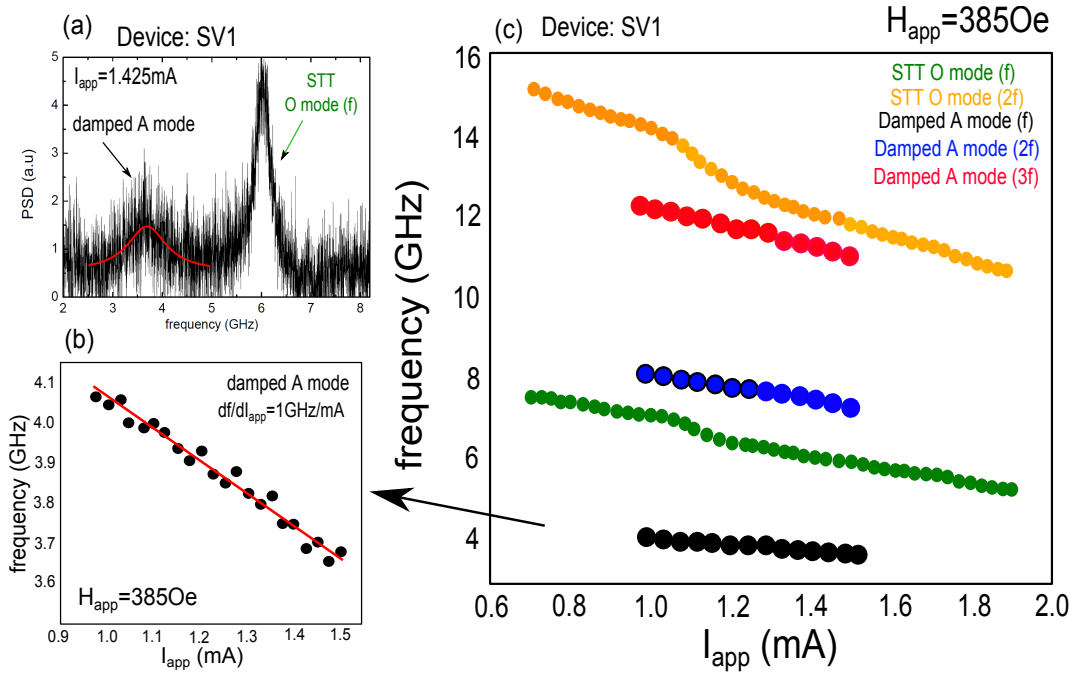

Figure 6.45 – (a) STT O mode and damped A mode peaks. (b) The damped A mode shows a redshift tendency. (c) the harmonic of the damped A mode do not cross the STT O mode and its second harmonic.

During the measurement of the kink, we observe two peaks together, the STT and the damped SO mode (f/3), that could be analysed as an "envelope" of both, due to the proximity of frequencies. In Fig. 6.46 we show the analysis of the frequency and linewidth as a function of the current for two cases: taking into account the envelope of the two peaks or only the STT peak. The open circles ∘ correspond to the case of the envelope while the solid circles • only to the STT O mode. We remark that using the peak of the damped SO mode (f/3) we can estimate the frequency of the damped SO mode in <21GHz.

We can notice in Fig. 6.46 (a)-(b) that the frequency and the linewidth follow the same tendency until the region labelled as '2'. The reduction of the linewidth for both cases appears in the flattening red region '1'. The inset in Fig. 6.46 (a) shows the fitting of two peaks for I_{app}=1.075mA. The frequency of the STT mode in the manual analysis shows

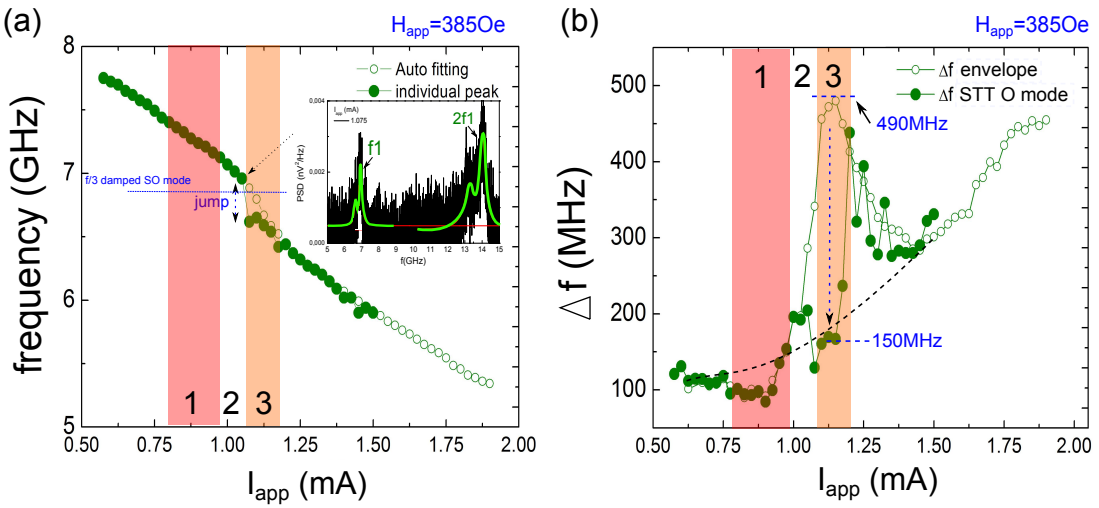

Figure 6.46 – (a) The interaction in the frequency crossing of a damped SO mode with the fundamental STT O mode is evidenced in a form of a kink (two peaks together) or a jump (following the STT peak). (b) Linewidth as a function of the dc current. In the crossing of modes we observe a decrease and increase of linewidth values.

a jump of 0.3GHz in region '3', orange region. The linewidth should be reduced because now we are fitting only one peak and not an envelope. The reduction of the linewidth is shown in the orange region, while the envelope gives us a 490MHz the fitting of the STT O mode give us 150MHz. The region with smaller linewidth is still the region "1".

In conclusion, the interaction of the STT O mode with a damped mode will give rise to a reduction of the linewidth in the flattening region (df/dI_{app}) of the frequency dispersion. This could be the reduction of the non linearity of the system following the equation 5.4. The abrupt increase in the linewidth tendency is a evidence of the presence of the peak of the damped SO mode (envelope) in the region of interactions.

6.4.2.2 Evidence of interaction between the (3f) STT A mode (SyF dominant precession) with a damped O mode in SV structure

Features described above for the FL are also observed for the SyF. They will be shown in this section. The STT A mode (SyF dominant precession,I_{app}=-1.85mA) in the SV devices (**SV1**), presents a deviation from its normal tendency, close to 500 Oe. As we notice in the Fig. 6.47, the STT A mode does not have any evident crossing or interactions with any of the other modes. However if we superpose its 2f and 3f harmonics, we notice the 3f STT A mode frequency crosses the damped O mode

The solid circles correspond to the STT A mode, f in red, 2f in green and 3f in yellow.

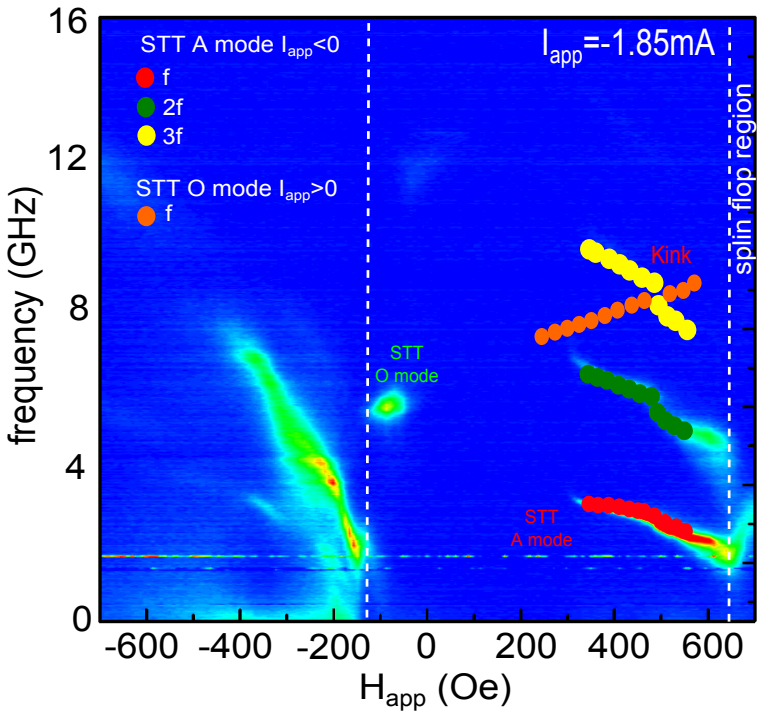

Figure 6.47 – (a) Frequency diagram as a function of the field for the STT A mode for device SV1. The dc current was I_{app}=-1.85mA. Dashed line corresponds to the switching of the FL. The STT A modes are indicate by circles (f red, 2f green and 3f yellow) and the tendency of the STT O mode is shown in orange (from I_{app} ≈0.6mA).

The third harmonic is not possible to visualize but we multiply by three the fundamental mode. The orange circles correspond to the STT A mode for the smaller positive current (I_{app}=0.6mA), in order to be close to the hybridized mode. We notice the crossing between the (3f) STT A mode (yellow) and damped O mode (orange). The frequency tuning of the fundamental STT A mode and its linewidth show us two interesting regions that we will analyse, see Fig. 6.48. The green circles corresponds to the fitting of the peaks taking into account the envelope (if we see two peaks in the interaction region) and black circles to the individual peak. The red shadow region of Fig. 6.48 represents the first approach between the modes, i.e. when the STT A mode start to feel the crossing of the damped O mode. In this region we observe a decrease of the linewidth, in the case when the hybridized damped O modes and the (3f) STT A mode coexist. The amplitude of the PSD peak is higher (24nV^2/Hz) in comparison with the two peaks of the region 2 (5.5nV^2/Hz) or 3 (7.8nV^2/Hz), see Fig. 6.48 (c).

Comparing both curves of Fig. 6.48 (a)-(b), we cannot conclude that a reduction of the linewidth appears in the interaction between the (3f) STT A mode and the damped O mode, only a kink/jump. We should measure this region with more detail.

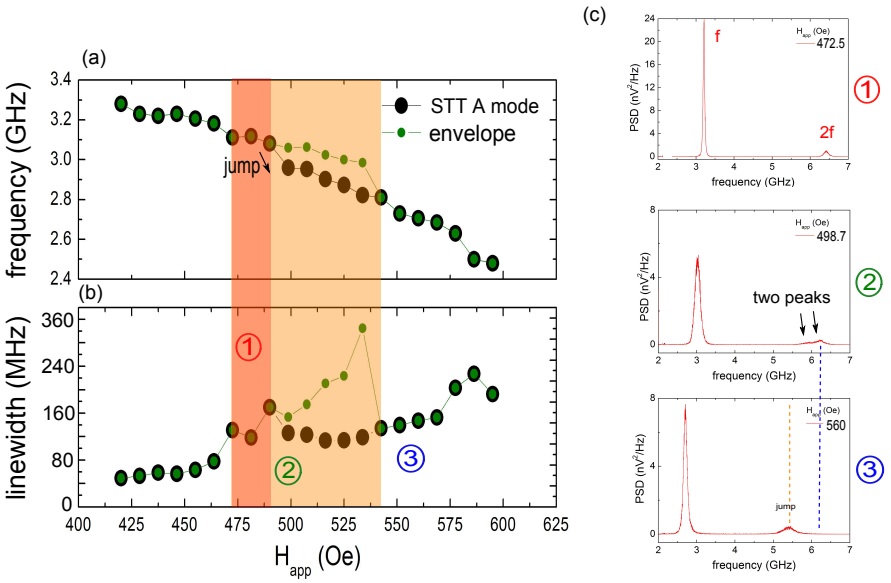

Figure 6.48 – (a)-(b) Frequency and linewidth dispersion of the STT A mode for SV1. The dc current was I_{app}=-1.85mA. The fitting following the individual STT A peak is indicates with the black circles and the envelope which includes the two peaks is indicated by the green circles. The crossing of the modes is represented by the red region. (c) PSD peaks for three regions of (b). Looking at the 2f harmonic peak, we realized that for 498.75 Oe the system present two peaks. The damped O mode amplitude increases while the STT A mode amplitude decreases.

6.4.3 Frequency tuning in the STO based on MTJ structure

In the case of a STO based on the MTJ, before to study the frequency tuning or another feature, it is necessary to know if the excited mode is in the damped regime or in the steady state oscillation. The criteria to obtain the critical current of the excitations is shown in Fig. 6.52. We will study in this section the damped modes and the steady state oscillation of the emitted spectra.

6.4.3.1 Damped A and O modes

The damped mode frequency dispersion as a function of the magnetic field for the device **MTJ4** is shown in Fig. 6.49, for 0.8mA and 1.2mA. This frequency dispersion diagram is measured at 30° because it is not possible to identify the acoustic and optical hybridized damped A and O modes at 0°. It should be compared with the frequency diagram shown in Fig. 6.13.

The M3 optic mode shows the discontinuity due to the crossing of the M5 mode, second

harmonic of M1 (black dashed line). The gap between the damped M1 and M2 modes decreases with the increase of the current. There are two region red-shifted indicated by the blue arrows. We indicate in Fig. 6.49 (b) the decrease of the splitting between the modes, a confirmation of the numerical simulation, see Fig. 5.16 (a).

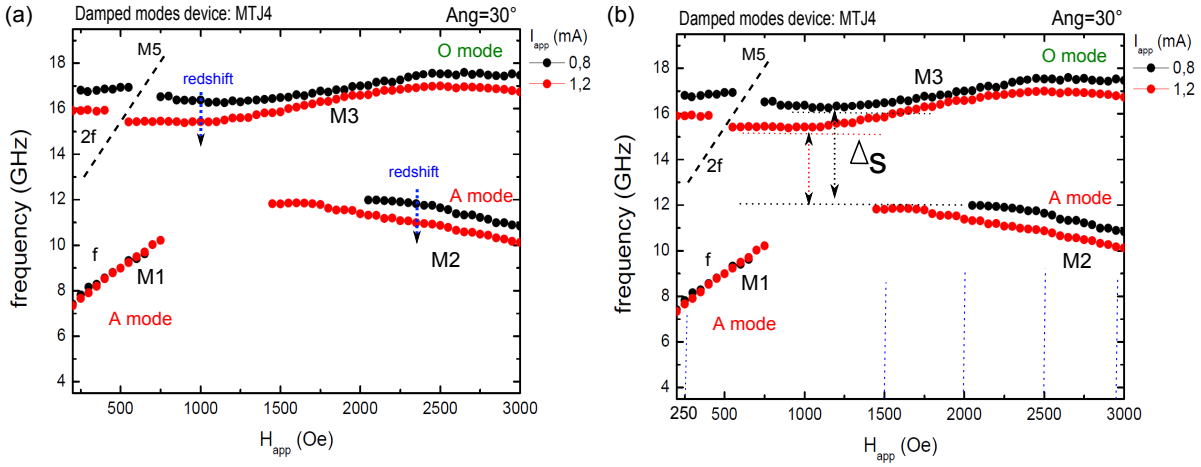

Figure 6.49 – Frequency dispersion diagram as a function of the field. We identify the damped A and O mode. (a) Arrows represent the region of the mode which are red-shifted. (b) We will study the linewidth behaviour for field values indicate in blue dashed lines.

We show the linewidth dispersion as a function of the current for H_{app}=250, 1000, 2000, 2500 and 3000Oe in order to be sure that we are measuring a damped mode, see Fig. 6.49 (b). In Fig. 6.50 (a)-(b) the three values of magnetic field correspond to the damped A and O mode respectively. The criteria $\Delta f=0 \longrightarrow I_{app}=I_c$ shows that I_c is more larger than the used current, hence those modes are damped modes. The smaller I_c is $I_c \approx > 1.125$mA.

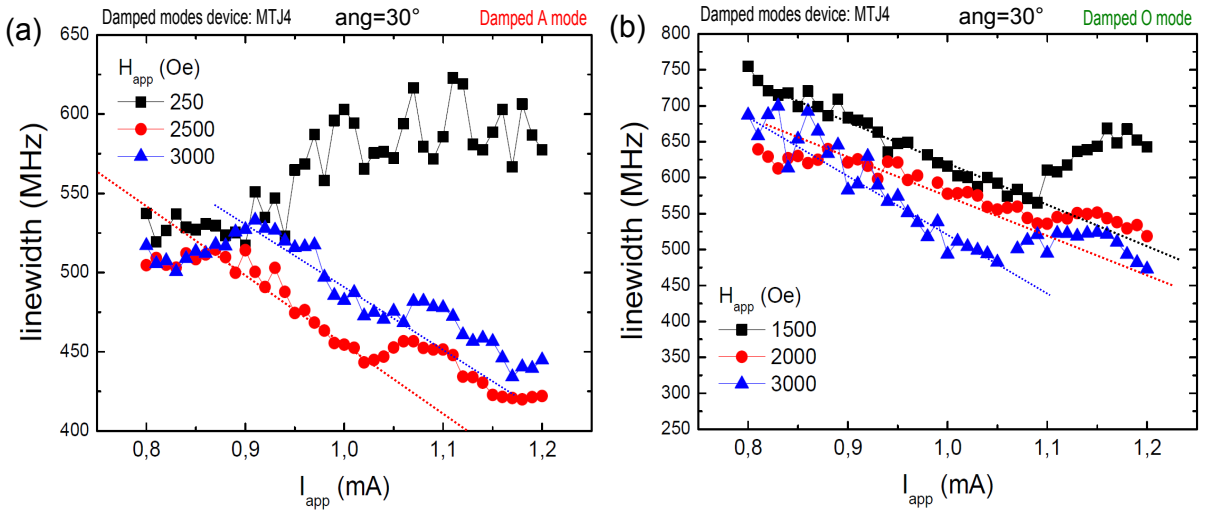

Figure 6.50 – Linewidth as a function of the current for different values of applied field. The damped A and O mode are show in (a) and (b) respectively, see Fig. 6.49 (b). The tangential line cross the I_{app} axis over the 1.2mA.

In order to study the linewidth or attenuation of the system as a function of the magnetic

field we show the frequency and linewidth dispersion in Fig. 6.51. Following the numerical results, we should expect that applying positive current, the damped A and O mode will follow the tendency of Fig. 5.13, passing from high to small linewidth in the case of the damped O mode or from small to high linewidth in the case of the damped A mode. For negative current the linewidth should show an inverse behaviour, see Fig. 5.15.

In the case of 0.8mA in Fig. 6.51 (a) we observe a decrease of the linewidth for the optic mode, which is expected. In the case of the damped A mode, for the branch of small fields the linewidth decreases (not in agreement with simulations). One possibility could be that this branch is not in a damped mode due to the positive current it will be excited first towards the STT mode. The other branch, high fields is in agreement with simulations, showing an increase of linewidth.

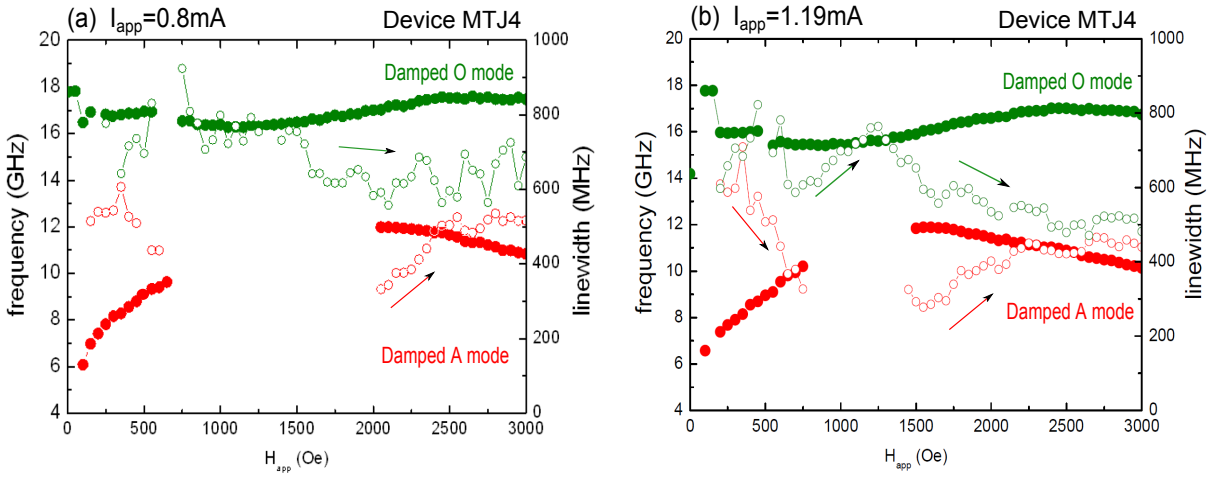

Figure 6.51 – (a)-(b) Frequency and linewidth of the A and O damped modes of the standard STO for 0.8mA and 1.19mA. Device MTJ4.

Increasing the current into 1.19mA the linewidth shows the same tendency, see Fig. 6.51 (b). The only difference is the increase of the linewidth for 500Oe<H_{app}<1150Oe which is not in agreement with the simulations. Again maybe the transition between the damped to the STT mode could change the expected tendency of the linewidth. In the next section we will increase the applied current in order to reach the STT modes.

6.4.3.2 STT modes, $|I_{app}|>|I_c|$

An important study has already done in our group, focused in the STT modes in the FL of the standard STO, [Houssameddine et al., 2008]. We will focus our study on the STT modes for the SyF dominant precession ($I_{app}<0$). We can be sure that the system reaches the STT excitation is with the criteria $\Delta f=0 \longrightarrow I_{app}=I_c$. We show I_c for two cases in Fig.

6.52 (a). The STT mode is accompanied by a increase in the power, see Fig. 6.52 (b)

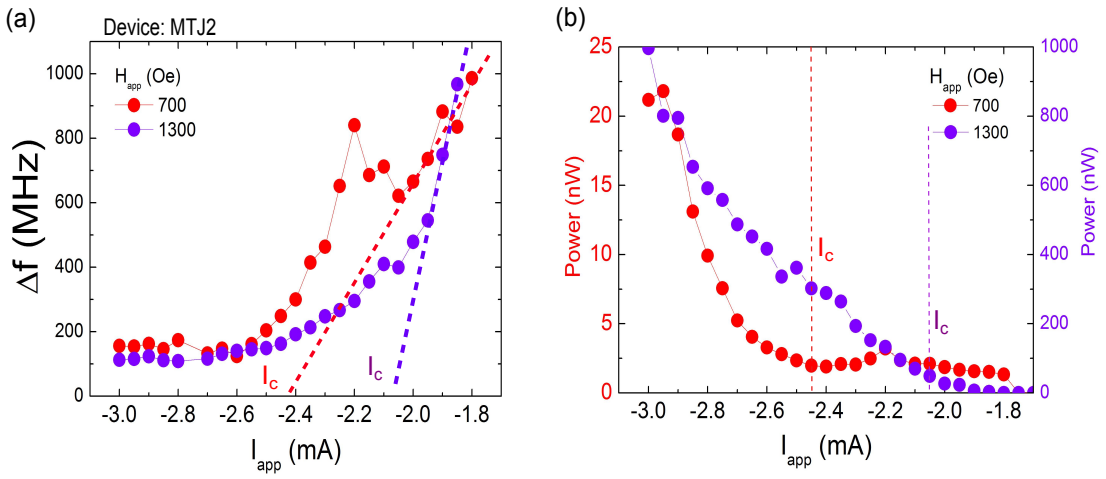

Figure 6.52 – (a) The linewidth versus applied current of SyF dominant precession on the MTJ2 device (I_{app}<0). The dashed lines are plotted in order to obtain the critical current which is the value of the crossing with the I_{app} axis. (b) The power of the emitted signal as a function of the current. The increase of power corresponds with the value of the critical current.

6.4.3.3 Frequency versus magnetic field

The state diagram of the **MTJ2** device for negative dc current values is shown in Fig. 6.53. We identify the STT O and A regions, of the SyF dominant precession, which are separated by the characteristic gap. In the case of STO based on MTJ it is not possible to reach the STT O mode of the steady state oscillations in the SyF pinned layer without the degradation of the MgO barrier. Between 0<H_{app}<250Oe the system shows a reversal of the FL magnetization. These are not excitations, just a huge band of noise.

In Fig. 6.54 we present four figures, corresponding to the evolution of the frequency as a function of the applied field, I_{app}=-2, -2.5, -2.8 and -3mA. The damped A mode is always present in the measurements. As in the case of the SV devices, the gap disappears upon increasing the applied current density. Using the results of the PSD of the magneto-resistance, Fig. 5.48 (b), the splitting seems to be closed by a low power peak (damped mode), giving the impression that the STT mode follows the tendency of a straight line. This mode is labelled as $f_{n,ex1}$. We can observe the closing of the gap also in the state diagram, indicated by a circle, see Fig. 6.53.

The frequency dispersion versus applied field is shown in Fig. 6.55 (a). We have included the damped modes as open circles. We notice how for applied dc current of -2mA and

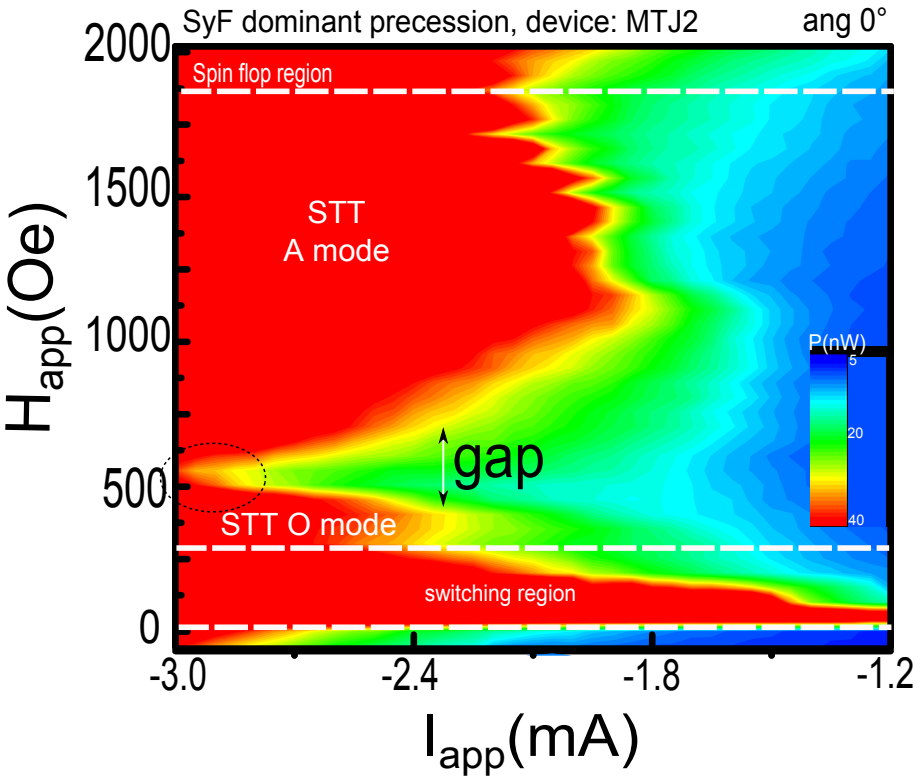

Figure 6.53 – (a) The state diagram of the MTJ2 device for negative dc current values (SyF dominant precession). We can observe the STT A and O regions separated by a gap. The closing of the gap is indicated by the circle. Device:MTJ2

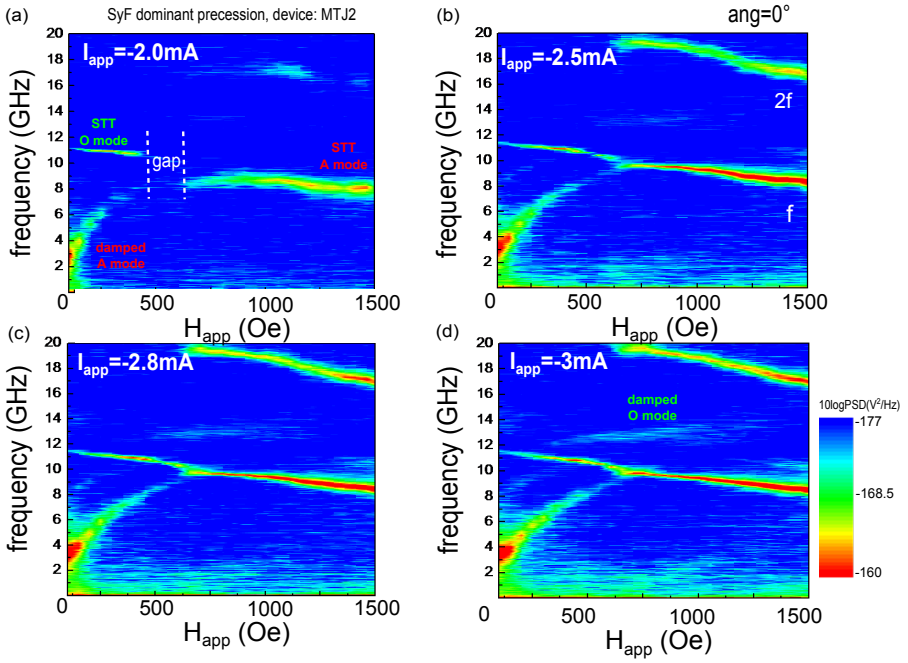

Figure 6.54 – The STT A and O mode for the SyF dominant precession are shown for different current values I_{app}=-2, -2.5, -2.8, -3mA. The gap disappears upon increasing the current.

-2.2mA, the excitations want to follow the damped A mode. For -2.8mA the gap is already close and the excitation does not present damped mode. The splitting also becomes small. In Fig. 6.55 (b) we show the frequency and linewidth for I_{app}=-2.8mA. The minimum linewidth found in the STT O mode was $\Delta f \approx 45$MHz for H_{app}=300Oe and for the STT A mode was $\Delta f \approx 56$MHz for H_{app}=850Oe.

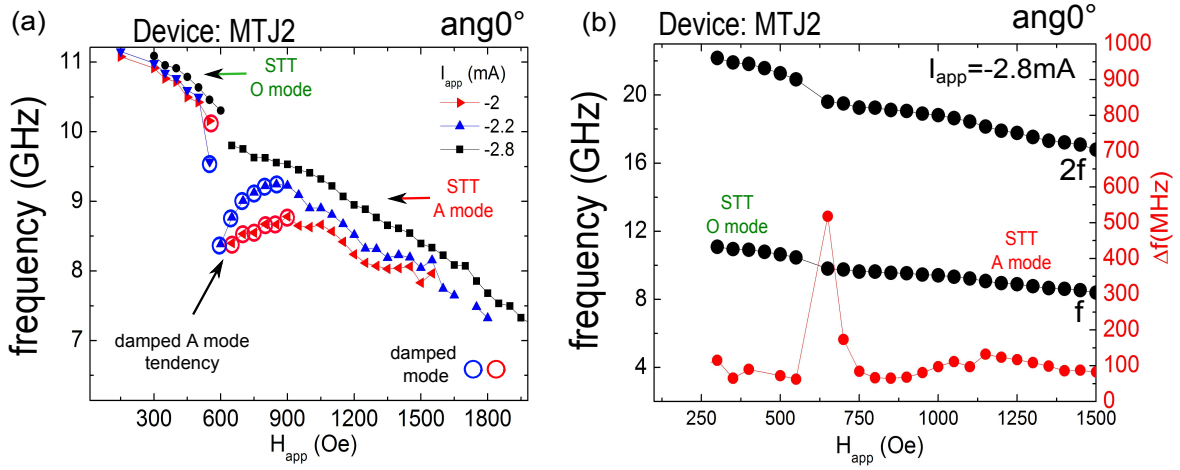

Figure 6.55 – (a) Frequency tuning as a function of the magnetic field with the STT and damped modes for the MTJ2 device. The open circles correspond to the damped modes. It is possible to observe the closing of the gap.

6.4.3.4 Frequency versus current

Now, we show the frequency as a function of the current for the same device **MTJ2**. In order to find the critical current we show the linewidth as a function of the current, see Fig. 6.56 (a). Then we can identify the damped and STT mode on the frequency dispersion of Fig. 6.56 (b). The shadow regions correspond to the damped modes. In Fig. 6.56 (b) the red curve corresponds to the highest critical current and only the symbols over -2.6mA could be taken into account. We notice that for H_{app}=400Oe the frequency current tuning shows a small tendency into the redshift regime, in all the rest of the field range the STT mode shows a blueshift regime. The transition from redshift to blueshift in a MTJ device is quite small. Even in the STT O mode the system is already in the blueshift regime so it dominates the STT mode. In comparison with the SV devices, in both cases the linewidth is smaller in the blueshift regime. The minimum $\Delta f \approx 67$MHz in the blueshift regime, I_{app}=-2.5mA. This blueshift regime is a feature of the STO with less than 50% of TMR [Houssameddine et al., 2008].

In some cases, as in the device **MTJ1**, we can measure the STT mode with several damped modes present in the spectrum. We show the frequency dispersion for the device **MTJ1**

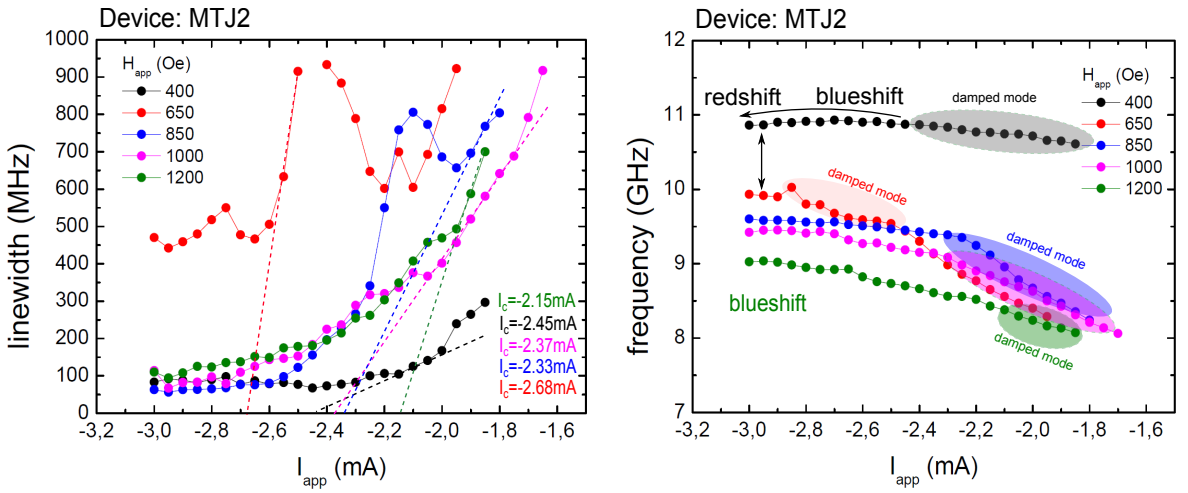

Figure 6.56 – (a) Linewidth as a function of the applied current to identify the critical current.(b) Frequency tuning of the STT A and O mode as a function of the applied dc current (device MTJ2). The open circles correspond to the damped modes. We identify excitation for three regions, corresponding to the small and high magnetic field (before and after the gap) and the spin-flop region.

of TMR=55%, for positive and negative current (FL and SyF dominant precession). It has been chosen four values of magnetic field see Fig.6.57. For small values of magnetic field (a)-(b) for H_{app}=0 and 252 Oe and for high field values (c)-(d) for 1111 Oe and 1414 Oe.

In Fig.6.57 (a), H_{app}=0 we observe three modes well defined for positive current. In the case of (b), for H_{app}=252Oe presents a small linewidth and a redshift $df/dI_{app}<0$. Taking into account the previous results from Helmer [Helmer et al., 2010] the lower frequency mode (below M1) could be defined as an edge mode. In this region, the negative current is not high enough to measure the STT O mode.

In Fig. 6.57 (c) and (d), for high field values (after the gap) and positive current the STT O mode (M3) present a blueshift regime (which is a features found by [Houssameddine et al., 2008] in low TMR devices). For negative current the mode M2 and M_{23} shows a blueshift regime. As it has been shown for the case of the MTJ2, Fig. 6.56 the region of redshift regime is small for the MTJ devices.

In the Fig. 6.58 (a), we show the frequency dispersion as a function of the field close to the spin flop field for negative current, M2 mode is excited. We realize the coexistence of at least four modes. The STT A mode is labelled as M_{23}, the higher order modes M_{21} and M_{22} and the damped mode M2. It is important to remark that the large size (90×190nm) of the sample contributes to the creation of the edges modes in this devices. The linewidth as a function of the dc current of M2 and M_{23} are shown in Fig. 6.58 (b)

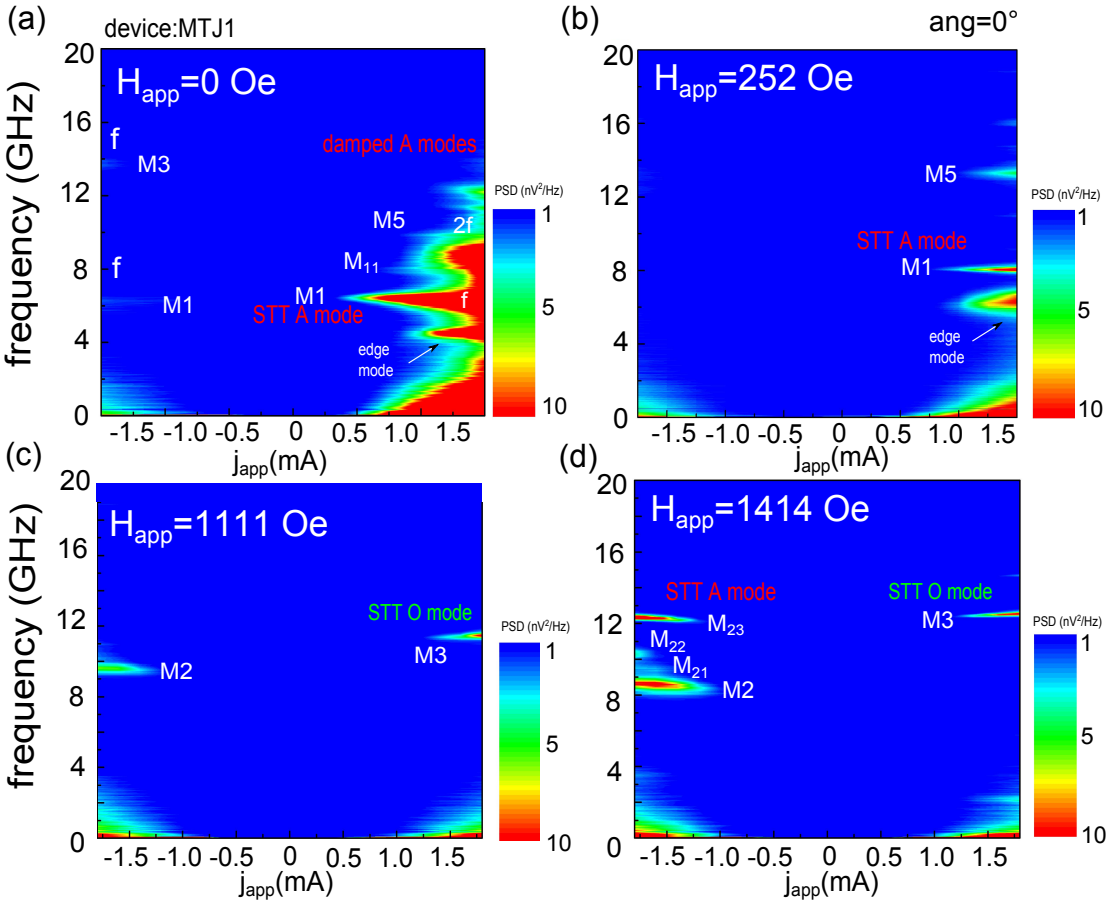

Figure 6.57 – Frequency tuning measured in the device MTJ1 of TMR=55%. For small field (before the gap), H_{app}=0 and 252Oe, we identify the different STT and damped modes for positive and negative current. The dc current is not enough to observe the STT O mode. For high fields (after the gap), H_{app}=1111Oe and 1414Oe, the STT A and O modes appear. A low frequency mode is identify as an edge mode.

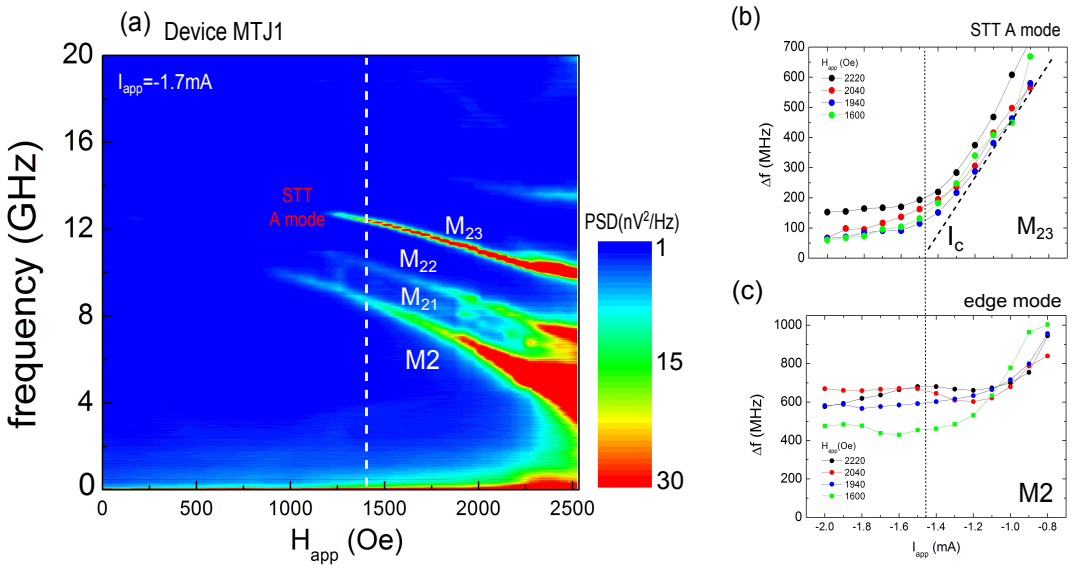

Figure 6.58 – (a) Frequency dispersion of the SyF dominant precession for I_{app}=-1.7mA. (b)-(c) Linewidth as a function of the dc current density for the auto-oscillations (M_{23}) and the edge mode (M2). The noisy region is close to the spin flop value.

and (c) to be sure that the mode is in a STT regime. A small linewidth is found in this STT A mode, Δf=50MHz. We found that the position of the STT mode is not always the low frequency mode and the STT as in this case could be follow the frequency dispersion of a higher order mode.

6.5 Summary

In this chapter we have shown the main features and the performance of the standard STO nanopillars, based on SV and MTJ. We characterized several devices, of circular and elliptical cross sections, finding features that could be defined as general characteristics of this type of devices. Structurally the SV devices can endure high current (metallic spacer) which is a difference with the STO based on MTJ. This is the main limiting factor to a deep study for the MTJ devices.

The dipolar field plays a crucial role in understanding the magnetization dynamics of the STO. Due to its conservative origin the system will suffer a hybridization generating a new acoustic and optical modes of a mix between the SyF pinned layer and FL modes. Experimentally it is possible to identify the influence of the dipolar field which is proportional to the gap and splitting in the state diagrams and frequency dispersion diagrams for the SV and MTJ, a confirmation of the predictions of the numerical simulations.

Furthermore the influence of the dynamical RKKY coupling in the SyF pinned layer has been evidenced. The gradual evolution of the tuning df/dI_{app} from redshift to blueshift is an effect directly related with the dynamical RKKY torque in the SyF pinned layer. The **smaller linewidth** was found in the blueshift regime, where the dynamical RKKY coupling has more impact in the dynamics. In agreement with the numerical simulations.

The existence of the interaction between the STT mode with the damped modes (or higher order modes) depends fundamentally of the intrinsic parameters as the RKKY coupling, dipolar field or shape anisotropy. These parameters will change the damped modes tendency. These interactions and its influence in the magnetization dynamics were predicted in the numerical chapter and found in the experiments. A consequence of the interaction is the appearance of kinks or jumps.

The reduction of linewidth could be product of the previous enhance due to the crossing of modes, which is common in MRJ devices, or a reduction in the region were the STT O mode and the damped SO mode interact, which was observed in SV devices as it was predicted in simulations. During this interaction a reduction of the non-linear character of the system were found.

One advantage of the STO is the possibility to obtain STT FL excitations (STT O mode) at smaller field, even at zero field. However the IPP regime is presented only for a small range of dc current. This IPP regime evolves into an OPP non periodic regime, generating a change in the frequency tuning.

As a summary of the STO nanopillars performance, we show the state diagram with the corresponding features of the different regions of steady state excitations. We present the regions with redshift, blueshift regime, the out-of plane (OPP) and non-coherent precession. The crossing of modes is indicated as well. In Fig. 6.59 (a) and (b) we shown the final state diagram for a SV and MTJ STO respectively.

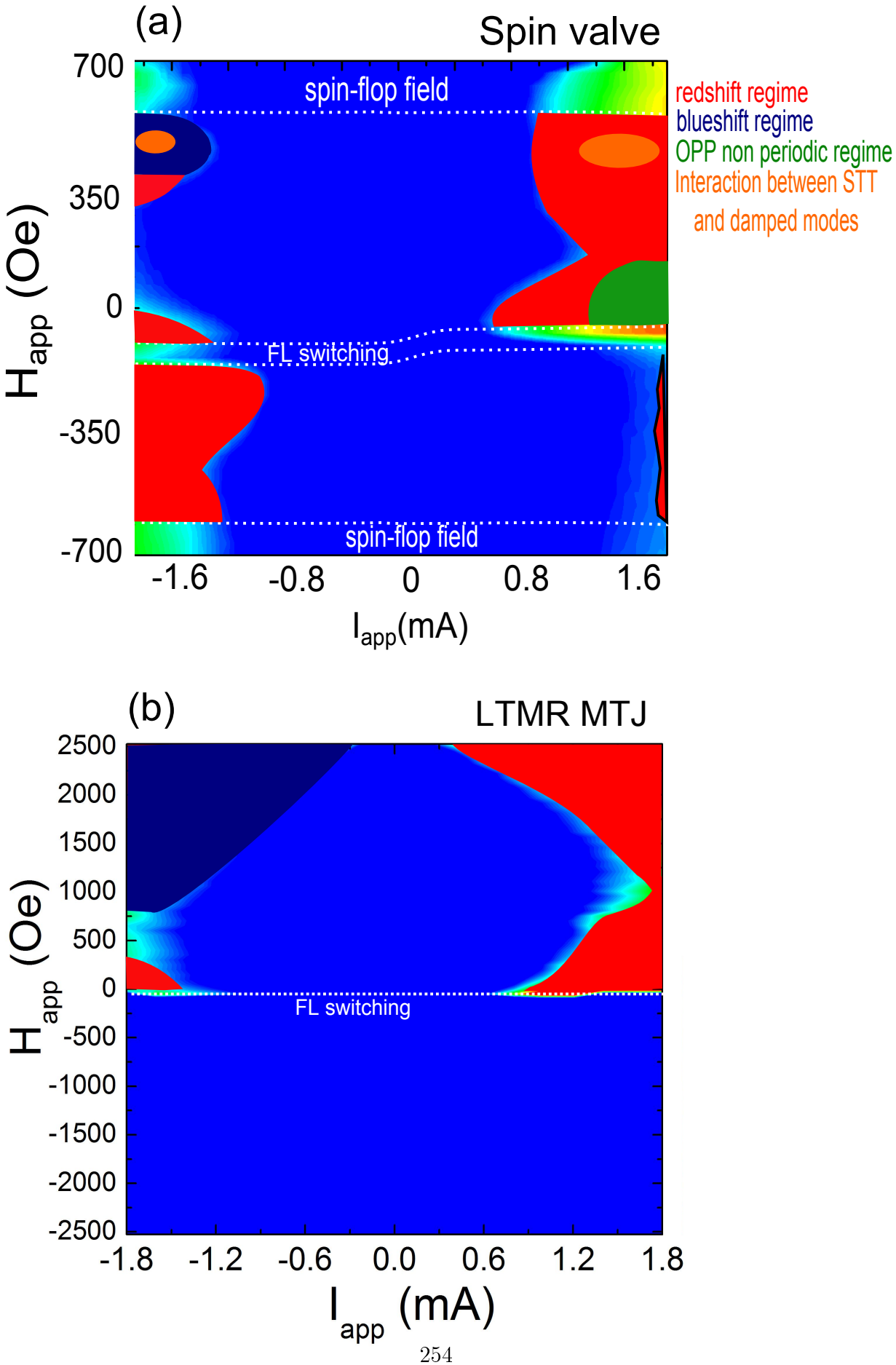

Figure 6.59 – Summary of features of the STO in the state diagram for the SV devices in (a) and for a MTJ in (b).

Chapter 7

Spin Transfer Torque Nano-oscillator based on Magnetic Tunnel Junction with double SyF layer

In this last chapter we present a new STO structure based on an MTJ and composed by two SyF layers, called double SyF (D-SyF) STO. In this structure, the SyF on bottom will be labelled SyF pinned layer (pinned by an exchange bias) and the SyF unpinned on top as SyF free layer (SyF-FL), see Fig. 7.1 (b). As it has been explained, the different couplings between the layers of the structure will generate features, that will be studied. The samples to be studied in this chapter were introduced in sec. 3.3.4. This chapter shows the following structure.

1. **Magnetic static properties**. The experimental MR loops of the magnetic structure provide important information, about the magnetic configuration, P and AP states (low and high resistance) of the D-SyF STO.
2. **Numerical simulations**. We show the numerical simulated hysteresis, MR loops and the FMR modes of the D-SyF STO, in order to verify and quantify the RKKY coupling of the SyF-FL and the SyF pinned layer.
3. **Excitations modes**. We will identify the different STT and damped modes of the emitted spectrum. We will explain the different features of the measured frequency field and current dispersion.
4. **Further results** In the end of this chapter we will show some further results with interesting features.

7.1 Static properties of the STO with double SyF layer

In magnetic multi-layer structures, the MR curve will provide the first picture about the magnetic configuration of the system as a function of the applied field. This curve will be measured for the D-SyF STO in order to identify the magnetic configuration of each SyF layer and the high and low resistance states. In Fig. 7.1 (a) we show an experimental MR curve of the device **D-SyF1**. Arrows correspond to the magnetization of each layer.

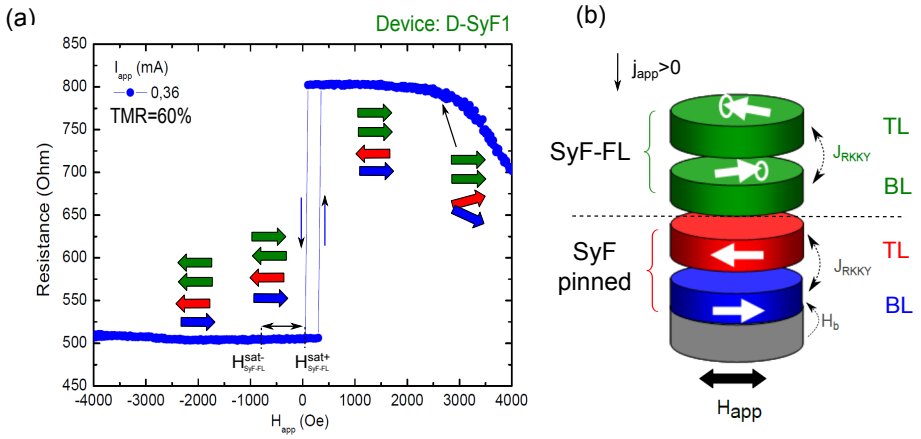

Figure 7.1 – (a) MR curve of the device D-SyF1. Arrows correspond to the magnetization of each ferromagnetic layer. Sweeping the magnetic field from negative to positive, the plateau of the SyF-FL is defined between H^{sat-}_{SyF-FL} and H^{sat+}_{SyF-FL}. In (b) the D-SyF STO structure is showed. Following the convention for $j_{app}>0$ it is induced dominant precession in the SyF-FL.

Sweeping the magnetic field from high positive towards negative field values, the first layer to rotate away from the saturation state is the TL of the SyF pinned layer, due to the strong RKKY coupling. In this spin flop region ($H_{app}>3000$Oe) the SyF-FL magnetizations remain in the saturation state (positive direction, green arrows). The SyF pinned layer reaches its plateau region close to 3000 Oe, where the high state of resistance is reached as well, see Fig. 7.1 (a).

When the magnetic field decreases towards to zero one of the layers of the SyF-FL switches abruptly, as in the numerical predictions of Fig. 4.6 (a)-(b) for a SyF with weak RKKY coupling. The switching corresponds to the layer which can minimize the Zeeman energy. The product of the saturation magnetization times the thickness for the TL is larger than for the BL in the case of the SyF-FL, $M_{S,SyF-FL,TL}.d_{SyF-FL,TL}>M_{S,SyF-FL,BL}.d_{SyF-FL,BL}$, see structure in sec. 3.3.4. The BL of the SyF-FL presents the smaller net magnetic moment, switching first than the TL. Due to this magnetization reversal, the total MR loop switches from AP to P (high towards low resistance). We have to remark in this point that the SyF-FL, with weak RKKY, does not present a spin flop region and there is only

a plateau region (SyF-FL plateau). The static dipolar field along the x axis, from the SyF pinned layer does not stabilize the SyF-FL plateau, due to the orientation of the magnetizations, see Fig. 7.2 (a).

One idea in order to obtain a SyF-FL plateau in the AP state (high resistance) should be fabricated the structure with the inverse order of layers i.e the $M_{S,TL}d_{TL}<M_{S,BL}d_{BL}$, Fig. 7.2 (b). If the magnetic field is increased towards high negative values, the SyF-FL

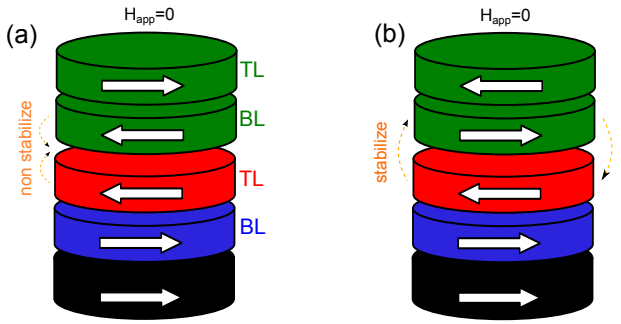

Figure 7.2 – Magnetic configuration of the D-SyF STO structures. (a) The case studied in this thesis where the SyF is not stabilized by the dipolar field of the SyF pinned. (b) The ideal magnetic configuration where the SyF-FL is stabilized.

will be saturated first and then, the SyF pinned layer will reach the spin flop region and the saturation. If the magnetic field is swept from negative to positive the first layer of the SyF-FL to switch is the TL, generating the SyF-FL plateau in the P state. Then the SyF-FL is saturate when the BL switched and the system comes back to the AP state.

In appendix B section 9 we show the magnetic characterization of D-SyF structures that were realized at SPINTEC/Leti at the start of the thesis. These studies show that the RKKY coupling of the SyF-FL is reduced 10 times for equal ruthenium thickness due to the roughness of the interfaces. This fact produces a quite important reduction of the plateau and the disappearance of the spin flop region of the SyF-FL, see Fig. 9.3. Roughness effects have been discussed earlier theoretically by Bruno [Bruno and Chappert, 1991], [Bruno and Chappert, 1992] and experimentally by Parkin [Parkin et al., 1990], see Fig. 1.11 (a)-(c). Hence the RKKY of the top SyF is always weaker than the bottom SyF. This has been corroborated for Cu and MgO spacer. One example of the degradation of the MgO barrier is shown in Fig. 7.3 (a) for the device D-SyF4. The TMR decreases from 75% to 38%. Increasing the current I_{app}=1.3mA, the MR curve of the same device shows fluctuation in the resistance of the AP state, pink shadow region in Fig. 7.3 (b). We note that the switching of the BL of the SyF-FL is reduced.

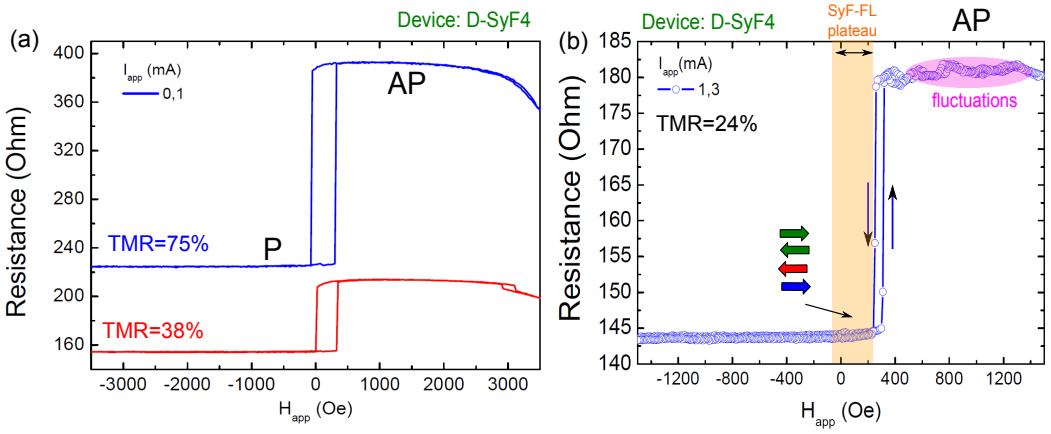

Figure 7.3 – (a) MR curve of the device D-SyF4 before and after degradation. (b) MR curve of the device D-SyF4 for I_{app}=1.3mA. Arrows correspond to the magnetization of each ferromagnetic layer in the SyF-FL plateau, orange shadow region. The positive high current produces fluctuations in the magnetization in the AP state, pink shadow region.

7.2 Static and dynamic numerical simulation of SyF-FL

Numerical simulation of the hysteresis loops and the FMR modes of the D-SyF STO structure will be shown in this section. Parameters of the numerical simulations are given in table 7.1. We study the hysteresis loop of the SyF-FL for several conditions of the RKKY coupling, see Fig. 7.4 and its corresponding FMR modes are shown in Fig. 7.5.

7.2.1 MH loops

In Fig. 7.4 (a) the hysteresis loop of an isolated SyF-FL is shown for a weak RKKY coupling of SyF-FL, J_{RKKY}=-0.1mJ/m^2. The magnetizations (green arrows) switch directly from the saturation into the plateau due to weak RKKY coupling. In all the cases, the sweeping of magnetic field was from high positive values to negatives values. Fig. 7.4 (b) corresponds to a SyF-FL with positive RKKY coupling J_{RKKY}=0.1mJ/m^2, (ferromagnetic coupling) which is coupled by dipolar field with the SyF pinned layer. The hysteresis loop shows the reversal of both ferromagnetic layers together. In Fig. 7.4 (c) we present the hysteresis loop of the case of two uncoupled layers (J_{RKKY}=0.1mJ/m^2=0) but coupled by dipolar field with the SyF pinned layer. The shape of the hysteresis loop is quite similar to Fig. 7.4 (a) but with a small shift in field. The Fig. 7.4 (d) we show the numerical simulation for a hysteresis loop for the D-SyF STO of the experiments, using a weak RKKY coupling of the SyF-FL of J_{RKKY}=-0.1mJ/m^2 and including dipolar field coupling between the pinned SyF and SyF-FL.

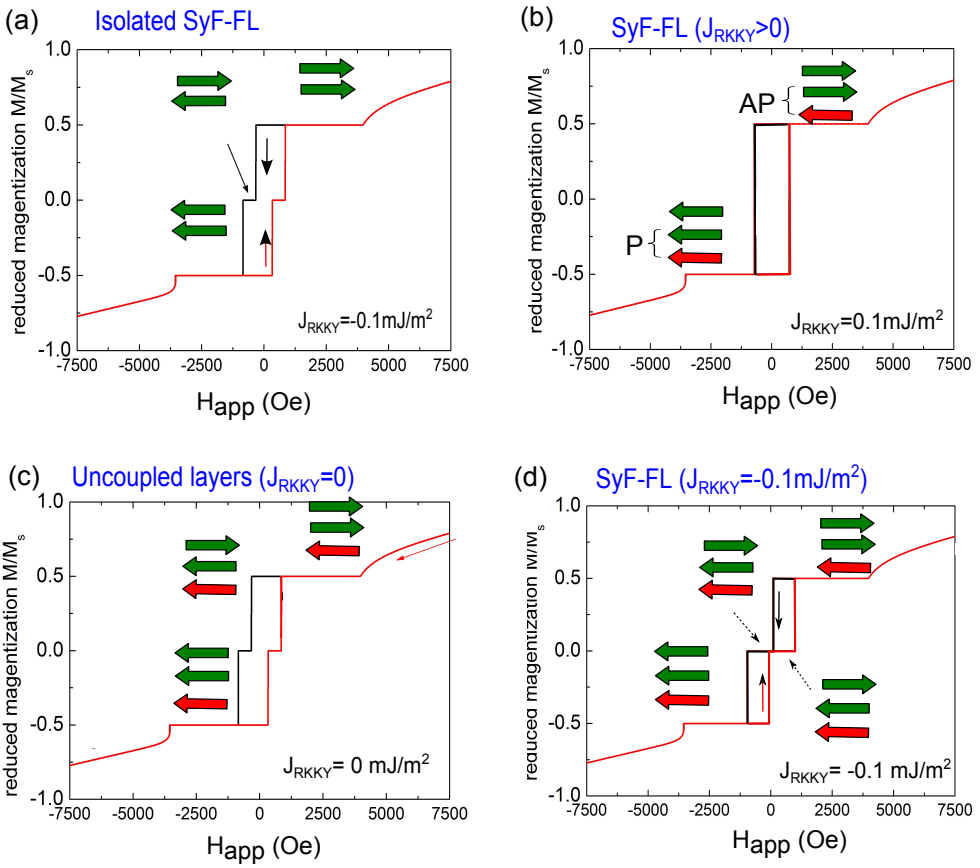

Figure 7.4 – Hysteresis loop of the D-SyF STO taking into account a isolated SyF-FL (without dipolar field) in (a). A coupled by dipolar field SyF-FL is shown for different cases. In (b) the SyF-FL with ferromagnetic RKKY coupling, (c) two uncoupled layers and (d) SyF-FL with weak RKKY coupling. In all the figures the black line indicate the sweeping from positive to negative fields and the red one from negative to positive. Parameters in table 7.1.

	SyF-FL				SyF pinned		
	TL	Ru	BL	MgO	TL	Ru	BL
Ms	1470kA/m		1112.5kA/m		1060kA/m		1470kA/m
K_u	7957.75J/m^3		7957.75J/m^3		7957.75J/m^3		7957.75J/m^3
t	3.6nm	0.8nm	3.9nm	1.0nm	2.0nm	0.8nm	1.8nm
N_x N_y N_z	0.042085 0.078372 0.879543		0.044620 0.083119 0.872260		0.027061 0.050280 0.922658		0.024952 0.046343 0.928705
H_b			0		0		1000 Oe
J_{RKKY}	-0.1 mJ/m^2				-1.5 mJ/m^2		
α	0.02						
h	0.3						
$\bar{p}$			m_{TL}		m_{BL}		

Dipolar tensor

$N^{\infty}_{x,BL\to TL}$ = 1.706766x10^-25 $N^{\infty}_{x,BL\to TL}$ = 1.435170x10^-25
$N^{\infty}_{y,BL\to TL}$ = 3.195475x10^-25 $N^{\infty}_{x,TL\to TL}$ = 1.860979x10^-25
$N^{\infty}_{z,BL\to TL}$ = -4.902441x10^-25 $N^{\infty}_{x,BL\to TL}$ = 5.075982x10^-25

$N^{\infty}_{x,BL\to BL}$ = 2.172154x10^-25 $N^{\infty}_{y,BL\to TL}$ = 2.666935x10^-25
$N^{\infty}_{y,BL\to BL}$ = 4.071497x10^-25 $N^{\infty}_{y,TL\to TL}$ = 3.476933x10^-25
$N^{\infty}_{z,BL\to BL}$ = -6.243651x10^-25 $N^{\infty}_{y,BL\to TL}$ = 9.517479x10^-25

$N^{\infty}_{x,TL\to BL}$ = 3.079646x10^-25 $N^{\infty}_{z,BL\to TL}$ = -4.102105x10^-25
$N^{\infty}_{y,TL\to BL}$ = 5.773958x10^-25 $N^{\infty}_{z,TL\to TL}$ = -5.337912x10^-25
$N^{\infty}_{z,TL\to BL}$ = -8.853604x10^-25 $N^{\infty}_{z,BL\to TL}$ = -1.459346x10^-24

Table 7.1 – Parameters of numerical simulation of the D-SyF structure.

7.2.2 FMR loops

The FMR modes of the isolated SyF-FL for J_{RKKY}=-0.1mJ/m^2 system are shown in Fig. 7.5 (a). As we showed in numerical simulation we observe here two modes (acoustic and optic) in comparison with a single FL. The FMR modes of the SyF-FL (with positive RKKY coupling J_{RKKY}=0.1mJ/m^2, ferromagnetic coupling) which is coupled by dipolar field with the SyF pinned layer is shown in Fig. 7.5 (b). We can observe a splitting in the crossing of the modes around H_{app}=1125Oe. The FMR modes in Fig. 7.5 (c) correspond to the dipolar coupling between a SyF pinned with two uncoupled layers. In all these three cases we superposed the frequency dispersion of the single BL to observe the difference with the case of a SyF. The Fig. 7.5 (d) shows the SyF-FL with weak RKKY and with dipolar coupling from the SyF pinned layer. We will focus our study in the AP state, orange shadow region. We observe a weak splitting in the crossing of the FMR modes of both SyF layers, see sec. 3.3.6.

Fig. 7.5 (d) shows three low frequency modes that we will label as follow. Overcoming the two splitting, we define the low mode as acoustic (A) mode, and the high as the optic (O) mode, following the convention of the standard STO. The intermediate mode is labelled as AO mode and while highest mode is the super optic (SO) damped mode.

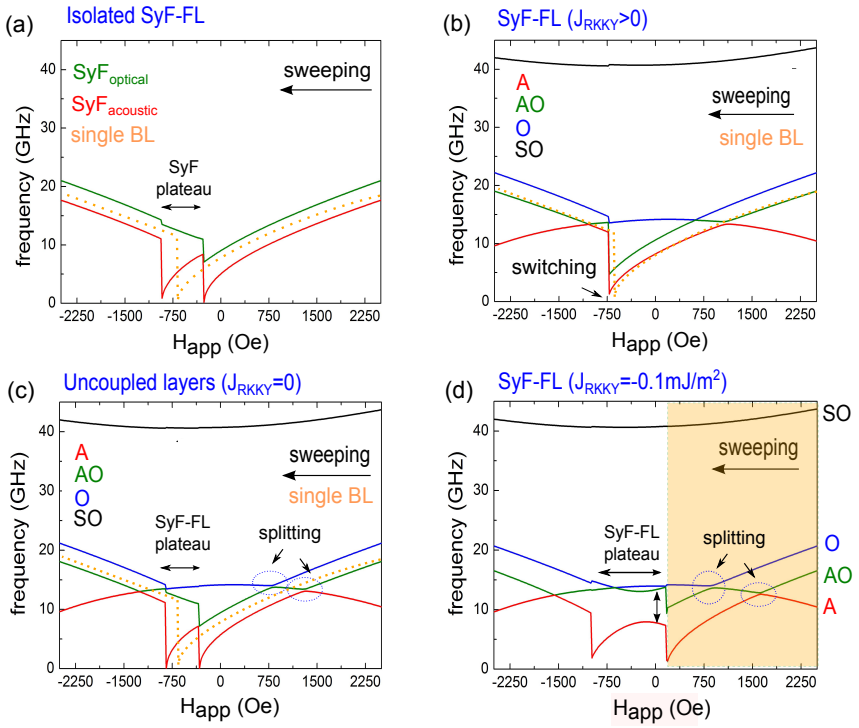

Figure 7.5 – FMR modes of the D-SyF STO taking into account an isolated SyF-FL (without dipolar field) in (a). In (b) a SyF-FL with ferromagnetic RKKY coupling, (c) two uncoupled layers and (d) SyF-FL with weak RKKY coupling. The orange region indicates the region over study (AP state). We superposed the frequency dispersion of the single BL. Parameters in table 7.1.

In Fig. 7.6 we show the numerical simulation of the hysteresis loop, the MR curve and FMR modes for the simulated structure D-SyF which will be studied in this chapter. In Fig. 7.6 (b) the dashed circles indicate the two splitting in the crossing of the damped modes and the orange shadow region indicate the AP state where we will focus the study of the STT modes. The size of the plateau of the SyF-FL is about ≈1000Oe for J_{RKKY}=-0.1mJ/m^2 which is larger in comparison with the experimental results as we will show later.

7.2.3 State diagram

The experimental state diagram will be compared to the numerical simulation of the critical boundaries for the D-SyF STO. The state diagram of the D-SyF STO is shown in Fig. 7.7. We can observe a small gap due to the small dipolar field from the SyF pinned layer on the FL and the two regions of excitations for positive and negative current density. At H_{app}=0 the critical current for the SyF-FL is comparable to the corresponding one of the SyF pinned layer. The crossing of modes of Fig. 7.6 (d) are indicated in the state diagram, green dashed lines.

7.3 Experimental state diagram of the the D-SyF STO

As in the case of the standard STO based on MTJ, the state diagram (H_{app} vs I_{app}) of the D-SyF provides the magnitude of applied field and current that the system needs, in order to reach the auto-oscillations. The experimental state diagram is shown in Fig. 7.8 for the device **D-SyF3**. The arrows indicate the magnetic configuration of the layers. In (a) the full range of the state diagram is shown where the gap is weak in comparison with the case of the standard STO. This was shown in the previuos section of simulations. In this gap region, the state diagram shows also the PSD of all modes including acoustic and optical modes for the SyF-FL and SyF pinned layers.

In Fig. 7.8 (b) the zoom of the state diagram shows that for positive current the small gap which appears (H_{app}<600Oe) also in the the numerical simulation, Fig.7.7. The critical current of the SyF-FL dominant precession is almost the same in comparison with the SyF-pinned dominant ±1.2mA. The critical current of the SyF-FL dominant precession decreases towards 1.0mA for H_{app}>600Oe.

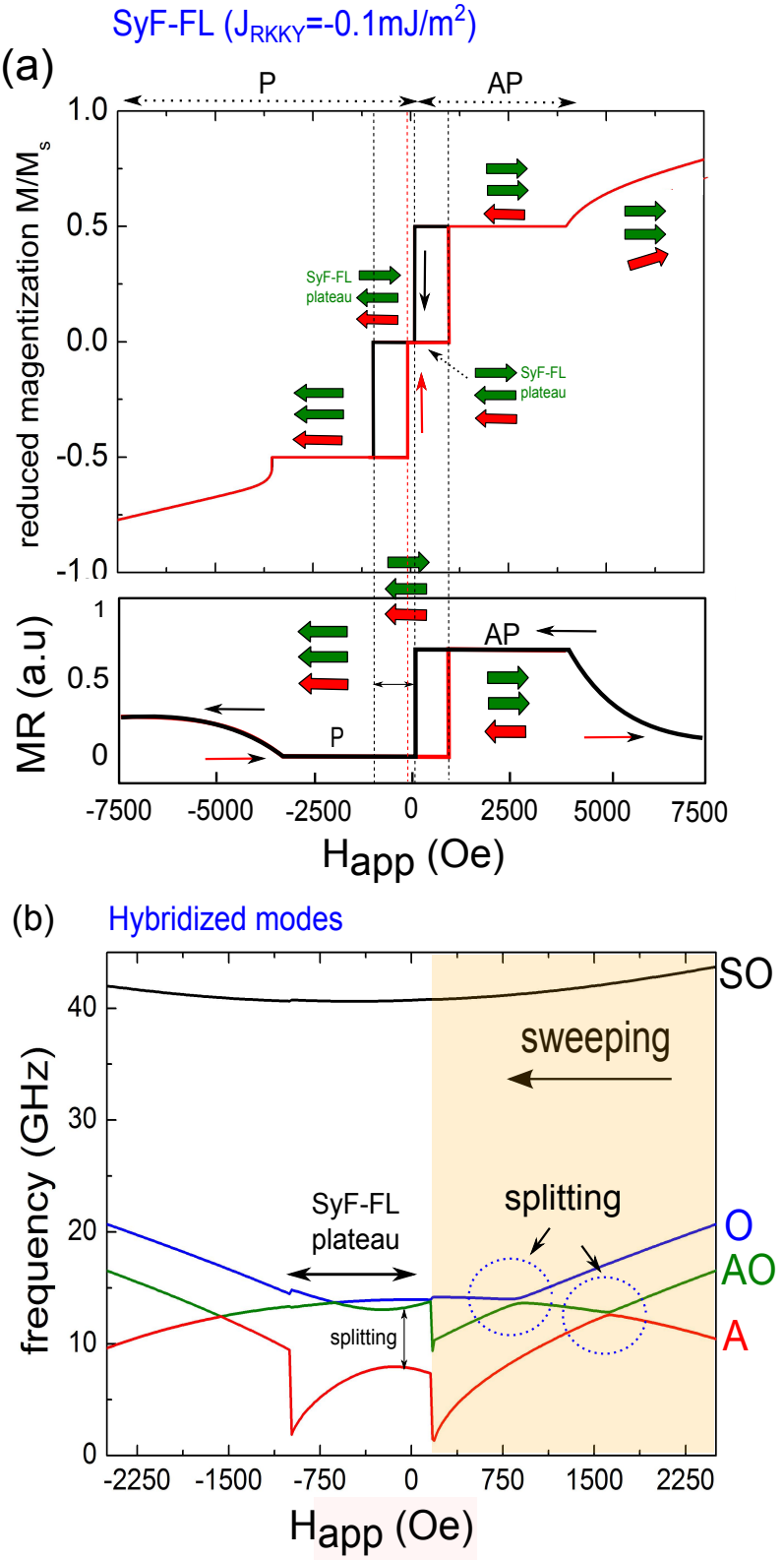

Figure 7.6 – Numerical simulation of the structure D-STO under study. (a) Hysteresis and MR curves for a SyF-FL with weak RKKY coupling J_{RKKY}=-0.1mJ/m^2. (b) The corresponding FMR modes. The orange region indicates the region over study (AP state). Parameters in table 7.1.

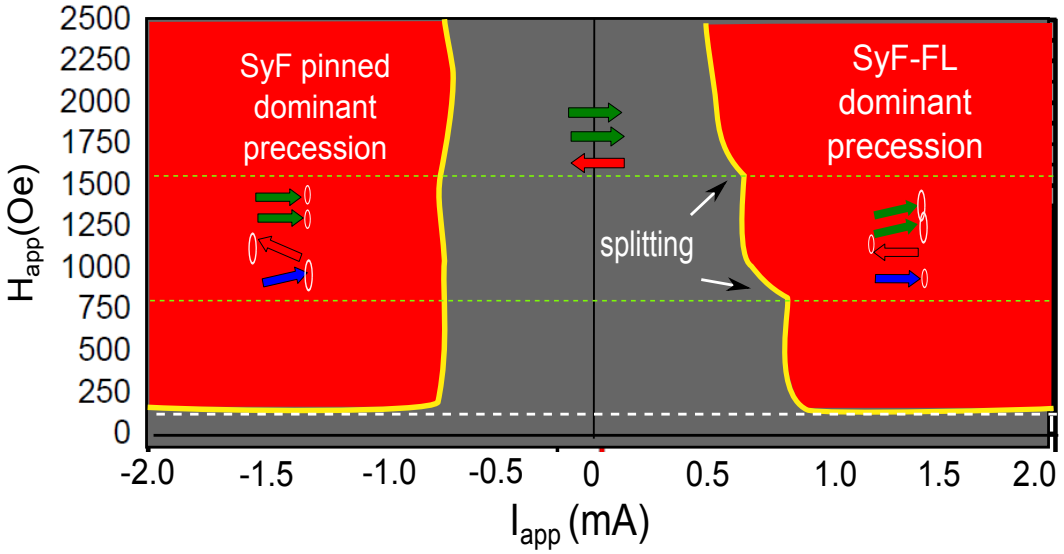

Figure 7.7 – Numerical simulation of the state diagram of the D-SyF STO. Splitting are indicated by the green dashed lines. Parameters in table 7.1.

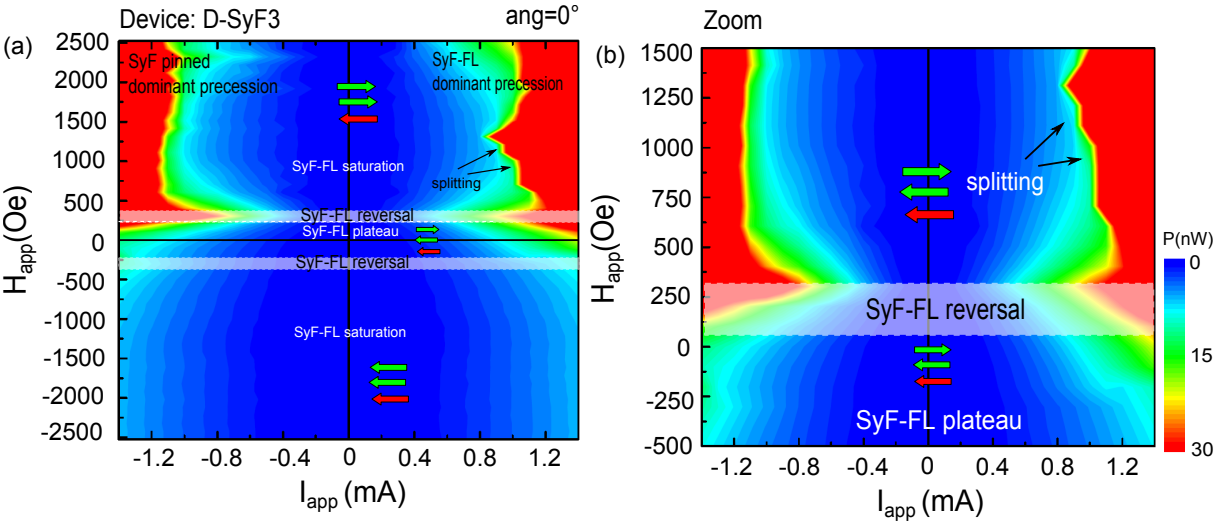

Figure 7.8 – State diagram of device D-SyF3 for the full magnetic field range. (b) Zoom close to zero applied field in order to show the SyF-FL excitations.

7.4 Evidence of influence of the dipolar field in the D-SyF STO structure

In the chapter 6 we showed the influence of the dipolar field in the form the hybridization of the modes, the appearance of a gap (in the damped A mode) and the splitting (between the damped A and O mode). In the case of the D-SyF STO we start with the damped modes to evidence the dynamical dipolar field interaction. A corresponding diagram is shown in Fig. 7.9 for the device **D-SyF3** and for an angle of 30°.

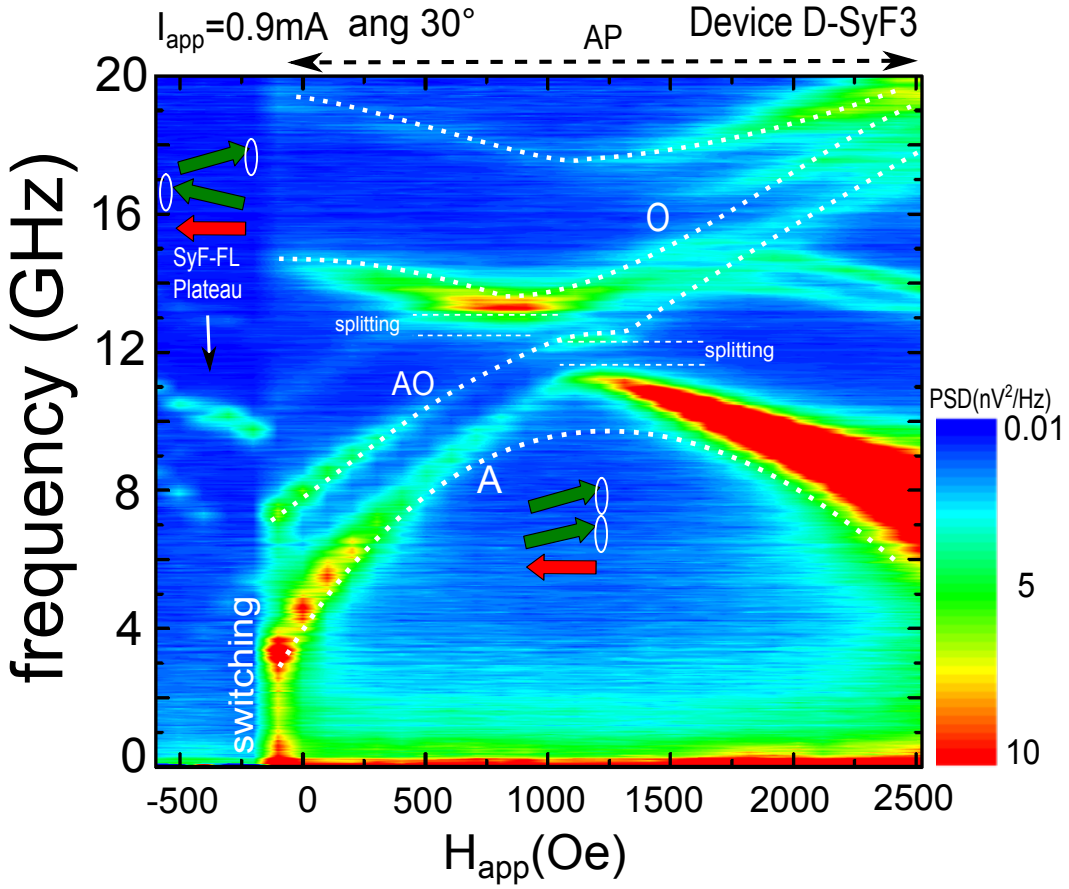

Figure 7.9 – (a) Frequency vs. field diagram, in the AP state (high resistance), of device D-SyF3 for I_{app}=0.9mA. Dashed lines correspond to the damped A, AO, and O modes defined in the numerical section, see Fig. 7.5 (d) only as a visual reference. We observe the excitation of the plateau region of the SyF-FL close to zero applied field. Device D-SyF3.

Comparing the AP region of this frequency diagram with the corresponding one of the standard STO of Fig. 6.16 for 30° we notice the similarities in the frequency dispersion. In the case of the standard STO, the FL precession frequency (positive current) will increase with the magnetic field. Now for the device D-SyF3, the frequency dispersion of the SyF-FL also increases with the field but shows two modes[1]. The full frequency dispersion

[1]The TL and BL of the SyF-FL will be in the saturated state in almost all the positive range of

diagram is given by the four hybridized modes, as shown in the numerical simulation in Fig. 7.6 (b). In Fig. 7.9 the characteristic gap is almost closed for this structure and we notice the presence of the three hybridized damped modes (dashed lines). In experiments the SO mode is not visible since the frequency range is limited to 20GHz. We should remark that in the case of the standard STO the distance between the higher order mode M_{11} and the fundamental mode is almost 1GHz and for the case of the D-SyF the A and AO mode are separated 2.4GHz for small fields, showing an important difference. We observe also the two splittings around 1000Oe, between the A and AO and between AO with O modes.

7.5 Frequency field dispersion of the SyF-FL

In this section we show the frequency dispersion as a function of the magnetic field for the SyF-FL (I_{app}=0.84mA) around zero field, in order to observe the damped modes in the plateau region of the SyF-FL and clarify the existence of a weak RKKY coupling. We started with an elliptical device **D-SyF2** because the anisotropy will help us to stabilize the magnetization in the direction of the easy axis[2]. The sweeping from positive towards negative magnetic field will give us the frequency tendency of the damped modes in the three regions of magnetic configuration (positive and negative saturation and in the plateau). As we know the SyF-FL is not pinned by an anti-ferromagnetic layer, thus its critical current will be smaller than the SyF pinned layer.

In Fig. 7.10 (a), (b), we can observe the three regions of excitations, characteristic of the SyF-FL. For instance in (a), for high fields (positive H_{app}>100Oe and negatives H_{app}<-250Oe) the system is in the saturation state and around zero field (-250<H_{app}<100Oe) in the plateau region (AP state). We used a logarithmic scale to observe the modes with small power. If we compare both figures (a) and (b), the plateau region is shifted, i.e the switching for positive and negative current is not the same. Since for the measurement the current was fixed and the field is swept from positive to negative, we confirmed that for positive current values the parallel state between the TL of the SyF pinned and the BL of the SyF-FL is reached at H_{switch}=+100Oe. In the case of negative values of dc current the anti-parallel state is favoured and with this fact, the switching or reversal of the BL is induced at lower field value H_{switch}=-60Oe. For positive current, 7.10 (a), we indicate the more important damped modes, A, AO and M5 (M5 is the 2f harmonic of

magnetic field.

[2]In the case of the standard STO the FL is always pointing in the direction of the magnetic field but in this case the D-STO the SyF-FL can present an arbitrary direction.

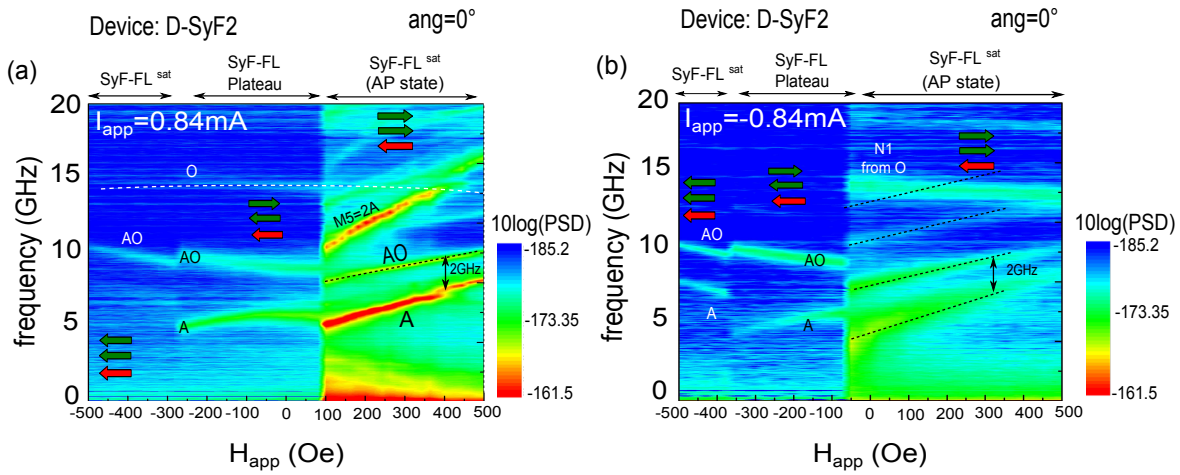

Figure 7.10 – Frequency field dispersion of the SyF-FL for positive (a) and negative current (b) (I_{app}=±0.84mA). In both figures we identify three regions, the right correspond to the saturation magnetization of the SyF-FL, in the centre the plateau of the SyF-FL and in the left the saturation towards the negative field direction. In (a) we identify the modes, A and AO modes, the M5 is the second harmonic of the A damped mode, in the SyF-FL plateau region the A, AO and O modes and in the P state A and AO. The arrows correspond to the magnetic direction of magnetizations (SyF-FL in green and TL of the SyF pinned in red). (b) The O mode appears clearly. Device measures was D-SyF2.

A). For negative current, Fig. 7.10 (b), the hybridized damped O mode appears clearly in the AP state.

In the plateau region of the SyF-FL we observe the splitting and curvature of modes which correspond to the weak conservative RKKY coupling in the SyF-FL, see Fig. 7.5 (d). The splitting seems to be larger in the case of negative dc current. Since the resistance is small in the P state, we can apply higher values of dc current. However one has to be careful since the SyF-FL is switched for high dc current. Thus the system will pass from P to AP state (high resistance), and the increase in voltage can degrade the MgO barrier. We notice that in the SyF-FL plateau region of Fig. 7.10 (a), the acoustic mode presents a higher PSD emitted signal but in the case of (b), it is the optical mode. In the negative saturation range of figure (a) it is the acoustic mode which shows the higher PSD. One hypothesis could be that as in the case of the standard STO the attenuation of the modes is inverted with the sign of current, generating the change in the PSD amplitude.

In the AP state (positive saturation of the SyF-FL), we observe the evidence of several damped modes (as in the standard STO). We will show first the fundamental and higher order modes. In Fig. 7.11 (a) the dashed lines correspond to these damped higher modes, following the results in literature [Helmer et al., 2010]. In. Fig. 7.11 (b) the dashed lines correspond to the harmonics of the A damped modes as we showed in the previous

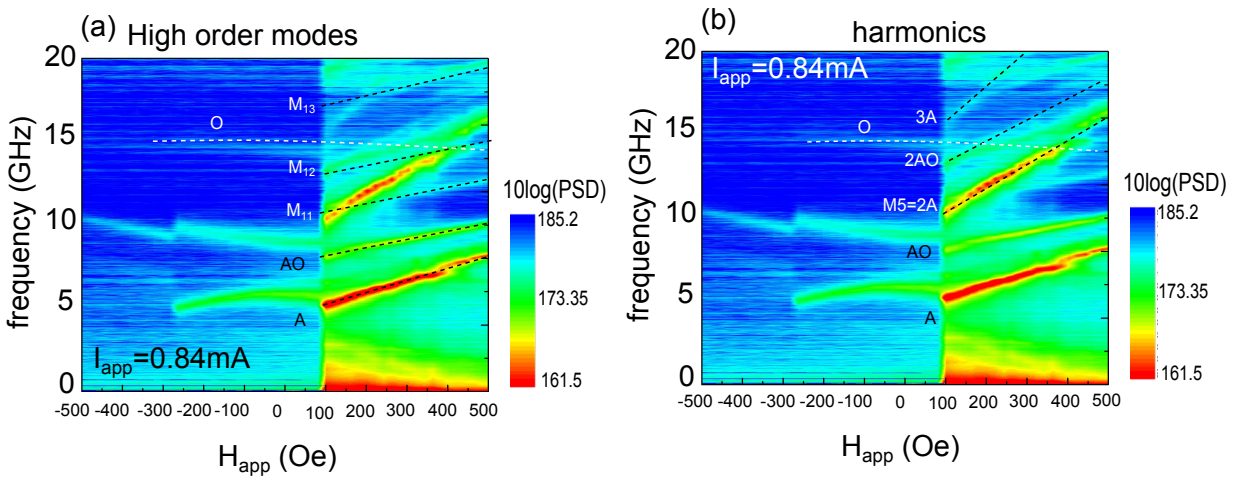

Figure 7.11 – Frequency dispersion of the SyF-FL for positive (a) and negative current (b). In (a) the high order damped modes and in (b) the harmonic of the low frequency modes. The dashed lines are included to identify the modes only as a reference. Device D-SyF2

chapter (standard STO), these higher order modes can be a disadvantage for the D-SyF STO spectra because they will interact with the STT modes. Spectra in the plateau region for a circular device, **D-SyF5** is shown in Fig. 7.12, applying I_{app}=1.45mA.

7.6 Frequency field dispersion of D-SyF STO

Now we will present the damped modes in all the range of fields, to have a global view. In order to measure the damped modes for the P and AP state (full field range), we divided the measurements in two parts.

First we measure the damped modes of the P region applying I_{app}=-0.55mA. Secondly, for the AP state we measure applying I_{app}=0.36mA. The low resistance in the P state allows us to increase the negative current without reaching the break-down voltage.

In Fig. 7.13 the damped modes of the SyF-FL and SyF pinned layer are shown in the full magnetic field range for the device **D-SyF1**. The arrows of Fig. 7.9 correspond to the magnetization of the SyF-FL (saturated state) and the TL of the SyF pinned layer. In the centre of the figure we can distinguish the characteristic SyF-FL modes on the small plateau region. In the negative field region we notice the absence of hybridization.

In the next section we will study the steady state oscillation in the D-SyF STO.

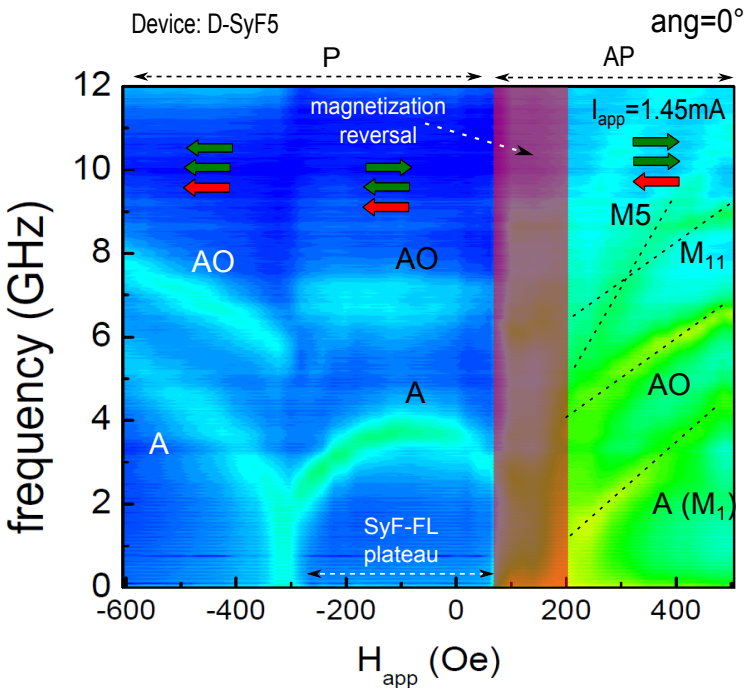

Figure 7.12 – Frequency dispersion of the SyF-FL in the plateau region for I_{app}=1.45mA. Dash lines correspond to the higher damped modes on the circular device **D-SyF 5**.

7.7 General frequency dispersion diagram of the D-SyF STO

In order to explain the different features of the frequency tuning as a function of the magnetic field and current, first we will identify which mode is in STT and which is damped. We will take into account the experimental results of the standard STO of chapter 6.

The study of the frequency field dispersion will focus in the high resistance region (AP state, positive magnetic field). We can not study the STT modes of the SyF-FL dominant precession in the plateau region of the SyF-FL (P state, low resistance) due to the possibility of an abrupt switching, generating a degradation of the device (high voltage).

As we explained in the previous chapter, the interaction between the STT mode and the damped or higher order modes changes the frequency dispersion, generating kinks or jumps. Moreover this interaction is transmitted to the linewidth[3].

In Fig. 7.14 (a) we show the frequency dispersion as a function of the field for the device **D-**

[3]In numerical simulations we found that the interaction of the (3f) STT O mode with the damped SO mode will induce a decrease in the linewidth. This has been corroborated in experimental results with the SV devices.

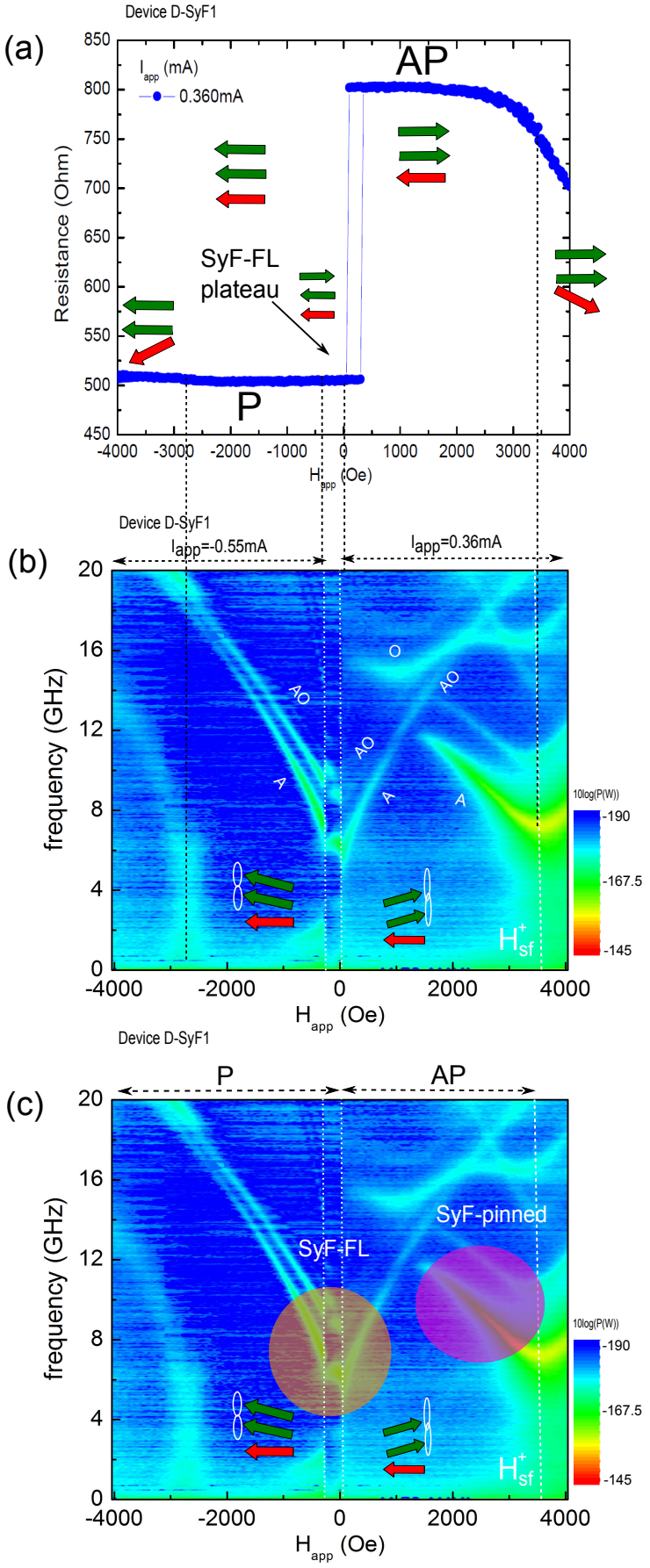

Figure 7.13 – (a) MR curve for the device D-SyF1. (b) Frequency dispersion for the whole magnetic field range, for I_{app}=-0.55mA (negative fields) and for I_{app}=0.36mA (positive fields). We identify the damped modes of the SyF-FL and for the SyF pinned layer. In (c) the shadow region represent the SyF-FL and the SyF pinned layer hybridized damped modes. Device D-SyF1.

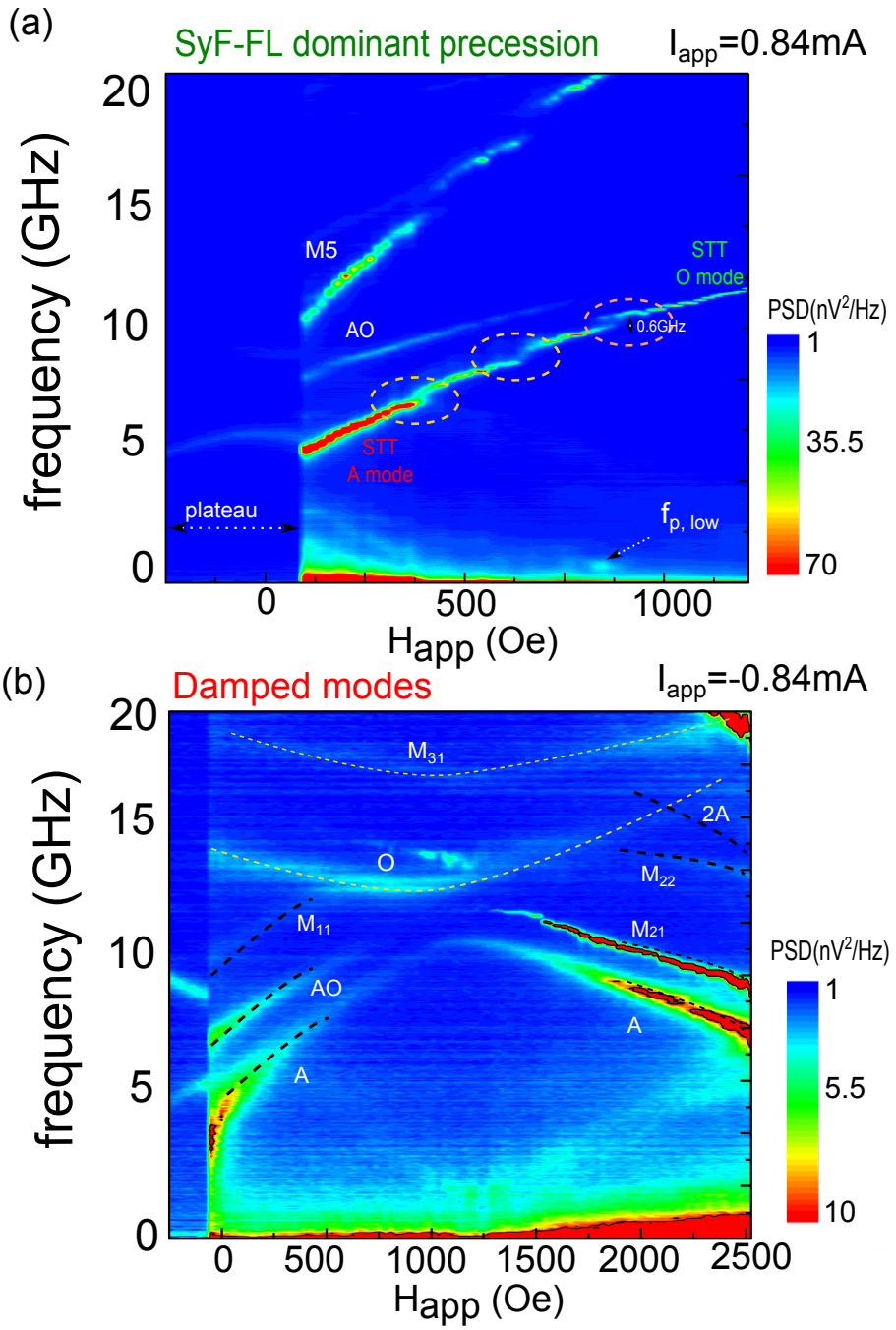

Figure 7.14 – (a) Frequency dispersion as a function of the field for the SyF-FL dominant precession, I_{app}=0.84mA. The circles indicate the kink and jumps in the STT A mode. In (b) it is shown the damped modes applying negative current, I_{app}=-0.84mA. For this values of current the system remains in the linear regime, damped modes. We observe that the characteristic gap is already close by the A damped modes. Device D-SyF3 (TMR=60%)

SyF3 with TMR=60% (angle<5°). For positive current I_{app}=0.84mA we observe the STT mode (SyF-FL dominant precession) which is the evolution from the damped A mode[4]. The frequency dispersion shows several deviations (dashed circles) in the tendency that are not predicted in the macro-spin simulations.

We observe that a low frequency mode ($f_{p,low}$) appears around 875 Oe and a jump of ≈0.6GHz between two branches of the STT A mode, see dashed orange circle in Fig. 7.14 (a), around 900Oe.

In Fig. 7.14 (b), for the same value of current (but negative) the frequency dispersion diagram shows the damped modes (dashed lines). Close to zero and for high field we observe the hybridized damped modes, A, AO, and higher order modes M_{11}, M_{21} and M_{22}. The hybridized O mode seems to have a higher order damped mode M_{31}. Coming back to Fig. 7.14 (a), we observe that the STT A mode finishes at 875Oe when a low frequency excitation ($f_{p,low}$) appears. As in the case of the standard STO the splitting between the STT A and O mode seems to disappears.

As we showed in Fig. 7.14 (b), I_{app}=-0.84mA is not enough current to overcome the critical current and reach the STT modes. Now we will increase the current up to ±1.4mA, with a degradation of the MgO barrier and a decrease in the TMR to 30%. The frequency dispersion versus applied field shows important branches in the STT A and O modes, see Fig. 7.15 (a) and (b) respectively. The frequency dispersion has changed in comparison with Fig. 7.14.

In the STT mode SyF-FL dominant precession we identified 11 kinks and in the SyF pinned dominant precession 5 deviations, see Fig. 7.15 (a) and (b) respectively. The flattening in the STT mode (H_{app}=750Oe) is accompanied by a low frequency mode ($f_{p,low}$), see Fig. 7.15. In the case of negative current, Fig. 7.15 (b), the SyF pinned dominant precession shows low frequency modes in the region of the splitting region H_{app}≈1000Oe and before to reach the spin flop field H_{app}≈1750Oe in another crossing of modes, see vertical dashed lines.

Using the macro-spin simulation of the standard STO, we found the evidence of a flattening in the damped A mode, in the region of the interaction of the 3f STT O mode with the SO mode. However in the STO based on MTJ we observe features that we supposed are more related to the interaction with the high order modes. In order to clarify the crossing of modes we show the frequency versus field in a different scale, for the SyF FL and SyF pinned dominant precession, see Fig. 7.17.

[4]In order to identify the modes see Fig. 6.22 of the standard STO.

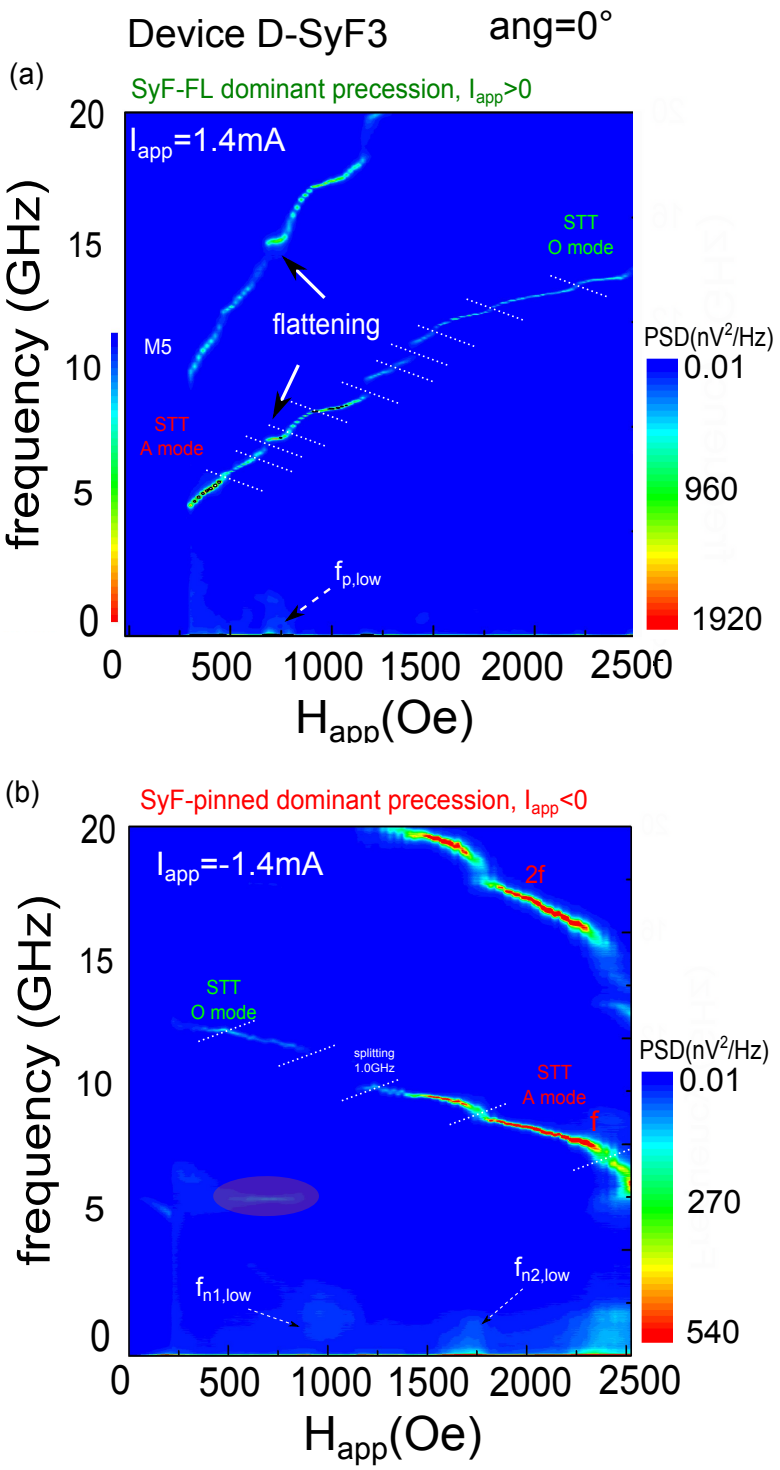

Figure 7.15 – Deviations (kinks and jumps) of the fundamental and second harmonic in the frequency versus applied field dispersion. (a) SyF-FL dominant precession and (b) SyF pinned dominant precession, I_{app}=±1.4mA. Device D-SyF3 (TMR=30%).

We can observe in Fig. 7.17 how the frequency dispersion versus field shows more kinks and jumps (more branches) when the device is degraded (reduction of the TMR), i.e the applied current is higher. The degradation of the devices will produce pinholes and a different features in the electronic transport. We should be able to avoid this degradation in the future.

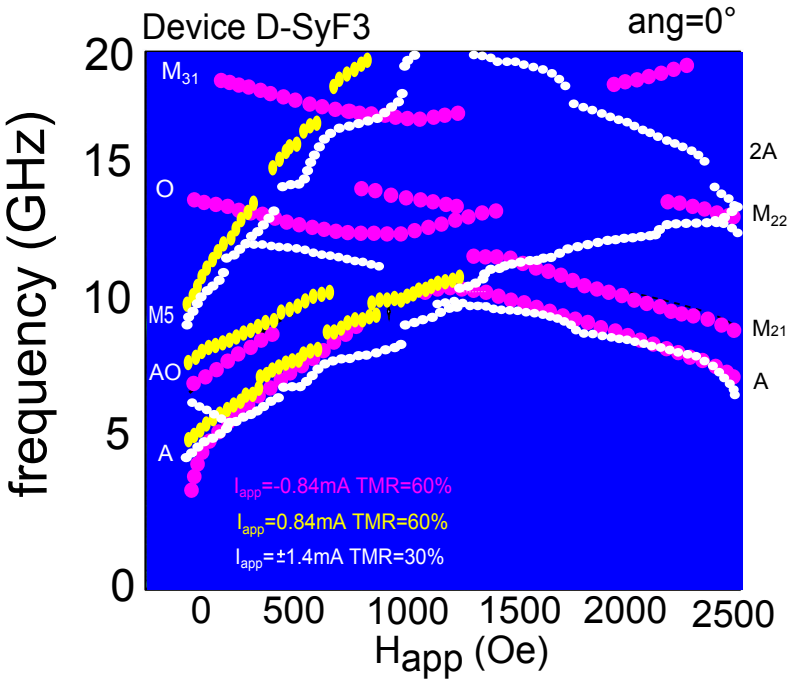

Figure 7.16 – Superposition of the damped modes tendency (harmonic and higher modes) and the STT modes for the frequency field dispersion. I_{app}=±0.84mA and ±1.4mA. Device D-SyF3 (TMR=60%-30%).

In Fig. 7.17 (a) and (b) we included dashed black lines to identify the hybridized or high order damped modes. We notice that for small fields the crossing of the damped and high order modes (A, O and M_{31}) with the 2f of the STT A mode of the FL dominant precession, see vertical arrows in Fig. 7.17 (a). For high fields, we observe the crossing of A, M_{21}, M_{22} and 2M2. All these interactions produce deviations in the STT A and O mode.

In Fig. 7.17 (b) the SyF-pinned dominant precession shows the expected splitting between the two branches (STT A and O modes). This splitting is closed by a narrow excitation mode (dashed circle), simultaneously the low frequency mode appears $f_{n1,low}$. After this measurement we found that the TMR was decrease until 20%.

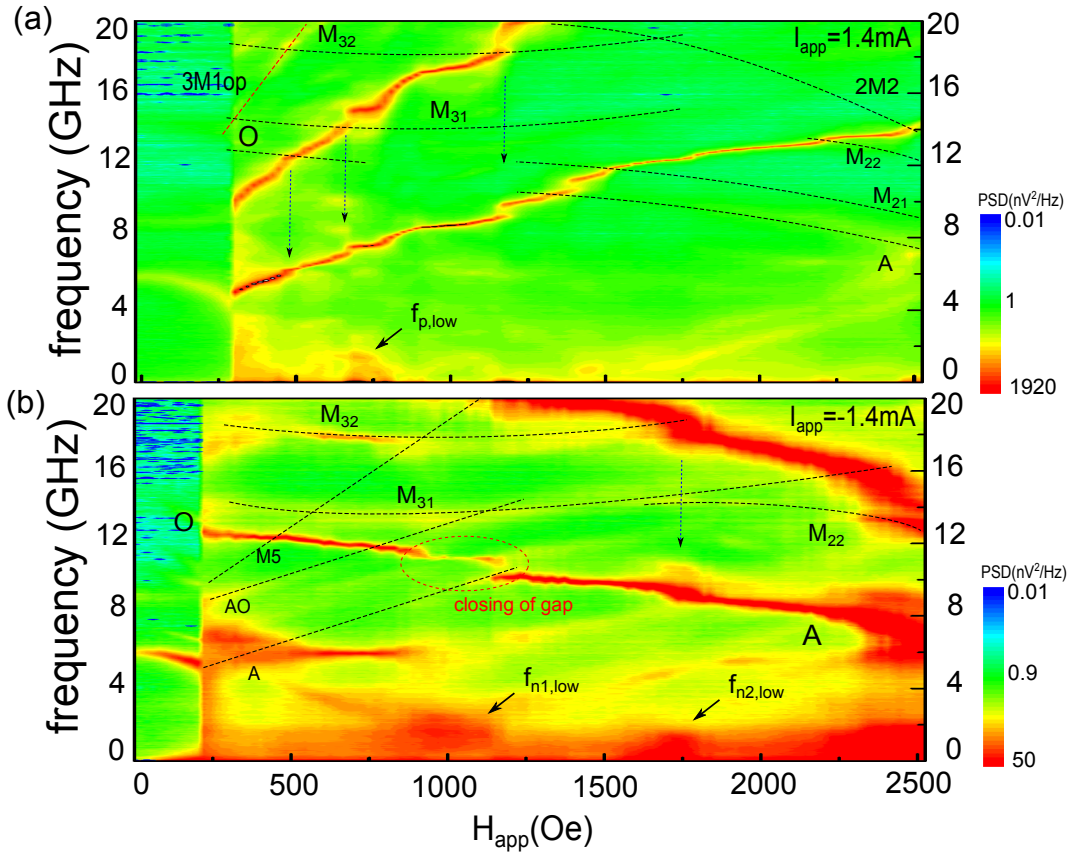

Figure 7.17 – Superposition of the damped modes tendency (harmonic and higher modes) for the frequency field dispersion. Dash lines correspond to the damped modes crossing the harmonics or the fundamental modes. (a) SyF-FL dominant precession and (b) SyF pinned dominant precession, I_{app}=±1.4mA. Device D-SyF3 (TMR=30%).

7.7.1 Crossing between the excitations modes

As we showed in the chapter 5, the interactions between the modes will be transmitted in changes of the normal tendency of the linewidth. We show the linewidth of the SyF-FL dominant precession in Fig. 7.18 for I_{app}=0.74mA, device **D-SyF3** with TMR=60 %. We indicate three yellow shadow regions which correspond to the crossing of the STT mode with the damped or the harmonic of the STT mode with high order modes. These crossings produce the increase of the linewidth.

The red shadow region corresponds to an abrupt decrease of the linewidth and a flattening region on the frequency. We can see this flattening also in Fig. 7.14 (a).

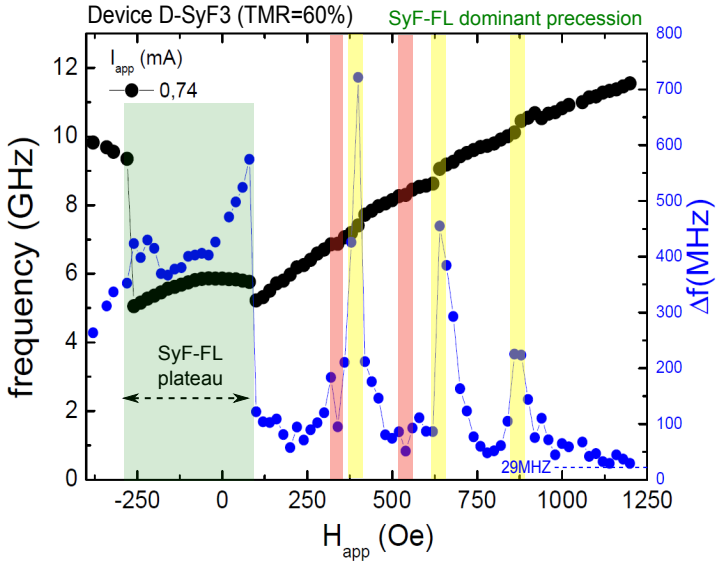

Figure 7.18 – Frequency and linewidth (black and blue) field dispersion for the SyF-FL dominant precession. It is noticed that each flattening of the frequency corresponds to the deviations in frequency correspond to the abrupt decrease in linewidth (red shadow region) and a abrupt increase later (yellow shadow region). The green shadow region corresponds to the plateau region. The minimal linewidth in the STT A mode was Δf=29MHz. Device D-SyF3 60%. It was applied a current of I_{app}=0.78mA.

In Fig. 7.19 the frequency and linewidth of the STT modes are shown for I_{app}=±1.4mA device **D-SyF3** with TMR=20 %, where we show the abrupt increase of linewidth corresponding to the crossing of the STT modes with damped or high order modes (see yellow shadow regions). The minimum linewidth was found for the SyF-FL ≈13MHz and for the SyF pinned on ≈40MHz. Around 2000Oe the branch is relatively large ≈250Oe and the corresponding linewidth small.

The same study was done for another sample (**D-SyF4** with TMR=38%), in Fig. 7.20 for the SyF-FL and SyF pinned dominant precession (green and red respectively). We

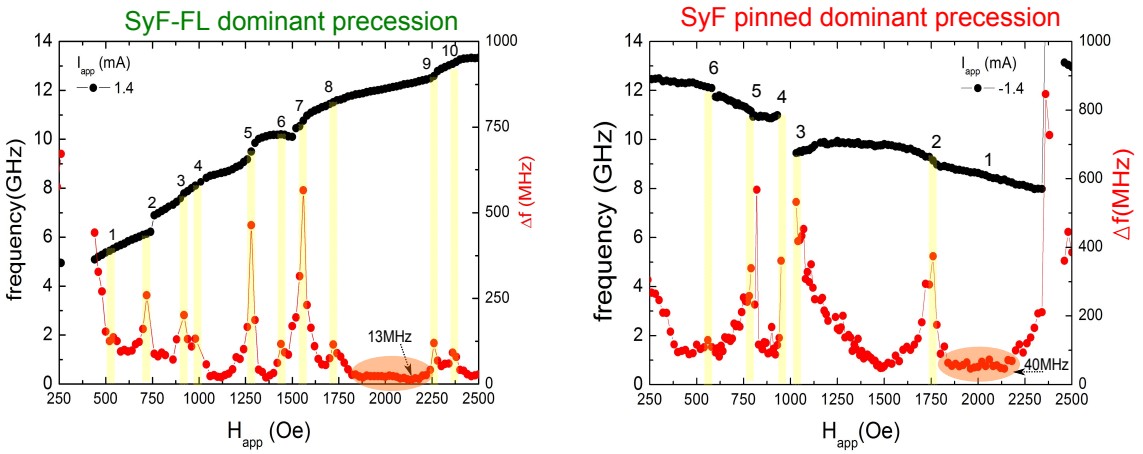

Figure 7.19 – Frequency and linewidth (black and red) field dispersion for the SyF-FL and SyF pinned dominant precession which were depicted in (a)and (b) respectively. It is noticed that each deviation in frequency correspond to the abrupt increase in linewidth. It was applied a current of I_{app}=±1.4mA. Device D-SyF3 20%.

notice that the SyF-FL linewidth presents a decrease in the region where the frequency does not present distortions, large branch between 1750Oe<H_{app}<2250Oe.

We superposed both frequency and linewidth dispersion, in order to see if the jumps or kinks correspond in both cases for the same applied field. The crossing of both fundamental and second harmonic are represented by the orange circle. Due to the several jumps, we cannot be sure that the flattening region of the STT O mode will be the interaction of the (3f) STT O mode with the second harmonic because we cannot observe an abrupt decrease of the linewidth, to help us to identify it.

The minimum linewidth was found for the SyF-FL ≈12.5MHz and for the SyF pinned on ≈15.75MHz, again the SyF-FL shows the smaller linewidth. In this point we conclude that the linewidth for the SyF-FL could be smaller than the corresponding for the SyF pinned dominant precession for this conditions.

This subsection clarify that adding more layers to the system will produce more higher order modes, crossing and branches of the fundamental STT mode.

7.8 Frequency current tuning of the D-SyF STO

In the D-SyF structure it is complicated to reach the STT modes in the SyF-FL without degrading the MgO barrier and reducing the TMR, see Fig. 7.16. We show the results of

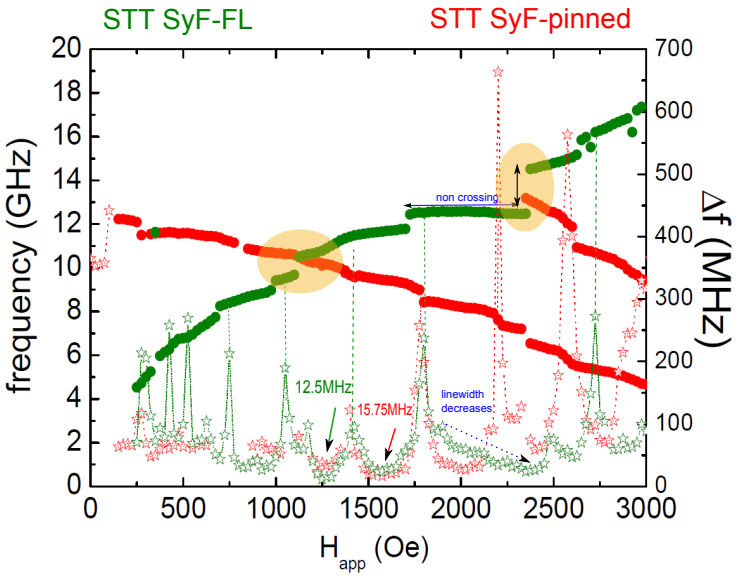

Figure 7.20 – Frequency and linewidth (green and red) field dispersion for the SyF-FL and SyF pinned dominant precession. It is noticed that deviations in the frequency corresponds to the abrupt increase in linewidth. Device D-SyF4 with TMR=38% and I_{app}=±1.3mA

a device with small TMR=20% (device **D-SyF3**), see Fig. 7.19.

The frequency tuning of the SyF-FL is shown in Fig. 7.21 for four values of magnetic field. Only for small fields, Fig. 7.21(a) H_{app}=242Oe (SyF-FL plateau), the system shows a damped mode. In the cases of H_{app}=545Oe and 707Oe the system shows a blueshift regime ($df/dI_{app}>0$). In the case of H_{app}=707Oe the mode changes its tendency into a redshift regime. This point correspond to the abrupt increase in linewidth just in the change of mode. For high field, H_{app}=1414Oe the narrow STT mode presents also the two branches, blueshift (small current) and redshift regime (high current).

In the case of the SyF pinned dominant precession we notice that the tuning as a function of the current shows for small fields, Fig. 7.22 (a)-(c) H_{app}=242Oe, 545Oe, and 868Oe, a redshift and a flattening behaviour. For H_{app}=1898Oe high fields Fig. 7.22 (e) the frequency diagram is noisy. The evolution from the redshift towards the blueshift is not evident as in the case of a single FL in a structure with low TMR. In Fig. 7.22 (d) the tuning df/dI_{app} is almost ≈1GHz/mA.

The frequency tuning of the D-SyF based on MTJ is smaller in comparison with the case of the tuning of the STO based on SV.

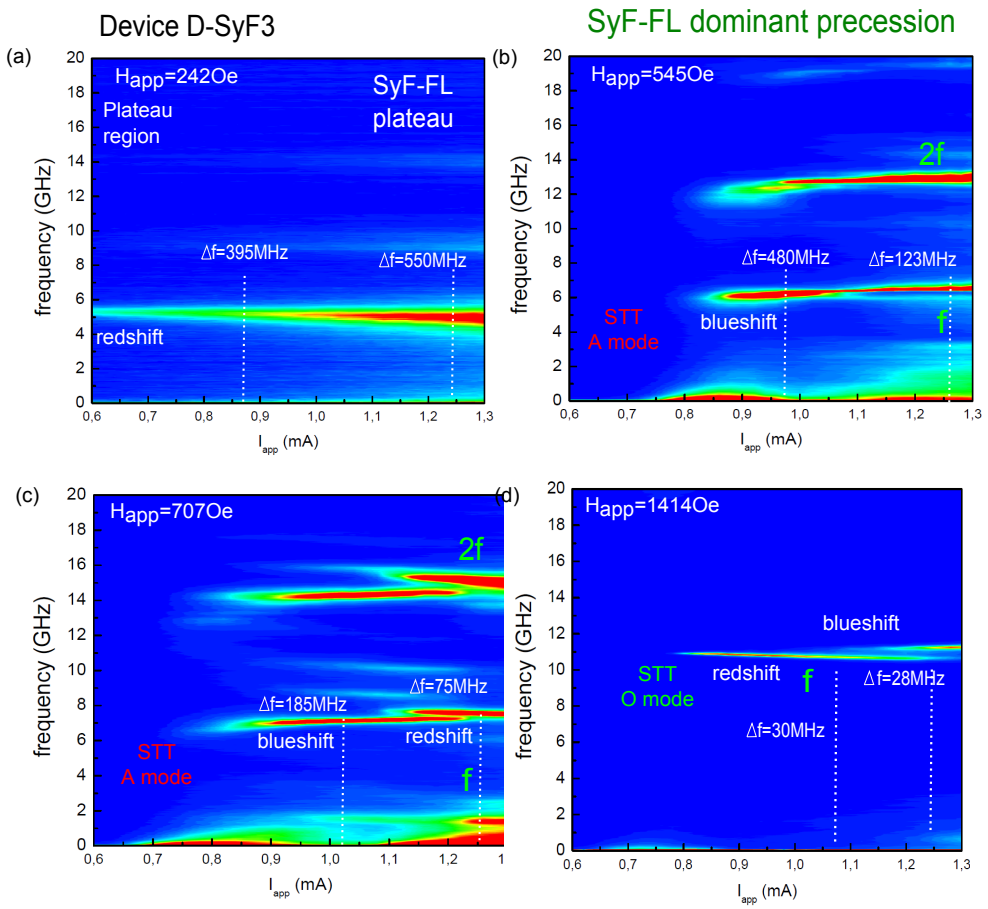

Figure 7.21 – Frequency tuning as a function of the current density for I_{app}>0 (SyF-FL dominant precession) for different field values. In (a) the damped A mode of the SyF-FL plateau. In (b) H_{app}=545Oe the system shows a blueshift regime. Increasing the field the frequency increases then, in (c) H_{app}=707Oe the system starts in the blueshift regime and for I_{app}>1.1mA it changes towards another mode showing a redshift regime. In (c) H_{app}=707Oe the system shows the same change in the tuning. (d) For H_{app}=1414Oe the STT O mode shows a minimum linewidth of 28MHz. Device D-SyF3 (20%).

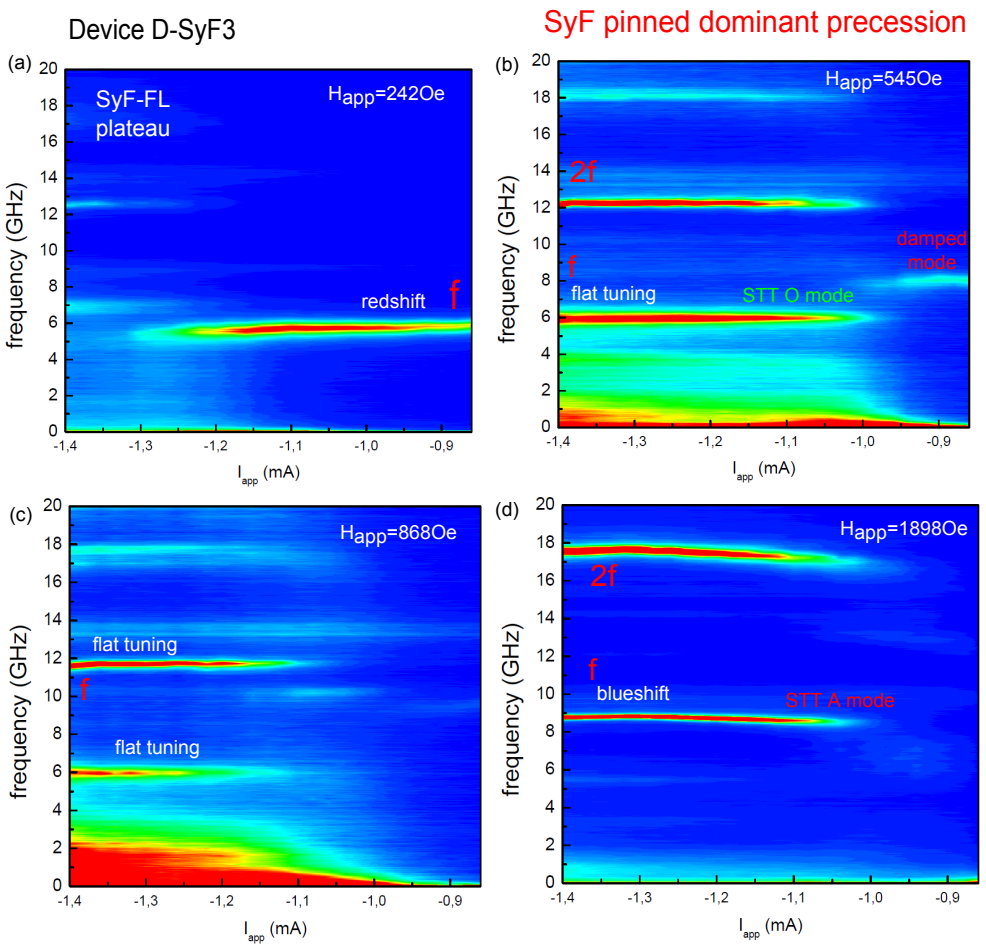

Figure 7.22 – Frequency tuning as a function of the current density for $I_{app}<0$ (SyF pinned dominant precession) for different field values. In (a)-(d) H_{app}=242Oe, 545Oe, 707Oe and 868Oe the system show a redshift regime and flattening tuning. In (e) for H_{app}=1010Oe the system is in the gap region, where for high current values we observe the appearance of one narrow STT mode, Δf=100MHz. In he case after the gap region (f) H_{app}=1898Oe the tuning shows a blueshift regime. Device D-SyF3.

7.9 Additional features of the D-SyF STO

7.9.1 Side bands

In some devices, the frequency dispersion diagram shows interesting features. An example is given in Fig. 7.23 where we show the frequency as a function of the magnetic field for I_{app}=-0.9mA for the device **D-SyF1**. The distance from the STT mode to the side bands is 1.4GHz, exactly the value of the low frequency mode. This could be a kind of modulation from the low frequency modes, which appears just in the crossing of modes.

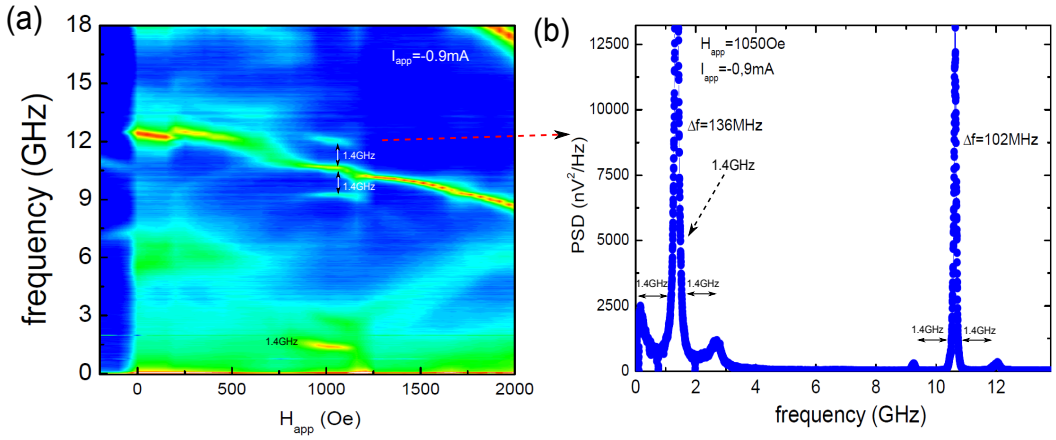

Figure 7.23 – Frequency dispersion as a function of the magnetic field shows side bands around H_{app}=1000Oe. Device D-SyF1.

7.10 Summary

The double SyF (D-SyF) STO based on MTJ characterized in this thesis work has shown the following features.

The RKKY coupling of the SyF-FL is weak (J_{RKKY}=-0.1mJ/m^2) in comparison with the coupling in the SyF pinned layer of the structure (J_{RKKY}=-1mJ/m^2). We associate this feature to the roughness of the interfaces on top of the structure. This has been corroborated in similar structures SV and MTJ in films. In consequence the SyF-FL does not present a spin flop region and only a plateau region that is smaller that the one of the pinned SyF.

The structure studied is characterized by a plateau of the SyF-FL in the P state and the saturation in the AP state. We can observe STT modes only in the saturation state of

the SyF-FL.

The state diagram shows a small gap, as in the numerical simulations. The frequency versus field show several branches, that we attributed to the crossing of the STT mode with other damped hybridized or higher order modes of the layers. We found that the minimum linewidth was around ≈12-15MHz for SyF-FL and SyF pinned dominant precession.

The tuning frequency versus current of the SyF-FL and SyF pinned layer is almost flat (1GHz) and with and important blueshift tendency in almost all the field range. This blueshift was also found in single layers, for devices with small TMR (LTMR). It has been shown a jump from the blueshift regime into the redshift regime for high values of current in the case od the SyF-FL tuning.

Conclusions

In conclusion, the dynamical interactions between the layers based of the different STO structures play an important role in the understanding of the emitted spectra of the STO nanopillars. It is not possible to predict the frequency dispersion diagrams, as a function of the field and current, without them. These dynamical interactions result, in the crossing of modes, in changes of the frequency tuning as well as in changes of the linewidth, both in an increase and in a decrease

The most simple case of dynamical coupling studied was the RKKY interlayer coupling. It was found, using numerical simulations, as the responsible of the transition from $df/I_{app}<0$ (redshift) towards $df/I_{app}>0$ (blueshift) in an isolated SyF structure or in a isolated SAF pinned layer. The small linewidth was found numerically and experimentally in the blueshift region, where the RKKY plays an important role.

In the case of the standard STO, the dynamical dipolar field between the three FM layers (SyF and single FL) will define hybridized damped modes which will give us a first view of the frequency versus field dispersion. Also the state diagram, field vs. current shows a gap in the STT mode regions, evidence of the influence of the dynamic dipolar field in the spectra. The frequency vs. current of the STT modes of the FL dominant precession have shown different features, such as the small region of IPP regime and its transition towards OPP regime for small fields (STT A mode), the highest df/dI_{app} tuning for high fields (STT O mode) and the evidence of the interaction between the damped SO mode with the STT O mode. This interaction produces a kink or jump in the frequency dispersion (as a function of the field or current). Around this interaction the emitted spectra presents a reduction of the linewidth. For the SyF dominant precession the frequency dispersion as a function of field or current shows the transition from $df/I_{app}<0$ (redshift) towards $df/I_{app}>0$ (blueshift) as in the isolated case.

These features were corroborated in experiments during the study of the STO based on SV devices. In STO based on MTJ the influence of the dynamic dipolar field is shown in the

gap of the state diagram. The frequency vs. current tuning shows a dominant blueshift regime for the SyF dominant precession, this due to LTMR behavior. In these devices the higher order modes play an important role, crossing the STT mode and producing branches. Due to this fact the linewidth will increase and decrease continuously, upon varying current and field.

The introduction of a SyF-FL instead a single layer in the STO based on MTJ (double SyF (D-SyF) STO) will generate more higher order modes which produces more branches in the main STT mode. We found that with an increase of current the numbers of branches in the STT mode increases. For this structure the linewidth found was comparable with the corresponding to the SyF pinned layer but lower than single FL STO.

Perspectives

This thesis work has opened questions that must be answered in the future. The simulations focused on the AP state where the hybridization of the SyF and FL modes were observed. This is confirmed in experiment. However in experiments the hybridization of modes in the P state is absent while the modes show narrow linewidth. This needs to be further analyzed in numerical simulations where the excitations in the P state of the standard STO should be studied. due to the evidence in experiments of narrow STT modes (34MHz) without of hybridization.

The PSD of the magneto-resistance ($\mathbf{m}_{TL}.\mathbf{m}_{FL}$) should be computed for high current values (positive and negative), in order to better compare to experiments results.

We have to compute the angular dependence of these PSD of the magneto-resistance ($\mathbf{m}_{TL}.\mathbf{m}_{FL}$) diagrams in order to better understand why certain features of mode hybridisation is more visible.

The SyF-FL of the D-SyF structure should be simulated for different values of RKKY coupling and changing the influence of the dipolar field from the others layers.

It should be important to compare more carefully the single FL spectra with the SyF-FL spectra for LTMR devices, in order to quantify the similarities in the performance Δf and power.

The STO structure should be modified in order to obtain the SyF-FL plateau in the AP state (high resistance of the structure). In order to increase the RKKY coupling of the SyF-FL we proposed the deposition of the inverted structure. The performance of the spectra of the SyF-FL and pinned structure, changing the RKKY coupling, must be studied in numerical simulation and experiments.

Part IV

Appendix

Chapter 8

Appendix A

8.1 Analytical equations for the spin flop and saturation field values of the SyF layer

In this section will be present the analytical equations of the spin flop and saturation magnetic field, $H_{sf}^{\pm}$ and $H_{sat}^{\pm}$ respectively, as a function of the exchange bias and the RKKY coupling of a SyF layer. We start taking into account the total energy of an isolated SyF layer, see eq. 8.1 neglecting the dipolar contribution between the layers (due to the strong RKKY coupling). For this calculations we supposed that both layers are in the plane magnetized, $\theta = \pi/2$ (due to the strong demagnetizing field out of plane).

$$\begin{aligned} E_{Tot} = & -\mu_0 M_{S,BL}(H_{app}+H_b)\cos\phi_{BL}V_{Vol,BL} - \mu_0 M_{S,TL}H_{app}\cos\phi_{TL}V_{Vol,TL} \\ & -\frac{\mu_0 M_{S,BL}^2}{2}(\cos\phi_{BL}^2 N_{xx,BL} + \sin\phi_{BL}^2 N_{yy,BL})V_{Vol,BL} \\ & -\frac{\mu_0 M_{S,TL}^2}{2}(\cos\phi_2^2 N_{xx,TL} + \sin\phi_2^2 N_{yy,TL})V_{Vol,TL} \\ & +K_{u,BL}(\cos\phi_{BL}^2)V_{Vol,BL} + K_{u,TL}(\cos\phi_{TL}^2)V_{Vol,TL} \\ & -J_{RKKY}(\cos\phi_{BL}\cos\phi_{TL} + \sin\phi_{BL}\sin\phi_{TL})S_{surface}. \end{aligned} \tag{8.1}$$

The angles of these equations are defined in Fig. 3.4. In order to simplify the expressions we supposed the constant B equal to: $B_{BL(TL)}$=$K_{BL(TL)}$+ $\frac{\mu_0 M_{S,BL(TL)}^2}{2}$ ($N_{xxBL(TL)}$-$N_{yyBL(TL)}$). The first step is find the state of minimal energy doing the derivatives of the

total energy equation as a function of the angles.

$$\frac{\partial E_{Tot}}{\partial \varphi_{BL}}, \frac{\partial E_{Tot}}{\partial \varphi_{TL}} = 0. \tag{8.2}$$

We will found the determinant of the characteristics matrix of the system, composed by the second derivatives terms, $\lambda_{1,2}>0$.

$$det \begin{bmatrix} \frac{\partial^2 E_{Tot}}{\partial \varphi_{BL}^2} - \lambda & \frac{\partial^2 E_{Tot}}{\partial \varphi_{BL} \partial \varphi_{TL}} \\ \frac{\partial^2 E_{Tot}}{\partial \varphi_{TL} \partial \varphi_{BL}} & \frac{\partial^2 E_{Tot}}{\partial \varphi_{TL}^2} - \lambda \end{bmatrix} = 0 \tag{8.3}$$

In these two equations we should replace the critical angles of the equilibrium position. If we want to obtain the saturation field we will use φ_{BL}=φ_{TL}=0 or π depending of the sense of the magnetic field sweeping, i.e in the structure is saturated. If we want to obtain the spin flop value we will use φ_{BL}=0 (π) and φ_{TL}=π (0), i.e the sample is in the plateau region. It is not possible to solve the equations supposing φ_{BL}=-φ_{TL} for the spin flop region.

$$H_{sf}^{\pm} = \frac{1}{2\mu_0^2 M_{S,BL} M_{S,TL} d_{BL} d_{TL}} [\mu_0 J(M_{S,BL} d_{BL} - M_{S,TL} d_{TL}) + d_{BL} d_{TL} (2\mu_0 (B_{TL} M_{S,BL} - B_{BL} M_{S,TL}) + H_b \mu_0^2 M_{S,BL} M_{S,TL}) \pm (J^2 \mu_0^2 (M_{S,BL} d_{BL} - M_{S,TL} d_{TL})^2 + 2J\mu_0^2 d_{BL} d_{TL} (M_{S,BL} d_{BL} + M_{S,TL} d_{TL})(2(B_{BL} M_{S,TL} + B_{TL} M_{S,BL}) + H_b \mu_0 M_{S,BL} M_{S,TL}) + \mu_0^2 d_{BL}^2 d_{TL}^2 (2(B_{BL} M_{S,TL} + B_{TL} M_{S,BL})^2 + H_b \mu_0 M_{S,BL} M_{S,TL})^2)^{1/2}] \tag{8.4}$$

$$H_{sat}^{\pm} = \pm \frac{1}{2\mu_0^2 M_{S,BL} M_{S,TL} d_{BL} d_{TL}} [\mu_0 J(M_{S,BL} d_{BL} + M_{S,TL} d_{TL}) - d_{BL} d_{TL} (2\mu_0 (B_{TL} M_{S,BL} + B_{BL} M_{S,TL}) \pm H_b \mu_0^2 M_{S,BL} M_{S,TL}) + (J^2 \mu_0^2 (M_{S,BL} d_{BL} + M_{S,TL} d_{TL})^2 + 2J\mu_0^2 d_{BL} d_{TL} (M_{S,BL} d_{BL} - M_{S,TL} d_{TL})(2(B_{BL} M_{S,TL} - B_{TL} M_{S,BL}) \pm H_b \mu_0 M_{S,BL} M_{S,TL}) + \mu_0^2 d_{BL}^2 d_{TL}^2 (2(B_{BL} M_{S,TL} - B_{TL} M_{S,BL})^2 \pm H_b \mu_0 M_{S,BL} M_{S,TL})^2)^{1/2}] \tag{8}$$

If the J_{RKKY} is strong enough ($>0.2 mJ/m^2$) the hysteresis loop of the SyF will not present

bi-stability and the $H_{sf}\pm$ and $H^{\pm}_{sat}$ will separated by the spin flop region, Fig. 4.7. In the case of J_{RKKY} <0.1mJ/m^2 an important bi-stability region appears, the spin flop region disappears and the critical values have to be defined as in the Fig. 4.6 and 4.7.

In chapter 4, the isolated system was a SAF with symmetric parameters for the TL and BL, as the saturation magnetization, anisotropy constant, thickness, see table 3.1. In this case the equations will be reduced to,

$$H^{\pm}_{sf} = -\frac{H_b}{2} \pm \frac{\sqrt{(\mu_0 M_S H_b + 4B + 2\frac{J}{d})^2}}{2\mu_0 M_S}. \tag{8.6}$$

$$H^{\pm}_{sat} = \pm\frac{1}{2\mu_0 M_S}(\frac{J}{d} - (4B \pm H_b\mu_0 M_S) + \sqrt{\frac{4J^2}{d^2} + (H_b\mu_0 M_S)^2}). \tag{8.7}$$

8.2 Calculation of FMR modes in a SyF layer

Following the same procedure of sec.3.1.4.1 we will derivate the ferromagnetic equations of a couple system SyF. The term i=1,2 correspond to each ferromagnetic layer.

$$\frac{\partial \mathbf{M}_i}{\partial t} = -\gamma_0(\mathbf{M}_i \times \mathbf{H}^i_{eff}). \tag{8.8}$$

The effective field was defined in 3.32 and the gradient operator in spheric coordinates is $\nabla_i = \frac{\partial}{\partial \rho_i}\mathbf{e}_\rho + \frac{1}{\rho_i}\frac{\partial}{\partial \theta_i}\mathbf{e}_\theta + \frac{1}{\rho_i \sin\theta_i}\frac{\partial}{\partial \varphi_i}\mathbf{e}_\varphi$. Writing the magnetization $\mathbf{M}_i$ in spheric coordinates we must re-write the 8.8. The left side for each layer will be written as,

$$\frac{\partial \mathbf{M}_i}{\partial t} = M_{Si}\mathbf{e}_{\rho_i} = M_{Si}(\sin\theta_i\dot{\phi}\mathbf{e}_\phi + \dot{\theta}_i\mathbf{e}_\theta) \tag{8.9}$$

The energy of the system which is defined by equation 3.8 for the $i = BL, TL = 1, 2$ is given by,

$$
\begin{aligned}
E_{\mathrm{T}ot} &= E_{Zeeman,i} + E_{\mathrm{b},BL} + E_{\mathrm{a}ni,i} + E_{\mathrm{d}emag,i} + E_{\mathrm{RKKY},i\leftrightarrow j} \\
&= -\mu_0 M_{S1}(H_x + H_b)\sin\theta_1\cos\phi_1 V_{Vol1} - \mu_0 M_{S2} H_x \sin\theta_2\cos\phi_2 V_{Vol2} \\
&\quad -\frac{\mu_0 M_{S1}^2}{2}(\sin\theta_1^2\cos\phi_1^2 N_{xx1} + \sin\theta_1^2\sin\phi_1^2 N_{yy1} + \cos\theta_1^2 N_{zz1})V_{Vol1} \\
&\quad -\frac{\mu_0 M_{S2}^2}{2}(\sin\theta_2^2\cos\phi_2^2 N_{xx2} + \sin\theta_2^2\sin\phi_2^2 N_{yy2} + \cos\theta_2^2 N_{zz2})V_{Vol2} \\
&\quad +K_{u1}(\sin\theta_1^2\cos\phi_1^2)V_{Vol1} + K_{u2}(\sin\theta_2^2\cos\phi_2^2)V_{Vol2} \\
&\quad -J_{RKKY}(\sin\theta_1\cos\phi_1\sin\theta_2\cos\phi_2 + \sin\theta_1\sin\phi_1\sin\theta_2\sin\phi_2 + \cos\theta_1\cos\theta_2)S_{surface}.
\end{aligned} \tag{8.10}
$$

As we observe the energy is a function of the spherical angles, $E_{Tot}(\theta_1, \phi_1, \theta_2, \phi_2) = E$. In order to study the small fluctuation of the magnetization around an equilibrium state define as,

$$\theta_i = \theta_{i0} + \delta\theta_i; \qquad \delta\theta_i << \theta_{i0} \tag{8.11}$$

$$\varphi_i = \varphi_{i0} + \delta\varphi_i; \qquad \delta\varphi_i << \varphi_{i0} \tag{8.12}$$

We expanded the energy equation around this equilibrium position eq=$(\theta_{10}, \varphi_{10}, \theta_{20}, \varphi_{20})$. It is important to remark, as in the case of the single layer, that the derivative as a function of the angles of the energy evaluated in the equilibrium position is zero.

$$
\begin{aligned}
E &= E|_{(eq)} + E_{\theta_1}|_{(eq)}\delta\theta_1 + \frac{1}{\sin\theta_1}E_{\varphi_1}|_{(eq)}\delta\varphi_1 + E_{\theta_2}|_{(eq)}\delta\theta_2 \\
&\quad + \frac{1}{\sin\theta_2}E_{\varphi_2}|_{(eq)}\delta\varphi_2 + O^2.
\end{aligned} \tag{8.13}
$$

where the energy sub-index corresponds to the derivative, $\dfrac{\partial E}{\partial\theta} = E_\theta$. In the plateau region our equilibrium state is given by the angles eq=$(\pi/2, 0, \pi/2, \pi)$. Neglecting all contribution of the second order we can obtain the gradient of the energy E, in order to find the right side term of the equation 8.8,

$$-\gamma_0 \mathbf{M}_i \times H^i_{eff} = -\frac{\gamma_0}{\mu_0 M_{Si}} \mathbf{M}_i \times \nabla E_i, \tag{8.14}$$

$$\begin{aligned}
\nabla_1 E &= \mathbf{e}_\theta (E_{\theta_1} + E_{\theta_1\theta_1}\delta\theta_1 + \frac{1}{\sin\theta_1} E_{\theta_1\varphi_1}\delta\varphi_1 + E_{\theta_1\theta_2}\delta\theta_2 + \frac{1}{\sin\theta_2} E_{\theta_1\varphi_2}\delta\varphi_2) \\
&\quad + \mathbf{e}_\varphi (\frac{1}{\sin\theta_1} E_{\varphi_1} + \frac{1}{\sin\theta_1} E_{\varphi_1\theta_1}\delta\theta_1 + \frac{1}{\sin^2\theta_1} E_{\varphi_1\varphi_1}\delta\varphi_1 \\
&\quad + \frac{1}{\sin\theta_1} E_{\varphi_1\theta_2}\delta\theta_2 + \frac{1}{\sin\theta_1 \sin\theta_2} E_{\varphi_1\phi_2}\delta\varphi_2),
\end{aligned} \tag{8.15}$$

$$\begin{aligned}
\nabla_2 E &= \mathbf{e}_\theta (E_{\theta_2} + E_{\theta_2\theta_1}\delta\theta_1 + \frac{1}{\sin\theta_1} E_{\theta_2\varphi_1}\delta\varphi_1 + E_{\theta_2\theta_2}\delta\theta_2 + \frac{1}{\sin\theta_2} E_{\theta_2\varphi_2}\delta\varphi_2) \\
&\quad + \mathbf{e}_\varphi (\frac{1}{\sin\theta_2} E_{\varphi_2} + \frac{1}{\sin\theta_2} E_{\varphi_2\theta_1}\delta\theta_1 + \frac{1}{\sin\theta_2 \sin\theta_1} E_{\varphi_2\varphi_1}\delta\varphi_1 \\
&+ \quad \frac{1}{\sin\theta_2} E_{\varphi_2\theta_2}\delta\theta_2 + \frac{1}{\sin^2\theta_2} E_{\varphi_2\phi_2}\delta\varphi_2),
\end{aligned} \tag{8.16}$$

where the derivatives of the total energy have to be evaluated in the equilibrium state. The procedure to find $\nabla_i E$ is the same. Comparing these equations with the the equation 3.33 for each layer of the SyF, supposing the periodic behavior of our small deviation $\delta\theta_i = Re(\delta\theta_{max} e^{i\omega t}) \rightarrow \delta\dot{\theta}_i = i\omega\delta\theta_i$ and finding the temporal derivative of eq.8.12 we obtain,

$$\begin{aligned}
0 &= -\frac{\gamma_0}{\mu_0 M_{S1}\sin\theta_1} E_{\theta_1\theta_1}\delta\theta_1 - (\frac{\gamma_0}{\mu_0 M_{S1}\sin^2\theta_1} E_{\theta_1\varphi_1}\delta\phi_1 + i\omega) \\
&\quad - \frac{\gamma_0}{\mu_0 M_{S1}\sin\theta_1} E_{\theta_1\theta_2}\delta\theta_2 - \frac{\gamma_0}{\mu_0 M_{S1}\sin\theta_1\sin\theta_2} E_{\theta_1\varphi_2}\delta\varphi_2
\end{aligned} \tag{8.17}$$

$$\begin{aligned}
0 &= (\frac{\gamma_0}{\mu_0 M_{S1}\sin\theta_1} E_{\varphi_1\theta_1} - i\omega)\delta\theta_1 + \frac{\gamma_0}{\mu_0 M_{S1}\sin^2\theta_1} E_{\varphi_1\varphi_1}\delta\varphi_1 \\
&\quad + \frac{\gamma_0}{\mu_0 M_{S1}\sin\theta_1} E_{\varphi_1\theta_2}\delta\theta_2 + \frac{\gamma_0}{\mu_0 M_{S1}\sin\theta_1\sin\theta_2} E_{\varphi_1\varphi_2}\delta\varphi_2
\end{aligned} \tag{8.18}$$

$$\begin{aligned}
0 &= -\frac{\gamma_0}{\mu_0 M_{S2}\sin\theta_2} E_{\theta_2\theta_1}\delta\theta_1 - \frac{\gamma_0}{\mu_0 M_{S2}\sin\theta_2\sin\theta_1} E_{\theta_2\varphi_1}\delta\varphi_1 \\
&\quad - \frac{\gamma_0}{\mu_0 M_{S2}\sin\theta_2} E_{\theta_2\theta_2}\delta\theta_2 - (\frac{\gamma_0}{\mu_0 M_{S2}\sin^2\theta_2} E_{\theta_2\varphi_2} + i\omega)\delta\varphi_2
\end{aligned} \tag{8.19}$$

$$\begin{aligned}
0 &= \frac{\gamma_0}{\mu_0 M_{S2}\sin\theta_2} E_{\varphi_2\theta_1}\delta\theta_1 + \frac{\gamma_0}{\mu_0 M_{S2}\sin\theta_2\sin\theta_1} E_{\varphi_2\varphi_1}\delta\varphi_1 \\
&\quad + (\frac{\gamma_0}{\mu_0 M_{S2}\sin\theta_2} E_{\varphi_2\theta_2} - i\omega)\delta\theta_2 + \frac{\gamma_0}{\mu_0 M_{S2}\sin^2\theta_2} E_{\varphi_2\phi_2}\delta\varphi_2
\end{aligned} \tag{8.20}$$

These four equations can be written in a matrix as in the form of eq.3.40 but in this case it will be 4×4.

$$\begin{bmatrix} -\frac{\gamma_0 E_{\theta_1\theta_1}}{\mu_0 M_{S1}\sin\theta_1} & -(\frac{\gamma_0 E_{\theta_1\varphi_1}}{\mu_0 M_{S1}\sin^2\theta_1}+i\omega) & -\frac{\gamma_0 E_{\theta_1\theta_2}}{\mu_0 M_{S1}\sin\theta_1} & -\frac{\gamma_0 E_{\theta_1\varphi_2}}{\mu_0 M_{S1}\sin\theta_1\sin\theta_2} \\ (\frac{\gamma_0 E_{\varphi_1\theta_1}}{\mu_0 M_{S1}\sin\theta_1}-i\omega) & +\frac{\gamma_0 E_{\varphi_1\varphi_1}}{\mu_0 M_{S1}\sin^2\theta_1} & +\frac{\gamma_0 E_{\varphi_1\theta_2}}{\mu_0 M_{S1}\sin\theta_1} & -\frac{\gamma_0 E_{\varphi_1\varphi_2}}{\mu_0 M_{S1}\sin\theta_1\sin\theta_2} \\ -\frac{\gamma_0 E_{\theta_2\theta_1}}{\mu_0 M_{S2}\sin\theta_2} & -\frac{\gamma_0 E_{\theta_1\varphi_1}}{\mu_0 M_{S2}\sin\theta_2\sin\theta_1} & -\frac{\gamma_0 E_{\theta_1\theta_2}}{\mu_0 M_{S2}\sin\theta_2} & -(\frac{\gamma_0 E_{\theta_1\varphi_2}}{\mu_0 M_{S2}\sin^2\theta_2}+i\omega) \\ \frac{\gamma_0 E_{\varphi_2\theta_1}}{\mu_0 M_{S2}\sin\theta_2} & +\frac{\gamma_0 E_{\varphi_2\varphi_1}}{\mu_0 M_{S2}\sin\theta_2\sin\theta_1} & +(\frac{\gamma_0 E_{\varphi_2\theta_2}}{\mu_0 M_{S2}\sin\theta_2}-i\omega) & +\frac{\gamma_0 E_{\varphi_2\phi_2}}{\mu_0 M_{S2}\sin^2\theta_2} \end{bmatrix} \begin{bmatrix} \delta\theta_1 \\ \delta\varphi_1 \\ \delta\theta_2 \\ \delta\varphi_2 \end{bmatrix} \tag{8.21}$$

Solving and looking for non trivial numerical solution of this matrix, we found the two solutions which correspond to the acoustic and optical mode of the SyF.

8.3 Calculation of the effective field in SyF

Each contribution of energy is related with a magnetic field through the equation,

$$H_i = -\frac{1}{\mu_0 M_{Si} V_{Vol,i}} \frac{\partial E}{\partial \mathbf{m}_i} \tag{8.22}$$

The fields values related with each energy contribution are fundamentals in order to obtain the total effective field of the structure over study, and in order to understand the magnetization dynamics equation which will be presented in the future. In the following we present the fields values related with each energy term,

$$\mathbf{H_{Zeeman}} = \mathbf{H_{app}} \tag{8.23}$$

$$\mathbf{H_{ani,x}} = \frac{2K_u}{\mu_0 M_S}\hat{\mathbf{i}} \tag{8.24}$$

$$\mathbf{H_{demag}} = -4\pi M_S \cos\theta \hat{\mathbf{k}} \tag{8.25}$$

$$\mathbf{H_b} = \mathbf{H_b} \tag{8.26}$$

$$\mathbf{H_{RKKY,i}} = -\frac{J_{RKKY}}{\mu_0 d_i M_{S,i}}\mathbf{m}_j \tag{8.27}$$

$$\mathbf{H^i_{dip}} = -\frac{M_{S,j} N_{dip}}{Vol_i}\mathbf{m}_j \tag{8.28}$$

8.3.1 Dipolar Field

In the following we introduce the method to obtain the different components of the dipolar tensor N_{dip}. The magnetic layers are simulated as rectangular films, see Fig. 8.1. The magnetization is homogeneous pointing in one direction.

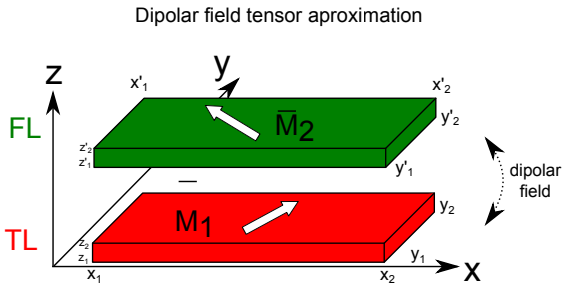

Figure 8.1 – The components of the dipolar field tensor are found using an approximation of two magnetic rectangular layers.

The layers are defined for $\mathbf{M}_1$ by the points (x_1,x_2), (y_1,y_2), (z_1,z_2) and for $\mathbf{M}_2$ by (x'_1,x'_2), (y'_1,y'_2), (z'_1,z'_2). The dipolar field interaction and the demagnetized energy are defined as,

$$E_{dip} = -\mu_0 \int_{Vol} \mathbf{M}_1(\mathbf{r}).\mathbf{H}_{dip,2\longrightarrow 1} d_{Vol} \tag{8.29}$$

$$E_{demag} = -\frac{1}{2}\mu_0 \int_{Vol} \mathbf{M}_1(\mathbf{r}).\mathbf{H}_{demag} d_{Vol} \tag{8.30}$$

$$\tag{8.31}$$

The demagnetized field can be expressed in terms of the gradient of the scalar potential $\mathbf{H}_{demag}$=-$\nabla\phi(\mathbf{r})$.

$$E_{demag} = \frac{1}{2}\mu_0 \int_{Vol} \mathbf{M}_1(\mathbf{r}).\nabla\phi(\mathbf{r}) d_{Vol} \tag{8.32}$$

Using the surface and volumetric magnetic charges $\sigma(\mathbf{r})$ and $\rho(\mathbf{r})$ and the divergence theorem we can wrote,

$$E_{demag} = \frac{1}{2}\mu_0 \oint_S \phi(\mathbf{r})\sigma(\mathbf{r}) d_S + \frac{1}{2}\int_{Vol} \phi(\mathbf{r})\rho(\mathbf{r}) d_{Vol} \tag{8.33}$$

We suppose a system with a homogenisation magnetization producing charges in the surface.

$$E_{demag} = \frac{1}{2}\mu_0 \oint\!\!\!\!\!\!\int_S \phi(\mathbf{r})\sigma(\mathbf{r})d_S \tag{8.34}$$

Finding the scalar potential $\phi(\mathbf{r})$ using the green function we obtain the global interaction due to the surfaces of the rectangular layers.

Chapter 9

Appendix B

This appendix is constituted by two sections. The first one corresponding to the development of a D-SyF STO structure and the second one to the influence of the annealing temperature in the SyF layer which composes most of the spintronic devices.

9.1 Development of the double SyF STO (D-SyF)

In this section it will be shown a brief summary of the development of the double SyF STO (D-SyF) based on SV. The main objective is the study of the degradation of the RKKY coupling in the SyF top layer. This features will be corroborate using numerical static simulations (hysteresis loops of the structure). In chapter 7 has been measured the FMR spectra of a D-SyF based on MTJ which presents the same weak RKKY coupling, due to the degradation. The samples were deposited by Dra. M.C. Cyril and Dra. E.Hanssen in CEA/LETI during the her Phd thesis. These samples has been annealed at 265°C during 1h.

The study starting with a pinned layer, sample S1. The structure is shown in Fig. 9.1 (a). Measuring the hysteresis loops, the exchange bias is obtain, H_b=197Oe. Now we will show the hysteresis loop of a structure SyF but with positive RKKY coupling which corresponds to a Ru thickness of 1.4nm, see Fig. 9.1 (b). In this figure we can observe the comparative with a single pinned layer, the red curve corresponds to the sample S2 (SyF pinned layer with $J_{RKKY}>0$) and the blue one to the sample S1. The arrows correspond to the magnetic configuration of the sample S2.

When the coupled system (S2) pass from the positive saturation into negative, the first layer to turn is the unpinned layer (on top) and then the pinned layer. For this reason the curve shows two behaviours, a abrupt switching TL and a soft reversal of the BL. The hysteresis of the BL reversal is smaller due to the RKKY coupling which favours the parallel state.

Now a SyF free layer will deposited over the single layer S1, separated by a Cu(3.5nm) layer. This new structure will be the sample S3 which is introduced with its corresponding hysteresis loop (red curve) in Fig. 9.2 (a). The hysteresis loop of the S3 is compare with the S1 (blue curve), which is the base of the structure. Arrows correspond to the magnetization direction of the S3 layers. We observe that the S3 curve shows several steps corresponding to the reversal of the SyF on top. The point labelled A and B correspond to the changing of sense of the TL and BL of the SyF free layer from positive to negative sweeping of field. the points C and D will be the same but in the opposite sense. It is important to remark that the layer with the less net magnetic moment ($M_{S,i}\times$ d_i) will be the first layer to change its sense. This fact in order to keep in the minimum energy system state. From the hysteresis loop it is possible to notice that the size of the steps in a and A corresponds to the size of the plateau region of the SyF free layer and the saturation field for the SyF free layer will be $\approx$ 58.5 Oe.[1]. Both $H_{sat}{}^{\pm}$ should be equals but due to the dipolar field we found a difference of 7Oe.

Following with the development of the D-SyF structure, the SyF FL structure will be deposited in top of a SyF pinned layer. The structure of the sample S4 and its hysteresis loop are shown in Fig. 9.2 (b). We observe that the A step keep the same size that in the case of structure of Fig. 9.2 (a).

We will try to obtain an approximate value of the RKKY coupling of the SyF free layer removing the contribution of the pinned layers of the structures S3 and S4. The results are introduced in Fig. 9.3.

Using this method, the plateau of the SyF FL was $\approx$ 105Oe. In a double SyF structure, see Fig. 9.4, the plateau of the FL measured directly from the hysteresis loop was $\approx$90Oe. The difference between this to measurement maybe correspond with some coupling between the SyF pinned and the SyF FL (RKKY or weak dipolar field).

In conclusion the roughness of the structure destroys the RKKY coupling of the SyF FL on top of the structure, in comparison of the $\approx$2000 Oe for the SyF pinned layer the SyF FL shows only in average $\approx$100 Oe.

[1] Average between both values $H_{sat}{}^{\pm}$

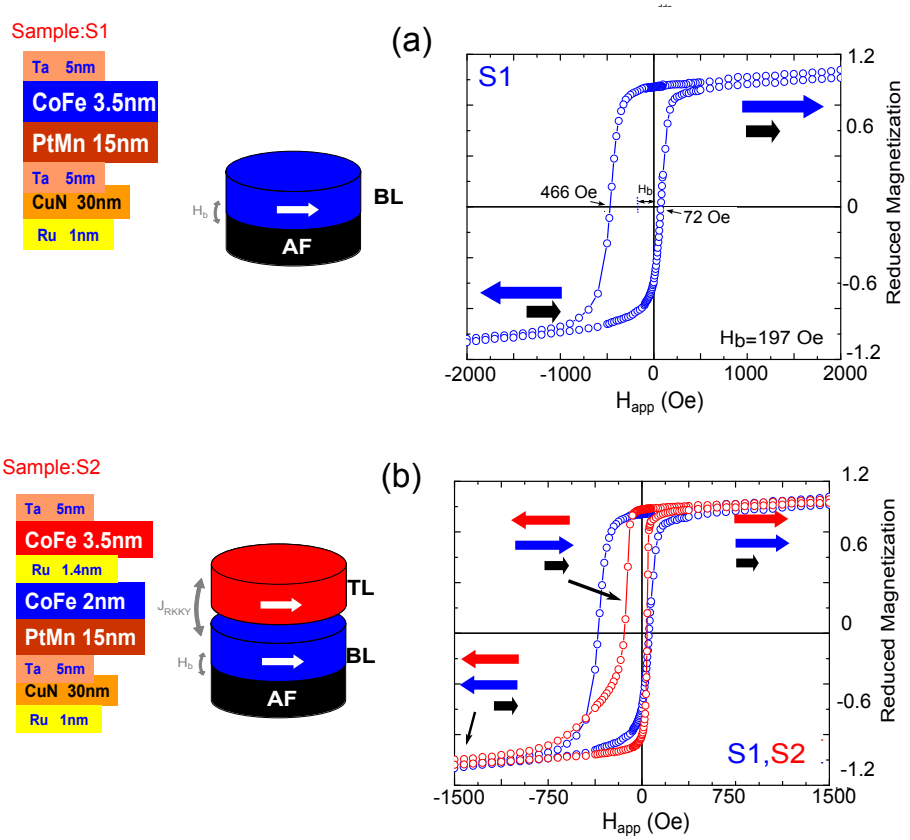

Figure 9.1 – Structure and hysteresis loop of a (a) Single layer and (b) SyF pinned ($J_{RKKY}>0$) layer (red curve), compared with the previous cases.

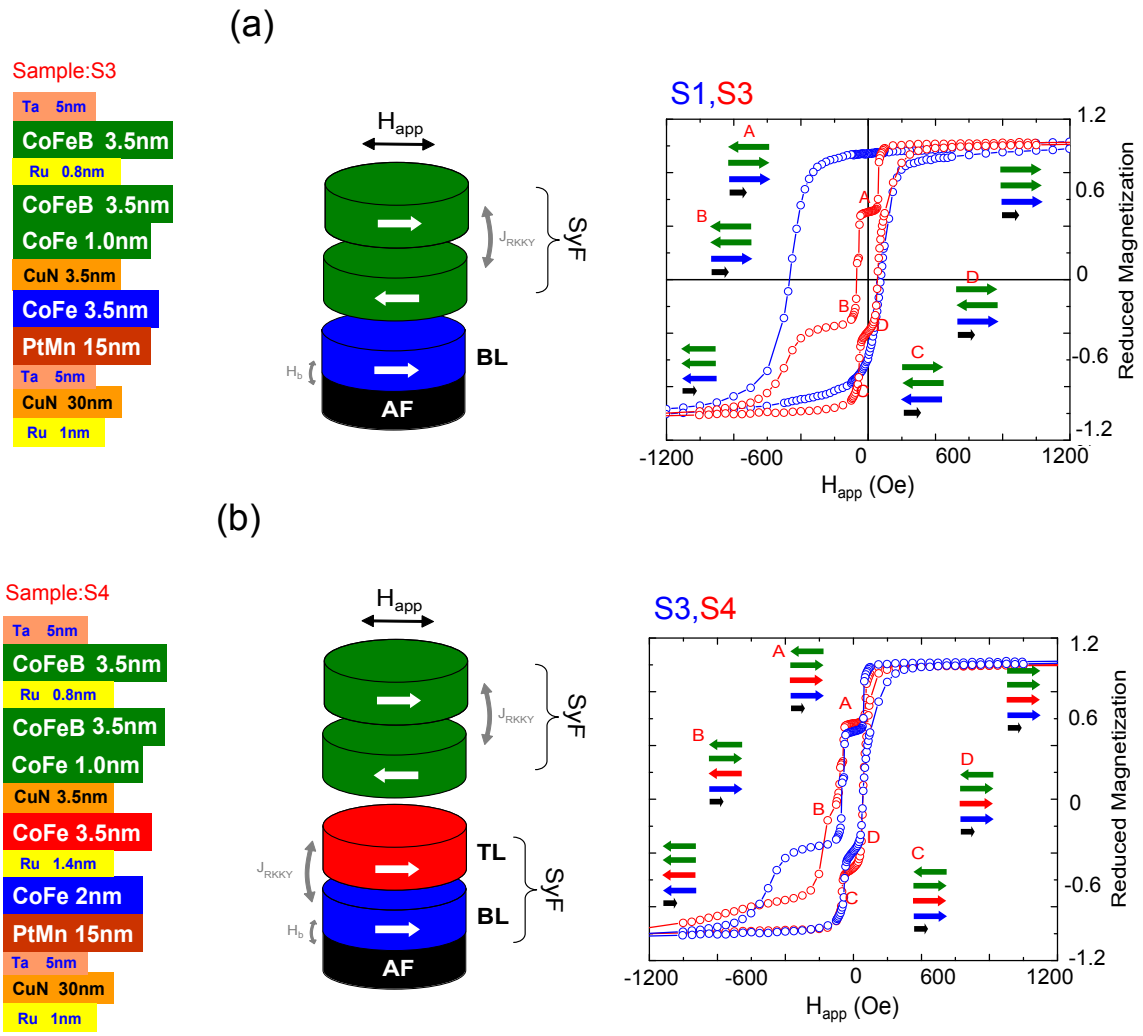

Figure 9.2 – Hysteresis loop of two structures. (a) Single layer with a SyF-FL on top and in (b) the double SyF structure.

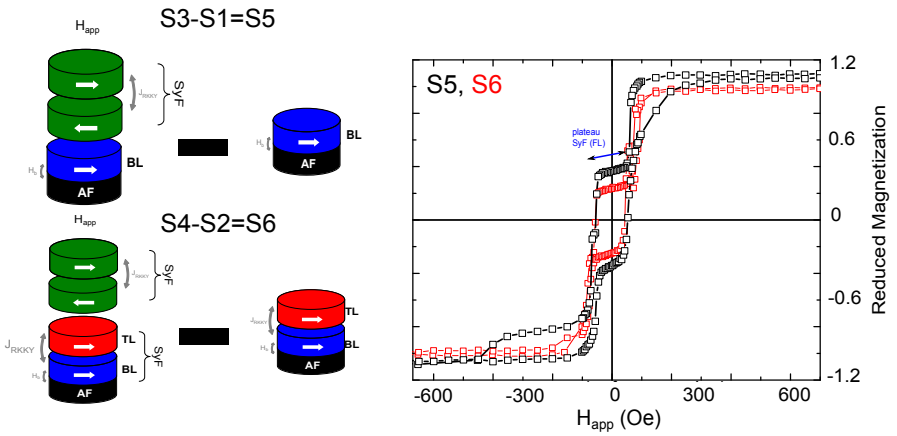

Figure 9.3 – Hysteresis loop of the SyF FL (from S3 and S4) obtained removing the single or SyF pinned layer, on bottom of the structure.

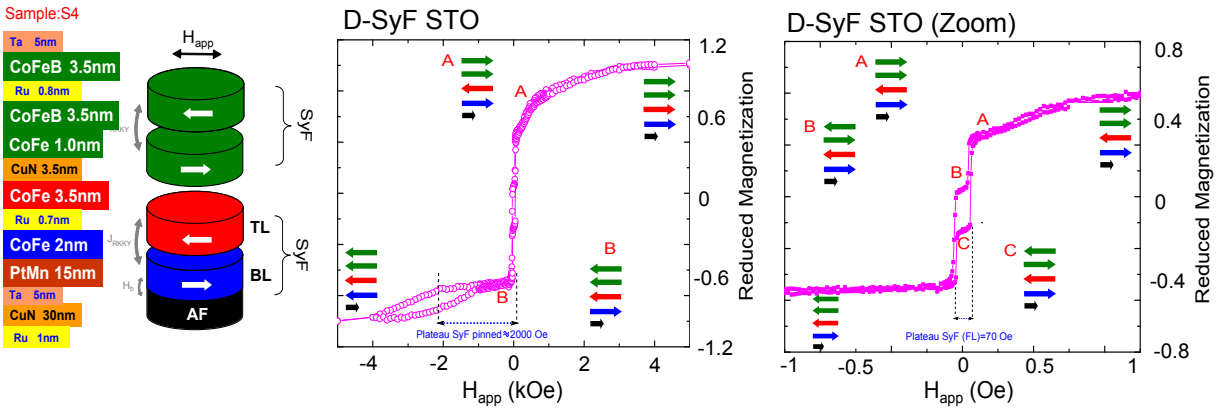

Figure 9.4 – Structure and hysteresis loop of the D-SyF STO based on SV. We observe that the plateau of the SyF (FL) is small (70Oe) in comparison with the SyF pinned layer (≈2000Oe)

9.2 Influence of the annealing temperature in the RKKY strength

During the development of the STO devices the structure must be submitted over a thermal process for two reasons. First the as-deposited AF layer needs an annealing process in order to induce an uni-directional exchange bias field, H_b. The pinning is given by the interface field between a the BL of the SyF which is in contact with an antiferromagnetic layer (AF) like PtMn, IrMn, FeMn, NiMn or PtPdMn [Anderson et al., 2000]. This annealing process also gives rise a change in the structure of the PtMn from FCT[111] to FCC[111]. For our studies we used PtMn already optimized at LETI laboratories, founding the optimal thickness of the layers in order to obtain the highest exchange bias field. It has been studied [Kim et al., 2002] that high temperatures of annealing process (≈350°C) generates a interlayer diffusion of Mn just in the transition from FCT to FCC, decreasing the MR and the H_b. The applied field during the annealing process must be enough strong to saturate the SyF layer. If the magnetic field reaches only the spin-flop region, the direction of the pinning will be unknown, [Negulescu et al., 2011].

Secondly, for the STOs based on MTJ structures, the thermal process is fundamental in order to obtain a good crystallization of the MgO barrier. We would like to remark that in our study we present the destruction of the RKKY coupling in a SyF due to the temperature effect. For our samples, the crystallization temperature must be of $\sim 340^{o}$C during 1h 30', and it is high enough to be used as annealing temperature as well.

Another problem of the thermal process is the Mn or B diffusion into the Ru of the SyF (PtMn/BL/Ru/TL/MgO/FL) or the MgO barrier. In order to avoid the Mn diffusion

into the Ru of the SyF pinned, currently a CoFeB/CoFe layer is deposited as BL. The B present before the annealing avoid the Mn and Ru diffusion increasing the stability of the plateau of the SyF pinned layer [Schreiber et al., 2011]. If the CoFeB is placed as TL (PtMn/CoFe/Ru/CoFeB) the Ru diffusion into the PtMn will be enhanced by the B diffusion destroying the RKKY coupling. Using a TL as CoFeB/CoFe and the FL as CoFe/CoFeB it is obtained a high TMR because the CoFe works as a template for a good crystallization of the MgO.

In order to show the temperature influence in a STO structure, we will show some examples structures for different annealing temperatures. These studies always in continuous films. In Fig. 9.5 (a) we introduced the hysteresis loop of a SyF structure deposited in CEA/LETI[2]. The sample called *S5* is composed by Ta(3)/CuN(20)/Ta(5)/CoFe(5)/Ru(0.8)/CoFeB(2)/T in which the thickness in nanometers are in parenthesis.

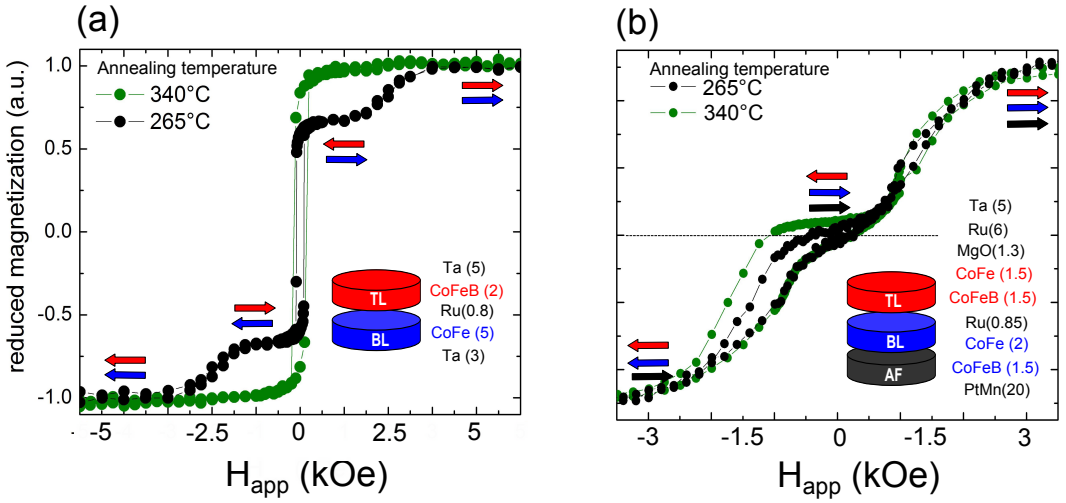

Figure 9.5 – (a) Structure of a SyF unpinned where the temperature induced degradation of the Ru spacer and decreasing the RKKY coupling. (b) Structure of a SyF pinned where the high temperature increases the pinning, and the RKKY coupling is not affected.

In Fig. 9.5 (a) the hysteresis loops for two temperatures (265^{o}C and 340^{o}C) values show the destruction of the RKKY coupling due to the high temperature is presented (340^{o}C) due to the migration of the B and Ru. A similar study was presented by [Takenaga et al., 2009] in SyF structures. The plateau region which is the characteristic of the negative RKKY coupling (antiferromagentic configuration) disappears gradually until reach 340^{o}C.

In Fig. 9.5 (b) the sample *S6*: Si/SiO2/Ta(3)/CuN MP (30)/Ta(5)/PtMn(20)/CoFeB(1.5)/CoFe(2.0) /Ru(0.85)/CoFeB(1.5)/CoFe(1.5)/MgO(0.9)NOX 0.5torr 10sec/Mg(0.4)/ Ru(6)Ta(5)/Ru(7)

[2]Samples were deposited by Dra. M.C. Cyril and Dra. E.Hanssen in CEA/LETI during the its Phd thesis.

was annealed during 1H 30' at 265^{o}C and 340^{o}C. We can observe that the plateau region present a flattering region larger for 340^{o}C. The annealing is much better in this case. The RKKY coupling remains with the same strength for the two different temperature.

In conclusion the optimization of the annealing and crystallization process is an important step in order to avoid the degradation RKKY coupling due to the Ru diffusion or MgO barrier (tunnel magnetorresistance).

Bibliography

[Anderson et al., 2000] Anderson, G. W., Huai, Y., and Pakala, M. (2000). Spin-valve thermal stability : The effect of different antiferromagnets. 87(9):5726–5728.

[Baibich, 1988] Baibich, M. N. (1988). Giant magnetoresistance in (001)Fe/(001)Cr Magnetic Superlattices.

[Bayer et al., 2005] Bayer, C., Jorzick, J., Hillebrands, B., Demokritov, S., Kouba, R., Bozinoski, R., Slavin, a., Guslienko, K., Berkov, D., Gorn, N., and Kostylev, M. (2005). Spin-wave excitations in finite rectangular elements of Ni80Fe20. *Physical Review B*, 72(6):064427.

[Berger, 1996] Berger, L. (1996). Emission spin waves magnetic multilayer traversed current. 54(13):9353–9358.

[Bertotti et al., 2005] Bertotti, G., Serpico, C., Mayergoyz, I., Magni, A., DAquino, M., and Bonin, R. (2005). Magnetization Switching and Microwave Oscillations in Nanomagnets Driven by Spin-Polarized Currents. *Physical Review Letters*, 94(12):127206.

[Bianchini et al., 2010] Bianchini, L., Cornelissen, S., Kim, J.-V., Devolder, T., van Roy, W., Lagae, L., and Chappert, C. (2010). Direct experimental measurement of phase-amplitude coupling in spin torque oscillators. *Applied Physics Letters*, 97(3):032502.

[Brown, 1963] Brown, W. F. (1963). Thermal Fluctuations of a Single-Domain Particle. 34(1951).

[Bruno and Chappert, 1991] Bruno, P. and Chappert, C. (1991). Oscillatory coupling between ferromagnetic films separated by a non-magnetic metal spacer. 67(12):1602–1606.

[Bruno and Chappert, 1992] Bruno, P. and Chappert, C. (1992). Ruderman-Kittel theory of oscillatory interlayer exchange coupling. *Physical review. B, Condensed matter*, 46(1):261–270.

[Carbone et al., 1993] Carbone, C., Vescovo, E., Rader, O., Gudat, W., and Eberhardt, W. (1993). Exchange split quantum well states of a noble metal film on a magnetic substrate. *Physical review letters*, 71(17):2805–2808.

[Cornelissen et al., 2010] Cornelissen, S., Bianchini, L., Devolder, T., Kim, J.-V., Van Roy, W., Lagae, L., and Chappert, C. (2010). Free layer versus synthetic ferrimagnet layer auto-oscillations in nanopillars processed from MgO-based magnetic tunnel junctions. *Physical Review B*, 81(14):144408.

[Cornelissen et al., 2009] Cornelissen, S., Bianchini, L., Helmer, a., Devolder, T., Kim, J.-V., Op de Beeck, M., Van Roy, W., Lagae, L., and Chappert, C. (2009). Effect of patterning on the saturation magnetization in MgO based nanopillars. *Journal of Applied Physics*, 105(7):07B903.

[Demidov et al., 2007] Demidov, V., Hansen, U.-H., and Demokritov, S. (2007). Spin-Wave Eigenmodes of a Saturated Magnetic Square at Different Precession Angles. *Physical Review Letters*, 98(15):157203.

[Deranlot et al., 2010] Deranlot, C., Ulysse, C., Faini, G., Klein, O., and Fert, A. (2010). Dynamics of two coupled vortices in a spin valve nanopillar excited by spin transfer torque. pages 1–4.

[Devolder et al., 2011] Devolder, T., Bianchini, L., Miura, K., Ito, K., Kim, J.-V., Crozat, P., Morin, V., Helmer, a., Chappert, C., Ikeda, S., and Ohno, H. (2011). Spin-torque switching window, thermal stability, and material parameters of MgO tunnel junctions. *Applied Physics Letters*, 98(16):162502.

[Dieny, 1991] Dieny, B. (1991). Giant magnetoresistance in soft ferromagnetic multilayers. 43(1).

[Dussaux et al., 2010] Dussaux, A., Georges, B., Grollier, J., Cros, V., Khvalkovskiy, A. V., Fukushima, A., Kubota, H., Yakushiji, K., Yuasa, S., Zvezdin, K. A., Ando, K., and Fert, A. (2010). Large microwave generation from d.c. driven magnetic vortex oscillators in magnetic tunnel junctions. pages 1–18.

[G. Binash, 1988] G. Binash (1988). Enhanced magnetoresistance in layered magnetic structures. 39(7):4828–4830.

[Garcia Palacios and Lazaro, 1998] Garcia Palacios, L. and Lazaro, F. J. (1998). Langevin dynamics study of the dynamical properties of small magnetic particles. *Physical Review B*, 58(22):937–958.

[Garrison et al., 1993] Garrison, K., Chang, Y., and Johnson, P. (1993). Spin polarization of quantum well states in copper thin films deposited on a Co(001) substrate. *Physical review letters*, 71(17):2801–2804.

[Grollier et al., 2006] Grollier, J., Cros, V., and Fert, a. (2006). Synchronization of spin-transfer oscillators driven by stimulated microwave currents. *Physical Review B*, 73(6):060409.

[Grünberg et al., 1986] Grünberg, P., Schreiber, R., Pang, Y., Brodsky, M., and Sowers, H. (1986). Layered magnetic structures: Evidence for antiferromagnetic coupling of Fe layers across Cr interlayers. *Physical review letters*, 57(19):2442–2445.

[Gubbiotti et al., 2005] Gubbiotti, G., Carlotti, G., Okuno, T., Grimsditch, M., Giovannini, L., Montoncello, F., and Nizzoli, F. (2005). Spin dynamics in thin nanometric elliptical Permalloy dots: A Brillouin light scattering investigation as a function of dot eccentricity. *Physical Review B*, 72(18):184419.

[Gubbiotti et al., 2007] Gubbiotti, G., Tacchi, S., Carlotti, G., Singh, N., Goolaup, S., Adeyeye, a. O., and Kostylev, M. (2007). Collective spin modes in monodimensional magnonic crystals consisting of dipolarly coupled nanowires. *Applied Physics Letters*, 90(9):092503.

[Gusakova et al., 2009] Gusakova, D., Houssameddine, D., Ebels, U., Dieny, B., Buda-Prejbeanu, L., Cyrille, M., and Delaët, B. (2009). Spin-polarized current-induced excitations in a coupled magnetic layer system. *Physical Review B*, 79(10):104406.

[Gusakova et al., 2011] Gusakova, D., Quinsat, M., Sierra, J. F., Ebels, U., Dieny, B., Buda-Prejbeanu, L. D., Cyrille, M.-C., Tiberkevich, V., and Slavin, a. N. (2011). Linewidth reduction in a spin-torque nano-oscillator caused by non-conservative current-induced coupling between magnetic layers. *Applied Physics Letters*, 99(5):052501.

[Hamadeh et al., 2013] Hamadeh, A., Locatelli, N., Naletov, V. V., Lebrun, R., Loubens, G. D., Grollier, J., Klein, O., and Cros, V. (2013). Perfect and robust phase-locking of a spin transfer vortex nano-oscillator to an external microwave source. pages 3–6.

[Hamadeh et al.,] Hamadeh, A., Loubens, G. D., Klein, O., Naletov, V. V., Locatelli, N., Lebrun, R., Grollier, J., and Cros, V. Origin of spectral purity and tuning sensitivity in a vortex-based spin transfer nano-oscillator. pages 1–5.

[Helmer et al., 2010] Helmer, A., Cornelissen, S., Devolder, T., Roy, W. V., Lagae, L., and Chappert, C. (2010). Quantized spin wave modes in magnetic tunnel junction nanopillars. pages 1–17.

[Houssameddine, 2009] Houssameddine, D. (2009). *Dynamique de l aimantation de nano-oscillateurs micro-ondes à transfert de spin*. PhD thesis.

[Houssameddine et al., 2007] Houssameddine, D., Ebels, U., Delaët, B., Rodmacq, B., Firastrau, I., Ponthenier, F., Brunet, M., Thirion, C., Michel, J.-P., Prejbeanu-Buda, L., Cyrille, M.-C., Redon, O., and Dieny, B. (2007). Spin-torque oscillator using a perpendicular polarizer and a planar free layer. *Nature materials*, 6(6):441–7.

[Houssameddine et al., 2008] Houssameddine, D., Florez, S. H., Katine, J. a., Michel, J.-P., Ebels, U., Mauri, D., Ozatay, O., Delaet, B., Viala, B., Folks, L., Terris, B. D., and Cyrille, M.-C. (2008). Spin transfer induced coherent microwave emission with large power from nanoscale MgO tunnel junctions. *Applied Physics Letters*, 93(2):022505.

[Houssameddine et al., 2010] Houssameddine, D., Sierra, J. F., Gusakova, D., Delaet, B., Ebels, U., Buda-Prejbeanu, L. D., Cyrille, M.-C., Dieny, B., Ocker, B., Langer, J., and Maas, W. (2010). Spin torque driven excitations in a synthetic antiferromagnet. *Applied Physics Letters*, 96(7):072511.

[Ikeda et al., 2008] Ikeda, S., Hayakawa, J., Ashizawa, Y., Lee, Y. M., Miura, K., Hasegawa, H., Tsunoda, M., Matsukura, F., and Ohno, H. (2008). Tunnel magnetoresistance of 604 at 300K by suppression of Ta diffusion in CoFeB/MgO/CoFeB pseudo-spin-valves annealed at high temperature. *Applied Physics Letters*, 93(8):082508.

[J. Storn,] J. Storn, H. S. *Magnetism From Fundamentals to Nanoscale Dynamics*.

[Julliere, 1975] Julliere, M. (1975). Tunneling between ferromagnetic films. 54(3):225–226.

[Kaka et al., 2005] Kaka, S., Pufall, M. R., Rippard, W. H., Silva, T. J., Russek, S. E., and Katine, J. a. (2005). Mutual phase-locking of microwave spin torque nano-oscillators. *Nature*, 437(7057):389–92.

[Khvalkovskiy et al., 2009] Khvalkovskiy, A., Grollier, J., Dussaux, A., Zvezdin, K., and Cros, V. (2009). Vortex oscillations induced by spin-polarized current in a magnetic nanopillar: Analytical versus micromagnetic calculations. *Physical Review B*, 80(14):140401.

[Kim et al., 2008] Kim, J.-V., Tiberkevich, V., and Slavin, A. (2008). Generation Linewidth of an Auto-Oscillator with a Nonlinear Frequency Shift: Spin-Torque Nano-Oscillator. *Physical Review Letters*, 100(1):017207.

[Kim et al., 2002] Kim, M. J., Kim, H. J., Kim, K. Y., Jang, S. H., and Kang, T. (2002). The annealing effect on GMR properties of PtMn-based spin valve. 239:195–197.

[Kiselev et al., 2003] Kiselev, S. I., Sankey, J. C., Krivorotov, I. N., Emley, N. C., Schoelkopf, R. J., Buhrman, R. a., and Ralph, D. C. (2003). Microwave oscillations of a nanomagnet driven by a spin-polarized current. *Nature*, 425(6956):380–3.

[Kodzuka et al., 2012] Kodzuka, M., Ohkubo, T., Hono, K., Ikeda, S., Gan, H. D., and Ohno, H. (2012). Effects of boron composition on tunneling magnetoresistance ratio and microstructure of CoFeB/MgO/CoFeB pseudo-spin-valve magnetic tunnel junctions. *Journal of Applied Physics*, 111(4):043913.

[Komagaki et al., 2009] Komagaki, K., Hattori, M., Noma, K., Kanai, H., Kobayashi, K., Uehara, Y., Tsunoda, M., and Takahashi, M. (2009). Influence of Diffused Boron Into MgO Barrier on Pinhole Creation in CoFeB/MgO/CoFeB Magnetic Tunnel Junctions. *IEEE Transactions on Magnetics*, 45(10):3453–3456.

[Kudo et al., 2012] Kudo, K., Nagasawa, T., Suto, H., Yang, T., Mizushima, K., and Sato, R. (2012). Influence of dynamical dipolar coupling on spin-torque-induced excitations in a magnetic tunnel junction nanopillar. *Journal of Applied Physics*, 111(7):07C906.

[Lee et al., 2012] Lee, S. C., Pi, U. H., Kim, K., Kim, K. S., Shin, J., and Chung, U.-i. (2012). Current Driven Magnetic Damping in Dipolar-Coupled Spin System. pages 1–7.

[Mancoff et al., 2005] Mancoff, F. B., Rizzo, N. D., Engel, B. N., and Tehrani, S. (2005). Phase-locking in double-point-contact spin-transfer devices. *Nature*, 437(7057):393–5.

[McMichael and Stiles, 2005] McMichael, R. D. and Stiles, M. D. (2005). Magnetic normal modes of nanoelements. *Journal of Applied Physics*, 97(10):10J901.

[Mistral et al., 2008] Mistral, Q., van Kampen, M., Hrkac, G., Kim, J.-V., Devolder, T., Crozat, P., Chappert, C., Lagae, L., and Schrefl, T. (2008). Current-Driven Vortex Oscillations in Metallic Nanocontacts. *Physical Review Letters*, 100(25):257201.

[Moodera J. S., 1995] Moodera J. S. (1995). Large magnetoresistance at room temperature in ferromagnetic thin film tunnel junction. *Physical review letters*, 74(16).

[Negulescu et al., 2011] Negulescu, B., Lacour, D., Hehn, M., Gerken, A., Paul, J., Negulescu, B., Lacour, D., Hehn, M., Gerken, A., Paul, J., and Duret, C. (2011). On the control of spin flop in synthetic antiferromagnetic films On the control of spin flop in synthetic antiferromagnetic films. 103911.

[P. M. Tedrow, 1971] P. M. Tedrow (1971). Spin-Dependent Tunneling into Ferromagnetic Nickel. *Physical review letters*, 26(4).

[Parkin et al., 1990] Parkin, S., More, N., and Roche, K. (1990). Oscillations in exchange coupling and magnetoresistance in metallic superlattice structures: Co/Ru, Co/Cr, and Fe/Cr. *Physical review letters*, 64(19):2304–2307.

[Petit, 2008] Petit, S. (2008). *Influence du couple de transfert de spin sur les fluctuations magnétiques thermiquement activées dans les jonctions tunnel magnétiques.* PhD thesis.

[Pribiag et al., 2007a] Pribiag, V. S., Krivorotov, I. N., Fuchs, G. D., Braganca, P. M., Ozatay, O., Sankey, J. C., Ralph, D. C., and Buhrman, R. a. (2007a). Magnetic vortex oscillator driven by d.c. spin-polarized current. *Nature Physics*, 3(7):498–503.

[Pribiag et al., 2007b] Pribiag, V. S., Krivorotov, I. N., Fuchs, G. D., Braganca, P. M., Ozatay, O., Sankey, J. C., Ralph, D. C., and Buhrman, R. a. (2007b). Magnetic vortex oscillator driven by d.c. spin-polarized current. *Nature Physics*, 3(7):498–503.

[Quinsat, 2012] Quinsat, M. (2012). *Thesis: Etude d'un auto-oscillateur non-isochrone : Application à la dynamique non-lineaire de l'aimantation induite par transfert de spin.* PhD thesis.

[Quinsat et al., 2010] Quinsat, M., Gusakova, D., Sierra, J. F., Michel, J. P., Houssameddine, D., Delaet, B., Cyrille, M.-C., Ebels, U., Dieny, B., Buda-Prejbeanu, L. D., Katine, J. a., Mauri, D., Zeltser, a., Prigent, M., Nallatamby, J.-C., and Sommet, R. (2010). Amplitude and phase noise of magnetic tunnel junction oscillators. *Applied Physics Letters*, 97(18):182507.

[Ruotolo et al., 2009] Ruotolo, a., Cros, V., Georges, B., Dussaux, a., Grollier, J., Deranlot, C., Guillemet, R., Bouzehouane, K., Fusil, S., and Fert, a. (2009). Phase-locking of magnetic vortices mediated by antivortices. *Nature nanotechnology*, 4(8):528–32.

[Schneider et al., 2007] Schneider, M. L., Pufall, M. R., Rippard, W. H., Russek, S. E., and Katine, J. a. (2007). Thermal effects on the critical current of spin torque switching in spin valve nanopillars. *Applied Physics Letters*, 90(9):092504.

[Schreiber et al., 2011] Schreiber, D. K., Choi, Y.-S., Liu, Y., Chiaramonti, A. N., Seidman, D. N., and Petford-Long, a. K. (2011). Enhanced magnetoresistance in naturally oxidized MgO-based magnetic tunnel junctions with ferromagnetic CoFe/CoFeB bilayers. *Applied Physics Letters*, 98(23):232506.

[Slavin and Tiberkevich, 2005] Slavin, A. and Tiberkevich, V. (2005). Spin Wave Mode Excited by Spin-Polarized Current in a Magnetic Nanocontact is a Standing Self-Localized Wave Bullet. *Physical Review Letters*, 95(23):237201.

[Slavin and Tiberkevich, 2009] Slavin, A. and Tiberkevich, V. (2009). Advances in Magnetics Nonlinear Auto-Oscillator Theory of Microwave Generation by Spin-Polarized Current. 45(4):1875–1918.

[Slonczewski, 1996] Slonczewski, J. (1996). Current-driven excitation of magnetic multilayers. *Journal of Magnetism and Magnetic Materials*, 159(1-2):L1–L7.

[Stancil, 2009] Stancil (2009). *Spin waves theory and applications*. Springer, Stancil2009, 2009 edition.

[Takenaga et al., 2009] Takenaga, T., Takada, H., Tomohisa, S., Furukawa, T., Kuroiwa, T., Takenaga, T., Takada, H., Tomohisa, S., and Furukawa, T. (2009). Evaluation of distribution of exchange coupling in CoFe / Ru / CoFe synthetic antiferromagnetic structure after annealing Evaluation of distribution of exchange coupling in CoFe / Ru / CoFe synthetic antiferromagnetic structure after annealing. 310.

[Takiguchi et al., 2000] Takiguchi, M., Ishii, S., Makino, E., and Okabe, A. (2000). Thermal degradation of spin valve multilayers caused by Mn migration. *Journal of Applied Physics*, 87(5):2469.

[T.Kasuya, 1956] T.Kasuya (1956). A Theory of Metallic Ferro and Antiferromagnetism on Zener's Model. 16(1):45–57.

[Tsoi et al., 1998] Tsoi, M., Jansen, A., Bass, J., Chiang, W.-C., Seck, M., Tsoi, V., and Wyder, P. (1998). Excitation of a Magnetic Multilayer by an Electric Current. *Physical Review Letters*, 80(19):4281–4284.

[Xiao et al., 2005] Xiao, J., Zangwill, a., and Stiles, M. (2005). Macrospin models of spin transfer dynamics. *Physical Review B*, 72(1):014446.

[Yosida, 1957] Yosida, K. (1957). Magnetic Properties of Cu-Mn Alloys. *Physical Review*, 106(5):893–898.

[Yuasa and Djayaprawira, 2007] Yuasa, S. and Djayaprawira, D. D. (2007). Giant tunnel magnetoresistance in magnetic tunnel junctions with a crystalline MgO(0,0,1) barrier. *Journal of Physics D: Applied Physics*, 40(21):R337–R354.

[Zhou et al., 2007] Zhou, Y., Persson, J., and Akerman, J. (2007). Intrinsic phase shift between a spin torque oscillator and an alternating current. *Journal of Applied Physics*, 101(9):09A510.

[Zhou et al., 2013] Zhou, Y., Xiao, J., Bauer, G. E. W., and Zhang, F. C. (2013). Field-free synthetic-ferromagnet spin torque oscillator. *Physical Review B*, 87(2):020409.